STRONG MICROWAVES IN PLASMAS

2006

Volume 1

Institute of Applied Physics
Nizhny Novgorod

RUSSIAN ACADEMY OF SCIENCES
INSTITUTE OF APPLIED PHYSICS

STRONG MICROWAVES IN PLASMAS

PROCEEDINGS
OF THE INTERNATIONAL WORKSHOP

Nizhny Novgorod,
25 July – 1 August 2005

Edited by

A.G. Litvak

In two volumes

Volume 1

Nizhny Novgorod – 2006

ISBN 5-8048-0037-X

Editor's Preface

The 6th International Workshop «Strong Microwaves in Plasmas», July 25 – August 1, 2005 was held on board the river ship «Georgii Zhukov» cruising from Nizhny Novgorod to Saint-Petersburg. The Workshop traditionally had an essentially interdisciplinary character bringing together developers of a new type microwave sources and scientists using such sources in basic and applied researches.

The Workshop's title does not define completely the topics under consideration, it originated from the first conferences of this series, when the major attention was focused on the applications of high-power microwaves in plasma research, in particular at the experiments on RF plasma heating and current drive in nuclear fusion setups with magnetic confinement. More recently, the Program Committee of the Workshop has expanded essentially the range of the problems of microwaves applications under consideration. Their list includes problems of the development of new types of radars and remote sensors of environmental and atmospheric objects, microwave technique for the next generation of charged particles accelerators (linear collider, heavy-ion accelerators etc.), microwave technologies of material processing (nanoceramic sintering, annealing of semiconductors, deposition of diamond films, production of gradient coating, carbon nanotube growth etc.).

The 6th Workshop hosted 134 scientists from 16 countries. Overall, 140 papers were presented by 127 speakers at scientific sessions including 20 invited plenary lectures, 23 invited topical presentations, 83 con-

tributed oral talks and 14 posters. Three topical sections were working at the Workshop:

- Development of high-power microwave sources.
- Current drive and microwave plasma heating in fusion installations.
- Gas discharges and other applications of high-power microwaves.

This two-volume edition is the collection of a major part of invited lectures and original contributions at the Sixth International Workshop «Strong microwaves in plasmas». As usual, the text of a few papers have not been submitted by their authors mainly since they have been already published as original papers. Nevertheless, the material of this book gives a sufficiently complete information about the state of art and new trends in the development of high-power microwave sources and their applications.

Alexander Litvak

DEVELOPMENT OF HIGH-POWER MICROWAVE SOURCES

FORTY YEARS OF RESEARCH ON CHARGED PARTICLE–WAVE INTERACTION

Uwe Schumacher

Institute of Plasma Research, University of Stuttgart,
Pfaffenwaldring 31, D-70569 Stuttgart, Germany

High power electromagnetic waves are successfully applied for generating, heating, controlling and diagnosing of fully ionized high temperature plasmas suitable for a future fusion reactor. Moreover, microwave generated plasmas are a new tool for an increasingly high number of successful low temperature plasma applications, and strong charged particle–wave interaction (e. g. in the interaction of intense femto-second lasers with matter) leads to fascinating new results for the state of matter and for new particle acceleration mechanisms. Most of these developments during the last four decades rely on brilliant new ideas – mostly from Russian scientists – like the understanding of collisionless shock waves, the use of intense relativistic electron beams or of plasmas for collective-effect acceleration, the invention and successful operation of the gyrotron and the understanding of wave damping. Some of these investigations and their results, that are important conditions for the present-day developments, are presented.

Introduction

A plasma is an ensemble of charged (electrons and ions) and neutral (atoms or molecules) particles that is characterized by collective behavior [1–4]. Processes, where charged particle–wave interaction is involved, hence belong to the most important and most common processes in plasmas. Strong waves in plasmas allow to accelerate charged particles to high energies and – vice-versa – high energy charged particle beams are able to generate high power waves. Strong waves in plasmas and charged particle–wave interaction on the one side are responsible for the experimentally observed extremely wide range of charged particle energies ranging from about 1 eV up to more than 10^{20} eV. On the other side intense charged particle beams of specific properties of their phase space density are an important condition for the generation of strong electromagnetic waves.

However, normally these processes are closely related and interwoven. Very often they may drive collective instabilities. Therefore, it is extremely important to understand in detail the mechanisms of charged particle–wave interaction and the limits of instability onset as well. The aims of research on charged particle–wave interaction hence are concentrated on the generation of high energy particle distributions, e. g. in plasma heating, current drive, plasma profile shaping, microwave plasma diagnostics, instability suppression [5–8], and in several different devices of charged particle accelerators [9], by interaction with electrostatic, electromagnetic, magnetic field, and shock waves. This research certainly also includes the aim to understand the experimentally observed extremely high charged cosmic particle energies in excess of 10^{20} eV.

In connection to this it is very important to deeply understand and optimize wave damping in plasmas and in intense charged particle beams as well [10]. On the other hand since many decades charged particle-wave interaction plays an important role in the generation of high power waves by intense charged particle beams, e. g. in slow wave and fast wave structures, in klystrons, travelling wave tubes, magnetrons, magnicons, gyrotrons, orbitrons, electron cyclotron masers (ECM), cyclotron autoresonance masers (CARM), free electron lasers and many others [11–13].

Strong shock wave–ion interaction for plasma heating

In the 1960ies – besides investigations on toroidal plasma confinement – the fusion oriented plasma research mainly concentrated on the generation of fully ionized high temperature plasmas by the pinch principle, which applies strong shock wave – charged particle interaction. In one of the experimental devices, the so-called *Theta-* or θ-*pinch* [1, 2, 14], a large axial magnetic field **B** is suddenly applied to the surface of a cylindrical plasma by high densities of currents **j** flowing in azimuthal (θ) direction. For the rapidly rising magnetic field Ohm's law, assuming large conductivity, becomes

$$d/dt\,[\,\mathbf{B} - (c^2/\omega_p^2)\,d^2\,\mathbf{B}/dx^2\,] = 0, \qquad (1)$$

where $\lambda_s = c/\omega_p$ is called the *collisionless skin depth*, and ω_p is the electron plasma frequency, $\omega_p = (n_e e^2/\varepsilon_0 m_e)^{1/2}$ [1–4, 14], with the electron density n_e and electron mass m_e. Due to the high density and high electrical conductivity this skin depth is much less than the radius of the plasma cylinder, such that strong shock waves are developed and radially imploded. For lower particle densities and very fast compression collisionless shock waves play the important role, the theory of which is carefully worked out by Roald Z. Sagdeev and Albert A. Galeev [15]. The magnetic field pressure $\mathbf{B}^2/2\mu_0$ is always much larger than the plasma pressure gradient ∇p, such that the implosion transfers the stored electric energy into kinetic energy. The plasma thermalizes partly during compression or by the shock wave reflection on the axis, but remains anisotropic, which is shown in Fig. 1 as results of spectroscopic investigations on hydrogen ions in a θ-pinch with a temporal magnetic field rise of as much as $d\mathbf{B}/dt > 10^7$ T/s [16].

Another very effective fast shock wave ion heating system is the plasma focus, proposed and developed by Nicolai V. Filippov [17] at the Kurchatov Institute at Moscow and by Joseph W. Mather [18] in the US.

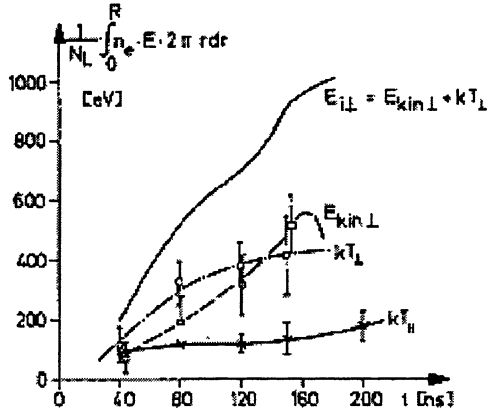

Fig. 1. The development of anisotropic hydrogen ion energy distributions from spectroscopy of the first compression phase of a fast θ-pinch versus time [16]: kinetic energy $E_{\text{kin}\perp}$ in radial direction (perpendicular to the axial magnetic field direction), the thermal ion energies $kT_\perp$ perpendicular and $kT_\parallel$ parallel to the magnetic field as well as the sum $E_{i\perp}$.

Charged particle – wave interaction for collective ion acceleration

Strong waves are extremely attractive for charged particle acceleration. While conventional particle accelerators are characterized by vanishing space charges ρ as well as vanishing current densities **j** at the location of the charged particle to be accelerated, i. e.

$$\text{div}\,\mathbf{E} = 0,\ \text{rot}\,\mathbf{B} = \varepsilon_0\mu_0\,\partial\mathbf{E}/\partial t = 0, \tag{2}$$

Vladimir I. Veksler [19] and G. I. Budker [20] nearly half a century ago proposed collective-effect accelerators, e. g. by using very intense relativistic electron beams of high charge density $\rho = -\,en_e$ and high current density **j**, hence resulting in

$$\text{div}\,\mathbf{E} = \rho/\varepsilon_0\ \text{rot}\,\mathbf{B} = \varepsilon_0\mu_0\,\partial\mathbf{E}/\partial t = \mu_0\,\mathbf{j}. \tag{3}$$

These collective fields **E** and **B** strongly depend on the charged particle densities ρ, and they have the fascinating property to be maximum at the location of the particles to be accelerated. Moreover, synchronization of the accelerating fields with the charged particles to be accelerated is automatically given [19].

There exist several different attractive systems of collective field accelerators, a few of them should be mentioned: The ionization front accelerator scheme proposed by Craig L. Olson [21] applies the strong space charge field generated and controlled by intense light pulses through light pipes of different lengths leading to ionization of the low pressure working gas and hence to an ion bunch with controlled accelerating motion in an intense relativistic electron beam.

The wake field charged particle acceleration scheme applies the wake fields, that an intense relativistic particle beam, passing near to a conducting surface, leaves behind, generally regarded as an adverse effect. Since the wake will not be large, if the particles to be accelerated are located in the same region as the wake-producing beam, a "wake-field-transformer" was proposed and tested by Gustav Voss and Thomas Weiland in 1982 at DESY in Hamburg [22]. This concept uses a ring-shaped low-energy electron beam passing through a cylindrical cavity conducting structure, which leaves behind a wake, which is then transmitted radially towards the axis, where it becomes a strong accelerating field of gradients exceeding 100 MeV/m. In the plasma-wake-field accelerator [23] one would excite a plasma with an intense bunch train of high-energy electrons, but the condition of wake-field transformation has not been achieved yet. Presently there is much activity in the exploration and development of a dielectric wake field resonator accelerator [24, 25], which applies wake field excitation in a dielectric cavity by a sequence of short electron bunches.

In the electron ring accelerator device (ERA) a cluster of relativistic electrons in form of a ring generates the collective fields. According to the proposal of Veksler, Sarantsev et al. [19, 26] the ring is formed by injecting an intense relativistic electron beam into a magnetic field (Fig. 2). Budker's [20] concept of a relativistic ring beam, partly neutralized by the ions to be accelerated (hence self-stabilized, see Eq. 5) easily solves the problem of the electrostatic repulsion of the charges. The rings are radially (and axially) compressed in the rising magnetic field, thereby increasing the electron kinetic energy, by which the difference between the electrostatic repulsion and the magnetic attraction decreases.

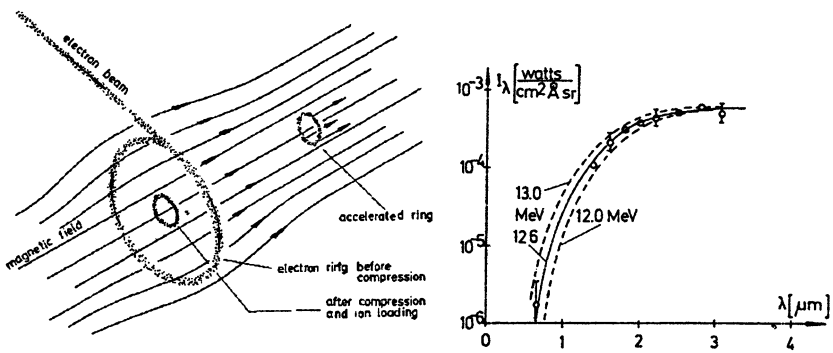

Fig. 2. Scheme of an electron ring accelerator (ERA) using electron ring compression in a slightly focussing fast rising magnetic field and axial acceleration in the slightly expanding magnetic field (left part) [27]. Measured synchrotron radiation spectrum of the compressed ring of electrons having attained 12.6 MeV (right part) [27].

Complete compensation of this difference is attained by the ions, that are particles created by electron collisional ionization of the residual gas just in the potential well of the electron ring. The ions hence have two functions: They provide the missing focussing and they are the collectively accelerated particles.

The axial acceleration can be carefully controlled. The acceleration limit is given by the "holding power", the maximum electric field strength E_{max}, which holds the ions in the accelerated ring [27]:

$$E_{max} = -I_e / (2\pi \cdot \varepsilon_0 \cdot \beta \cdot c \cdot a) = -e \cdot n_e \cdot a / (2 \cdot \varepsilon_0), \tag{4}$$

where I_e is the electron current, n_e the electron particle density, β is the ratio of the electron azimuthal velocity related to the speed of light c, and a is the electron ring minor radius. In order to avoid beam destruction and "kink" instability the electron current I_e has to be smaller than the Alfvén–Lawson current I_{AL} [27, 28], and the Budker parameter ν_{Budker} [20, 27] should not exceed the relativistic factor $\gamma = (1 - \beta^2)^{1/2}$:

$$I_e < I_{AL} = ec\beta\gamma / r_0 = \beta\gamma \cdot 17 \text{ kA or } \nu_{Budker} = r_0 \int_0^\infty n_e(r) 2\pi r dr < \gamma, \tag{5}$$

where $r_0 = e^2 / (4\pi\varepsilon_0 m_e c^2) = 2.82 \cdot 10^{-15}$ m is the classical electron radius.

For a slender electron ring the equilibrium condition is given by the Budker limits [20]

$$1/\gamma^2 < Zn_i / n_e < 1, \tag{6}$$

where Z and n_i are charge and particle density of the ions, respectively, and γ is the relativistic mass factor.

The electron rings were formed from an intense electron beam generated by a 2 MeV Marx generator (with a large number of stages) and injected perpendicular into a magnetic field [19, 26, 27]. Due to flux conservation the electron ring is compressed and the electron particle energy and density are increased as well (see Fig. 2).

The electron ring properties during compression, axial roll-out and acceleration were carefully diagnosed using magnetic probe measurements and optical observations like the synchrotron radiation (see Fig. 2 right and Fig. 4 left). As a specific very attractive diagnostic application of charged particle – wave interaction the laser scattering diagnostics at relativistic electrons was explored [27]. Laser photons of wavelength λ_0 in the visible spectral region are scattered at electrons of relativistic factor γ into the X-ray region at a wavelength of $\lambda = \lambda_0 / 4\gamma^2$. The spectrally resolved scattering measurements offer a diagnostic potential for precise measurements of the electron energy and the phase space distributions [27]. However, they could not be detected yet.

The successful operation of the ERA principle was demonstrated by collective acceleration of light elements like hydrogen and helium with a holding power of 3 to 4 MV/m [27, 29].

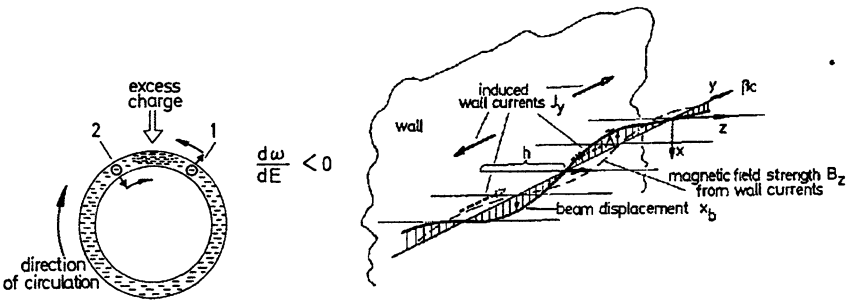

Fig. 3. The scheme of the negative mass instability (left), where due to the negative derivative of the electron angular velocity ω with respect to electron energy *E* the repulsive forces of an excess charge on the electrons lead to further bunching and widening of the ring, and that of the transverse resistive wall instability (right) generated and excited by currents induced in near-by conducting walls [27].

The main aim of the experiments, however, was the study of the electron ring properties as influenced by collective instabilities: in the longitudinal direction by electromagnetic bunching forces like in the negative mass instability, in the transverse direction by the forces of eddy currents like in the transverse resistive wall instability, or by the attractive forces of ions like in the transverse ion-electron and in other instabilities. The results obtained three decades ago are of major importance still now, because the complicated behavior of collective instabilities governs the investigations and developments of high power RF wave generators and of high energy new particle accelerators based on charged particle – wave interaction as well.

The negative mass instability or longitudinal collective instability (see Fig. 3 left) is driven by space charge forces acting upon the azimuthal motion of the circulating electrons. For relativistic electrons with speed near to c the mechanism is easy to explain: Electrons (particle *1* in Fig. 3 left) in front of an arbitrary extra charge gain energy due to repulsion and hence go to a higher radius, thus approaching the extra charge, as does particle *2*, when being repulsed, loosing energy and approaching the extra charge on slightly reduced radius, too. Hence bunching occurs, followed by electron ring widening and holding power reduction.

The beam displacement and the induced magnetic field strengths as driving elements of the resistive wall instability are sketched in Fig. 3 (right) for the model case of a straightened electron beam between resistive walls. The forces driving the resistive wall instability are produced by the magnetic field of currents, which are induced in the imperfectly-conducting layers by the transverse electron ring displacement. These Lorentz forces are in quadrature with the radial (or axial) displacement. The particle trajectories at coherent radial motion are sketched in Fig. 4 (right) [27].

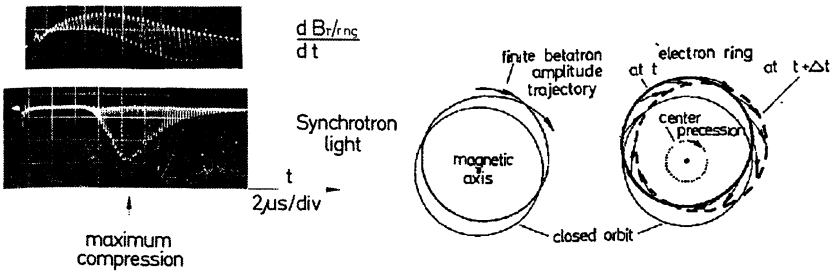

Fig. 4. Magnetic field (top left) and synchrotron radiation measurements (bottom left) of a strong transverse ion-electron instability of an electron ring during magnetic compression and corresponding particle trajectories at coherent radial motion (right) [27].

Without resistive walls the same electron ring behavior may occur, when replacing the Lorentz forces by electrostatic forces from a small number of ions in the electron ring. The experimental results – in close agreement with the theoretical analysis – give impressive wide collective oscillations of the electron ring in radial direction, as observed by magnetic probes and by synchrotron radiation as well (see Fig. 4 left) [27].

There are several other collective instabilities of importance like the two-stream instabilities, the diocotron (slipping stream) instability [3] of a hollow electron beam and others.

Strong laser wave – charged particle and material interaction

Very recent results of collective particle acceleration were reported from experiments with Petawatt lasers in plasmas by interaction of an underdense plasma with the Vulcan Petawatt Nd:glass laser system at intensities in excess of $3 \cdot 10^{20}$ W·cm^{-2} [30]. Electron energies of more than 300 MeV are measured. They are obtained by stochastic acceleration, while self-modulated wakefield mechanisms are excluded.

The beat-wave accelerator scheme, invented by John Dawson and Toshi Tajima in 1979 [31], converts the transverse electromagnetic field of a wave, e. g. by a laser, which is ineffective for charged particle acceleration, into a longitudinal wave in a plasma by injecting two intense laser beams of angular frequencies ω_1 and ω_2, whose difference is just the fundamental plasma frequency ω_p (see Eq. 1). In this resonant condition of the beat wave the plasma becomes strongly bunched, and a "ponderomotive well" develops, which acts like stimulated Raman forward scattering. This process is very effective, if the bunching would be strong: For complete plasma bunching the maximum longitudinal electric field strength $E_\parallel$ according to Poisson's equation would be given by

$$eE_\parallel = m_e c\omega_p = 4\pi n_e r_0 \lambda_s m_e c^2, \tag{7}$$

where ω_p, λ_s, e, $m_e = 0.511$ MeV/c^2 and $r_0 = e^2/(4\pi\varepsilon_0 m_e c^2) = 2.82 \cdot 10^{-15}$ m (see Eq. 5) are, respectively, the plasma frequency (see Eq. 1), the collisionless skin depth, the charge, rest mass and the classical radius of the electron. For a plasma electron density of $n_e = 10^{22}$ m^{-3} the longitudinal electric field strength hence would be as large as 9.3 GV/m. These values have not yet been obtained in beat-wave acceleration schemes.

The dramatic increase of laser intensities (power densities) in excess of 10^{20} W/cm^2 in the last few years, however, which is mainly due to the chirped pulse amplification (CPA), explains the increasing interest in intense laser-plasma interactions, that produce relativistic electrons, X-rays and very fast ions [32]. They support very high electric field strengths much greater than those in conventional radio frequency accelerators, which are limited to less than about 100 MV/m. For laser intensities of 10^{20} W/cm^2 the electric field strength in the plasma will be 10^{13} V/m, the magnetic fields may reach values of 10^5 T, and the pressure might be as high as 10^{16} Pa. The related collective phenomena like self-focussing, "bubble" acceleration and other nonlinear processes lead to extremely high particle energies [32].

High intensity ultrashort pulse laser wave – material interaction is able to transform matter into an extremely hot and dense plasma with temperatures in the MeV and pressures in the 100 TPa (Gigabar) range. These relativistic laser plasmas are unique sources of electrons, ions and photons, also emitted in pulses of ultrashort duration [33]. The laser generated bremsstrahlung may result in photo fission of heavy nuclei as the two actinides ^{232}Th and ^{238}U [34]. Hence the high intensity ultrashort pulse laser wave – material interaction may open new horizons in laser induced nuclear reactions [34] as fission of, e. g. ^{232}Th and ^{238}U, as transmutation of long living fission products or fusion of light nuclei as, e.g. deuterium.

Charged particle – magnetic shock wave interaction generates the cosmic ray energy spectrum

The fundamental scientific problems related to the origin, the acceleration mechanism and the reason for the observed energy spectrum of cosmic rays belong to the most important and difficult questions of astrophysics. The energy density of the cosmic rays is comparable with that of the visible stellar radiation or with that of the microwave background radiation or with that of the interstellar magnetic fields. The cosmic ray energies E are observed with a flux dependence proportional to $E^{-2.7}$ up to values as high as 10^{20} eV (see Fig. 5) [35, 36]. The mechanism of this charged particle acceleration – mainly protons, light and heavy nuclei - can be explained as charged particle – magnetic well interaction in supernovae remnants [35]: In supernovae shells the material of the star explodes into the interstellar space at velocities of about 0.1 c, generating shock waves and magnetic fields by collective effects. According to the acceleration

mechanism (of first order), that Enrico Fermi found in 1942 (constancy of the second adiabatic invariant J) the charged particles gain extreme energies ($> 10^{20}$ eV) by frequent stochastic reflections at the moving magnetic field structure. The motion of the magnetic fields is determined by different streaming velocities in front and behind the shock waves.

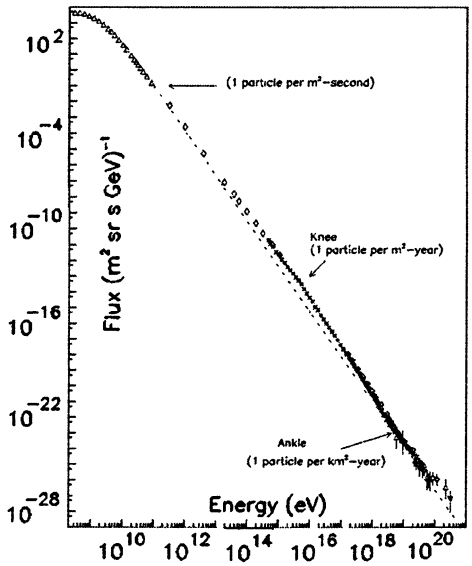

Fig. 5. Energy spectrum of the cosmic rays above 100 MeV: the detected particle flux drops by more than 30 decades over 13 decades of particle energy down to less than one particle per square kilometer and century (from [35]).

This mechanism is very similar to some processes in fusion plasma heating like TTMP (transit time magnetic pumping) or the gyro-relaxation effect [37]. It is interesting to note, that protons at an energy above $5 \cdot 10^{19}$ eV interact strongly with the microwave background radiation, another type of wave – charged particle interaction [35, 36].

Microwaves for plasma generation and plasma-technological applications

While all mechanisms of charged particle – wave interactions discussed so far are related to pulsed processes, most of the attractive microwave supported plasma applications need the availability of continuously emitting reliable microwave sources. The recent progress in continuous power microwave generators enables numerous new plasma-technological applications for industry and

research. There are several different devices of microwave plasma generators with specifically high potentials for industrial applications [38]. Here we will concentrate on the applications using surface wave sustained plasmas generated with the Duo-Plasmaline [39] at a frequency of 2.45 GHz. In principle this device is a coaxial waveguide at atmospheric pressure replacing the outer conductor by a dielectric tube, when entering the vacuum vessel, which is filled with the process gas at low pressure. Feeding microwave power into both sides generates a low pressure plasma surface wave sustained plasma and thus results in linearly homogeneous plasmas (Fig. 6). For large area plasma homogeneity the parallel arrangement of several of these lines is applied.

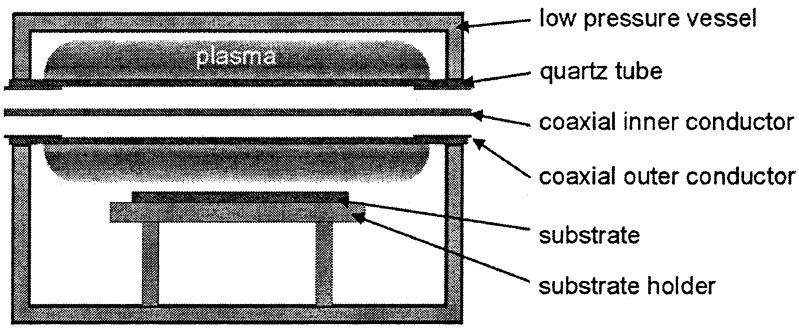

Fig. 6. Scheme of the large-area surface wave sustained microwave plasma generator Duo-Plasmaline [39, 41].

At the Institute of Plasma Research at Stuttgart University a variety of methods of microwave applications using Duo-Plasmaline devices for large area surface applications at a frequency of 2.45 GHz were developed. Most attractive applications – among many others – are plasma-polymerized thin film barrier coatings as isolation layer and as plasma technological encapsulation for flexible solar cells [40, 41] as well as for fuel cell membranes, the deposition of silicon nitride, silicon oxide and other layers [42] and the sterilization of food packaging materials by low pressure microwave plasmas in Duo-Plasmaline and related devices as further developments [43]. The results showed, that plasma-polymerized thin films can be produced with remarkably good quality with respect to low permeability for liquids and gases, with high surface resistance, and with excellent homogeneity and surface properties.

The generation and applications of dense low temperature plasmas by microwaves is of special interest in combination with a magnetic field B [4, 38, 39]. If the rotating electric field vector of the R-wave is in resonance with the electron cyclotron motion of the frequency [2, 4, 38]

$$\omega_{ce} = 2\pi f_{ce} = eB/m_e \text{ or } f_{ce}\,[\text{Hz}] = 2.8 \cdot 10^{10}\, B\,[\text{T}] \qquad (8)$$

and the electron collision frequency is not too high, the electrons can absorb maximum energy in the case of the electron cyclotron resonance (ECR, when $\omega = \omega_{ce}$). The power is absorbed due to electron collisions (Ohmic heating) or due to stochastic heating. A magnetic field strength of 87.5 mT corresponds to the frequency of 2.45 GHz.

Microwaves are not the only source for quasi-continuous energy input into a plasma. The availability of much shorter wavelength sources as those of high power continuous lasers offers to generate very dense plasmas and hence new applications even from wave – material interaction.

Laser wave – particle interaction for material welding and cutting

Since several years impressive progress has been made in the applications of intense laser wave interaction with materials. New methods for welding, cutting and drilling of metals and alloys using high power continuous lasers were developed, resulting in high quality machining, mainly for automobile industry. Since very dense plasmas are generated in the interaction zone of the laser wave, its radiation is optically thick [44]. The spectral lines show extreme line broadening and strong self absorption, which is another form of wave – particle interaction, such that the temperature and density distributions can easily be determined from emission and absorption spectroscopy. An example of the scheme of laser welding of a 2 mm thick metal sheet with a CO_2 laser (λ = = 10.6 μm wavelength) of 4 kW maximum power and of a MgI spectral line with strong self absorption is presented in Fig. 7.

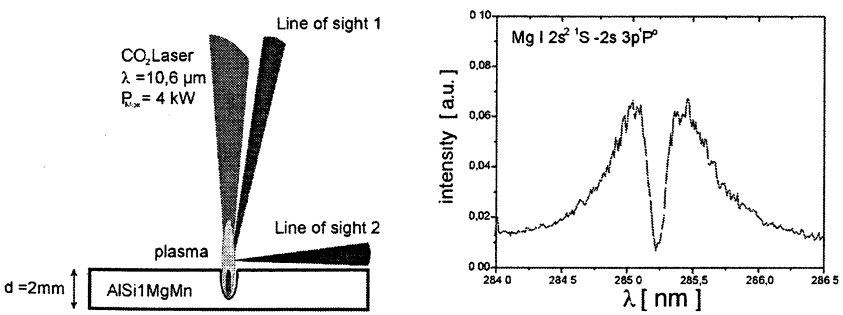

Fig. 7. Scheme of the laser welding with two optical sight lines (left) and a spectral line of neutral Magnesium showing strong line broadening and strong self absorption (right).

The measured spectra show strong Stark and Van der Waals broadening and self reversal of resonance lines. This phenomenon of self reversal results from strong temperature inhomogeneity and high optical depth of the laser generated plasma due to high electron (n_e = 10^{22} m^{-3}) and gas densities (n_{gas} = = 10^{26} m^{-3}).

Strong microwaves in fusion plasmas

After the invention of the gyrotron and after the successful pioneering work at IAP Nizhny Novgorod [46–50] strong microwaves were applied in fusion oriented magnetically confined plasmas. These waves demonstrated an impressively high potential for quite different tasks in fusion research [5–8, 45, 51]. Since these developments belong to the main results of this workshop, we will restrict ourselves to refer to these contributions [8, 51]:

In magnetically confined fusion plasmas the gyrotrons first of all allow electron cyclotron resonance heating (ECRH), when the resonance condition Eq. (8) or its first harmonic is fulfilled. At these high frequencies only electrons are heated directly, mainly by Landau damping [10]. Under reactor-like conditions the ions are heated by collisions with the electrons. In order to overcome the 1st harmonic O-mode cut-off density (when the plasma frequency, Eq. (7), reaches the microwave frequency), the gyrotron frequency was increased and mode conversion heating on the basis of the O-X-B process was successfully introduced [51].

Moreover, under specific conditions the microwave injection can generate electromotive forces, i. e. electron cyclotron current drive (ECCD) can be applied. As a consequence the current density distribution can be optimized and controlled, such that improved plasma confinement can be obtained. As a consequence ECCD can also be applied to suppress magnetohydrodynamic instabilities, e. g. neoclassical tearing modes (NTMs) [7]. Furthermore, wave – charged particle interaction using strong microwaves in plasmas allows scattering diagnostics for ion energy distributions [52], and certainly several other attractive applications will come up in the future.

Acknowledgments

The author would like to express his gratitude to Hartmut Zwicker[+], Rolf Wilhelm, Michael Kaufmann, Claus Andelfinger, Arnulf Schlüter, Rudolf Wienecke, Klaus Pinkau, Gerd Fussmann, Volker Erckmann, Hartmut Zohm, and many coworkers at IPP Garching, Germany, to Andrew Sessler, Andrew Faltens, Denis Keefe[+], and Jackson Laslett[+] at LBL Berkeley, California, to Manfred Thumm at FZK Karlsruhe, Roland Sauerbrey at Jena University, as well as to Walter Kasparek, Jochen Krüger, Peter Lindner, Andreas Schulz, Matthias Walker and coworkers at IPF Stuttgart, Germany.

References

1. *Artsimovich L.A.*, Nucl. Fusion **12**, 215-252 (1972); *Artsimovich L. A., Sagdeev R. Z.*, Plasmaphysik fuer Physiker. Stuttgart: B.G. Teubner, 1983 (Transl. from Russian edition published in Atomisdat, Moscow, 1976, by *H.-P. Zehrfeld*).

2. *Chen, Francis F.*, Introduction to Plasma Physics and Controlled Fusion, 2nd ed. New York: Plenum Press, 1985.
3. *Davidson, Ronald C.*, Physics of Non-neutral Plasmas. Redwood City: Addison-Wesley Publishing Company, 1990.
4. *Dinklage A. et al.* (eds.), Plasma Physics: Confinement, Transport and Collective Effects, Springer Lecture Notes in Physics LNP 670, Berlin, Heidelberg, New York: Springer-Verlag, 2005.
5. *Litvak A.G.*, High Frequency Plasma Heating. New York: American Institute of Physics, 1992.
6. *Stix T. H.*, The Theory of Plasma Waves. New York: Mc Graw-Hill, 1992.
7. *Zohm H.*, Nucl. Fusion **39**, 577-580 (1999).
8. These proceedings: *Lohr J et al.*, vol. 2, p. 434-447; *Schüller F.C. et al.*, vol. 2, p. 389-397; *Thumm M. et al.*, vol.1, p. 33-45.
9. *Kolomenskii A.A.*, Particle Accelerators, Moscow 1983.
10. *Landau L.D.*, J. Phys. USSR **10**, 25 (1946).
11. *Granatstein V.L., Alexeff I.* (eds.), High-Power Microwave Sources. Boston, London: Artech House, 1987.
12. *Bhartia P., Bahl I.J.*, Millimeter Wave Engineering and Applications. New York, Chichester: John Wiley and Sons, 1984.
13. *Hirshfield J.L., Granatstein V.L.*, IEEE Trans. **MTT-25**, 522-527 (1977).
14. *Krall N., Alvin W. Trivelpiece*, Principles of Plasma Physics. New York: McGraw-Hill Book Company, 1973.
15. *Sagdeev R.Z., Galeev A.A.*, Nonlinear Plasma Theory, Eds. T.M. O'Neil and D.L. Book. Benjamin, New York, London, 1969; *Sagdeev R.Z.*, Reviews of Plasma Physics **4**, 23. New York: Consultants Bureau, 1966.
16. *Schumacher U.*, Plasma Phys. Contr. Fus. Res. **1**, 93-101 (1969); Z. Phys. **227**, 162-178 (1969).
17. *Filippov N.V., Filippova T.I., Vinogradov V.P.*, Nucl. Fus. Suppl. **2**, 577 (1962).
18. *Mather J.W.*, Phys. Fluids Suppl. **7**, 28-34 (1964).
19. *Veksler V.I.*, At. Energ. **2**, 427 (1957).
20. *Budker G.I.*, At. Energ. **1**, 9 (1956); Proc. CERN Symp on High Energy Accelerators and Pion Physics (Geneva) **1**, 68 (1956).
21. *Olson C.L.*, Springer Tracts in Modern Physics **84**. Berlin, Heidelberg, New York: Springer-Verlag, 1979.
22. *Voss G., Weiland T.*, in "The Challenge of Ultra-High Energies", ECFA 83/68, J. Mulvey, ed. Rutherford Laboratory, Didcot, UK, 1982. P. 287.
23. *Chen P., Dawson J.M., Huff R.W., Katsouleas T.*, Phys. Rev. Lett. **54**, 693 (1985).
24. These proceedings: *Marshall T.C. et al.*, vol.1, p. 277-282; p. 294-302.
25. *Marshall T.C., Fang J.M., Hirshfield J.L., Park S.J.*, Proc. 9th Workshop Advanced Accelerator Concept (P. Colestock, S. Kelley eds.), 316 (2001); *Balakirev V.A., Onishchenko I.N., Sidorenko D.Yu., Sotnikov G.V.*, Techn. Phys. Lett. **29**, 589 (2003).
26. *Veksler V.I., Sarantsev V.P. et al.*, At. Energiya **24**, 317 (1968).
27. *Schumacher U.*, Springer Tracts in Modern Physics **84**. Berlin, Heidelberg, New York: Springer-Verlag, 1979.
28. *Alfvén H.*, Phys. Rev. **55**, 425 (1939).
29. *Schumacher U., Andelfinger C., Ulrich M.*, Phys. Lett. **51A**, 367 (1975); IEEE Trans. Nucl. Sci. **NS-22**, no. 3, 989 (1975).
30. *Mangles S.P.D. et al.*, Phys. Rev. Lett. **94**, 245001, June 24 (2005).
31. *Tajima T., Dawson J.M.*, Phys. Rev. Lett. **43**, 267 (1979).
32. *Pukhov A.*, Rep. Prog. Phys. **66**, 47-101 (2003); *Pukhov A., Sheng Z.-M., Meyer-ter-Vehn J.*, Phys. Plasmas **6**, 2847 (1999).
33. *Schwoerer H., Gibbon P., Düsterer S., Behrens R., Ziener C., Reich C., Sauerbrey R.*, Phys. Rev. Lett. **86**, 2317 (2001).
34. *Schwoerer H., Ewald F., Sauerbrey R., Galy J., Magill J., Rondinella V., Schenkel R., Butz T.*, Europhys. Lett. **61**, 47 (2003).

35. *Cronin J.*, Rev. Mod. Phys. **71**, 165 (1999); Hans Blümer, Phys. Bl. **56**, 39-45 (2000); www.chicos.caltech.edu/collaboration/education/spectrum html.
36. *Biermann P.L.*, New Astr. Rev. **48**, 41-46 (2004).
37. *Schlüter A.* Z. Naturforsch. **12a**, 822-825 (1957).
38. *Lebedev Y.A.*, Proc. Vth Int. Workshop on Strong Microwaves in Plasmas (Ed. by A.G. Litvak), Vol. 2, 605-617. Nizhny Novgorod, 2003.
39. *Räuchle E.*, J. Phys. **8**, 99 (1998); *Petasch W., Räuchle E., Mügge H., Mügge K.*, Surf. and Coat. Technol. **93**, 112-118 (1997).
40. *Herrmann D., Kessler F., Lammer M., Powalla M., Schulz A., Schneider J., Schumacher U.*, Contr. 19th Europ. Photovoltaik Solar Energy Conf. Paris, 2004.
41. *Schulz A., Baumgärtner K.-M., Feichtinger J., Walker M., Schumacher U., Eike A., Herz K., Kessler F.*, Surface and Coating Technology **142-144**, 771-775 (2001).
42. *Krüger J., Kubach T., Feichtinger J., Hirsch K., Lindner P., Quell S., Schulz A., Stirn R., Walker M., Schumacher U.*, Surf. & Coat. Techn. **174-175**, 933-937 (2003).
43. *Feichtinger J., Schulz A., Walker M., Schumacher U.*, Surf. & Coat. Technol. **174-175**, 564-569 (2003).
44. *Lindner P., Stirn R., Schumacher U.*, Verhandl. DPG VI 41, P 21.24 (2005).
45. *Schumacher U.*, Naturwissenschaften **88**, 102-112 (2001).
46. *Twiss R.O.*, Austr. J. Phys. **11**, 564 (1958), *Schneider J.*, Phys. Rev. Lett. **2**, 504 (1959).
47. *Gaponov-Grekhov A.V.*, Izv. VUZ Radiofizika **2**, 837 (1959); *Gaponov-Grekhov A.V., Petelin M.I., Yulpatov V.K.*, Radiophys. Quant. Electron. **10**, 794-813 (1967).
48. *Flyagin V.A., Gaponov-Grekhov A.V, Petelin M.I., Yulpatov V.K.*, IEEE Trans. **MTT-25**, 514-521 (1977).
49. *Andronov A.A., Flyagin V.A., Gaponov A.V., Goldenberg A.L., Petelin M.I., Usov V.G., Yulpatov V.K.*, Infrared Phys. **18**, 385-393 (1978).
50. *Denisov G.G., Litvak A.G., Myasnikov V.E., Tai E.M., Illin V.I., Zapevalov E.V.*, these proceedings, vol. 1, p. 62-75.
51. *Erckmann V., Gasparino U., Laqua H.P., Maassberg H., Marushenko N.B., Renner H., Rome M.*, W7-AS Team, *Kasparek W., Müller G.A.*, Proc. Vth Int. Workshop on Strong Microwaves in Plasmas (Ed. by A.G. Litvak), Vol. 1, 281-295, Nizhniy Novgorod, 2003.
52. *Suvorov E.V. et al.*, Plasma Phys. Contr. Fusion **39**, B337-B351 (1977).

MICROFABRICATION OF RF DEVICES

Lawrence Ives[1], *Carol Kory*[1], *Michael Read*[1], *Purobi Phillips John Booske*[2], *Sudeep Bhattacharjee*[2], *John Welter*[2], *Matt Genack*[2], *Hongrui Jiang*[2], *Dan van der Weide*[2], *Steve Limbach*[2], *Steve Schwartzkopf*[3], *Ron Witherspoon*[3], *Philipp Borchard*[4], *Ross Wilcox*[4]

[1]Calabazas Creek Research, Inc., Saratoga, CA
[2]University of Wisconsin, Madison, Wisconsin, USA
[3]Ron Witherspoon, Inc., Campbell, CA USA
[4]Consultants, Palo Alto, CA USA

Research is underway at Calabazas Creek Research, Inc., in collaboration with the University of Wisconsin and Ron Witherspoon, Inc., to create the next generation of high frequency RF sources. There is increasing interest in these sources for defense, homeland security, medical, communications, and industrial applications. As the frequency increases, the size of the RF structures decreases, and new fabrication and assembly techniques are required. In addition, new demands are placed on electron sources to produce high quality beams with reduced area compression. This requires cathodes operating with higher emission current densities. Improved magnetic circuits are also required. This presentation describes research to produce components for several high frequency sources.

There is currently great interest in applications using submillimeter RF power. The U.S. Department of Defense ranked the early-warning detection of chemical and biological agents at highest priority [1]. Significant research is in progress to develop techniques for remote sensing of these agents for protection of troops in the field, as well as highly populated areas, such as airports, train stations, ball parks, and public buildings. There is an abundance of molecular rotational energy levels of free molecules in this frequency range that can be used to identify specific molecules and materials. DNA, for example, possesses unique resonances in this frequency range due to localized phonon modes, providing a means for identifying biological agents [1]. Previous experiments demonstrated use of submillimeter radiation to identify various powder substances in envelopes, including flour, salt, baking soda, and Bacillus thruengiensis bacteria [2]. There are additional applications in medicine, microelectronics, agriculture, forensic science, and many other fields [3].

Detection of chemical and biological agents using terahertz radiation is particularly attractive in areas where people are present. The photon energy of terahertz radiation is a million times less than that of x-rays and produces no biological tissue damage [4]. Terahertz radiation also easily penetrates most dielectrics, including paper, cardboard, clothes, non-metallic luggage containers, wood, and many building materials.

Submillimeter radiation can not only provide spectroscopic information, but also produce high resolution images of objects and secure communications.

Both these applications require fairly high average power sources operating continuously or at high duty.

The terahertz (THz) region of the electromagnetic spectrum (approximately 300 to 3000 GHz in frequency or approximately 1 to 0.1 mm free space wavelength) has enormous potential for high-data-rate, short-range terrestrial and airborne communications. Using carrier frequencies above 300 GHz, oscillator and amplifier sources with approximately 10% fractional bandwidths would enable very high data rate (> 10 Gbits/s) wireless communications with high security protection. If adequately powerful, compact, and wideband sources were available, this capability could be achieved with extremely simple, low-cost, amplitude modulation schemes (for example, simple amplitude modulation and diode receivers).

Unfortunately, there are no economical, high average power sources of submillimeter radiation. Two techniques are currently used for experimental studies [3]. Both methods use ultra-fast pulses of laser radiation. A typical source is an ultra-fast Ti:sapphire laser with an average power of 1 W delivering 100 femptosecond pulses at 800 nm. In the photoconductive approach, high speed photoconductors serve as transient current sources for radiating antennas. Typical conversion efficiency of the optical power to RF power is 10-3 to 10-6. The second approach uses electro-optic crystals to provide optical rectification. Conversion efficiency is from 10-4 to 10-6. Output power for these approaches is from 0.1 to 100 microwatts. For a 2D imaging system, average powers of milliwatts or higher would be required for a practical device with sufficient response [3]. Using the technology described above, it requires approximately eight minutes to scan an envelope [2].

The submillimeter frequency range provides unique challenges for high power RF generation. The frequency is too low for most photonic sources, which are used routinely at higher frequencies. At lower frequencies, RF sources based on vacuum electronics and semiconductor physics are available. As frequencies increase, however, problems occur for semiconductors related to the electron mobility in the semiconductor material. This appears to be a fundamental barrier for high power RF generation at submillimeter frequencies. For vacuum electron devices, the principle challenges relate to fabrication and assembly. It becomes difficult to convert electron beam energy to RF energy using resonant structures with existing fabrication technology. There are possibilities to utilize lithographic fabrication to construct certain components, and research in this area is in progress [5, 6, 7].

Calabazas Creek Research, Inc. (CCR) is developing RF sources at W-Band for communications applications and at sub-millimeter wave frequencies for homeland security and defense applications. Research is also in progress to develop high current density cathodes for these sources. The source development activities are focused on circuit fabrication and assembly techniques to create the required micron-scale structures. Techniques under investigation include deep reactive ion etching (DRIE) with deposition of copper and diamond,

micro electro-discharge machining (EDM), and laser ablation of chemically vapor deposited (CVD) diamond. The cathode research initially focused on field emission structures, but is now primarily working on controlled porosity dispenser cathodes. Progress in these research efforts will be described in the following sections.

Electron guns

All vacuum electron sources require a high quality electron beam for efficient production of RF power. Typically, this electron beam is produced by a cathode operating in an accelerating electric field with the beam guided by a magnetic field. Traditionally, these applications used Pierce-type electron guns. In a Pierce gun, a spherical cathode emits an electron beam focused toward a region where a beam of the correct diameter is captured by a magnetic field and transported through the RF circuit. In lower frequency devices, this is a fairly simple design and fabrication process. As the frequency increases and the size of structures become smaller, it is becomes more difficult to properly shape the cathode and position and align the gun with other structures and the magnetic field. It is much simpler to fabricate a cathode that generates the proper size beam at the emission surface. One can then immerse the cathode in a flat magnetic field, and alignment and positioning becomes much simpler.

Unfortunately, this requires the emission surface to produce beams with the full current density required by the circuit. In conventional dispenser cathodes, high current density leads to rapid depletion of barium and reduced lifetime. Barium reduces the work function of the cathode to facilitate efficient emission of electrons from the surface, which is traditionally porous tungsten.

Research is in progress to develop cathodes capable of operating at increased current density. Spindt-type field emission array (FEA) cathodes use a lithographic process to create small cones of metal surrounded by cylindrical openings serving as a gate electrode. Figure 1 shows scanning electron microscope (SEM) photos of a Spindt FEA. Small arrays have

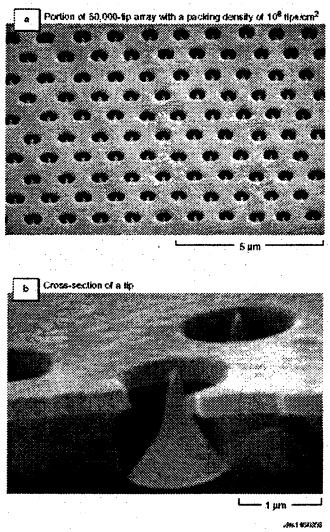

Fig. 1. SEM photos of field emission arrays. The top photo shows the array, and the bottom photo shows a close up of one emitter and its associated gate electrode.

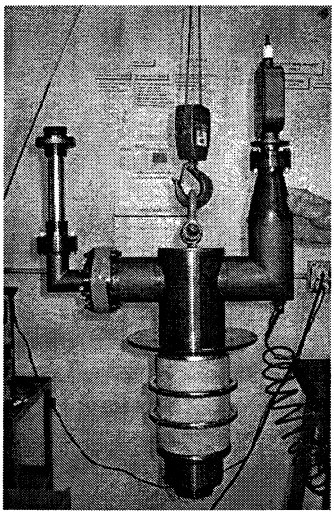

Fig. 2. High voltage device for testing field emission array cathodes.

demonstrated current emission densities exceeding 500 A/cm^2 in laboratory experiments.

Spindt FEAs, however, are not robust. Arcs between the gate and emission tip can lead to shorting of the electrode, and arcs between the emitter and the anode can lead to complete destruction. Unfortunately, such arcs are common in normal processing of RF sources. Another problem is damage from back streaming ions. These ions can be created from back ground gas or emitted from surfaces subjected to electron beam impact. Ion damage leads to reduced emission in certain regions leading to an electron beam with reduced, non-uniform current emission. Severe damage can also lead to destruction. Again, such ions are common in RF sources.

CCR developed an effective technique for reducing damage from cathode to anode arcs. A support structure was designed where the highest field gradient was located between the anode and a focus electrode around the cathode. The cathode was operated at the same potential as the focus electrode, but was electrically isolated by a ceramic sleeve. In the event of a breakdown between the gun and the anode, it is anticipated that the arc would first occur between the focus electrode and the anode. The subsequent increase in voltage between the focus electrode and cathode would create a high field gradient at a location between the FEA and its power supply. The resultant arc current would flow around the FEA, which would not be damaged. This technique was used in the test vehicle shown in Fig. 2. No FEA cathodes were destroyed by arcs during testing; however, it is not clear that any cathode to anode arcs occurred. Therefore, the concept is not fully validated.

CCR was able to test several FEA cathodes before the program was terminated. The cathodes could not be operated at more than a few percent duty. Any gassing of the device resulted in a reduction in beam current, apparently from gas adsorption on the emitter tips. Typically, full current would return with lower duty operation.

While FEA cathodes may be capable of high current density operation, their ability to operate in typical vacuum devices at high duty is not demonstrated. There are still serious concerns about their ability to handle arcs and ion bombardment.

The National Aeronautics and Space Administration is developing cathodes using carbon nanotubes (CNTs) [8]. Manohara et al. are attempting to develop cathodes for a 300 GHz reflex klystron operating at vacuum levels of 10^{-6} to 10^{-7} Torr using bundles of CNTs. Figure 3 shows an SEM photograph of a CNT bundle with a close-up photograph of a single bundle.

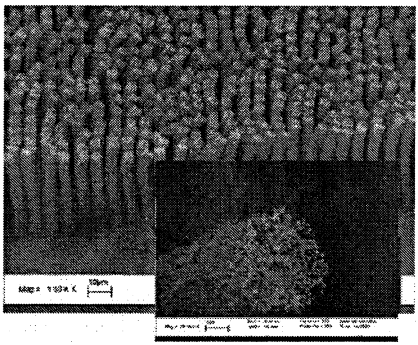

Fig. 3. Carbon nanotube bundles

They have demonstrated current densities of 6 A/cm^2 with a goal of 10 A/cm^2. The emission, however, does not appear to be uniform with bright spots of emission scattered over the surface. This has traditionally been an issue with CNT cathodes. The research is continuing, but has not resulted in a practical cathode for production RF sources.

CCR is investigating a new approach to improve dispenser cathodes. As previously mentioned, the current generation of dispenser cathodes exhibit reduced lifetime at high current density due to excessive barium depletion. In porous tungsten cathodes, the barium producing compound is imbedded in the porous tungsten matrix. The quantity of the barium compound is limited by the structure of the tungsten material. CCR is developing cathodes where the barium compound is contained in a reservoir cavity with the rate of barium diffusion carefully controlled.

Creating a controlled porosity tungsten surface has been the goal of cathode research for many years. There are numerous patents on this issue, though none have achieved success in a practical, production environment [9–14]. Previous efforts used laser drilling or lithographic techniques to create holes of a controlled size and pattern through a tungsten sheet. Unfortunately, the holes could only be created in very thin sheets which buckled or creased when heated to operating temperatures. The approach under investigation by CCR allows creation of controlled, micron size holes through tungsten of arbitrary thickness.

The process is based on an experiment performed by B. H. Alexander and R. W. Balluffi [15] and subsequently described in *Principles of Power Metallurgy* by W. D. Jones in 1960 [16]. Scientists studying sintering of spherical particles simplified the experiment by creating a bundle of closely packed wires. As the bundle was heated, the wires sintered together in a controlled manner such that the spacing between the wires was gradually reduced. At various times, the sintering process was terminated and the structure examined. The result was a metal structure with a hexagonal pattern of pores extending entirely through the structure. Figure 4 shows a cross section cut of tungsten material CCR produced using this procedure. The periodicity and pore size are close to ideal for many current RF sources.

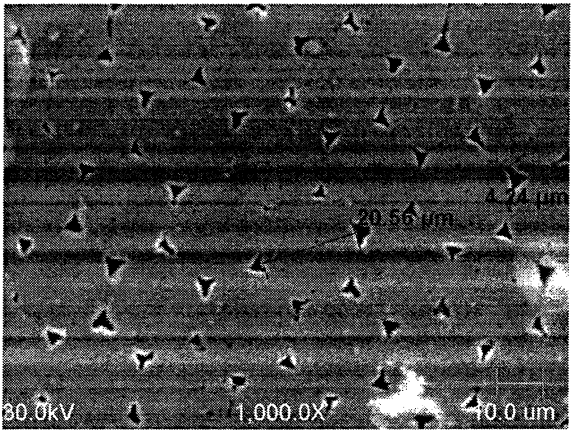

Fig. 4. SEM photograph of 20 micron diameter tungsten wires sintered at 2075 °C for 75 minutes. The periodicity is approximately 20 microns with extent of the pores being approximately 4 microns.

This material would be an ideal cap for a reservoir cathode. In a reservoir cathode, barium is placed in a chamber and allowed to diffuse through a porous cap to the surface. Previously, this cap consisted of porous tungsten as found in typical dispenser cathodes. These cathodes are capable of extremely long life but still suffer from the same problems with nonuniform barium diffusion as in standard dispenser cathodes.

The tungsten structure shown in Fig. 4 is structurally robust and can be custom manufactured to optimize either the thickness, pore distribution, or pore size. Consequently, the barium diffusion rate can be controlled and uniformly dispersed over the emission surface. The result would be extremely long life cathodes with unprecedented emission uniformity in a structurally robust package. Control of the diffusion rate allows control of the potential cathode emission density. Hence, high current density emission appears feasible. Large barium reservoirs could provide long lifetimes, and tungsten wire cathodes are currently being produced for testing. More information will be available in an article scheduled for publication in IEEE Transactions of Electron Devices [17].

Circuit fabrication techniques

As the frequency of RF sources increases, fabrication issues dominate the design of the RF circuit. At 600 GHz, for example, the periodicity in a backward wave oscillator (BWO) circuit is approximately 50 microns. The metal structures are only 25 microns in axial length. Creating robust structures with these dimensions is the greatest challenge for the designer. A number of fabrication techniques are in development to produce these structures, including micro EDM, LIGA, DRIE, dicing, and laser ablation. Of these, micro-EDM is the most widely used fabrication technique in production devices.

EDM fabrication uses thermal energy from an electric discharge to erode metal. The discharge can be generated along a wire or along the surface of a

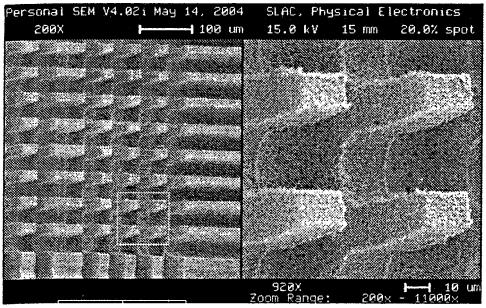

Fig. 5. SEM photos of BWO test circuits fabricated with wire EDM.

shaped electrode. Wire EDM is used for planar structures where the geometry allows cutting of metal between two supports for the wire. CCR's BWO circuits are manufactured using wire EDM. The BWO circuit consists of five parallel rows of 25×25 micron towers, or pintles, that are 80 microns high. There are approximately 300 pintles in each row. Figure 5 shows a test section of the BWO circuit produced from wire EDM.

Sinker EDM uses a shaped electrode to erode the metal. The advantage is that three dimensional structures can be created. Figure 6 shows an output waveguide section created with sinker EDM. The system consists of a section of rectangular waveguide with transitions in width and depth, followed by a non linear taper in circular waveguide. The structure was made in two halves that were bonded together. The width of the waveguide on the right of the image is 300 microns, and the depth is 30 microns.

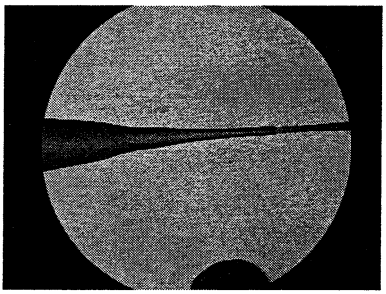

Fig. 6. Micro photograph of a BWO output waveguide system. The right end is a 300×30 micron rectangular guide and the left is a non-linear uptaper in circular guide.

Lithographe, Galvonoformung, und Abformung (LIGA) is a lithographic process where synchrotron radiation passes through a metallic mask containing a planar, negative image of the circuit. The radiation reacts with a plastic material that is removed and replaced with a metal, such as copper. Micron size structures can be created with extremely high surface finish. Figure 7 shows a section of a BWO circuit created using LIGA. The circular pintles are 25 microns in diameter, 80 microns high, and approximately 30 microns apart. One can compare the surface finish with that achieved with EDM in

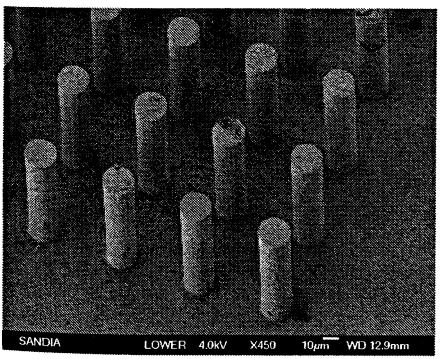

Fig. 7. Section of a BWO circuit fabricated using LIGA.

Figure 5 to see the obvious advantage. Unfortunately, LIGA requires access to a high energy synchrotron, and there are only a few available for production manufacturing in the world. Also, the process is still not well understood or reliable. The circuit shown in Fig. 7 was one of only four that were successfully produced on a wafer containing more than 50 circuits.

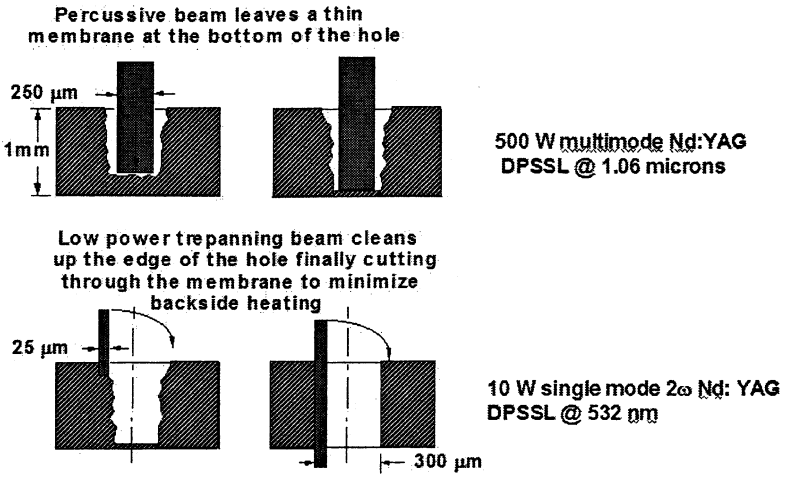

Fig. 8. The laser ablation process for creating small holes in metal

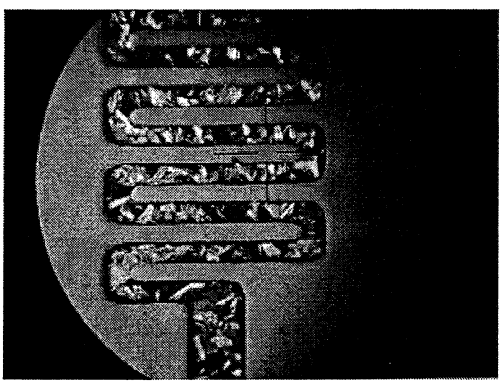

Fig. 9. TWT circuit pattern created using laser ablation of CVD diamond.

Laser ablation is a relatively new process where laser radiation ablates metal from a surface. The precision depends on the wavelength and power of the lasers. Figure 8 shows the process used for drilling precision holes in metal. CCR is investigating use of this technique to produce a meander line traveling wave tube (TWT) circuit in CVD diamond. Figure 9 shows a section of a test laser cut where the width of the cut is 30 microns*.

* Courtesy of Victor Ralchenko, General Physics Institute, Russian Academy of Sciences, Moscow, Russia.

CCR and the University of Wisconsin-Madison are also attempting to create the meander line TWT circuit using deep reactive ion etching. DRIE will be used to create a mold in silicon of the negative of the meander line base structure. CVD diamond will be grown directly into the mold [19], the mold will be removed by etching, and selective metallization will be performed on the meander trace.

Other fabrication techniques are available or in development. Dicing is used routinely in the semiconductor industry to separate individual circuits from large wafers and can create 25 micron wide cuts. Dicing is used by Vermont Photonics to create Smith Purcell gratings for their line or THz sources [18]. SU-8 is a lithographic process similar to LIGA that uses UV radiation instead of radiation from a synchrotron. Figure 10 shows a circuit pattern created at the University of Wisconsin for a 400 GHz folded waveguide TWT. Unfortunately, this process is still in development and does not appear to be very reproducible or robust.

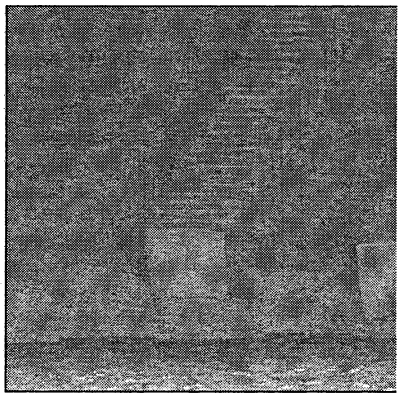

Fig. 10. 400 GHz folded waveguide TWT pattern created using DRIE.

Not surprisingly, the simplest techniques appear to be the most reliable. EDM and laser ablation are machining operations directly on the final material. LIGA and DRIE are multi-step processes that are complex and time consuming, and the final product is electro-deposited metal. LIGA and DRIE do, however, offer the promise of smaller and higher quality structures. Hopefully, continuing research will result in reliable, robust techniques suitable for RF source production.

RF source development

A number of RF sources are in development using a variety of microfabrication techniques. Stanford Linear Acceleratory Center (SLAC) constructed a W-Band klystron circuit using LIGA. The goal of the research was to produce a 100 kW RF source at 95 GHz. LIGA was used to fabricate the RF cavities, and wire EDM was used to create the beam tunnel. Figure 11 shows sections of the RF circuit and the periodic permanent magnet support structure. The device was successfully fabricated but was damaged by a problem with the magnetics circuit. This was one of the first implementation of LIGA structures in a high power RF circuit. SLAC is currently using LIGA to develop a sheet beam klystron at W-Band.

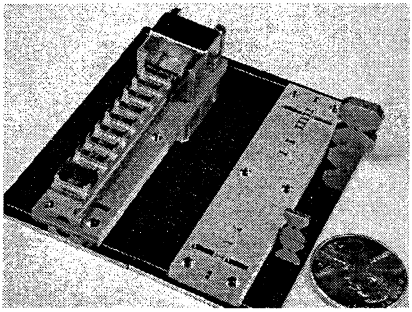

Fig. 11. Klystrino circuit produced using LIGA. The ppm support structure and magnet sections are also shown.

CCR is developing BWOs operating in the submillimeter-wave region. Figures 5 and 6 and showed images of the BWO test circuit and the output waveguide system. The approach is based on a design developed by Istok Company in Russia. CCR is using a similar electron gun and adding a depressed collector to improve the operating efficiency and an improved output waveguide system to improve the output mode purity. The next prototype BWO is scheduled for testing in spring 2006.

CCR is also developing two W-Band TWTs to produce approximately 10 W of RF power with a 5% bandwidth. Two different circuits are under development. The first is a folded waveguide that is approximately 120 mm long and contains an attenuator between the input and output sections. The attenuator was produced using DRIE by the University of Wisconsin. Approximately 100 attenuators were successfully fabricated on a single wafer. All parts for this TWT are fabricated and assembled except the RF circuit. The challenge is to fabricate the 200 micron diameter beam tunnel through the 120 mm circuit structure, and a number of attempts resulted in failure. The current approach is to machine a square beam tunnel in a flat section of copper and diffusion bond a cover plate on one side. Wire EDM will be used to fabricate the serpentine circuit along the square beam tunnel, and copper plates will be diffusion bonded to each side to form the RF circuit. It is anticipated that the circuit fabrication will be completed by December 2005 with testing of the TWT in spring 2006.

The other TWT circuit will use a meander line circuit fabricated from CVD diamond. A solid model of the circuit is shown in Figure 12. The width of the meander line is 30 microns Simulations show that compared to the folded waveguide circuit, the meander line circuit will be about one third the length for a 10 W TWT with a 49% increase in RF efficiency. In addition, the beam is not required to propagate through a small beam tunnel.

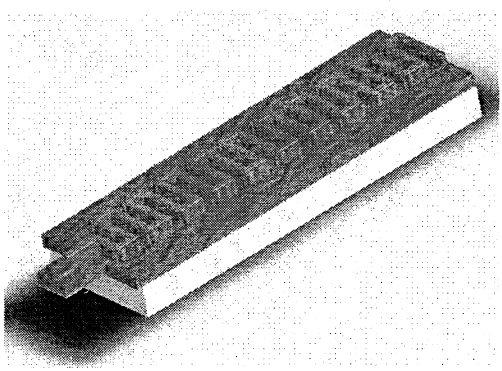

Fig. 12. Solid model of meander line circuit

As previously mentioned, both laser ablation and DRIE will be used to create the circuits. The laser approach will start with a CVD diamond wafer and directly machine the meander line on the surface. An important issue is the vertical walls of the diamond cut structure. There is some evidence the diamond may be converted to graphite along this surface. Since graphite is somewhat conductive, this could have an adverse impact on the circuit. Currently it is assumed that the diamond meander line structure is an insulator. It may be necessary to develop an etching process to remove any graphite; however, a technique for properly performing this operation is not finalized.

A critical issue in both approaches is selective deposition of a gold layer on the surface of the meander line. It is critical that gold is not deposited on other surfaces of the structure. Several approaches are in development, and experiments are planned in the next few weeks.

Magnetics

An issue for all high frequency electron beam sources is magnetic focusing. For most applications, size and weight are critical issues, particularly for mobile sources or for satellites. Traditionally, TWTs utilized periodic permanent magnet focusing for beam transport. As the frequency increases, the period of the magnetic field becomes smaller. This requires the magnet structures be closer to the electron beam to achieve the required field strength. Consequently, it becomes necessary to incorporate the magnet structure within the vacuum envelope of the device. This has serious implications for compensating for transverse fields and for baking and processing.

If there is no flexibility for externally adjusting the magnetic field, then the field strength and uniformity of the magnetic structures becomes more critical. Unfortunately, there appears to be little research focused on this issue. Nor is there equipment available for accurately measuring transverse fields in small diameter (less than 1 mm) periodic permanent magnet structures prior to sealing within an electron beam device. The permanent magnet version of CCR's W-Band folded waveguide TWT will be designed so that the magnet structure can be inserted over the device following final assembly. The output window will be in line with the circuit and collector, which adds significantly to the complexity of the tube. While this may work at W-Band, it is probably not practical for submillimeter wave devices.

An alternative is to use non-periodic permanent magnets. The submillimeter wave BWO produced in Russia and under development by CCR uses such magnets; however, they are quite large and heavy. More compact magnets will be required for mobile and hand-carried RF sources.

More research in this area is required. Currently there appears to be more research in cathodes and circuit fabrication techniques then in magnetics for high frequency sources.

Summary

There are many important applications for high frequency RF sources. The challenge for electron beam devices is to develop techniques for fabricating micron scale structures that are economical, robust, and practical in production environments. There is also a need for high current density cathodes that provide sufficient lifetime for these devices. Fortunately, research is in progress in these areas, and progress is being achieved. A more critical need may be for additional development on magnetic circuits for these devices.

References

1. *Woolard D., Kaul R., Suenram R., Hight Walker A., Globus T., Samuels A.* Terahertz Electronics for Chemical and Biological Warfare Agent Detection. IEEE MTT-S Digest, 1999. P. 925-928.
2. *Shaohong Wang, Ferguson B., Mannella C., Abbott D., Zhang X.-C.* Powder detection using THz imaging, in Technical Digest. Summ. Quantum Electronics and Laser Sci. Conf. Conference Edition, Long Beach, CA, USA, May 2002.
3. *Zhang X-C.* Terahertz wave imaging: horizons and hurdles, Phys. Med. Biol., Vol. 47, 3667-3677 (2002).
4. *Smye S.W., Chamberlain J. M., Fitzgerald A.J., Berry E.* The interaction between terahertz radiation and biological tissue, Phys. Med. Biol., Vol. 46, R101-R112 (2001).
5. *Scheitrum G.* 95 GHz klystron Design and Fabrications, Multidisciplinary University Res. Initiative Teleconf. October 2000.
6. *Kurayev A.A., Sinitsyn A.K., Sherbakov A.V.* Optimization Peniotron in View of Features of the T-Wave Near to Oscillation Wires, Sixth Intern. Vacuum Electronics Conf. Noordwjik, The Netherlands, 2005. P. 287-288.
7. *Han S.T., So J.K., Jang K.H., Shin Y.M., Jeon S.G., Kim J.H., Cahng S.S., Ryskin N.M., Park G.S.* Experimental Investigations of Folded-Waveguide TWT Oscillators, Fifth IEEE Intern. Vacuum Electronics Conf., Monterey, CA, April 2004. P. 69-70.
8. *Manohara H.M., Bronilowski M.J., Hunt B., Siegel P.H.* High-current-density field emitters based on arrays of carbon nanotube bundles, J. Vac. Sci. Technol. B 23(1), Jan/Feb 2005.
9. *Garner C.E., Deininger W.D., Gibson J., Thomas R.* Patterning of Dispenser Cathode Surfaces to a Controlled Porosity, IEEE Trans. Electron Devices, Vol. 26, No. 1, January 1989.
10. *Hwan-Chu Rho, Seog-Lae Cho, Hae-Taek Yang*, Cathode for electron tube and method of preparing the same," U.S. Patent 2002/0041141A1, April 11, 2002.
11. *Thomas R.E., Green R.F.* Controlled porosity sheet for thermionic dispense cathode and method of manufacture, U.S. Patent 4,379,979, April 12, 1983.
12. *Falce L.R., Breeze G.S.* Controlled porosity dispenser cathode, U.S. Patent 4,587,455, May 6, 1986.
13. *Greene R.F., Thomas R.E.* Method of manufacturing integral shadow gridded controlled porosity dispenser cathodes, U.S. Patent 4,745,326, May 17, 1988.
14. *Wijen J.F.C.M.* Impregnated cathodes with a controlled porosity, U.S. Patent 5,118,317, June 1992.
15. *Alexander B.H., Balluffi R.W.* Acta Met., 5 (11), 666-677 (1957).
16. *Jones W.D.* Principles of Powder Metallurgy, Edward Arnold Publishers LTD, London, 1960.
17. *Ives R.L., Falce L., Schwartzkopf S., Witherspoon R.* Controlled Porosity Cathodes from Sintered Tungsten Wires, Schedule for publication in IEEE Trans. Electron Devices, December 2005.
18. *Mross M., Lowell T.H., Durant R., Kimmitt M.F.* Performance Characteristics of a Smith-Purcell Tunable Terahertz Source, J. Biolog. Phys. 29(2), 295-302, Jan. 2003.
19. *Dayton J.A., Kory Jr.C.L., Mearini G.T.* Diamond-based Sub-millimeter Backward Wave Oscillator, SPIE, Philadelphia, PA, October 2004.

STATUS OF 1 MW, 140 GHz, CW GYROTRON FOR W7-X

M. Thumm[1a,2], *S. Alberti*[3], *A. Arnold*[2], *G. Dammertz*[1a], *V. Erckmann*[7], *G. Gantenbein*[6], *E. Giguet*[4], *R. Heidinger*[1b], *J.-P. Hogge*[3], *S. Illy*[1a], *W. Kasparek*[6], *H. P. Laqua*[7], *C. Lievin*[4], *R. Magne*[5], *G. Michel*[7], *B. Piosczyk*[1a], *K. Schworer*[6], *M. Q. Tran*[3], *X. Yang*[1a]

[1]Forschungszentrum Karlsruhe, Association EURATOM-FZK, [1a]IHM, [1b]IMF-I
Postfach 3640, 76021 Karlsruhe, Germany
[2]IHE Universitat Karlsruhe, Germany, [3]CRPP Lausanne, Switzerland
[4]TED Velizy-Villacoublay, France, [5]CEA Cadarache, France
[6]IPF Universitat Stuttgart, Germany, [7]IPP Greifswald, Germany

The program aims towards the development and installation of a 10 MW, continuously (30 minutes) operated ECRH system at 140 GHz for the stellarator W7-X at the Max-Planck-Institute of Plasma Physics (IPP) Greifswald (in collaboration with CRPP Lausanne, IPF Stuttgart, CEA Cadarache and TED). The conventional-cavity gyrotron operates in the TE28,8 cavity mode and provides a linearly polarized, fundamental Gaussian output beam. It is composed of a diode-type electron gun, an improved beam tunnel, a high-mode-purity low-ohmic-loss cavity with rounded transitions, an optimized non-linear uptaper, a highly efficient internal quasi-optical mode converter employing an improved launcher together with one quasi-elliptical and two beam shaping reflectors, a large single-stage depressed collector (SDC) with a beam shaping magnet, and a horizontal RF output through a largeaperture, water edge-cooled, single-disk CVD-diamond window. With the first series tube an output power of 1 MW has been achieved in short-pulse operation (ms) at an electron beam current of 40 A and an efficiency of 31% (without SDC), and 1.15 MW at 50 A. With a pulse duration of 3 minutes, limited by the available high-voltage (HV) power supply, a record output power of 0.92 MW at a beam current of about 40 A and an efficiency of 45% (with SDC) has been obtained. The output mode purity is 97.5% in the fundamental Gaussian beam mode. At a reduced beam current of 29 A an output power of 0.57 MW was measured at a pulse length of 31.5 minutes (pulse energy: 1.08 GJ) without any significant increase of the internal tube pressure. The detailed results and conclusions of the three development stages of this gyrotron are reported.

Introduction

High plasma temperatures are needed for initiating thermonuclear fusion reactions in magnetically confined plasmas. One possibility for heating the plasma to the necessary temperature of about 120 mil. °C is the injection of millimeter waves with a frequency corresponding to the cyclotron motion of the electrons in the confining magnetic field.

Gyrotron oscillators have proven to be highly efficient sources of coherent millimeter wave radiation at the interesting frequencies between 110 and 170 GHz [1, 2]. They have been used successfully for electron cyclotron resonance heating (ECRH) and electron cyclotron current drive (ECCD) [3]. ECRH has been proven to be an important tool for plasma devices especially for stel-

larators as it provides both net current free plasma start up from the neutral gas and efficient heating of the plasma.

The application of ECRH is limited due to the lack of powerful sources operating at an appropriate frequency. The major problems of high-power, high-frequency long-pulse gyrotron oscillators were given by the dielectric output windows, by the power capability of the collector and by the stray radiation absorbed inside the gyrotron [1, 2].

The development of gyrotrons with an output power in the megawatt range has been subject of investigation worldwide for a number of years. Microwave powers of 2 MW and more have been achieved in short-pulse operation and great progress has been made in the development of 1 MW long pulse gyrotrons during the last years [4–16].

The 140 GHz gyrotron for the stellarator Wendelstein 7-X at IPP Greifswald has been designed, constructed and fabricated in a collaboration between European research laboratories and the European tube industry Thales Electron Devices (TED) in France. The gyrotrons are equipped with a single-stage depressed collector (SDC) for reducing the thermal loading and for increasing the overall efficiency, an advanced quasi-optical mode converter and a single-disk diamond window made by chemical vapor deposition (CVD diamond).

Gyrotron design

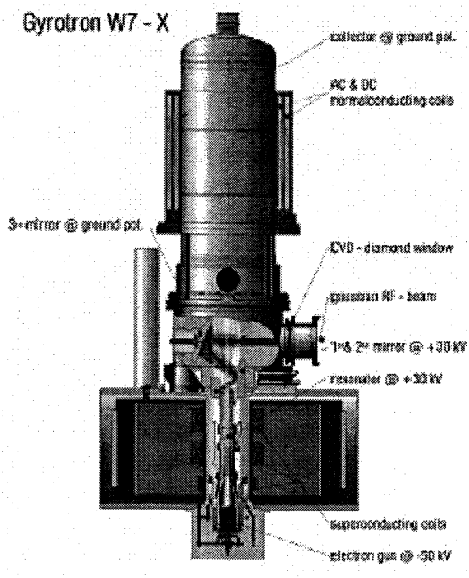

Fig. 1. Schematic view of the gyrotron

The 140 GHz gyrotrons (Fig. 1) with conventional cavity (hollow waveguide) for the stellarator Wendelstein 7-X (W7-X) consist of a diode-type magnetron injection gun without intermediate anode. It operates at an accelerating voltage of V_{acc} = = 81 kV with respect to the body (beam tunnel, cavity, quasi-optical launcher and first two mirrors) and a beam current of I_{beam} = 40 A.

Between gun and interaction region, an aperiodic loading structure composed of a stack of copper and absorbing dielectric rings has been implemented in order to suppress spurious oscillations in the beam tunnel. The RF cavity has been designed to

operate in the TE28,8 mode. It is a standard cylindrical cavity with a length of 14.5 mm and a diameter of 40.96 mm, a linear input taper of 2.5° and a non-linear output uptaper with an input angle of 3°. Mode conversion has been strongly reduced by the use of smooth transitions between cylindrical and taper sections with a transition length of 4 mm at the input and 6 mm at the output taper. The resulting mode purity has been calculated to be 99.9%.

Special care has been taken for the design of the quasi-optical mode converter to have very little amount of stray radiation. The operating mode belongs to a class of cavity modes for which the ratio of caustic to cavity radius is approximately 0.5. For this case, helical triangular perturbations of a dimpled-wall launcher provide perfect azimuthal focusing. The input radius of the launcher is 21.9 mm, the radius is slightly uptapered towards the output by an angle of 0.004 rad. This configuration reduces the quality factor of the section between cavity and helical cut and suppresses spurious oscillations. The wall perturbations have an amplitude of 0.041 mm, however, the perturbations for longitudinal and azimuthal field bunching start and end at different positions along the launcher axis. The dimpled-wall section is followed by a smooth-wall phasing section and the helical cut [7].

Due to the low fields along the edge of the helical cut, this advanced dimpled-wall launcher generates a well-focused Gaussian-like field pattern with low diffraction. In combination with a three-mirror system the desired Gaussian beam output pattern can be obtained. The first mirror of this quasi-optical system is a cylindrical mirror with quasielliptical curvature, the second and third mirror are toroidal ones.

With this design, theoretically an efficiency of more than 98% can been achieved for the conversion of the high-order TE28,8 cavity mode to the fundamental Gaussian beam.

The output vacuum window unit uses a single, edge-cooled CVDdiamond disk [18] with an outer diameter of 106 mm, a thickness of 1.8 mm (four half wavelengths inside the material) and a window aperture of 88 mm. The average loss tangent of the disk had been determined in a low-power measurement to be $4 \cdot 10^{-5}$. These measurements were performed with a scanning version of a hemispherical Fabry–Perot resonator. For this loss tangent, the losses in the disk are calculated to be about 700 W at an output power of 1 MW. The Cu/Ag-based brazing of the disk to copper cuffs at about 750–850 °C avoids corrosion of the braze by the cooling water and allows high baking temperatures of the gyrotron.

To reduce the power density on the collector surface, the body and the collector are insulated in order to allow a decelerating voltage to be applied (SDC). The collector with the mirror box, the last mirror of the quasi-optical mode converter system and the window unit are on ground potential, whereas beam tunnel, cavity, launcher and the first two mirrors are at depression voltage V_{body}. At the design values the cathode voltage is set to $V_{cath} = -51$ kV and the body to $V_{body} = +30$ kV.

The specifications of the gyrotron are summarized in Table 1.

Table 1. Specifications of the 140 GHz W7-X gyrotron

Cavity Mode	$TE_{28,8}$
Power, Pulse length	1 MW, CW (1800 s)
Electronic efficiency / Electrical efficiency	> 30% / > 45%
Magnetron injection gun	Diode
Current density at cathode	2.5 A/cm^2
Electron beam radius at cavity	10.1 mm
Magnetic field at cavity	5.58 T
Beam thickness at cavity	0.2 mm
Electron beam voltage	81 kV
Electron beam current	40 A
Velocity ratio α	1.3
Collector depression voltage	27–30 kV
Cavity heat load (ideal Cu, σ= 5.9·107S/m)	< 1 kW/cm^2
Gaussian output mode purity	> 900 kW
Waist of output beam	22 mm
Collector magnetic field	Universal Current (UC) field (1 coil)

Experimental results in development phase

During the development phase, a pre-prototype tube "Maquette" and an improved version, the prototype tube, have been fabricated and tested. For these tubes, the results of the output power, efficiency and the energy content for different pulse lengths are summarized in Table 2 [7]. With these results, the specified value of 1 MW for the output power has almost been achieved. However, two problems were faced: firstly the output power of 1 MW was not completely achieved, and secondly the pulse length of 30 minutes could not be obtained, even at reduced output power.

Table 2. Output power, efficiency and energy content for different pulse lengths of the prototype gyrotron [7]

Pulse length	Output power	Efficiency	Energy	Limitation
11.7 s	970 kW	44 %		Arcing
180 s	890 kW	42 %	160 MJ	HV-PS
939 s	539 kW		505 MJ	Pressure
1300 s	257 kW		350 MJ	Pressure

The first problem is seen in a degraded electron beam quality caused by an inhomogeneous emission from the cathode surface. Short-pulse measurements performed after long-pulse operation showed a saturation of the output power at

beam currents between 40 to 50 A. Increasing the beam current did not increase the output power significantly. This saturation is thought to be due to a non-homogeneous distribution of the electron emission from the surface. This inhomogeneity deteriorates the quality of the electron beam [19]. Other effects as for example spurious mode oscillations or a misalignment of the gyrotron might be excluded as this effect has not been observed in the pre-prototype tube. Further evidence for an inhomogeneous electron emission was given by a visual inspection of the cathode after dismantling the tube. The pictures taken with a scanning electron microscope clearly showed different surface structures with different surface roughness or porosity.

As mentioned before, the quasi-optical mode converter had been optimized with respect to high mode purity and low stray radiation [17]. Though the stray radiation turned out to be only 3% (the internally absorbed one is only about 1% of the output power), the pulse length of the gyrotron was limited to 939 s at an output power of 539 kW due to a pressure increase inside the gyrotron. At the end of this pulse, the temperature of the parts inside the mirror box could be measured with an infrared camera through the transparent diamond window. An increase in temperature of the internal ion getter pumps to values of more than 260 °C was found.

Experimental results of first series tube

Knowing the reasons for the limitation in output power and in pulse length, the development phase for the gyrotron had been finished. The series gyrotrons and the superconducting magnets were ordered.

To avoid the saturation of output power with beam current, a better quality assurance has to be performed before installing the emitter ring in the tube. According to the measurements on the prototype, the inhomogeneity of an emitter ring can easily be seen by an optical view with a scanning electron microscope, and poor material can be avoided. Homogeneous cathode heating is checked by a pyrometer.

The limitation in pulse length due to an overheating of the internal ion getter pumps could be avoided by a better RF shielding of the pumps. This turned out to be rather difficult due to the HV feed-throughs inside the gyrotron. Therefore, it was decided, to place the pumps outside the gyrotron and to shield the pump against RF radiation by a simple grid. Figure 2 shows a photography of the first series tube in the test facility of FZK. Two of the four ion getter pumps installed outside the gyrotron can be clearly seen.

The first series tube arrived at FZK in February 2005 and was tested in short and long-pulse operation. Figure 3 shows the dependence of the output power on the electron beam current in short-pulse operation (1 ms). In contrast to the results of the prototype, the output power does not show any saturation up to beam currents of 50 A proving the good quality of the electron emitter ring.

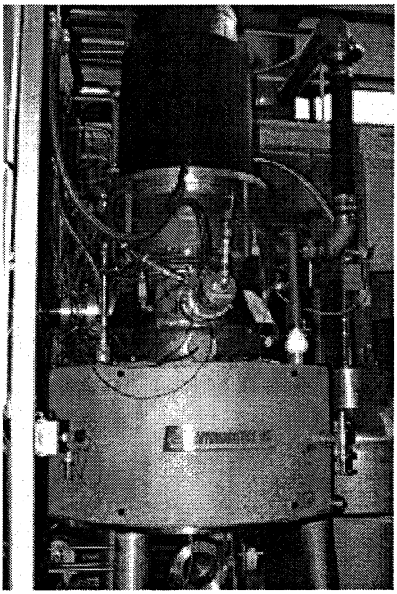

Fig. 2. Photography of the series tube at the test facility.

The corresponding output power was 1.15 MW with an efficiency of 30% (without SDC). For this measurement the magnetic field and the electron beam radius at the cavity was kept constant at 5.53 T and 10.36 mm, respectively. It turned out that the output power is strongly dependent on the electron beam radius (see Fig. 7). This leads to the very low values of output power at $I_{beam} < 30$ A (Fig. 3). For these values, the beam radius should have been changed to excite the desired TE28,8 mode at a reasonable output power.

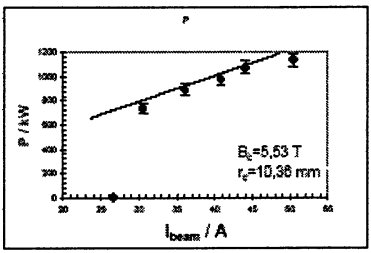

Fig. 3. Dependence of output power on the electron beam current

Field profile measurements were performed using an IR camera by inserting a target into the RF beam. Figure 4 shows the RF-beam pattern at different distances from the window. The phase reconstruction of the beam and the subsequent mode analysis yielded a Gaussian beam content of 97.5%.

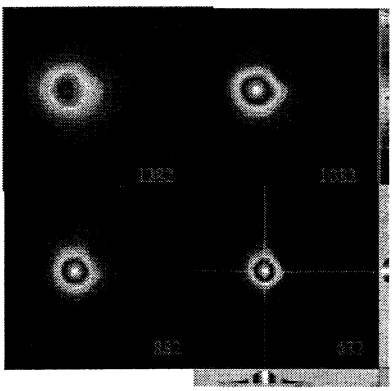

Fig. 4. Profile measurements of the RF beam at different distances from the window. The distances (in mm) are given in the lower right corner.

However, a horizontal shift of 12 mm has been found for the RF beam in a direction opposite to what had been observed during measurements with the prototype. It is thought that this is due to the tolerances of the mirror system, especially in position and angle of the first quasielliptical one, which are very sensitive to the position of the beam at the window.

Cavity expansion due to Ohmic heating, leading to a frequency downshift, electron emission cooling of the cathode, leading to a reduction of the beam current, and electron beam space charge neutralization, leading to an increase of the electron energy inside the cavity make the finding of the optimal long-pulse operating parameters quite difficult [6]. Stationary conditions are obtained after 40 to 60 s, depending on the cathode heater boosting scheme.

The optimisation procedure for finding the operating parameters at high output power in long pulse operation was performed in 1s pulses assuming that the instantaneous power is well described by the frequency difference between the initial frequency and the instantaneous frequency (after one second). Figure 5 shows the frequency shift during a 1 s pulse at 0.57 MW output power. The frequency shift is approximately proportional to the output power. Figure 6 shows frequency shift and accelerating voltage for maximum frequency shift that is at maximum output power for different magnetic field values in the cavity region. The measurements were performed at a constant beam current of 40 A, but with optimising the electron beam radius inside the cavity. The straight line for the frequency shift corresponds to the maximum output power at a given magnetic field. These values are related to an accelerating voltage which follows the equation B/γ = const with the magnetic cavity field B and the relativistic factor γ. Increasing the voltage beyond this value leads to an excitation of the neighbouring mode.

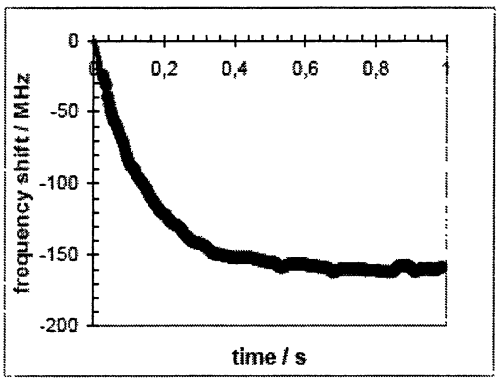

Fig. 5. Frequency shift during a 1 s pulse for an output power of 0.57 MW

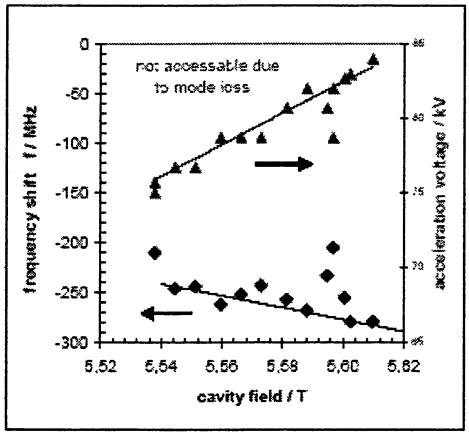

Fig. 6. Frequency shift (measure for output power) and corresponding (optimal) accelerating voltage for different magnetic fields in cavity region. The diamonds correspond to the measured frequency shift, the triangles show the measured optimal accelerating voltages. The solid line shows a fit to the frequency measurement according to B/γ = const, the thin dashed line the same for the accelerating voltage. Values which are not on the lines are either within the tolerance or correspond to lower output power.

A strong dependence of the output power has been found for different electron beam radii inside the cavity (Fig. 7). The desired mode can only be excited in a narrow range between 10.25 mm and 10.45 mm. At lower beam radii, arcing occurs, at higher radii a wrong mode (or the counterrotating mode) is excited. The optimum value of the beam radius decreases slightly with decreasing cavity field and beam current.

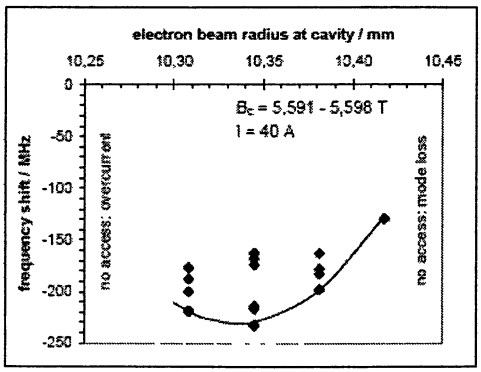

Fig. 7. Dependence of maximum frequency shift (maximum output power) on electron beam radius. The allowed range for excitation of the desired mode is only 10.27–10.43 mm.

It is interesting to know the individual power distribution on different components, that is to know the internal and external stray radiation, the Ohmic losses, the generated power and so on, resulting in an overall power balance. The water cooling loops of the gyrotron are equipped with a lot of thermocouples which allow very accurate temperature measurements of the water inlet and outlet of different components and diagnostic devices. A relief window (sapphire) equipped with a small calorimeter provides additional information on the internal stray radiation. Figure 8 shows the microwave chamber in front of the gyrotron where the most parts of the diagnostics are installed. Figure 9 shows the corresponding difference of water temperature (temperature of outlet minus inlet) for the cooling loops inside the microwave chamber as for example the temperature difference of the two parts of the beam tube (RF tubes, see Fig. 8), the two polarizers, the pre-load and an absorber placed inside the chamber. The absorber is not shown in Fig. 8. The gyrotron itself is also equipped with thermocouples in order to measure the power dissipated in the different components.

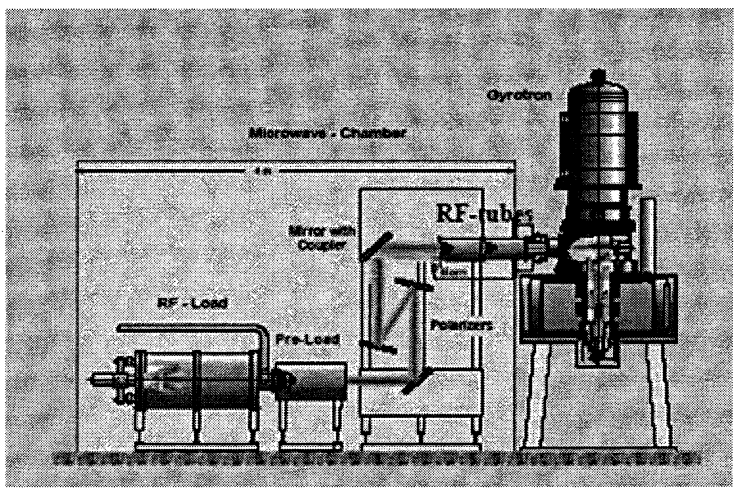

Fig. 8. Microwave chamber for RF diagnostics

These measurements allowed to make the power balance of the series tube: Table III summarizes the Ohmic losses, internal and external stray radiation and the losses inside the diamond window for two different pulse lengths and output powers. Compared to the prototype the values are similar, however, the losses of the diamond window are increased by a factor of 2 which is due to the spread of the loss tangent for different CVD-diamond disks.

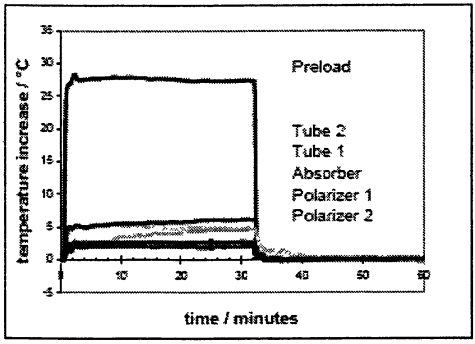

Fig. 9. Increase of water temperature of some water loops inside the microwave chamber.

Table 3. Power balance and dissipation in the various gyrotron components

Pulse length		180 s		1893 s
Efficiency (with depression)		44%		37%
Parameter	Power (kW)	Relative power / %	Power (kW)	Relative power / %
Generated power	970±50	100	607±30	100
Ohmic losses	40±8	4.2	26±5	4.2
Internal stray radiation	9.6±2	1.0	7.5±1.5	1.2
Window losses	1.5	0.2	1.0	0.2
Output power	920±45	95.0	569±30	93.8
External stray radiation	14±3	1.4	12±3	1.9
Directed power	906±45	93.5	557±28	91.8

It should be mentioned that the amount of stray radiation agrees very well with the theoretically predicted of 2%. The sum of the internal and external stray radiation adds to about 3%.

The highest output power for three minutes pulses (limit of the HV power supply at FZK) was measured to be 0.92 MW with a directed power of 0.91 MW. (The directed power is the power measured inside the load, the preload, on the mirrors and on the polarizers). The efficiency of the gyrotron for this pulse was 28% without and 44% with a depression voltage of 28.5 kV. The averaged electron beam current was 40.6 A and the accelerating voltage was 81 kV. Figure 10 shows the time dependence of the gyrotron parameters for this pulse. The increase in beam current during the pulse is caused by manual cathode heater boosting in order to counteract the electron cooling (usually the manual boosting is much better than shown here).

A reduction in beam current to values less than 30 A allows operation of the gyrotron with longer pulse duration. Figure 11 shows the gyrotron parameters for a pulse length slightly longer than 30 minutes (1893 s). The pressure increase during this pulse is less than a factor of 2 and stays well within the 10^{-9} mbar range. In these plots also an RF-diode signal for the output power is shown. The diode is installed in front of the first mirror (Fig. 8) and detects a small part diffracted from the RF output beam. This signal is very stable during the pulse. The output power was measured to be 0.57 MW and the Gaussian beam power to 0.56 MW.

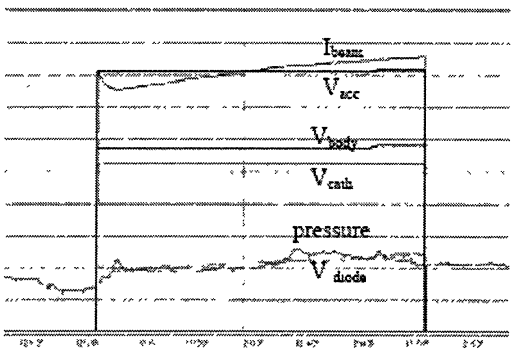

Fig. 10. Gyrotron parameters for the 180 s, 0.92 MW record pulse. Shown are the beam current I_{beam}, the accelerating voltage V_{acc}, the body (depression) voltage V_{body}, the cathode voltage V_{cath}, the pressure and the diode signal.

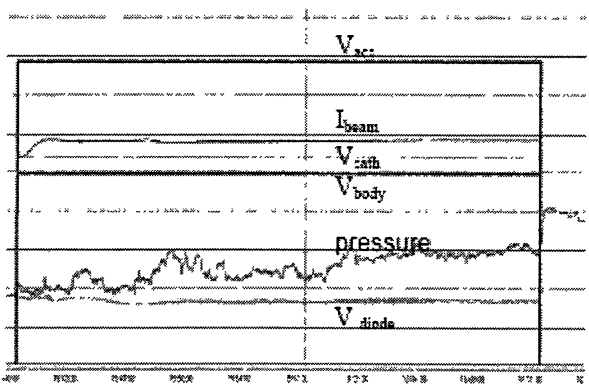

Fig. 11. Gyrotron parameters for the 1893 s, 0.57 MW pulse

The reliability of the gyrotron at high output power has been checked in long pulse operation. Eight consecutive pulses were successful at a power level of about 0.9 MW and a pulse length exceeding 170 s. The ninth was stopped due to arcing inside the tube after 168 s. After arcing, short pulse operation is necessary with a few pulses in order to recover the behaviour of the gyrotron. Though the output power of 1 MW has not been achieved completely, the directed power (Gaussian contribution) is about 0.9 MW, as specified. It is thought that by increasing the electron beam current by 10% (from 41 A to 45 A) also the output power and the directed RF power could be increased by this amount. Due to lack of time this could not be proven up to now.

Though not all measurements which were foreseen during these tests have been performed, the experimental tests at FZK were finished and the first series gyrotron was delivered to IPP Greifswald for long pulse operation at high power, that is 1 MW for 30 minutes.

Conclusions

The first European 140 GHz series gyrotron for W7-X was tested at Forschungszentrum Karlsruhe. In order to avoid the same problems as in the prototype, a better quality assurance of the electron emitter ring has been performed. This was done before installation into the tube by an optical inspection with an electron microscope. The reduction of the pressure rise and thus an increase in pulse length was achieved by placing the ion getter pumps outside the gyrotron in a way that the high voltage can be supplied from the outside. The pump itself is protected in the usual way by a copper grid between mirror box and pump.

The series tube yielded an output power of 1 MW in short pulse operation (1 ms), with an efficiency of 31% without depressed collector, and of about 0.92 MW in long pulse operation (180 s) with an efficiency of about 45% at a depression voltage of 28.5 kV.

The efficiency of the mode converter for the conversion of the TE28,8 cavity mode to the Gaussian output mode was calculated to be 98% and measured to about 97%. An amount of about 1% stray radiation is absorbed inside the gyrotron, without causing any limitation in the pulse length at an output power of 0.57 MW up to a pulse length exceeding 30 minutes (pulse energy: 1.08 GJ).

The gyrotron was delivered to IPP Greifswald for further tests at high power levels and 30 minutes pulse duration.

Acknowledgments

The authors would like to acknowledge the outstanding scientific and technological work of all persons from the different laboratories and industries, which have been involved in the gyrotron R&D program. They are especially indebted to the technical personal at the FZK gyrotron test facility.

This work was supported in part by the European Fusion Programme under the Project Nuclear Fusion at Forschungszentrum Karlsruhe and through the Contract of Associations of the different laboratories and by the Swiss National Science Foundation.

References

1. *Thumm M.*, Fusion Eng. Des., 2003, **66-68**, 69-90.
2. *Thumm M.*, Int. J. Infrared and Millimeter Waves, 2005, **26**, 483-503.
3. *Luce T.C.*, IEEE Trans. Plasma Sci., 2002, **30**, 734-754.
4. *Dammertz G. et al.*, IEEE Trans. Plasma Sci., 1996, **24**, 570-578.
5. *Dammertz G. et al.*, IEEE Trans. Plasma Sci., 2000, **28**, 561-566.
6. *Alberti S. et al.*, Fusion Eng. Des., 2001, **53**, 387-397.
7. *Dammertz G. et al.*, IEEE Trans. Plasma Sci., 2002, **30**, 808-819.
8. *Dammertz G. et al.*, IEEE Trans. Electron Devices, 2005, **52**, 808-817.
9. *Piosczyk B. et al.*, IEEE Trans. Plasma Sci., 1999, **27**, 484-489.
10. *Piosczyk B. et al.*, IEEE Trans. Plasma Sci., 2002, **30**, 813-827.
11. *Felch K. et al.*, IEEE Trans. Plasma Sci., 1996, **24**, 558-569.
12. *Felch K. et al.*, Proc. of the IEEE, 1999, **87**, 752-781.
13. *Blank M. et al.*, IEEE Trans. Plasma Sci., 2004, **32**, 867-876.
14. *Anderson J.P. et al.*, IEEE Trans. Plasma Sci., 2004, **32**, 887-883.
15. *Zapevalov V. et al.*, Fusion Eng. Des., 2001, **53**, 377-385.
16. *Sakamoto K. et al.*, Nucl. Fusion, 2003, **43**, 729-737.
17. *Thumm M. et al.*, IEEE Trans. on Electron Devices, 2005, **52**, 818-824.
18. *Heidinger R. et al.*, IEEE Trans. Plasma Sci., 2002, **30**, 800-807.
19. *Nusinovich G.S. et al.*, Phys. Plasmas, 2001, **8**(7), 3473-3479.

HIGH-POWER GYROTRON OSCILLATOR AND BROADBAND GYRO-AMPLIFIER DEVELOPMENT AT CPI

M. Blank, P. Borchard, P. Cahalan, S. Cauffman, T. S. Chu, K. Felch, H. Jory

Communications and Power Industries, Palo Alto, CA, USA

The results of experimental demonstrations for two long-pulse, megawatt-class gyrotron oscillators and a low-voltage, broadband gyrotron-traveling-wave-tube (gyro-TWT) amplifier are described. Recent gyrotron oscillator development at CPI has been focused on a 140 GHz, 900 kW CW device, which was delivered to the Max Planck Institute for Plasma Physics in Greifswald, Germany, and a 1.3 MW, CW device. Features of both the 140 GHz and 110 GHz gyrotron oscillators include a single-anode magnetron injection gun, a highly-efficient internal converter that produces a TEM_{00} output mode, an 88-mm-diameter chemical vapor deposition (CVD) diamond output window, and a single-stage depressed collector. In tests at CPI, the 140 GHz gyrotron achieved pulse lengths up to 700 s in duration at the 500 kW output power level and powers up to 930 kW for short pulses. Long-pulse testing at beam currents above 25 A, which is a long-pulse power supply limit at CPI, were performed in Griefswald where 30-minute pulses at 900 kW were achieved. For the 110 GHz gyrotron, measured power levels up to 1.28 MW at ms pulse lengths were demonstrated. In long-pulse tests performed at CPI, power levels of 500 kW were obtained for 10-s pulses. Long-pulse tests at the 1.3 MW power level will be carried out at General Atomics in San Diego, CA, following a minor repair of the output window assembly.

In addition, the development and test of a broadband, W-band gyro-TWT amplifier is discussed. The gyro-TWT will be used as a driver for previously developed and planned high-power gyrotron amplifiers. The device was designed for 500 W peak and 200 W average output power centered at 96 GHz, with a full-width-half-maximum (FWHM) bandwidth of 8 GHz at a nominal operating point of 30 kV and 0.8 A. Features of the gyro-TWT include a double-anode magnetron injection gun, a 32-cm loaded TE_{01} mode interaction circuit, and a double-disk CVD diamond output window for bandwidth enhancement. Peak output powers up to 1.5 kW and FWHM bandwidths of 7 GHz have been achieved in recent experimental demonstrations. Ongoing tests will be aimed at increasing the bandwidth while maintaining the peak output power level.

140 GHz, 0.9 MW, CW gyrotron oscillator

The detailed design and initial tests on the 140 GHz gyrotron have been discussed elsewhere [1] but are summarized below along with the main results of the recent tests in Greifswald.

Key features of the 140 GHz gyrotron are shown if the schematic diagram in Fig. 1.

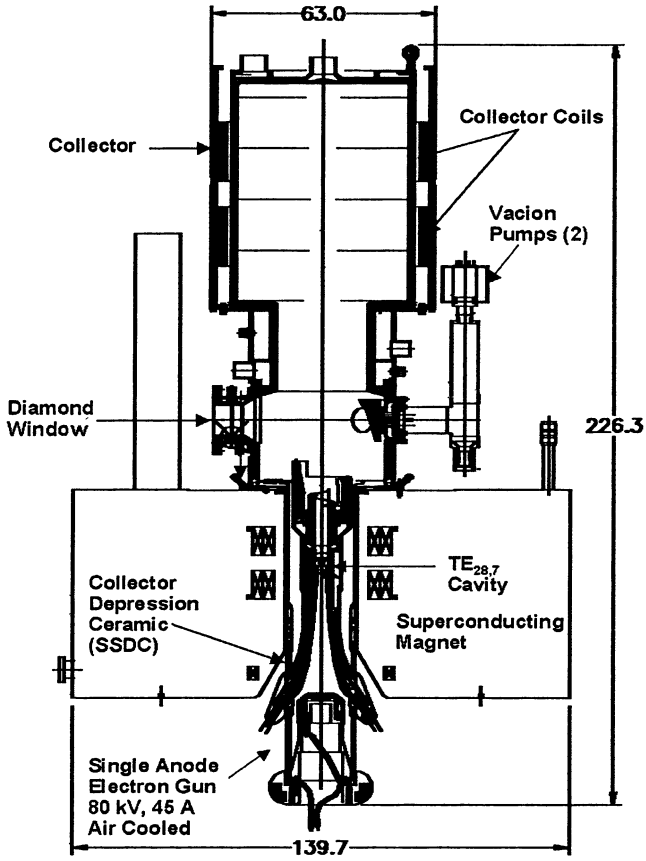

Fig. 1. Schematic diagram of 140 GHz gyrotron

The single-anode, or diode, magnetron injection gun was designed to operate at a nominal accelerating voltage of 80 kV and a nominal beam current of 40 A. The average cathode radius is 5.64 cm and the average cathode loading, at 40 A beam current, is 2.3 A/cm^2. The electron gun was designed to operate with air insulation and was operated in air in the initial tests at CPI. In the recent tests in Greifswald, oil insulation was employed, which facilitated cooling of the collector-depression ceramic shown in Fig. 1.

The interaction cavity was designed to support the $TE_{28,7,1}$ mode at 140 GHz. The cavity, which consists of an input taper, straight section and an output taper, was designed for a cold Q of 1200 and an output mode purity of 99.8%. The predicted peak power density in the cavity was 1.6 kW/cm^2. Multi-mode efficiency calculations were carried out with a self-consistent, time-dependent code [2].

These calculations indicated that, for a cathode voltage of 80 kV, a beam current of 40 A, and a perpendicular-to-parallel velocity ratio of 1.5, 1.2 MW would be generated in the cavity, resulting in 1 MW output power. DC space-charge depression, which is approximately 5.5 kV in the cavity, was included in the simulation. The total predicted efficiency, assuming a cathode-to-body voltage of 80 kV and a cathode-to-collector voltage of 60 kV, or 20 kV depression, was 41.7%.

The internal mode converter was designed to efficiently transform the $TE_{28,7}$ mode produced in the cavity to a Gaussian beam that exits the gyrotron perpendicular to the axis. The converter consists of a rippled-wall launcher and three focusing and steering mirrors, designed to optimize the shape and mode purity of the Gaussian beam and to bring the waist into the proper position to exit through the output window. The calculated diffraction losses for the internal converter system were about 5%, including 0.6% predicted loss at the output window due to spillover. Cold tests were performed to align the mirrors and verify the properties of the output beam. The measured beam pattern near the position of the window is shown in Fig. 2. Although a circular Gaussian beam was predicted by the theory, the cold tests showed that the output beam was slightly elliptic, but that at least 99% of the power would be transmitted through the output window.

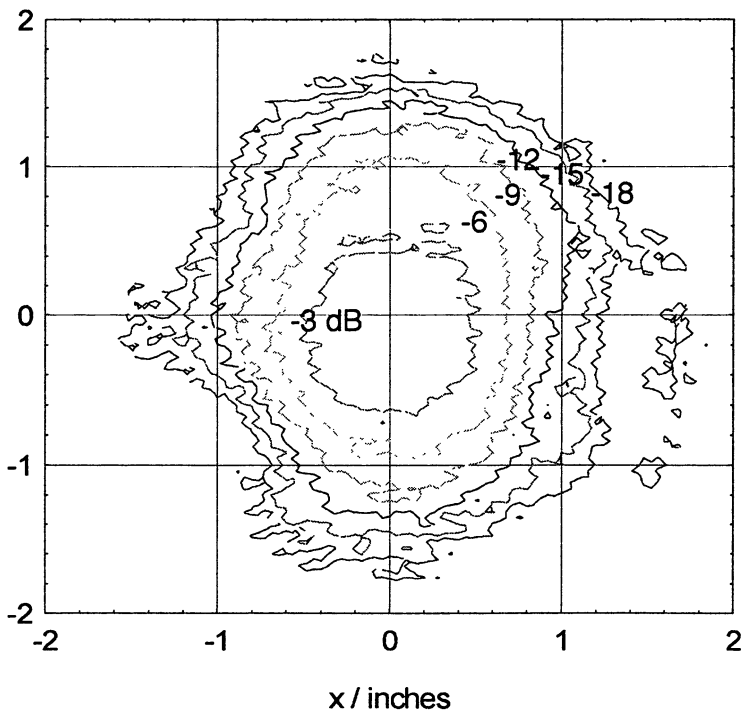

Fig. 2. Cold test measurement of output beam pattern near output window position

The output window consists of an edge-cooled CVD diamond disc. The clear aperture diameter of the window is 88 mm and the thickness is 1.8 mm, which is two wavelengths in the material at 140 GHz. A high-temperature braze technique was used in the fabrication of the window assembly. Detailed thermal-mechanical analyses indicated that the maximum tensile stress for 1 MW operation was two to three times lower than the ultimate tensile strength of the diamond for the measured loss tangent of 5×10^{-5} for the final brazed window.

A single-stage, depressed collector (SSDC) is used for efficiency enhancement. Since the body operates above ground potential, an additional insulator, the collector-depression ceramic shown in Fig. 1, is required. The two collector coils shown in Fig. 1 are used to generate an axial magnetic field to spread the spent beam in the collector. Both coils are driven with an AC current to sweep the spent electron beam with time to reduce the average power level in the collector. These coils are mounted close to the collector cylinder and are enclosed inside a magnetic shield. For the nominal cathode-to-collector voltage and beam current, 60 kV and 40 A, respectively, the maximum power density in the collector is predicted to be 650 W/cm^2.

The magnetic field for the gyrotron is generated by a superconducting magnet that has a warm-bore diameter of 20.32 cm. The nominal axial magnetic field at the cathode is 0.18 T and the ratio of the magnetic field at the cathode to the magnetic field in the interaction cavity is 29.5. A photograph of the 140 GHz gyrotron is shown in Fig. 3.

The initial tests on the 140 GHz gyrotron that were performed at CPI have been discussed in detail elsewhere [1]. Peak power levels above 900 kW were achieved with

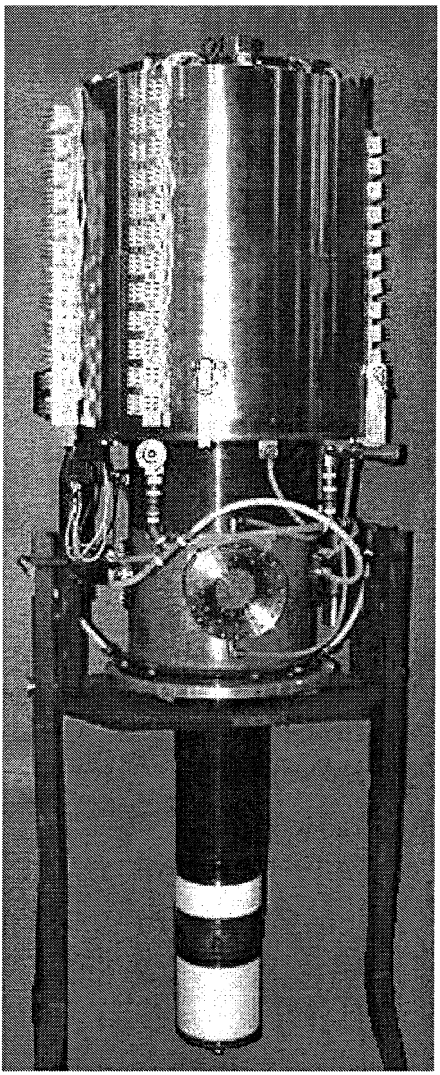

Fig. 3. Photograph of 140 GHz gyrotron

efficiencies of 34%. However, it was not possible to reach the design power level of 1 MW. Reasons for this shortcoming are not yet understood but could involve electron beam quality or mode competition. Figure 4 shows a map of output power for varying gun coil current, which results in a variation in the perpendicular-to-parallel velocity ratio in the beam and taper coil current, which varies the magnetic field in the interaction region. For each point on the curve, the cathode-to-body and cathode-to-collector voltages were held fixed at 80 kV and 60 kV, respectively. Although the filament power was held constant, the beam current varied from 43.2–45.1 A throughout the measurement. As seen in the figure, the maximum output power was measured to be 923 kW, which corresponds to 34% efficiency. Due to power supply limitations at CPI, pulse lengths longer than a few milliseconds could not be achieved at beam currents greater than 25 A. Therefore, long-pulse demonstrations were carried out at the 500 kW output power level with 80 kV cathode-to-body voltage, 55 kV cathode-to-collector voltage, and 24.7 A beam current. The pulse length was extended to 700 seconds with very little difficulty. During the tests, numerous 600-second pulses were taken, including a sequence of ten in a row without a fault. Pulses longer than 700 seconds at the 500 kW output power level were not attempted due to heating in the collector depression ceramic (see Fig. 1) caused by stray RF power not directed through the output window by the internal converter system.

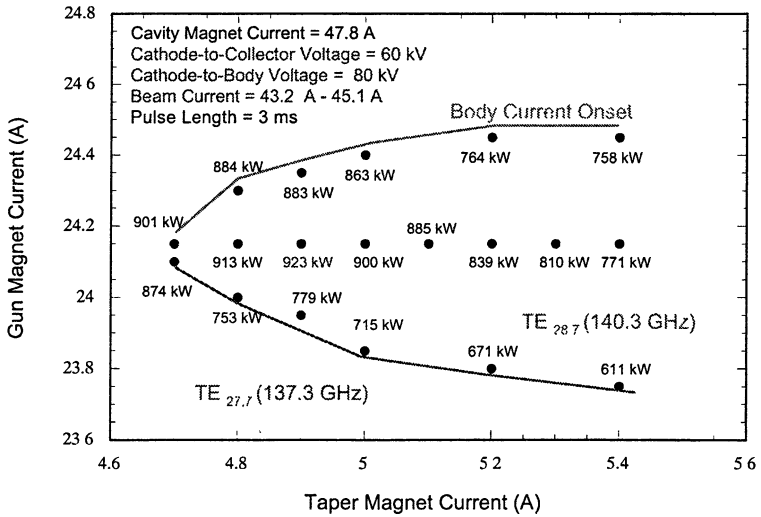

Fig. 4. Mode map showing parameters for maximum output power of 923 kW

The later addition of oil cooling for the tests in Greifswald enabled higher-power and longer-pulse operation. The tests in Greifswald were carried out by personnel from the Max Planck Institute for Plasma Physics with assistance

from CPI. Following a series of initial activities to verify the correct operation of the gyrotron and superconducting magnet in the new power supply system at Greifswald, output power levels and pulse duration were both gradually increased. In March 2005, output power levels of 820 kW were measured in the final calorimetric load for the system for a continuous pulse duration of 30 minutes. Since it is estimated that about 10% of the output power from the gyrotron is not captured in the dummy load due to a number of factors, the gyrotron output power was about 900 kW. Parameters for the 30 minute pulse were: collector voltage 55 kV, body voltage 25 kV, beam current 45 A and body current 26 mA. In Figure 5, a plot of the vac-ion current, which is a measure of the internal vacuum pressure, is shown over the duration of the 30-minute pulse. The increase in current (vacuum pressure) at the end of the pulse is due to the pumping effects of the electron beam. Output power as measured in the final calorimetric load over the duration of an earlier 27-minute pulse is shown in Fig. 6. Two 2-minute pulses precede the 27-minute pulse.

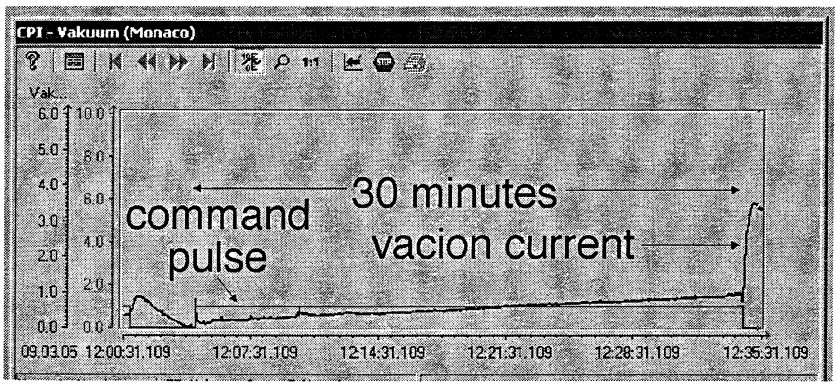

Fig. 5. Vacion current during 900 kW, 30-minute pulse on 140 GHz gyrotron

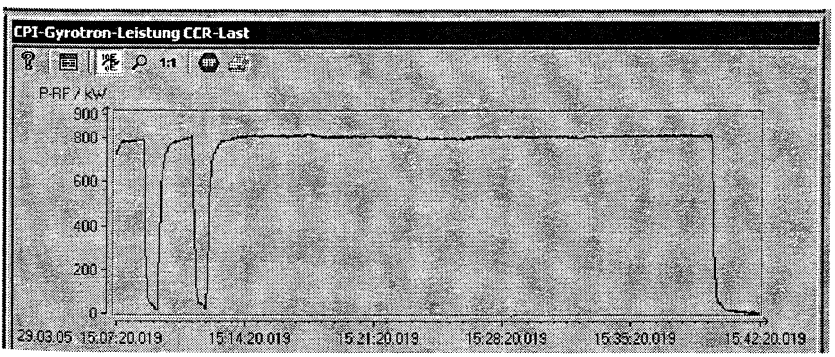

Fig. 6. Output power in the final calorimetric load during a 27-minute pulse

Operation of the gyrotron appeared to be quite stable over the long pulse durations, validating the basic CW design of the gyrotron. Unfortunately, a water to vacuum leak in the collector due to over heating developed in subsequent testing. The gyrotron was returned to CPI so that it could be repaired and sent back to Greifswald for future use.

110 GHz, 1.3 MW, long-pulse gyrotron oscillator

In many respects, the design of the 1.3 MW, 110 GHz gyrotron is similar to that of the 1 MW device previously developed and demonstrated by CPI [3]. A schematic diagram of the 110 GHz, 1.3 MW gyrotron and magnet is shown in Fig. 7. Although the optics and high-voltage designs of the electron gun for the higher-power gyrotron have been altered for operation at a beam voltage of 96 kV (up from 80 kV for the 1 MW design) and beam current of 40 A, the single-anode gun makes use of the same size cathode as that employed in the 1 MW device. As with the 1 MW gyrotron, the 1.3 MW design utilizes oil insulation in the electron gun region. The interaction cavities of both the 1 and 1.3 MW gyrotrons are designed to operate in the $TE_{22,6,1}$ mode, but the cavity has been modified to optimize the efficiency for an output power level of up to 1.5 MW, while keeping ohmic losses on the cavity walls at values that are consistent with standard cooling techniques.

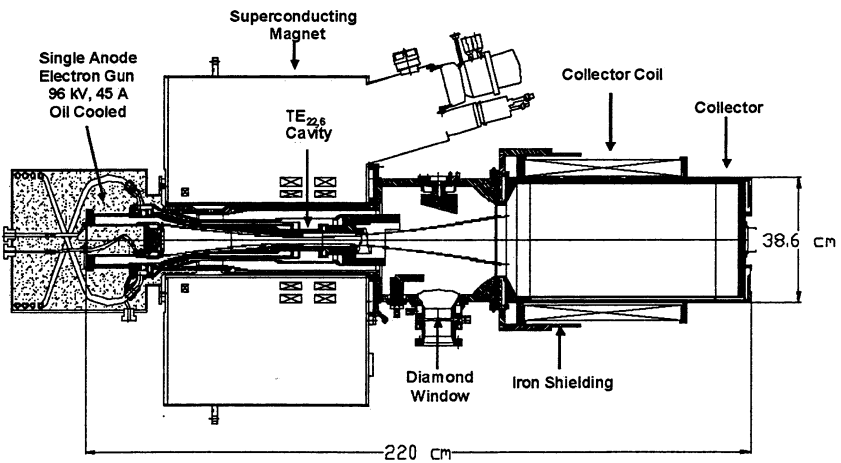

Fig. 7. Schematic diagram of 110 GHz, 1.3 MW gyrotron and magnet

Like the 110 GHz, 1 MW gyrotron, the internal converter for the 1.3 MW device consists of a rippled-wall launcher and four mirrors to convert the $TE_{22,6}$ mode produced in the cavity into a fundamental Gaussian mode at the output of

the gyrotron. The CVD diamond output window for the 1.3 MW gyrotron has a clear aperture of 88 mm, which is somewhat larger than the 50.8 mm aperture of the earlier 110 GHz, 1 MW gyrotrons, but the same size as the aperture of the 140 GHz gyrotron. To accommodate the larger window, the internal converter mirrors have been changed to produce a larger output beam at the window. The collector design has been modified in two ways from that of the 110 GHz, 1 MW gyrotrons. First, for the 1.3 MW gyrotron, collector depression is employed to reduce the amount of power that must be dissipated in the collector and also to increase the overall device efficiency. A single-stage, depressed collector, with a configuration similar to the 140 GHz gyrotron, is employed. Nominally, the collector voltage would operate at 71 kV and the body voltage would be 25 kV to yield the full 96 kV accelerating or cathode-to-body voltage. A second departure from the 1 MW collector design involves the collector size and collector-coil geometry. The collector for the 1.3 MW gyrotron is significantly longer and somewhat smaller in diameter than that of the 1 MW gyrotron, and, thereby, easier to manufacture. While the 1 MW design employs a collector magnet coil near the entrance of the collector, the 1.3 MW design relies on a room-temperature coil that covers much of the collector length as well as iron shielding to tailor the magnetic field in the collector region. Both the 1 MW and 1.3 MW collector designs rely on modulation of the collector coil current to spread the distribution of the spent electron beam over the surface of the collector in the axial direction. A photograph of the 110 GHz gyrotron prior to bakeout processing (no collector coils or hardware attached) is shown in Fig. 8.

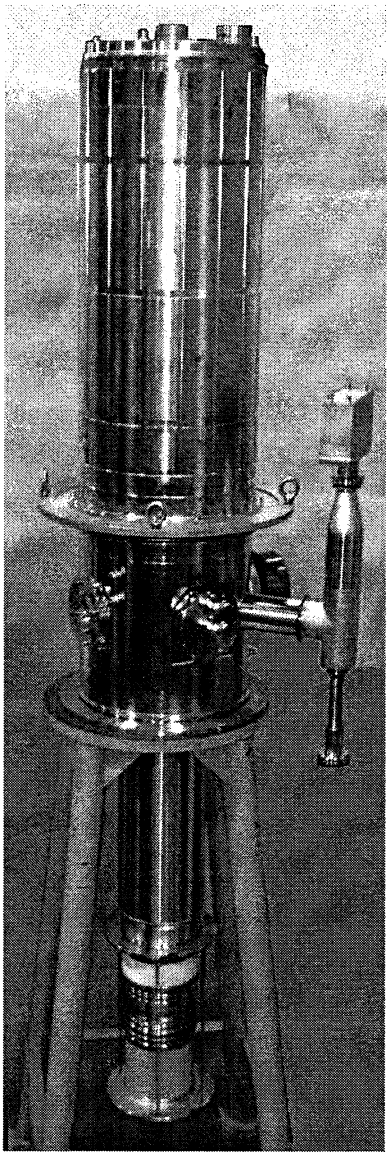

Fig. 8. Photograph of 110 GHz, 1.3 MW gyrotron before bakeout processing.

Initial tests were carried out under short-pulse conditions at CPI. The maximum output power observed in these tests was 1.28 MW with an efficiency of 42.3%. The collector voltage was 73.3 kV, the body voltage was 26 kV and the beam current was 41.2 A. At the nominal operating conditions, output power levels of 1.25 MW were obtained.

Following short-pulse tests on the gyrotron, the tube was aged out to pulse durations of 10 s at the 25 A long-pulse, beam-current limit of the CPI power supply. Output power levels for long-pulse operation ranged from 500 to 520 kW for beam currents of 24–25 A. Collector and body voltages for the 10 s pulses were 73.5 kV and 20.9 kV, respectively. Future tests will be performed at General Atomics where increased power supply capabilities should enable operation up to the maximum output power levels of 1.2–1.3 MW for 10-s pulses.

W-band, broadband gyro-TWT amplifier

CPI is also involved in the development of high-frequency gyrotron amplifiers. For example, a broadband W-band gyro-TWT amplifier, intended to be used as a driver for higher-power gyrotron amplifiers, has recently been fabricated and tested. The design goals are 500 W peak output power at 40% duty factor and an 8 GHz, –3 dB bandwidth centered at 96 GHz. Efficiency, which is normally low for a low-voltage gyrotron, is not of great importance for the intended application. Design features and measured performance are described below.

A double-anode magnetron injection gun was designed to produce a high-quality electron beam at the nominal operating point: 30 kV cathode voltage, 14 kV mod-anode voltage, relative to cathode, 0.8 A beam current, 33.5 kGs axial magnetic field in the interaction region, and perpendicular-to-parallel velocity ratio, α, 0.65. The average guiding center radius of the beam is 0.1 cm, which is near the electric field maximum of the TE_{01} operating mode in a 0.20 cm radius cylindrical waveguide. At the nominal operating point, the RMS perpendicular velocity spread is predicted to be 1.2%.

The TE_{01} mode interaction circuit was designed with a large-signal gyrotron modeling tool, MAGY [2]. The circuit, which is 28 cm long, consists of a 23.75 cm section of alternating metal and lossy ceramic (80% BeO, 20% SiC) pieces, followed by a 4.25 cm unloaded, metal-walled output region. The inner diameters of the metal and ceramic circuit components are 0.20 cm. A detailed analysis of the interaction circuit stability, including the effects of reflections from the window, was performed. At the nominal values of beam voltage, α, and magnetic field, the TE_{01} mode is not predicted to oscillate at beam currents below 1.2 A, which provides a 50% margin of safety at the design beam current, 0.8 A. All other potential competing modes, including the TE_{11} at ~73 GHz, TE_{21} at ~79 GHz, and the second harmonic TE_{02} at ~169 GHz, have predicted start-oscillation currents above 1.8 A. The maximum predicted peak output power is

approximately 1.7 kW and the predicted –3 dB and –1 dB bandwidths are 7.1 and 8.8 GHz, respectively. For all frequency points, an input power of 0.01 W in the TE_{01} mode of the circuit was assumed. This input power is consistent with the performance of the available broadband solid-state driver, which was designed to provide a minimum output power of +17 dBm over the 92–100 GHz frequency band.

A coaxial input coupler was designed to efficiently convert power from the TE_{10} rectangular waveguide mode to the TE_{01} cylindrical waveguide mode in the interaction circuit over the frequency band of interest. The power is transferred from the fundamental rectangular guide into the TE_{51} mode of an outer cavity and magnetically coupled to the TE_{01} mode through five slots in the wall between the outer cavity and the interaction circuit. A cylindrical section of waveguide between the input coupler and electron gun that is cut-off for the operating mode preferentially couples power in the forward direction, the direction of the interaction circuit. Cold tests of the input coupler showed better than –1.5 dB coupling to the TE_{01} mode over the 92–100 GHz frequency range.

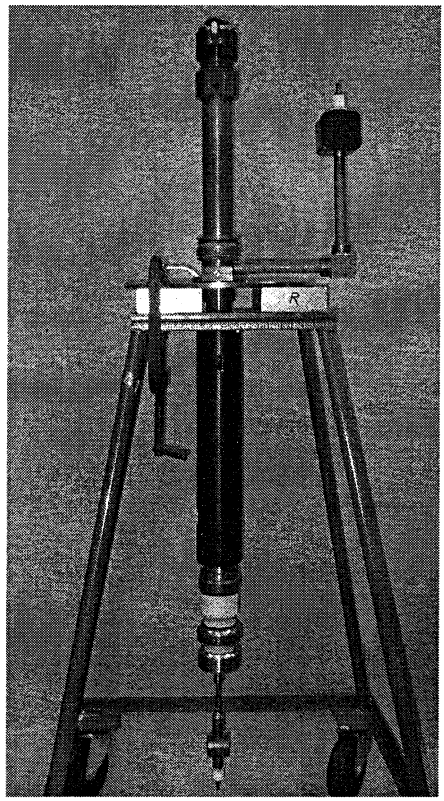

Fig. 9. Photograph of the W-band gyro-TWT amplifier.

The 0.8 inch (20.32 mm) diameter collector, which also serves as the output waveguide, was designed with water cooling for power densities up to 600 W/cm^2. Two room-temperature coils are used to tailor the falling field of the superconducting magnet and effectively spread the spent electron beam.

In order to achieve good transmission over the broad operating bandwidth, a double-disk chemical vapor deposition (CVD) diamond output window was used. The two disks, which are separated by air, are spaced such that a VSWR better than 1.1 is achieved over the band. The air-side window is mechanically tunable to allow adjustments during operation. A photograph of the gyro-TWT amplifier is shown in Fig. 9.

The gyrotron and superconducting magnet were installed in the test stand and operation began late in 2004. A plot of calorimetrically measured peak

output power as a function of frequency is shown in Fig. 10. The input power measured at the gyrotron flange is also shown on the plot. Taking into account losses in the drive line between the input flange and the input coupler, as well as coupler losses, the power arriving in the TE_{01} mode in the interaction circuit is approximately 6 dB less than the power measured at the flange. As shown in the figure, a peak output power of 1.5 kW with 7 GHz –3 dB bandwidth was achieved at 15% RF duty factor. Measurements of output power versus drive power showed that at the lower edge of the frequency band (92–93 GHz) the gyro-TWT is over driven, at the middle of the band (94–96 GHz) the output power is nearly saturated, and at the high end of the band (97–100 GHz) the gyro-TWT is operating in or near the linear gain region.

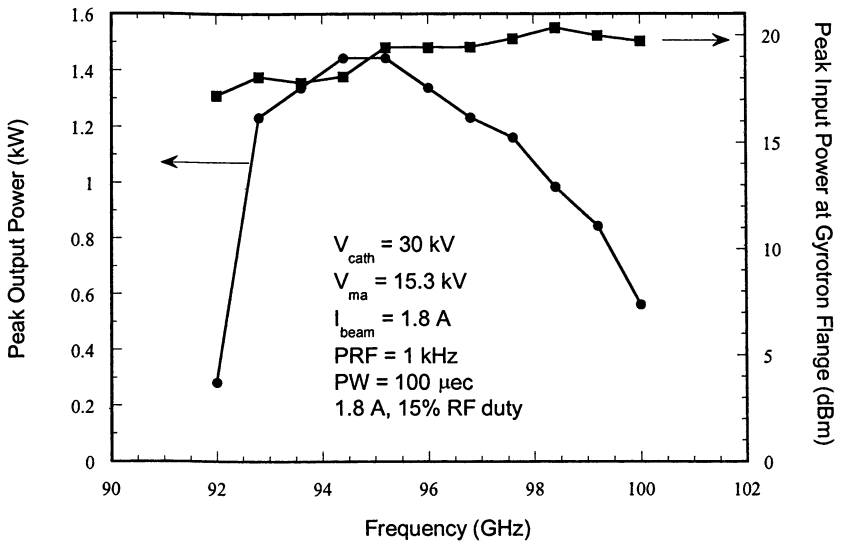

Fig. 10. Measured peak output power (circles) and drive power (squares) as a function of frequency at 15% RF duty factor.

Although the measured peak output power and bandwidth are similar to the design point, the beam current and drive power required to achieve the results shown in Fig. 10 are significantly different from the design. At lower beam currents, closer to the design value of 0.8 A, the bandwidth was reduced to below 5 GHz. The reasons for the better performance at higher beam currents and the less than predicted gain are currently under investigation.

Measurements of the limiting oscillation, the frequency of which corresponded to the TE_{01} operating mode, as a function of beam current, interaction magnetic field, and gun coil current (pitch factor) were compared with theory.

The agreement between the observed onset of the TE_{01} mode oscillation and the predictions of theory was excellent over a wide range of operating parameters.

Future work will include optimizing the bandwidth of the gyro-TWT, conducting measurements of phase as a function of frequency, and a detailed comparison of measured data and predictions of theory.

References

1. *Blank M., Felch K., Borchard P., Cahalan P., Cauffman S.R., Chu T.S., Jory H.,* Demonstration of a high-power long-pulse 140 GHz gyrotron oscillator, IEEE Trans. Plasma Sci., **32,** 867-876 (2004).
2. *Botton M., Antonsen Jr.T.M., Levush B., Vlasov A., Nguyen K.,* MAGY: A time dependent code for simulation of electron beam devices, IEEE Trans. Plasma Sci., **26**, 882-892 (1998).
3. *Felch K., Blank M., Borchard P., Cahalan P., Cauffman S.R., Chu T.S., Jory H.,* Recent Tests on 500 kW and 1 MW, Multi-second-Pulsed Gyrotrons, Proc. 12th Joint Workshop on Electron Cyclotron Emission and Electron Cyclotron Heating, Ed. by Giruzzi G. Singapore, World Scientific Publishing Co. Pte. Ltd., 2003. P. 565-570.

GYROKLYSTRON OPERATING AT A SEQUENCE OF HIGH-ORDER MODES

E. V. Ilyakov, I. S. Kulagin, S. V. Kuzikov, M. A. Moiseev, M. I. Petelin, A. S. Shevchenko, N. I. Zaitsev

Institute of Applied Physics, Nizhny Novgorod, Russia

A 30-GHz gyroklystron operating at a sequence of TE_{511}, TE_{521} and TE_{531} modes and driven with a 300–500 kV electron beam is hoped to deliver ~10 MW power in ~1 μs pulses.

Introduction

In future "warm" TeV electron-positron colliders, accelerating structures are planned to be fed by 30–100 GHz amplifiers. In this frequency band, multi-megawatt powers can be produced by amplifiers of only the fast-wave type [1]: ubitrons (free electron masers) [1, 2], magnicons [3] or gyroklystrons [4–6]. This paper deals with a version of gyroklystron (Fig. 1) [6] featured with using high order (space-developed) modes common for modern high-power gyro-monotrons.

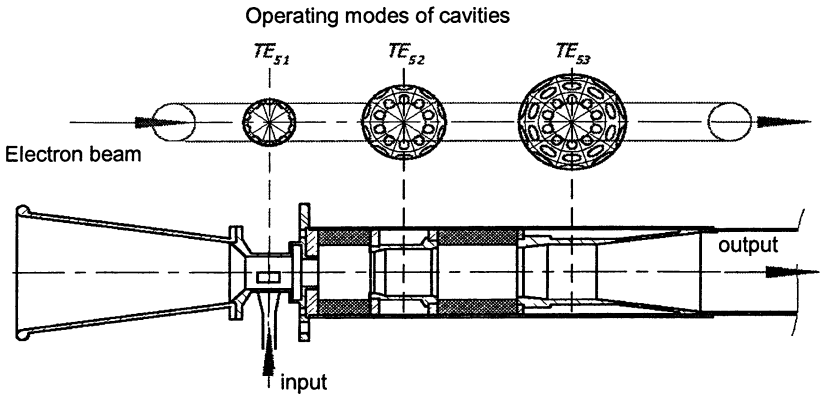

Fig. 1. Scheme of 3-cavity gyroklystron

Principle and design of gyroklystron

At the shortest microwaves, especially at millimetre waves, the gyroklystron is advantageous over the conventional klystron amplifier due to the opportunity to operate at high order modes of oversized cavities. Only the very first

gyroklystron (realized in 1967 and published in 1978 [7]) operated at the lowest mode TE_{11}. Later the preference was given to axis-symmetrical, TE_{0n}, modes, because their electric RF field at the cavity wall is zero. However, any TE_{0n} mode

1) has a non-zero surface magnetic field fraught with the pulse periodic heating fatigue,
2) cannot withstand, if the radial index n is large, competition with modes possessing non-zero azimuthal indexes.

From the latter viewpoint operating modes possessing non-zero azimuthal indexes are preferable: if the tubular electron beam formed with the high-compression magnetron injection gun is injected into the inner caustic of such a mode, rival modes loose in coupling to the beam and, hence, in competition with the operating one. As for the relevant RF electric and magnetic fields at the cavity wall, they are relatively low compared with those at the caustic, which favours to avoid the RF breakdown and fatigue – of course, if the pulse duration is not excessively long.

The above considerations were put into the basis of scheme shown in Fig. 1. In all cavities of the axis-symmetric system, operating modes have a common azimuthal index. In the output cavity, to reduce the RF field at the metal surface, the radial index of the mode is relatively high. In the input and penultimate cavities, to enlarge the RF field coupling with the electron beam, to loosen tolerances on the beam azimuthal inhomogeneity and to provide a high gain of the amplifier, the radial indexes are chosen relatively small. Drift tubes between cavities, outside the tubular electron beam, are filled with a distributed RF absorber in order to suppress parasitic self-excitation. The electron beam is formed with a magnetron injection gun of the triode configuration (Fig. 2).

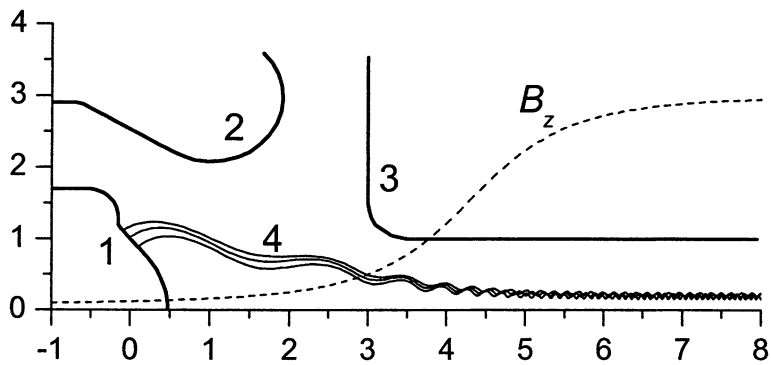

Fig. 2. Electron gun profile: *1* – cathode, *2* – control anode, *3* – RF and collector block, *4* – electron beam, B_z is longitudinal magnetic field distribution.

Introductory experiments

A gyroklystron of the type shown in Fig. 1 was designed for operation at 30 GHz. Cavities were optimised, in succession, for modes TE_{511}, TE_{521} and TE_{531}. The magnetron-injection gun (Fig. 2) designed with account of space charge had to form the helical electron beam with orbital velocity spread less than 20% and the pitch-factor in the range from 1.3 to 1.6.

At first, to check the electron beam quality, a single cavity was used instead of the 3-cavity system shown in Fig. 1. Experimental investigation was carried out at the accelerator "Saturn" in the single pulse regime [8]. The cavity was sufficiently long and, correspondingly, self-excited. The free-running gyrotron fed with 300 kV/80 A electron beam delivered 12 MW output power with 50% efficiency at the pulse duration 0.2 μs [9].

After that, experiments with the gyroklystron began. 2- [10] and 3-cavity versions were tested. The structure underwent some modifications to exclude various kinds of self-excitation and to enlarge power, efficiency and gain. Presently, to the paper submission date, one of the best combinations of parameters obtained with the 3-cavity 30 GHz gyroklystron (with the sequence of TE_{511}, TE_{521} and TE_{531} modes) is

- output power 6.5 MW,
- efficiency 18 %,
- gain 31 dB,
- gun voltage 320 kV,
- electron beam current 110 A,
- RF pulse duration 0.5 μs.

The relevant voltage pulse and RF pulse envelope are shown in Fig. 3.

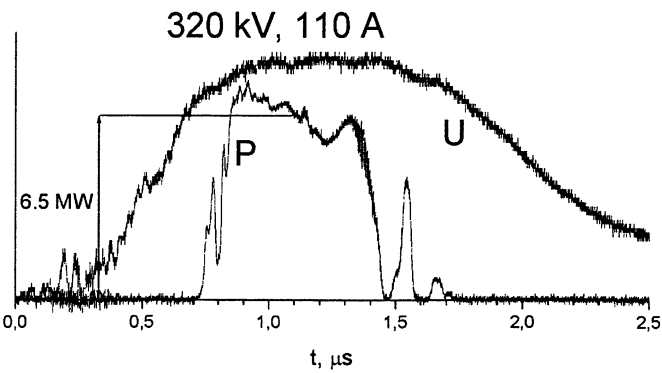

Fig. 3. Performance of 30-GHz gyroklystron

Further plans

For further experiments, instead of the present-date single-pulse machine, a test stand based on a 500 kV / 300A / 1 μs modulator with a pulsed transformer manufactured by Stangenes, California, is being constructed and a relevant electron gun is being manufactured.

Supported by grants of ISTC and RFBR, assisted by SLAC and CLIC, the IAP plans to develop, during 2–3 years, a 30-GHz three-cavity gyroklystron delivering output power of 20–30 MW in 0.5 μs pulses.

Acknowledgement

The IAP gyroklystron team is grateful to A. Litvak, I. Wilson, G. Caryotakis, and M. Thumm for moral and financial support, to SLAC experts R. Koontz, S. Gold and A. Krasnykh for technical assistance and to J. Hirshfield, E. Jensen, R. Ruth and W. Manheimer for valuable consultations.

The research is supported by the International Science and Technology Center, grant No. 3169, and the Russian Foundation for Basic Research, grants No. 03-02-16650, 04-02-16340.

References

1. *Whittum D.H.* Millimeter Wave Drivers For Future Linear Colliders: Preprint SLAC-Pub-7809, 1998. 5 p.
2. *Freund H.P., Jackson R.H., Danly B.G., Levush B.*, IEEE Trans. Plasma Sci., 1999, **27**, 243.
3. *Nezhevenko O A., LaPointe M.A., Yakovlev V.P., Hirshfield J.L.*, Proc. 2003 Particle Accelerator Conf., Portland, Oregon, 2003.
4. *Gouveia E.S., Lawson W., Hogan B. et al.*, Proc. RF-2003, Berkeley Springs, **AIP-691**, 79.
5. *Neilson J., Ives R.L., Read M.E. et al.*, Proc. IVEC-2003, Seoul, 346.
6. *Ilyakov E., Krasnykh A., Kulagin I. et al.*, Proc. IVEC-2004, Monterey, 61.
7. *Andronov A.A., Flyagin V.A., Gaponov A.V. et al.*, Infrared Phys., 1978, **18**, 385.
8. *Zaitsev N.I., Ilyakov E.V., Korablyov G.S. et al.*, Instrum. Exper. Techniques, 1995, **38**, 380.
9. *Zaitsev N.I., Zavolsky N.A., Zapevalov V.E. et al.*, Radiophys. Quantum Electron., 2003, **46**, 816.
10. *Zaitsev N.I., Ilyakov E.V., Kuzikov S.V. et al.*, Izv. Vyssh. Uchebn. Zaved. Radiofizika, 2005, **48**, 830.

MEGAWATT-POWER GYROTRONS FOR FUSION

G. G. Denisov[1], *A. G. Litvak*[1], *V. E. Myasnikov*[2], *E. M. Tai*[2], *V. I. Ilin*[3], *V. E. Zapevalov*[1]

[1]Institute of Applied Physics, Nizhny Novgorod, Russia
[2]GYCOM Ltd, Nizhny Novgorod, Russia
[3]Kurchatov Institute, Moscow, Russia

Introduction

Gyrotrons are the most powerful sources of millimetre wavelength radiation [1–7]. They are widely used in electro-cyclotron-wave systems of plasma fusion installations (e. g. see [8–12]). For the next generation of fusion installations gyrotrons with unit power at least 1 MW in CW regime are required. The present paper continues in the frames of SMP Conference proceedings [6, 7] to monitor general tendencies in MW-power gyrotron development.

First experiments with gyrotrons were done in 1964 [1–3]. In 70-s great parameters for microwave sources were demonstrated with gyrotrons – we can mention here just two of them: 28 GHz/100 kW/CW and 100 GHz/1 MW/100 μs. The first application of gyrotrons for plasma fusion setups TM-3 and TUMAN-2 took place [13]. In 80-s many scientific and industrial institutions worked on development of gyrotrons. Lots of scientific and technological tasks were solved at that time. Even nowadays young gyrotron researchers very often surprised that their "new" ideas were already published in 80-s. Real fruitful collaboration and simultaneously strong competition of the main gyrotron developers began in 90-s with start of ITER activity and wide use of gyrotrons at plasma installations. The requirement of 1 MW/CW gyrotron operated at very high frequency (above 100 GHz) was issued.

In the similar review papers of the previous conferences two first periods of "modern gyrotorn history" in MW gyrotron development were observed. In the period of 1995–1999 the following principal steps were made:

- Efficient gyrotron operation was shown at very high-order modes (e. g. $TE_{25.10}$, $TE_{31.8}$). This solves the problem of cavity thermal loading.
- Demonstration of a depressed collector gave a great move in solving collector and power supply problems.
- Gyrotron windows made of artificial diamond discs were developed. This is still the only option for megawatt gyrotrons.

The highlights of the next period 1999–2002 were also very important:

- Demonstration of a very long-pulse (hundreds seconds) operation of MW tubes equipped by diamond windows and depressed collectors.
- Tests of prototypes for multi-frequency gyrotrons and for 1.5–2 MW gyrotrons.
- Integration and use of MW gyrotron complexes at major fusion installations.

The period 2002–2005 between the two last SPM Conferences gave us: demonstration of CW operation of megawatt power gyrotron, plasma experiments with CW gyrotrons, successful tests of multi-frequency long-pulse tubes, tests of models for 1.5–2 MW gyrotrons, and also interesting effects observed in gyrotrons including demonstration of very high efficiency, output wave reabsorption, frequency stabilization and tuning in gyrotrons, precise control and characterization of output wave beams.

Gyrotrons are developed by four groups (in EU, Japan, Russia and US) and each of them cooperate efforts of several scientific and industrial institutions. In the mentioned period all parties demonstrated very interesting and important results. Let us briefly discuss some of them.

CW operation of MW power level gyrotrons

According to requirements for ECW microwave sources for future stellarator W7-X the gyrotrons should produce 1MW at 140 GHz frequency in "pulses" of 30 minutes tubes. Several years ago [14] EU team was already very close to the goal when they demonstrated 0.9 MW power in 3 minutes pulses. Even for such long pulses the gyrotron operation was limited by overheating of some hidden inner parts of the gyrotron. CPI (US) was also developing a similar gyrotron for W7-X [15].

Gyrotron conditioning towards full power, CW operation started June 2004 at IPP and completed March 2005 (Fig. 1). The power 0.83 MW was measured in the load at the end of the test line in 1800 s pulse. The line consist of 7 quasi-optical mirrors and

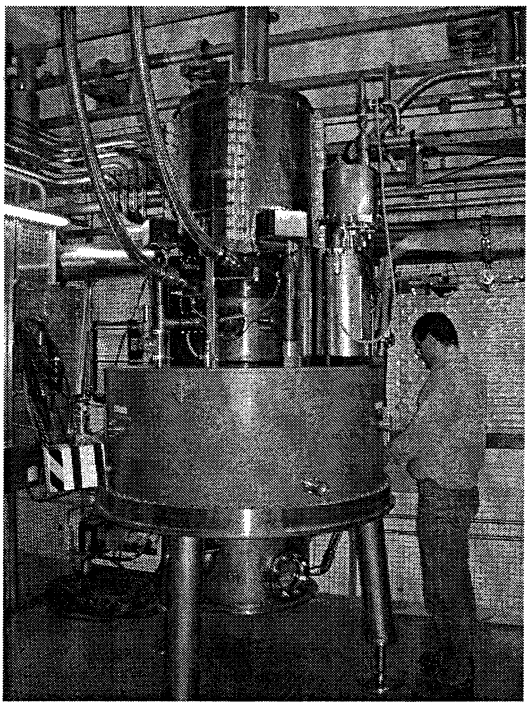

Fig. 1. CPI 140 GHz/1 MW/CW gyrotron under tests at IPP, Greifswald.

diffraction losses in it are estimated as 50–70 kW so the gyrotron output power is close to 0.9 MW. Gyrotron efficiency 33% for this long-pulse test was not optimized.

The gyrotron showed real CW features (Fig. 2).

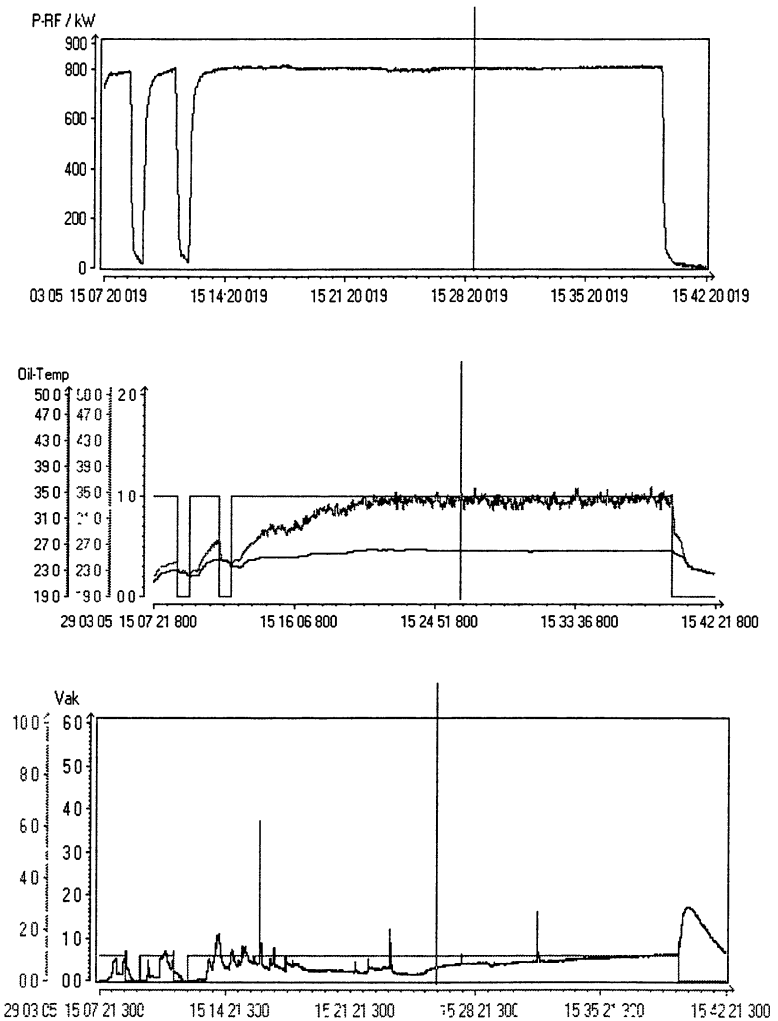

Fig. 2. Some CPI gyrotron parameters in 35 minutes pulse: power (*a*), temperature of some parts (*b*), gas pressure in the tube (*c*). The pictures taken from presentation of Dr. H. Laqua on German–Russian Workshop on ECRH and gyrotrons, 2005.

Use of CW gyrotrons in plasma experiments

Practically all main plasma fusion installations are equipped by gyrotron complexes. Among them there is LHD where 8 pulsed and 1 CW gyrotrons are used. 84 GHz/200 kW/CW gyrotron which is capable to oscillate also in 0.5 MW/10 s mode is described in [16, 17]. Last year the gyrotron was used in a plasma experiment.

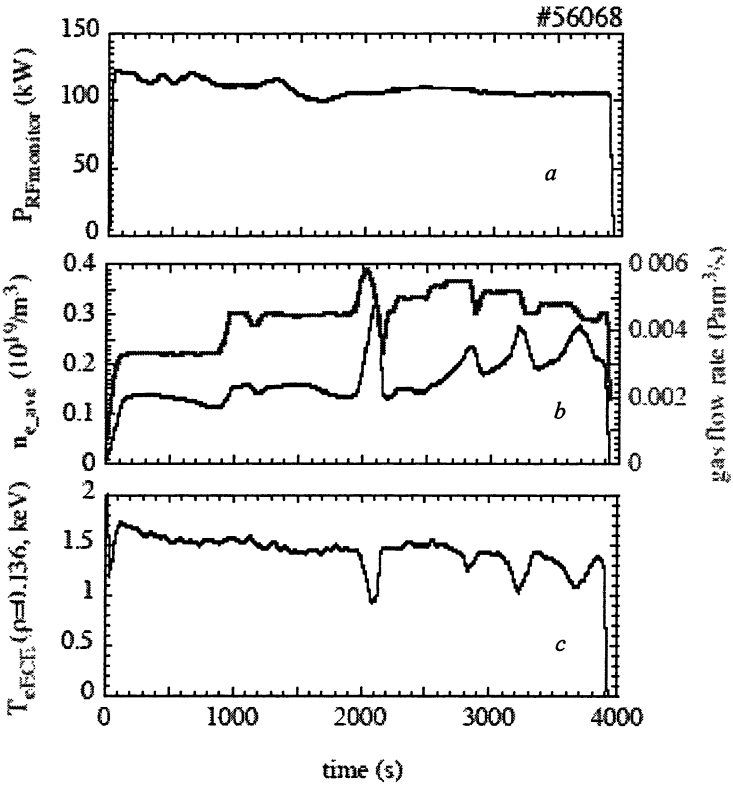

Fig. 3. 3900 seconds plasma discharge (# 56068) at LHD. RF power injected into plasma (*a*), electron concentration (*b*) and temperature (*c*).

The plasma start-up was provided by the pulsed gyrotrons and then CW power successfully sustained the plasma for 3900 seconds [11]. Plasma was quite stable: fluctuations of n_e and T_e were caused by intended change of gas fuelling (Fig. 3). Heating power was terminated at 3900 second. Since near-future fusion machines as W7-X and ITER will operate in pulses of comparable duration the experiment caused great interest.

Dual- and multi-frequency long-pulse gyrotrons

A gyrotron capable to operate at several frequencies is very attractive for plasma experiments. The use of step-tunable gyrotrons can greatly enhance flexibility and performance of ECRH/ECCD systems due to larger accessible radial range, possible replacement of steerable antennas, higher CD efficiency for NTM stabilization. Even two-frequency gyrotrons can bring real improvements of the system. Russian and European teams jointly develop a dual- and multi-frequency gyrotrons for 105–140 GHz frequency range [17, 18, 28].

The main problems in development of multi-frequency gyrotrons are to provide:

- efficient gyrotron operation at different modes,
- efficient conversion of different modes into a Gaussian beam,
- broadband or tuneable window.

The multi-frequency gyrotron under development is based on a diode type of electron gun. This resulted in the change of optimal electron beam radius (approximately as $f^{1/3}$, f is frequency) and consequently in the necessity of an additional collector coil correcting position of the beam on the collector surface. Two window concepts were considered: Brewster window and two-disc adjustable window. Both concepts imply the use of CVD diamond discs with diameter of brazed cuffs of 88 mm. The Brewster window is very attractive because of very wide instant frequency band, however the converter design in this case is more complicated and it was decided that in initial tests the first frequency tunable gyrotrons would be equipped with the two-disc windows (Fig. 4).

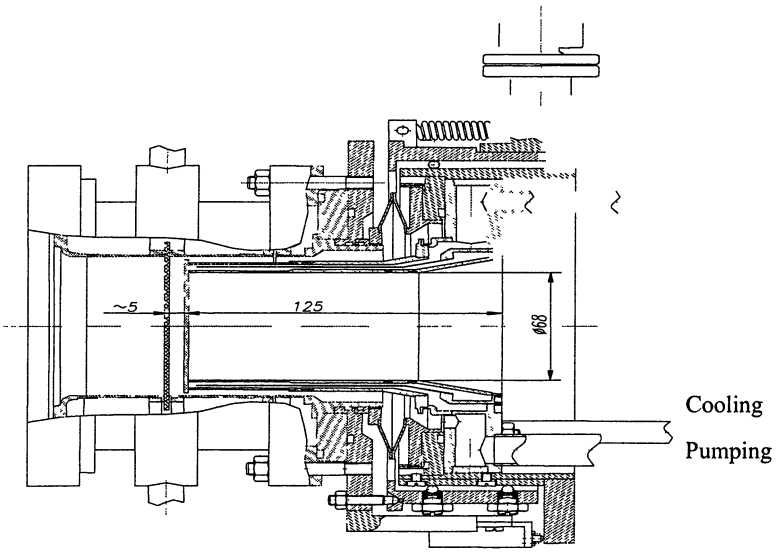

Fig. 4. Double-disc window for a multi-frequency gyrotron. The window consists of a single-disc window, a carrier unit with a flexible copper cuff for adjusting of the second disc, tunable unit with the second disc.

Dual-frequency gyrotron has a cavity using $TE_{22.8}$ and $TE_{17.6}$ modes correspondingly for 140 GHz and 105 GHz operation, internal quasi-optical converter of the cavity mode in the output wave beam, output window based on diamond disk transparent for both frequencies at its 1.8-mm thickness and collector with additional coil sweeping electron beam over its surface. In the two tested dual-frequency gyrotrons, power in the output Gaussian beam exceeding 0.9 MW at 140 GHz (radiated power over 1 MW) and 0.7 MW at 105 GHz (radiated power of 0.8 MW) was attained at specified 10-s pulse duration with acceptable current waveform.

Stray radiation, which was measured for both operating frequencies as 12–15% of generated power, is not dangerous at 10-s pulses from the viewpoint of any gyrotron part overheating but represents the essential loss of power. Internal mode converter with a pre-shaping procedure consisting of a dimpled-wall waveguide launcher and four mirrors recently developed for the dual frequency gyrotron reduces the power fraction carried away by stray radiation to about 3%.

In parallel to double-disc development a Brewster window is under study (Fig. 5). A window version based on a circular disc was chosen since the brazing of a circular disc is much simpler than of elliptical one. A set of mirrors forms a required wave beam size at the discs and provides an oblique incidence of the beam. The window scheme was checked in a special experiment with 105–140 GHz gyrotron and BN ceramics disc. In short pulses (0.1 seconds) limited by ceramic heating the gyrotron showed a reliable operation at 11 modes in the frequency range of interest.

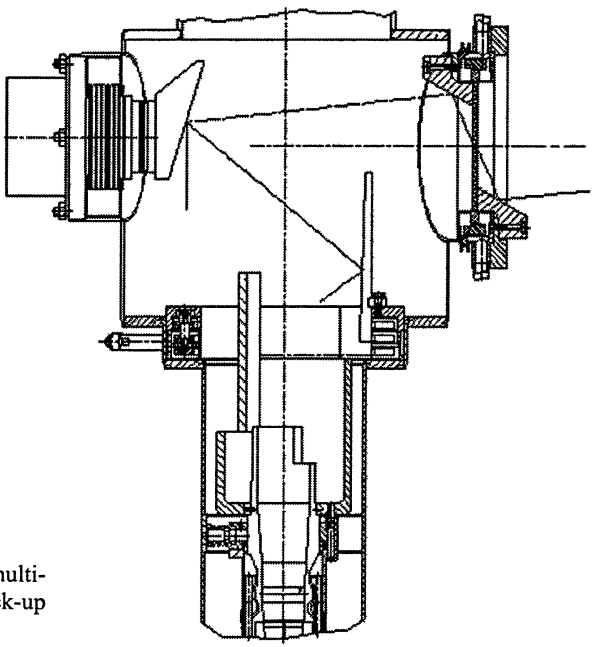

Fig. 5. Output unit of the multi-frequency gyrotron mock-up with BN Brewster window.

Development of 1.5–2 MW power gyrotron prototypes

There are two lines in development of gyrotrons with enhanced power: to advance conventional-type gyrotrons with cylindrical cavities and to develop more complicated but promising gyrotrons with coaxial cavities.

IAP/GYCOM and JAERI/Toshiba teams study a possibility to use a higher order mode in a conventional cavity and hence increase power of a gyrotron (Fig. 6). Similar design based on $TE_{28.12}$ and $TE_{31.12}$ modes are in consideration (see Table) [17, 19, 28].

Main parameters of the GYCOM/IAP 1.5 MW gyrotron

Cylindrical Cavity Mode	$TE_{28\,12}$
Cavity diameter	41.5 mm
Peak thermal load for ideal copper	< 1.35 kW/cm^2
Beam voltage	100 kV
Beam current	50 A
Pitch-factor	1.2
Efficiency (without DC)	30–33%

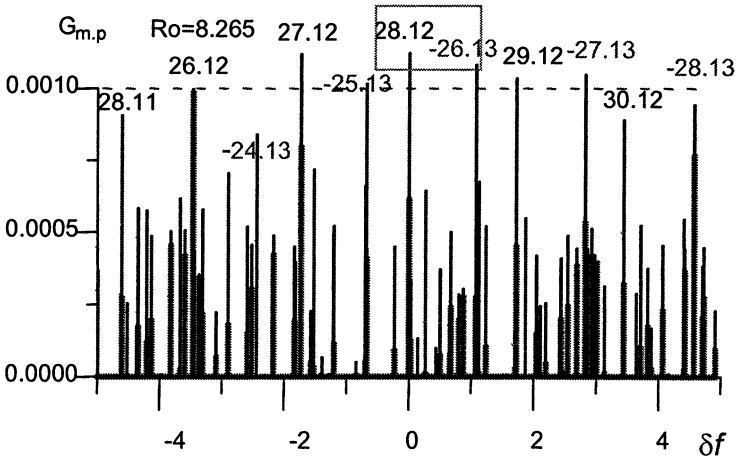

Fig. 6. Spectrum of critical frequencies/coupling coefficients of parasitic modes relatively operating mode frequency and G_{mn} factors for 1.5 MW IAP/GYCOM gyrotron.

So far both teams showed gyrotron output power 1.1–1.2 MW, however efficiencies were somewhat less than required ones (Fig. 7). Experiments continue.

It was demonstrated many years ago that a coaxial cavity gyrotron can operate at high-order mode. Real design of 1.5–2 MW coaxial gyrotron and its magnet is rather complicated. The main effort in the development of the coaxial tube is carried out by EU team [20]. Many encouraging results (e. g. 2.2 MW at 165 GHz frequency) have been obtained in short pulse experiments though there are some open questions as discrepancy in predicted and measured de-

pendences of the output power versus electron energy (Fig. 8). No long-pulse experiment was carried out so far.

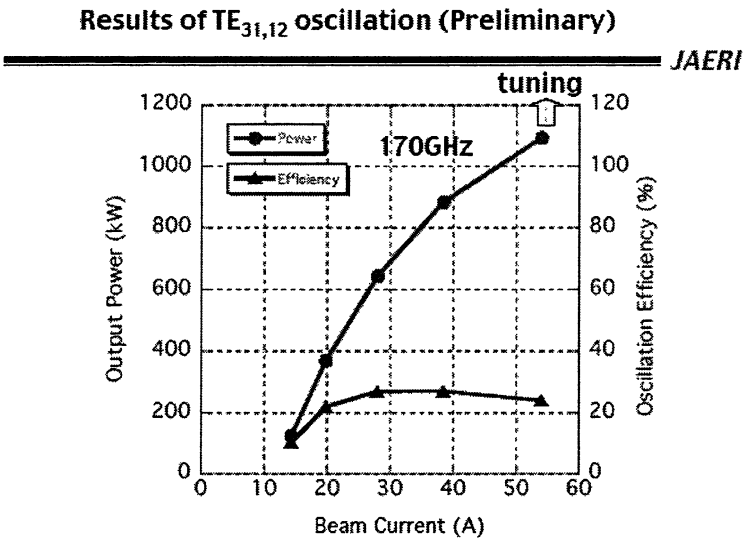

Fig. 7. First test results for JAERI gyrotron with increased power

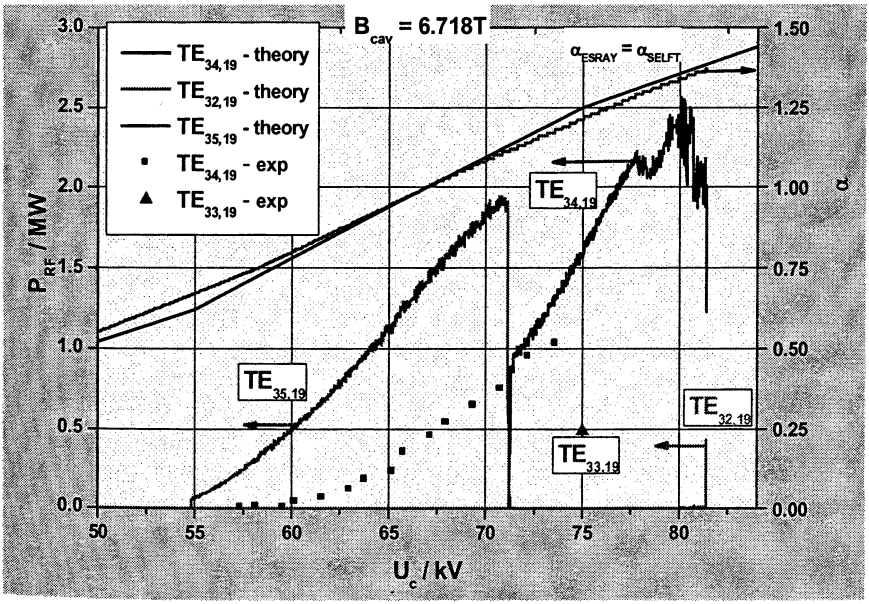

Fig. 8. Preliminary test results for the EU coaxial gyrotron. Short-pulse (5 ms) model

Some other development results

During last 3–4 years some supplementary interesting experiments and studies were performed which were very important to understand processes in gyrotrons and to enhance gyrotron parameters. There is no possibility to observe all of them and here we just mention very few things.

High-efficiency gyrotron

A megawatt power gyrotron with a very high efficiency up to 70% was tested (Fig. 9). The 75 GHz gyrotron is equipped with a single-stage depressed collector. The tests were performed for electron beam energy 77 keV = (52 keV + 25 keV).

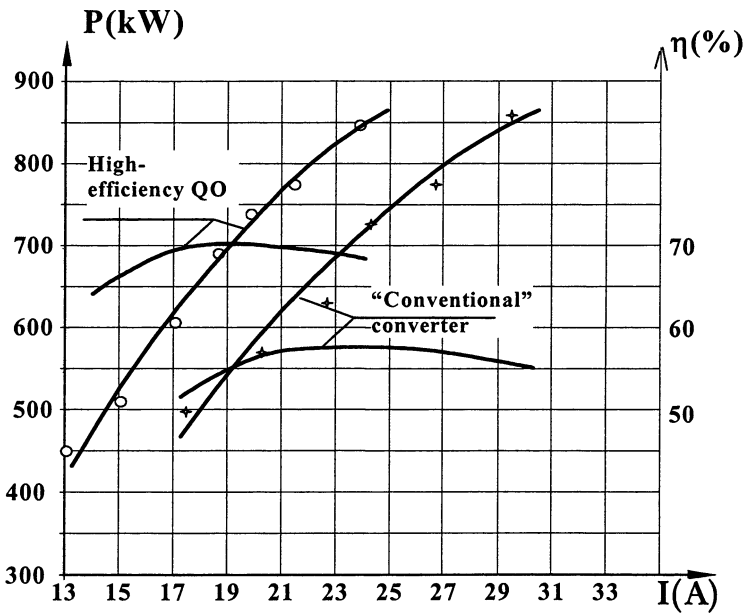

Fig. 9. Power and efficiency of 75 GHz gyrotron versus current for the tube equipped with conventional and high efficiency quasi-optical mode converter.

Since the gyrotron efficiency was not usual for a megawatt power tube the gyrotron was carefully analyzed. It was discovered that this high efficiency resulted from two factors: very good electron beam quality at currents around 20 A and very good performance of the mode converter providing near 99% Gaussian mode content in the output beam and only about 1% diffraction losses inside the tube (Fig. 10).

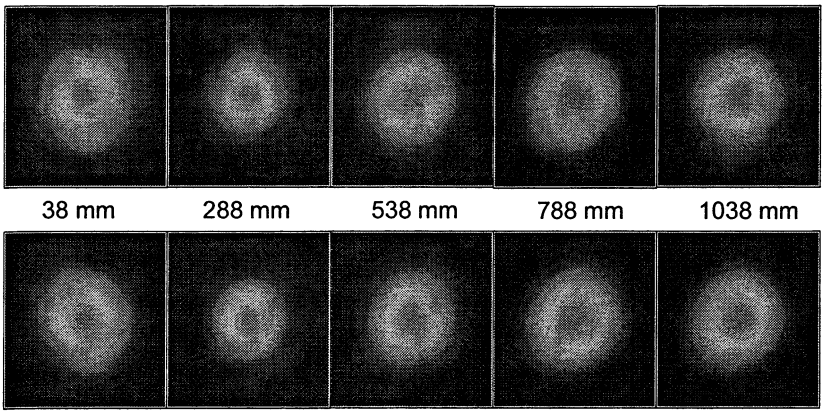

Fig. 10. Wavebeam structures (amplitude distributions) at various distances from the gyrotron window: measured structures (upper row) and calculated (lower row) ones. Gaussian mode content is near 99%.

It is important to note that the gyrotron was fabricated by use of industrial technology and tested at pulse duration of 0.1 seconds which defines in general the tube behaviour at longer pulses.

CVD diamond window growing and brazing

The windows based on a CVD diamond are very expensive but today they are the only option for a megawatt CW window. Calculations show that the windows based on the best discs are capable to transmit even 2–3 MW power. Diamond windows allow edge cooling of discs by water at room temperature. This makes their use much more comfortable as compared with previous window schemes operating at cryogenic temperatures or using some sophisticated coolants.

It is necessary to note that a very extensive study of electrical, mechanical and heat properties of CVD discs is carried out at FZK and their papers content a lot of information [21–22].

Diamond discs for gyrotron windows must be brazed to metal constructions with a high temperature alloy in order the tube can pass the process of baking out.

Last years significant efforts were done by IAP/GYCOM, Nizhny Novgorod in order to solve the whole scope of problems associated with the use of CVD diamond windows in gyrotrons: growing of discs (Figs. 11, 12), their cutting and polishing, and then high-temperature brazing and mounting to a tube [23].

Two setups have been put into operation: the first one bought from Aixtron company, Germany (but without technology) is based on a magnetron and conventional receipts for discs growing, the second one is an experimental gyrotron based setup operating at high frequency 30 GHz and it aims to increase the growth rate of the procedure.

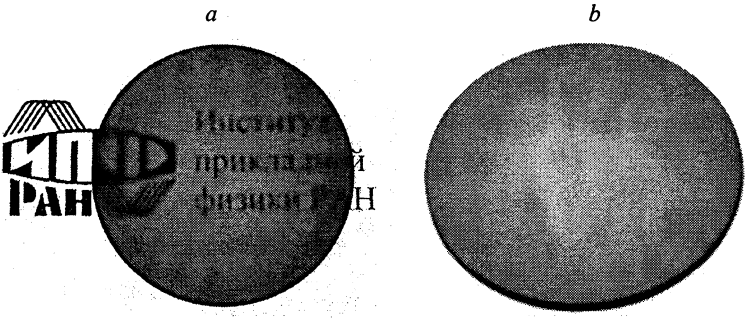

Fig. 11. IAP diamond disk of 75 mm in diameter: *a* – as grown (1.6 mm thickness at the center), *b* – the disc after polishing, 1.35 mm thickness.

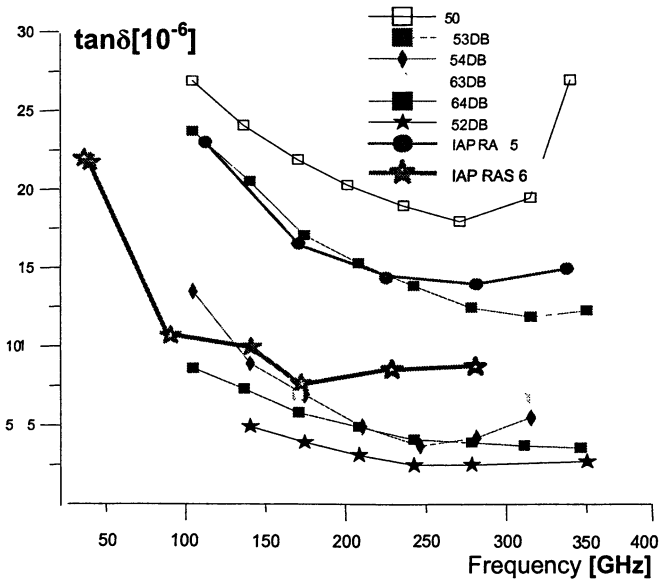

Fig. 12. Loss tangent for some De Beers and IAP/GYCOM CVD diamond discs. Measurements done at IAP by V. V. Parshin.

The IAP/GYCOM discs have been successfully brazed at near 800 °C temperature to metal constructions and will be tested soon with high-power gyrotrons.

Advanced methods for calculation of gyrotron microwave systems

Last years a great progress was demonstrated in development of numerical methods for analysis and synthesis of oversized gyrotron systems: cavities, up-

tapers and quasi-optical mode converters. One particular important task is a design of gyrotron mode converter which transforms high-order operating mode into a Gaussian wavebeam with minimal diffraction, polarization and Ohmic losses. For one chosen mode the amount of mentioned losses can be brought down to a very low value about 1%. The analysis and synthesis methods are based on vector [25] or scalar [26] integral equations or system of coupled waves [27]. Advanced methods allow optimization of the systems also for many frequencies simultaneously. For example, optimization of the mode converter for a multi-frequency gyrotron results in low losses (2–3%) for 10 gyrotron operating modes in the range of 105–140 GHz. Such a mode converter is now under measurements. The optimized launchers look more sophisticated (see Fig. 13) than the conventional ones and their fabrication requires more efforts, nevertheless no doubts that new advanced tubes will be equipped with such quasi-optical components.

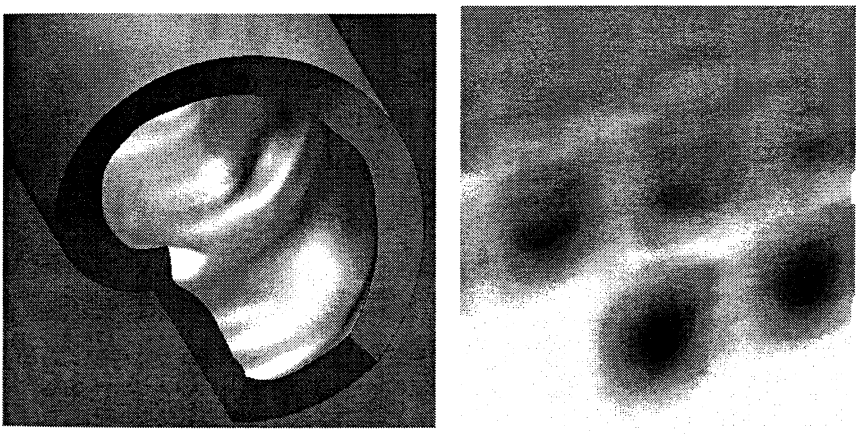

a *b*

Fig. 13. Exaggerated (surface distortion increased about 10 times) inner surface of the launcher for $TE_{25.10}$ mode converter (*a*); *b* – current distribution on the unrolled wall surface (azimuth coordinate is shown as horizontal one). It is seen that just before its launch the wavebeam has near Gaussian spatial distribution.

Summary and future tasks

Strong collaboration and competition of gyrotron developers resulted in great progress in the device performance. Megawatt power level gyrotrons operating in CW regime have been demonstrated. Development studies of multi-frequency gyrotrons and gyrotrons with enhanced power are in progress. First results of these studies are encouraging.

Gyrotron efficiency enhancement is probably even more strategic task than the power increase with some drop of efficiency. High-efficiency gyrotron sys-

tem consumes less power and water for cooling systems, and also more compact. There are no physical limitations for MW gyrotrons to operate with efficiency of 60–70%.

Acknowledgments

The authors are very grateful to their colleagues for discussions and valuable help in preparing the paper.

References

1. *Gaponov A.V. et al.,* Induced synchrotron radiation of electrons in cavity resonators, Pis'ma ZhETF, 1965, 15, 430-435; JETP Lett., 15, 2267-269.
2. *Gaponov A.V., Flyagin V.A., Goldenberg A.L., Nusinovich G.S, Tsimring Sh. E, Usov V.G., Vlasov S.N.* Powerful millimeter-wave gyrotrons, Int. J. Electronics, 1981, v. 51, No. 4, p. 277-302.
3. *Nusonovich G.,* Introduction to the Physics of Gyrotrons, The Johns Hopkins Univ. Press, 2004.
4. *Felch K.L., Danly B.G., Jory H.R. et al.,* Characteristics and Applications of Fast-Wave Gyrodevices, Proc. IEEE, 1999, v. 87, No. 5, p. 752-781.
5. *Thumm M.,* State-of-the-Art of High power Gyro-Devices and Free Electron Masers. Update 2003. Forschungcentrum Karlsruhe, Germany, 2004.
6. *Denisov G.G.,* Megawatt gyrotrons for fusion research. State of the art and trends of development, Strong Microwaves in Plasmas: Proc. 4th Int. Workshop, Nizhny Novgorod, 2000, p. 967-986.
7. *Denisov G.G.,* Development of 1 MW output power level gyrotrons for fusion systems, Strong Microwaves in Plasmas: Proc. 5th Int. Workshop, Nizhny Novgorod, 2003, p. 29-45.
8. *Zohm H. et al.,* Confinement and stability studies with ECRH in ASDEX upgrade, Strong Microwaves in Plasmas: Proc. 5th Int. Workshop, Nizhny Novgorod, 2003, p. 281-295.
9. *Erckman V. et al.,* 20 years of ECRH at W7-A and W7-AS, Strong Microwaves in Plasmas: Proc. 5th Int. Workshop, Nizhny Novgorod, 2003, p. 281-296.
10. *Shimozuma T. et al.,* Recent results of ECH experiment by an upgrated teating system in LHD, Strong Microwaves in Plasmas: Proc. 5th Int. Workshop, Nizhny Novgorod, 2003, p. 307-319.
11. *Yoshimura Y. et al.,* Achievement of one hour discharge with ECH at LHD, Third IAEA Technical meeting on ECRH Physics and technology for ITER, 2-4 May, 2005, Como, Italy.
12. *Lohr J. et al.,* Tests and performance of the six-gyrotron system on the DIII-D tokamak, Strong Microwaves in Plasmas: Proc. 5th Int. Workshop, Nizhny Novgorod, 2003, p. 364-371.
13. *Alikaev V.V. et al.,* Electron cyclotron heating at the TM-3 tokamak, Pis'ma ZhETF, 1972, 15, 41-44; JETP Lett., 2, 27-29.
14. *Dammertz G. et al.,* Status of the 1MW, 140 GHz, CW gyrotron for W7-AS, Strong Microwaves in Plasmas: Proc. 5th Int. Workshop, Nizhny Novgorod, 2003, p. 16-28.
15. *Felch K. et al.,* Recent advances in increasing output power and pulse duration in gyrotron oscillators, Digest of the Joint 30th Int. Conf. on Infrared and Millimeter Waves and 13th Int. Conf. on Terahertz Electronics, Williamsburg, Virginia, USA, September 19-23, 2005, p. 237-238.
16. *Denisov G.G. et al.,* 200 kW/CW Gyrotrons and Transmission Line Components for Fusion Systems, Proc. 6th Int. Vacuum Electronics Conf. IVEC2005, Noordwijk, The Netherlands, April 20-22, 2005, p. 119-120.
17. Denisov G.G., Litvak A.G., Myasnikov V.E., Tai E.M., Recent Results in GYCOM/IAP Development of High-Power Gyrotrons for Fusion Installations, Proc. 6th Int. Vacuum Electronics Conf. IVEC2005, Noordwijk, The Netherlands, April 20-22, 2005, p. 497-500.

18. *Wagner D. et al.,* Current status of the new ECRH system for ASDEX Upgrade, Digest of the Joint 30th Int. Conf. on Infrared and Millimeter Waves and 13th Int. Conf. on Terahertz Electronics, Williamsburg, Virginia, USA, September 19-23, 2005, p. 24-25.
19. *Kasugai A. et al.,* Development of a 170 GHz High-power CW gyrotron for Fusion Application, Digest of the Joint 30th Int. Conf. on Infrared and Millimeter Waves and 13th Int. Conf. on Terahertz Electronics, Williamsburg, Virginia, USA, September 19-23, 2005, p. 287-289.
20. *Piosczyk B. et al,* A 2 MW, CW coaxial cavity gyrotron. Experimental and technical conditions, Proc. 5th Int. Workshop on Strong Microwaves in Plasmas. 2003, Nizhny Novgorod, v. 1, p. 104-110.
21. *Hiedinger R. et al.,* CVD diamond windows for High power gyrotrons, Proc. 23rd Int. Conf. Infrared and Millimeter Waves, Sept. 1998, p. 223-224.
22. *Thumm M.,* Development of output windows for high-power long-pulse gyrotrons and EC wave applications, Int. J. Infrared and Millimeter Waves, 1998, v. 19, p. 3-14.
23. *Vikharev A.L. et al.,* Development of MPACVD technology for high-rate diamond production, these proceedings, v. 2, p. 613-625.
24. *Thumm M. et al.,* Frequency step-tunable (114–170 GHz) megawatt gyrotrons for plasma physics applications, Fusion Engineering and Design, 2001, 53, p. 407-421.
25. *Nielson J.,* Optimal Synthesis of Quasi-optical converters for High-Power Gyrotrons, Proc. 6th Int. Vacuum Electronics Conf. IVEC2006, Monterey, USA, April 22-27, 2006, p. 413-414.
26. *Chirkov A.V. et al.,* Huygens principle application for the field analysis and synthesis in oversized waveguides, J. Radiophys. and Quantum Electronics, 2006, v. 49, No. 5.
27. *Denisov G.G. et al.,* Method for synthesis of waveguide mode converters, J. Radiophys. and Quantum Electronics, 2004, v. 47, No. 8, p. 615-620.
28. Litvak A.G. et al., Recent Results in GYCOM/IAP Development of High-Power Gyrotrons for Fusion Installations, Digest of the Joint 30th Int. Conf. on Infrared and Millimeter Waves and 13th Int. Conf. on Terahertz Electronics, Williamsburg, Virginia, USA, September 19-23, 2005, p. 233-234.

GENERATION OF COHERENT TERAHERTZ RADIATION

V. L. Bratman, E. V. Suvorov

Institute of Applied Physics, Russian Academy of Sciences, Nizhny Novgorod, Russia

Radiation sources based on methods of vacuum electronics and optoelectronics are being now intensively developed for many applications in THz frequency range. Among most prospective THz devices providing higher power than existing ones there are orotrons, conventional and large orbit gyrotrons, and Free Electron Lasers. Contemporary optoelectronics provides generation of THz radiation based on optical radiation rectification at "fast" photo-conductors or at nonlinear optical crystals. Broad-band coherent pulses with high repetition rate are also generated using femtosecond laser technique, while cw and quasi-cw frequency tunable THz radiation is generated using two lasers with frequency difference in THz region, one of them being tuneable.

Terahertz frequency range conventionally defined (not generally adopted) as 0.1–10 THz is also called "terahertz gap" having in mind that these frequencies are still too high for well elaborated means of vacuum electronics and too low for well elaborated optical technique. Nevertheless, the interest to this range is permanently increasing due to numerous important research and technical applications, which are mainly concentrated within two vast domains – spectroscopy and radio-vision (tera-vision). Among them there are fundamental spectroscopy, radio-astronomy, aeronomy, environmental investigations, identification of complex chemical and bio-molecules (including drugs and powder explosives), chemical analysis of composites, solid-state physics and technology, defectoscopy, noninvasive medical diagnostics, communication, material processing, package inspection etc. At present, "terahertz gap" is actively filled from both sides (radio and optics). Harmonic progress assumes appropriate development of both generation and detection techniques and their correspondence to each other depends on the specific problem under investigation. On the other hand, in many laboratories the natural independent development of both generation and detection means takes place irrespectively of any concrete applications. In our presentation, we confine ourselves to the problems and achievements in the field of THz radiation generation. Moreover, we concentrate on the frequencies 0.3 THz and higher having in mind that very impressive results on the long pulse (up to cw regime) gyrotrons of 1 MW power level at frequencies approaching 0.2 THz were presented and discussed to large extent at the Workshop (see, e. g., papers by *M. Thumm et al.*, p. 33-45, and *G. G. Denisov et al.*, p. 62-75, of these proceedings). Even with these restrictions the field is too large to be observed within this short paper, so our review is far from being exhaustive. The main part presented on classical (vacuum) electronics will be devoted to the results obtained with essential contribution from the Institute of Applied Physics, while in optoelectronics part the main ideas and some of impressive results will be presented.

Classical high-frequency electrovacuum devices

In principle, vacuum electronics allows production of coherent Terahertz radiation at any required power level. The most widespread devices – low-voltage Backward Wave Oscillators (BWOs) – enable CW radiation with output power of order $1–10^{-3}$ W at the frequencies of 0.1–1.0 THz with a broad frequency tuning. Gyrotrons provide a fantastic high power up to 1 MW in quasi-CW regime in low-frequency part of the range and tens kW in long pulses at the frequencies up to 0.65 THz. Free Electron Lasers (FELs) also demonstrate very high pulsed power as well as possibility of broadband frequency tuning within entire Terahertz range and even at significantly higher frequencies. It should be noticed, however, that gyrotron operation requires very strong magnetic field: 35 T at the frequency of 1 THz if one would try to generate at the fundamental cyclotron resonance. Terahertz FELs use basically very high electron energy 2–12 MeV that can be only produced in large accelerators. Many applications require relatively compact oscillators with power higher than it can be generated in BWOs, but with operating magnetic field much lower than in conventional gyrotrons and with electron energy much lower than in FELs. In the Institute of Applied Physics (IAP) a few ways for realization of more available and relatively powerful sources with the operating frequency up to 1 THz have being developed. Main efforts are directed now on development of high-harmonic gyrotrons (Large Orbit Gyrotrons, gyromultipliers) and orotrons.

High-frequency vacuum devices are based on use of all mechanisms of collective (stimulated) radiation of electron beams, namely, Cherenkov and transition radiation, Bremsstrahlung and wave scattering. Realization of a stimulated process includes providing conditions, first, for corresponding individual (spontaneous) radiation of a particle and, second, for particle bunching and coherent radiation of formed bunches into a fixed wave. Cherenkov and transition radiation of particles involve slowed-down waves, which are synchronous with moving particles. Such waves are basically concentrated near small-scale electrodynamical elements (periodic structures, gaps in cavities) that complicates obtaining powerful radiation at high frequencies. Unlike this, in Bremsstrahlung and scattering radiation processes electrons can be in resonance with fast waves and respectively they can move far from the walls of electrodynamical systems. Because of this very important distinction, devices based on different radiation mechanisms are more or less distributed over frequency ranges. At relatively low frequencies, $f \leq 30$ GHz, rf devices based on stimulated Cherenkov and transition radiation of rectilinear electron beams (Traveling Wave Tubes, Backward Wave Oscillators, conventional electron valves, klystrons) as well as devices based on Cherenkov radiation of self-arising rotating bunches (spokes) in magnetic field (magnetrons) are almost exclusively utilized. In the range of $f = 30–300$ GHz, all these devices are also very widespread, but their power is sharply decreases with the frequency and the highest power is provided by devices based on stimulated Bremsstrahlung (gyrotrons, FELs), which exploit

interaction of electrons with fast waves[1]. At the frequencies $f > 300$ GHz basically low-voltage BWOs have been widespread during long time, though more complicated devices, namely gyrotrons and FELs demonstrate significantly higher output power and efficiency.

Cherenkov electron devices

The stimulated Cherenkov radiation of rectilinear electron beams is the most spread mechanism, which is used in electrovacuum devices. In such process electrons interact with a synchronous wave whose phase velocity, $v_{ph} = \omega / k_{\|}$, is close to particle velocity, v,

$$v \approx v_{ph} . \tag{1}$$

Here ω, $k_{\|}$ are wave frequency and longitudinal number. The condition (1) can be fulfilled in a case of slow wave only. Therefore, in vacuum such a wave is located near the slowing-down structure that determines surface character of interaction between the electrons and the wave. Actually, in such situation the transverse wave number

$$k_{\perp} = \sqrt{\left(\frac{\omega^2}{\tilde{n}^2} - \frac{\omega^2}{v^2} \right)} \tag{2}$$

is imaginary. Respectively, the wave amplitude exponentially decreases at the distance $L_{\perp}$ from the slowing-down structure, where

$$L_{\perp} = \frac{\beta\gamma}{2\pi}\lambda , \tag{3}$$

$\beta = v/c$, $\gamma = \left(1-\beta^2\right)^{-1/2}$ are electron velocity, normalized to the speed of light, and Lorenz-factor, $\lambda = 2\pi\tilde{n}/\omega$ is the wavelength. At low electron velocity, $\beta << 1$, the characteristic scale is much smaller than wavelength (e. g., $L_{\perp} = 0.01\lambda$ at the accelerating voltage 1 kV).

Because of small characteristic scale a very dense and strongly guided electron beams propagating near the slowing-down structures should be used at high frequencies. However, there are methods for some softening these requirements. The beam can propagate inside a slowing-down structure consisting e. g. from relatively high rods (multi-rod periodic structure). In this case, the wave amplitude inside the structure changes not exponentially, but sinusoidally and significantly slower. This method is used in the most spread electron de-

[1] At relativistic electron energy short-pulse Cherenkov devices also demonstrate very high power because phase velocity of synchronous waves in such devices is close to speed of light and correspondingly these waves are significantly weaker concentrated near the electrodynamical structures than in analogous low-voltage devices (see below Eq. (3)).

vices of millimeter- and submillimeter-wavelength range, namely in BWOs that were designed and manufactured in "Istok" Company, Fryazino [1]. The thickness of the electron beam in such BWO is many times larger than the characteristic scale (3). At the same time because of severe limitations from mode competition the beam width can not be larger than $\lambda/2$. The set of 13 Fryazino's BWOs overlaps continuously the frequency range of 36 GHz – 1.4 THz with typical power level from 40 to 0.5 mW (about 10 mW at 0.3 THz). Another method of enlarging effective beam thickness is utilized in clinotron [2], which represents a variety of BWO. In this device, electrons fall at the angle to the slowing-down structure. Unlike the conventional BWOs, not only relatively thick, but also wide electron beams are used in clinotrons in spite of mode competition and incoherence of radiation probably caused by it. This allows one to generate significantly higher power.

The problem of mode competition can be avoided by use of open electrodynamical systems. As for Cherenkov devices, this method is used in the orotron only [3] (this device is also called Diffraction Radiation Generator, DRG [4] and laddetron [5]). A selective open cavity allows utilizing broad electron beams with high current that provides increasing of output RF power. Another advantage is the high cavity Q-factor that ensures high stability of the frequency generated. At the same time, it results in a narrow band of fine electronic frequency tuning. The orotrons and DRGs have been successfully used at millimeter waves for many years and for a number of applications. In the THz region they can provide higher output power and stability than BWOs [6, 7]. The orotrons are now under development at the IAP and Gycom Ltd. in collaboration with the Institute of Metrology for Time and Space and with the Institute of Spectroscopy, Russian Academy of Sciences. In such a device (Fig. 1), a smooth concave mirror and a flat mirror with multiple-rod periodic structure form the cavity. The periodic structures with periods of 100–170 μm, rod thickness of 30–40 μm and height of 500–700 μm are fabricated using Electric Discharge Machining. The operating voltage and current in the orotrons are within 0.5–5 kV and 50–250 mA, respectively, at pulse duration from 50 ns to 10 ms. The beam with transverse dimensions of 3×0.3 mm propagates between the rods in field of 1.25 T provided by a permanent magnet. The microwave power is radiated from the cavity through the slots in the concave mirror into oversized rectangular waveguide. Output power ranges from 1 W at 0.10–0.18 THz to 60 mW at 0.37 THz. Changing of the operating voltage and the distance between the mirrors provides smooth frequency tuning with a

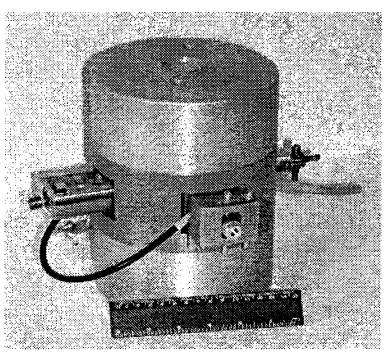

Fig. 1. Photo of a low-voltage orotron

typical range of about of octave. The electronic frequency tuning in the band of 30 MHz in the single pulse and 70 MHz from pulse to pulse (at the single cavity mode) was demonstrated in the experiments. The measured frequency stability amounts to 10^{-7} without additional systems of frequency control.

During a long time orotrons with relativistic electron energy have been also developed at the IAP at centimeter and millimeter waves. A new relativistic orotron is now studied at the IAP with the aim of obtaining a MW power level at THz waves. A preliminary experiment using a conventional quasi-flat cavity, which enables a mechanical frequency tuning, is being carried out. Unlike conventional orotrons and like gyrotrons a diffraction radiation output is used in the oscillator (Fig. 2). A 500 keV/0.5 kA/20 ns electron beam provides a MW power level at the frequency of 0.14 THz with pulse duration of 10 ns [7].

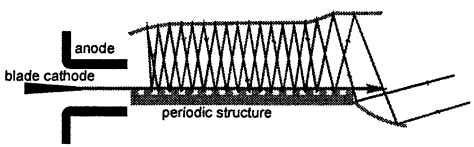

Fig. 2. Schematic of frequency-tunable relativistic orotron.

High-harmonic gyrotrons

Operation of conventional gyrotrons at the fundamental or second cyclotron harmonics is a clear way of producing high power at the frequencies up to 1 THz. However, it requires very strong working magnetic fields (up to 37 T). As an alternative, one can use operation at higher harmonics, which suffers, however, from parasitic excitation of low harmonics. The latter problem can be partially overcome in Large Orbit Gyrotrons (LOGs) and gyromultipliers. In a LOG [8–11], a helical beam of electrons encircling the axis of axisymmetric microwave system provides a better mode selection and more efficient operation at high harmonics in comparison with polyhelical electron beams which are exploited in conventional gyrotrons. Only co-rotating cavity modes $TE_{m,p}$ with the azimuthal index m equal to the resonance harmonic number s can be excited by a thin centered beam in a LOG. It should be, however, noticed that generation of appropriate beams with a small velocity and position spreads is a rather complicated task that cannot be solved using conventional magnetron injection guns.

The LOG was proposed and demonstrated for the first time in Ref. [8]. Later such devices were studied by a number of American research groups [9–11]. Last 10 years LOGs have been investigated in the IAP, where highest operating frequencies up to 0.414 THz were recently achieved at the 3rd cyclotron harmonic (see [7] and *V. L. Bratman et al.*, p. 150-155 in this volyme). This THz oscillator has been realized at the high-voltage installation with electron

energy of 250 keV and operating magnetic field of 6.6 T. To produce the axis-encircling electrons, a thin rectilinear beam was first formed in a "Pierce-like" gun, and then the electrons acquired the transverse velocity passing through a magneto-static kicker. After that the transverse velocity was further increased in tapered magnetic field. The helical axis-encircling electron beam entered a conventional gyrotron cavity. Operating modes $TE_{3,p}$ with high radial index of p = 5–9 were chosen to decrease Ohmic losses and simplify fabrication of the cavity. The radiation with frequencies of 0.374 and 0.414 THz was observed at the $TE_{3,8}$ and $TE_{3,9}$ modes. Because of the mode competition (Fig. 3), selective generation at these modes was obtained for the beam current below 2 A only and radiation power was measured to be 10 kW. More selective operation with 20 kW output power was achieved in the cavity of lower diameter at the mode $TE_{3,5}$ with the frequency of 0.369 THz.

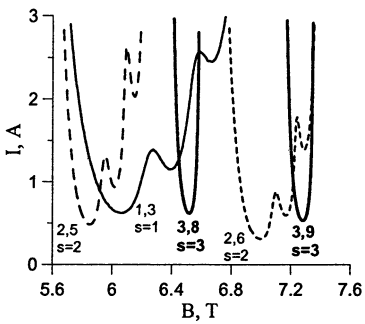

Fig. 3. Calculated starting current of modes observed in the LOG (electron pitch factor g = 1, velocity spread $\delta v_\perp / v_\perp = 0.6$, off-center shift 0.1 mm).

A challenging project of a 1-THz LOG with a kW-level of power at lower electron energy of 80 keV is also under development in IAP [7].

Another alternative for creation of simple THz devices can be gyromultipliers [13–19]. Since generation of input LF signal for conventional versions of THz multipliers is a rather complicated task, new varieties with self-excitation of LF wave at the fundamental resonance were recently proposed (see *I. V. Bandurkin et al.*, p. 156-161, and *I. I. Antakov et al.*, p. 162-166, in this volume and [7, 20]). In such a device, the same electron beam is used for generation of the LF wave and its multiplied HF harmonic. Unlike high-harmonic gyrotrons, in the proposed self-exciting multipliers it is not required to exceed the starting current of the HF mode and these devices can provide better selectivity at high harmonics. The simplest klystron-like variant with a self-exciting fundamental-harmonic cavity and a third-harmonic cavity excited by the bunched electron beam has been already recently realized at the IAP (paper by *I. V. Bandurkin et al.*, p. 156-161, of this volume and [20]). Another way is to "build in" the high-harmonic oscillator into the low-harmonic one and organize both low- and high-harmonic electron-wave interactions in one electrodynamical system [7]. According to simulations, it is

possible to realize such oscillator, where THz wave is generated at the 3rd – 4th (or even higher) cyclotron harmonic with the efficiency of the order of 1% and frequency tuning in the band of 1–2%.

Free electron lasers

Operation of FELs (see [21] and Proceedings of the Int. Free Electron Lasers Conferences e. g. [22]) is based on the stimulated radiation of electrons moving with a relativistic translational velocity, $v_{\|}$, and oscillating in transverse spatio-periodical magnetic field of a undulator. In a FEL, the radiation frequency, ω, is connected with the frequency of electron oscillations, $\Omega = 2\pi v_{\|} / d$, by Doppler formula

$$\omega - k_{\|} v_{\|} \approx \Omega , \tag{4}$$

where d is the undulator period, $k_{\|} = (\omega / \tilde{n})\cos\theta$ is the longitudinal wavenumber. At a ultrarelativistic particle energy, $\gamma >> 1$, and small radiation angles, $\theta \le \gamma^{-1}$, the radiation wavelength is many times smaller than the undulator period:

$$\lambda \sim d / \gamma^2 . \tag{5}$$

In accordance with these formulas the electrons with sufficiently high energy moving in a undulator with a small period can radiate very short waves with possibility of very broadband frequency tuning. In reality, period d is usually not smaller than 2–3 cm because of difficulties of producing sufficiently high transverse component of a periodical field and because of its fast decrease in transverse direction. Respectively, 1-THz FEL requires a rather high electron energy $E \sim 5$ MeV.

First Terahertz FEL installation that has been operated in UCSB at the electrostatic accelerating facility (E = 2–12MeV) during many years provides coherent radiation in the very broadband frequency range of 0.12–4.8 THz with power of kW-level in 1–20 μs pulses at 1 Hz repetition rate that makes this unique radiation source very attractive for many research applications [23]. Recently set into operation first stage of Novosibirsk FEL (E = 12 MeV) provides 0.6 MW of peak power in 50 ps pulses at 5.6 MHz repetition rate (0.2 kW of average power) within the frequency range of 1.5–2.5 THz [24]. A number of other FELs and similar devices with relativistic electrons initially intended for higher frequencies are now reconstructing for operation at THz waves.

Various versions of FELs have been also studied for many years both theoretically and experimentally at millimeter waves (in collaboration with other Institutions and independently) in the IAP. Among prospective ideas developed and successfully tested in these studies which can be very competitive in the THz range is the cyclotron version of FEL (CARM) and high selective cavities for FELs. The proposed original cavities providing mode selection in very large

systems are based on the using one- and two-dimensional Bragg waveguide reflectors, as well as on the effect of image multiplication (famous Talbot effect in optics).

Being much more voluminous and complicated in comparison with THz gyrotrons the FELs are nevertheless very attractive due to their possibility of broadband frequency tuning and higher operating frequency. Many attempts of different kinds are made in order to realize compact versions of FELs that are more available for small laboratories.

Optoelectronics

FELs, in principle, can provide THz radiation of sufficiently high power with possible tunability in a wide frequency range but they are unique installations placed close to huge and expensive electron accelerators providing relativistic electron beams. So, the customer must bring all the necessary equipment to FEL and perform investigations near it; the number of customers is also limited. Thus, the need for compact THz sources which may be used in any laboratory is quite evident. The development of such sources became a reality due to essential progress during last decades in a laser technique and optical crystals with unique properties.

All photo-optical means of THz radiation generation are mainly based on the two varieties of optical crystals. They are "fast" photo-conducting crystals (so called "photo-switches") and nonlinear optical crystals with high nonlinearity. Both techniques are able to provide short pulse generation (SPG) with high peak power and repetition rate using the optical rectification of the radiation from femtosecond lasers. CW or quasi-cw THz radiation is generated by means of mixing of two optical frequencies (so called "difference frequency generation" – DFG technique) using two cw or quasi-cw lasers (one of them tunable, as a rule) with their frequency difference being in the THz range. Photo-switches can provide low power cw THz radiation with a rather narrow line width; they are limited over frequency by the finite conductivity relaxation time. Nonlinear DFG has no frequency limitations but requires high optical beam intensities; this means quasi-cw generation with high enough peak power and with the natural limitation on the line-width as the inverse pulse duration.

Short pulse generation (SPG)

The beginning of very important branch of investigations - free space generation of short THz pulses is associated with the paper [25]. Both emitting and receiving antennas were identical elementary (Hertzian) dipoles manufactured of "fast" photo-switch material – radiationally damaged silicon-on-sapphire with conductivity rise and decay times in the ps range. The length of dipoles was 10 μm, the "diameter" was about 1 μm. The medium for THz pulse propa-

gation was alumina slab; its thickness (1.15 mm) defined the distance of free space propagation of THz pulses (Fig. 4). The bias of 45 V was applied to the electrodes of the transmitting photoconductor; this provided the photo-current in the emitting dipole when the latter was irradiated by a femtosecond laser pulses (about 50 pJ per 100 fs pulse, the photo-current pulses were coincided with the envelope of the light pulses). Identical THz pulses were generated with high repetition rate (about 100 MHz) and this allowed recording the wave-form of THz pulse by varying the delay of probing optical pulse at the receiving photoconductor with respect to THz pulse. The photo-current in the receiving dipole was proportional to the electric field strength in the THz pulse (Fig. 5).

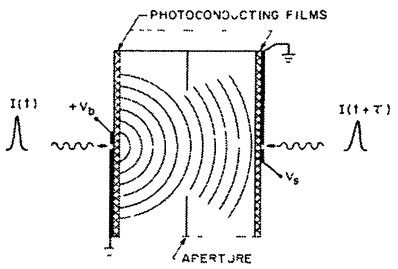

Fig. 4. Experimental configuration for free space generation and detection of short THz pulses [25].

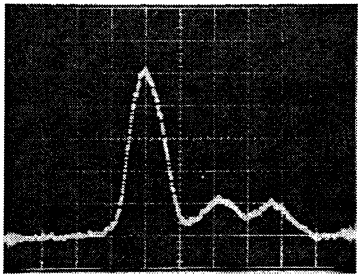

Fig. 5. Registered photo-current in the experiment shown in Fig. 4 (the horizontal time scale is 2 ps/division).

Using the focusing lenses (e. g., sapphire) allowed to increase the distance between emitting and receiving dipoles to meter range [26], to govern the transverse shape of THz pulse by means of quasi-optical mirror technique and to place different objects on the way of THz pulse for investigation of dielectric properties, for time-domain spectroscopy or for the imaging (see e. g. [27, 28]).

The next important step in SPG was the usage of large aperture photo-conducting emitters, which means that the aperture transverse dimension is large compared to longitudinal dimension of femtosecond pulse. The idea is schematically illustrated in Fig. 6. Let the plane femtosecond pulse with large transverse aperture (sheath of light radiation) is incident to the large aperture photoconducting plane layer (photo-conducting sheath) at the incidence angle θ. A photo-conducting line, corresponding to the crossing of these two sheaths will be running over photo-conducting surface with the super-light velocity. With dc electric field in the semiconductor surface this conductivity pulse is easily transformed into the current pulse which radiates THz pulses in the direction of Cherenkov angles which coincide with the transmission and reflected angles for femtosecond laser pulse. The dc electric field providing the photo-current may be of "built-in" nature like in InP near air/semi-conductor interface [29], in which case the photo-current is directed transverse to the semi-conductor surface, or due to bias voltage applied to the photo-conducting layer

(e. g. [30]), in this case the photo-current is directed along the radiating surface. Close to the radiating surface the THz pulses reproduce the transverse structure of optical pulse, while in the longitudinal direction the wave-form of THz pulses corresponds to the time derivative of the optical pulse envelope. In the case of bias voltage applied the incidence angle of femtosecond pulse may be equal to zero (normal incidence); in this case two THz pulses are generated; one – in forward direction and other – in backward direction normal to photo-conducting surface. Generated THz pulses have the shape of plane sheath with transverse dimension (up to a few cm) essentially greater than characteristic wavelength and the longitudinal depth of few characteristic wavelengths (typically fractions of mm). Such pulses are propagating in a free space with low divergence corresponding to diffraction limit and are easily controlled by large aperture appropriately shaped mirrors.

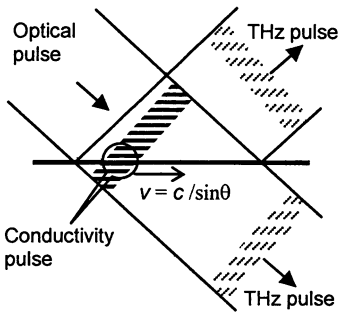

Fig. 6. The scheme of wide aperture emitters of short THz pulses.

Electric field strength in the near zone of large aperture emitter can reach the value of order of applied bias electric field, and the formally introduced efficiency of SPG generation (as the ratio of energy emitted in THz pulse to the optical pulse energy) may exceed 100% due to additional energy input from the bias voltage source. Energy per THz pulse can exceed 10 pJ with the peak power in the region of hundreds kW. Maximum electric field after appropriate focusing of THz pulse may reach hundreds kV/cm. Short pulse generation, in principle, may be obtained from "fast" photo-conductors with short conductivity rise time and long conductivity decay time [30]; in this case, only the first front of photo-current is responsible for THz pulse generation.

In spite of such impressive successes in SPG by "fast" photo-switches there are two main drawbacks which put some limitations to the wide using of such emitters. The first one is the necessity to use high technology in manufacturing large aperture photo-conducting surfaces and the electrode system for applying the bias voltage to the structure. The second one is the finite conductivity raise (and decay) time which puts frequency limitation to the spectrum of generated short THz pulse.

Both of these limitations are overcome by using wide aperture non-linear optical crystals in which non-linear rectification of femtosecond optical pulses takes place. Nonlinear polarization excited in a crystal due to finite band-width of an optical pulse is a source of THz radiation:

$$E_{\mathrm{THz}}(t) \propto \frac{\partial^2 \boldsymbol{P}(t)}{\partial^2 t}, \; P_i(\Omega) = d_{ijk}(-\Omega, \omega+\Omega, -\omega) E_j(\omega+\Omega) E_k^*(\omega) .$$

The wave-form of generated THz pulses is dependent on the parameters of both optical pulses and nonlinear crystals, the most important of latter being the thickness, synchronism between propagating optical and THz pulses and the dispersion properties in THz band. Generating efficiency is naturally increasing with the optical radiation intensity and can reach the values about 10^{-6} and higher. The most popular nonlinear crystals for SPG are <110> ZnTe [31] and organic crystal DAST [32], which possesses the highest nonlinearity. The energy characteristics of THz pulses generated at nonlinear crystals are approaching to those of similar pulses generated by "photo-switches", but their frequency spectrum may be extended far above 10 THz.

Difference frequency generation

The same principles are used for the generation of a narrow-band THz radiation; the natural way is using difference frequency generation (DFG) technique. Both photo-switches and nonlinear crystals being irradiated by two monochromatic optical beams provide generation at the difference frequency which may lie in THz range and may be tuned by the frequency tuning of one of light beams. In the first case, monochromatic modulation of the photoconductivity at the difference frequency provides monochromatic photo-current due to dc bias voltage, while in the second case the same effect is produced due to nonlinear monochromatic polarization.

Nonlinear DFG may be realized only under condition of high enough optical intensity, which means pulsed regime of light generation with reasonable laser mean power. The bandwidth of THz radiation is usually defined in this case by the inverse optical pulse duration. An impressive example is shown in Fig. 7 with three plots of output peak power versus generation wavelength, taken from Ref. [33]. The THz radiation is in the form of pulses with 5 ns duration following with the repetition rate 10 Hz, it is easily tunable within the wide range from 60 to 1600 μm. The maximum peak power (upper curve in Fig. 7) corresponds to approximately 60 W at the frequency 1.5 THz. Generation of THz radiation is realized with averaged optical power about 60 mW by illuminating GaSe crystal with the 3 mm aperture of optical beams. Peak intensity in the pump beam was ~17 MW/cm^2 (about half of optical damage threshold); maximum of generated THz power was obtained with the crystal length 15 mm (lower than absorption length for THz radiation). Maximum conversion efficiency $4.4 \cdot 10^{-4}$ was reached.

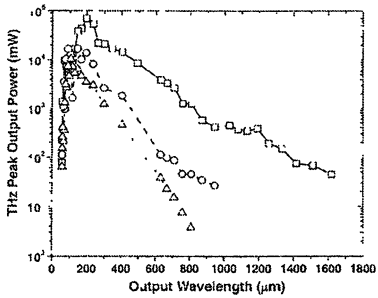

Fig. 7. Peak output power versus wavelength for 3 GaSe pure crystals with thicknesses of 4 mm (triangles), 7 mm (circles) and 15 mm (squares) [33].

Two or three orders of improvement in the line-width may be provided with DFG based on fast photo-switches. But there is essential decrease in the generation efficiency as compared to that of SPG. The reason is that in the case of SPG pulsed current is provided simply by relaxation of bias electric field, which is restored from bias voltage during rather long time between generated pulses. In the case of photo-conductivity oscillating at THz frequencies, in order to get corresponding reaction from bias voltage source, the micro-structure elements are needed. To provide operation of DRG THz source in a wide frequency range either elementary dipole structures with focusing lenses [34, 35] or logarithmic spiral antennas [36–38] are used. The best material for this type of THz generators is low-temperature-grown GaAs which demonstrates the shortest photo-conductivity decay time (about 0.25 ps) and allows operation up to frequencies about 3 THz. An example of 10×10 μm generating structure incorporated into 3-turn logarithmic spiral antenna is shown in Fig. 8 [38]. With the bias voltage 10 V and optical power 60 mW the output power at 1 THz reached 0.5 μW. The registration of such low power was provided with cryogenically cooled bolometer.

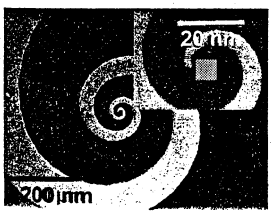

Fig. 8. Optical view of generating device (the insert has 10 times more detailed scale) [38].

"Exotic" generation

Obtaining the THz radiation under various conditions became nowadays rather fasionable. So, before the conclusion we would like to mention briefly few examples of other ways of THz radiation generation.

Frequency tripling of a gyrotron radiation at 110 GHz propagating inside the oversized waveguide by the array of 10^3 surface oriented Shottky barrier

diods was demonstrated in [39]. The output power at 330 GHz was registered at the level about 50 mW with the pulsed (50 μs) gyrotron power 10 kW. There are projects to use the same technique for mutiplying the gyrotron radiation with the frequency 170 GHz by factor 3 (or even 5). Evident problems on this way are efficiency decrease of the generation mechanism with the frequency increase, limitation on the gyrotron radiation power density and not so good quality of gyrotron radiation line.

Quantum cascade lasers (QCLs) may be still considered as "exotic" source of THz radiation, but in the very recent years a rather rapid progress in the shift of generation frequency from IR region to THz one and in the increase of operation temperature has been achieved. For example, the operation of QCL at the frequency 3.8 THz up to temperatures 137 K was reported in [40].

A plasma mechanism of THz radiation generation in a laser spark of optical axicon discharge is proposed in [41] (see also *S. V. Golubev et al.*, p. 691-696, in these proceedings). It is based on the forced excitation of plasma oscillations in a plasma cylinder with its ionization front moving with super-light velocity; the wave of decaying plasma oscillations moving with the same velocity emites THz radiation into the Cherenkov cone. There is a little chance of practical utilization of this radiation, but it is of great interest from the viewpoint of fundamental physics.

Conclusions

Nowadays the "terahertz gap" is successfully filling from both sides of classical (vacuum) electronics and of optoelectronics. A number of classical electron oscillators seem prospective and available for many applications. For example, a low-voltage (up to 5 kV) orotrons can provide power up to 0.1 W at the frequencies 0.3–1.0 THz with possibility of very broad-band electromechanical frequency tuning. Gyrodevices with electron energy 30–80 keV and relatively low magnetic field 3–7 T are presumably capable to generate in this range 10^1–10^4 W. Free Electron Lasers with high electron energy 2–12 MeV already demonstrate kW-level of power and very broad-band frequency tuning over the whole THz range.

Optoelectronics demonstrated a considerable progress in short pulse generation using wide aperture emitters irradiated by a femtosecond laser pulses. Record values of electric field in THz pulses (up to hundreds kV/cm) and peak power (up to hundreds kW) are obtained on the basis of "fast" photo-conducting emitters. More simple technique of short pulse generation is based on the nonlinear rectification of femtosecond laser pulses at electro-optic crystals. In spite of low generating efficiency (typically ~ 10^{-6}) THz pulses following with high repetition rate are widely used for time-domain spectroscopy and for radiovision in THz range (tera-vision).

Quasi-cw THz radiation with the bandwidth limited by laser pulse duration (really $\Delta\omega/\omega$ up to 10^{-4}) may be generated by bi-frequency laser emission mixing at nonlinear crystals (difference frequency generation technique) at the power level up to 100 W. Similar mixing at fast "photo-switches" provides more narrow THz line; the power level is essentially lower (typically fractions of μW). These two types of THz radiation may be successfully used for spectroscopy with high or super-high resolution.

Acknowledgments

This work has been supported by the GYCOM Ltd. (Nizhny Novgorod, Russia), by the Russian Foundation for Basic Research (grants 03-02-16780, 03-02-17064, 03-02-16831, 05-02-16852, 05-02-17517) and by the Presidium of the Russian Academy of Sciences (Programs "Electromagnetic radiation of Terahertz frequency range" and "Basic Problems of Nano- and Picosecond High-Power Electronics").

References

1. *Gershenson E.M., Golant M.B., Negirev A.A., Savel'ev K.S.* Backward Wave Oscillators of Millimeter and Submillimeter Wavelength Ranges / Ed. by N.D. Devyatkov. Moscow: Radio and Communications, 1985.
2. *Levin G.Ya., Borodkin A.I., Kirichenko A.Ya., Usikov A.Ya., Churilova S.A.*, The Clinotron. Kiev: Naukova Dumka Press, 1992.
3. *Rusin F.S., Bogomolov G.D.* // Pis'ma v JETF, **4**, 236 (1966).
4. *Shestopalov V.P.* Diffraction Electronics. Kharkov: Vischa shkola, 1976.
5. *Mizuno K., Ono S., Shibata Y.* // Symp. Submillimeter Waves. Polytechnic Inst. of Brookline, 1970. P. 115.
6. *Bratman V.L., Dumesh B.S., Fedotov A.E., Grishin Yu.A., Rusin F.S.* // Int. J. Infrared and Millimeter Waves, **23**, 1595 (2002).
7. *Bratman V.L., Bandurkin I.V., Dumesh B.S. et al.* // High Energy Density and High Power RF, AIP Conf. Proc. 807, 356 (2006).
8. *Jory H.R.*, Research and Development Technical Report ECOM-01873-F, Varian Associates, Palo Alto, California, 1968.
9. *McDermott D.B., Luhmann N.C., Jr., Kupiszewski A., Jory H.R.* // Phys. Fluids **26**, 1936 (1983).
10. *Lawson W., Destler W.W., Striffler C.D.* // IEEE Trans. Plasma Sci. **13**, 444 (1985).
11. Nusinovich G.S. // Int. J. Electronics **72**, 959-967 (1992).
12. *Bratman V.L., Fedotov A.E., Kalynov et al.* // IEEE Trans. Plasma Sci. 27, 456 (1999).
13. *Gaponov A.V., Petelin M.I., Yulpatov V.K.* // Radiophys. Quantum Electron. **10**, 794 (1967).
14. *Zhurakhovskiy V.A.* Nonlinear electron oscillations in magneto-guided beams. Kiev: Naukova Dumka Press, 1972.
15. *Ergakov V.S., Moiseev M.A.* // Radiotekhnika i Electronika **22**, 789 (1977).
16. *Belousov V.I., Ergakov V.S., Moiseev M.A.* // Electronnaya Tekhnika. Ser. 1. Electronika **41** (1978).
17. *Hirshfield J.L.* // Phys. Rev. A **44**, 6845 (1991).
18. *Guo H., Chen S.H., Granatstein V.L., Rodgers J., Nusinovich G.S., Walter M.T., Levush B., Chen W.J.* // Phys. Rev. Lett. **79**, 515 (1997).

19. *Walter M.T., Nusinovich G.S., Lawson W.G., Granatstein V.L., Levush B., Danly B.* // IEEE Trans. Plasma Sci. **28**, 688 (2000).
20. *Denisov G.G., Antakov I.I., Gachev I.G., Zasypkin E.V.* // Conf. Digest of the Joint 30th Int. Conference on Infrared and Millimeter Waves and 13th Int. Conference on Terahertz Electronics. Willamsburg, Virginia, USA, 2005. P. 435.
21. *Deacon D.A.G., Elias L.R., Madey J.M.J. et al.* // Phys. Rev. Lett. **38**, 892 (1977).
22. Proc. of the 26th Int. Free Electron Lasers Conference and 11th FEL Users Workshop / Eds R. Bakker et al. Trieste, Italy, 2004.
23. http://sbfel3.ucsb.edu/
24. *Bolotin V.P., Vinokurov N.A., Kayran D.A. et al.* // Proc. of the 26th Int. Free Electron Lasers Conference and 11th FEL Users Workshop, Eds R. Bakker et al. Trieste, Italy, 2004, P. 226.
25. *Auston D.H., Cheung K.P., Smith P.R.* // Appl. Phys. Lett., **45** (3), 1 August 1984.
26. *Fattinger Ch., Groischkowsky D.* // Appl. Phys. Lett., **54** (6), 6 February, 1989.
27. *Hu B.B., Nuss M.C.* // Opt. Lett., **20**, 1716 (1995).
28. *Cheville R.A., Grischrowsky D.* // Appl. Phys. Lett., **67** (14), 2 October 1995.
29. *Zhang X.-C., Hu B.B., Darrow J.T., Auston D.H.* // Appl. Phys. Lett., **56** (11), 12, March 1990.
30. *Darrow J.T., Hu B.B., Zhang X.-C., Auston D.H.* // Opt. Lett., **15** (6), 323 (1990).
31. *Rice A., Jin Y. et al.* // Appl. Phys. Lett., **64** (11), 14 March 1994. P. 1324.
32. *Zhang X.-C., Ma X.F. et al.* // Appl. Phys. Lett., **61** (26), 28 Dec. 1992.
33. *Shi W., Ding Y.J. et al.* // Opt. Lett., **61** (26), 28 Dec. 1992.
34. *Matsuura S., Blake G.A. et al.* // Appl. Phys. Lett., **74** (19), 10 May 1999.
35. *Matsuura S., Tani M., Sakai K.* // Appl. Phys. Lett., **70** (5), 3 Febr. 2002. P. 559.
36. *Brown E.R., Mcintosh K.A. et al.* // Appl. Phys. Lett., **66** (3), 16 January 1995. P. 285.
37. *Mcintosh K.A., Brown E.R. et al.* // Appl. Phys. Lett., **67** (26), 25 Dec. 2002. P. 3844.
38. *Peytavit E., Arscott S. et al.* // Appl. Phys. Lett., **81** (7), 12 August 2002.
39. *Shashkin V.I.* Russian seminar on the radiophysics of mm/smm waves, Abstracts. N. Novgorod, 2005. P. 63.
40. *Williams B.S., Kumar S. et al.* // Appl. Phys. Lett., **83** (25), 22 Dec. P. 5142.
41. *Golubev S.V., Suvorov E.V., Shalashov A.G.* // Piz'ma v JETF, 79 (8), 443 (2004).

PROGRESS IN THE DEVELOPMENT OF THE 170 GHz COAXIAL CAVITY GYROTRON FOR ITER

B. Piosczyk[1a], *S. Alberti*[3], *D. Bariou*[4], *P. Benin*[4], *T. Bonicelli*[5], *G. Dammertz*[1a], *O. Dumbrajs*[6], *D. Fasel*[3], *E. Giguet*[4], *T. Goodman*[3], *R. Heidinger*[1b], *M. Henderson*[3], *J. P. Hogge*[3], *S. Illy*[1a], *J. Jin*[1a], *C. Lievin*[4], *G. Michel*[7], *P. L. Mondino*[5], *L. Porte*[3], *T. Rzesnicki*[1a], *M. Thumm*[1a,2], *M. Q. Tran*[3,5], *X. Yang*[1a], *I. Yovchev*[3]

[1]Forschungszentrum Karlsruhe, Association EURATOM-FZK,
[a]IHM, [b]IMF-I, Postfach 3640, D-76021 Karlsruhe, Germany;
[2]also IHE Universitat Karlsruhe, Germany; [3]CRPP Lausanne, Switzerland;
[4]Thales ED, Velizy, France; [5]EFDA-CSU, Garching, Germany;
[6]HUT Helsinki, Finland; [7]IPP Greifswald, Germany;
e-mail: bernhard.piosczyk@ihm.fzk.de

For use at ITER the EFDA (European Fusion Development Agree-ment) CSU (Close Support Unit), Garching, supports the development of a 2 MW, CW, 170 GHz coaxial cavity gyrotron in cooperation between European Research Institutions (FZK Karlsruhe, CRPP Lausanne, HUT Helsinki) together with European tube industry (TED, Velizy, France). The design of the gyrotron components has been finished already. The manufacturing phase of the first industrial prototype started last year and the delivery is expected for spring 2006. A suitable superconducting magnet has been ordered and a facility for testing the gyrotron is under construction at CRPP Lausanne. At FZK an experimental 170 GHz pre-prototype tube which uses the same cavity and same quasioptical RF-output system as designed for the industrial prototype and a very similar electron gun, has been operated, in order to verify the design of critical component under relevant conditions.

Introduction

In ITER microwave power at 170 GHz is foreseen not only for electron cyclotron heating and current drive (ECH & ECCD) but it is also considered to be essential for stabilizing neoclassical tearing modes (NTM) by localized current drive [1]. In the reference design ITER requires a total of 20 MW, CW power provided by 24 conventional gyrotrons with 1 MW output power. The increase of the RF output power per unit would result in a reduction of the installation costs of the electron cyclotron wave system (ECW) at ITER and it would allow, if necessary, to enhance the total amount of microwave power injected into the plasma.

In proof of principle experiments carried out at FZK Karlsruhe on a 165 GHz coaxial tube during the last years, the feasibility of manufacturing a 2 MW, CW coaxial cavity gyrotrons at 170 GHz has been demonstrated and information necessary for a technical design has been obtained [2, 3]. Based on these results and on the experience acquired during the development of the 1 MW, CW, 140 GHz gyrotron for W7-X, firstly EFDA CSU, Garching, assessed the technical feasibility with a study contract with TED and secondly

placed a contract at TED for procurement of a first industrial prototype of a 2 MW, CW, 170 GHz coaxial cavity gyrotron as could be used for ITER. The development work on the prototype tube is performed in cooperation between European research centers (FZK Karlsruhe, CRPP Lausanne, HUT Helsinki) together with TED. Within this cooperation the physical specifications and the design of the components are done by the research institutions and TED is responsible for the technological aspects and manufacturing [4].

In parallel to the work on the industrial prototype, the previously used 165 GHz coaxial gyrotron has been modified for operation at 170 GHz. This short pulse ($\leq$ 10 ms) experimental gyrotron ("pre-prototype") operates in the same $TE_{34,19}$ mode and uses the same cavity with uptaper, the same launcher and mirrors as designed for the industrial prototype, and in addition, a very similar electron gun. Therefore, the pre-prototype tube is suitable to be used for verification of the design of the main components of the industrial prototype under relevant conditions.

In the following first the pre-prototype tube will be described and recent results on verification of the design will be given and then the status of the industrial prototype tube will be reported.

Pre-prototype of the 170 GHz coaxial cavity gyrotron

In Table 1 the main design parameters are summarized both for the experimental pre-prototype tube and for the 2 MW, CW industrial prototype. The SC-magnet available at FZK for operation of the pre-prototype delivers only a magnetic field up to about 6.7 T. Due to this the beam voltage had to be reduced to values below 80 kV in order to be able to excite the $TE_{34,19}$ mode at 170 GHz. According to simulations, operation at a lower voltage results in an RF output power reduced to about 1.5 MW, depending on the finally obtained magnetic field.

A coaxial magnetron injection gun (CMIG) [5], similar to the gun foreseen for the prototype tube, is used (Fig. 1). The emitter ring has an diameter of 108 mm and a radial width of 1.8 mm. At a beam current I_b = 75 A the emitting current density is ~ 4.2 A/cm^2. The cathode heating power needed for emission of this current is about 550 W. The coaxial insert with a length of about 1.2 m is supported from the bottom of the gun. The inner part of the insert is water cooled and its position can be adjusted under operating conditions. Special care has been taken in designing the geometry of the bottom part of the cathode body and of the insert in order to avoid regions in which electrons can be trapped. In such regions a Penning discharge could be built up and limit the high voltage performance, as observed in earlier experiments [4].

In order to keep the Ohmic losses at the cavity wall below 1 kW/cm. (ideal copper at 273 K) for 2 MW RF output power the $TE_{34,19}$ mode has been selected as the operating mode [6]. The corresponding peak losses at the insert are expected to be less than 0.1 kW/cm. The cylindrical part of the cavity has a radius of 29.55 mm and a length of 16 mm. Inside the cavity the coaxial insert is longitudi-

nally corrugated and down-tapered with an angle of 1° [3]. The problem of mode competition has been investigated with a time dependent, self consistent multimode code considering up to 13 competing modes [6]. The main competition has been found to occur between the two mode triplets, {$TE_{-33,19}$, $TE_{-34,19}$, $TE_{-35,19}$} and {$TE_{+32,20}$, $TE_{+33,20}$, $TE_{+34,20}$}. Ac-cording to the calculations, single-mode oscillation of the $TE_{34,19}$ mode is expected for accelerating voltages between about 65 and 75 kV for B_{cav} = 6.68 T. This voltage range shifts to higher values with increasing magnetic field.

The aim of the quasi optical (q.o.) RF output system is to convert the RF-power generated in the $TE_{34,19}$ mode inside the cavity into a free-space beam with high content of the fundamental Gaussian mode. To keep the microwave losses inside the gyrotron tube within technically acceptable limits, a dimpled-wall launcher with reduced diffraction losses at the edge of the launcher cut is used [7]. However, because of limitations in the accuracy of mechanical fabrication of the surface structure of the non-quadratic mirror a compromise had to be made between the Gaussian content of the RF output beam and the amount of microwave stray losses inside the tube. According to calculations the total amount of stray losses is expected not to exceed a value of 5% to 6% of P_{out}.

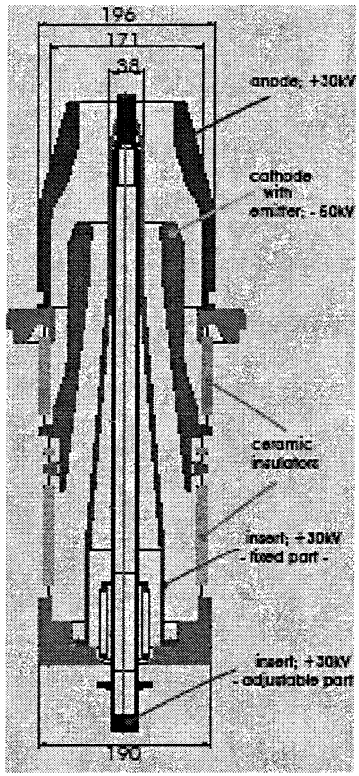

Fig. 1. View of the CMIG gun

Table 1. Design parameters of the prototype and short pulse tube

	Pre-prototype	Prototype
Operating cavity mode	$TE_{34,19}$	
Frequency, f	170 GHz	
RF output power, P_{out}	~ 1.5 MW	2 MW
Beam current, I_b	75 A	
Accelerating voltage, U_{acc}	~ 75 kV	90 kV
Cavity magnetic field, B_{cav}	~ 6.7 T	6 87 T
Efficiency (with depressed collector), η		≥45 %
Velocity ratio, α	~ 1.3	
Beam radius inside the cavity, R_b	10.0 mm	

As RF output window a disc made of fused silica with an optical thickness of 15λ/2 at 170 GHz is used in the pre-prototype tube, whereas for the 2 MW prototype a 5λ/2 disc made of CVD diamond is foreseen.

Operation of the pre-prototype and results:

Electron gun and electron beam: The performance of the electron gun has been found to be in agreement with the design objective. No limitations on high voltage performance due to build up of a Penning discharge have been observed. Stable operation up to $I_b \approx 80$ A and $U_c \approx 80$ kV has been observed without any beam instabilities. The current to the insert was measured to be below 0.1% of the beam current, in agreement with the results of previous experiments.

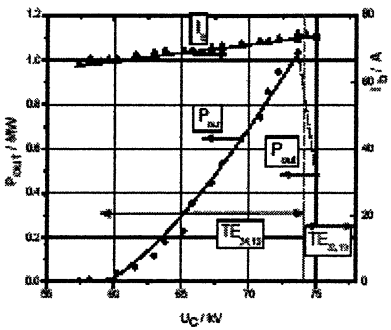

Fig. 2. RF output power and beam current versus cathode voltage at B_{cav} = = 6.718 T.

Cavity and RF-interaction: The experiments were carried out with short-pulses (< 10 ms), limited by the power loading at the collector surface.

First the inner conductor has been radially aligned with respect to the electron beam within ± 0.1 mm and the concentricity between the electron beam and the cavity wall has been verified. The obtained results can be summarized as follows: the nominal co-rotating $TE_{-34,19}$ mode has been excited stably in single-mode operation over a wide parameter range. Figure 2 shows a typical behavior of the RF output power measured as a function of the applied accelerating voltage U_c. The corresponding dependence of the beam current from U_c due to the Schottky effect is indicated, too. The magnetic field has been kept constant at $B_{cav} = 6.718$ T. The beam radius has been optimized for maximum output power by varying the magnetic compression ratio. With increasing beam voltage first the $TE_{-34,19}$ mode at 170.02 GHz occurs followed by the $TE_{-33,19}$ mode at 167.85 GHz above $U_c \sim 73$ kV. At voltages above ~80 kV the $TE_{-32,19}$ mode at 165.74 GHz has been observed. The experimentally obtained mode sequence ($TE_{-34,19} \rightarrow TE_{-33,19} \rightarrow TE_{-32,19}$) with increasing beam voltage is not in agreement with the theoretical results. In particular, in simulations the $TE_{-33,19}$ mode does not occur at these parameters and instead the nominal $TE_{-34,19}$ mode remains until nearly 80 kV followed by the $TE_{-32,19}$ mode. Contrary to the simulations, in the experiment the $TE_{-34,19}$ mode stops to oscillate at the fairly low voltages $U_c \approx 73$ kV with a low velocity ratio $\alpha \approx 1.1$. This has limited the maximum RF output power to $P_{out} \cong 1.15$ MW with a corresponding efficiency of about 20% (without depressed collector). The reasons

for the discrepancy between theory and experiment are not clear yet and need further investigations. In particular, the influence of alignment on the gyrotron performance will be studied in more detail.

Quasi-optical (q.o.) RF-output system: The performance of the q.o. RF output system has been studied both at low power levels ("cold") and at high power ("hot") with the pre-prototype gyrotron. A good agreement has been found between the "cold" and "hot" measurements and calculations. However, by mistake the optimization of the mirrors built in the pre-prototype tube was performed for a launcher different from the manufactured one. In the mean time the mirrors have been redesigned and manufactured. "Cold" measurements performed with the redesigned mirrors are in good agreement with design calculations as shown in Fig. 3. Thus this design of the RF output system will be used in the first industrial prototype tube. However, further improvements, in particular of the Gaussian content in the output beam, are under investigations.

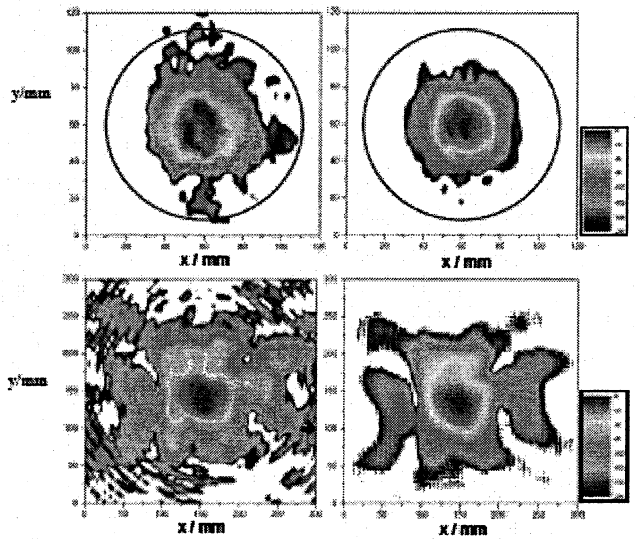

Fig. 3. Power distribution (in steps of 3 dB) of the RF output beam at the window plane (upper row) and 1 m outside the window (lower row). Aperture of the output window (96 mm) is indicated. "Cold" measurements are on left side and calculations on right side.

Microwave stray losses and internal absorber: The amount of stray losses inside the tube has been determined to be $0.08 \times P_{out}$ for the RF out-put system with the incorrect mirror design. The measurement will be repeated with the correct mirrors for which a slightly reduced value is expected. In order to reduce the amplitude of the microwave losses inside the tube, internal microwave

absorbers are proposed. To measure the absorption efficiency a test version of internal absorbers consisting of an array of four water cooled Al_2O_3 tubes (diameter 20 mm, length 100 mm) has been installed inside the mirror box and the power dissipated in that tubes has been measured calorimetrically. As a result it has been found that 2.2% of P_{out}, corresponding to 25% of the stray losses, has been absorbed by the tubes. This value is approximately 3 times the power radiated through one relief window with 100 mm diameter. The operation with the internal absorbing tubes did not show any significant influence on the microwave generation.

First prototype of the 170 GHz, 2 MW, CW coaxial cavity gyrotron

The design of all compone nts of the prototype has already been finished. The overall view of the tube (integration of all components) is shown in Fig. 4. The gyrotron is foreseen to be operated with a single stage depressed collector with the gyrotron body including the mirror box and RF output window at +35 kV and the collector on ground potential. Therefore, the use of an insulator between the gyrotron body and the SC magnet, as well as an insulator above the mirror box is needed. In addition, a DC break has to be used between the gyrotron window and the transmission system. A 3D view of the electron gun with the insert is shown in Fig. 5. A mock-up coaxial insert made of Glidcop and stainless steel was realized to validate the fabrication process. The structure was exposed to vibrations according to a road transport. To limit the amplitude of vibrations some shock absorption during transport is needed. The amplitude of vibrations due to flow of the cooling water was proven to be very low (< 0.1mm). The cavity will be made out of Glidcop. Taking into account the resistivity of Glidcop and the effect of surface roughness a peak ohmic loading at the outer wall of 1.7 kW/cm^2 has been estimated (compared to 1 kW/cm^2 for ideal copper) corresponding to a total dissipated power of 45 kW. In a mock-up of the cavity the cooling system has successfully been tested with a heat exchange coefficient as high as 15 W/(cm^2×K). The total losses at the insert are expected to be around 1 kW. Special care has been devoted to the handling of the microwave stray losses inside the gyrotron. Internal microwave absorbers consisting of six water cooled Al2O3 tubes (diameter 25 mm, length 150 mm) distributed inside the mirror box will be installed (Fig. 6) which, according to the results obtained with the pre-prototype tube, should dissipate around 2/3 of the microwave stray losses. The output window has an aperture of 96 mm and uses a 1.852 mm disc out of CVD diamond. For dissipation of 2.2 MW power under nominal conditions a collector with a diameter of 600 mm and a maximum peak power density of < 500 W/cm^2 (time averaged, sweeping frequency 7 Hz) has been designed. The influence of the eddy currents in the collector wall on the sweeping magnetic field has been taken into account. Further optimization is needed to make the distribution of the power along the surface less sensitive to variation of gyrotron operating parameters.

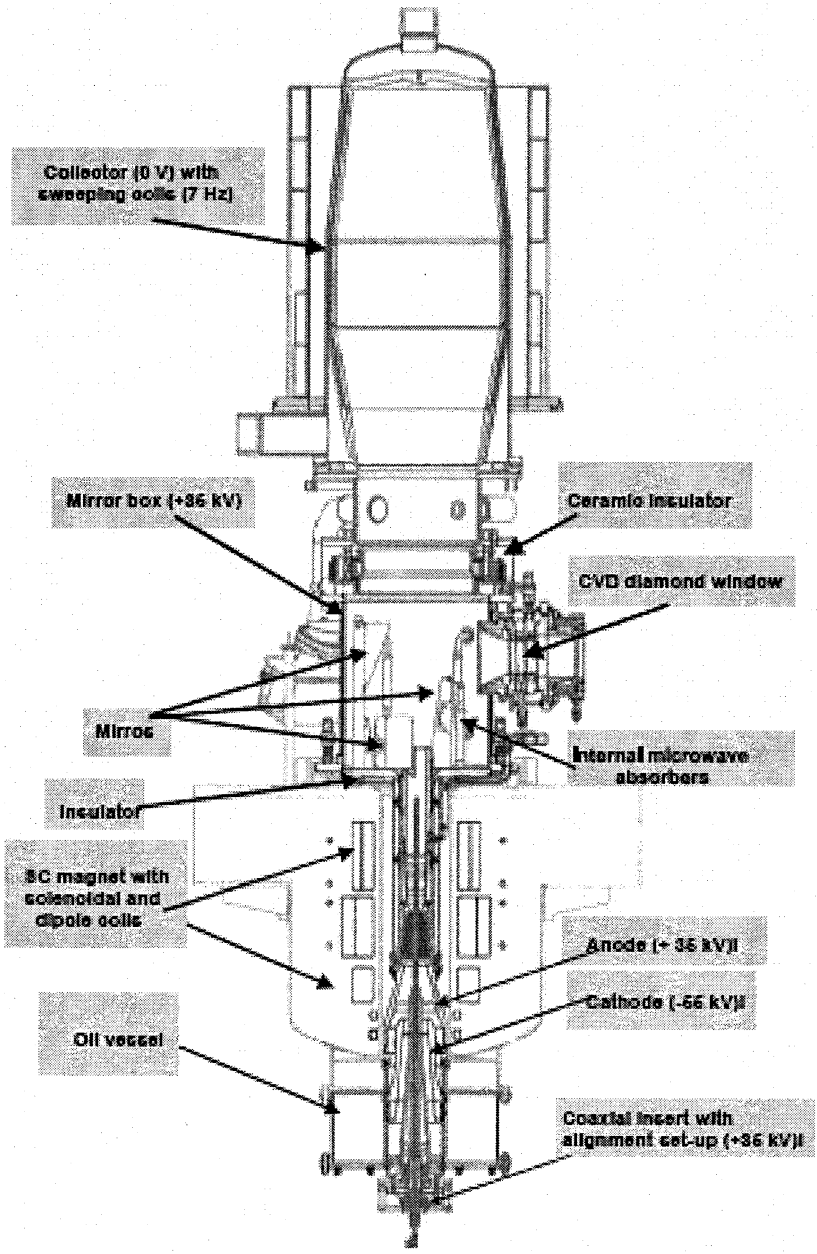

Fig. 4. Schematic view of the 170 GHz, 2 MW, CW prototype tube

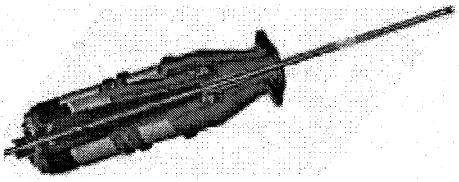

Fig. 5. 3D view of the electron gun

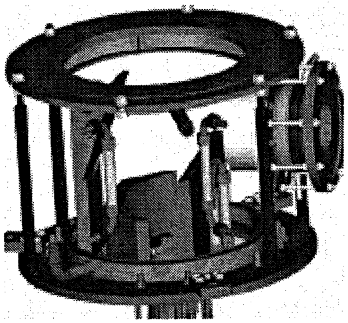

Fig. 6. The mirror box with the internal absorbers.

The first prototype tube is expected to be delivered in spring 2006. A suitable SC-magnet has already been ordered and is under fabrication. A facility suitable for testing the 2 MW, CW gyrotron is under construction at CRPP Lausanne. Tests with the first prototype tube are foreseen to start in summer 2006.

Summary and outlook

The fabrication of the first industrial prototype of the 2 MW, CW 170 GHz coaxial cavity gyrotron is progressing well. The design of critical gyrotron components as electron gun, cavity and RF output system of the 1st industrial prototype of the 2 MW, CW 170 GHz coaxial cavity gyrotron has been verified experimentally. The performance of the electron gun is in agreement with the design. The gyrotron has been operated stably up to an electron beam current of 80 A. The nominal $TE_{34,19}$ mode has been excited at 170 GHz over a reasonably wide parameter range. However, there is some discrepancy between design simulations and experimental observations. Experimentally a more dense mode spectrum has been observed than expected from simulations. Due to this the oscillation range of the nominal mode is limited to ~73 kV at $B_{cav} = 6.718$ T. At these parameters a maximum RF output power of about 1.15 MW has been measured. The measured power distribution of the RF output beam is in good agreement with design calculations. However, a mistake in optimization of the mirrors has been discovered thus the design had to be repeated and the mirrors have been newly manufactured. The distribution of the RF output beam measured at low power is in good agreement with design calculations. High power measurements with the pre-prototype tube will be performed next. The design of all components for the industrial prototype tube is now frozen and the manufacturing of the tube is in progress. The delivery is expected in spring 2006.

References

1. *Zohm H. et al.,* Nucl. Fusion, **41,** 197-202 (2001).
2. *Piosczyk B. et al.,* IEEE Trans. Plasma Sci. **32**(3), 853-860 (2004).
3. *Piosczyk B. et al.,* IEEE Trans. Plasma Sci. **32**(3), 413-417 (2004).
4. *Hogge J.P. et al.*, 3 rd IAEA Techn. Meet. ECRH Physics and Technology for ITER, 2 May – 4 May 2005, Como, Italy.
5. *Piosczyk B.,* IEEE Trans. Electron. Devices, **48**(12), 2938-2944 (2001).
6. *Dumbrajs O. et al.*, 26th Int. Conf. Infrared and Millimeter Waves, 2001, Toulouse, France. P. 10-14.
7. *Michel G.,* EC13 conf., May 17-20, 2003, Nizhny Novgorod, Russia.
8. *Piosczyk B. et al.,* 29th Int. Conf. Infrared and Millimeter Waves, 2004, Karlsruhe, Germany. P. 107-108.

DEVELOPMENT OF HIGH POWER GYROTRON FOR ITER

R. Minami, A. Kasugai, K. Takahashi, N. Kobayashi, K. Sakamoto

Japan Atomic Energy Research Institute, Ibaraki, Japan

A 170 GHz/1 MW/50% efficiency gyrotron has been developed for the International Thermonuclear Experimental Reactor (ITER). For a stable 1 MW/continuous wave (CW) operation, the gyrotron and test facility were under modification: efficiency improvement of a quasioptical (QO) mode converter, beam current and output power stabilization by a pre-programmed control of cathode heater power and voltage between an anode and a cathode. To reduce the diffraction loss from the QO mode converter, a high efficiency QO mode converter was designed and optimized. More than 99% of the radiated power enters the first mirror of QO mode converter. One method to compensate the electron beam current reduction is to boost the heater power of the electron gun. By integration of the above-mentioned modification, preliminary experiments of stable long pulse operations such as 0.13 MW/600 s and 1000 s electron beam pulse (without RF oscillation) were carried out for the 170 GHz ITER gyrotron. Besides, a study of the high order mode oscillation was demonstrated using a short pulse gyrotron.

1. Introduction

A 100 GHz band gyrotron is necessary for a fusion reactor. In ITER, twenty-four 170 GHz/1 MW/continuous wave (CW) gyrotron with 50% efficiency required for electron cyclotron heating (ECH), current drive (ECCD), suppression of plasma instability, and start up of plasma [1]. Key technologies for the 170 GHz/1 MW gyrotron such as a diamond window [2–5], a depressed collector for high efficiency operation [6] and an oversized open cavity for higher mode [7, 8] have been developed. Next issue is a demonstration of long pulse operation. Up to now, experimental results of 0.5 MW/100 s and 0.9 MW/9.2 s were demonstrated in Japan Atomic Energy Research Institute (JAERI) [9, 10]. For further pulse extension at high power, some modifications were carried out. One problem was stray radiation of 8–10% of the output power. The stray radiation should be suppressed as much as possible to avoid the risk of damage of inner components, in particular the ceramic parts, and to minimize the capacity of the cooling system. Another problem was large beam current decrease due to so called the emission cooling of a cathode.

During the operation, the oscillation mode shift from $TE_{31,8}$ to $TE3_{0,8}$ was caused by the current decrease. Then, the magnetic field of the cavity should be increased to avoid the downshift of the oscillation mode, however, the efficiency decreases and the parasitic oscillation in a QO mode converter appears.

In this paper, the recent activities on the development of 170 GHz gyrotron for ITER are described. Also, the studies of the high order oscillation mode for future advanced gyrotron are described.

2. Design of the 170 GHz gyrotron and improvement for long pulse operation

2.1. Configuration of the gyrotron

A conceptual view of 170 GHz gyrotron is shown in Fig. 1. The gyrotron is installed in the superconducting magnet coil of 7 T (at center), whose bore radius is 120 mm at the room temperature. An electron beam is generated at a magnetron injection gun (MIG), and accelerated by voltage V_b from a beam acceleration power supply. A main power supply with output voltage of V_c is connected to a collector, which receives the electron beam. A voltage difference V_d between the power supplies ($V_b - V_c$) arises at a ceramic insulator between a gyrotron body (a cavity and a mode converter section) and a collector. This voltage acts as a retarding voltage on the spent beam (the electron beam after RF-beam interaction) to improve total RF power generation efficiency of the gyrotron, i. e., a depressed collector operation. The RF oscillation takes place in a cavity with the use of an electron cyclotron resonance maser (CRM). The cavity is a standard cylindrical open cavity. A beam radius in the cavity is 9.1 mm, and a radius of the cavity is 17.9 mm. An operation mode is $TE_{31,8}$ mode, and an unloaded quality factor Q_0 of the cavity is 1530. The $TE_{31,8}$ mode RF wave is converted to a Gaussian beam by a launcher and phasecorrection mirrors (QO mode converter). The RF beam is transmitted to outside of the tube through an edge cooled diamond window. A collector is made of copper and its inner diameter is 320 mm and receives the spent electron beam with rather lower heat load because of the collector potential depression effect. The design value of the QO mode converter efficiency from the oscillation mode to a Gaussian beam is 94% in the calculation. A rest of oscillation power is trapped in the gyrotron as stray radiation. A large part of the stray radiation is extracted from the ceramic insulator. As the stray radiation often heats up internal components of the gyrotron and limits the pulse length, it must be reduced as low as possible to get the stable long pulse operation. The aperture of the window is 80 mm. The loss tangent of the diamond disk is $2 \cdot 10^{-5}$. By edge watercooling, the temperature rise of the disk center is stabilized at $\Delta T = 45$ K (0.9 MW transmission). The pulse extension experiment was performed at the output power of 0.5 MW level up to

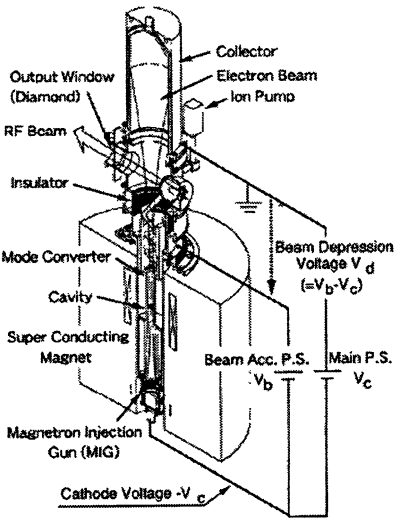

Fig. 1. Conceptual view of 170 GHz gyrotron.

100 s. The temperature of key components was stabilized during the shot. The outgas level was as low as 10^{-5} Pa. The stray radiation is extracted from a sub-window and a ceramic insulator (DC break made of Si_3N_4 cylinder) installed for depressed collector operation. In the experiment, absorbed stray radiation at the outside of the gyrotron was 8% of the output power. The DC break is cooled by fluorinert. A Silicon Carbide (SiC) cylinders are installed in the beam tunnel in order to suppress the parasitic oscillation.

2.2. High efficiency launcher of the QO mode converter

The launcher has a tapered dimpled-wall. To form a sidelobe-free fundamental Gaussian output beam, the launcher must have surface deformations such that an incident rotating TE mode is converted to a mode mixture generating a Gaussian beam distribution. The inner wall has complex perturbations indicated by the following equation:

$$r(\phi, z) = r_0 + \alpha z + \sum^{N} \left[a_n(z) \cos(l_n \phi) + b_n(z) \sin(l_n \phi) \right], \quad (1)$$

where z is a distance from an input of the launcher and parallel to the launcher axis, φ is an azimuthal angle, r_0 is the radius of initial input to the launcher, α is the slope of the launcher taper and l_n is an integer which is the number of azimuthal variations for the n-th surface deformation. Here, $a_n(z)$ and $b_n(z)$ are numerically optimized to form a Gaussian like field pattern at far field [11, 12].

For 170 GHz gyrotrons for ITER developed at JAERI, the oscillation mode of $TE_{31,8}$ is used [9, 10]. The previous launcher has simple surface perturbation, where $a_n(z)$ and $b_n(z)$ in eq. (1) are constant and only $l = 3$ is used. A new built-in launcher, where the azimuthal variations of eq. (1) is $l = 1, 2, 3$ and 6, is designed for $TE_{31,8}$ at 170 GHz. A taper angle is 0.2 degrees and the mean output radius is 21.5 mm. The calculated results of the electric field intensity on a cylindrical surface surrounding the launcher axis for the previous and improved design are shown in Fig. 2, *a* and 2, *b*, respectively. Each square in Fig. 2 corresponds to area of each first mirror of the QO mode converter. In the previous launcher, the radiated power collected by the parabolic mirror is 97%. On the other hand, the radiated power of the new one is 99.5% at the first mirror.

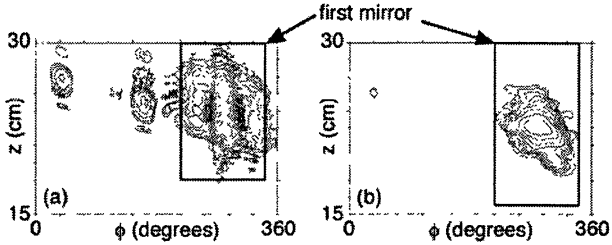

Fig. 2. Radiated field patterns of the previous design launcher (*a*) and the improve design launcher (*b*). Each contour line is 3 dB.

2.3. Recovery of an electron beam current reduction by the control of heater voltage

The pulse duration was extended up to 100 s at 0.5 MW. The beam voltage was 71.5 kV. Then, the beam current decrease was observed from 35 to 25 A due to the cathode cooling, which is accompanied by the output RF power drop from 0.56 to 0.44 MW. In order to recover the electron beam current reduction, it is necessary to compensate the temperature decrease resulted from the electron emission. Control of the heater voltage is carried out to compensate the emission belt temperature reduction, where the heater voltage is increased just before onset of RF oscillation, it is called "heater boost". The long pulse experiments with the heater boost are carried out to verify the heater boost effectiveness for improvement to the electron beam current reduction. Figure 3 shows the result of heater boost experiments by pre-programming control. In Figure 3, solid lines correspond to beam current and dashed lines correspond to heater voltage. Thin line data is without control of heater power, and bold line data is with pre-programming control of heater power. In the case of no control of heater power, beam current was decrease with pulse duration. On the other hand, due to a heater boost with pre-programming control, constant beam current during 1000 s was achieved. One can predict the temporal evolution of electron beam current for a longer pulse such as CW oscillation and control the electron beam current to keep the stable oscillation.

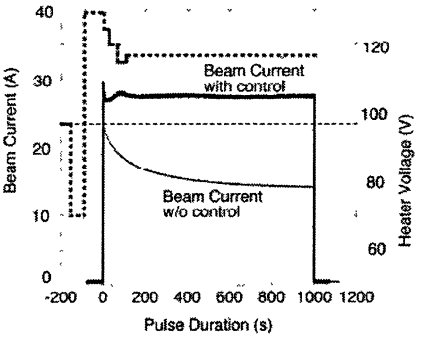

Fig. 3. The result of heater boost experiments by pre-programming control.

3. Experimental results of long pulse oscillation

Based on improvement of mode converter and pre-programming control of heater voltage of electron gun, long pulse operation was carried out. Figure 4 shows the example results of long pulse operation for 170 GHz gyrotron. In Figure 4, the waveforms of heater voltages, beam current, signal of photomultiplier (arcing), vacuums and the output power at 600 s operation are shown. The RF power is absorbed by the dummy load with the water in the teflon tube. The power is monitored by the temperature increase of the water. A flow rate of the water is 50 L/min. The dummy load is evacuated to avoid the RF breakdown. The constant power was measured by dummy load during 600 s. In this initial experiment, power level was limited 0.2 MW because of the capacity of

the teflon dummy load. The current keeps a constant value by the pre-programming control of the heater power. The vacuum in the tube was the order of the 10^{-6} Pa, and no arcing was observed. In the initial experiment, 0.13 MW/600 s and 0.2 MW/400 s were achieved.

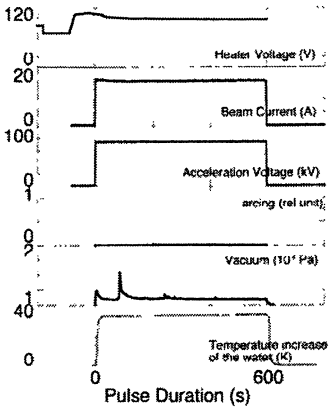

Fig. 4. Waveforms of heater voltage (pre-programming control), beam current, beam acceleration voltage, signal of photo-multiplier (arcing), vacuum, and power measured calorimetrically at 600 s operation.

4. Study of high order mode oscillation

For higher power gyrotron, much higher order mode oscillation will be required because of lower heat load on the cavity. Figure 5 shows the wall field intensity and radiated field pattern. The source field is $TE_{31,20}$ mode. The frequency is 170 GHz. The radiated field pattern is calculated at $r = 6$ cm from the launcher axis. It is found that the single beam is formed with no side lobes of over –30 dB. Such profile will be enough to convert to Gaussian beam by use of phase correlating mirrors.

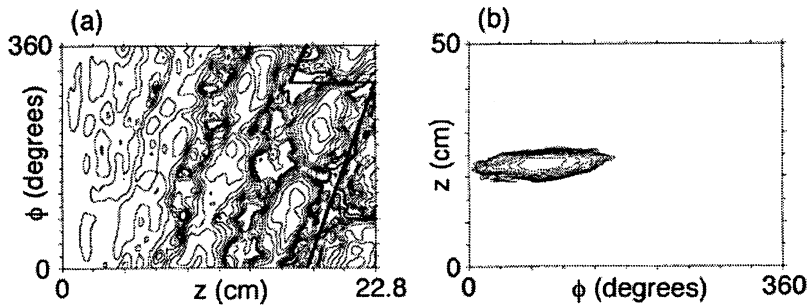

Fig. 5. The wall field intensity (*a*) and radiated field intensity (*b*) for $TE_{31,20}$/170 GHz. Each contour line is 3 dB.

Next, a short pulse gyrotron was designed and fabricated for a study of high order mode oscillation. The operation mode is $TE_{31,12}$, and its Q-factor is 1660. The frequency is 170 GHz. The peak heat load on the cavity wall is 1.8 kW/cm^2 at the oscillation power of 1.5 MW. The operation is done using a super conducting magnet (SCM) of the long pulse 170 GHz gyrotron. A configuration of MIG is the same with that of 170 GHz/$TE_{31,8}$ gyrotron since the beam diameter in the cavities are 18.26 mm for both modes. The oscillation mode is converted to Gaussian beam mode using a launcher and a parabolic mirror. Using two additional mirrors, the power is extracted through the window obliquely. The power profile is shown in Fig. 6, *a*. The designed power profile is indicated in contours for every 10% of the peak power. The measured one by infrared camera is shown in gray gradation. Almost perfect agreement was obtained between them. These indicate the oscillation mode is $TE_{31,12}$, and the launcher works well at high order volume mode. As no phase correlation is adopted on the mirror surfaces, the output profile is noncircle. The transmission efficiency from the cavity to the window is 93.3% in calculation, which can be increased furthermore by optimizing the mirror surfaces. In Figure 6, *b*, the electron beam current dependence of the output power and the efficiency are shown. The pulse duration is 1 msec. The beam voltage is 84 kV. The maximum efficiency is 30% at 1 MW oscillation, and 1.56 MW oscillation was obtained at the beam current of 69 A. It can be concluded that the stable single mode oscillation is possible at higher order mode $TE_{31,12}$, which indicates a possibility of the 1.5 MW level long pulse operation.

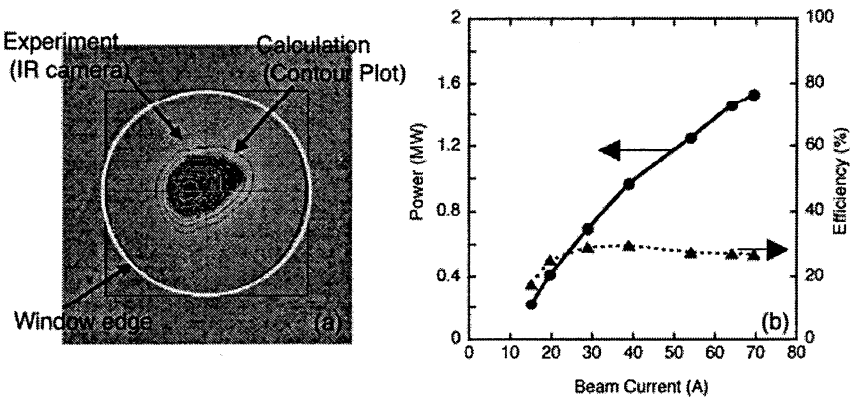

Fig. 6. Power profile at the window (*a*). Beam current dependence (*b*) of output power (filled circles) and efficiency (filled triangles).

Summary

The recent research and development of 170 GHz gyrotron were presented. For the development of ITER gyrotron, the gyrotron and the test facility was modified for CW operation. The pre-programming control of heater power was effective to obtain the constant current to avoid the power decrease during the shot. The QO mode converter system was improved to reduce the stray radiation. In the preliminary experiment, the results of 0.2 MW/400 s and 0.13 MW/600 s were obtained. The study of the high order mode oscillation was carried out. The experimental results indicate the stable oscillation over 1 MW at 170 GHz is possible using the simple cylindrical cavity.

References

1. Technical Basis for the ITER Final Design Report (2001).
2. *Braz O. et al.*, Int. J. Infrared Millimeter Waves, 18 (1997), 1495.
3. *Thumm M.*, Int. J. Infrared Millimeter Waves, 19 (1998), 3.
4. *Kasugai A. et al.*, Rev. Sci. Instrum., 69 (1998), 2160.
5. *Sakamoto K. et al.*, Rev. Sci. Instrum., 70 (1999), 208.
6. *Sakamoto K. et al.*, Phys. Rev. Lett., 73 (1994), 3532.
7. *Sakamoto K. et al.*, J. Phys. Soc. Japan, 65 (1996), 1888.
8. *Shoyama H. et al.*, Jpn. J. Appl. Phys., 40 (2001), 906.
9. *Sakamoto K. et al.*, Nucl. Fusion, 43 (2003), 729.
10. *Kasugai A. et al.*, Nucl. Instrum. Methods, Phys. Res. A, 528 (2004), 110.
11. *Neilson J., Bunger R.*, IEEE. Trans. Plasma Sci., 30 (2002), 794.
12. *Neilson J., Bunger R.*, Proc. 28th IRMMW (2003), Th. 5-6, p. 377.

DEVELOPMENT STATUS OF 1 MW AND 1.5–1.7 MW/ 170 GHz GYROTRONS FOR ITER

M. V. Agapova[1], *A. A. Bogdashov, A. V. Chirkov, G. G. Denisov, A. Ph. Gnedenkov*[1], *V. I. Ilyin*[2], *V. N. Ilyin*[1], *D. V. Khmara*[1], *A. N. Kostyna*[1], *A. N. Kuftin, V. I. Kurbatov, A. G. Litvak, V. K. Lygin, V. I. Malygin, S. A. Malygin*[1], *M. A. Moiseev, V. E. Myasnikov*[1], *V. O. Nichiporenko*[1], *L. G. Popov*[1], *E. A. Soluyanova*[1], *N. A. Shamanova*[1], *E. M. Tai*[1], *S. V. Usachev*[1], *V. E. Zapevalov*

Institute of Applied Physics, Nizhny Novgorod
[1]GYCOM Ltd, Nizhny Novgorod
[2]Nuclear Fusion Institute, Russian Research Center "Kurchatov Institute"

Design and test results of 170 GHz/1 MW/CW industrial gyrotron being developed in Russia for ITER are presented. The output power and pulse duration combinations of 1.15 MW/0.1 s, 0.9 MW/20 s, 0.7 MW/40 s and 0.5 MW/80 s ware attained. Transmission line elements rather than gyrotron itself were responsible for pulse limitation.
To reduce the stray radiation new Denisov converter was designed and verified on short-pulse gyrotron mock-up. Modified industrial gyrotron with this new converter was tested with BN window and is testing now with CVD-diamond window. Total stray radiation is estimated as 4% of generated RF power instead of 10% in previous design. The industrial gyrotron test is planned to complete in this year.
Searching an ability to have higher output power project of 1.5–1.7 MW/170 GHz/CW gyrotron has been started. Short-pulse mock-up using $TE_{28\,12}$ mode of conventional cylindrical cavity was made. Its test is planned to start this year and long-pulse gyrotron prototype will appear in 2006.

During some years Russian specialists are developing super-high-power CW gyrotrons for ITER. The main ITER requirements for gyrotrons are summarize in Table 1.

Table 1

Frequency	170 GHz
Nominal RF Power	1 MW
Output radiation	TEM_{00}
RF Output Efficiency	50%
Accelerating Voltage	80–90 kV
Depression Voltage	27–35 kV
Beam Current	40–50 A
Pulse duration	1000 s

Large experience accumulated in the recent years was used to modify sequentially gyrotron design aiming at improvement of cooling, rise of efficiency, reduction of internal losses and stray radiation [1, 2]. Present design of 170 GHz/1 MW/CW gyrotron, which is shown in Fig. 1, stipulates usage of following main components and principles.

- Depressed-collector with longitudinal sweeping of worked-out electron beam.
- Main output window with 88-mm CVD diamond disk complemented by relief window with 102-mm BN disk.

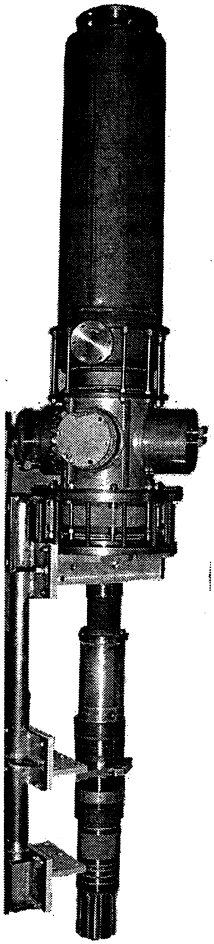

Fig. 1. Industrial gyrotron

• Built-in quasi-optical converter with four mirrors – three mirrors under beam accelerating voltage and the last adjustable mirror – under ground potential.

• Retarding voltage isolator placed above the cryomagnet (the gyrotron body must be isolated from cryomagnet housing) and provided by flexible cuffs for welding, outside ceramic supports to remove any mechanical stress and inner copper shield to protect ceramic from overheating by scattered RF power.

• Cavity designed for $TE_{25.10.1}$ mode operation.

• Diode type electron gun designed for beam current up to 50 A.

• Copper solely used as a material for all inner surfaces with intense water-cooling adequate to CW operation.

Two gyrotrons of this design with few intermediate modifications, which were fabricated and tested, demonstrated stable reassuring results.

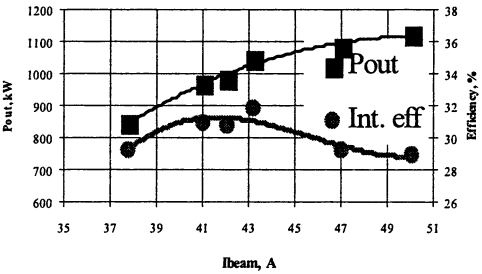

Fig. 2. Gyrotron output power and efficiency vs. beam current.

Gyrotron features are illustrated by Fig. 2 where behavior of power transported by output Gaussian beam along with oscillation power and corresponded efficiency are shown as functions of electron beam current at beam voltage of 76 kV. Measurements were made at 0.1 s pulse duration acceptable for used calorimetric load.

Table 2 given below shows the summary of test results ranged following attained power of output Gaussian beam, P_{out}, and pulse duration, τ. Operating regimes are illustrated by values of beam current, I_{beam}, beam voltage, U_{beam}, and efficiency at correspondent recuperation voltage, U_{rec}.

Table 2. Summary of test results

P_{out}, MW	*Eff.*, %	I_{beam}, A	U_{beam}, kV	U_{rec}, kV	Pulse duration	
					τ, s	Limited by
1.15	42	49	84	29	0.1	Load capacity
0.9	44	38	81	28	19	Load arcing
0.7	44	30	80	28	42	MOU arcing
0.5	40	26	76	22	80	Load arcing

Arcing arisen in terminating load or elements of mirror transmission line prevented from either reaching named source limit even at further reduced power level or disclosure of gyrotron serious intrinsic shortcomings. Low drift of operating frequency (~50 MHz) instilled confidence in efficient cavity cooling. Problem with long-term instability of beam current was managed to solve by step tuning of heater current.

Most important shortcoming inhere in previous gyrotron design was relatively high fraction of stray radiation, measured as 10% of output power. This radiation could cause overheating of DC break ceramic insulator and BN relief window. Temperature monitoring of these ceramic parts allowed to forecast that the retarding voltage insulator under forced air-cooling will not actually impede 1 MW/CW operation whereas window overheating will be the potential reason of pulse duration restriction.

For elimination of the found out potential restrictions development of new quasi-optic gyrotron system with pre-shaping was conducted. An upgrade internal converter consisting of a dimpled-wall waveguide launcher (so called Denisov launcher) and four mirrors produces an output beam with theoretical Gaussian mode content of 99,5% and diffraction losses as little as 2,3%.

To verify the proper behavior of the converter, a short-pulse gyrotron mock-up has been built and tested. The measured power of stray radiation was decreased from 8% to 3% with simple quadratic mirrors and about to 2% with phase correcting mirrors of synthesized shape.

After this experiment, new converter was fabricated and built into the following prototype of ITER industrial gyrotron, which was tested with BN window and is testing with CVD-diamond window now.

Output power of 1.05 MW in Gaussian beam with total efficiency of 47% at 0.1 s pulse duration was reached. Total stray radiation is estimated as 4% of generated RF power. It means that potential restriction due to BN relief window overheating is eliminated.

0.5 MW/30 s pulses were observed. Output power and pulse duration were limited by breakdowns in the water-cooled load. After summer holiday and installation of new water cooled load the gyrotron testing will be continued.

170 GHz, 1.5–1.7 MW gyrotron

GYCOM started to develop project of more powerful 170 GHz gyrotron basing on experience of 1 MW-tubes building.

Increases of output power up to 1.7 MW at expected electron efficiency of about 30% means increase of electron beam power up to 5 MW and consequently increase of beam voltage and current up to 100 kV/50 A. To have the total efficiency more then 45% single stage depressed collector was implemented.

Table 3

Parameter	Value
Frequency	170 GHz
Nominal RF Power	1.5–1.7 MW
RF Output Efficiency	> 45%
Accelerating Voltage	100 kV
Retarding Voltage	35–40 kV
Beam Current	50–60 A
Cavity type	Cylindrical
Cavity mode	$TE_{28\ 12}$
Cavity magnetic field	< 7 T
Pulse duration	1000 s
Depressed Collector	Single stage
Window	Diamond (CVD)
Output radiation	TEM_{00}

After comparative analysis of conventional and coaxial gyrotron advantages and disadvantages a design basing on cylindrical cavity was chosen.

The design parameters are presented in Table 3.

The gun was thoroughly calculated aiming in electron beam velocity ratio of 1.2 and velocity spread of 20–30%. The pitch-factor value of 1.2 was chosen to make compromise between such conflicting factors as electron beam stability and highest possible efficiency of beam-wave interaction in the cavity.

The gun is to operate at voltage up to 100 kV and current up to 50 A. At this current value the emitted current density is of 2.7 A/cm^2. Proper operation of electron gun at 90–100 kV/ 50–60 A and pitch-factor 1.2 will be checked in the mock-up which is manufacturing now to search for desired gyrotron parameters. Gyrotron mock-up is shown schematically in Fig. 3.

In the mock-up, the electron beam is emitted by a hexaboride lanthanum cathode at operating temperature of about 1400 °C.

$TE_{28.12}$ mode was selected as an operating one taking into account cavity heat load, mode converter efficiency and available cathode radius.

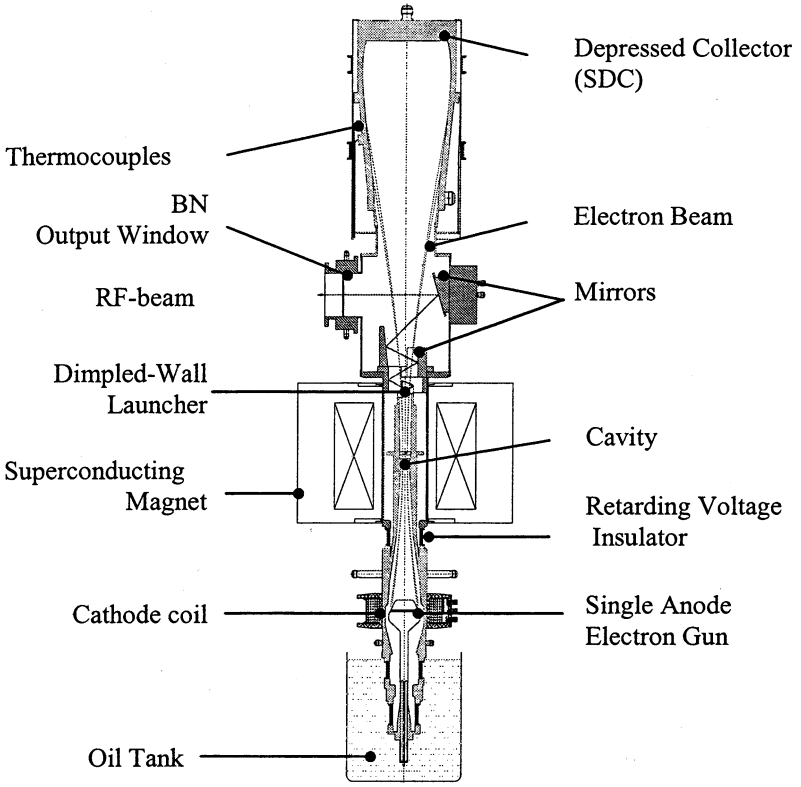

Fig. 3. Schematic view of 170 GHz/1.7 MW/100 ms gyrotron mock-up

Enlarging of a working space and usage of higher order modes yields the mode selection problem including start-up scenario as well as the problem of efficient mode conversion. However, calculation predicts that chosen $TE_{28.12}$ operating mode permits to reach near 1.7-MW output power with efficiency about 33% at moderate RF Ohmic losses. Cavity wall losses were calculated as 2.3 kW/cm^2 considering hot copper with real surface roughness. The mode excitation scenario will be checked in the mock-up too.

For so powerful gyrotron the principal problem is reduction of a stray radiation, which could cause overheating of the internal surface and ceramic units.

An internal mode converter utilizes a dimpled-wall launcher and three mirrors to transform the $TE_{28.12}$ mode excited in the cavity to fundamental Gaussian mode at the output of the gyrotron. Usage of specially profiled mirrors allows to

increase Gaussian mode content in the RF output radiation up to 98% at the level of stray radiation near 3%.

Early designed collector is utilized in the mock-up. Under usage of specially calculated electron sweeping it can withstand ~2.5 MW power at pulse duration not exceeding 150 ms. The set of thermocouples is imbedded in the collector wall for temperature monitoring.

Its test at 100-ms pulses is planned to carry out this year.

Basing on the test results long-pulse gyrotron prototype will be designed end manufactured to the end of the next year.

References

1. *Litvak A.G. et al.* Development of 170 GHz/ 1 MW/ 50%/ CW Gyrotron for ITER, Joint 29th Int. Conf. Infrared and Millimeter Waves and 12th Int. Conf. Terahertz Electronics. Karlsruhe, Germany, September 27-October 1, 2004. P. 111-112.
2. *Denisov G.G., Litvak A.G., Myasnikov V.E., Tai E.M.* Recent results in GYCOM/IAP Development of High-Power Gyrotrons for Fusion Installations, Proc. Int. Vacuum Electronics Conf. IVEC2005. Noordwijk, The Netherlands, April 2005. P. 497-500.

CW GYROTRONS AND ATTENDANT COMPONENTS AT 200 kW MICROWAVE POWER LEVEL

V. I. Kurbatov, S. A. Malygin, V. B. Orlov, E. A. Solujanova, E. M. Tai, A. A. Bogdashov[1], A. V. Chirkov[1], G. G. Denisov[1], V. I. Malygin[1], A. B. Pavelev[1]

Gycom Ltd, Nizhny Novgorod, Russia
[1]Institute of Applied Physics, Nizhny Novgorod, Russia
e-mail: tai@gycomnn.nnov.ru

Information about GYCOM CW gyrotrons manufactured and tested in 2004 – 2005 is presented. Designed output parameters of 84 GHz gyrotron were 200 kW continuously and 500 kW during 10 s pulse. During the operation at NIFS (Japan) the outputs 400 kW / 10 s, 200 kW / 1000 s, 160 kW / 3900 s were achieved. Another 82.7 GHz gyrotron operated at IPR (India) and generated 200 kW during 1000 s pulses. The equipment necessary for the gyrotron testing, conditioning and using is described. The test results of the pulse gyrotron with the built-in converter planned to be used in CW gyrotrons are reported.

Introduction

Usual way of CW high output power (~ 1 MW) gyrotron development is the design of gyrotron with maximum power and the increasing of the pulse duration step by step. During the rise of pulse length different difficulties are met and this problems are solved as they appear [1–3].

Presented work is the trial of another way. At first the gyrotron with output power smaller than 1 MW (~ 200 kW) is created, but this gyrotron is just really CW. After that is possible to think about how to increase the power up to the higher value. During the operation with this gyrotron different features are observed and investigated. Some difficulties begin to appear after ten minutes and even hour from the operation start. These problems may be investigated and solved only with the real CW gyrotron. Also that is right for the equipment necessary for the use of the gyrotron i. e. the elements of the transmission line, measuring load, water and vacuum systems and so on.

Two 200 kW CW gyrotrons with neighboring frequencies have built and tested at the factory and at the work placed together with the attendant equipment. There were 82.7 GHz gyrotron for Institute for Plasma Research (IPR, India) and 84 GHz gyrotron for National Institute for Fusion Science (NIFS, Japan).

Very preventing factor for the increase of the power is a heating of the gyrotron insides by stray radiation made by the built-in converter. 75 GHz pulse gyrotron containing the high efficiency converter was successfully tested. There is a possibility to use similar converters in future CW gyrotrons.

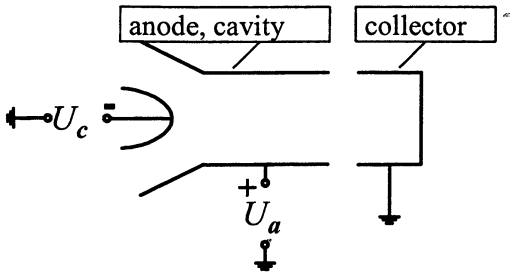

Fig. 1. Supplying scheme of the single step CPD gyrotrons. U_c – cathode voltage, U_a – anode, cavity voltage.

Depressed electron beam power at the collector is very useful for CW tubes. Single step collector power depression (CPD) scheme is shown on Fig. 1. Anode of the electron gun is connected with cavity (diode-type gun). Low power supply with positive voltage relatively ground is applied to the anode-cavity unit and creates additional acceleration of electrons in the interaction region. After the interaction on the way to the collector additional acceleration disappears.

External view of the gyrotron is shown on Fig. 2. At the microwave output Gaussian-like beam goes through the CVD diamond window. The cavity modes $TE_{10.4}$ and $TE_{12.5}$ were operating in 82.7 GHz and 84 GHz gyrotrons respectively. Built-in quasioptical converters consist of the Vlasov antenna with optimized nonsquare matching mirrors. Stray radiation from converter partly loosed in the inner microwave absorbers. Also 82.7 GHz gyrotron has the relief BN window. Even with this efforts against the stray radiation that is necessary to cool all the gyrotron elements i. e. mirrors, body, screens, pumps, insulators and so on.

Gyrotrons are pumped by inner getter pump continuously and by inner powerful ion pump during operation. Current of the ion pump is used for protection system.

Although frequencies are very close the gyrotrons are different because 84 GHz gyrotron has two operating regimes 200 kW / CW (1000 s at least) and 500 kW / 10 s. Test results of both gyrotrons in the 1 s pulse regime are shown on Fig. 3.

Also during the pulse tests stray power losses in different elements relatively the clear Gaussian output power were measured. Microwave heating of the gyrotron body and inner absorbers were 11% and 6% in 84 GHz and 82.7 GHz gyrotrons

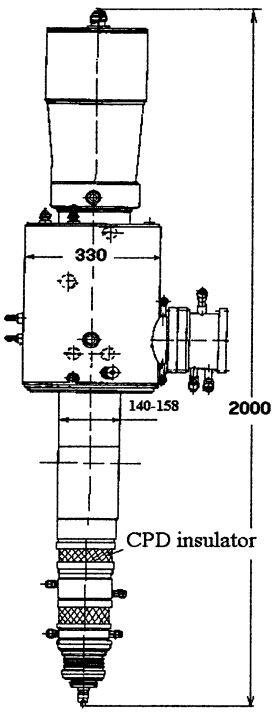

Fig. 2. External view of CPD gyrotron.

respectively. In the outside two matching mirrors box 9% and 12% were loosed. As 82.7 GHz gyrotron has the relief window, 5% were radiated through this window.

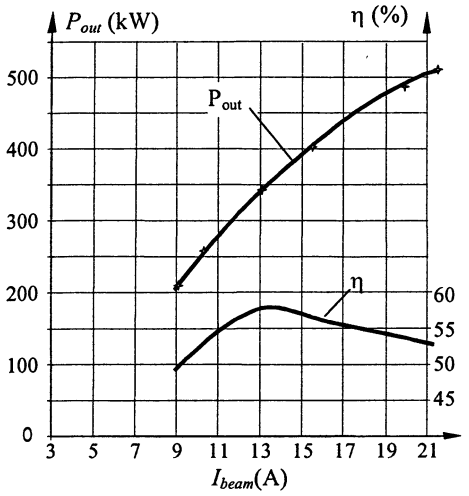

• Test regimes: U_c = –46 kV, U_a = +22 kV
P_{out} = 205 kW, I = 9 A, η = 49.5%
P_{out} = 505 kW, I = 21 A, η = 52%
• Optimum regime:
P_{out} = 360 kW, I = 13.5 A, η = 58%

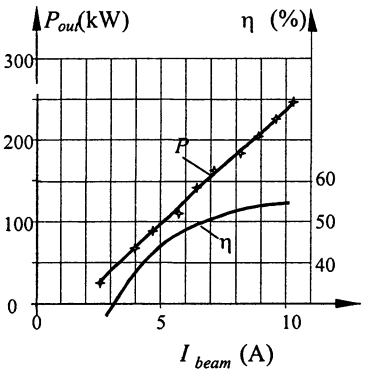

• Test regimes:
U_c = –43.5 kV, U_a = +19.5 kV
P_{out} = 205 kW, I = 9 A, η = 52%

Fig. 3. Gyrotron tests results (pulse regime, τ = 1 s).

82.7 GHz gyrotron was tested together with attendant equipment in CW regime on May, 2004 at GYCOM site. Scheme of the test is shown on Fig. 4.

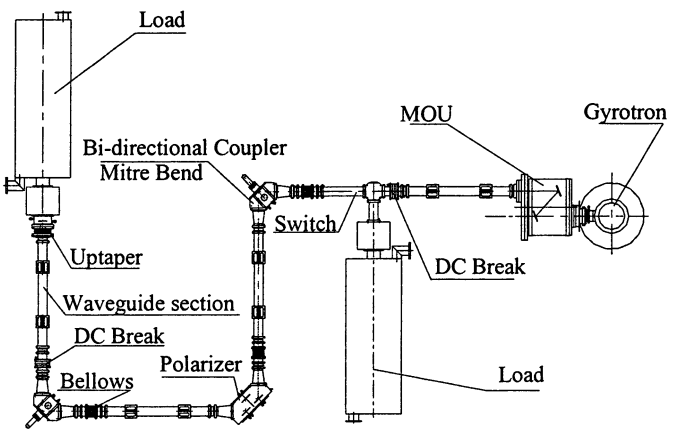

Fig. 4. Scheme of 82.7 GHz gyrotron system test at GYCOM

That were the matching optic unit (MOU) – two matching mirrors filter separating clear Gaussian component of the microwave power and forming required dimensions of Gaussian beam. Also the DC-breaks for electrical insulation, mitre bends containing directional copler and polarizer, bellows to neutralize mechanical movements, the wavequide sections, measuring calorimetric load and preload to reduce reflection from the load. Special switch dependently on its position directs the microwave power to the measuring load immediately after MOU or after all transmission line. Test was made under atmospheric pressure.

200 kW / CW calorimetric load is the big steel cylindrical volume (see Fig. 5) filled by the cooled steel pipes so much as volume allows. Assuming that the microwave power propagates in the load chaosly the reflection coefficient may be estimated as relation between the squares of the input hole and steel pipes, regarding that the reflection from the input hole back to the volume is zero but the reflection from the steel surface is 99%.

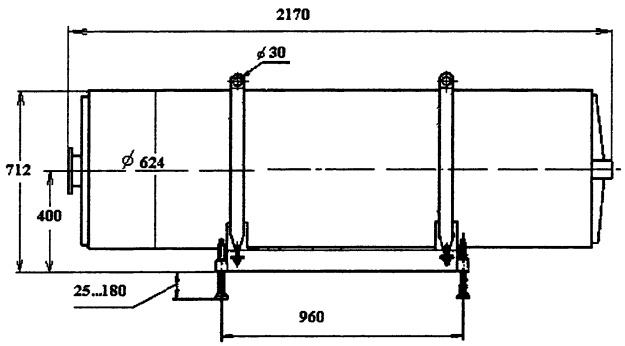

- Flow rate 3 l/s
- Reflection less than 3% at 82.7 GHz

Fig. 5. 200 kW/CW calorimetric load external view.

Scheme of the waveguide filter (preload) is shown on Fig. 6. It is the big gap in the waveguide in the volume filled by the cooled absorbing pipes. Power from the gyrotron is directed and most part of this power goes to the receiving waveguide. The power reflected from the load is in the form of stray radiation and most part of the reflected power goes to absorber. At the atmospheric pressure as absorber the teflon pipe with water may be used. In vacuum it must be another absorber available for the vacuum. Big gap between the waveguides may be used for the pumping of the evacuated transmission lines.

During factory test of 82.7 GHz gyrotron the clear Gaussian output power after MOU P = 200 kW was achieved in regime of cathode voltage U_c = –44.5 kV relatively ground, anode voltage U_a = +18.5 kV, beam current I_b = 10.5 A, efficiency η = 42.8%. At the place of work the similar regime was demonstrated: P = 206 kW, U_c = –44.5 kV, U_a = +18.8 kV, I_b = 9.1 A, η = 50.9%.

84 GHz gyrotron was tested mainly in NIFS because of the evacuated transmission line. For tests different attendant equipment was developed for the op-

eration with vacuum inside. MOU was developed by GYCOM and magnet, calorimetric load, corrugated waveguide line 31.75 mm diameter were developed by NIFS.

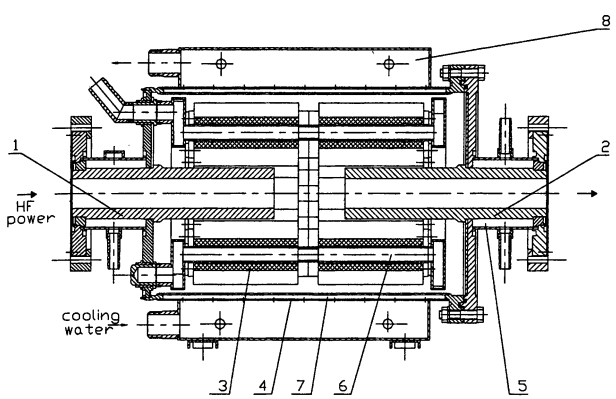

1 – input waveguide
2 – output waveguide
3 – absorbers
4 – body
5 – waveguides cooling
6 – absorbers cooling
7 – body cooling
8 – water collectors

Fig. 6. Waveguide filter scheme.

1000 s pulses were observed with $P = 200$ kW, $U_c = -49$ kV, $U_a = +17.7$ kV, $I_b = 10.1$ A, $I_a < 20$ mA. As the load the empty LHD-stellarator (without plasma) was used. During 10 s pulses $P = 400$ kW was achieved. Longest observed pulse 3900 s was to the LHD-machine with continuously firing plasma. Output power after MOU was 160 kW, injected power after the transmission line – 110 kW.

One of the possibility to reduce the difficulties on the CW way is the use of the high efficiency built-in converters with low level of the stray radiation. Converter with the corrugated launcher is considerable as the high efficiency converter. But the manufacture of this converter requires very high technological accuracy. That was observed during the creation of the first gyrotron with corrugated launcher – 110 GHz / 500 kW / 0.5 s gyrotron in 1992. After 10 years there was the next trial to use the corrugated launcher because of the new level of technology. 75 GHz / 800 kW / 0.1 s depressed collector gyrotron contains the $TE_{11.5}$ corrugated launcher, 3-mirrors scheme – quasiparabolic and two non-square mirrors for correction of the phase distribution (see Fig. 7, *a*).

There were two versions of gyrotron in test: without the corrugation of launcher and with it. Output power and efficiency dependencies are shown on Fig. 7, *b*. 70% efficiency was achieved with the corrugated launcher. Without corrugation efficiency was significantly lower because of the big Brilluen angle thereby big reflection and difraction at the end of launcher. That shows the high efficiency converters with corrugated launchers can allow to increase the output power of the future CW gyrotrons.

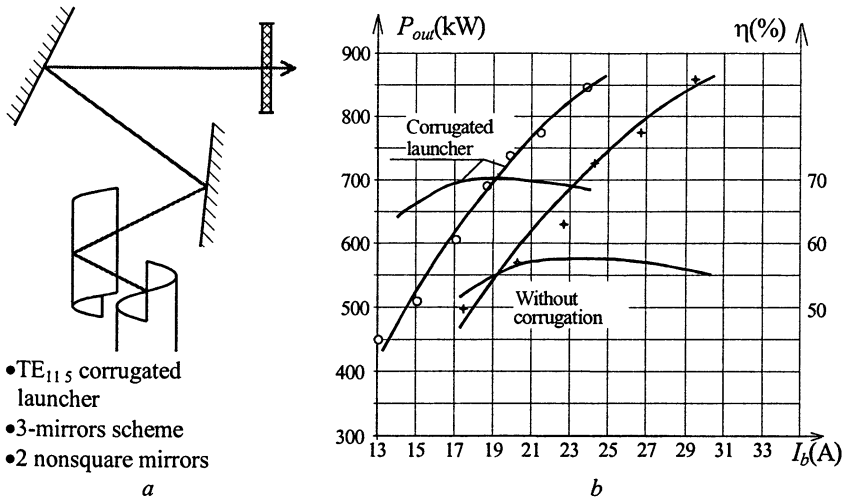

Fig. 7. 75 GHz / 800 kW / 0.1 s depressed collector gyrotron

Conclusion

Developed gyrotron design is acceptable for CW operation. Vacuum transmission line components (two mirrors MOU and waveguide filter) have tested at 200 kW power level. This components may be used at MW power level systems. Design of RF load is suggested. At present time it has modified to MW power level evacuated load. The tests demonstrated that significant output power rise is possible by increasing of converter efficiency. Efficiency of converters with corrugated launcher for different waveguide modes $TE_{10.4}$, $TE_{11\,5}$, $TE_{12.5}$, $TE_{25.10}$ are calculated and tested. Measured efficiency is about 97%.

References

1. *Blank M. et al.*, Development of long-pulse, Megawatt-class gyrotron oscillators at 110 and 140 GHz, EC-13, Proc. Joint Workshop. N. Novgorod, Russia, 2005. P. 383-387.
2. *Dammertz G. et al.*, Status of the 1 MW, 140 GHz, CW gyrotron for W7-X, in Strong Microwaves in Plasmas, Proc. Int. Workshop, N. Novgorod, Russia, 2003. V. 1, P. 16-28.
3. *Usachov S.V.*, Development of 170 GHz / 1 MW / CW gyrotron for ITER, EC-13, Proc. Joint Workshop, N. Novgorod, Russia, 2005. P. 398-402.

STATUS OF MULTI-FREQUENCY 105–140 GHz/1 MW/10 s GYROTRON AND RECENT TEST RESULTS

L. G. Popov[1], *M. V. Agapova*[1], *A. A. Bogdashov, G. G. Denisov, A. Ph. Gnedenkov*[1], *V. I. Ilyin*[2], *V. N. Ilyin*[1], *D. V. Khmara*[1], *A. N. Kuftin, A. G. Litvak, S. A. Malygin*[1], *V. I. Malygin, V. E. Myasnikov*[1], *V. O. Nichiporenko*[1], *A. B. Pavelyev, Yu. V. Roschin*[2], *N. A. Shamanova*[1], *E. A. Solujanova*[1], *E. M. Tai*[1], *S. V. Usachev*[1], *V. E. Zapevalov*

Institute of Applied Physics of Russian Academy of Science, Nizhny Novgorod, Russia
[1]GYCOM Ltd, Nizhny Novgorod, Russia
[2]Nuclear Fusion Institute, Russian Research Center "Kurchatov Institute", Moscow, Russia

First of Gycom gyrotrons designed for multi-frequency long-pulse operation yielded output power near 1MW at 140-GHz and near 0.8 MW at 105-GHz frequencies in up to 10-s pulses being tested at first on producer site and then on the site at IPP (Garching, Germany). Second gyrotron differing from the first one only in electron gun version under short pulse test produced similar output power for both frequencies. Both gyrotrons were equipped by diamond single disk window which could be matched only at the end frequencies of 105–140GHz range. For multi-frequency operation additional diamond disk should be installed to form tunable output window unit. Design of double disk gyrotron window has been completed in Gycom and is now ready for production. Nearest multi-frequency gyrotron prospect including possible usage of wide-band Brewster output window is presented.

Project of multi-frequency gyrotron based on possibility of gyrotron tuning to different operation mode within wide frequency range was initiated by IPP (Garching, Germany) to add more flexibility to ECRH as to the instrument of plasmas control. Desired gyrotron parameters are as follows:

Frequency range	105 – 140 GHz
Output power:	
at 140 GHz frequency	1 MW
at 105 GHz or at any intermediate frequency	0.8 MW
Pulse duration	10 s
Maximal beam voltage	90 kV
Maximal beam current	50 A
Efficiency with energy recuperation	40 – 50%
Output radiation	Gaussian beam

Considering results of prior theoretical end experimental investigations Gycom produced two gyrotrons using design conception which could be brought to the following features of main units:

Cavity has effectively cooled hard structure providing low frequency drift (most important for double disc output window) at ohmic losses less than 2 kW/cm^2.

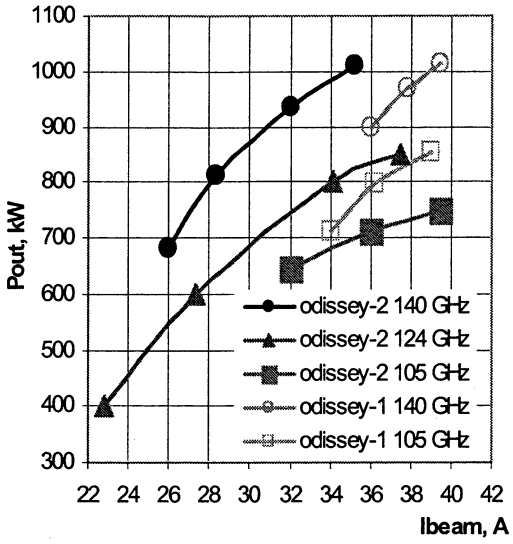

Fig. 1. Output power vs. beam current

Electron gun of diode type gun forms electron beam with radius tuned by gun coil when changing operation mode.

Mode converter of conventional type forms output radiation with Gaussian mode content more than 95% at diffraction losses 10–15%.

DC break insulator is located above the cryomagnet.

Collector uses depressed potential and sweeping of worked-out electron beam to withstand 1.2 MW power; sweep coil is fed by saw-tooth current with amplitude tuned under changing of operation mode.

Output window uses 106-mm diameter diamond disc mounted in conventional unit with 88-mm aperture; window can be converted in the double-disk one by mounting of external unit equipped with second disc of ~68-mm aperture; gap between two discs is tuned with high accuracy.

Relief window is formed by means of conventional unit with 133-mm diameter BN disc.

Figure 1 and Table show test results of two gyrotrons equipped with BN windows. BN window is thicker than diamond one and matched at 124 GHz as well as at 140 GHz and 105 GHz. Second gyrotron was tested at this frequency too. One can see that at the similar output power beam voltage and current are rather different which is consequence of different gun design following different used emitters.

Table

Gyrotron	Odissey-1		Odissey-2		
Operating frequency, GHz	105	140	105	124	140
Maximal output power, kW	850	1020	750	850	1010
U_{beam}, kV	70	75	84	81	85
U_{rec}, kV	25	26	25	21	22
I_{beam}, A	39	40	39	37	35
Interaction efficiency, %	31	34	25	28	34

Figure 2 illustrates long pulse test of the first gyrotron equipped by single disk diamond window. Most powerful regimes turned not to be available due to high rate of beam current increasing which started near 5 s. Nevertheless series of 10-s pulses were demonstrated with about 900-kW Gaussian beam power at 140 GHz and about 700-kW Gaussian beam power at 105 GHz. To damp current increasing heater power was manipulated during a pulse. Measured drift of operating frequency in both regimes was less than 100 MHz.

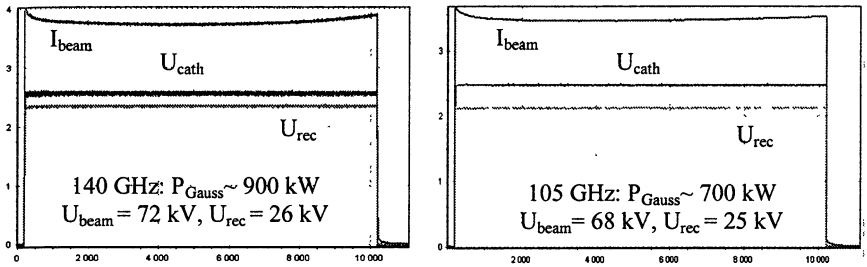

Fig. 2. Long-pulse test – monitored signals

Second gyrotron failed under long-pulse test because of collector melting-through. As analysis shows collector at first lost his shape under cooling water pressure due to processing errors taken place under its production. It will be restored and tested this year.

First gyrotron was shipped to IPP (Garching) where its commissioning was carried out. In the beginning, two problems embarrassed progress of test. First problem arose due to fluctuations appearing on beam current as well as on some other monitored signals. Protection system interpreted them as gyrotron arcing and tripped high voltage. Later on HV cable was identified as the source of harm and the problem escaped after grounding of cable armature. Second problem appeared as a necessity of long-term conditioning of the terminal water-cooled load produced by Gycom. Finally a moisture condensation on the internal load surfaces which temperature under water cooling was lower then ambient one was suspected as the reason of arcing started even in short pulses at lowered power. Remarkable progress in pulse extension was achieved when flow rate in the cooling circuit was varied during and after the pulse (up to complete switching it off) following an idea to keep the load walls warm. Series of 140 GHz/10 s pulses at Gaussian beam power exceeding 800 kW was demonstrated including pulses for which up to 20-kHz power modulation was used. Similar result was achieved with 105-GHz regime where measured Gaussian beam power was of 640 kW.

Output power measured on site at IPP in 140-GHz and 105-GHz regimes equivalent to long-pulse settings was found less than on site at Gycom. Differ-

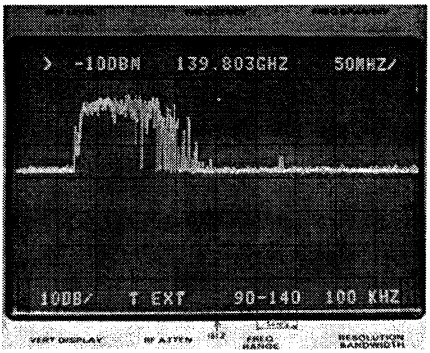

Fig. 3. Frequency spectrum at 140 GHz/ 9 s pulse.

ence looks not so dramatic considering both accuracy of calorimeter measurements and additional diffraction and ohmic losses brought by 4 additional mirrors as compared with Gycom set-up.

Frequency drift recorded by IPP spectrum analyzer as illustrated by Fig. 3 is higher than one measured in Moscow by Gycom frequency meter but still can be considered rather low even for case of double disk window tuning.

Traces of beam and body voltage and beam current in 140-GHz and 105-GHz regimes are similar to those ones in Fig. 2. Gaussian beam power monitored by RF detector looked pretty stable for both regimes.

Output window for multi-frequency gyrotron

To provide multi-frequency operation gyrotron is to be equipped with wide-band or tunable output window. Design of double disk version of multi-frequency gyrotron window has been completed in Gycom and it is now ready for production. The advantage of such a construction is that one can attach it to already existent dual frequency gyrotron and thus convert it to multi-frequency one. In the same time this assembly includes expensive additional diamond disk, means for its very accurate shift and positioning and means for exhausting of formed vacuum vessel.

Alternative way is to build a Brewster window and these attempts were made several times. Brewster angle for diamond is about 67°. To have more or less reasonable space for launching wave beam of 1 MW power through the conventional diamond disk of 106-mm diameter brazed with conventional cylindrical cuffs its length should be less than 10 mm. This kind of brazing is practically hardly feasible.

Two versions of thin copper cuffs of complicated shape having short cylindrical section and brazed seam placed closer to the disk rim were suggested. Calculations made independently in Gycom and FZK considering stresses remaining in the diamond disk after brazing and during operation as well as possibility of disk effective cooling gave encouraging results.

There is also an idea to use for diamond disk brazing into female cuff, which is conventional for BN-disk brazing. This manner of brazing gives following attractive opportunities.

– Principle absence of tensile stresses in CVD disk and in the joint after brazing.
– Maximal possible aperture for wave beam transmission.
– Guaranteed vacuum vessel isolation from cooling water in case of CVD disk crack.

Successful experiments on such type brazing carried out in Gycom with diamond disk of smaller diameter hopefully makes possible creation of compact window unit basing on diamond disk produced in Russia. In this case window unit could be used for building of a new multi-frequency gyrotron.

Compact window gives possibility to locate additional mirrors nearby the disk which in this case can be parallel to the gyrotron axis.

To check new ideas multi-frequency gyrotron mock-up is now preparing in Gycom. Early produced version of dual frequency gyrotron is put in the basis of this mock-up which scheme is shown in Fig. 4. New elements are adjustable last mirror combined with polarizer and BN Brewster window modeling future diamond window structure. Wave beam, which moves in horizontal plane at changing of operating mode but has here vertical polarization, will keep angle of incidence equal to Brewster one. It has elliptical cross-section and size which provides reasonable power density on the window itself and tight-fitting mirrors.

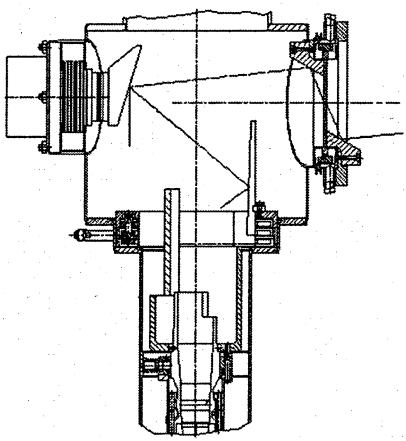

Fig. 4. Gyrotron mock-up with BN Brewster window.

Nearest future prospect

Global aim for the nearest future is to build new gyrotron including multi-frequency window and mode converter with pre-shaping reducing stray radiation to ~3%. Manufacturing and test of this gyrotron is planned to be done in 2006.

To achieve this object correction of the gyrotron technical documentation is to be completed in November 2005 basing on test results of both dual-frequency gyrotrons. Test of second restored dual frequency gyrotron will start in October 2005.

Type of the multi-frequency window which will be installed in a new gyrotron should be chosen to the end of this year basing on forthcoming test and processing results:

- Test of gyrotron mock-up with BN Brewster window.
- Brazing of diamond disk for double disk window.
- Brazing of diamond disk with shortened cuffs for Brewster window.

References

1. *Denisov G.G., Litvak A.G., Myasnikov V.E., Tai E.M.* Recent results in GYCOM/IAP Development of High-Power Gyrotrons for Fusion Installations, Proc. Sixth Int. Vacuum Electronics Conf. IVEC2005. Noordwijk, The Netherlands, April 2005. P. 497-500.

EXPERIMENTS AND SIMULATIONS OF A GYRO-BWO USING A HELICAL INTERACTION WAVEGUIDE

W. He, C. G. Whyte, A. W. Cross, A. R. Young, A. D. R. Phelps, K. Ronald, E. G. Rafferty, J. Thomson, C. W. Robertson, S. V. Samsonov[1], V. L. Bratman[1], G. G. Denisov[1]

Department of Physics, University of Strathclyde, Glasgow, G4 0NG, UK
[1]Institute of Applied Physics, Russian Academy of Sciences, Nizhny Novgorod, 603950, Russia

A gyrotron backward wave oscillator (gyro-BWO) with a helically corrugated interaction waveguide was studied experimentally using a thermionic electron beam of 90–215 keV in energy, 2–3 A in current and pitch alpha of up to 1.6. Simulated electron beam parameters from both MAGIC and SURETraj are in very good agreement with measured results. The oscillator achieved high efficiency frequency-tunable operation. At a fixed beam voltage of 185 kV and current 2 A, the output frequency was tuned by adjusting the B field in the interaction cavity. A maximum power of 62 kW and a 3-dB frequency-tuning band of 8.0–9.5 GHz (17% relative tuning range) with a maximum electronic efficiency of 16.5% were measured. In addition, the interaction frequency could be tuned by varying the electron beam energy. At a fixed cavity *B* field of 0.195 T and beam current of 2.5 A, A 3-dB relative voltage tuning bandwidth of 8% was measured when the electron beam voltage was changed from 215 kV to 110 kV. These measured results were found in excellent agreement with the simulations using MAGIC.

Introduction

It is well known that gyro-BWO is an efficient source of frequency-tunable high power coherent radiation. It is based on the resonant cyclotron interaction of electrons gyrating in the external magnetic field with an oppositely travelling electromagnetic wave. A number of gyro-BWOs have been investigated both in theory [1, 2, 3, 4] and experiments [5, 6, 7]. Two such experiments at the Naval Research Laboratory [5] and the National Tsing Hua University [6] operating at the fundamental cyclotron harmonic and the fundamental mode of a smooth cylindrical waveguide demonstrated excellent voltage tuning bandwidth of up to 5% and 13% respectively, with a high efficiency of nearly 20% at power levels of up to 100 kW at Ka-band frequencies.

A novel microwave system in the form of a helically corrugated waveguide has been demonstrated that its wave dispersion has a near constant group velocity in the region of small axial wave number [8]. This allows broadband microwave amplification to be achieved in a gyrotron travelling wave amplifier [9, 10]. Such a system is also favourable when used in a gyro-BWO [11, 12] in two ways. Firstly due to its larger group velocity as compared to conventional gyro-BWOs, it has a wider frequency tuning range. Secondly due to the non-symmetrical geometry of the helical interaction region, the electron beam interacts only with the wave in one direction (either backward or forward wave), and

hence has a pure frequency component. Helical waveguide gyro-BWO experiments performed at the Institute of Applied Physics, Russian, operating at the second harmonic at Ka-band frequencies generated a maximum output power of ~1 MW, an efficiency of 10%, a frequency tuning band of 15% using a 20 ns, 300 keV electron beam [13] and 10 kW of power, 5% efficiency, 10% tuning for a 10 μs, 45 keV electron beam [14, 15]. Latest gyro-BWO experiment performed at University of Strathclyde achieved a relative frequency-tuning band of 17% at X-band [16] with 16.5% electronic efficiency. The experiments also used a second harmonic interaction, halving the required magnetic field, but primarily to enable coupling between a special waveguide eigenmode having a strong quadrupole component and an axis-encircling electron beam. The dimension of the helical structure used in this experiment was designed to support the operating eigenwave of a higher group velocity as compared with the ones used in reference [11] to [15]. This allowed a higher electronic efficiency and wider frequency tuning range to be achieved. Both the experiments and its simulations of the gyro-BWO are presented in this paper.

The experimental set-up

A thermionic cathode electron gun in a Pierce-type geometry was used to generate a rectilinear electron beam in our experiment. A high voltage pulse of ~1 μs in duration and amplitude of up to 215 keV was applied to the electron gun to produce a beam current of 2–3 A in interaction cavity. The generation and propagation of the electron beam were simulated using both the 3D PIC code MAGIC [17] and the trajectory simulation code SURETraj, which was developed within the group. The beam parameter results calculated from both codes were found to be within 10% of the measured results. A schematic diagram of the gyro-BWO experiment is shown in Fig. 1.

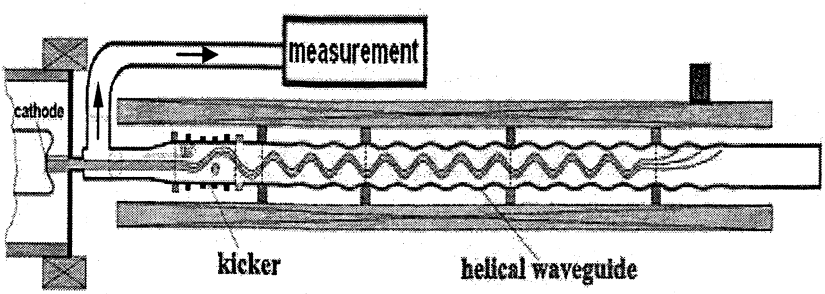

Fig. 1. A schematic diagram of the gyro-BWO experimental set-up

It is necessary to pump the transverse momentum of the electrons to obtain a beam-wave interaction based on the cyclotron resonance maser instability. Transverse velocity was imparted to the electron beam in a "kicker" consisting of 4 pairs of small rectangular multi-turn coils arranged in a Helmholtz-like configuration. In order to obtain the optimum cyclotron motion of the electron, the direction of the transverse magnetic fields produced by these coils underwent a total rotation within a distance equivalent to the cyclotron length of the "kicked" electrons. Electrons resonantly couple to this spatially inhomogeneous field to convert some of their axial momentum into transverse momentum. Figure 2 shows the simulated electron trajectories when passing through the kicker by using SURETraj simulation code. The rectilinear electron beam generated from the thermionic cathode was guided by an axial magnetic field and entered into the kicker region from the left. It should be noted that the magnitudes of both the radial position vectors and their projections in the y–z plane for the electrons are plotted in Fig. 2. When a pulsed current was applied to the kicker, the electron beam acquired a transverse velocity typically with a pitch factor of up to 1.6. Further increase of the kicker driving current resulted in the loss of part of the electron beam onto the beam tube although the pitch alpha of the remaining electron beam continued to increase. The simulations predicted a spread in the pitch alpha of the electron beam after the kicker to be approximately ±8% when the averaged pitch alpha of the electron beam was equal to 1. The resulting electron beam described a helical, axis-encircling trajectory. The pitch angle of such a large-orbit electron beam can be measured by the witness plate method [18], which was consistent with the results inferred from the radiation frequency as well as the simulation results from SURETraj. The beam voltage was measured using a two-tube, two-stage $CuSO_4$ voltage divider [19] and the electron beam current was measured using a Faraday cup at the end of the helical waveguide.

The cyclotron resonance maser (CRM) instability provided the effective interaction between the radiation and the axis encircling electron beam with the interaction harmonic number equal to the azimuthal mode index of the radiation. In this experiment the operating mode is synthesized by coupling the TE_{21} mode (azimuthal index, $m_A = 2$, Fig. 3) and the counter-rotating TE_{11} mode ($m_B = 1$, Fig. 3) on a three fold helical corrugation having a mean diameter 28.0 mm. The corrugated waveguide was 60 cm in length and the corrugation was 2.2 mm in amplitude with a period of 39.0 mm plus entrance tapers of 12 cm length at each end where the amplitude of the corrugation was tapered linearly to meet the smooth 28.0 mm bore of the input and output waveguides. The operating range was below the cut-off frequency of the TE_{21} mode of the smooth input/output waveguide. The backward wave co-rotating with the electron beam resonantly interacted with the 2nd harmonic of the electron cyclotron wave and underwent a partial reflection (6–20% in the frequency band of 8.0–9.5 GHz) from the upstream output coupler. The reflected forward wave propagated through the system without interaction with the electron beam. The forward wave then underwent a total reflection at the downstream end of the microwave system.

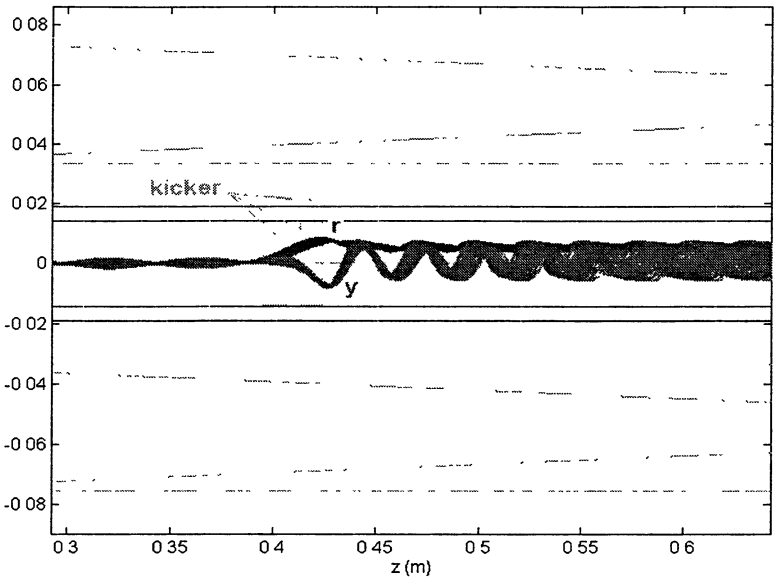

Fig. 2. Plot of $|r|$ vs z (indicated by r) and the projection of r in the y–z plane (indicated by y) for the simulation electrons in the kicker region.

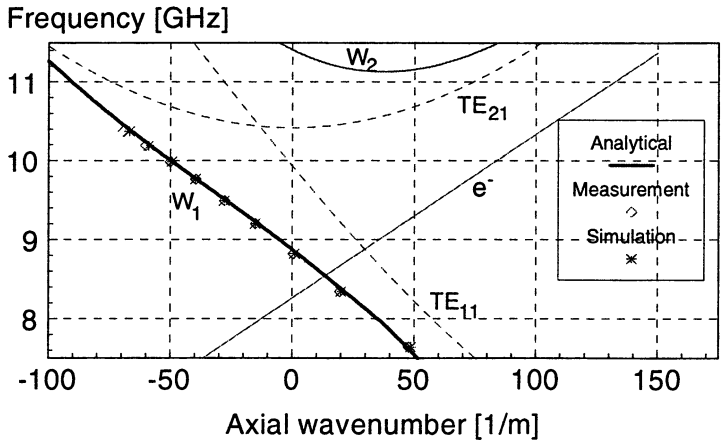

Fig. 3. Dispersion diagram of the operating eigenwave and the second harmonic electron cyclotron mode (e^-) from the gyro-BWO experiment.

Microwave output was measured using fast rectifying diodes after well-calibrated attenuators which were used to attenuate the microwave power from the output coupler. The oscillation frequency was measured using a heterodyne diagnostic.

The beam and wave dispersion

The three-fold helical waveguide structure can provide effective resonant coupling between two partial waves of the waveguide, i. e. the first spatial harmonic of the TE_{11} and TE_{21} modes when the period of the structure is properly chosen to meet Bragg resonance conditions. The resonant coupling of the waves corresponds to the intersection of their dispersion curves (Fig. 3). If the amplitude of the corrugation is small compared with the wavelength, the dispersions of the resultant eigenwaves, i. e. w_1 and w_2, can be calculated by analytical coupling theory [8, 20] and are shown in Fig. 3. One of the eigenwaves, i. e. w_1, having a near constant group velocity in the designed operating frequency range, is the operating eigenwave of the interaction. This operating eigenwave, resulting from the resonant scattering of the counter-rotating (with respect to the rotation of the helical waveguide) TE_{11} mode into the co-rotating TE_{21} mode inside the helical waveguide, is used in the experiment to resonantly interact with the second harmonic of the electron cyclotron mode as shown in Fig. 3.

The dispersion of the operating eigenwave can be measured by measuring the phase evolution of a counter-rotating circular polarized wave when it propagates through the waveguide by using a vector network analyser [21]. It can also be measured by detecting the polarization angle of a linearly polarized wave when it propagates through the waveguide by using a scalar network analyser (SNA) [8, 21]. In Figure 3 the measured results using the SNA method are shown and compared with the results simulated from the 3D PIC code MAGIC of the same operating eigenwave. In the simulation using the MAGIC code, a circular polarized wave of one frequency was injected into the helical waveguide, and a component of the electric field inside the waveguide was measured along the axial direction. The measured field was then numerically analysed and the axial wavenumber of the eigenwave was therefore obtained for that frequency.

The simulation of beam-wave interaction

The radiation of the gyro-BWO can be output in two positions. One is from an output coupler at upstream of the electron beam as shown in Fig. 1. The other is by an output window at downstream end. Obviously in the latter case the output window will act as a boundary of the cavity therefore some reflection from the window (can be as low as 1%) is desirable for the oscillation to start. Our experiments confirmed that the performance of the gyro-BWO is the same when using the two different output methods. In the simulation of the gyro-BWO, a simpler geometry from the latter output method (window type) was used to simulate the beam wave interaction as shown in Fig. 4. For the simplicity an electron beam of chosen parameter, i. e., beam energy, current and beam pitch angle, guided by a magnetic field in a beam tube of radius of 9mm, propagates downstream (right) direction. For the gyro-BWO to oscillate, the rotation of the electron beam should

rotate in opposite direction to the helical structure. At the downstream, a step-up (14 mm to 16 mm) of the output waveguide radius (instead of the output window) was used to define the interaction cavity. The step-up has a reflection coefficiency of a few percent for the operating frequency. In the simulation emitted electron beam can have either an annular or solid shape. However simulations shown that the radiation power and frequency are very similar by using either of the beam shapes when the beam parameters are kept the same. A snap shot of the simulation showing the geometry and electron beam trajectories is shown in Fig. 4. When the magnetic field is 0.2008 T, electron beam energy 185 keV, current 2 A, pitch alpha 1.1, a simulated output of ~64 kW and frequency of 8.575 GHz were obtained, which is very close to the measured output power of 58 kW and frequency of 8.58-8.60 GHz in the experiment. A typical simulated output spectrum and mode pattern are shown in Fig. 5.

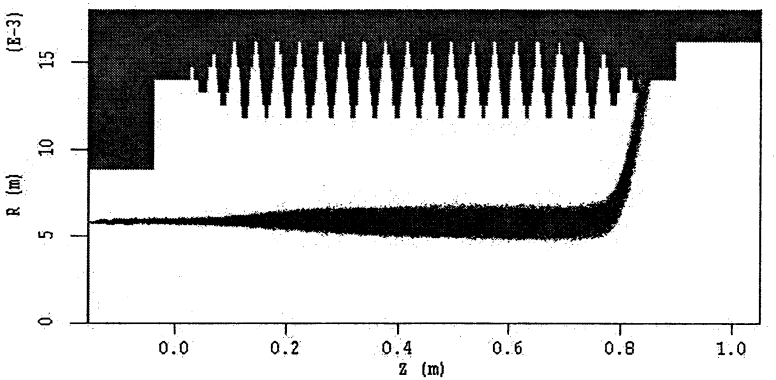

Fig. 4. Geometry of beam-wave interaction simulations by MAGIC and a snap shot of interacting beam trajectories.

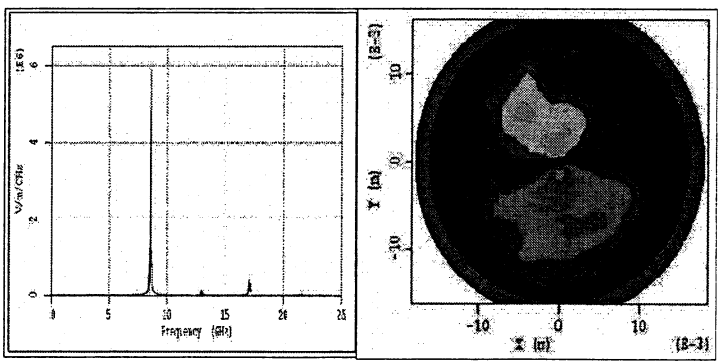

Fig. 5. A MAGIC simulation result showing the output spectrum of 8.575 GHz and mode pattern of TE_{11}.

The experimental results

Figure 6, *a* shows the measured electron beam voltage and current traces while Fig. 6, *b* shows the time-correlated microwave traces output from the gyro-BWO experiments. The measured electron beam results are in good agreement with the results from the simulations. The beam voltage and current traces show that there was some reflection in our pulsed power system. The microwave signal was observed at a lower voltage of about 90 kV up to a voltage of 185 kV in this case.

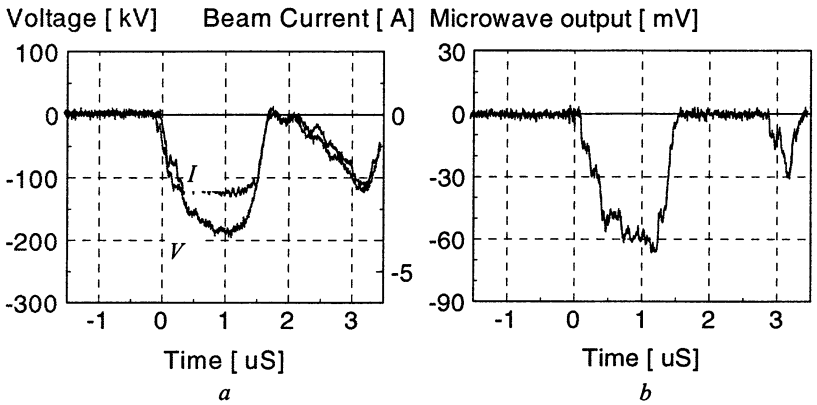

a *b*

Fig. 6. Measured beam voltage (*V*), current (*I*) (*a*) and time-correlated microwave output (*b*) wave traces.

A heterodyne frequency diagnostic was used to measure the frequency of the output radiation of the gyro-BWO. Microwave radiation from the gyro-BWO was mixed in a non-linear crystal with a local oscillator signal produced from a synthesised sweeper with the resultant intermediate frequency (IF) signal captured on a deep memory digitising oscilloscope. At a cavity magnetic field of 0.195 T, a fast fourier transformation of the IF signal showed significant output in the frequency spectral range of 9.00 to 8.40 GHz which was observed when the beam voltage was swept from about 120 to 185 kV respectively. Some of the measured frequency components at the corresponding beam voltages are shown in Fig. 7. From Fig. 6 and Fig. 7, the microwave output power is higher when the corresponding beam voltage is higher. This is due to the fact that the electron beam possesses higher power at higher voltages because the beam current is almost constant while the beam voltage was swept.

At beam energy of 185 keV and current of 2 A, the output frequency and power from the gyro-BWO were measured as a function of the tuning cavity magnetic field as shown in Fig. 8. In this case, only the frequency component at the peak voltage of 185 kV, which has the highest power in the pulse, was used as the output frequency. As shown in Fig. 8, a 3-dB relative frequency tuning

range of 8.0–9.5 GHz, which corresponds to a 17% relative tuning range, was measured. A maximum output power of 62 kW was measured which corresponds to an electronic efficiency of 16.5%. As a comparison the simulation results using MAGIC are also shown in Fig. 8. It clearly shows that the simulation results are in very good agreement with the measured results from the experiments. It should be noted that when a cavity magnetic field in excess of 0.240 T was applied, microwave radiation of similar power level was still generated. However, the frequency of the microwave radiation in such a case was measured to be around 10.5–10.6 GHz, which corresponded to the normal gyrotron interaction, in this case, the forward wave 2nd harmonic gyrotron interaction with the TE_{21} mode.

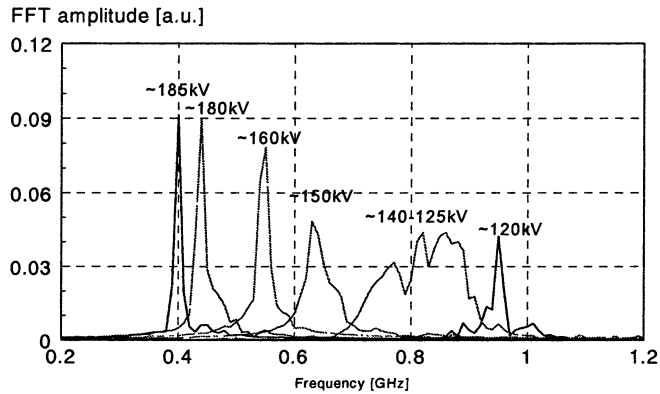

Fig. 7. A FFT spectrum of the IF signal at different sweeping electron beam voltage

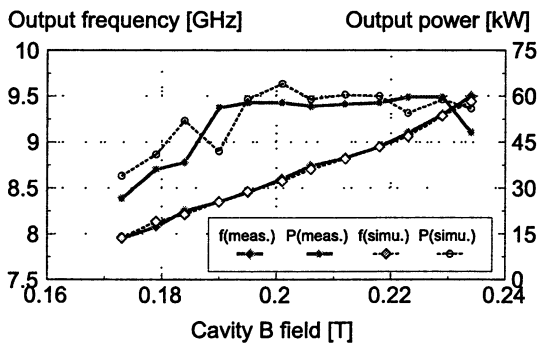

Fig. 8. Measured and simulated output frequency and power of the gyro-BWO as a function of tuning cavity magnetic field.

Frequency tuning characteristics of the gyro-BWO using beam voltage as a tuning parameter can be accurately measured by varying the electron beam energy from pulse to pulse. In this case the output frequency and microwave

output power were measured at the peak of the voltage pulses at a fixed cavity magnetic field of 0.195 T. Measured microwave frequency and electronic efficiency of the interaction from the gyro-BWO as a function of the tuning electron beam voltage is shown in Fig. 9. In this case the beam current was maintained at 2–2.5 A with an output power of 70 kW at a beam voltage of 215 kV and 7.5 kW at a beam voltage of 90 kV. A 3dB relative frequency tuning range of 8% (from 8.3–9.0 GHz) was measured when the electron beam voltage was changed from 215–110 kV.

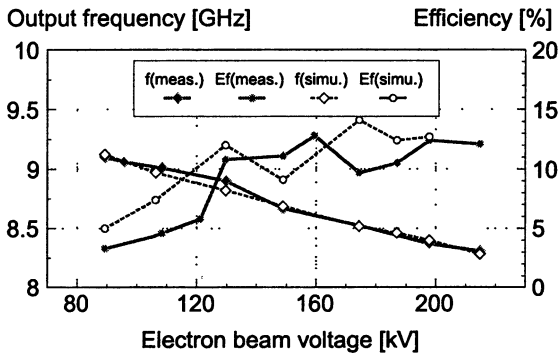

Fig. 9. Measured output frequency and interaction efficiency as a function of tuning e-beam voltage in comparison with the simulation.

Conclusions

A frequency-tunable gyro-BWO experiment using a novel helical waveguide was designed and investigated. A higher group velocity of the eigenwave inside the cavity allowed a wider frequency tuning range and higher interaction efficiency to be achieved. At a fixed beam voltage of 185 kV and current 2 A, a maximum power of 62 kW and a 3-dB frequency-tuning band of 8.0–9.5 GHz (17% relative tuning range) with a maximum electronic efficiency of 16.5% were measured when using the magnetic field as a tuning parameter. The relative frequency tuning range was measured at 8% when the beam voltage was used as the tuning parameter. Excellent agreement was shown between the simulations of the gyro-BWO using MAGIC and the measured results in the experiments.

Acknowledgement

The work was supported by the UK Engineering and Physical Sciences Research Council (EPSRC), Dstl, e2v, TMD and the UK Faraday Partnership in High Power Radio Frequency Engineering, Gycom Ltd., Nizhny Novgorod, Russia and the Russian Foundation for Basic Research under Grant 01-01-16780.

References

1. *Yulpatov V.K.* Radiophys. Quantum Electron., 1967, **10**, 471.
2. *Ginzburg N.S., Zaritsyna I.G., Nusinovich G.S.* Radio Eng. Electron. Phys., 1979, **24**, 113.
3. *Ganguly A.K., Ahn S.* Int. J. Electron., 1989, **67**, 261.
4. *Nusinovich G.S., Dumbrajs O.* IEEE Trans. Plasma Sci. 1996, **24**, 620.
5. *Park S.Y., Kyser R.H., Armstrong C.M., Parker R.K., Granatstein V.L.* IEEE Trans. Plasma Sci., 1990, **18**, 321.
6. *Kou C.S., Chen S.G., Barnett L.R., Chen H.Y., Chu K.R.* Phys. Rev. Lett., 1993, **70**, 924.
7. *Spencer T.A., Gilgenbach R.M., Choi J.J.*, J. Appl. Phys. 1992, **72**, 1221.
8. *Denisov G.G., Bratman V.L., Phelps A.D.R., Samsonov S.V.* IEEE Trans. Plasma Sci., 1998, **26**, 508.
9. *Denisov G.G., Bratman V.L., Cross A.W., He W., Phelps A.D.R., Ronald K., Samsonov S.V., Whyte C.G.* Phys. Rev. Lett., 1998, **81**, 5680.
10. *Bratman V.L., Cross A.W., Denisov G.G., He W., Phelps A.D.R., Ronald K., Samsonov S.V., Whyte C.G., Young A.R.* Phys. Rev. Lett., 2000, **84**, 2746.
11. *Samsonov S.V., Bratman V.L., Denisov G.G., Glyavin M.Yu., Lygin V.K., Luchinin A.G., Bykov Yu.V., Bogdashov A.A., Thumm M.*, IEEE Trans. Plasma Sci., 2004, **32**, 884.
12. *Denisov G.G., Bratman V.L., Glyavin M.Yu., Lygin V.K., Luchinin A.G., Manuilov V.N., Ofitserov M.M., Thumm M., Volkov A.B.*, IEEE IVEC 2003, Seoul, Korea, Proc., 338.
13. *Bratman V.L., Denisov G.G., Manuilov V.N., Samsonov S.V., Volkov A.B.* Digest Int. Conf. Infrared and Milimeter Waves, Toulouse, France, O. Portugall and J. Leotins Eds. 2001, 5.
14. *Samsonov S.V., Bratman V.L., Denisov G.G., Kolganov N.G., Manuilov V.N., Ofitserov M.M., Volkov A.B., Cross A.W., He W., Phelps A.D.R., Ronald K., Whyte C.G., Young A.R.* Phys. Proc. 12th Symp. On High current Electronics, Tomsk, Russia, G. Mesyats, B. Kovalchuk and G. Remnev Eds., 2000, 403.
15. *Bratman V.L., Cross A.W., Denisov G.G., Glyavin M.Yu., He W., Luchinin A.G., Lygin V.K., Manuilov V.N., Phelps A.D.R., Samsonov S.V., Thumm M., Volkov A.B.* Proc. 5th Int. Workshop Strong Microwaves in Plasmas, A.G. Litvak Ed. Nizhny Novgorod, Russia, 2002, 46.
16. *He W., Ronald K., Young A.R., Cross A.W., Phelps A.D.R., Whyte C.G., Rafferty E.G., Thomson J., Robertson C.W., Speirs D.C., Samsonov S.V., Bratman V.L., Denisov G.G.* IEEE Trans. Electron devices, 2005, **52**, 839.
17. *Gray T., Smithe D.N., Ludeking L.D.*, Mission Research Corporation, 2003.
18. *He W., Cooke S.J., Cross A.W., Phelps A.D.R.* Rev. Sci. Instrum., 2001, **72**, 2268.
19. *He W., Yin H., Phelps A.D.R., Cross A.W., Spark S.N.* Rev. Sci. Instrum., 2001, **72**, 4266.
20. *Cooke S.J., Denisov G.G.* IEEE Trans. Plasma Sci., 1998, **26**, 519.
21. *Burt G., Ronald K., Phelps A.D.R., Cross A.W., Konoplev I.V., He W., Young A.R., Whyte C.G., Thomson J.* Phys. Rev. E, 2004, **70**, 046402.

EFFECT OF ELECTRON EMISSION INHOMOGENEITY ON ELECTRON BEAM CHARACTERISTICS AND OUTPUT PARAMETERS OF A 4-mm GYROTRON

O. I. Louksha, B. Piosczyk[1], G. G. Sominski, M. Thumm[1], D. B. Samsonov

Saint-Petersburg State Polytechnical University, St. Petersburg, Russia
[1]Forschungszentrum Karlsruhe, Association EURATOM-FZK,
Institut für Hochleistungsimpuls- und Mikrowellentechnik (IHM), Karlsruhe, Germany

This paper describes the results of experiments performed with a pulse 74.2 GHz, 100 kW gyrotron at the St. Petersburg State Polytechnical University. Two LaB_6 cathodes and two impregnated dispenser cathodes, differing greatly in emission homogeneity, have been used for studying of the emission inhomogeneity effect on the amplitude of parasitic low-frequency oscillations, on the threshold pitch-factor corresponding to appearance of the oscillations as well as on the gyrotron output power and efficiency. The amount of transverse velocity spread related with inhomogeneity of the cathode emission was estimated using the data on electron energy distributions measured in the gyrotron. The obtained results allowed to determine the requirements for emission homogeneity of gyrotron cathodes.

Introduction

The requirement of high performance efficiency of a gyrotron is high quality of helical electron beam (HEB). One of the important sources of beam quality deterioration is inhomogeneous emission from thermionic cathodes of magnetron-type injection guns [1–3]. Typically, these guns operate in the regime of temperature limited emission. Therefore, the inhomogeneities of both the work function and the emitter temperature result in a non-uniform distribution of current density in the beam cross-section. The beam spatial non-uniformities can lead to degradation of the gyrotron efficiency through the increase of electron velocity spread due to non-uniform space-charge fields and through the excitation of parasitic modes in the resonator [4]. The inhomogeneities of electron emission can result from the imperfections in manufacturing of the large-size conical cathodes used in gyrotrons. Besides, the degree of emission inhomogeneity and, therefore, its influence on beam characteristics can change during long-time operation of a gyrotron, in particular, due to ion and electron bombardment of the emitter surface.

Our paper presents new data relating to the influence of cathode emission inhomogeneities on gyrotron output power and efficiency and on the parasitic low-frequency oscillations (LFO) of the space charge accumulated in the trap between the gun and the magnetic mirror.

Experimental gyrotron and measuring methods

The measurements have been performed with the experimental pulse gyrotron at the Saint-Petersburg State Polytechnical University. The main operating-regime design parameters of this tube are summarized in Table 1. The gyrotron is equipped with a room-temperature pulse magnetic system and operates in the regime of 30 – 60 μs single pulses with output power of ~ 100 kW. This tube includes a number of diagnostics, in particular, the electron energy analyzer, special probe and antenna to register the low-frequency instabilities in the beam and the parasitic low-frequency oscillations [5, 6].

Table 1. Main operating-regime parameters of the experimental gyrotron

Accelerating voltage	$U_0 = 30$ kV
Beam current	$I_b = 10$ A
Pulse duration	$\tau = 30 - 60$ μs
Cavity magnetic field	$B_0 = 2.75$ T
Cathode magnetic field	$B_c = 0.152$ T
Operating mode	$TE_{12\,3}$
Operating frequency	$f_0 = 74.2$ GHz
Average pitch-factor	$\alpha = 1.28$

In the sectional cathode assembly of the gyrotron, the emitter is changed via replacement of the molybdenum element equipped with an emissive strip. The experiments were performed with LaB_6 emitters C1 and C2 (operating temperature $T = 1500 - 1600$ °C), and with impregnated dispenser emitters C3 and C4 ($T = 950 - 1050$ °C). It is possible to rotate the cathode assembly with a bellows-type feedthrough. The azimuthal distribution of the cathode emission current density $j_e(\theta)$ is obtained by measuring the electron current passing through a 1-mm-diameter pin-hole in the anode versus cathode azimuthal position in the absence of applied magnetic field. The relative spread of emission current density is determined as the root-mean-square value:

$$\delta j_e = \frac{\sigma_{j_e}}{\bar{j}_e}, \tag{1}$$

where $\sigma_{j_e} = \sqrt{\frac{1}{n}\sum_{i=1}^{n}\left[j_e(\theta_i) - \bar{j}_e\right]^2}$ and $\bar{j}_e = \frac{1}{n}\sum_{i=1}^{n} j_e(\theta_i)$. In most cases, the dependencies $j_e(\theta)$ were measured with the azimuthal step $\Delta\theta = 5$ degree, which corresponds to the number of measuring points $n = 72$ per one 360-degree turn of the cathode.

Emission inhomogeneity of the cathodes

Studied cathodes differed in the azimuthal inhomogeneity of electron emission. The emission spreads δj_e was equal to 23% for cathode C1 and 50% for cathode C2. During a period of tube operation between its exposures to the atmosphere, the azimuthal distributions of emission current density didn't change significantly for these LaB_6 cathodes.

W-Ba cathodes C3 and C4 demonstrated higher sensitivity of their characteristics to external influence in comparison with LaB_6 cathodes. It was observed that emission activity and emission homogeneity of these cathodes decreased with time during standard gyrotron operation. However, a special conditioning at increased temperature and strongly reduced applied voltage in the CW regime allowed to smooth partially emission non-uniformities.

Parasitic low-frequency oscillations

The dependencies of the LFO amplitude measured for cathodes C1 – C3 and the calculated pitch-factor versus magnetic field are presented in Fig. 1. For a cathode with better emission uniformity, we obtained a decrease of the LFO amplitude for a fixed magnetic field and an increase of the threshold pitch-factor value α_{thr} corresponding to LFO appearance. This correlation was observed not only at the comparison of different emitters but also for one of the cathodes when its emission homogeneity was changed. Fig. 2 shows two dependencies obtained for cathode C4 in the states with different spreads of emission current density.

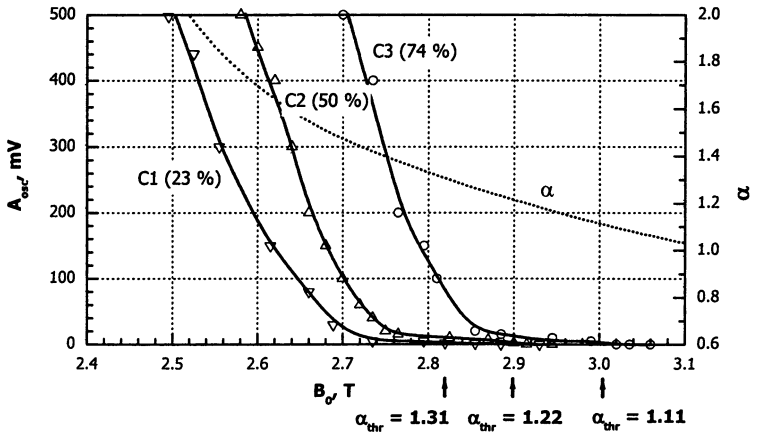

Fig. 1. Amplitude of low-frequency oscillations A_{osc} for cathodes C1, C2, C3 (emission spread δj_e are indicated in brackets) and calculated pitch-factor α as functions of magnetic field B_0.

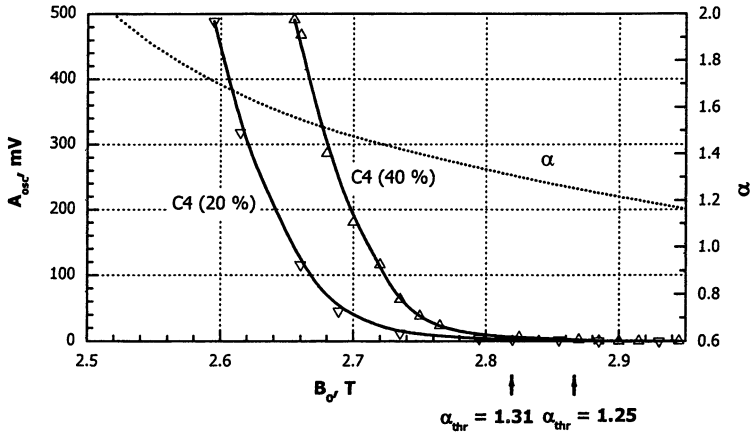

Fig. 2. Amplitude of low-frequency oscillations A_{osc} for cathode C4 (emission spread δj_e are indicated in brackets) and calculated pitch-factor α as functions of magnetic field B_0.

It was also observed that the increase of emission inhomogeneity resulted in reduction of the maximum output power and efficiency in the main $TE_{12,3}$ mode. The values of emission spread, threshold pitch-factor and maximum efficiency achieved with all cathodes are summarized in Table 2. The data of Table 2 put in the order of increase of cathode emission inhomogeneity.

Table 2. Emission inhomogeneity, maximum efficiency, threshold pitch-factor corresponding to LFO appearance and total transverse velocity spread for cathodes C1–C4

Cathode	δj_e	η_{max}	α_{thr}	$\delta v_{\perp rms}$
C4 (W-Ba)	20%	32%	1.31	8.8%
C1 (LaB_6)	23%	31%	1.31	8.8%
C4 (W-Ba)	40%	28%	1.25	9.6%
C2 (LaB_6)	50%	26%	1.22	10%
C3 (W-Ba)	74%	20%	1.11	11.8%

Obtained data can be explained if we are based on the model of parasitic oscillations caused by the reflection of electrons from magnetic mirror and accumulation of space charge in the trap between the gun and the resonator. From

this model, the LFO amplitude increases with growth of the coefficient of electron reflection from the mirror. This coefficient can be determined by the average values of pitch-factor and velocity spread and by the shape of the electron velocity distribution function. Most likely, the observed increase of the LFO amplitude in the case of emission inhomogeneity growth is a result of corresponding increase of the velocity spread in the beam. The inhomogeneous emission contributes to the velocity spread due to the non-uniform space charge fields as well at the cathode surface and along the whole beam trajectory.

To estimate the velocity spread from cathode emission inhomogeneity, we used the data on electron energy spectra measured in the gyrotron with cathode C2 [6]. Comparison of the experimental and calculated energy spectra let us assume the transverse velocity spread for this cathode in the regime without parasitic oscillations is equal to 10%. Knowing the values of threshold pitch-factor and velocity spread, the threshold reflection coefficient corresponding to appearance of the oscillations can be defined. The data of cathode C2 give us the threshold reflection coefficient equal to $1.7 \cdot 10^{-3}$. Having defined coefficient as a constant, we can estimate the total transverse velocity spread for another cathodes. These data are shown in the final column of Table 2.

As followed from Table 2, the factor connected with cathode emission inhomogeneity can affect the beam quality through increase of velocity spread. It should be noted that this factor is one of the sources of the total velocity spread along with spread of initial thermal velocities, cathode surface roughness, static and rf space-charge fields and others. Our data show that cathode emission inhomogeneity doesn't influence velocity spread against the background of another sources if coefficient of emission spread is less than approximately 20%.

As regards gyrotron efficiency, its degradation with emission inhomogeneity growth can be caused by (1) the increase of velocity spread, (2) by the excitation of parasitic modes in the cavity and the reduction of interaction efficiency with an operating mode, (3) or by the increase of energy spread from the parasitic low-frequency oscillations.

Conclusions

- The comparison of the cathodes differing in emission characteristics shows that the inhomogeneity of electron emission has a strong negative influence on gyrotron beam quality and efficiency.
- The decrease of emission homogeneity causes an increase of the electron velocity spread and the amplitude of parasitic low-frequency oscillations.
- The emission spread of $\delta j_e \cong 20\%$ can be accepted as a threshold value. Emission inhomogeneity below this threshold value doesn't influence neither the gyrotron efficiency no the beam characteristics (velocity spread and LFO amplitude).

Acknowledgements

This work was supported in part by the INTAS (grant no. 03-51-3861) and the RFBR (grant no. 05-02-08024).

References

1. *Tsimring Sh.E.* Int. J. Infrared Millimeter Wave, 2001, **22**, 1433.
2. *Louksha O.I., Sominski G.G., Kas'yanenko D.V.* J. Comm. Tech. Electron., 2000, **45** (1), S71.
3. *Glyavin M.Yu. et al.* IEEE Trans. Plasma Sci., 1999, **27**, 474.
4. *Nusinovich G.S. et al.* Phys. Plasmas, 2001, **8**, 3473.
5. *Kas'yanenko D.V. et al.* Proc. 5th Int. Workshop Strong Microwaves in Plasma (Nizhny Novgorod, Russia, 2003), 162.
6. *Kas'yanenko D.V. et al.* Proc. 10th ITG-Conf. Displays and Vacuum Electronics (Garmisch-Partenkirchen, Germany, 2004), 81.

DEVELOPMENT OF THz GYROTRONS IN FIR FU

T. Idehara[1], *M. Kamada*[1], *H. Tsuchiya*[1], *T. Hayashi*[1], *La Agusu*[1], *S. Mitsudo*[1], *I. Ogawa*[1], *V. N. Manuilov*[1,2], *K. Naito*[3], *T. Yuyama*[3], *W. Jiang*[3], *K. Yatsui*[3]

[1]Research Center for Development of Far Infrared Region, University of Fukui
Bunkyo 3-9-1, Fukui-shi 910-8507, Japan
[2]Radiophysical Department of Nizhny Novgorod State University,
690005, Gagarin av., 23, Nizhny Novgorod, Russia
[3]Extreme Energy-Density Research Institute, Nagaoka University of Technology,
Kamitomioka 1603-1, Nagaoka-shi, Niigata 940-2188, Japan

An ultra-high frequency gyrotron is being developed as a THz radiation source by using a pulse magnet. We have achieved the highest field intensity of 20.2 T. High frequency operation at the second harmonic will achieve 1.01 THz. Corresponding cavity mode is $TE_{6,11,1}$. On the other hand, an ultra-high power gyrotron with a pulse magnet is also being developed as a millimeter to submillimeter wave radiation source. The gyrotron is a large orbit gyrotron (LOG) using an intense relativistic electron beam (IREB). A pulsed power generator "ETIGO-IV" is applied for generation of IREB. A prototype relativistic LOG was constructed for fundamental operation. The output of the LOG will achieve 144 GHz and 9 MW. Corresponding cavity mode is $TE_{1,4,1}$. Cavities for 2nd and 4th harmonic operations were designed by numerical simulation for achievement of higher frequency. The progress of development for prototype high frequency gyrotrons with pulse magnets is presented.

1. Introduction

The development of gyrotrons is being advanced in two ways. One is the development of high power, millimeter wave gyrotrons. At the present, a gyrotron with a diamond window has achieved 2 MW output power at 170 GHz in a pulse of several seconds long [1]. Such high power gyrotrons are being used for the electron cyclotron heating of fusion plasmas. The other is the development of high frequency, medium power gyrotrons as millimeter to submillimeter wave radiation sources for a broad range of applications.

Our gyrotrons developed in the Research Center for Development of Far Infrared Region at University of Fukui (FIR FU) belong to the second type. In FIR FU, we have developed the Gyrotron FU Series which consists of 9 gyrotrons. The gyrotron series has achieved frequency tuning over a wide range (from 38 GHz to 889 GHz) with output powers ranged from several tens of watts to several tens of kilowatts. The highest frequency 889 GHz corresponds to a wavelength of 337 μm. This is a current record for high frequency operation of gyrotron [2].

In order to develop such high frequency gyrotrons, we usually require high magnetic fields generated by superconducting magnets [3] and/or operation at high harmonics of the electron cyclotron frequency [4, 5]. For Gyrotron FU IVA [6], for example, a 17 T superconducting magnet is used. However, operation with a superconducting magnet is complicated, because we need to transfer

liquid helium from a container to cryostat, recover the evaporated helium and liquefy it again.

Recently, we have developed a high harmonic gyrotron with an axis-encircling electron beam and a permanent magnet instead of a superconducting magnet. The treatment is much more simplified [7], but the field intensity is quite low compared with a superconducting magnet. It is only around 1 T. We have to use higher harmonic operation in order to obtain high frequencies. A gyrotron with an axis-encircling electron beam (a so-called Large Orbit Gyrotron, LOG) is capable of n-th harmonic operation, when we employ the TE_{n11} cavity mode. In this case, the frequency of electromagnetic wave f is equal to n times of the electron cyclotron frequency f_c and the axis-encircling electron beam feels n cycles of alternating electric field during one cycle of the electron gyration. Therefore, the interaction between an electron and electromagnetic wave is optimized and highly efficient operation is expected. In addition, the mode competition with fundamental or lower harmonic operations is removed, because only the TE_{n11} cavity mode is excited when $f = nf_c$ [8].

. In the case of the conventional gyrotron, higher harmonic operation is difficult to be realized. The Gyrotron FU Series easily achieved second harmonic operations but third harmonic operation was very rare. [9] In addition, efficiency is decreased with harmonic number. On the other hand, in the case of LOG, higher harmonic operation (n = 2, 3, 4, 5) is easily excited [10, 11]. At the present, our LOG has achieved fifth harmonic operation and the output power is around 0.1 kW.

At the present, we are intending to achieve a breakthrough of 1 THz by using high field pulse magnet. The design of the whole system, simulation of the operation and test results of the pulse magnet are described in the next section. On the other hand, use of high harmonic operations is also important for increasing the frequency of the gyrotron. Using an intense relativistic electron beam (IREB) from ETIGO IV which is included in the series of intense pulsed power generators installed in Extreme Energy-Density Research Institute at Nagaoka University of Technology, we are developing a Relativistic LOG with an ultra-high output power. We have designed the LOG operating at fundamental cyclotron frequency and constructed it. Also, we have designed a high harmonic LOG for higher frequency operation. Combination of high harmonic operations and high-field pulse magnet enables us to achieve the breakthrough of 1 THz. In this paper, the present status of ultra-high frequency gyrotrons with pulse magnets developed in FIR FU is described.

2. A THz gyrotrons using a pulse magnet

2.1. Design of the whole system and operation test

Figure 1 shows the overall view of the gyrotron system which has been designed and constructed in FIR FU. The system consists of a gyrotron tube, a pulse magnet, a condenser bank, power supplies, vacuum pumps and a control system. A pulse magnet is designed to achieve highest field intensity exceeding

20 T. The gyrotron tube is installed on the center axis of a pulse magnet which is connected to a condenser bank localized downstairs. The capacitance is 6 mF and maximum and charging voltage 10 kV. The maximum stored energy is 300 kJ. It is discharged through an ignitron to operate the pulse magnet. The whole system is controlled from upstairs by using a control system.

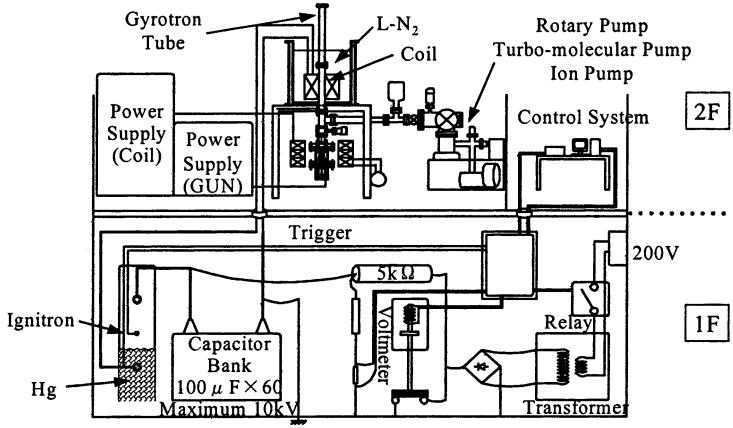

Fig. 1. Overall view of the gyrotron system

Figure 2 shows the cross section of the pulse magnet coil. The inner diameter is 43 mm, the length 112 mm and copper wire is wound 305 turns. The magnet is installed in a cryostat and cooled down by the liquid nitrogen. Water with alumina powder surrounding the coil is frozen and fixes the coil tightly in order to protect the coil from expanding. Figure 3 shows the test results of the magnet. The highest field intensity reaches 20.2 T and the pulse width is 6 ms. We are using a simple cylindrical cavity whose diameter is 3.9 mm and the length 10 mm.

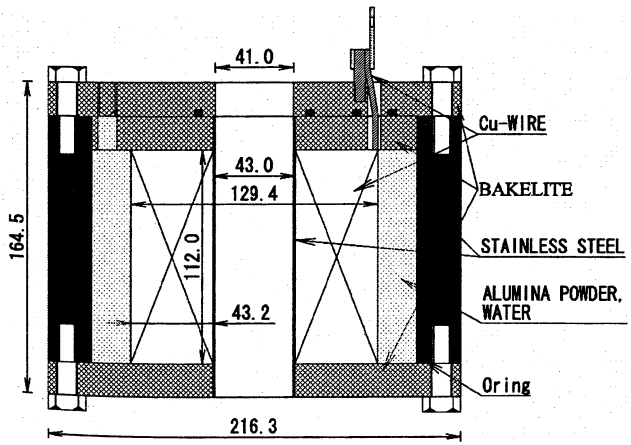

Fig. 2. A cross section of a high field pulse magnet.

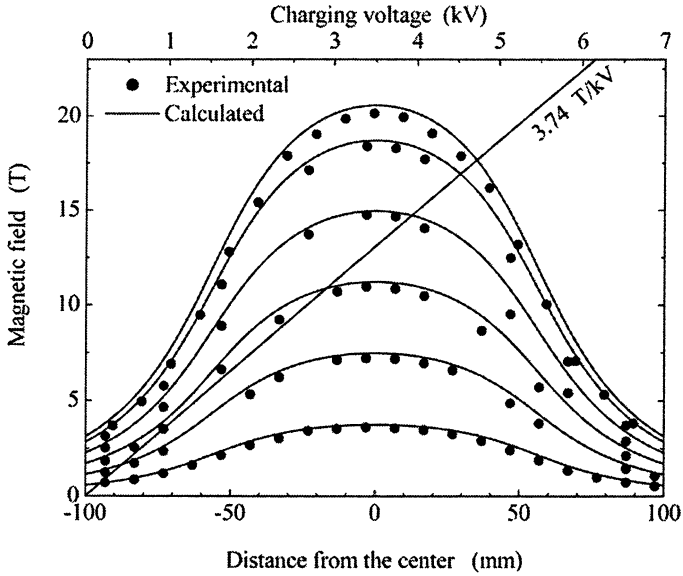

Fig. 3. Test result of pulse magnet

2.2. Simulation results for high frequency operation

Figure 4 shows starting currents for several cavity modes operating at the fundamentals (broken line) and second harmonics (solid lines) as functions of magnetic field intensity. Simulation results suggest possibility of a single mode operation of $TE_{6,11,1}$ at the second harmonic. The corresponding frequency is 1.01 THz.

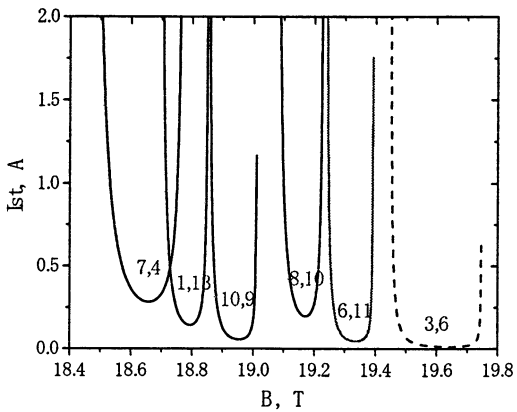

Fig. 4. Calculation of starting current in A

Figure 5 shows mode competition between $TE_{3,6,1}$ at the fundamental operation and $TE_{6,11,1}$ at the second harmonic operation. At the initial stage, a fundamental operation at $TE_{3,6,1}$ cavity mode occurs dominantly. However, it is suppressed with time. On the contrary, a second harmonic operation at $TE_{6,11,1}$ mode grows up and becomes dominant in the final stage. Coresponding frequency is around 1.01 THz.

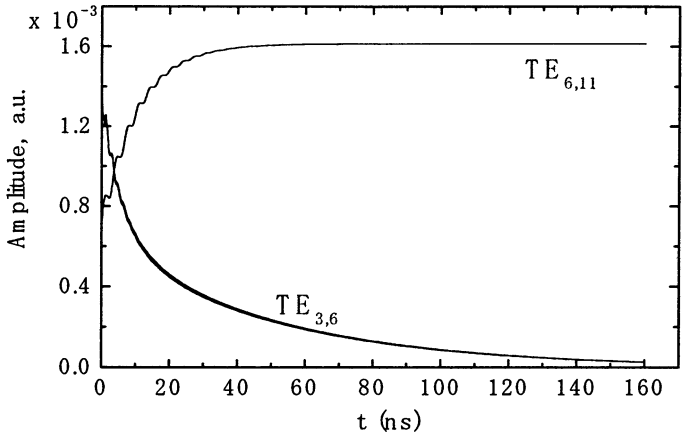

Fig. 5. Mode competition between $TE_{3,6}$ mode at fundamental and $TE_{6,11}$ at second harmonic.

3. High-power, short pulse, large orbit gyrotron

3.1. A prototype relativistic LOG for fundamental operation

Figure 6 shows the side view of a pulsed power generator "ETIGO-IV" installed in Nagaoka University of Technology [12]. It is aimed at applications to material development, pulsed ion beam acceleration, and high power microwave generation. It is capable of delivering to matched load an output pulse of 400 kV in peak voltage, 13 kA in peak current and 120 ns in pulse length at the repetition rate of 1 Hz. It is about 3.9 m long, 2.7 m high, 1.1 m wide, weighting about 6200 kg.

Figure 7 shows the cross section of the gyrotron tube. The LOG system is connected to the output edge of ETIGO-IV shown on the right hand side in Fig. 6. An IREB is generated from cold cathode by explosive emission. Beam energy is controlled by charged voltage of ETIGO-IV. An axis-encircling electron beam is formed by passing through the thin slit of the anode plate in the cusp magnetic field. Beam current is controlled by shape of the slit. The cusp magnetic field is produced by cw coils and pulse magnet coil. The electron beam is injected into the cavity following to line of force of the magnetic field. The pulse magnet coil produces a magnetic field of 8 T on the center of the cavity. After interaction in the cavity, the electron beam enter to the collector. The oscillated millimeter or submillimeter wave is radiated from the sapphire window. The whole LOG system is pumped out by a cryo-pump.

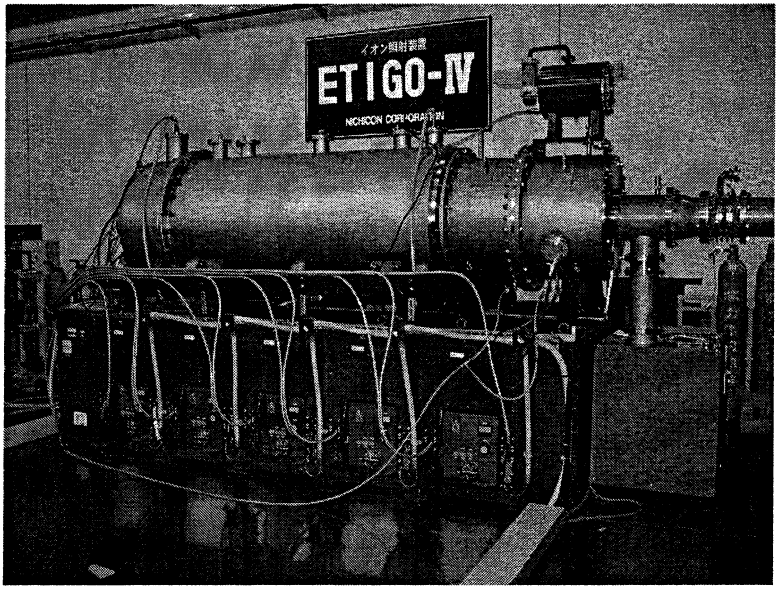

Fig. 6. Side view of a pulsed power generator "ETIGO-IV"

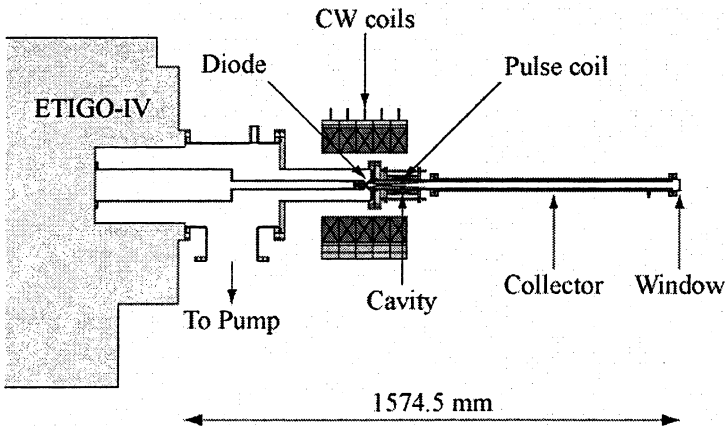

Fig. 7. Cross section of the gyrotron tube

As a first trial, a prototype LOG was designed and constructed. Numerical simulation was carried out for optimization of the diode, the cavity and the collector [13, 14]. Table 1 shows some parameters of the LOG for fundamental operation. The frequency achieved is 143.6 GHz. Corresponding cavity mode was $TE_{1,4,1}$. The output power was predicted at 18 MW from simulation of the

interaction in the cavity. But, it is necessary to consider the space charge effect and the ohmic loss. Actual output power is expected to be decreased to 9 MW in the experiment.

Table 1. Parameters of the LOG for fundamental operation

Operation mode	$TE_{1,4,1}$
Harmonic number	1
Beam energy	400 keV
Pitch factor	1.51
Cavity radius	3.9 mm
Cavity length	10.0 mm
Magnetic field	8 T
Beam current	200 A
Frequency	143.6 GHz
Q value	678
Output power	9 MW
Efficiency	11.3%

3.2. Operation test of the pulse coil

Structure of the pulse magnet is similar to that for a THz gyrotron which is described in the previous section. Operation test of the pulse magnet was already carried out. The pulse coil is 30 mm in inner diameter, 99.2 mm in length and copper wire is wound 217 turns. The coil is operated by the capacitor bank system of 1 mF. The maximum charging voltage is 5 kV. The upper bound of the field intensity is expected 12 T by the strength of the wire to the electromagnetic force. The highest field intensity reached 11.7 T when the charged voltage was 4 kV and the pulse width 2.5 ms as shown in Fig. 8. In Figure 8, a parameter is a charged voltage of the condenser bank.

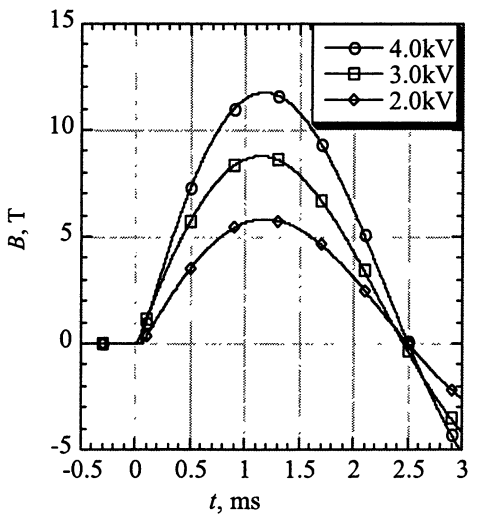

Fig. 8. Magnetic field intensity on the center of the cavity.

3.3. Cavity design for higher harmonic operation

In near future, higher harmonic LOG will be constructed for higher frequency operation. Cavities for 2nd and 4th harmonic operation were designed by numerical simulation. Table 2 shows some parameters for 2nd and 4th harmonic operation. On the second harmonic operation, the frequency achieved 256.3 GHz. Corresponding cavity mode was $TE_{2,4,1}$. The output power was expected 1.5 MW. On the 4th harmonic operation, the frequency achieved 312 GHz. Corresponding cavity mode was $TE_{4,4,1}$. The output power was expected 0.2 MW. In the next trial, we will install these cavities in order to achieve higher harmonic operation with higher frequency.

Table 2. Parameters of the LOG for harmonic operation

Operation mode	$TE_{2,4,1}$	$TE_{4,4,1}$
Harmonic number	2	4
Beam energy	381 keV	381 keV
Pitch factor	1.6	1.6
Cavity radius	2.45 mm	2.44 mm
Cavity length	10.0 mm	15.0 mm
Magnetic field	7.6 T	4.57 T
Beam current	60 A	30 A
Frequency	256.7 GHz	312 GHz
Q value	2317	7398
Output power	1.5 MW	0.2 MW
Efficiency	6.5%	1.7%

4. Summary

A THz gyrotron using a pulse magnet system generating a high magnetic field up to 20.2 T has been constructed. The operation test of the magnet was excellent. Computer simulation results indicate that the breakthrough of 1 THz can be achieved. The operation test of the whole system will be carried out soon.

A prototype relativistic LOG using a pulsed power generator "ETIGO-IV" generating a high voltage up to 400 kV has been constructed. As for the output characteristic of the relativistic LOG, frequency of about 144 GHz and power of 9 MW are expected. The experiment of the LOG will be carried out soon. As further development, high harmonic LOGs are designed. In near future, those LOGs will be constructed for achievement of higher frequency.

Acknowledgements

This work was partly supported by a Grant in Aid from the Ministry of Education, Culture, Sports, Science and Technology (MEXT) and Project Allocation Fund of the University of Fukui and was carried out in the framework of

the collaboration and Agreement for Scientific Exchange between the Research Center for Development of the Far-Infrared Region (FIR FU) at the University of Fukui and Extreme Energy-Density Research Institute at Nagaoka University of Technology.

References

1. *Piosczyk B., Braz O., Dammertz G., Iatrou C.T., Kern S., Kuntze M., Michel G., Moebius A., Thumm M.* Operation of a coaxial gyrotron with a dual RF-beam output, Digest 22nd Int. Conf. Infrared and Millimeter Waves. Wintergreen, Virginia, USA, July 1997. Ed. by H.E. Freubd. P. 114-115.
2. *Idehara T., Mitsudo S., Sabchevski S., Glyavin M., Ogawa I.* Gyrotron FU Series – current status of development and applications, 62, 123 (2001).
3. *Idehara T., Tatsukawa T., Ogawa I., Tanabe H., Mori T., Wada S., Kanemaki T.* Development of a second cyclotron harmonic gyrotron operating at 0.8 mm wavelength, Appl. Phys. Lett., 56, 1743 (1990).
4. *Idehara T., Tatsukawa T., Matsumoto S., Kunieda K., Hemmi K., Kanemaki T.* Development of high frequency, cyclotron harmonic gyrotron oscillator, Phys. Lett. A, 132, 344 (1988).
5. *Idehara T., Tatsukawa T., Ogawa I., Tanabe H., Mori T., Wada S., Brand G.F., Brennan M.H.* Development of a second cyclotron harmonic gyrotron operating at submillimeter wavelengths, Phys. Fluids B, 4, 267 (1992).
6. *Idehara T., Ogawa I., Mitsudo S., Pereyaslavets M., Nishida N., Yoshida K.* Development of frequency tunable, medium power gyrotrons (Gyrotron FU Series) as submillimeter wave radiation sources, IEEE Trans. Plasma Sci., 27, 340 (1999).
7. *Kikunaga T., Asano H., Yasojima Y., Sato F., Tsukamoto T.* A 28 GHz gyrotron with a permanent magnet system, Int. J. Electronics, 79, 655 (1995).
8. *Glyavin M., Sabchevski S., Idehara T., Ogawa I., Mitsudo S., Ohashi K., Kobayashi H.* Numerical analysis of weakly relativistic large orbit gyrotron with permanent magnet system, Int. J. Infrared and Millimeter Waves, 21, 1211 (2000).
9. *Idehara T., Tatsukawa T., Ogawa I., Wada S., Yoshizue K., Inoue F., Brand G.F.* Single mode operation of a submillimeter wave gyrotron at the third harmonic resonance, Phys. Fluids B, 4, 769 (1992).
10. *Sabchevski S., Idehara T., Ogawa I., Glyavin M., Ohashi K.* Simulation of a high harmonic gyrotron with axis-encircling electron beam and permanent magnet, Int. J. Infrared and Millimeter Waves, 23, 675 (2002).
11. *Sabchevski S., Idehara T., Ogawa I., Glyavin M., Mitsudo S., Ohashi K., Kobayashi K.* Computer simulation of axis-encircling beams generated by an electron gun with a permanent magnet system, Int. J. Infrared and Millimeter Waves, 21, 1191 (2000).
12. *Tokuchi A., Ninomura N., Jiang W., Yatsui K.* Repetitive Pulsed-Power Generator ETIGO-IV, IEEE Trans. Plasma Science, 30, 1637 (2002).
13. *Manuilov V.N., Idehara T., Glyavin M.Y., Agusu La, Kamada M., Kanemaki T., Jiang W., Yatsui K.* Electron optic system of powerful large orbit gyrotron with pulse magnetic field, Int. J. Infrared and Millimeter Waves, 26, 15 (2005).
14. *Agusu La, Idehara T., Kamada M., Hayashi T., Manuilov V.N., Dumbrajs O., Yatsui K., Jiang W.* Design of Cavities for a Short Pulse Powerful Large Orbit Gyrotron, Int. J. Infrared and Millimeter Waves, 26, 637 (2005).

LARGE-ORBIT GYROTRON OPERATION AT SUBMILLIMETER WAVES

V. L. Bratman, Yu. K. Kalynov, V. N. Manuilov, S. V. Samsonov

Institute of Applied Physics, Russian Academy of Science,
Nizhny Novgorod, Russia

A successful operation of a Large Orbit Gyrotron (LOG) at submillimeter waves has been demonstrated. The LOG utilized a 250 keV/4 A/10 μs axis-encircling electron beam produced by a thermionic-emission electron optical system. The third cyclotron harmonic, single-mode oscillations at the frequencies of 370 GHz and 414 GHz with a power up to 20 kW have been measured. Future work will be concentrated on realization of THz LOGs with reduced electron beam voltage (30–80 kV) attractive for many applications.

Introduction

Large Orbit Gyrotrons (LOG) [1–6] enable operation at higher cyclotron harmonics and hence at lower magnetic fields in comparison with conventional gyrotrons. The LOG configuration uses an axis-encircling electron beam in axisymmetric cavity that simplifies essentially discrimination of parasitic modes: only co-rotating modes $TE_{m,p}$ with the azimuthal index m equal to the resonance harmonic number s can be excited by a thin centered beam. It should be noted that generation of appropriate beams with small velocity and position spreads is a rather complicated task that cannot be solved using conventional magnetron injection guns. The electron-optical systems for millimeter-wave LOGs with explosive and thermionic emission guns were developed in Institute of Applied Physics [7–10]. Radiation with peak power of 100 kW and pulse duration of 10 μs was obtained at the 3rd and 4th cyclotron harmonics for the modes $TE_{3,2}$ and $TE_{4,2}$ with the frequencies of 115 and 130 GHz, respectively [9]. Based on these results, a new third-harmonic LOG had been designed and generation of the submillimeter waves on several high modes was obtained. In this paper, experimental results and new projects of low-voltage LOGs with frequencies of 0.37 and 1.0 THz are represented.

Modification of electron-optical system

Like the previous millimeter-wave oscillator [9], the submillimeter-wave 3rd harmonic LOG has been realized at the high-voltage installation "CARM". The LOG was designed for the same electron energy of 250 keV, but for 4-time higher value of operating magnetic field, 6.6 T [10]. Magnetic field in the cathode and kicker regions was not changed in comparison with the millimeter-wave LOG that was provided by enlarging separation between the main sole-

noid and the cathode and by using an additional solenoid (Fig. 1). Correspondingly, higher beam compression up to 4,400 was needed.

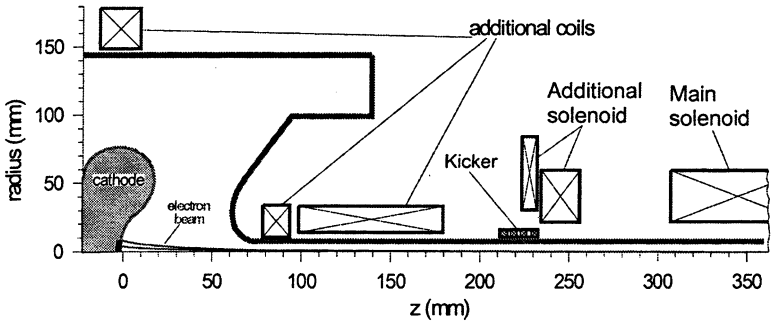

Fig. 1. Schematic of the modified electron-optical system

To produce the axis-encircling electron beam, a thin rectilinear beam was first formed in a "Pierce-like" gun, and then the electrons acquired the transverse velocity passing through a kicker (Fig. 1). To avoid excitation of large transverse velocities before the kicker, magnet coils was configured to match axial magnetic field profile and particle trajectories. The kicker was located in the area with the magnetic field of 0.4 T. Small changes of field in the cathode region provided minimization of the transverse velocity spread by means of optimization of parasitic electron pulsations phase before the kicker. After the kicker, the transverse velocity was further increased in the tapered magnetic field. In order to diminish parasitic transverse velocity before the kicker, the initial electron beam radius and current were decreased to 5 mm and 3 A, respectively.

A conventional axisymmetric gyrotron cavity consisting of a cut-off narrowing at the cathode end, a cylindrical part, and an output taper, was used in the LOG. The operating modes $TE_{3,p}$ with a higher radial index of $p = 5–8$ were chosen to decrease Ohmic losses and simplify fabrication of the cavity. According to calculations, such modes can be selectively excited by a centered electron beam, possessing small spread in transverse particle velocity, with efficiency of several percent and output power of tens of kW.

Electron-optical experiments

The modified electron-optical system was preliminarily tested in a modeling low-current regime, which allowed observation of beam imprints at a scintillating target (Fig. 2). In this regime, potentials and magnetic fields were reduced 2 and $2^{1/2}$ times, respectively, as compared to the operating values, but in

contrast to conventional scaling the electron current was reduced many times larger than by factor $2^{3/2}$ and was close to the scintillating threshold. Choice of such a regime was caused by too weak magnetic field at the cathode that could not be further reduced and by too high electron density that would occur in the proper scaling regime. The scintillating phosphor target was located at the distance of 40 mm down-stream the kicker position. The mean value of electron pitch-factor was determined by beam trace on the scintillator (Fig. 2, *a*). Volt-ampere characteristics at various emitter temperatures have been obtained for the operating regime (Fig. 2, *b*). Maximal current density in the cavity region amounted to 20 kA/cm^2 for a rectilinear electron beam. Detailed comparison of measured and calculated characteristics for the modes $TE_{2,5}$ [11] and $TE_{3,8}$ (see the following section) showed that the electron beam had a pitch-factor about 1.0 and transverse velocity spread up to 60%.

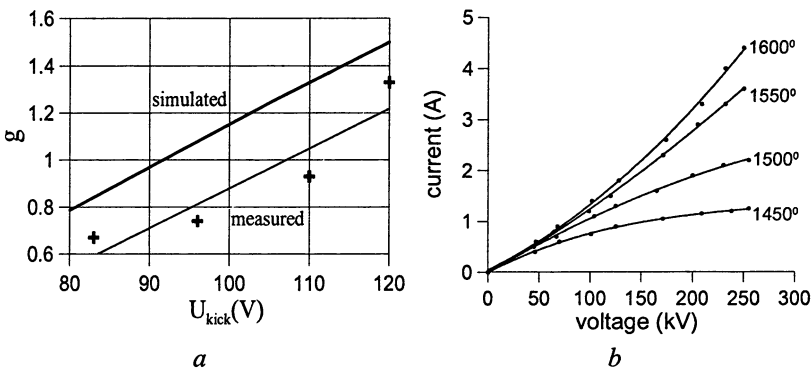

Fig. 2. Simulated and measured particle pitch-factor versus kicker voltage (*a*) and volt-ampere characteristics of the gun (*b*).

RF generation

In experiments involving electron-wave interaction in the LOG cavity for the operating range of magnetic field, stable selective generation of various modes at the 1st–3rd cyclotron harmonics was observed (Fig. 3). The excited modes were identified by the values of resonant magnetic field, oscillation frequency and mode pattern measurements across the output horn aperture (for the $TE_{1,3}$ mode). The submillimeter radiation was measured for the $TE_{3,8}$ and $TE_{3,9}$ modes interacting with the beam at the 3rd cyclotron harmonic. The frequency was measured using a heterodyne technique with a Shottky-diode mixer. The measured frequencies were found to be in good agreement with the calculated ones (Table).

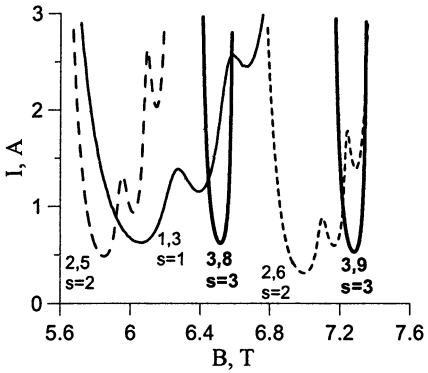

Fig. 3. Calculated starting currents of experimentally observed modes (electron pitch factor g = 1, velocity spread $\delta V_{\perp}/V_{\perp}$ = 0.6, off-center shift 0.1 mm).

f, GHz/ mode	$TE_{1,3}$	$TE_{2,5}$	$TE_{3,8}$
calculated	116,45	223,02	372,56
measured	115,7	222,7	371

Because of mode competition, selective generation at the $TE_{3,8}$ mode was observed for the beam current below 2 A and maximum power was measured to be about 10 kW with efficiency 2% (Fig. 4, *a*). At higher magnetic field and beam current up to 1.8 A, stable generation of the $TE_{3,9}$ mode at the frequency of 414 GHz, output power of 8 kW and efficiency of 1.7% was obtained (Fig. 4, *b*).

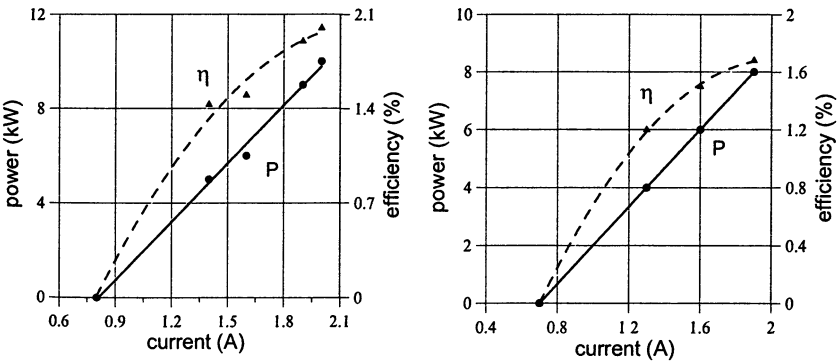

Fig. 4. Power and efficiency for $TE_{3,8}$ (*a*) and $TE_{3,9}$ (*b*) modes vs. beam current

In order to realize more selective operation the LOG cavity having diameter of 7 mm was replaced by one of 4.6 mm in diameter. In this case a lower oper-

ating mode $TE_{3,5}$ was used instead of the $TE_{3,8}$. As a result, a stable single-mode operation was realized at higher beam current (up to 3 A). Correspondingly, higher output power of 20 kW with efficiency of 2.5% was achieved at the frequency of 369 GHz (Fig. 5).

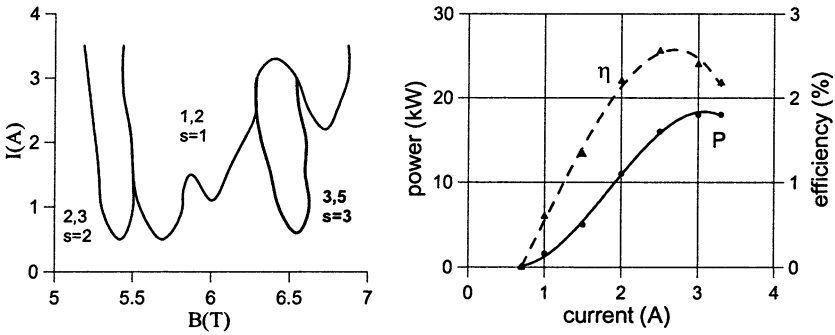

a *b*

Fig. 5. Measured starting currents for the 1st–3rd harmonic $TE_{1,2}$, $TE_{2,3}$, $TE_{3,5}$ modes (*a*); output power and efficiency for the $TE_{3,5}$ mode (*b*).

New projects

The study of submillimeter-wave LOG has shown that the limit of compression and pumping of an electron beam in guns with kickers is in essence achieved and creation of axis-encircling beams of satisfactory quality for a LOG at higher radiation frequency is a complicated task. Theoretical analysis showed that an appropriate electron beam for a THz LOG can be produced using the so-called cusp guns [11, 12] with reverse magnetic field at the cathode, which require lower electron density in the intermediate formation region. Two THz 3rd harmonic LOGs with such guns are now under development in the IAP.

The first oscillator is designed for CW operation at relatively low voltage of 30 kV for the $TE_{3,4}$ mode at frequency of 370 GHz. According to the calculations, this mode can be selectively excited by an electron beam with pitch-factor of 1.7 and current of 1 A in a magnetic field of 4.7 T. In order to produce such a beam a special coil will produce a negative magnetic field 1.7 mT at the ring emitting area and beam compression 2700 will be provided. Calculated power and efficiency are 0.7 kW and 2%, respectively.

The second LOG is designed for pulse operation at the voltage of 80 keV and magnetic field of 13.6 T for the mode $TE_{3,5}$ with record frequency of 1.0 THz. According to calculations, this mode can be selectively excited by an electron beam with pitch-factor 1.7, current 0.7 A and realistic transverse velocity spread 30% in spite of dangerous competition from parasitic 1st harmonic

backward wave $TE_{1,2}$. Negative magnetic field at the cathode and beam compression are to be 5 mT and 2800. Calculated radiation power is 0.8 kW at efficiency 1.5%.

The work was supported by Russian Foundation for Basic Research (Grants 03-02-17064, 05-02-16015), Programs for Basic Research of Presidium of Russian Academy of Sciences "Electromagnetic radiation of terahertz range" and "Basic problems of nano- and picosecond high-power electronics". The authors gratefully acknowledge the help of Yu.A. Dryagin, L.M. Kukin, A.F. Krupnov, M.A. Moiseev, V.E. Nechaev and M.Yu. Tretyakov.

References

1. *Jory H.R.* Research and Development Technical Report, ECOM-01873-F. Varian Associates, Palo Alto, California, 1968.
2. *Lau Y.Y., Barnett L.R.*, Int. J. Infrared Millimeter Waves, 1982, **3**(5), 619-644.
3. *McDermott D.B., Luhmann N.C., Kupiszewski Jr., A., Jory H.R.*, Phys. Fluids, 1983, **26**, 1936-1941.
4. *Lawson W., Destler W.W., Striffler C.D.*, IEEE Trans. Plasma Sci., 1985, **13**, 444-453.
5. *Nusinovich G.S.*, Int. J. Electronics, 1992, **72**, 959-967.
6. *Bratman V.L., Kalynov Yu.K., Fedotov A.E.*, J. Technical Phys., 1998, **68**(10), 91-98.
7. *Bratman V.L., Kalynov Yu.K., Kolganov N.G., Manuilov V.N., Ofitserov M.M., Samsonov S.V., Volkov A.B.*, Strong Microwaves in Plasmas: Proc. Int. Workshop. Nizhny Novgorod, Russia, 1996. P. 745-761.
8. *Bratman V.L., Fedotov A.E., Kalynov Yu.K., Manuilov V.N., Ofitserov M.M., Samsonov S.V., Savilov A.V.*, IEEE Trans. Plasma Sci., 1999, **27**, 456.
9. *Bratman V.L., Kalynov Yu.K., Manuilov V.N., Ofitserov M.M., Samsonov S.V.*, Radioteknika i Electronika, 2001, **6**, 744-751 (in Russian).
10. *Bratman V.L., Dumesh B.S., Fedotov A.E., Grishin Yu.A., Kalynov Yu.K., Manuilov V.N., Samsonov S.V.*, Digest of the 29th Int. Conf. IR and MM Waves. Karlsruhe, Germany, 2004. P. 193-194.
11. *Rhee M.J., Destler W.W.* The Physics and Fluids, 1974, **17**, 1574-1581.
12. *Samsonov S.V., Bratman V.L., Denisov G.G. et al.* Proc. 12th Symp. High Current electronics. Tomsk, Russia, 2000. P. 403-407.

FREQUENCY MULTIPLICATION IN GYRO-OSCILLATORS

I. V. Bandurkin, V. L. Bratman, G. G. Denisov, A. V. Savilov

Institute of Applied Physics, Nizhny Novgorod, Russia

New schemes of gyro-multipliers with self-exciting low-frequency sections proposed. Such devices, operating without external signal, appear to be effective and convenient sources of coherent THz radiation.

It is well known that an attempt to increase frequency of conventional gyrodevices faces a number of serious problems. The most obvious of them is a necessity for the strong magnetic field. This problem can be softened using operation at high cyclotron harmonics. However, in the most practical case of subrelativistic electron energy, electron-wave coupling rapidly weakens with growing harmonic number. This increases starting currents and intensifies competition between the operating mode and spurious oscillations at low harmonics. Moreover, due to high ohmic losses in Terahertz range, one inevitably has to use high cavity modes, which makes the problem of spurious modes excitation quite complicated. Practically, the number of operating harmonic rarely exceeds 2 for conventional gyrotrons and 3–4 for large orbit gyrotrons.

On the other hand, it is also well known that an output radiation of a gyrotron always contains a small part at multiple frequencies. This occurs due to nonlinear properties of the electron beam, when along with the electron bunching at the operating harmonic, bunching at multiple harmonics also takes place [1]. Produced electron bunches excite in the operating cavity oscillations at multiple frequencies. For some applications, even this relatively low-power radiation is of a certain interest, but the effect could be much more attractive if one managed to increase its efficiency. It is important, that for obtaining of induced radiation in frequency multipliers there is no need to exceed starting currents at high harmonics. Besides, since the multiplied frequency is bound to the low one, such an approach increases selectivity. In the work, electron bunching at high cyclotron harmonics is studied in detail, and new methods of purposeful use of this effect for frequency multiplication are proposed.

Conventional gyro-multipliers with external LF signal

The simplest gyro-multiplier [2–4] consists of three sections (Fig. 1, *a*). In the first section electrons interact with low-frequency (LF) wave at the fundamental cyclotron resonance:

$$\omega_L \approx h_L v_{\|} + \Omega . \qquad (1)$$

Here ω_L and h_L are the LF wave frequency and longitudinal wavenumber, $v_{\|}$ and Ω are the electron longitudinal velocity and gyrofrequency. The wave

modulates energy of the particles, which leads to appearance of the electron current harmonics $\rho_n = \langle \exp(-in\theta_L) \rangle$ at frequency ω_L and at multiplied frequencies $n\omega_L$ in the drift section. Here $\theta_L = \omega_L(t-t_0) - h_L z - \int_{t_0}^{t} \Omega dt - \varphi_0$ is the relative phase between the electron and the wave, t_0 is the time of the electron appearance at the entrance of the interaction region ($z = 0$), φ_0 is the initial gyrophase and the $\langle ... \rangle$ means averaging over the whole particle ensemble (over t_0 and φ_0). In the third section the resonance between the electrons and high-frequency (HF) wave at the N-th cyclotron harmonic takes place:

$$\omega_H = n\omega_L \approx h_H v_{\parallel} + N\Omega . \qquad (2)$$

For the induced excitation of this wave, the bunched beam must contain the harmonic of electron current $\rho_1^{(H)} = \langle \exp(-i\theta_H) \rangle$, $\theta_H = \omega_H(t-t_0) - h_H z - -N\int_{t_0}^{t} \Omega dt - N\varphi_0$ at wave's frequency ω_H. Such a harmonic appears in the beam due to bunching in the field of LF-wave, $\rho_1^{(H)} = \rho_n$, if $\theta_H = n\theta_L$. For uniform distribution of initial gyrophases, φ_0, this means that multiplication factor should coincide with cyclotron harmonic number: $n = N$ (for close initial gyrophases it is not necessary).

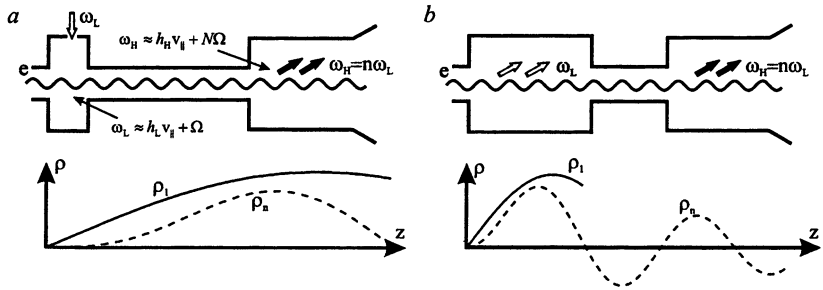

Fig. 1. Multipliers with external (*a*) and self-exciting (*b*) LF signals

If the modulating signal is weak enough, amplitudes of electron current harmonics obey the known formula

$$\rho_n(z) \propto J_n(Xnz), \qquad (3)$$

where J_n is the Bessel function of the n-th order, and factor X characterizes the intensity of LF wave-electron interaction. According to this expression, coordi-

nate z_n^{max}, where $\rho_n(z)$ reaches saturation, decreases with growing harmonic number n. In other words, the higher cyclotron harmonic one wants to use for operation, the shorter distance for optimal bunching he should choose.

Gyro-multipliers with self-exciting LF-sections

Described situation is common for the sources based on the inertial electron bunching. It is important that this effect takes place in the scheme with self-exciting LF-section as well. In the simplest scheme of such kind (Fig. 1, *b*), more or less effective generation at high cyclotron harmonic is possible only if the LF-oscillator operates closely to starting regime. To illustrate this, let us consider the LF-section in the form of a gyrotron backward-wave oscillator (gyro-BWO). This device is convenient for multiplication due to its frequency tunability and, hence, possibility to synchronize the two sections, $\omega_H = n\omega_L$.

In the framework of simplified (asymptotic) equations [5] the gyro-BWO operation (like a usual BWO one) is determined by the only parameter $\hat{L} \sim L\sqrt[3]{I}$ – the length of the system normalized by the cubic root from the beam current. The solution of spatio-temporal self-consistent problem shows that the gyro-BWO operates in stationary single-mode regime in the region $\hat{L}_S < \hat{L} < \hat{L}_A$ between the starting value $\hat{L}_S = 1.95$ and the threshold of auto-modulations $\hat{L}_A = 2.82$. When the parameter $\hat{L}$ is far enough from $\hat{L}_S$, which is necessary for effective LF-excitation, first harmonic reaches saturation near the end of the first section, $z_1^{max} \approx \hat{L}$. Correspondingly, higher harmonics become saturated inside the LF-section, $z_n^{max} < \hat{L}$, and after that rapidly oscillate and fade (Fig. 2). This leads to essential limitation of the length of the second section and to very low efficiency of the HF-generation in the scheme shown in Fig. 1, *b*. For more effective excitation of the both waves, the HF-section should be put inside or before the LF one, where the corresponding current harmonic has maximum. In particular, one may consider a LF-oscillator of a klystron type, whose drift space is used for HF-generation.

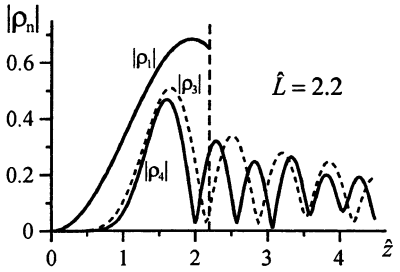

Fig. 2. Distribution of current harmonics in gyro-BWO.

BWO-BWO and BWO-gyrotron schemes

As an evolution of the latter idea we propose the BWO based on the effect of electron bunching in the field of nonresonant wave [6] (Fig. 3). This allows using microwave system in the form of a piece of regular waveguide with cut-off narrowing at the entrance, reflecting the both waves. In this case, klystron-like interaction takes place due to special stepped profile of the magnetic field. The LF-wave is in the resonance with the beam only in the second part of the interaction region ($z > L_b$), whereas in the first part it is relatively far from it. It is shown in [3] that the first section can work like the modulating and bunching sections of a conventional gyroklystron: the short interval $0 < z < L_0$, where $L_0 \sim v_\parallel / (\omega_L - h_L v_\parallel - \Omega)$, plays the role of modulating section, and the region $L_0 < z < L_b$ is the analogue of a drift section. In the second section, where the fundamental harmonic reaches the maximum and the magnetic field becomes resonant, a part of the beam energy converts into LF-radiation. High harmonics reach saturation earlier than the fundamental one, i. e. in the region $L_0 < z < L_b$, where magnetic field should be resonant for the HF-wave.

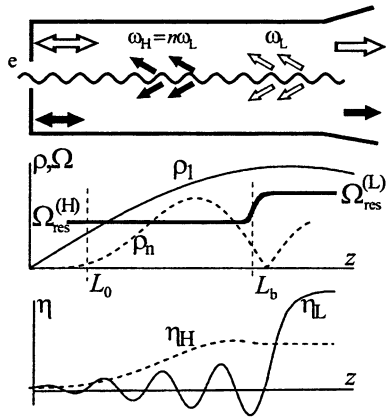

Fig. 3. Gyromultiplier in BWO-BWO configuration: HF-section "built in" inside the LF-generator. Cyclotron frequency profile $\Omega(z)$, current harmonics ρ_n and efficiencies of generation $\eta_{L,H}$ are shown.

The described gyromultiplier is especially attractive in BWO-BWO configuration (Fig. 3), when the both HF and LF sections generate in the regime of backward wave oscillator. Tuning the magnetic field in the both sections, one can tune the operating frequencies of the multiplier, keeping them synchronized, $\omega_H = n\omega_L$. Simulations show, that for multiplier using 80 kV/10 A electron beam and operating at fourth cyclotron harmonic ($\lambda_1 = 6\,\text{mm}, \lambda_4 = 1.5\,\text{mm}$), the bandwidth is of about 2%. However, the efficiency of HF generation is rather small in such a configuration and amounts to 1%. One of the reasons for

small efficiency is that the length of the HF-generator is limited by the requirement that the first section shouldn't be excited in the regime of conventional gyro-BWO at the fundamental cyclotron harmonic. The efficiency at the high frequency can be increased up to 3% if the gyrotron-like resonance with the HF-wave is provided in the first section. In this case, however, high frequency's being fixed deprives the scheme of such an advantage as frequency tunability.

Single-cavity gyrotron-gyrotron multiplier

In the scheme with nonresonant bunching the HF-generator precedes the LF one. Another way to put the HF-generator in the maximum of corresponding harmonic is to combine two cavities, so that the resonance conditions for the both waves were fulfilled simultaneously. Generally speaking, this problem is far from being a trivial one; however, the following remarkable property of gyrotron eigenmodes makes it solvable. As is known, the operating frequency of conventional gyrotron is close to the cut-off one of corresponding circular waveguide. At the same time, the cut-off frequencies of a circular waveguide are proportional to zeros of corresponding Bessel functions, $\omega_{cr} = cj_{\nu,s}/R$ (TM-modes), or their first derivatives, $\omega_{cr} = cj'_{\nu,s}/R$ (TE-modes). Here ν is the azimuthal index coinciding with the order of Bessel function, s is the radial index (zero's number), and R is the waveguide radius. According to McMahon's expansions for large zeros ($s >> \nu$) of Bessel functions [7],

$$\begin{aligned} j_{\nu,s} &= \left(s + \nu/2 - 1/4\right)\pi + O\left(\nu^2/s\right), \\ j'_{\nu,s} &= \left(s + \nu/2 - 3/4\right)\pi + O\left(\nu^2/s\right). \end{aligned} \qquad (4)$$

It follows from expressions (4) that $5j'_{\nu,s} - j'_{5\nu,5s-3} = O\left(s^{-1}\right)$ for large s. Thus, the chance of efficient multiplying of the gyrotron frequency by a factor of 5 exists. Besides, there appears a possibility to convert the $TE_{1,s}$ mode to the $TM_{3,3s-2}$ mode, since $3j'_{\nu,s} - j_{3\nu,3s-2} = O\left(s^{-1}\right)$. Minimization of the frequency discrepancy can be achieved by shortening the cavity, so that the second term in the expression for eigenfrequency $\omega_{op} \approx c\sqrt{(j^{(,)}_{\nu,s}/R)^2 + (q\pi/L_{\|})^2}$, which is responsible for longitudinal mode structure, introduces a significant contribution. After that, more precise mode synchronization should be provided by adjusting of magnetic field.

Preliminary simulations show, that for 20 kV/1 A electron beam this scheme allows converting of about of 0.1% of the beam energy to the radiation at fifth cyclotron harmonic, which makes the described approach quite attractive.

Acknowledgments

This work was supported by the Russian Foundation for Basic Research (Grants 04-02-14118 and 05-02-16852), by the Russian Science Support Foundation, and by the Programs of Presidium of the Russian Academy of Sciences "Electromagnetic radiation of Terahertz frequency range" and "Basic Problems of Nano- and Picosecond High-Power Electronics".

References

1. *Gaponov A.V., Petelin M.I., Yulpatov V.K.*, Radiophys. Quantum Electron. 10, 794 (1967).
2. *Zhurakhovskiy V.A.* Nonlinear electron oscillations in magneto-guided beams. Naukova Dumka, Kiev, 1972 (in Russian).
3. *Ergakov V.S., Moiseev M.A.*, Radiotekhnika i Electronika 22, 789 (1977) (in Russian).
4. *Hirshfield J.L.*, Phys. Rev. A 44, 6845 (1991).
5. *Bratman V.L., Ginzburg N.S., Kovalev N.F. et al.*, Relativistic HF Electronics. Institute of Applied Physics, Gorky, USSR, 1979. P. 249-274.
6. *Bandurkin I.V., Savilov A.V.*, Cyclotron resonance maser in the regime of non-resonant electron bunching (accepted for publication in Technical Physics Letters in 2006).
7. Handbook of Mathematical Functions with Formulas, Graphs and Mathematical Tables, Ed. by M. Abramowits and I.A. Stegun. U.S. Department of Commerce. 1972. P. 371.

DEVELOPMENT AND EXPERIMENTAL STUDY OF A TWO-CAVITY 285 GHz CW GYROTRON-MULTIPLIER

I. I. Antakov, I. G. Gachev, G. G. Denisov, V. K. Lygin, E.V. Zasypkin

Institute of Applied Physics RAS, N. Novgorod, Russia

A new type of oscillator – two-cavity gyrotron-multiplier with self-excited input cavity is proposed. A simplest theory of a gyrotron-multiplier has been developed. The design and experimental results of a 285 GHz two-cavity gyrotron-multiplier are presented. Initial experiments have demonstrated of about 30 W CW output power with a 24 kV, 0.3 A electron beam.

Development of terahertz band gyrotrons is restricted by maximum value of magnetic field, provided by the existing superconducting coils. Generation of a terahertz radiation in gyrotrons is possible due to the operation at high cyclotron harmonics.

Unfortunately, a relatively weak interaction of RF field with electron beam at high harmonics results in high starting currents of the operating mode and intense mode competition. Moreover, an attempt to reduce the starting current of the operating mode to acceptable level using a longer cavity results in ohmic loses growing.

The problem of the operating mode selection may be solved in a two-cavity gyrotron with frequency multiplication (Fig. 1). Its circuit consists of two cavities separated by a drift tube. First cavity is self-excited at the first cyclotron harmonic at low operating mode. The electron beam is modulated by the first cavity RF field and then it is bunched in the drift region. Eigenfrequency and azimuthal index of operating mode in the second (output) cavity exceed those for the input cavity in three times.

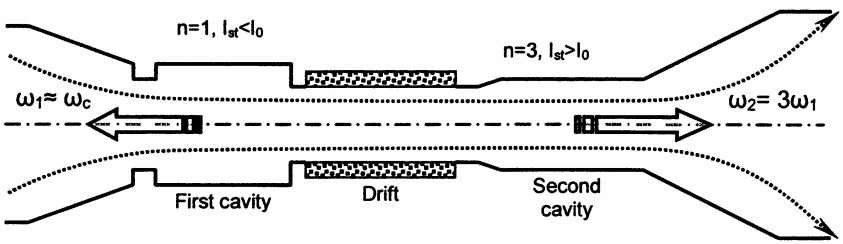

Fig. 1. Layout of a two-cavity gyrotron-multiplier

Since the electron current contains high harmonic components it excites forced oscillations in the second cavity at the multiplied frequency. As far as the starting current of the output cavity operating mode may be higher than the beam current, spurious oscillation are also not exited here. This paper presents

the design and test results of a two cavity gyrotron-multiplier operating at frequency of 285 GHz.

Design

A two cavity gyrotron-multiplier was designed, manufactured and tested. An electron beam is formed by a diode type, 25 kV, 0.3 A magnetron injection gun. Beam pitch factor is about 1.4, the velocity spread is equal to 20%. Pitch factor is controlled by the additional coil that changes the magnetic field over the cathode.

The gyrotron interaction circuit is positioned in the flat magnetic field produced by a 3.8 T superconducting coil. A cryomagnet bore diameter is 42 mm, the magnetic field length is 45 mm.

The circuit is comprised by two cavities separated by a cut-off drift tube. Ceramic absorbing rings are placed to the drift tube to suppress spurious oscillations. The first cavity operates in the TE_{01} mode at fundamental cyclotron frequency of about 95 GHz. Its design allows to adjust mechanically the cavity length by shifting cut-off plunger within 8÷12 mm, and thus to turn the multiplied frequency of generation to the output cavity eigenfrequency.

The diagrams on Fig. 2 present the starting current, frequency of dimensionless field amplitude of the oscillations excited in the first cavity.

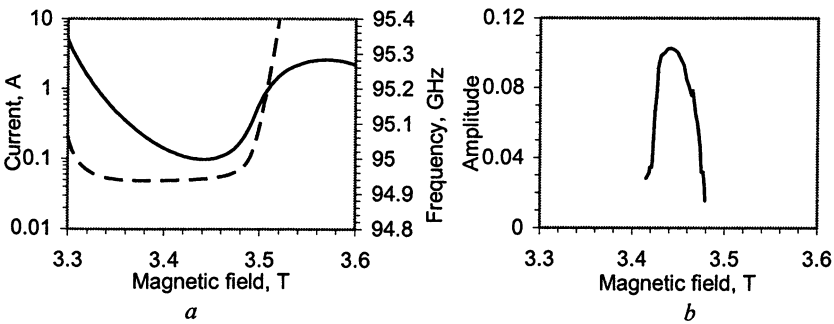

Fig. 2. Starting current (solid line) and frequency of oscillations (dashed) in the first cavity vs. magnetic field: TE_{01}, $U = 25$ kV, $g = 1.4$, $dV = 0.2$, $L_1 = 10$ mm (*a*). Dimensionless field amplitude in the first cavity vs. magnetic field, $J = 0.3$A (*b*).

The output cavity operates in the TE_{03} mode at the third cyclotron harmonic. Its eigenfrequency is 285 GHz, Q-factor is equal 3400. The cavity length is 12 mm.

Calculated starting currents of the operating and neighboring spurious modes versus magnetic field are depicted on Fig. 3. One can see that starting currents of all this modes exceed the beam current. So, electron beam excites only forced oscillations in the output cavity.

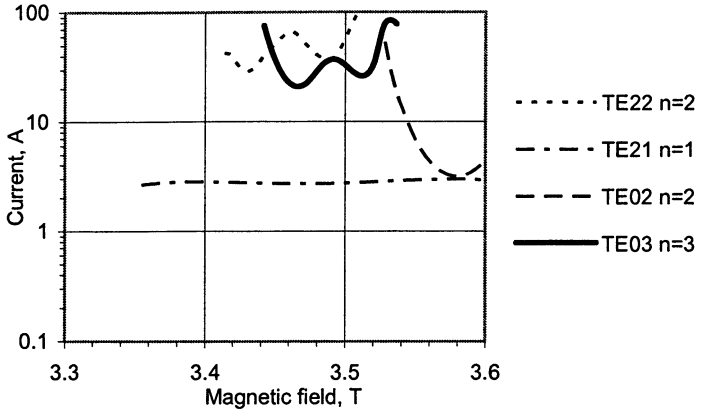

Fig. 3. Starting current and frequency of oscillations in the output cavity vs. magnetic field (TE_{03}, $U = 25$ kV, $g = 1.4$, $dV = 0.2$).

The curve at Fig. 4, *a* illustrates the dependence of the gyrotron efficiency on beam current. Since starting current of the operating mode is essentially higher than the beam current, maximum efficiency is not achieved. Fig. 4, *b* shows the dependence of the efficiency on the RF field amplitude in the first cavity. One can see that the RF field exited in the firs cavity is quite enough to realize saturated regime in the output cavity. Simulations also showed that the efficiency strongly depends on electron beam velocity spread and magnetic field structure in the circuit (Fig. 5). Typical for magnetron injection guns velocity spread of 20% leads to the sharp efficiency drop. Here dB is relative detuning of magnetic field in the drift region from exact cyclotron resonance.

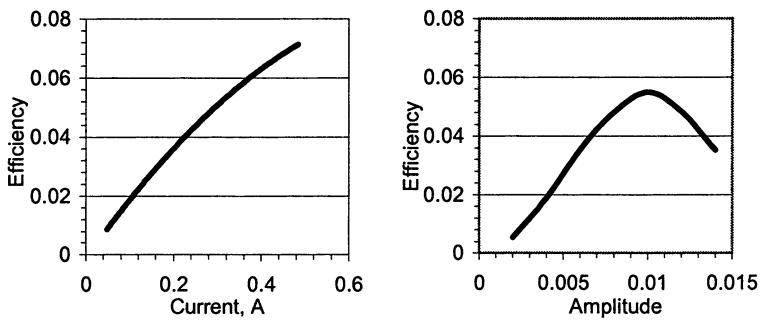

Fig. 4. Gyrotron efficiency vs. beam current, than field amplitude in the first cavity is optimized ($U = 25$ kV, $g = 1.4$, $dV = 0$).

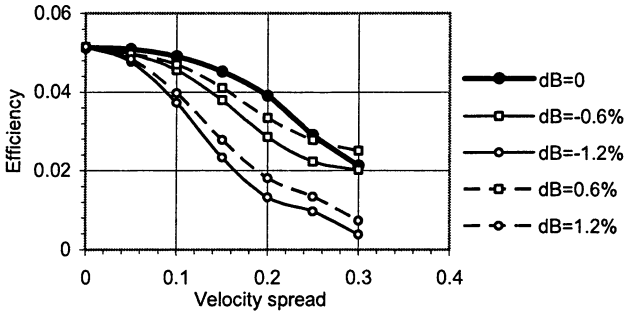

Fig. 5. Gyrotron efficiency as a function of velocity spread ($U = 25$ kV, $J = 0.3$ A, $g = 1.4$)

Test results

A series of experiments was undertaken to optimize the first cavity length, diameter and magnetic field in the circuit.

Firstly, the magnetic field and the first cavity length were varied to excite the first cavity operating mode with an optimal frequency and amplitude. This test results are presented in the diagram Fig. 6, *a*. In this figure, gyrotron output power is presented as a function of the first cavity length. Maximum output power corresponds to 10 mm input cavity length. Magnetic field was optimized at each operating point. Optimal values of the magnetic field are also depicted in Fig. 6, *a*.

Figure 6, *b* illustrates the dependence of the output power and frequency on the first cavity length in the case of the fixed magnetic field. A deviation of the cavity length accompanied by frequency shift within 50 MHz dramatically drops the output power. Frequency tuning band is inversely proportional to the output cavity Q-factor.

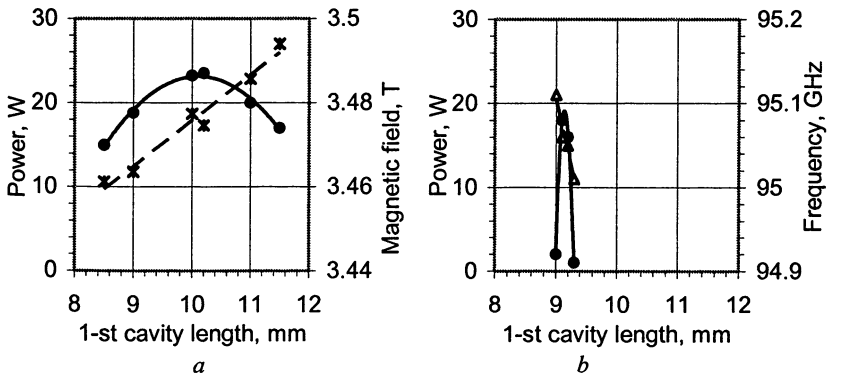

Fig. 6. Output power and optimized magnetic field vs. first cavity length at $U = 23$ kV, $J = 0.25$ A (*a*). Output power and frequency of oscillations in the first cavity vs. its length at $B = 3.47$ T, $U = 23$ kV, $J = 0.25$ A (*b*).

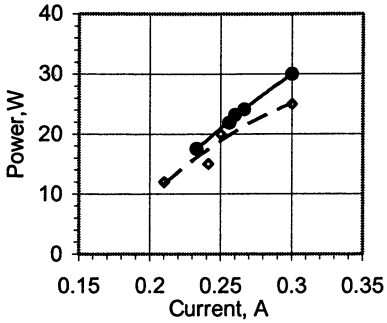

Fig. 7. Output power vs. beam current at $U = 23.5$ kV, $f = 285.2$ GHz.

The Figure 7 illustrates the dependences of output power on beam current, at different longitudinal positions of gyrotron in the cryomagnet. Magnetic fields in the circuit and in the cathode region were optimized. A maximum CW power of 30 W was obtained.

Conclusion

A successful operation of a compact low voltage two-cavity gyrotron-multiplier was demonstrated. The proposed gyrotron design is promising for production of high frequency microwaves up to terahertz. Further efforts will be focused at the optimization of circuit parameters and magnetic field structure.

Acknowledgements

This project was sponsored by the Institute of Applied Physics, RAS, Gycom Ltd., and Russian Foundation for Basic Research.

References

1. *Ergakov V.S., Moiseev M.I.*, CRM-amplifier with frequency conversion // J. Radiotechniques and Electronics. 1977. № 4. P. 789-794.
2. *Belousov V.I., Ergakov V.S., Moiseev M.I.*, Two-cavity CRM on electrons cyclotron harmonics // Electronnaya Tekhnika. Ser. 1, Electronika SVCh. 1978. № 9. P. 41-50.
3. *Sokolov E.V., Zasypkin E.V.*, Two-cavity gyroklystron with self-excited input cavity // Int. J. Electronics. 1995. V. 79. P. 495-503.
4. *Antakov I.I., Gachev I.G., Sokolov E.V.*, Experimental study of a two-cavity gyrotron with feedback between cavities // Intense Microwave Pulses III, Howard E. Brandt, Editor, Proc. SPIE 2557. P. 380-385 (1995).
5. *Zasypkin E.V., Antakov I.I., Gachev I.G., Vlasov S.N., Sokolov E.V.* Continuously tunable 35-190 GHz powerful gyrotrons at GYCOM // Conf. Digest 23d Int. Conf. Infrared and Millimeter Waves. 7-11 September, 1998, University of Essex, Colchester, Essex, UK. P. 323-324.

DEVELOPMENT OF THE 300 GHz/4 kW/CW GYROTRON

V. E. Zapevalov, V. K. Lygin, O. V. Malygin, M. A. Moiseev, V. P. Karpov, V. I. Khizhnjak, E. M. Tai, T. Idehara[1], I. Ogawa[1], S. Mitsudo[1]

Institute of Applied Physics, Russian Academy of Sciences,
GYCOM Ltd. Nizhny Novgorod, Russia
[1]Research Center for Development or Far Infrared Region, University of Fukui,
Fukui, Japan
E-mail: zapev@appl.sci-nnov.ru

The report presents results for design elaboration of 300 GHz/4 kW/CW gyrotron. The gyrotron will be used with 12T LiHe-free superconducting magnet. The possibilities to optimize an electron gun, mode converter and processes of mode interaction in the electron beam-cavity system are discussed for different versions of the 300 GHz gyrotron. The influence of Ohmic load on the cavity, mode competition and other effects are investigated also.

Introduction

For some applications RF sources with CW power 3–5 kW and frequency 300 GHz are requested [1]. In the framework of joint project, the program for design of the 300 GHz gyrotron with output power 4 kW for operation in the continuous regime was implemented at IAP RAS in cooperation with Fukui University FIR Center FU and industrial company GYCOM Ltd. Gyrotron specifications are shown in the Table 1.

Table 1. 300 GHz/4 kW/CW Gyrotron Specifications

Frequency	GHz	300 ± 2
Maximal CW output power	kW	3.5, not less
Range of CW output power	kW	0.5 – 3.5
Type of gun		quasi-diode
Maximal beam voltage,	kV	16 ± 1
Maximal beam current	A	1.1 ± 0.1
Output window diameter	mm	80
Output mode		wave beam
Overall dimensions (approximate)	m	0.3 (W) × 0.4 (D) × 2.0 (H)

On the basis of the analysis of scientific and technical information the general design concept of the gyrotron has been developed and possible operating modes and the value of accelerating voltage have been chosen. The main problems of gyrotrons at present are following:

- development of electron guns that form helical electron beams with sufficient power at minimal velocity spread;
- selection of high-efficiency operating mode with small ohmical loses in oversized cavities;

- efficient conversion of a complex operating mode into a wave beam with optimization of its field structure;
- development of a reliable collector which is stable to external perturbing magnetic fields;
- creation of an output window capable to transmit 300 GHz RF radiation in CW regime with small loses.
- Our work on a new gyrotron includes the following stages usually [2, 3]:
- calculations and design;
- test of an experimental version of the tube in a short-pulse regime;
- work on an industrial tube operating in the full-scale regime.

But in this situation we have to exclude second stage and in the case of necessity introduce modification directly to experimental-industrial tube after initial tests. Several possible operating modes like $TE_{6,4}$, $TE_{15,4}$, $TE_{22,8}$ were considered. Finally on the basis of the analysis of technical limitations $TE_{22,8}$ operating mode have been chosen for experimental-industrial tube, which give us the possibility to check different scientific and technical solution.

Results of this activity are summarized in this report.

Cryomagnet

Gyrotron tube has to be used together with 12 T liquid Helium (LiHe) free cryomagnet. Magnet specifications are shown in the table 2.

Table 2. 12 T LiHe free cryomagnet specifications

Height (max)	mm	713
Diameter (max)	mm	664
Diameter of a "warm" aperture	mm	100
Length of a "warm" aperture	mm	730
Number of coil		2
Coil material		Nb_3Sn, NbTi
Working current	A	160

Gyrotron design

The gyrotron has the same principal design concept as the earlier developed 70–140 GHz gyrotrons [3]. This includes the use of a quasi-diode gun with a LaB_6 cathode, a build-in mode converter to transform cavity mode to wave beam with radial directed output, and an electron beam collector, all designed for CW operation. Magnetic system of the tube includes a 12 T cryomagnet and optionally a cathode coil for fine adjustment of electron beam parameters.

Cavity

Stable single-mode CW oscillation in an oversized cavity with high efficiency η, at the 300 GHz and 4 kW output power level becomes a rather complicated problem [2]. An essential circumstance here is that this problem has to be solved within a number of limitations. Results of numerical simulation for the gyrotron detailed model demonstrate that efficiency is limited due to limitation on density of ohmic losses in cavity walls, voltage depression and mode competition also. Dependences of an output power and efficiency on beam current at different beam voltage are shown on Fig. 1. Possibilities to improve efficiency of the gyrotron have been theoretically revealed.

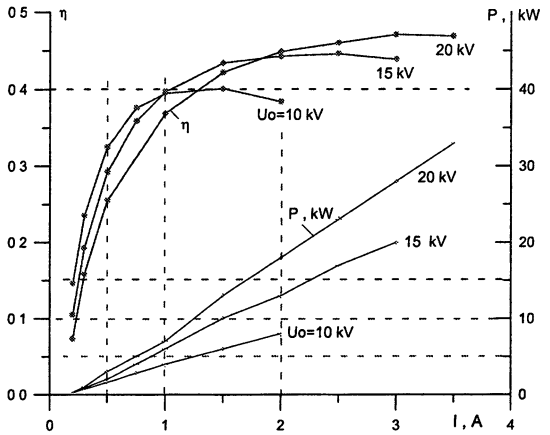

Fig. 1. Output power and efficiency vs. beam current

Electron gun and collector

Formation of high quality helical electron beams (HEB) with required parameters is one of the main problems for creating of high efficiency gyrotrons. For the 300 GHz gyrotron main electron gun design parameters are summarized in the Table 3.

Table 3. Main electron gun design parameters

Beam voltage	kV	15
Nominal beam current	A	1
Cathode radius	mm	21.5
Beam radius in cavity	mm	3.71
Density of emitter current	A/cm^2	<1
Pitch-factor		1.3
Velocity spread	%	<25

In result of numerical simulation the shapes of gun electrodes were optimized and dependence of velocity spread $\delta v_\perp$ (I) and ratio of oscillatory energy to the total one – $t_\perp(I)$ on the beam current is received (Fig. 2). Simulations were performed taking into account initial velocities (EPOS-V [4]).

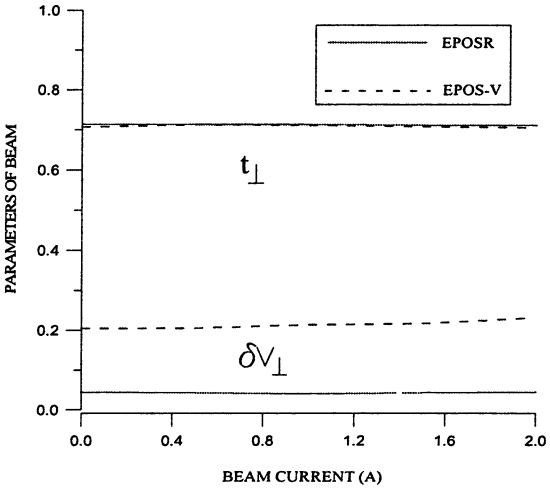

Fig. 2. Velocity spread $\delta v_\perp$ and $t_\perp$ vs. beam current

The tube collector has been designed to withstand up to 15 kW electron beam power for the CW regime of operation and up to 20 kW when the RF oscillation breaks. The collector profile is optimized to provide a thermal load and temperature increase below as admissible ones.

Mode converter and output window

The mode converter separates RF radiation from the worked-out electron beam, transforms a complicated cavity mode to a paraxial wave beam with an optimized structure and allows one to minimize harmful action of possible reflections of RF power back to the gyrotron. The converter includes a specially shaped waveguide end and three profiled mirrors, to provide: low diffraction losses inside the tube, optimal RF power distribution over an output window; matching of the output wave beam to a transmission line.

For the output window of 300 GHz/4 kW CW gyrotron will be used the selected BN disks with small RF loses (near 10% of transmitting power).

Industrial 300 GHz/4 kW gyrotron

The first version of the 300 GHz/4 kW experimental-industrial gyrotrons with $TE_{22,8}$ operation mode has been designed. General view of gyrotron tube is shown on the Fig. 3. The experimental-industrial 300 GHz CW gyrotron tube was constructed and manufactured.

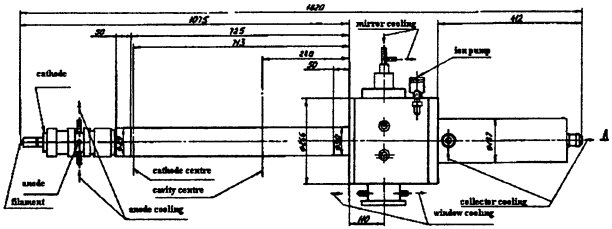

Fig. 3. General view of gyrotron tube

Preliminary test results

After fabrication the experimental-industrial 300 GHz CW gyrotron tube was delivered to Research Center for Development or Far Infrared Region, University of Fukui, Japan installed to the 12 T liquid Helium (LiHe) free cryomagnet for preparation for the test (see Fig. 4). The original test of the 300 GHz/ 4 kW/ CW gyrotron tube was made at May 2005. Pulse test results demonstrated good agreement with calculations. The CW operation test has carried out up to 0.5 kW, CW by using the existing water load. The power tested is restricted by the capability of the water load.

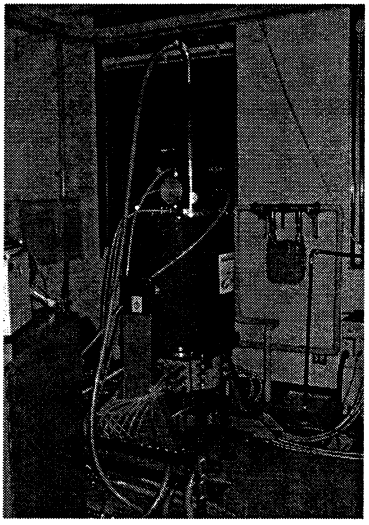

Fig. 4. Photo of the 300 GHz gyrotron with cryomagnet.

Conclusion

- Design versions and development of 300 GHz/CW, gyrotron with output power 4 kW, including its specific property details are presented.

- Main and special technical problems of 300 GHz gyrotron and test set-up are outlined and discussed.
- The CW version of the 300 GHz gyrotron tube was manufactured and delivered to the Research Center for Development or Far Infrared Region, University of Fukui.
- The original test of the 300 GHz/ 4 kW/ CW gyrotron tube was made at May 2005 at the Research Center for Development or Far Infrared Region, University of Fukui.
- The operation test has carried out up to 0.5 kW, CW by using the existing water load. The power tested is restricted by the capability of the water load.
- The efforts to increase the output power and efficiency of gyrotron operation will be continued.

Acknowledgements

The described research was supported by the Grant INTAS № 03-51-3861 and Grants of Russian Foundation of Fundamental Researches № 03-02-17560, № 05-02-16015 and № 05-02-08024-офи-а.

References

1. *Ogawa I., Idehara T. et al.* Application of Submillimeter Wave Gyrotron to plasma diagnostics 28th Int. Conf. Infrared and Millimeter Waves, Otsu, Japan, September 29-October 26, 2003. P. 403-404.
2. *Zapevalov V.E.* Problems and Advances of High Power Gyrotrons. Proc. 4th Int. Symp. Physics and engineering of millimeter and sub millimeter waves, June 4-9, 2001, Kharkov, Ukraine. P. 117-122.
3. *Kurbatov V.I. et al.* 70–140 GHz gyrotrons on their way to CW operation: Proc. Int. workshop Strong Microwaves in Plasmas. N. Novgorod, 2000. P. 641-650.
4. *Kuftin A.N. et al.* Advanced numerical and experimental investigation for gyrotrons helical electron beams. Int. J. Infrared and Millimeter waves, **20**(3), p. 361-382 (1999).

GYROTRON PHASE LOCKED BY RESONANT LOAD: THEORY

Yu. V. Novozhilova[1], *A. Fernandez*[2], *R. Martin*[2], *M. I. Petelin*[1]

[1]Institute of Applied Physics RAS, Nizhny Novgorod, Russia
[2]CIEMAT, Madrid, Spain

A simple analytical theory is built to describe 1) the autooscillator phase locked by the external wave and 2) the autooscillator frequency stabilization by the small reflection from high-Q resonant load. For the gyrotron, a sequential analysis of coupling the cavity to the incident wave is presented.

Autooscillator locked by external signal

Let us assume that in an autooscillator the time of transition process is much longer than the lifetime T of excited particles:

$$T << \frac{Q_1}{\omega_s}, \tag{1}$$

here ω_s and Q_1 are eigen-frequency and Q-factor of the empty autooscillator cavity. In this case the complex amplitude of the autooscillator field

$$Y_1 = A_1 \exp(i\varphi_1) \tag{2}$$

satisfies the equation [1]

$$\dot{Y}_1 + i\Delta Y_1 + Y_1 + i\chi Y_1 = F. \tag{3}$$

Here F is the external field, in the formula $\tau = \frac{\omega_2 t}{2Q_1}$ for dimensionless time, ω_2 is the external wave frequency taken as the reference one, $\Delta = 2Q_1 \frac{\omega_2 - \omega_s}{\omega_2}$ is normalized mismatch between this frequency and the cavity eigen-frequency ω_s,

$$\chi(A_1, \dot{\varphi}_1) = \chi_1 + i\chi_2 \tag{4}$$

is the normalized complex susceptibility being a non-linear function of the field amplitude and frequency.

In the absence of external force ($F = 0$), under condition $(\chi_2)'_A \big|_{A=A_{10}} < 0$, the free running autooscillator, according to (3), tends to stabilize

$$\dot{A}_{10} = 0, \ \dot{\varphi}_1 = 0, \tag{5}$$

here the amplitude A_{10} and the frequency ω_0 are defined by equations

$$\chi_{20} = 1, \ 2Q_1 \frac{\omega_0 - \omega_s}{\omega_2} = -\chi_{10}. \tag{6}$$

Let a weak ($|F| << 1$) external force have a frequency close to the frequency of free running autooscillator:

$$|\delta_0| = \left|\frac{\omega_0 - \omega_2}{\omega_2}\right| 2Q_1 << 1. \qquad (7)$$

Let us expanded the electron beam susceptibility into a series:

$$\chi \approx \chi_0 + a_1 (\chi)'_A \Big|_{A_1 = A_{10}}, \qquad (8)$$

where $a_1 = A_1 - A_{10}$ is the amplitude shift. Under the condition (1), the derivative (χ) on the mismatch δ can be neglected. The stationary phase locked operation is described with equation (2) linearized over a_1, that gives dependence of the amplitude shift a_1 on the frequency mismatch δ_0:

$$a_1 = \left(\delta_0 (\chi_1)'_A \pm \sqrt{\left(\frac{m_1 A_2}{A_{10}}\right)^2 |(\chi)'_A|^2 - (\delta_0 (\chi_2)'_A)^2} \right) \Big/ |(\chi)'_A|^2, \qquad (9)$$

where $(\chi)' = (\chi_1)' + i(\chi_2)'$. At the (a_1, δ_0) plane (Fig. 1), the equation (9) describes an asymmetrical ellipse of

$$|\delta_{0max}| = |F(\chi)'_A / (A_{10}(\chi_2)'_A)| \qquad (10)$$

frequency bandwidth. The ellipse inclination is due to the dispersion of active component of electron susceptibility $\chi_1(A)$. At the simplified description of the locking effect [2] the dispersion is not taken into account, but according to the causality principle (resulting in the Kramers–Kronig relations) it is non-zero [3].

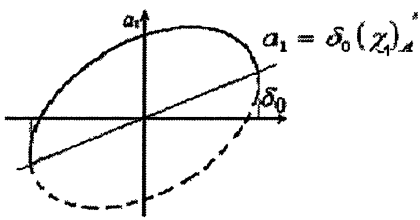

Fig. 1. Amplitude deviation caused by external force vs. frequency mismatch. The dashed line corresponds to instable solution of Eq. (2).

The upper part of ellipse corresponding to the upper sign in (9) describes stable locked oscillations.

Autooscillator frequency stabilization by resonant load

From the above analysis it is clear that the partial reflecton from resonant load can stabilize the autooscillator frequency, if

- the reflecting resonant load has the eigen-frequency close to that of the autooscillator free oscillation,
- the load Q-factor is sufficiently high,
- the wave returned to the autooscillator is properly phased.

The method is used in a number of practical systems [4, 5].

The autooscillator coupling to the external resonator is described with equations (compare with (2))

$$\dot{Y}_1 + i\Delta Y_1 + Y_1 + i\chi Y_1 + im_1 Y_2(\tau - T) = 0, \tag{11a}$$

$$\dot{Y}_2 + \gamma Y_2 + im_2 Y_1(\tau - T) = 0, \tag{11b}$$

where the reference frequency is taken equal to that of the external resonator, $m_{1,2}$ are the coupling parameters, $\gamma = Q_1/Q_2 << 1$ is the ratio of autooscillator and resonator Q-factors, T (to be optimized) is the time of wave propagation from the autooscillator to the load.

The stationary solution of the system (11)

$$Y_{1,2} = Y_{1,2_0} \exp(i\delta\tau), \quad \dot{Y}_{1,2_0} = 0 \tag{12}$$

takes place under condition

$$(i\delta + \gamma)(i\delta + i\Delta + 1 + i\chi) + m\exp(-2iT) = 0, \tag{13}$$

where $m = m_1 m_2$ is the product of coupling coefficients, $\delta = 2Q_1(\omega - \omega_2)/\omega_2$ is the mismatch of the coupled oscillation frequency and the external resonator eigen-frequency. Separating the real and imaginary parts of (13), one gets a relation between the frequency mismatch of coupled oscillation δ and the free-running frequency mismatch $\delta_0 = -\chi_{1_0} - \Delta$ (see Fig. 2):

$$\delta_0 = \delta + \chi_1 - \chi_{1_0} - \left(\delta m \cos(2T) + \gamma m \sin(2T)\right)/\left(\delta^2 + \gamma^2\right). \tag{14}$$

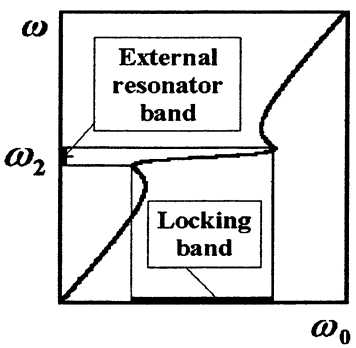

Fig. 2. Coupled oscillation frequency vs. the free-running autooscillator frequency.

If 1) the external resonator Q-factor is high enough, 2) the delay time satisfies condition $\cos(2T) < 0$ and 3) δ_0 changes within the band $|\delta_0| \le |m\cos(2T)/\gamma|$, then the coupled oscillation frequency is kept within the external resonator band: $|\delta| \le \gamma$ (Fig. 2).

Gyrotron excitation by external wave

The above theory can be applied to the gyrotron locking by external field, provided the gyrotron cavity coupling to the waveguide is described with a proper formalism. The gyrotron cavity represents a section of slightly irregular waveguide (Fig. 3) where the field $f(z)$ satisfies the inhomogeneous string equation

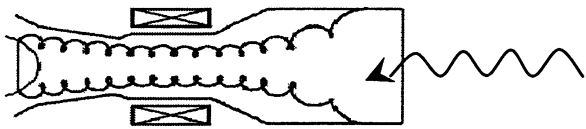

Fig. 3. The gyrotron excitation by the external wave

$$f'' + h^2 f = u(z), \tag{15}$$

$h^2 = \omega^2/c^2 - \kappa^2$, $\kappa(z)$ is the transverse wave number, $u(z)$ is a source. At the gun side, in below-cut-off neck, the field can be put zero

$$f|_{z=-L} = 0. \tag{16}$$

At the collector end $(z = 0)$, where

$$|h_z'| << h^2, \tag{17}$$

the boundary condition corresponds to the external wave incidence and to free radiation from resonator:

$$f_z'|_{z=0} = (-ihf + 2ihb)|_{z=0}, \tag{18}$$

where b is the incident wave amplitude.

Let us consider the excitation of the only lowest single-humped mode. The field can be expanded into the series

$$f(z) = \sum_s a_s f_s(z) \tag{19}$$

of functions representing solutions of Eqs. (15), (16) at $u(z) \equiv 0$, $b = 0$ and

$$f|_{z=0} = 0, \tag{20}$$

where z is put zero at the output waveguide cross section corresponding to zero of the main mode of empty cavity excited with the wave incident from the outer direction. Accordingly

$$a_s = c^2 \int_{-L}^{0} u(z) f_s^*(z) dz \left[\left(\omega^2 - \omega_s^2 \right) \int_{-L}^{0} |f_s|^2 \, dz \right]^{-1} . \tag{21}$$

The boundary condition (18) for the single-humped mode $f = a_0 f_0(z)$ can be described with an equivalent source placed near the cross section $z = 0$:

$$u(z) = \left[-a_0 i h_0^{-1} \left(df_0/dz \right) - 2b \right] \Big|_{z=0} \left(d\delta(z-0)/dz \right) . \tag{22}$$

At $b = 0$, the combination of (21) and (22) gives the radiation decrement of the main mode:

$$\operatorname{Im} \omega_0 = c^2 \left[\frac{1}{h_0} \left| \frac{df_0}{dz} \right|^2 \right] \Bigg|_{z=0} \left(2 \operatorname{Re} \omega_0 \int_{-L}^{0} |f_0|^2 \, dz \right)^{-1} . \tag{23}$$

If a stationary flow of a medium (a stationary electron beam) is injected into the cavity, the stimulated RF current can be described by a term $a_0 g(a_0, z)$ to be included into $u(z)$:

$$u(z) = a_0 g + \left[-a_0 i h_0^{-1} \left(df_0/dz \right) - 2b \right] \Big|_{z=0} \left(d\delta(z-0)/dz \right) . \tag{24}$$

Accordingly, Eqs. (21)–(24) can be combined into

$$a_0 i \left(\omega - \operatorname{Re} \omega_0 - i \operatorname{Im} \omega_0 \right) = -i \chi a_0 \operatorname{Re} \omega_0 / (2Q) - i b h_0 \operatorname{Im} \omega_0 / \left(df_0/dz \big|_{z=0} \right) , \tag{25}$$

where $\chi = \chi_1 + i\chi_2 = i \int_{-L}^{0} g f_0^* dz$ is the injected flow susceptibility, and the wave is reflected from resonator with the coefficient

$$R = \frac{\omega - \operatorname{Re} \omega_0 + i \operatorname{Im} \omega_0 + \operatorname{Re} \omega_0 \left(\chi_1 + i\chi_2 \right) / (2Q)}{\omega - \operatorname{Re} \omega_0 - i \operatorname{Im} \omega_0 + \operatorname{Re} \omega_0 \left(\chi_1 + i\chi_2 \right) / (2Q)} . \tag{26}$$

The gyrotron stabilization by the external high-Q resonator is exemplified with Fig. 4 where a partial reflection from a quasi-optical cavity is provided with a shallow mirror corrugation. If the gyrotron operates at a mode with non-zero azimuthal index, a proper azimuthal corrugation of the gyrotron output horn may be necessary to couple the reflected wave to the cavity mode.

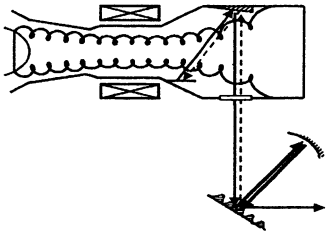

Fig. 4. Gyrotron stabilized by partial reflection from external mirror cavity.

Acknowledgement

Authors are grateful to K. Sarksyan, G. Batanov and V. Yakovlev for stimulating discussions.

References

1. *Ergakov V.S. et al.* Sov. Radiotehnika i Electr., 1978, 12, 2591-2599.
2. *Rabinovich M.I., Trubetskov D.I.* Oscillations and Waves in Linear and Nonlinear Systems. Dordrecht, Kluwer Academic, 1989.
3. *Landau L.D., Lifshitz E.M.* Electrodynamics of Continuous Media, 2nd edition, Pergamon Press, Oxford, England, 1984.
4. *Jory H.R.* Network for pulling a Microwave Generator to the Frequency of Its Resonant Load. US Patent 3714592, Jan. 30, 1973.
5. *Polovkov P.* The Stabilization of microwave oscillator frequency by the external cavity. Moscow, Sov. Radio, 1967.

SUPERRADIANCE IN THE PROCESS OF BACKSCATTERING OF PUMP WAVE ON THE INTENSE ELECTRON BUNCH (THEORY AND EXPERIMENT)

A. G. Reutova, M. R. Ulmaskulov, A. K. Sharypov, V. G. Shpak, S. A. Shunailov, M. I. Yalandin, V. I. Belousov[1], G. G. Denisov[1], N. S. Ginzburg[1], A. S. Sergeev[1], I. V. Zotova[1]

Institute of Electrophysics RAS, Ekaterinburg, Russia
[1]Institute of Applied Physics RAS, N.Novgorod, Russia

A novel mechanism of superradiance in the process of stimulated backscattering of powerful pump wave by intense electron bunch has been studied. Using a relativistic 38 GHz BWO as a pump wave source, the short superradiance pulses of scattered radiation were observed experimentally. Due to the Doppler up-shift, spectrum of scattered superradiance pulse included the frequencies up to 150 GHz.

Recently a significant progress was achieved in the generation of subnanosecond pulses in the millimeter and centimeter wave bands utilizing the cyclotron and Cherenkov mechanisms of superradiance (SR) of electron bunches [1–3]. The maximal peak power in the case of Cherenkov SR exceeded gigawatt level [3]. This paper is devoted to the novel mechanism of superradiance in the case of the stimulated backscattering of powerful pump wave by intense electron bunch. In this situation, due to the Doppler up-shift effect the radiation frequency can significantly exceed the frequency of the pump wave:

$$\omega_s = \omega_i \frac{1+V_{\|}/V_{ph.i}}{1-V_{\|}/V_{ph.s}}, \qquad (1)$$

where $V_{\|}$ is the translational electron velocity, $V_{ph\,i,s}$ are the phase velocities of the pump wave (index i) and the scattered wave (index s). With the relativistic microwave generator as a pump wave source such a mechanism is beneficial for generation of the powerful pulse radiation in the short millimeter and submillimeter wave bands. In this paper we present a basic theoretical description of the superradiance regime of stimulated backscattering. The results of theoretical consideration are confirmed by the first experimental observation of above SR mechanism.

Basic model

Let us consider the backscattering of the powerful pump wave by the hollow electron bunch with injection radius R_b and duration Δt_b that moves through a cylindrical waveguide with radius R along homogeneous guiding magnetic field $\mathbf{H_0} = H_0\mathbf{z_0}$. Under assumption of the fixed pump wave ampli-

tude, the generation of short single pulse of scattered radiation (SR pulse) can be described by the nonstationary equation for scattering signal amplitude A_s and the averaged equations for electrons' motion in the field of combination wave:

$$\frac{\partial a_s}{\partial \zeta}+\frac{\partial a_s}{\partial \tau}=if(\tau)a_i g\frac{I}{\pi}\int_0^{2\pi}e^{-i\theta}d\theta_0,$$
$$\frac{\partial^2\theta}{\partial\zeta^2}=\mu\,\mathrm{Im}\left\{a_s a_i\, g e^{-i\theta}\right\}. \qquad (2)$$

Here $\zeta=\omega_c z/c$, $\tau=\omega_c c\left(t-z/V_\parallel\right)\left(1/V_{gr}-1/V_\parallel\right)^{-1}$, $a_{i,s}=eA_{i,s}/2m_0\gamma c^2$ are the dimensionless amplitudes of pump and scattered waves, $\theta=\omega_{\tilde{n}}t-k_c z$ is the electrons phase with respect to the combination wave, $\omega_c=\omega_s-\omega_i$, $k_c=h_s+h_i$, $h_{i,s}$ are the longitudinal pump and scattered wave numbers, $\mu=\gamma_0^{-2}\beta_\parallel^{-3}$, $I=\left(eJ_0/mc^3\right)\cdot\left(2\gamma_0 h_s k_c R^2 N_s\right)^{-1}$, J_0 is the electron current, N_s is the norm of the scattered wave. Factor

$$g=J_{n_i-1}\left(k_{\perp i}R_b\right)J_{n_s-1}\left(k_{\perp s}R_b\right)\Omega/\left(\Omega-\omega_H\right) \qquad (3)$$

describes the increase of oscillation velocity of electrons near the cyclotron resonance, $\omega_H=eH_0/m_0c\gamma_0$ is the gyrofrequency, $\Omega=\omega_i+h_i V_\parallel$ is the bounce frequency, $k_{\perp i,s}$ is the transverse wave number, $J_n(x)$ is the Bessel function, $n_{i,s}$ are the azimuth indices of the waveguide modes. Function $f(\tau)$ defines the profile of electron current with normalized duration $\tau_b=\Delta t_b\omega_c c\left(1/V_{gr}-1/V_\parallel\right)^{-1}$.

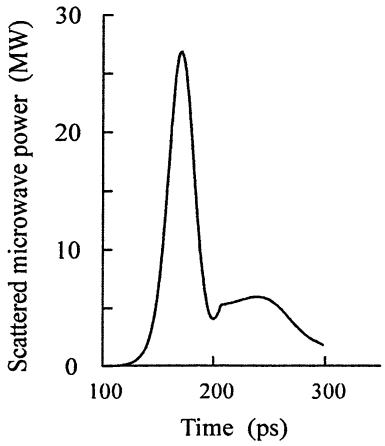

Fig. 1. Superradiance pulse (simulations).

Equations (2) describe the joint combinational action of the pump and the scattered waves on the electrons. Such an action leads to selfbunching that starts from small initial density perturbations. As a result the amplitude of scattered wave grows. In the absence of external feedback the synchronization of radiation from different parts of extended electron bunch is provided by slippage of the scattered wave with respect to electrons due to a difference between the electron velocity and the electromagnetic wave group velocity. As a result the scattered wave radiates in the form of a single short pulse, as is shown in Fig. 1. The parameters of simulation are chosen in

accordance with the performed experiment. The pump wave with 100 MW power and 38 GHz frequency has the transverse structure of the TE_{11} mode. This wave undergoes the backscattering by the 250 keV, 1 kA, 200 ps electron bunch guided in 24 kG magnetic field. According to the simulation the duration of the scattered SR pulse is about 50 ps with peak power ~25 MW. The scattered wave frequency should be about 150 GHz.

Experimental set-up

Experiments on the observation of the stimulated backscattering in the superradiance regime were carried out at Institute of Electrophysics (Ekaterinburg, Russia) based on two synchronized nanosecond and subnanosecond high-current RADAN-303 accelerators [4–5]. The 4 ns electron beam from the first accelerator was used to drive the low frequency pump wave generator. The pump wave undergoes backscattering with frequency up-conversion on the subnanosecond electron bunch produced by the second accelerator. The general view of experimental set-up is shown in Fig. 2.

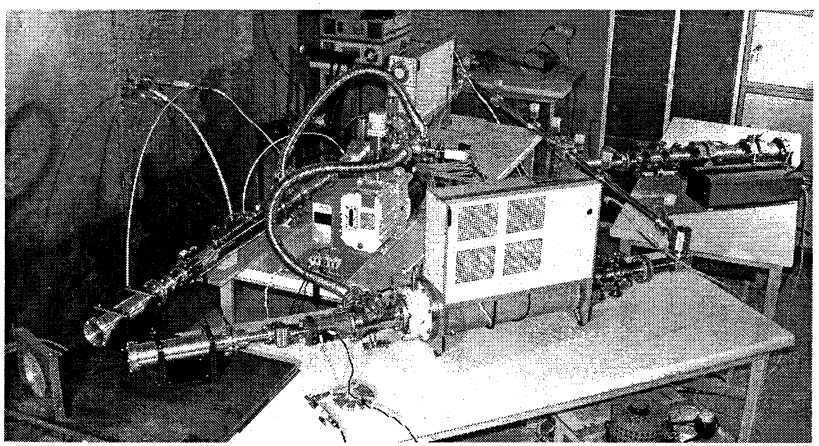

Fig. 2. Experimental set-up

In experiments the pump wave was generated by relativistic BWO with operating frequency 38 GHz. For transmission of the pump wave to the scattering section a specially designed quasioptical mirror has been used. The mirror possessed the high reflectivity 95% at the pump wave frequency 38 GHz. The partial transparency of the mirror for the scattered radiation at frequencies above 60 GHz was provided by the mesh of holes with diameter of 3 mm having a step of 4 mm.

Experimental results

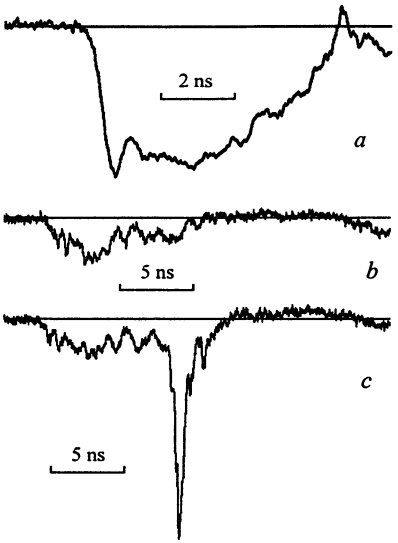

Fig. 3. Pulse of the pump wave (*a*). High frequency component of BWO radiation in the absence of electron e-bunch registered by detector after quasioptical mirror (*b*). Superradiance pulse caused by e-bunch backscattering (*c*).

Oscilloscope trace of the 4 ns, 100 MW pump wave pulse with duration is shown in Fig. 3, a. In absence of subnanosecond electron bunch, the signal from BWO registered by detector installed after quasioptical mirror is shown in Fig. 3, b. This signal is caused by parasitic high-frequency radiation from the pump wave generator at the harmonics of operating frequency. Presence of such harmonics in a spectrum of the pump wave is confirmed by the direct simulation based on PIC-code KARAT.

In the scattering section with 30 cm length the low frequency pump wave underwent stimulated backscattering by the high current relativistic subnanosecond bunch (250–300 keV, 1–1.5 kA, 500–700 ps). It is important to note that in absence of the pump wave the background noise radiation of electron bunch was below the threshold sensitivity of a microwave detector. When the pump wave generator was switched on, the short powerful pulse could be observed, as is shown in Fig. 3, *c*. This pulse has rather short duration (about 200 ps) and can be interpreted as a superradiance pulse. SR pulses were observed in a large area of magnetic field detuning. The maximal peak power was obtained for field strength 20–25 kG when the magnetic field strongly affects the amplitude of electron oscillations.

To analyze the radiation spectrum a set of cut-off waveguides was used. Amplitudes of detector signals after filters with different cut-off frequencies are shown in Fig. 4. Locations of vertical lines correspond to the cut-off wavelengths of different filters and the lengths of lines are proportional to the signals registered by the detector. Obviously the jumps of dashed line characterize the content of different spectrum components in the scattered radiation. The main components of radiation concentrate at the interval within wavelength 3.5–4.2 mm. But at the same time there are high frequency components with wavelength around 2 mm, which is rather close to the calculated one. However it should be noted that detector sensitivity decreases with frequency. So the real fall of intensity of high frequency components should be less than detector indi-

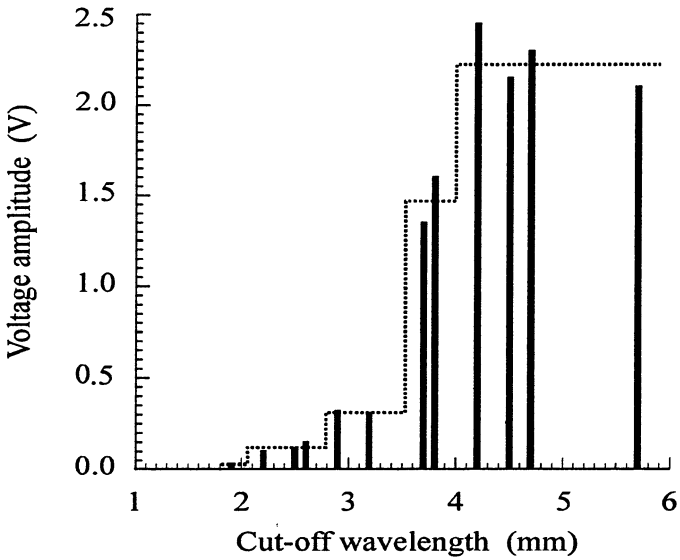

Fig. 4. Spectrum measurements. Relative amplitudes of detector signal after filters with different cut-off frequencies.

cations shown in Fig. 4. A rather wide spectrum of scattered radiation can be explained by the spread of electron velocities in the real electron bunch as well as by excitation of several waveguide modes. Integral (over frequency spectrum) peak power of SR pulse amounts up to 1 MW. It was estimated basing on the power level indicated by microwave detector taking into account the aperture of the reception antenna, the distance from a radiator and the width of the radiation pattern.

Conclusion

As a result of the experiments the effect of generation of short electromagnetic pulses was observed in the process of stimulated backscattering of the powerful pump wave by the intense electron bunch. Scattered radiation had the form of ultrashort pulse with peak power of 1 MW and duration of 200 ps. Due to the Doppler frequency up-conversion the spectrum of scattered radiation included the frequencies up to 150 GHz that exceeded the pump wave frequency in several times. This process can be interpreted as a superradiance of electron bunch since the radiation of the short pulse occurs in the absence of external high frequency signal and in the absence of external cavity and correspondingly cannot be attributed to traditional amplification or oscillation regimes. Due to the development of selfbunching inside the extended electron bunch the peak

power of scattered signal significantly exceeds the power of the spontaneous radiation of electrons in the pump wave and the duration of scattered pulse was essentially shorter than the duration of the background noise.

This work was supported by the Russian Fund for Fundamental Research, grant 05-02-17553-a and 05-02-08016.

References

1. *Ginzburg N., Zotova I., Sergeev A., Konoplev I., Phelps A., Cross A., Cook S., Shpak V., Yalandin M., Shunailov S., Ulmaskulov M.* Phys. Rev. Lett., 1997, 78(12), 2365.
2. *Ginzburg N., Novozhilova Yu., Zotova I., Sergeev A., Peskov N., Phelps A., Cross A., Ronald K., Shpak V., Yalandin M., Shunailov S., Ulmaskulov M., Tarakanov V.* Phys. Rev. E, 1999, 60(3), 3297.
3. *Korovin S., Mesyats G., Rostov V., Ul'maskulov M., Sharypov K., Shpak V., Shunailov S., Yalandin M.* Technical Phys. Lett., 2004, 30(2), 117.
4. *Shpak V., Shunailov S., Oulmascoulov M., Yalandin M.* In Digest 12th IEEE Int. Pulsed Power Conf., USA, 1999, 2, 1472.
5. *Mesyats G., Korovin S., Rostov V., Shpak V., Yalandin M.* Proc. of the IEEE, 2004, 92(7), 1166.

S-BAND SUPERRADIANCE IN SLOW WAVE STRUCTURE

K. Kamada, K. Yamamoto, R. Nakajima, R. Ando,
I. V. Zotova[1], *R. M. Rozental*[1], *A. S. Sergeev*[1], *N. S. Ginzburg*[1]

Graduate School of Natural Science and Technology, Kanazawa University, Kanazawa, Japan
[1]Institute of Applied Physics, Russian Academy of Sciences, Nizhny Novgorod, Russia

5 GHz, 300 MW microwave pulse with duration of 5 ns was obtained using a 600 keV, 5 kA, 12 ns intense relativistic electron beam injected into a periodical slow wave structure. PIC simulation indicated that the radiation was caused by superradiance. The modification of the beam energy waveform by inserting of additional coaxial cavity affected the output power of superradiance pulse.

1. Introduction

Stimulated emission from electron bunches – superradiance (SR) is an attractive method of generation of ultrashort electromagnetic pulses. Theoretical and experimental studies of superradiance have been reported with different mechanisms of stimulated emission (bremsstrahlung, Cherenkov, cyclotron) through the frequencies 10–150 GHz [1–5]. The most effective generation of SR pulses is obtained by Cherenkov mechanism with short electron bunch moving in corrugated waveguide. With increasing of electron bunch duration up to 10 ns it is possible to produce the SR pulses in long centimeter wave band (S-band). We report here the experimental and simulated results of S-band SR pulse production. The simulated peak output power of radiation is proportional to the square of the number of electrons as it is typical for superradiance. As it was proposed in [6] the peak power of SR pulse can be increased using an electron beam with time-increasing energy and current waveforms. In reported experiment the energy waveform was modified by transporting of electron beam through a coaxial cavity.

2. PIC Simulation

The cylindrically corrugated waveguide was designed for 5 GHz SR as shown in Fig. 1. PIC simulation code KARAT was used to optimize the precise parameters. The inner radius of the waveguide was decreased to be 22 mm (cut off frequency of 5.2 GHz) to reflect the expected backward wave to the downstream side at the entrance of the corrugated part. Gradually increasing radius regions ($\overline{AB}$ and $\overline{CD}$ in Fig. 1) were located at both sides of the interaction region to prevent parasitic wave reflections and to improve beam transport.

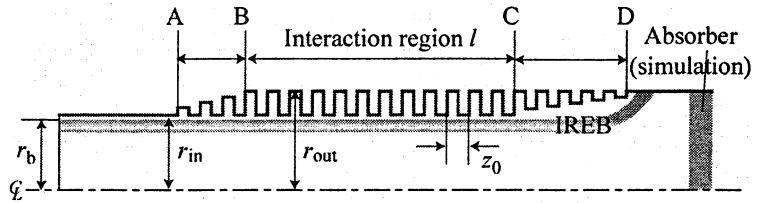

Fig. 1. Cross section of the cylindrical corrugated waveguide, where r_b = 20 mm, r_{in} = 22 mm, r_{out} = 28 mm, z_0 = 30 mm, l = 300 mm. In the simulation microwave was absorbed at the end of the tube.

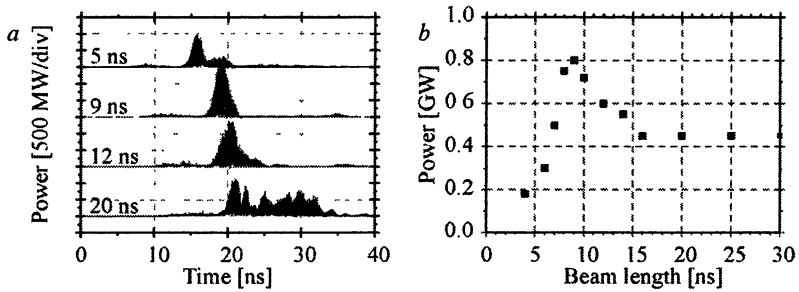

Fig. 2. Simulated microwave outputs for different beam lengths. Time dependence of microwave output (*a*). Output peak power vs. beam duration (*b*).

In the PIC simulation by code KARAT, the microwave pulse with frequency of 5 GHz, output power of 600 MW and duration of 4 ns was radiated when the electron beam with energy of 550 keV, current of 4.5 kA and duration of 12 ns was injected into the corrugated waveguide. The microwave pulse short duration and frequency spectrum corresponds to the SR emission. To clarify the dependency of the microwave output power on the total number of beam electrons, the beam duration was changed in the simulation. The simulated results of microwave outputs with different beam duration are shown in Fig. 2. As expected for SR the simulated output peak power of radiation is proportional to the square of the number of electrons for rather short electron beam.

3. Experimental setup

The system was composed of three sections, the diode, the coaxial cavity and the corrugated waveguide. An annular electron beam of 600 keV, 5 kA, 12 ns with diameter of 40 mm and thickness of 3 mm was injected from the diode into a conducting drift tube with inner diameter of 44 mm. At first, the coaxial cavity was removed. The corrugated waveguide was connected at

100 mm downstream of the diode. For the second experiment with modified energy waveforms, the coaxial cavity was inserted at 200 mm from the diode. The principle of the modification of the energy waveform is the same as the autoacceleration scheme [7]. Though the cavity length was changed, the entrance of the corrugated waveguide was located at 1100 mm from the diode for any cavity length. The schematic of the experiment with the modified waveforms is shown in Fig. 3. In both cases, the microwave was radiated into the air through a Lucite window. The system was immersed in axial magnetic field of 1 T applied by solenoid coils. The base pressure was maintained below 1×10^{-5} Torr.

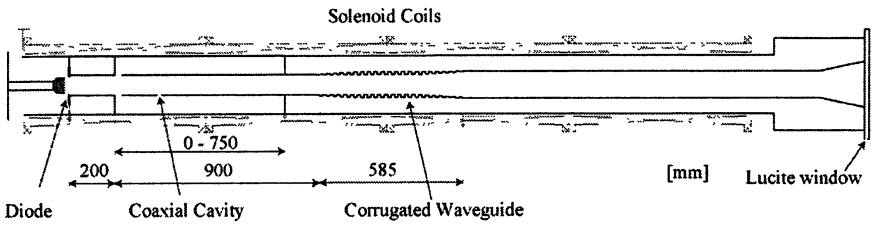

Fig. 3. Experimental Setup

The radiated microwave was detected by a horn located more than 1 m far from output window. The microwave received by the horn was attenuated by two variable attenuators. Five low pass filters with frequencies from DC-4 GHz to DC-8 GHz were utilized. Tunnel detectors detected microwaves passing through the low pass filters. The variable attenuators, low pass filters and tunnel detectors were calibrated by low power devices.

4. Experimental observation of S-band SR pulses

At first, the coaxial cavity was removed for the experiments of 5 GHz SR. The signals detected by tunnel detectors through low pass filters are shown in Fig. 4. No signal was detected without the corrugated waveguide. With corrugated waveguide, similar signals were detected through DC-5 to DC-8 GHz low pass filters, though no signal was observed through the DC-4 GHz. It corresponds to microwave signal frequency of around 5 GHz. The detected SR pulse duration was 5 ns that agreed with the simulated result. The microwave signals were not changed by the axial magnetic field from 0.7 to 1.0 T.

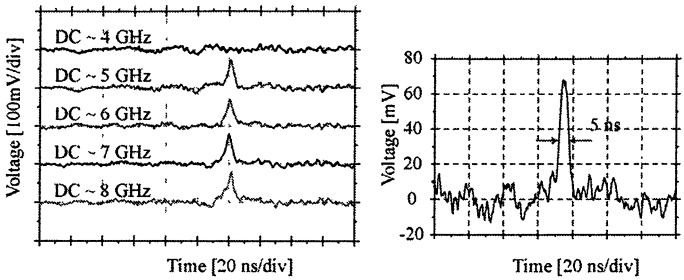

Fig. 4. Signals through low pass filters with cylindrical corrugated waveguide

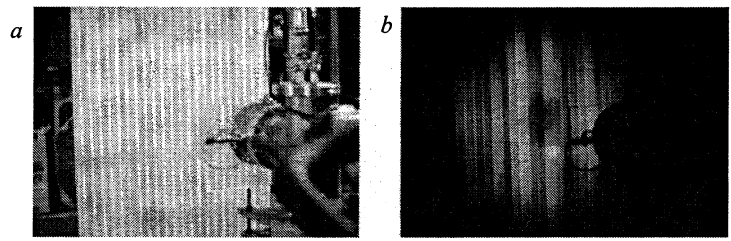

Fig. 5. Fluorescent tubes were located 550 mm far from the Lucite window (*a*). The donuts like pattern was observed (*b*).

Fluorescent tubes were located 550 mm far from the Lucite window to observe the radiation pattern. The observed donut like pattern is shown in Fig. 5 and corresponds to emission of TM_{01} mode.

The angular distribution of the radiated microwave was measured by the horn moved along the circumference with radius of 1500 mm from the center of the Lucite window. In agreement with the observed radiation pattern the microwave output has one peak around 20 degrees from the beam axis as shown in Fig. 6. Total output power was estimated to be 300 MW from the angular distribution.

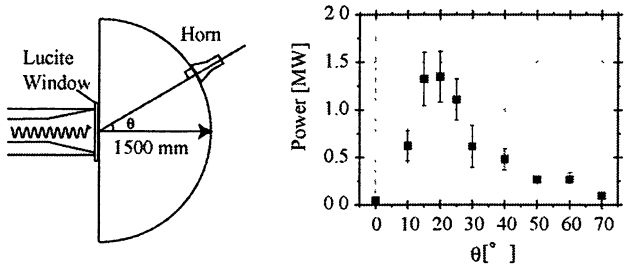

Fig. 6. The setup of the measurement of the angular distribution (left). The peak output power was plotted against the angle from the beam axis (right).

The frequency, the duration, the mode and the total power of the radiated microwave were in a good agreement with the simulated results of SR. Therefore, we concluded that the 5 GHz SR was observed.

5. Optimization of driving beam energy waveform

For the second experiment with the modified electron beam, the auto- acceleration coaxial cavity was inserted between the diode and the corrugated waveguide. The energy waveform was modified by the length of the coaxial cavity as shown in Fig. 7. The beam current waveform was little changed by the coaxial cavity. The frequency, the duration and the radiation mode of the microwave were not changed by the length of the cavity.

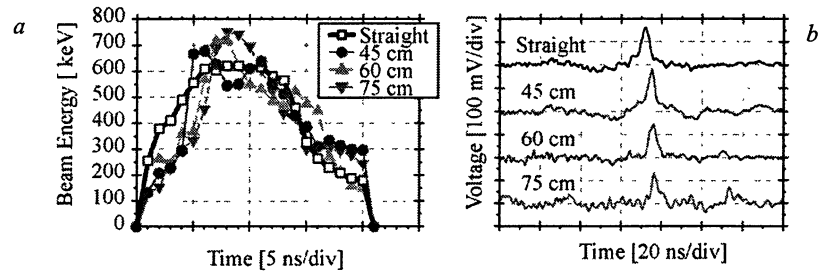

Fig. 7. The energy waveforms (*a*) and microwave signals (*b*) for different cavity length

The angular distribution of the peak output power of the microwave is shown in Fig. 8. The estimated peak output power is also plotted against the length of the coaxial cavity. The lower total power than in the experiment described in Sect. 5 should come from the difficulty of the beam alignment with increasing of the distance between diode and slow wave structure to insert the additional cavity.

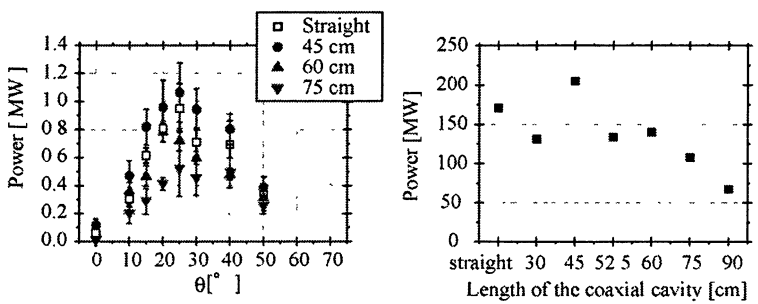

Fig. 8. Angular distribution of the peak output power of the microwave (left) and the estimated total output power (right) for the different cavity length.

The output power was changed by the modified energy waveform. When the cavity length was 45 cm, the power was 20% higher than that without coaxial cavity. Thus, there is a possibility to increase the output power of SR pulse by using an appropriately modified electron beam.

6. Conclusion

A 5 GHz, 300 MW, 5 ns superradiance microwave pulse was observed using the 600 keV, 5 kA, 12 ns electron beam injected into the slow wave structure. The experimental results showed good agreements with the simulation results. The modification of energy waveform of the beam affected the output power of SR pulse. It could be possible to increase the output power of superradiance pulse by modifying the energy waveform of an intense electron beam.

A part of this work is supported by a Grant-in-Aid for Scientific Research from Ministry of Education, Science, Sports and Culture, Japan.

References

1. *Ginzburg N.S., Zotova I.V.*, Sov. Tech. Phys. Lett., **15**, 573-574 (1989).
2. *Ginzburg N.S. et al.*, Phys. Rev. Lett., **78**, 2365-2368 (1997).
3. *Ginzburg N.S. et al.*, Phys. Rev. E, **60**, 3297-3304 (1999).
4. *Wiggins S.M. et al.*, Phys. Rev. Lett., **84**, 2393-2396 (2000).
5. *Elthaninov A.A. et al.*, Pis'ma v ZhETF, **77**(6), 314-318 (2003).
6. *Ginzburg N.S. et al.*, Opt. Comm., **231**, 303-308 (2004).
7. *Friedman M.*, Appl. Phys. Lett., **41**, 419–421 (1982).

HELICALLY CORRUGATED WAVEGUIDES FOR COMPRESSION OF PULSES FROM A RELATIVISTIC BWO

S. V. Samsonov, V. L. Bratman, G. G. Denisov, M. L. Kulygin, S. V. Mishakin, A. W. Cross[1], P. MacInnes[1], W. He[1], A. D. R. Phelps[1], G. Burt[1], K. Ronald[1], I. V. Konoplev[1], A. R. Young[1], C. G. Whyte[1]

Institute of Applied Physics, Nizhny Novgorod, 603950, Russia
[1]University of Strathclyde, Glasgow, G4 0NG, United Kingdom

The use of a metal overmoded circular waveguide with an appropriate helical corrugation of its inner surface as a dispersive medium enables effective compression of smoothly frequency modulated microwave pulses at very high powers. The paper presents results of on-bench experiments at kilowatt power levels demonstrating that X-band radiation of 80 ns duration with 5% frequency modulation can be compressed into a 1.5 ns pulse having 20–25 times higher peak power. Results of the simulations of an X-band relativistic BWO enabling a frequency-modulated pulse with power of hundreds of megawatts to be produced are also presented as well as the simulations of a helical waveguide with enhanced electrical strength designed to compress the BWO pulse up to multigigawatt power.

Introduction

As it was shown in Ref. [1], the use of a metal overmoded circular waveguide with an appropriate helical corrugation of its inner surface as a dispersive medium enables effective compression of smoothly frequency modulated microwave pulses. The helical corrugation couples a pair of circularly polarized partial modes of the smooth waveguide having significantly different group velocities, one mode (mode 1 in Fig. 1) is far from the cutoff whereas the other mode (mode 2) is close to cutoff. As a result, in the frequency region of their resonant coupling an eigenmode appears that has a strongly frequency dependent group velocity (mode W_1 in Fig. 1), which is favorable for the pulse compression. In contrast to a smooth or axially-symmetric corrugated waveguide, the helical corrugation allows the frequency regions with zero or negative group velocity of the eigenwave to be avoided, which ensures good RF matching of the compressor with the input source over a sufficiently wide frequency band.

The theoretical analysis and proof-of-principle experiments at kilowatt power levels [1] showed that X-band radiation of 50–70 ns duration with 3–5% frequency modulation can be compressed into 2–3 ns pulses having 10–20 times higher peak power and containing more than 50% of the input pulse energy. This region of operating parameters in conjunction with low reflection and high RF electric strength makes the helical waveguide compressor attractive for increasing the peak power from relativistic non-resonant electron devices such as BWOs and TWTs up to the multigigawatt level.

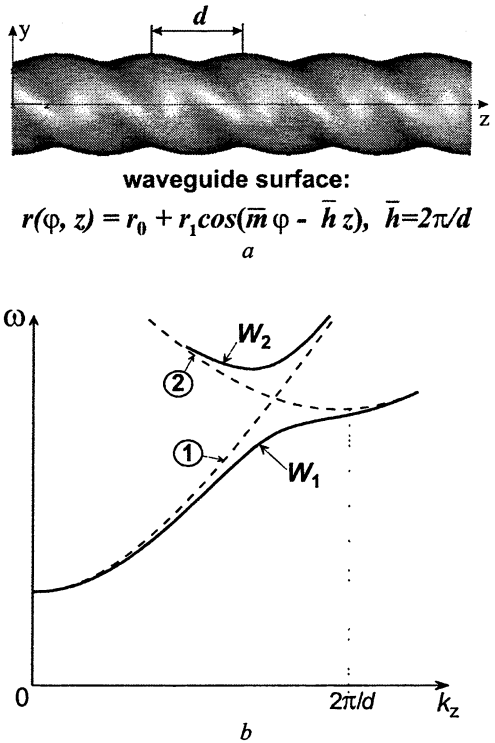

Fig. 1. Helically corrugated waveguide (*a*) and its dispersion diagram (*b*): ① is a lower partial mode of a smooth waveguide; ② is a spatial harmonic of a near-cutoff mode; W_1 and W_2 are the eigenmodes of the helical waveguide.

In this paper recent experimental results on the pulse compression with improved frequency modulation of the input pulse are presented. Simulation results on a relativistic BWO as a source of a powerful frequency modulated pulse are discussed. A design of a higher-order-mode helical waveguide for the BWO pulse compression, capable for handling gigawatt powers is also presented.

Helical-waveguide pulse compression experiment

Experiments on the pulse compression using helically corrugated waveguides were performed at the University of Strathclyde. Several helical structures with slightly different parameters, manufactured at the Institute of Applied Physics and the University of Strathclyde, were cold-tested with scalar and vector network analyzers and used as X-band pulse compressors. The tested waveguides had 3-fold right-handed corrugations ($\bar{m}=3$ in Fig. 1, *a*) which coupled the right-handed $TE_{2,1}$ near-cutoff mode with the left-handed $TE_{1,1}$ mode [2]. The input radiation was launched from a WG16 waveguide, then passed through a rectangular-to-circular adapter and then through an elliptical cross-section polarizer which converted the linearly polarized $TE_{1,1}$ mode to a circularly polarized mode. This mode was then adiabatically transformed into the operating mode (Fig. 1, *b*) passing through a four-period section with linearly increasing amplitude of the helical corrugation. Analogous sequence of the mode converters took place at the compressor output. The best results were achieved with a copper helical structure with a 2.08 m long, 14.7 mm in diameter section (consisting of 9 pieces) of regular corrugations having period of 28.9 mm and amplitude of 1.4 mm (Fig. 2). Recent experiments were performed using equipment loaned by Agilent, UK to generate an input signal with optimum parameters as

well as to monitor the input and output radiation from the compressor (Fig. 3). A conventional X-band TWT was used to amplify the input pulse up to kilowatt powers. The optimum frequency modulation of a quasi-rectangular input pulse was found from analysis of the measured helical waveguide dispersion. The sweep started from the frequency corresponding to the minimum value of the group velocity and went down to the frequency of higher group velocity in such a manner that the inverse group velocity was linearly decreasing function of time over the input pulse duration determined by the waveguide length. Due to some technical problems the input pulse top was not very flat but the measured frequency modulation practically coincided with the optimum one (Fig. 4, *a*). As a result, almost the maximum available (for this compressor) power compression ratio of 25 was achieved. The measured output pulse shape was in very good agreement with the simulations (Fig. 4, *b*) which included the measured compressor (Fig. 2) and input pulse (Fig. 4, *a*) characteristics.

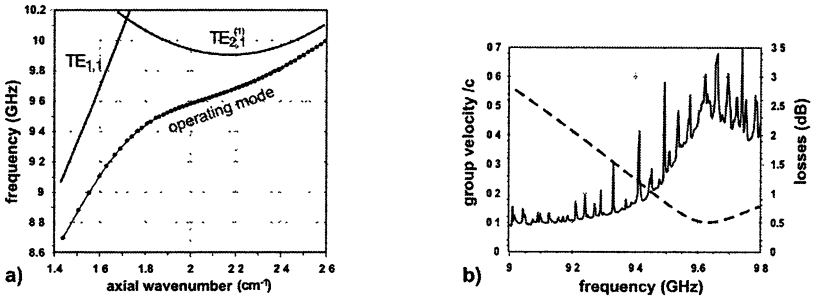

Fig. 2. Measured characteristics of helically corrugated waveguide used in the compression experiment: *a* – dispersion; *b* – group velocity of the operating mode (dashed line) and losses (solid line) for whole compressor.

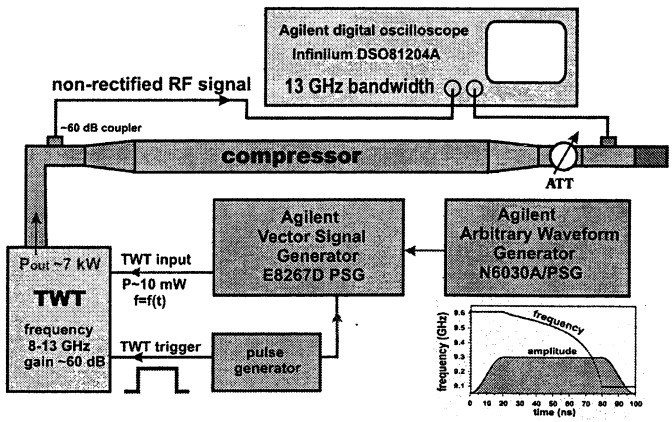

Fig. 3. Setup of the pulse compression experiment

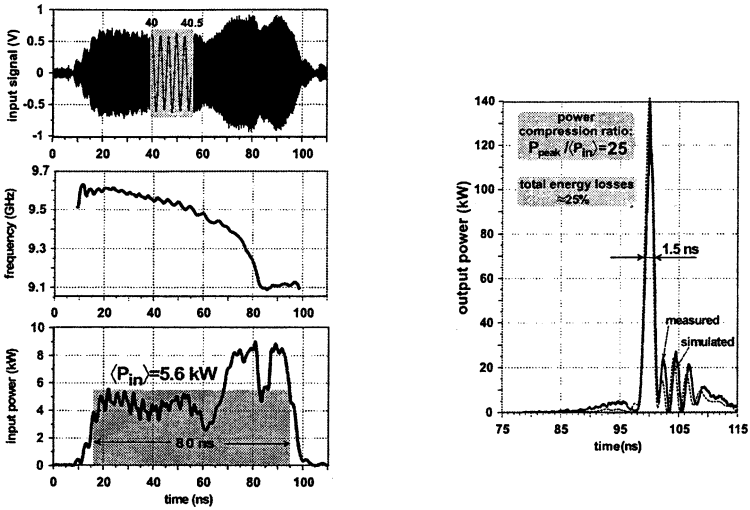

a *b*

Fig. 4. Experimental results on the pulse compression: *a* – input pulse details; *b* – measured (solid line) and simulated (dashed line) compressed pulse.

Relativistic BWO with fast frequency tuning

Backward-wave oscillators (BWOs) utilizing moderately relativistic (400–600 kV) high-current (5–10 kA) explosive-emission electron beams are now highly-developed reliable devices capable of producing gigawatt-level pulsed radiation in the centimeter and millimeter wavelength range [3, 4]. The principle of BWO operation allows for sufficiently broadband smooth frequency tuning by varying the accelerating voltage so that pulses similar to that shown in Fig. 4, *a* can be produced at gigawatt powers. Further 10–20 fold power increase due to the pulse compression may result in a unique source of multigigawatt radiation attractive for a number of advanced applications.

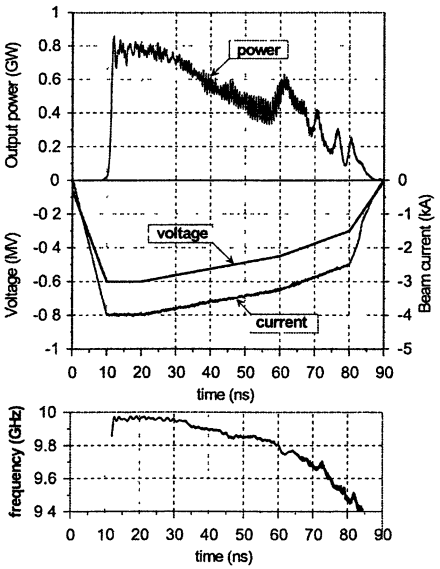

Fig. 5. Results of KARAT simulations for a frequency-swept BWO.

In Ref. [5] a BWO analysis based on 1D linear theory and more detailed numerical simulations using the time-domain PIC code KARAT [6] were performed resulting in a BWO configuration which combines high output power, high efficiency and a sufficiently wide frequency tuning for a moderately relativistic electron beam (Fig. 5).

Compression of the BWO pulse

Theoretical analysis of compression of the simulated BWO pulse showed that it is possible to adapt the dispersion of a helical waveguide to the BWO frequency sweep and increase (due to the compression) its peak power by 15–20 times. However, for a helical waveguide configuration similar to that which was used in the experiment discussed above, the amplitude of the RF electric field on the wall at a power of 1 GW amounted to 1.4 MV/cm which exceeded the breakdown threshold for a 50-ns long pulse. Therefore several different higher-order mode structures were analyzed resulting in the design of a waveguide with a 5-fold helical corrugation coupling $TE_{2,2}$ and $TE_{3,1}$ modes having about a two times larger diameter (Fig. 6). This allowed reduction of the maximum electric field at the wall down to 0.44 MV/cm (at 1 GW power) which is acceptable to handle the BWO pulse to be compressed. In addition, the higher-order-mode helical waveguide possesses lower ohmic losses. According to the simulations, the use of such a waveguide with optimized parameters enables the BWO pulse compression up to the power of 13.7 GW which is 17.1 and 27.4 times greater peak and averaged BWO power, respectively (Fig. 7). It is planned to test the designed BWO at the "SINUS-6" accelerator in the regime of short (15–20 ns) pulses as well as to manufacture and cold-test the higher-order-mode helical structure including the corresponding mode converters.

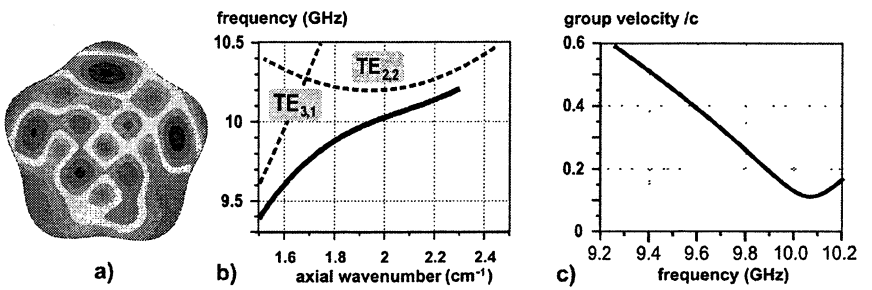

Fig. 6. Simulated characteristics of helically corrugated waveguide for compression of the BWO pulse: *a* – distribution of absolute value of the electric field across waveguide cross section; *b* – dispersions of the partial and operating eigenmodes; *c* – group velocity of the operating mode.

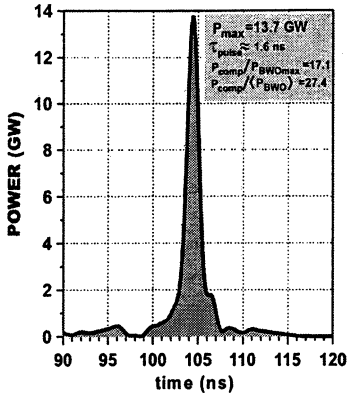

Fig. 7. Simulated BWO pulse after a 3.2 m long helical-waveguide compressor.

This work was supported by the Russian Foundation for Basic Research (Grant 04-02-16698), the Program for Basic Research of Presidium of Russian Academy of Sciences "Basic problems of nano- and picosecond high-power electronics", the EPSRC UK and the University of Strathclyde. The authors would like to thank Geoff Wild and Don Hamilton of Agilent UK for the loan of the Agilent equipment used in the experiments.

References

1. *Samsonov S.V., Phelps A.D.R., Bratman V.L., Burt G., Denisov G.G. et al.* Phys. Rev. Lett., 2004, **92**, 118301.
2. *Burt G., Samsonov S.V., Ronald K., Denisov G.G., Young A.R., Bratman V.L., Phelps A.D.R., Cross A.W., Konoplev I.V., He W., Thomson J., Whyte C.G.* Phys. Rev. E, 2004, **70**, 046402.
3. *Zaitsev N.I., Kovalev N.F., Kol'chugin B.D., Fuks M.I.*, J. Tech. Phys. (Sov.), 1982, **52**, 1161.
4. *Korovin S.D., Mesyats G.A., Rostov V.V., Shpak V.G., Yalandin M.I.*, Proc. 15th Int. Conf. High-Power Particle Beams, 2004, St. Petersburg, Russia, p. 479-482.
5. *Samsonov S.V., Bratman V.L., Burt G.C., Cross A.W., Denisov G.G., Phelps A.D.R., Ronald K.*, Proc. 15th Int. Conf. High-Power Particle Beams, 2004, St. Petersburg, Russia, p. 430-433.
6. *Tarakanov V.P.*, User's Manual for Code KARAT. Springfield, VA: BRA, 1992.

RECENT PROGRESS IN THE PASOTRON STUDIES

Yu. P. Bliokh, G. S. Nusinovich[1], J. Felsteiner, Y. Carmel[1], A. G. Shkvarunets[1], J. C. Rodgers[1], V. L. Granatstein[1]

Physics Department, Technion–Israel Institute of Technology, Haifa, Israel
[1]Institute for Research in Electronics and Applied Physics, University of Maryland, College Park, MD, USA

Plasma-assisted slow-wave oscillators (pasotrons) are unique sources of microwave radiation, in which beam propagation in the absence of external magnetic fields is provided by ion focusing and the electron interaction with the RF field is essentially two-dimensional.

The name "Pasotron" is an acronym for plasma-assisted slow-wave oscillator [1]. The pasotron utilizes the ion focusing mechanism [2] for the beam transport in the absence of a guiding magnetic field. The absence of solenoids makes the pasotron to be a compact, lightweight microwave source. A scheme of the pasotron is presented in Fig. 1. A plasma e-gun is used as a beam source. The electron beam ionizes the neutral gas which fills the chamber, the beam space-charge field expels the plasma electrons and the remaining ions form a channel which partially compensates the beam space charge and keeps the beam from radial divergence. The beam excites an electromagnetic wave in a slow-wave structure (SWS) in the same manner as in conventional TWT or BWO tubes. Typical parameters of the pasotron that is investigated experimentally at the University of Maryland are the following: beam current 30 – 120 A, voltage 40 – 55 kV, pulse duration 80 μs, microwave power from 0.5 MW with efficiency 50% to 1 MW with efficiency 30%.

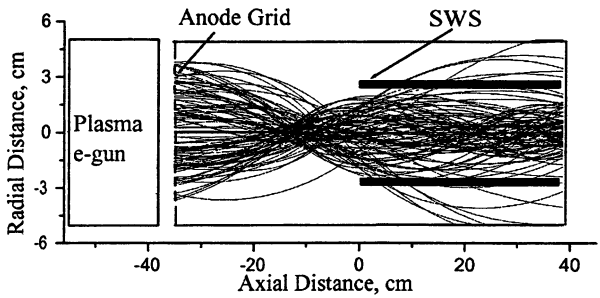

Fig. 1. Scheme of the pasotron

Let us consider at first the channel formation. The chamber forms an equipotential surface and the beam creates inside the chamber a bath-shaped po-

tential well (Fig. 2). Ions oscillate in the well and the most important are the axial oscillations [3]. In our experiments the characteristic time required for the beam charge compensation is large compared with the period of these oscillations and ions have time to visit any point along the system independently of their birth place. It means that an homogeneous ion channel is formed along the whole system even if the gas density is strongly inhomogeneous.

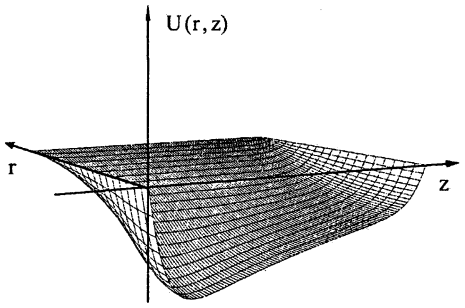

Fig. 2. Potential well

In the pasotron the gas density, on the one hand, should be large enough in order to provide the beam transport. On the other hand, the presence of the gas inside the SWS may cause a microwave breakdown at a high power level. These conflicting objectives have been satisfied using the above-mentioned effect of the ion motion. The gas is concentrated mainly in the drift region and inside the SWS the gas pressure is some orders of magnitude smaller. The measured gas pressure is shown in Fig. 3. The right-hand scale shows the local neutralization time which is calculated using the local gas density. The solid line marks the beam pulse duration, and the dashed line marks the measured time of the channel formation along all the system. One can see that the local neutralization time in the SWS is longer that the pulse duration and only the axial motion of the ions can explain the channel formation along the whole system. The calculated theoretically channel formation time (10 μs) is in a good agreement with experiment. The developed theory of the channel formation [3] allows us to explain two phenomena which are unusual for traditional microwave sources. There are the hysteresis-like dependence of the on-axis current density on the beam current [4] and the dependence of the starting current of the microwave excitation on the beam current rise time [5].

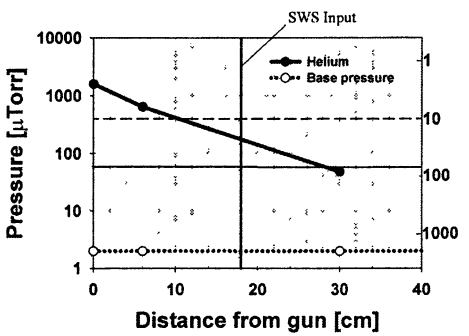

Fig. 3. Gas pressure distribution

Thus, the beam transport in pasotron is much richer in physical effects than the traditional method of beam transport in a guiding magnetic field. The microwave excitation in the pasotron also looks unusual. In contrast to a magnetically confined beam the beam particle motion in the pasotron is multi-dimensional

in principle [6]. The axial motion in the microwave field occurs in the same manner as in traditional devices and will not be considered here. The radial motion is determined by the common action of the ion channel and the beam self-fields and the radial fields of the excited synchronous wave. The profile of the resulting radial potential well depends on the wave phase θ. If the wave amplitude is small, the axially uniform potential well is slightly deformed by the wave fields, as it is shown in Fig. 4, *a*. Oscillating electrons fill this well and form a so-called phase-mixed beam [7].

If the wave amplitude is large enough, the shape of the well is transformed drastically (Fig. 4, *b*). The radial field of the wave becomes stronger than the channel focusing field. Depending on their phase, some electrons remain trapped by the well, while other electrons are ejected. The electron bunch which is formed during the beam instability development is placed exactly in the last region of phases. On the one hand, this radial motion increases the efficiency of the beam-wave energy exchange because the wave field is stronger near the SWS boundary. On the other hand, the most "active" electrons, which form the bunch, are excluded from the process of wave excitation when they reach the chamber wall. Under optimal conditions this happens when the wave amplitude reaches the saturation level. The theoretical determination of these conditions [8] and their experimental realization allowed us to achieve 50% efficiency of microwave excitation in the pasotron [9].

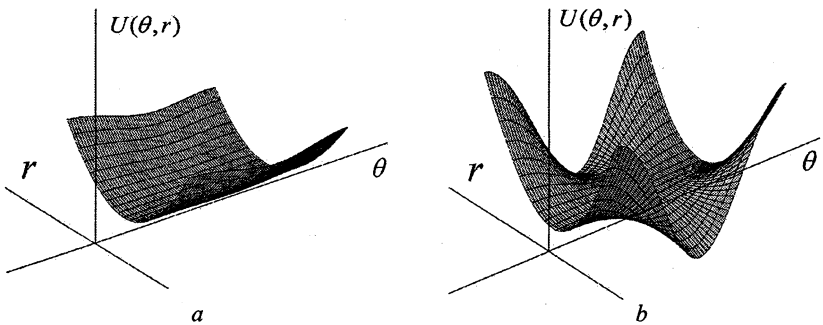

Fig. 4. Potential well for the small wave amplitude (*a*) and for the large wave amplitude (*b*).

The next effect has an absolutely different nature but leads to similar consequences. Let us consider the beam propagation in the ion channel in more detail. The density of ions in the channel is proportional to the beam density, $n_i = fn_b$, where f is the space-charge compensation ratio. The focusing force is proportional to the ion density, $F_{foc} \propto n_i = fn_b$. The defocusing force of the beam space charge is partially compensated by the focusing action of the mag-

netic field of the beam current and the resulting defocusing force is proportional to $F_{defoc} \propto n_b \gamma^{-2}$ (here γ is the beam relativistic factor). Thus, the resulting radial force is proportional to $F_r \propto -(f - \gamma^{-2}) n_b$.

Under the beam instability development the longitudinally homogeneous beam splits up into bunches. The beam density now depends on the wave phase θ. The ion density depends on the average beam density, $n_i = f < n_b >_\theta$, therefore the focusing force is proportional to $f < n_b >$. As regard to the defocusing force, it depends on the local beam density, that is on $n_b(\theta)$. As a result, the total radial force appears as

$$F_{tot} \propto -\left(f\gamma^2 - 1\right)\left\{< n_b(\theta) > -\left[n_b(\theta) - < n_b(\theta) >\right]\left(f\gamma^2 - 1\right)^{-1}\right\}. \qquad (1)$$

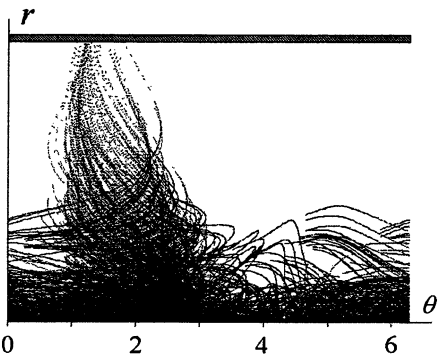

Fig. 5. Electon trajectories along the wave phase θ and in the radial direction.

The factor $f\gamma^2 - 1$ in the second term is always small for a weakly relativistic beam. It means that during the bunch formation the second term becomes larger than the first one and the focusing force changes into a defocusing one for the bunch electrons. These electrons move out from the axis. The longitudinal bunching continues and the electron motion along the wave phase and in the radial direction looks as it is shown in Fig. 5.

Figures 6*a*, 6*b* present the beam electron trajectories in the absence (Fig. 6, *a*) and in the presence (Fig. 6, *b*) of the excited wave. During the beam instability development, practically all electrons are grouped into bunches and when these bunches reach the chamber wall the beam disappears. Beyond the place where the beam reaches the wall, the wave amplitude does not change (see Fig. 6*b*). This is a specific nonlinear mechanism of the beam instability saturation in the pasotron. The saturation amplitude does not depend on the input amplitude, therefore the output amplitude also does not depend on the input amplitude. The output amplitude does not depend on the SWS length: one can cut part of the SWS and the output amplitude does not change. All these unusual properties of the pasotron have been confirmed experimentally: the collector current disappears when microwave generation is started, and the contraction of the SWS does not affect the output microwave power.

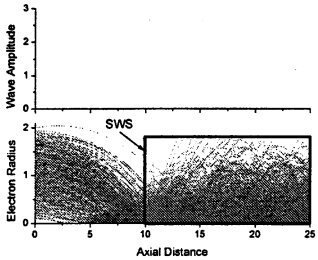

Fig. 6*a*. Electron trajectories in the absence of the wave.

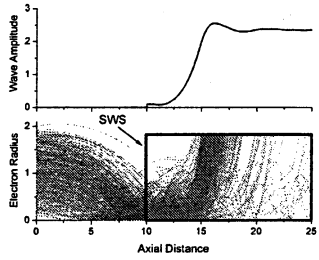

Fig. 6*b*. Wave amplitude (top) and electron trajectories (bottom).

The presence of ions in microwave devices is the source of the so-called ion noise. It seems natural to expect that the noise level in the pasotron should be very high. Surprisingly, this is not the case. The noise level in the pasotron is 50 dB below the carrier frequency (Fig. 7) [10].

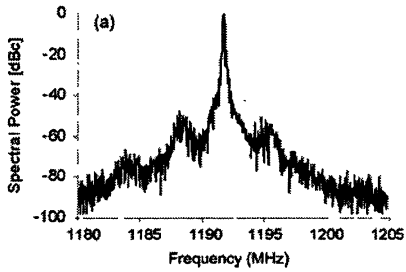

Fig. 7. Pasotron spectrum in the vicinity of the carrier.

Eq. (1) makes clear this phenomenon. Because of the smallness of the factor $f\gamma^2 - 1$, the second term becomes dominating early in the development of the beam instability. It is easy to see that in this case the radial force does not depend on the ion density. The ions do not affect the beam instability development and the role of the ion density fluctuations is strongly reduced.

References

1. *Schumacher R.W. et al.*, U.S. Patent 4912367, Mar. 27, 1990; *Goebel D.M. et al.*, IEEE Trans. Plasma Sci., 1994, **22**, 547.
2. *Bennett W.H.*, Phys. Rev., 1934, **45**, 890.
3. *Bliokh Yu.P., Nusinovich G.S.*, IEEE Trans. Plasma Sci., 2001, **29**, 951.
4. *Carmel Y. et al.*, Phys. Plasmas, 2003, **10**, 4865.
5. *Bliokh Yu.P. et al.*, Phys. Rev. E. 2004, **70**, 046501.
6. *Nusinovich G.S., Bliokh Yu.P.*, Phys. Rev. E, 2000, **62**, 2657; *Abu-elfadi T.M. et al.*, Phys. Plasmas, 2003, **10**, 3746.
7. *Lee E.P.*, Phys. Fluids, 1978, **21**, 1327.
8. *Abu-elfadi T.M. et al.*, IEEE Trans. Plasma Sci., 2002, **30**, 1126.
9. *Shkvarunets A.G. et al.*, Phys. Plasmas Lett., 2002, **9**, 4114.
10. *Nusinovich G.S. et al.*, IEEE Trans. Electron Dev., 2005, **52**, 845.

PLASMA RELATIVISTIC MICROWAVE AMPLIFIER

A. V. Ponomarev, P. S. Strelkov

A.M. Prokhorov General physics institute, Moscow, Russia

100 MW of the output power in plasma microwave amplifier was obtained with the efficiency of 10% and the gain of 32 dB. The frequency bandwidth of output radiation was found to be 0.17%. This width is defined by amplifier pulse duration.

Statement of the problem

The first successful experiment on Cherenkov plasma relativistic microwave amplifier was held in 1998 [1]. However, the amplification regime was rather unstable and was accompanied by the generation at frequencies different from the input signal frequency. Further modification of the experimental device as well as the use of another kind of microwave absorber allowed to suppress self-oscillations over a wide range of plasma densities. As a result, it became possible to measure main characteristics of the amplifier [2]. It was shown, in particular, that the frequency bandwidth of the amplified signal is less than 5% of the mean frequency. It does not contradict the theory but, according to it, the frequency bandwidth should be much less ($\sim 0.1\%$) and in our case should be determined by the microwave pulse duration.

The purpose of this work was to perform precise measurements of the output radiation frequency spectrum utilizing heterodyne method.

Experimental setup

A schematic of the device is shown in Fig. 1. Annular plasma 1 with a mean radius of 8 mm and a thickness of 1 mm was created in a smooth cylindrical waveguide 2 with a radius of 22 mm. The plasma was produced by an annular electron beam (see below) in xenon at a pressure of $2.5 \cdot 10^{-4}$ Torr over a time of about 30 μs. The system was placed in a strong longitudinal magnetic field **B**. Annular REB 3 with a mean radius of 10 mm, a thickness of 1 mm, electron energy of 500 keV and pulse duration of 100 ns was injected into the system from a diode located on the left (not shown in the Figure). The REB current could be varied. The experiments were carried out with the currents of 1.1 and 2 kA. The microwave signal from a magnetron went to the input 4 of the amplifier. Microwave power of 60 kW passed to the metal coaxial waveguide and excited slow plasma wave in the plasma waveguide. The frequency of the input power was 9.1 or 13 GHz. The REB amplified this wave and the electric field of this wave modulated the beam density. Then the absorber 6 absorbed microwaves completely, but the previously modulated beam excited the same slow plasma wave after the absorber. Then the most part of the microwave energy

went to the metal coaxial waveguide and was emitted by the horn 5. A part of the microwave energy was reflected from the right boundary of the plasma waveguide and could excite oscillations. However, the absorber eliminated the possibility of oscillations.

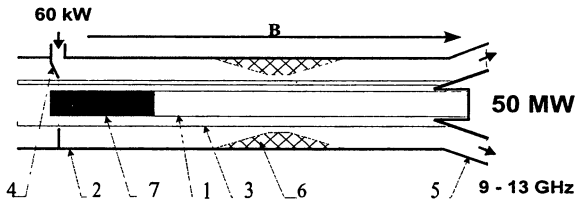

Fig. 1. Schematic of the amplifier: *1* – plasma, *2* – metal waveguide, *3* – REB, *4* – amplifier input, *5* – coaxial emitting horn, *6* – microwave absorber, *7* – central conductor of the input coaxial waveguide.

The source for plasma creation is shown in Fig. 2.

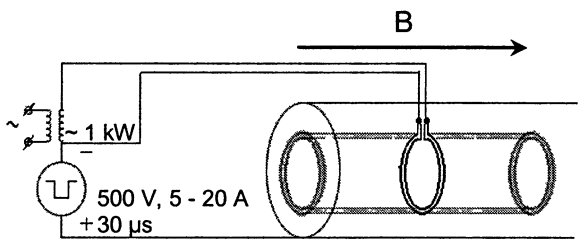

Fig. 2. Scheme of the plasma source

The tungsten ring, which is insulated from the ground, is heated up to the temperature of 3000 K. After that the negative 500 V, 30 μs pulse is applied to this ring. As a result, the 5 to 20 A electron beam propagates to the left and right sides along the magnetic field lines, creating annular plasma column. It is important that during the microwave pulse (~100 ns) the plasma concentration is constant and can be chosen in advance in the range $10^{11} - 10^{13}$ cm^{-3}. Cross section of xenon atoms ionization by relativistic electrons is small, the REB pulse duration is small also therefore, REB creates plasma with negligible density. The detailed description of the plasma source under consideration can be found in [3].

Measurement technique

Two methods of spectrum measurement were used: "filter method" and "heterodyne method" (Fig. 3). The "heterodyne method" was used for an input frequency 9.1 GHz only.

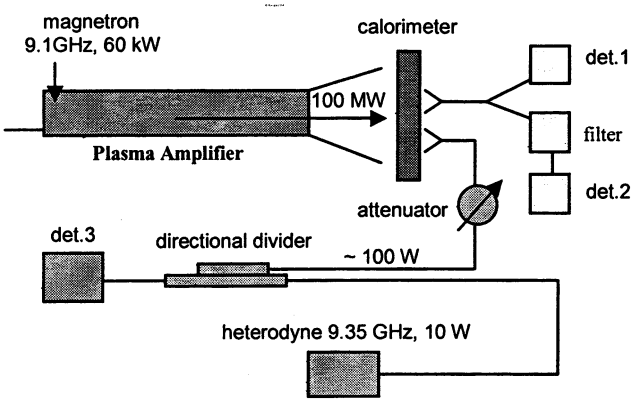

Fig. 3. The scheme of measurements

The "filter method" was a rough one and gave us the possibility to distinguish the regimes of amplification and oscillations in the plasma amplifier. To estimate the spectral width of the output radiation, we used a receiving transmission line consisting of two detectors and a narrowband filter. One of the detectors measured the total incident microwave power (det. 1 in Fig. 3). At the input of the other detector (det. 2 in Fig. 3) we placed a narrowband filter ($\Delta f / f = 5\%$), which was tuned to the frequency of the input signal. The sensitivities of the detectors were chosen so that in the case of a monochromatic signal at the receiving line input, the signals from the both detectors were identical. If the width of the radiation spectrum exceeded 5%, then the amplitude of the signal from the second detector was smaller than that from the first one. Thus, the width of the spectrum of the output microwave radiation could be estimated.

The well-known "heterodyne method" was used for precise measurements of the spectrum of the output radiation. Two waveguides went to the directional divider. One waveguide came from the plasma amplifier; the other one came from a steady-state microwave source (heterodyne). The attenuated signal from the amplifier was mixed with a signal from the heterodyne in the directional divider. The beating of microwave signals (they had different frequencies) was

measured by the detector 3. The beating signal had a frequency of 250 MHz and was measured by an oscilloscope with 350-MHz frequency band.

The total energy of the output microwave pulse was measured by a broad-band large-area (with the diameter of 30 cm) microwave calorimeter.

Experimental results

All the experiments have been carried out with the following parameters: plasma density $1.2 \cdot 10^{13}$ cm^{-3} ± 10%, input frequency 9.1 GHz, electron beam energy 500 keV, beam current 2 or 1.1 kA.

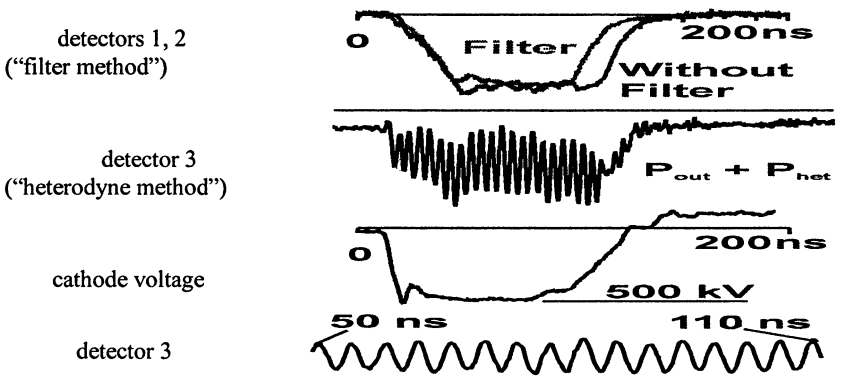

Fig. 4. $I_b = 1.1$ kA, $P_{in} = 60$ kW, $P_{out} = 40$ MW

Figure 4 illustrates the operation of the diagnostics. The signals from the detectors 1 and 2 coincide during the most part of the pulse. This means that the plasma amplifier frequency is about the input microwave frequency and the spectrum width at the output is less than 5%. The beating signal from detector 3 shows that the plasma amplifier radiation is almost monochromatic for these experimental parameters.

Figure 5 shows experimental results of 3 pulses with different levels of the input power. The left vertical row is identical to that in Fig. 4. The lowest row in Fig. 5 is the low-frequency beating signal spectrum.

The spectrum width for the first shot is equal to 15 MHz, $W = 3$ J, $P_{out} = 40$ MW. As soon as the input power decreases from 60 to 30 kW, the output energy and power decrease approximately twice also. The spectrum width does not change; it remains equal to 15 MHz. If the input power is zero, small microwave radiation is observed at the leading and trailing edges of the

beam current pulse only. In the middle of the pulse the output microwave power is equal to zero. The energy of that pulse is less than 0.3 J.

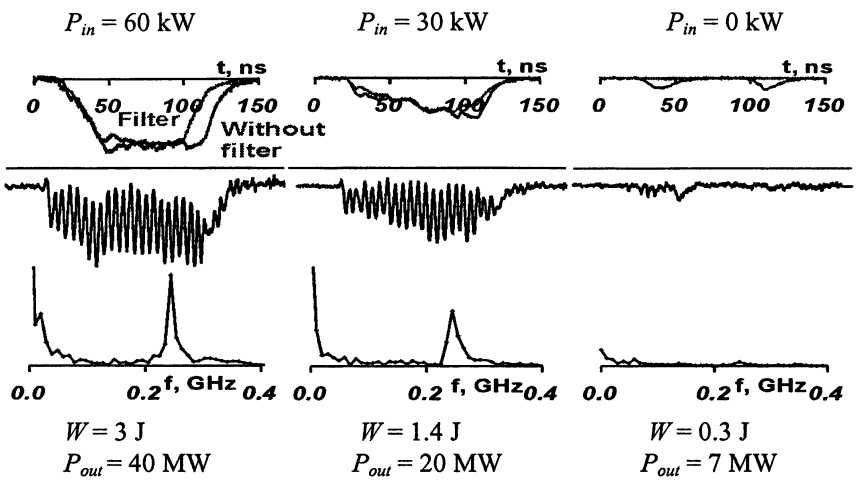

Fig. 5. The frequency spectrum measurements with the different values of input power, I_b = 1.1 kA.

An increase of the beam current up to 2 kA leads to an increase of the output power up to 100 MW, but the beating signal becomes worse.

Figure 6 represents the waveforms of the beating signals and their spectra (recalculated to the input frequency) for three different shots. The upper waveform is the beating signal of the input microwaves from the magnetron (f = 9.1 GHz) and the heterodyne microwaves. According to the theory an ideal plasma amplifier ought to give the same beating signal. The middle waveform is the beating signal of the heterodyne and plasma amplifier in the case of 1.1 kA electron beam and an output microwave power of 40 MW. It can be seen that the beating signal in this case is similar to the ideal one.

The lowest beating signal corresponds to 2 kA electron beam and 90 MW output microwave power. Clearly it is getting worse in this case, which is probably connected with much more considerable nonlinearity of the system.

The plasma amplifier spectrum calculated from these waveforms is presented at the bottom of Fig. 6. The frequency width on the half-height is the same for these three cases and is defined by the pulse duration of 80 ns. Nevertheless, the spectrum corresponding to the maximal power (90 MW) is the widest.

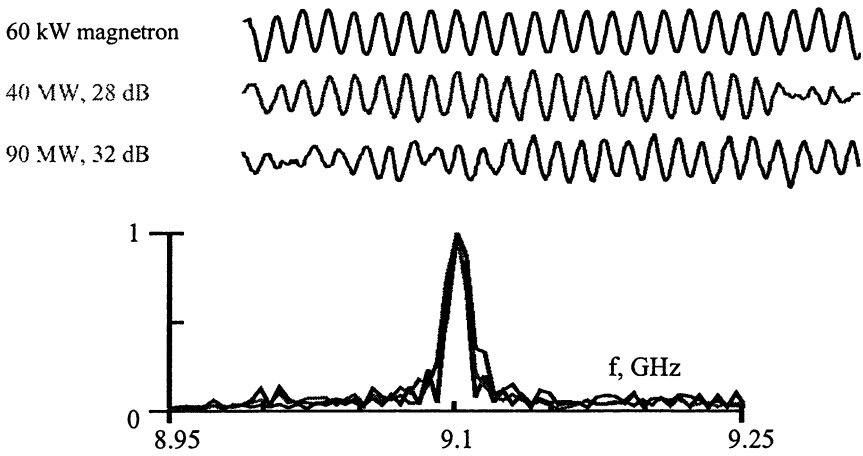

Fig. 6. Waveforms of beating signals and their spectra

Conclusions

Optimization of the plasma amplifier resulted in obtaining 100 MW of the output microwave power. It corresponds to the efficiency of 10% and to the gain of 32 dB.

The output radiation frequency bandwidth was equal to 15 MHz (0.17% from the mean frequency). This width is defined by the pulse duration (80 ns) of the amplifier.

The authors thank Dr. Denis Ulyanov who made all the calculations in obtaining the spectra from the waveforms of beating signals.

References

1. *Ponomarev A.V., Strelkov P.S., Shkvarunets A.G.*, Plasma Phys. Rep., 1998, **24**, 48.
2. *Ponomarev A.V., Strelkov P.S.*, Plasma Phys. Rep., 2004, **30**, 62.
3. *Loza O.T., Ponomarev A.V., Strelkov P.S. et al.*, Plasma Phys. Rep., 1997, **23**, 201.

STUDY OF CO-AXIAL FREE ELECTRON MASER BASED ON TWO-DIMENSIONAL DISTRIBUTED FEEDBACK

I. V. Konoplev[1], *A. W. Cross*[1], *N. S. Ginzburg*[2], *W. He*[1], *P. McGrane*[1], *N. Yu. Peskov*[2], *A. D. R. Phelps*[1], *C. W. Robertson*[1], *K. Ronald*[1], *A. S. Sergeev*[2], *M. Thumm*[3], *C. G. Whyte*[1], *V. Yu. Zaslavsky*[2]

[1]Department of Physics, University of Strathclyde, Glasgow G4 0NG, UK
[2]Institute of Applied Physics, RAS, Nizhny Novgorod 603950, Russia
[3]Forschungszentrum Karlsruhe, IHM, Karlsruhe D-76021, Germany

First studies of microwave radiation from a co-axial FEM based on 2D distributed feedback are presented. Measurements of the output radiation spectrum using a heterodyne technique demonstrate that a spectrum locates near the frequency of 37.3 GHz which corresponds to excitation of the fundamental azimuthally symmetric mode of the two-mirror 2D Bragg cavity. The output power of the FEM was measured to be ~15 MW. The possibility to optimise the cavity geometry to increase the RF-breakdown strength and further enhance the output power is discussed.

Introduction

Microwave sources such as Free-Electron Masers (FEM) operating in the millimetre and sub-millimetre wavelength range at MW and GW power levels can be attractive for a number of applications. To achieve the ultra-high power operation such radiation sources should be driven by an oversized (with respect to the wavelength of operation) electron beam, in order to maintain the current density and the RF power density inside the interaction space to a level which circumvents pulse shortening. A two-dimensional (2D) distributed feedback has been proposed to produce spatially coherent radiation from a large size electron beam of either planar [1, 2] or annular [3] geometry. The 2D distributed feedback can be realized in 2D Bragg resonators having a double-periodic corrugation.

This paper is devoted to progress in theoretical and experimental studies of the co-axial FEM scheme with 2D distributed feedback. The first results of the experimental study of the co-axial 2D Bragg FEM driven by an oversized annular electron beam are presented. The spectrum of the output radiation, the output power and output radiation mode pattern was measured and compared with theoretical predictions. The radiation spectrum was found to be located near the frequency of 37.3 GHz and was associated with excitation of the fundamental cavity mode, having a TEM azimuthally-symmetric output wave.

Study of the 2D Bragg structures

The analysis of the coaxial structures with corrugated inner and outer conductors (Fig. 1) was carried out. The experimental set-up used to measure the transmission coefficients through the 2D Bragg structures in the operating fre-

quency range 30–40 GHz has been designed and constructed (Fig. 2). For excitation of the structures a TEM-mode of a co-axial waveguide was formed at the input of the Bragg structure. The transmission line was made from three mode converters to provide mode transformation from the launched $TE_{0,1}$ wave of single mode rectangular waveguide to a TEM wave of a co-axial waveguide. An additional co- axial slowly up-tapered waveguide horn of length 60 cm was used to connect from the converters to the oversized co-axial structure. The structures on the inner conductor were machined from brass and were of length $l_z = 4.8$ cm with the corrugation depth 0.08 cm. A second structure manufactured from copper

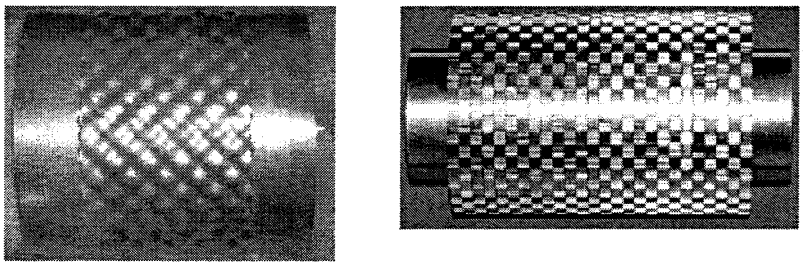

a *b*

Fig. 1. The photographs of the corrugated (*a*) outer and (*b*) inner conductors of co-axial 2D Bragg structures.

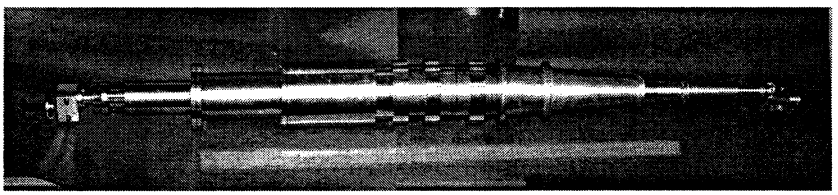

Fig. 2. The photograph of the experimental set-up used to measure property of the 2D Bragg co-axial structures.

had smooth 0.05 cm double-periodical sinusoidal corrugations on the inner surface of the outer conductor. The parameters of the corrugation were chosen to provide coupling between a TEM and $TE_{24,1}$ waves for the brass 2D Bragg reflector and between TEM and $TE_{28,0}$ waves for the copper 2D Bragg reflector and, thus, the number of azimuthal variations for the brass and copper 2D Bragg reflector was 24 and 28 respectively. The periods of corrugations corresponded to the frequencies of precise Bragg resonance (Bragg frequencies) of 37.3 GHz and 37.5 GHz for these two structures. In Figure 3 the snap-shots of the longitudinal component of the magnetic fields B_z found using the 3D MAGIC code simulation are presented. The TEM wave launched into the Bragg structures has no B_z field component and the field structure with large number of azimuthal variations is due to the coupling of partial waves on the corrugation.

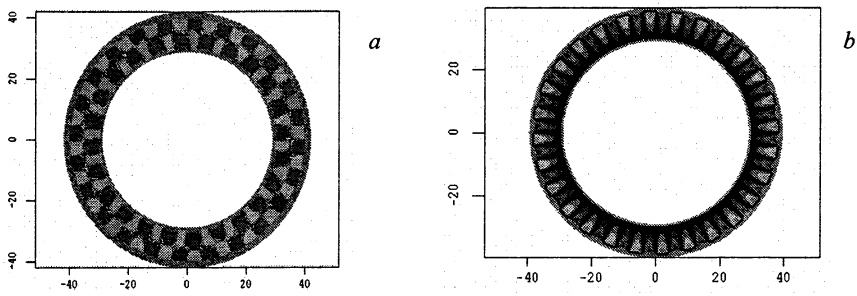

Fig. 3. The snap-shots of the B_z field distribution in the middle cross section of the 2D Bragg structures with number of azimuthal variations (*a*) 24 and (*b*) 28 associated with partial waves $TE_{24,1}$ and $TE_{28,0}$ respectively.

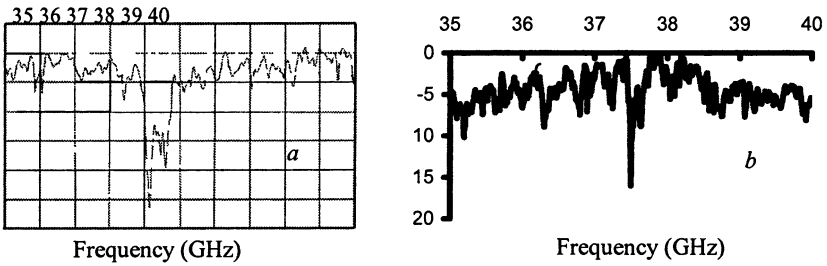

Fig. 4. Frequency dependence of the power transmission through the 2D Bragg co-axial structure with corrugated (*a*) inner and (*b*) outer conductors.

In Figure 4 the measured transmission coefficients from the 2D Bragg structures are presented. The minimum of the transmission coefficients corresponds to the calculated Bragg frequencies and is associated with the excitation of the fundamental mode. This mode consists of two longitudinally propagating TEM waves (one of them incident and another reflected wave) and two azimuthally propagating nearly cut-off waves with the azimuthally index equal to the number of azimuthal variations of the corrugation.

First operation of the coaxial 2D Bragg FEM

The 2D Bragg co-axial FEM includes an axially symmetric pulsed wiggler, large diameter (30 cm) pulsed solenoid of length 2.5 m and up to 0.6 T field strength, co-axial Bragg cavity and electron beam diagnostics, diode tank containing electron gun, low impedance (10 Ω) transmission line and 1.5 MV Marx bank generator. To drive the FEM a High Current Accelerator was used to pro-

duce a large mean diameter (7 cm) annular electron beam of current 0.5 kA and energy 450 keV. The electron beam propagated through the interaction space defined by a two-mirror 2D Bragg cavity. The 2D Bragg structures with corrugated inner conductors were used as input and output mirrors of length 10.4 cm and 5.6 cm respectively. The cavity had a total length of 86 cm. For the first experiments the length of the cavity and the mirror parameters were chosen to ensure FEM operation and, thus, a longer than optimal cavity length for high-efficiency operation was used.

Using time dependant equations [3] the operation of the FEM has been simulated (see Fig. 5). Taking into account the experimental data the gain parameter was estimated to be $\sim 0.6 \times 10^{-2}$. In the simulations the excitation of the fundamental mode with azimuthally symmetric output waves takes place. Nevertheless the cavity parameters used were not optimal in the sense of transition time minimization. As a result, in the current experiments the steady state regime could not be achieved due to short electron pulse duration.

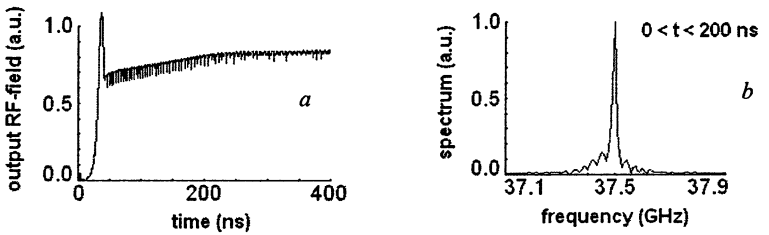

Fig. 5. Computer simulations of the FEM with 2D Bragg two-mirror cavity studied in the experiment: *a* – time dependence of the output RF-field, *b* – the spectrum of the output radiation.

In the experiments conducted reproducible RF pulses were observed. In Figure 6, *a* the trace of the RF pulse in comparison with the traces of the electron beam voltage are presented. It is clearly evident that the oscillations takes place after some transition time of ~75 ns and stops when the electron beam voltage decreases after ~200 ns. A heterodyne frequency diagnostic was used to measure the frequency of the output radiation. Microwave radiation from the FEM was mixed in a non-linear Farran Technology waveguide balanced mixer BMC-28B. The calibration of the mixer was confirmed in the frequency range 26.5 to 40 GHz in cold microwave measurements. Tuning the amplitude of the guide magnetic field and undulator field the operation of the FEM in the frequency band of effective Bragg reflections was observed. In the radiation spectrum (Fig. 6, *b*) a maximal spectral line at 37.3 GHz above the pedestal was presented while the total spectrum width correlated well with the width of the reflection band found in "cold" microwave measurements (Fig. 4, *a*). The fre-

quency distance between the spectral lines was ~40 MHz (Fig. 6, *b*). This is much smaller than the distance between the longitudinal modes of the cavity (~300 MHz) or azimuthally non-symmetric modes (~2 GHz). The individual lines clearly evident in the spectral measurements can be associated with transition processes (compare with the simulations, Fig. 5, *b*) and are the subject of further investigation.

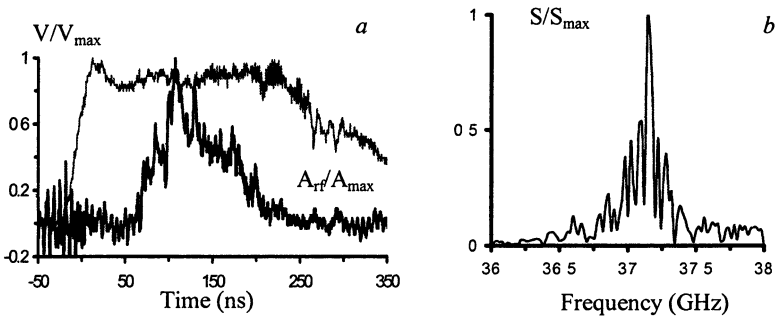

Fig. 6. The trace of electron beam voltage $V_{max} = 450$ kV and typical RF pulse observed A_{rf} (*a*) and the spectrum of the output radiation (*b*).

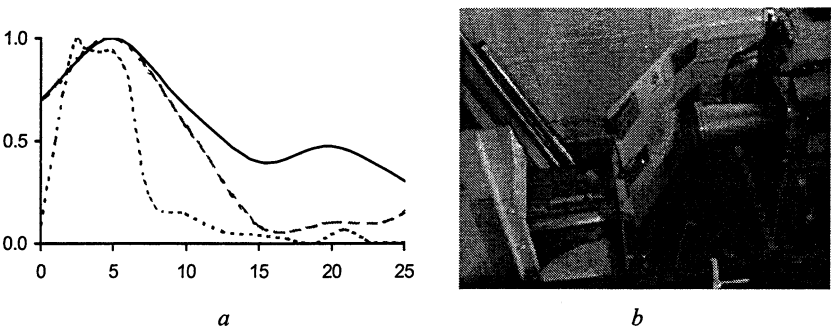

Fig. 7. The output horn mode pattern: "hot experiment (solid line), "cold" measurements (dotted line) and 3D code MAGIC simulation (dashed line) (*a*), the excitation of the neon bulb panel by the output RF pulse (*b*).

To measure the output radiation (A_{rf}) from the FEM two Ka-band receiving horns with detectors were located at a distance of 1.5 m from the output window. The first horn was "fixed" at the same position during all the experiments as a reference signal. The position of the second horn was free to move and was used to study the output radiation characteristics. In Figure 7, *a* the pattern measured in "hot" experiments (bold line) was compared with the radiation pattern in "cold" tests when the horn was excited by a TEM wave of frequency 37.3 GHz (dotted line) and with the results obtained from numerical simulations

using the 3D code MAGIC (dashed line). The output power of the FEM was estimated by integrating the power densities over the radiation pattern. The total power was calculated to be ~15 MW. Additional evidence of the high peak power was obtained from the observation of the neon bulb panel illumination at a distance of 20 cm from the output window (Fig. 7, *b*).

Conclusion

The FEM experimental set up has been assembled and tested. The first operation and lasing of the 2D coaxial FEM has been achieved. The radiation spectrum of the FEM was measured using a heterodyne frequency diagnostic and the output power estimated. The radiation parameters were compared with the theoretical predictions. It was found that the radiation spectrum corresponds to excitation of a single azimuthal mode of the co-axial 2D Bragg resonator with a perimeter equivalent to approximately 25 wavelengths. The results obtained can be interpreted as experimental demonstration of the feasibility of using 2D Bragg structures for the azimuthal mode control.

The novel 2D Bragg structure with corrugated outer conductor has been studied and results have been compared with 2D Bragg structures with a corrugated inner conductor. The use of smooth double-periodic sinusoidal corrugations allows the amplitude of the RF field on the surface of inner conductor to be reduced.

References

1. *Ginzburg N.S., Peskov N.Yu., Sergeev A.S., Arzhannikov A.V., Sinitsky S.L.*, Nucl. Instr. Meth., in Phys. Res. A, 1995, **A358**, 189.
2. *Ginzburg N.S., Peskov N.Yu., Sergeev A.S., Phelps A.D.R., Konoplev I.V., Robb G.R.M., Cross A.W., Arzhannikov A.V., Sinitsky S.L.*, Phys. Rev. E, 1999, **60**, 935.
3. *Ginzburg N.S., Peskov N.Yu., Sergeev A.S., Phelps A.D.R., Robb G.R.M.*, IEEE Trans. Plasma Sci., 1996, **24**, 770.
4. *Cross A.W., Konoplev I.V., Ronald K., Phelps A.D.R., He W., Whyte C.G., Ginzburg N.S., Peskov N.Yu., Sergeev A.S.*, Appl. Phys. Lett., 2002, **80**, 1517.

EFFECTS OF SPACE CHARGE WAVES ON SUPER-RADIANCE EMISSION FROM A PREBUNCHED E-BEAM FEM

M. Arbel, A. Eichenbaum[1], *A. Gover, H. Kleinman*

Tel-Aviv University, Tel-Aviv, Israel
[1]The College of Judea and Samaria, Ariel, Israel

There are several theoretical investigations of interaction and Super-radiant emission [or Prebunched Beam (PB)] radiation from prebunched e-beams in FELs. These include both analytical results and predictions based on a 3D simulation FEL model. Effects of space charge were taken into account in these investigations. As far as we know no thorough experimental study of the effect of space charge on the frequencies of Super-radiant emission and the power levels of radiation at each frequency was carried out and no comparison of predicted theoretical results with measured data was made.
In this presentation we shall report on such an experimental investigation and on a comparison between measured and predicted results in particular in regard to power levels vs. radiation frequency for differing e-beam space charge and differing current modulation levels. Like in other beam-wave interaction devices (Klystrons, TWTs etc.) FELs enable interaction between propagating electromagnetic waves at the slow and fast space charge waves (at a frequency below and above the frequency for synchronous operation respectively) if the e-beam current is high enough to allow for such interaction.
An experimental study of the effect of space charge on interaction requires the capability to vary and control the e-beam current and its modulation level in a wide e-beam current range. Such a capability exists in the experimental FEM developed at Tel-Aviv University, which serves as a flexible experimental tool for studies of gain, Super-radiance and stimulated Super-radiance modes of operation. It allows extensive study of the interaction mechanisms in each mode as well as studies of FEM behavior as an oscillator.
We report here on an experimental and theoretical investigation of Super-radiance over a wide range of e-beam dc currents and of e-beam modulation levels in a wide frequency range. In particular we shall discuss the splitting of the radiation frequency into two distinct frequencies as the e-beam current is raised (the frequency dependence and the radiation power level at each frequency as the e-beam current level is raised will be described).
The Super-radiance power emission level resulting from the slow space charge wave is higher than that due to the fast space charge wave. We shall show that if one takes into account a small amount of velocity modulation in the e-beam one can account for that behavior. Correlation between measured and theoretically predicted radiation frequencies and power levels will be shown and discussed.

1. FEM operation for various initial conditions

FEL/FEM radiation emission can be obtained for various Initial Conditions (I.C.) of the e-beam and of the signal entering the wiggler interaction region. Incoherent I.C. (Table 1) enable oscillator and Self Amplified Spontaneous Emission (SASE) FEL operation. Super-Radiance (SR) emission is one of the options for coherent I.C. (Table 2).

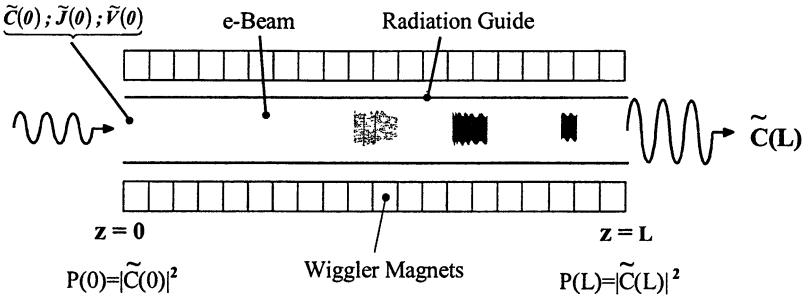

Fig. 1. Initial conditions at the wiggler input

Table 1 – Incoherent I.C.				**Table 2** – Coherent I.C.			
I.C. / Device	$\tilde{C}(0)$	$\tilde{J}(0)$	$\tilde{V}(0)$	I.C. / Device	$\tilde{C}(0)$	$\tilde{J}(0)$	$\tilde{V}(0)$
FEL Oscilla-tor	0 + Noise spectrum power	0 + Shot noise	0 + Random velocity spread	FEL Amplifier	$\neq 0$	0	0
SASE	0 + Noise spectrum power	0 + Shot noise	0 + Random velocity spread	Super-Radiance (PB radiation)	0	$\neq 0$	$\neq 0$
				Stimulated Super-Radiance	$\neq 0$	$\neq 0$	$\neq 0$

2. Analytical expression for Super-radiance

The Super-radiance power is a function of the e-beam space charge parameter $\bar{\theta}_p$, detuning parameter $\bar{\theta}$, current density modulation level M_J, velocity modulation M_V and the phase angle ϕ between them.

We shall consider two cases:

case 1: $M_V = 0$, $M_J \neq 0$, e-beam density: $0 < \bar{\theta}_p < 5$;

case 2: $M_V \neq 0$, $M_J \neq 0$, e-beam density: $0 < \bar{\theta}_p < 5$.

The Super-radiance power is proportional to $F_{PB}\left(\bar{\theta}, \bar{\theta}_p\right)$ [1, 2]:

$$F_{PB}(\bar{\theta}, \bar{\theta}_p) = \left(M_J \bar{\theta}\right)^2 \frac{\left(\frac{\bar{\theta}_p}{\bar{\theta}} \sin \bar{\theta}_p - \sin \bar{\theta}\right)^2 + \left(\cos \bar{\theta}_p - \cos \bar{\theta}\right)^2}{\left(\bar{\theta}^2 - \bar{\theta}_p^2\right)^2} +$$

$$\left\{\begin{array}{l} \text{for case 1} \\ \text{this sum is 0} \\ \text{as } M_V = 0 \end{array}\right. \quad \left\{\begin{array}{l} + M_V^2 \dfrac{\left(\dfrac{\overline{\theta}}{\overline{\theta}_p}\sin\overline{\theta}_p - \sin\overline{\theta}\right)^2 + \left(\cos\overline{\theta}_p - \cos\overline{\theta}\right)^2}{\left(\overline{\theta}^2 - \overline{\theta}_p^2\right)^2} + \\ + M_J M_V \left[2\sin\phi\sin c\overline{\theta}_p \dfrac{\left(\cos\overline{\theta}_p - \cos\overline{\theta}\right)}{\left(\overline{\theta}^2 - \overline{\theta}_p^2\right)^2} - \cos\phi F_{FEL}(\overline{\theta}, \overline{\theta}_p) \right]. \end{array}\right.$$

The sum of the last two terms in the equation is not equal to zero for case 2 as $M_V \neq 0$.

Super-radiance power vs. $\overline{\theta}$ for $M_V = 0$ is given in Fig. 2, *a* (for low and for high values of $\overline{\theta}_p$) and for $M_V \neq 0$ in Fig. 2, *b* (ϕ is parameter).

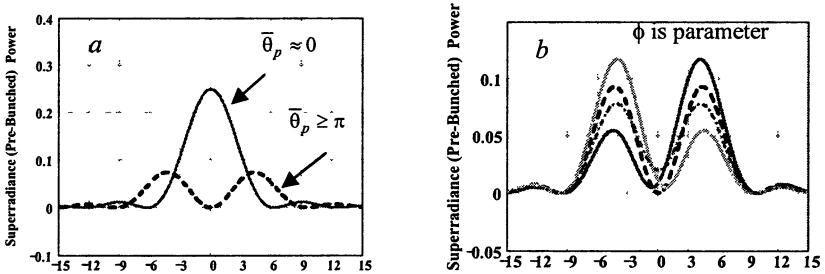

Fig. 2. Super-radiance power vs. $\overline{\theta}$ for $M_V = 0$ (*a*) and for $M_V \neq 0$ (*b*)

3. Experimental determination of Super-radiance vs. frequency (e- beam current and prebunching modulation level are parameters)

Experiments on Super-radiant power vs. modulation frequency were carried out on the prebunched e-beam FEM (Fig. 3) at Tel-Aviv University [2]. The dc current was changed in a wide range by control of the e-gun grid voltage and current modulation was controlled by adjustment of the r.f. input power to the traveling wave prebuncher. No external r.f. wave was injected at the waveguide input port in the wiggler; it was terminated in a matched load for Super-radiance experiments. The range of operating FEM parameters is given in Table 3.

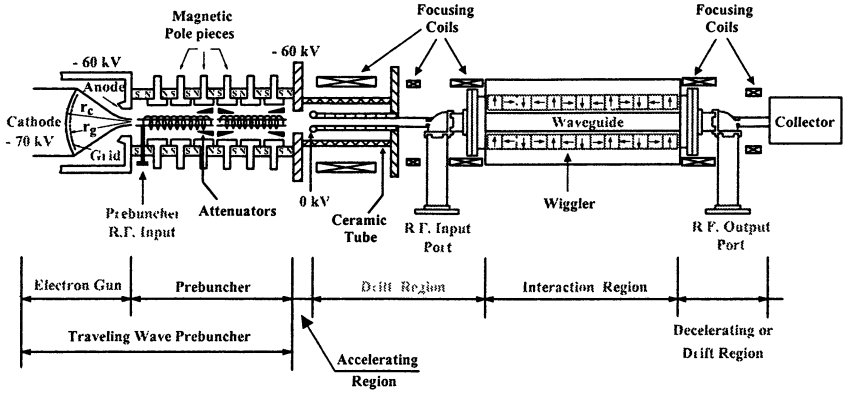

Fig. 3. Schematic of prebunched e-beam FEM

Table 3. Experimental parameters of the prebunched e-beam FEM

E-beam energy	70 keV	Wiggler magnetic field	300 Gauss
E-beam current – I	0.1–1.2 A	Wiggler period – λw	4.44 cm
E-beam radius – r	~3 mm	Number of periods – Nw	17
RF frequency – f	3.5 – 6.5 GHz	Waveguide cross-section	2.215 cm × ×4.755 cm
Modulation index	$0 \le M_J \le 0.28$	Mode	TE_{10}

4. Frequencies of Super-radiance power maxima

The dispersion diagram of the rectangular waveguide used is shown in Fig. 4. Only the TE_{10} mode intersects the e-beam line (for a 70 kV e-beam). For low space charge $\left(\overline{\theta}_p \cong 0\right)$ synchronism occurs near waveguide cutoff at $f_c = 3.156$ GHz (point "*d*") and at $f_s = 4.9$ GHz (point "*a*"). For $\left(\overline{\theta}_p \ge \pi\right)$ two frequencies of maximal radiation exist around "*a*" (points "*b*" and "*c*"), corresponding to slow space charge wave and fast space charge wave interaction respectively. The frequency difference between "*b*" and "*c*" goes from 0 for negligible space charge ($\overline{\theta}_p \cong 0$) to values determined by the e-beam space charge level $\overline{\theta}_p$.

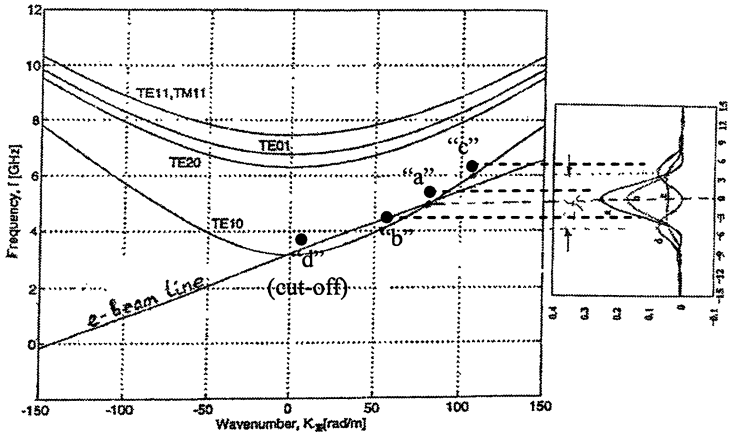

Fig. 4. Rectangular waveguide dispersion curves and e-beam line for $\overline{\theta} = 0$

5. Super-radiance power vs. modulation frequency

Super-radiance power vs. modulation frequency was measured for a wide range of e-beam dc currents (0.15 A < I_b < 1.2 A). The measured Super-radiance power was compared to calculated values. For currents in the range 0.15 A < I_b < 0.56 A the maximum of radiation power is at a nearly constant frequency (Fig. 5, *a*). The maximal radiated power level goes up with e-beam dc current. For currents in the range 0.56 A < I_b < 1.2 A (Fig. 5, *b* and *c*) maxima of radiated power occur at two frequencies spaced around "*a*". The lower frequency power maximum corresponds to efficient interaction with the slow space charge wave and the higher frequency power maximum corresponds to interaction with the fast space charge wave. As in all microwave tubes, a higher power is obtained for the slow space charge wave as greater beam to wave energy transfer takes place. The frequency difference between these two maxima increases as the e-beam current goes up.

The calculated frequency of maxima of SR power vs. e-beam current for $M_V = 0$ is shown in Fig. 6, *a*. Experimental results and best fit calculated results taking into account both current density and velocity modulation and the phase difference between them are shown in Fig. 6, *b*. Inclusion of these variables in the calculations is required to obtain better agreement with measurements.

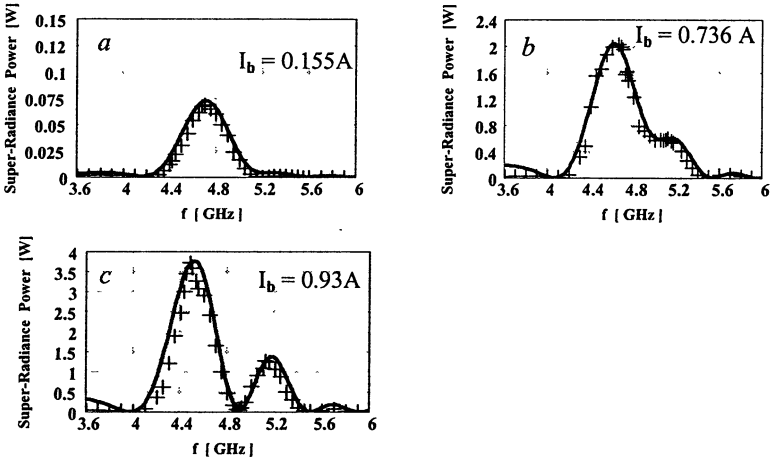

Fig. 5. Experimental (+) and theoretical (line) Super-radiance power vs. frequency

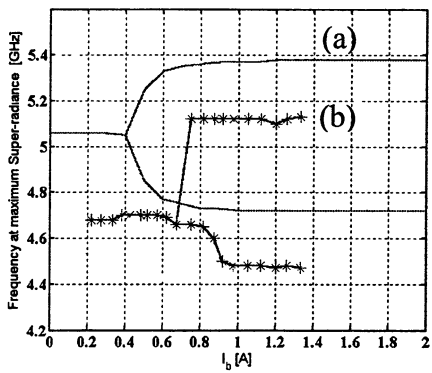

Fig. 6. Frequency of maximal power vs. e-beam current. Theoretical curve (*a*) for $M_V = 0$ and experimental and calculated curves (*b*) for best fit M_V and ϕ values.

Acknowledgement

We are grateful to Prof. Y. Pinhasi and Dr. Y. Lurie for their assistance and support in the theoretical and computer simulations.

References

1. *Schnitzer I., Gover A.*, Nucl. Instr. Meth., **A 237**, p. 124-140 (1985).
2. *Arbel M.*, Ph. D. Thesis (2005).
3. *Arbel M. et al.*, Phys. Rev. Lett., **86**, p. 2561-2564 (2001).

PHOTONIC BAND GAP ACCELERATOR DEMONSTRATION AT MIT

E. I. Smirnova, L. M. Earley, R. L. Edwards, A. S. Kesar[1], *I. Mastovsky*[1], *M. A. Shapiro*[1], *R. J. Temkin*[1]

Los Alamos National Laboratory, Los Alamos, NM, USA
[1]Massachusetts Institute of Technology, Cambridge, MA, USA

We report the demonstration of a metal photonic band gap (PBG) accelerator structure at 17.140 GHz. A photonic band gap (PBG) structure is a periodic metallic and/or dielectric system (for example, of rods), which acts like a filter, reflecting rf fields in some frequency range and allowing rf fields at other frequencies to transmit through. First, we applied PBG structures to construct an 11 GHz PBG cell with reduced long-range wakefields. The higher-order-modes suppression was proven. Next, the 17.140 GHz 6-cell PBG accelerator structure with reduced long-range wakefields was designed for the experiment. The copper structure was electroformed and cold-tested. Final cold test measurements were found to be in very good agreement with the design. The structure was installed on the beam line at the accelerator laboratory at Massachusetts Institute of Technology and powered with 2 MW of peak power from the Haimson 17.14 GHz klystron. The 16.5 MeV electron beam produced by the MIT-Haimson linac was accelerated by additional 1.4 MeV inside the PBG structure.

Introduction

In future linear colliders, the transition to higher operating frequencies will improve the energy efficiency of acceleration, thus minimizing the accelerator cost and complexity [1]. However, at high frequencies, long-range transverse wakefields are excited and induce transverse motion of electrons and subsequent emittance growth in the bunch [2]. Thus, it is crucial to use new accelerating cavities that suppress wakefields. A promising approach to eliminating the problem of long-range transverse wakefields is the use of photonic band gap (PBG) [3] structures. We report the study of metallic PBG structures and PBG resonators and the successful fabrication, tuning and operation up to 35 MeV/m of a six-cell PBG structure.

Possible applications of two-dimensional (2D) metallic PBG structures [4] in accelerators were initially discussed in [5, 6]. For accelerator applications, we employ a 2D PBG structure formed by a triangular array of copper rods [7]. It was demonstrated in [7], that such a structure possesses a global band gap, which is a range of frequencies, at which the electromagnetic wave in unable to propagate through the bulk of the lattice. We form a "PBG cavity" by removing a rod in the periodic structure (Fig. 1). The mode, which has a frequency in the global band gap, will be localized inside the PBG cavity around the defect. The complete global band gap theory developed in [7] allows us to prove the higher-order modes (HOM) suppression inside this PBG cavity, which yields a design of a single-mode PBG resonator. Several PBG resonators were constructed according to the design and cold-tested [8]. A single-mode confinement inside the

PBG resonators was demonstrated. The technology for fabrication of PBG resonators was developed.

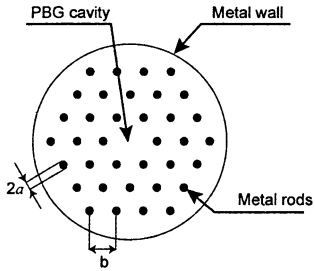

Fig. 1. The schematic of a "PBG cavity" formed by removing a single rod in a triangular array.

Next, we designed and constructed a PBG accelerator with long-range wakefield suppression. The PBG accelerator was successfully tested with the electron beam (hot tested). The hot test results are published in [9]. The structure was powered with 2 MW of microwaves and the electron beam was accelerated by 1.4 MeV. The accelerating gradient of 35 MV/m was demonstrated.

This paper summarizes the results of PBG structures study, single-mode PBG resonators design and testing, and the multi-cell PBG accelerator experiment.

Computation of global band gaps

We started with the computational investigation of bulk properties of the triangular lattice of metallic rods (Fig. 2) [7]. The electromagnetic field in a 2D PBG structure can be decomposed into two independent classes of modes: the transverse electric (TE) mode and the transverse magnetic (TM) mode. We restricted our study to the TM modes, since the TM modes are of the primary interest in accelerators. All the field components in the TM modes can be expressed through the axial component of the electric field, which we will further denote by ψ. Since the system is homogeneous along the z-axis, we take the Fourier transform of ψ in axial coordinate z and time t. The Helmholtz equation for $\psi(\mathbf{x}_\perp, k_z, \omega)$ follows from Maxwell's equations

$$\nabla_\perp^2 \psi = \left(k_z^2 - \frac{\omega^2}{c^2} \right) \psi = -\kappa^2 \psi. \qquad (1)$$

The boundary conditions on the surfaces S of the conducting rods are $\psi|_S = 0$ for the TM mode. The discrete translational symmetry of the conductivity profile allows us to write the fundamental solution of the Helmholtz equation in Bloch form $\psi(\mathbf{x}_\perp + \mathbf{T}) = \psi(\mathbf{x}_\perp) e^{i\mathbf{k}_\perp \cdot \mathbf{T}}$, where $\mathbf{x}_\perp = x\mathbf{e}_x + y\mathbf{e}_y$ is the transverse displacement, $\mathbf{T}$ is the lattice period, $\mathbf{k}_\perp$ is the transverse wave number. The Helmholtz equation (1) was solved numerically using the PBGSS code [7].

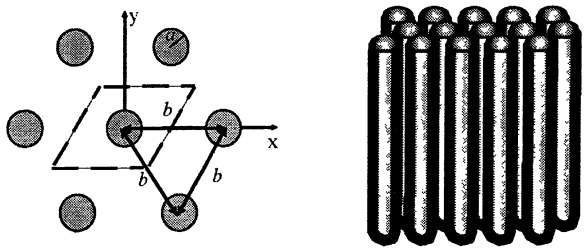

a *b*

Fig. 2. Triangular lattice of metallic rods: front view (*a*); side view (*b*).

The global band gaps were computed, which are the bands of frequencies, for which the Helmholtz equation (1) does not have a propagating solution. The plot of the band gap regions for different ratios of the radius of the rod, *a*, to the spacing between the rods, *b*, is shown in Fig. 3. For the frequencies from the shaded region in Fig. 3, the wave cannot propagate through the bulk of the PBG structure.

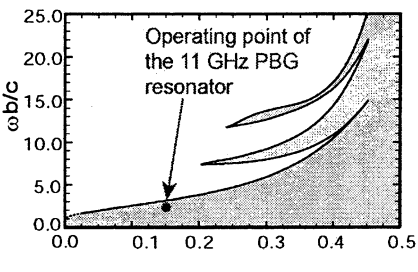

Fig. 3. The global band gap diagram for the triangular lattice of metallic rods. The operating point of the 11 GHz PBG resonator is shown with a dot.

11 GHz PBG resonators with HOM suppression

A PBG resonator was designed according to the schematic shown in Fig. 1 [8]. The metallic rods placed in a triangular lattice formed a PBG structure. A missing rod represents a defect in the structure and forms a PBG resonator. The outside metal wall can be partially removed for damping the higher order modes. The ratio of the rod's radius, a, to the spacing between the rods, b, was chosen, so that the eigenfrequency of the fundamental mode of the resonator was inside the band gap (Fig. 3). However, the eigenfrequencies of the HOM were outside the band gap, and the HOM were not confined by the PBG structure. The resonator was modeled with HFSS [10]. The electric field profile of the fundamental eigenmode of the PBG resonator is shown in Fig. 4(a). For comparison the field profile of the TM_{01} mode of a pillbox cavity is shown in Figure 4(b). The PBG resonator mode closely resembles the TM_{01} mode of a pillbox resonator, so we name it the TM_{01}-like mode.

The PBG resonator was constructed for the cold test at 11 GHz. The dimensions of the PBG resonator are summarized in Table 1. Rods and plates were

machined of high purity oxygen-free Class 1 copper. Brazing material was placed into the gaps between rods and plates and then the structure was heated in a hydrogen furnace. This ensured good electrical connection between the rods and the end plates. The photograph of the resonator is shown in Fig. 5. Half of the outer wall of the resonator was removed to obtain the HOM damping. The resonator was tested with the HP8720 network analyzer and the Ohmic Q-factor of 5000 was measured for the TM_{01} mode at 11 GHz, which is in excellent agreement with the theoretical value of 5300. This proved that the TM_{01} mode was confined by the PBG structure and was not leaking out through an open outside wall [8].

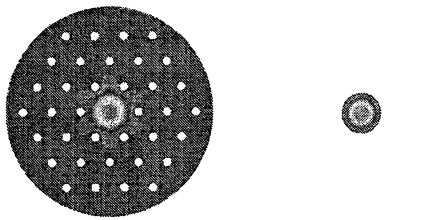

Fig. 4. The electric field profile in the TM_{01}-like mode of a PBG resonator (*a*), and in the TM_{01} mode of a pillbox resonator (*b*).

Table 1. Dimensions of the 11 GHz PBG resonator

Rod radius *a*	0.16 cm
Lattice spacing *b*	1.06 cm
a/*b*	0.15
Cavity radius	3.81 cm
Axial length	0.787 cm

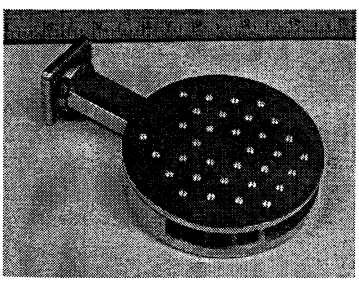

Fig. 5. Photograph of the 11 GHz PBG resonator.

17 GHz PBG accelerator demonstration

The successful construction of the PBG resonator formed the basis to proceed with demonstration of a PBG accelerating structure [8]. The accelerating structure schematic in the form of a disk-loaded PBG waveguide is shown in Fig. 6. The PBG waveguide was formed by removing the central rod in a triangular array of metal rods. The $\varphi = 2\pi/3$ phase shift per cell was chosen for the

accelerator structure. The ratio a/b was kept close to 0.15 for good HOM damping and high Ohmic Q. The dimensions of the PBG accelerator structure are summarized in Table 2. Table 2 also presents the computed accelerator characteristics of the designed PBG accelerator structure, including the structure Ohmic Q-factor, Q_w, the shunt impedance per unit length.

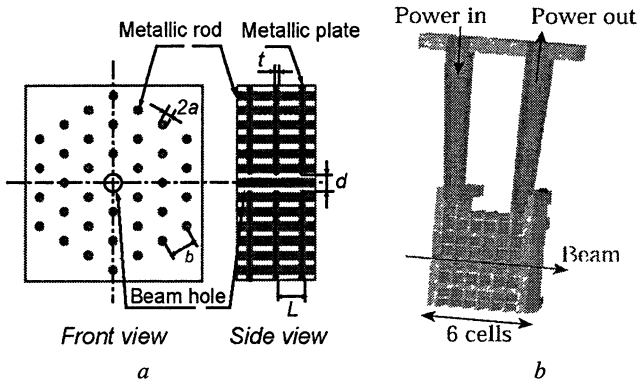

Fig. 6. A schematic of the multi-cell PBG accelerator structure (*a*). Cut-away drawing of the PBG accelerator (*b*).

Table 2. Parameters of the 17 GHz PBG accelerator

Rod radius (structure/coupler cell)	1.04/1.05 mm
Rod spacing	6.97 mm
Cavity length	5.83 mm
Iris radius	2.16 mm
Iris thickness	1.14 mm
Freq. (TM_{01})	17.140 GHz
Shunt impedance, r_s	98 MΩ/m
$[r_s/Q_w]$	23.4 kΩ/m
Group velocity	0.013 c
Gradient	$25.2\sqrt{P[MW]}$ MV/m

The accelerator structure was fabricated via electroforming. Rods and plates were grown together to form a single copper part. Then a good electrical connection between rods and plates in the structure was automatically ensured. The aluminum mandrels with holes in place of the rods were fabricated, and then placed into copper solution. Copper ions were deposited on the mandrels, and PBG cells consisting of the rods and two half-plates were formed. Then the aluminum was etched away. Cells were put together and soldered. Copper was flashed over the whole structure to cover the solder in the joints. The waveguides were bolted to the structure. Side pieces were bolted for additional mechanical strength. Photographs of the electroformed structure are shown in Fig. 7.

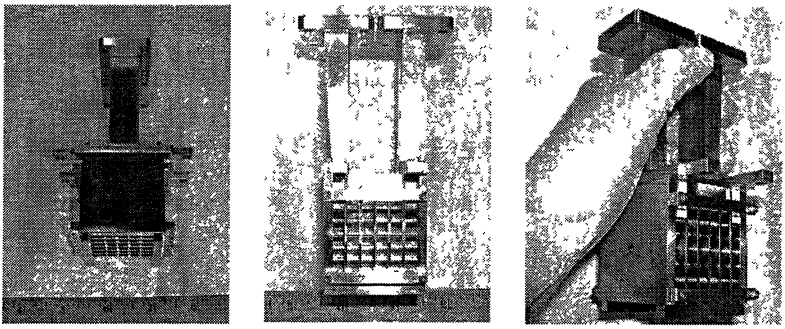

Fig. 7. Photographs of the electroformed PBG accelerator structure

The coupling curves for the new structure were measured with an HP8720 network analyzer. The comparison of the measured and computed reflection curves indicated that the fabricated structure was 40 MHz higher in frequency than the design. Tuning was performed by chemical etching of the copper rods in an acid solution. The tuned structure was cold-tested again. The measured reflection (S11) and transmission (S21) curves are shown in Fig. 8. For comparison, the S11 and S21 curves computed with HFSS [10] are shown. The agreement between the measured and the computed curves is excellent [8, 9].

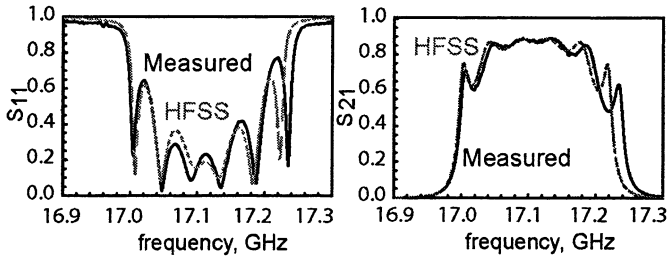

Fig. 8. Reflection and transmission curves for a 6-cell PBG accelerator as measured with the HP8720 network analyzer (black curve) and as computed with the HFSS (gray curve).

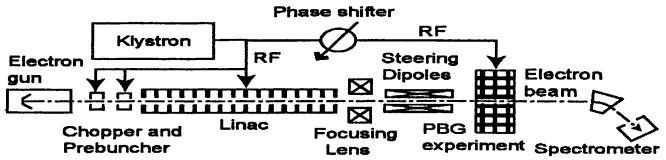

Fig. 9. The schematic of the PBG acceleration experiment

The PBG structure was installed inside a vacuum chamber at the end of the MIT linear accelerator (linac) beamline [9]. A diagram of the experimental accelerator laboratory setup is shown in Fig. 9. The Haimson Research Corpora-

tion (HRC) relativistic klystron amplifier [11] was employed to supply the power for the linac and the PBG structure. The klystron was operated at 10 to 15 MW for 100 ns. The klystron output was connected to a power splitter which directed the power into two WR-62 output waveguide arms. The power level ratio between the arms could be varied. One arm was connected to the linac and the second arm went to the PBG structure. A phase shifter on the PBG experiment arm allowed for different phase shifts between the field in the linac and in the PBG accelerator. The linac beam was generated by a DC (Pierce) electron gun at the energy of 0.51 MeV with a normalized RMS emittance of 1.8π mm-mrad and transported to the chopper-prebuncher section and the main linac. The resulting beam represented a train of 0.01 nC, 1 ps bunches at 17.140 GHz with an energy of 10–25 MeV [12, 13]. At 0.5 m beyond the linac on the beamline, a focusing solenoid produced magnetic fields up to 0.6 T, which provided a minimum beam spot size of about 1 mm. The focusing solenoid and a set of steering coils provided a means to center the beam on the PBG accelerator structure axis. A magnetic spectrometer was installed at the end of the beamline for measurements of changes in beam energy. The PBG accelerator structure was conditioned over a period of 1 week (approximately 100,000 pulses). Up to 2 MW of microwave power at 17.140 GHz in a 100 ns long pulse could be coupled into the PBG structure without breakdown. The filling time of the PBG structure was less than 10 ns. With 2 MW of input power, the calculated accelerating gradient in the PBG structure was 35 MV/m.

For 10.5 MW of input linac power, the linac electron beam had energy of 16.5 MeV with rms energy spread of 0.5 MeV. The phase shift between the linac and the PBG accelerator was scanned until the two were found to be in phase, thus allowing for the maximum energy gain. The electron beam energy was measured for different input powers into the PBG accelerator. The results are shown in Fig. 10. It was found that the beam energy increases as the square root of the input power, as expected from theory. Maximum energy gain for 2 MW of input power was found to be 1.4 MeV which is consistent with the estimated 35 MV/m accelerating gradient [9].

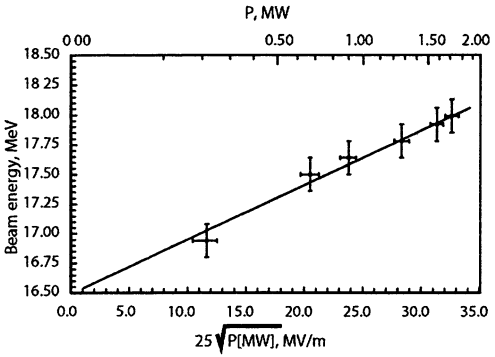

Fig. 10. The measured electron beam energy versus square root of the PBG accelerator input power, *P*.

Conclusion and future plans

We have demonstrated high gradient electron beam acceleration in a Photonic Band Gap accelerator. The PBG disk-loaded waveguide may be a promising candidate for future accelerator applications because of its ability to effectively damp higher order modes and thus suppress wakefields. We conducted extensive research of the metallic photonic band gap structures, designed fabricated and tuned PBG resonators and a PBG accelerator structure. We have shown that the PBG structure does in fact accelerate electrons at high gradient [9]. Future research on PBG accelerators should be directed towards improved fabrication techniques, studies of microwave breakdown and direct tests of wakefield suppression.

References

1. International Linear Collider Technical Review Committee. Second report. SLAC-R-606, 2003.
2. *Bane K.L.F., Li Z.* SLAC-PUB-8545, 2000.
3. *Yablonovitch E.* Phys. Rev. Lett., 1987, 258, 2059.
4. *Joannopoulos J.D., Meade R.D., Winn J.N.* Photonic Crystals: Molding the Flow of Light. Princeton: Princeton Univ. Press, 1995.
5. *Smith D.R., Schultz S., Kroll N., Sigalas M., Ho K.M., Souloulis C.M.* Appl. Phys. Lett., 1994, 65, 645.
6. *Shapiro M.A., Brown W.J., Mastovsky I., Sirigiri J.R., Temkin R.J.* Phys. Rev. Special Topics – Accelerators and Beams, 2001, 4, 042001.
7. *Smirnova E.I., Chen C., Shapiro M.A., Sirigiri J.R., Temkin R.J.* J. Appl. Phys., 2002, 91, 960.
8. *Smirnova E.I., Mastovsky I., Shapiro M.A., Temkin R.J., Earley L.M., Edwards R.L.* Phys. Rev. Special Topics – Accelerators and Beams, 2005, 8, 091302.
9. *Smirnova E.I., Kesar A.S., Mastovsky I., Shapiro M.A., Temkin R.J.* Phys. Rev. Lett., 2005, 95, 074801.
10. High Frequency Structure Simulator. Ansoft Corporation, Pittsburgh, PA 15219, www.hfss.com.
11. *Haimson J., Mecklenburg B., Stowell G., Kreischer K.E., Mastovsky I.* AIP Conf. Proc., 1999, 474,137.
12. *Haimson J., Mecklenburg B.* Proc. 1995 Particle Accelerator Conf., 1995, 2,755.
13. *Haimson J., Mecklenburg B., Stowell G.* Proc. 2001 Particle Accelerator Conf., 2001, 5, 3948.

INTERCAVITY SCATTERING SCHEME FOR TWO-STAGE GENERATION OF SUBMILLIMETER RADIATION ON THE BASE OF PLANAR 2D BRAGG FEM

A. V. Arzhannikov[1], *N. S. Ginzburg*[2], *P. V. Kalinin*[1], *S. A. Kuznetsov*[1], *N. Yu. Peskov*[2], *R. M. Rozental*[2], *A. S. Sergeev*[2], *S. L. Sinitsky*[1], *V. D. Stepanov*[1], *M. Thumm*[3], *V. Yu. Zaslavsky*[2], *I. V. Zotova*[2]

[1]Budker Institute of Nuclear Physics, Novosibirsk, Russia
[2]Institute of Applied Physics, N. Novgorod, Russia
[3]Institute fur Hochsleistungsimpuls-und Mikrowellentechnik, FZK, Karlsruhe, Germany

The paper describes the experimental project at the ELMI accelerator on two-stage generation of submillimeter radiation. At the first stage a sheet electron beam drives 2D Bragg FEM of planar geometry to generate 4-mm pump wave. At the second stage this wave undergoes stimulated scattering at the supplementary electron beam to produce submilimeter radiation.

Introduction

In recent ELMI-experiments the operation of 4-mm free electron maser (FEM) with 2D distributed feedback has been demonstrated [1]. These results can be served as a basis for development of a two-stage generator for the sub-mm band. A key feature of the proposed scheme is the use of two parallel sheet beams from single cathode with a few kiloampers currents that transported in two parallel channels, which are connected by special waveguide. At the first stage one of the sheet beams moving in an quasi-static undulator magnetic field would drive 2D Bragg FEM of planar geometry to generate 4-mm pump wave At the second stage this wave undergoes stimulated scattering at the supplementary electron beam to produce submilimeter radiation. Thus powerful 4-mm radiation from the first generation channel would be used as an EM-undulator of the secondary stage sub-mm FEL.

Schematic of proposed experiments and the main parameters

Let us outline the wavelength band that can be covered in experimental conditions at the ELMI-accelerator. At the first stage we plan to use a FEM with hybrid Bragg resonator which was developed in the recent experiments having the radiation wavelength $\lambda_0 = 4$ mm. Taking into account the wavelength of incident radiation we can estimate the wavelength of radiation λ scattered by the electrons with kinetic energy about 1 MeV. For the double Doppler effect the wavelength conversion is expressed by the following formula:

$$\lambda = \lambda_0 \frac{(1-\beta\cos\theta_s)}{(1-\beta\cos\theta_i)}, \qquad (1)$$

where $\beta = v/c$, v is the electron longitudinal velo-city, θ_i, θ_s are the angles of incident and scattered radiation respectively with the respect to direction of the electron drift velocity (Fig. 1). Thus, for back-scattering $\lambda \approx \lambda_0 / 4\gamma^2$ and for 90°-scattering $\lambda \approx \lambda_0 / 2\gamma^2$ can be achieved. Wavelength of the scattered radiation as a function of the beam γ-factor is shown in Fig. 1. The radiation in the band of 0.1÷0.3 mm by scattering the incident radiation in the direction opposite to the beam electron velocity can be obtained. If the incident radiation propagates in the transverse direction with the respect to the beam propagation the radiation wavelength can be ~ 0.2÷0.5 mm.

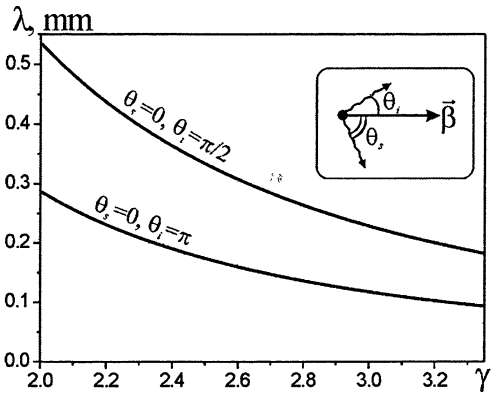

Fig. 1. Conversed wavelength due to scattering of 4-mm radiation by e-beam as the function of the beam γ-factor.

Schematic drawings of experimental realization of sub-mm generator based on two different scattering schemes are presented in Fig. 2 and Fig. 3. For both variants we suppose to use sheet beams with 3÷4 mm thickness and 10÷20 cm width and a current density more than 1 kA/cm. The e-beams pass the slit channels at presence of longitudinal guide magnetic field with the strength ~ 1 T. In the channel 1 of both variants the electrons oscillate in undulator magnetic field and generate 4-mm pump wave. Theoretical studies of planar FEM at ELMI-accelerator demonstrates that the electric field strength of 4-mm radiation inside the FEM resonator can amount $10^5 \div 10^6$ V/cm. In Figure 4 results of simulation of interactivity fields is presented for configuration shown in Fig. 3. The 2D Bragg resonator is optimized such a way to increase of amplitude of transverse propagating energy fluxes *B*. These fluxes by connecting waveguides are transported in the channel 2 for pumping electron transverse oscillations.

For the first experiments we plan to observe scattered signal amplification in the SASE (self-amplified spontaneous emission) [2] regime in the absence of the resonator (mirrors) for sub-mm radiation.

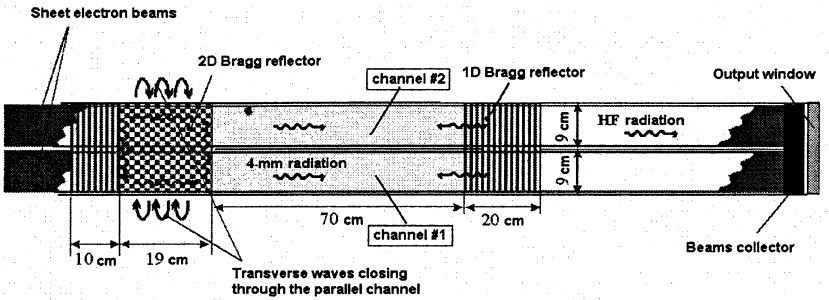

Fig. 2. Scheme of two-stage generation for the band of 0.1÷0.3 mm

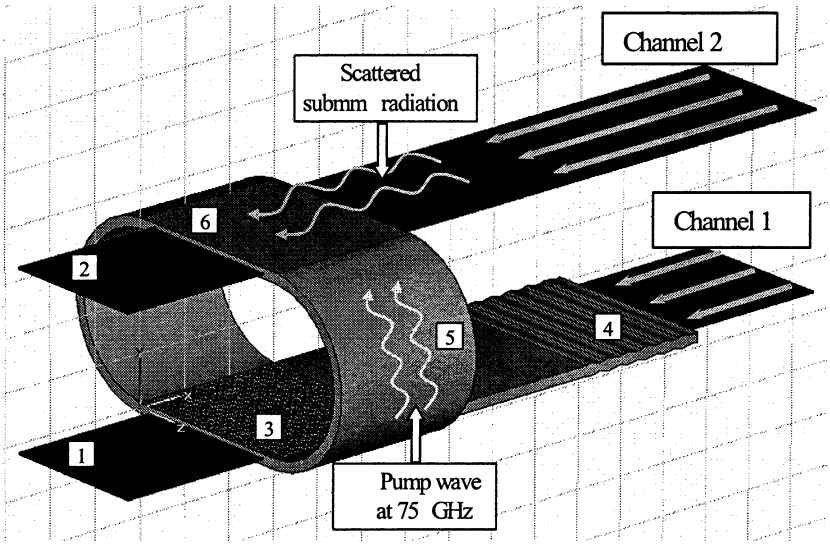

Fig. 3. Scheme of two-stage generation for the band of 0.2÷0.5 mm: *1* – sheet beam driving planar FEM; *2* – supplementary sheet beam driving the scattering channel; *3* – 2D Bragg reflector; *4* – 1D Bragg reflector; *5* – circuit for transverse e.m. fluxes; *6* – interaction space in the scattering channel.

The spatial growth rate for scattered short-wave radiation is given by the expression [3, 4]

$$\Gamma[\mathrm{cm}^{-1}] = 6.8 \cdot \left(\frac{j_b[\mathrm{kA/cm}]}{\lambda_0[\mathrm{mm}] \cdot b[\mathrm{mm}]} \right)^{1/3} \cdot \frac{a_0^{2/3}}{\gamma}, \qquad (2)$$

where b is the gap between the channel plates, j_b is the current density per unit transverse size (liner current density) in the second beam and $a_0 = 2.3 \cdot 10^{-8} \lambda_0[\mathrm{mm}] E_i[\mathrm{V/cm}]$ is the pump wave strength parameter, E_i is the pump wave amplitude. For the pump radiation of the wavelength $\lambda_0 = 4$ mm and the

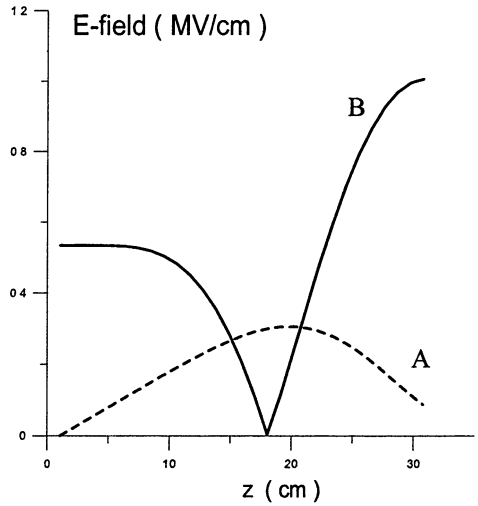

Fig. 4. Results of simulation of 4-mm generation in the 2D Bragg FEM: profile of transverse (B) and longitudinal (A) propagating partial waves inside 2D Bragg structure.

amplitude $E_i \sim 1$ MV/cm this parameter is estimated on the level $a_0 \sim 0.05 \div 0.1$. Thus, for the relativistic factor $\gamma \approx 3$, $j_b \approx 1$ kA/cm and $b \approx 10$ mm the spatial growth rate of sub-mm radiation is estimated as $\Gamma \sim 0.1$ cm^{-1}.

Expression for the gain (2) is valid for a "cold" beam with rather small velocity spread

$$\frac{\delta V_z}{c} << \lambda \cdot \Gamma \approx 0.04 . \qquad (3)$$

The required value of the velocity spread can be obtained by an accurate choice of geometry of magnetic field configuration in accelerator diodes and an appropriate strength of guide magnetic field. Analysis of this problem has shown that for experimental conditions of the ELMI-accelerator we can increase the guide magnetic field up to 2.5÷3 T. In addition to these changes some reconstructions in the accelerator diode and vacuum slit channels should provide appropriate parameters for the first step of two-stage experiments on production of sub-mm radiation in SASE regime. After that it will be possible to use either quasi-optical or some modifications of Bragg resonators to obtain generation regime with corresponding narrowing the radiation spectrum.

One of the problems related with observation of SASE regime in the over-moded waveguide is suppression of interaction with low frequency modes. Such a problem can be solved by using waveguide with variable gap between plates. In Figure 5 results of KARAT simulation of 200 GHz SASE in the case of regular and tapered waveguide are presented. One can see that the tapering provides possibility for suppression of low frequency amplification. This result is explained that variation of the waveguide parameters affects more strongly near cut-off modes with the large Brillouin angles.

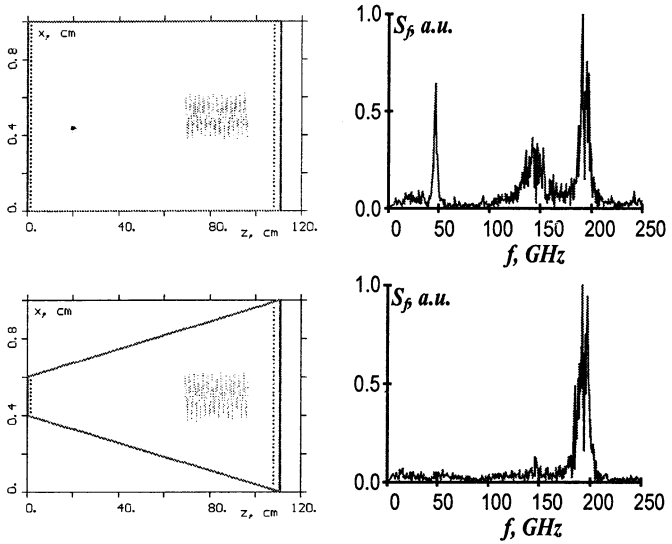

Fig. 5. Results of the KARAT simulations demonstrating suppression of amplification of spurious low-frequency components by the waveguide tapering: left column – geometry of the system, right column – spectrum of the radiation.

Acknowledgements. The work was partially supported by CRDF Grant NO-008-X1 and RFBR Grants 04-02-17118 and 05-02-17036.

References

1. *Arzhannikov A.V., Ginzburg N.S., Ivanenko V.G., Kalinin P.V., Kuznetsov A.S., Kuznetsov S.A., Peskov N.Yu., Sergeev A.S., Sinitsky S.L., Stepanov V.D., Zaslavsky V.Yu.*, these proceedings, vol. 1, p. 271-276.
2. *Bonifacio R., Pellegrini C., Narducci L.M.*, Opt. Comm., 1985, **50**, 6.
3. Bratman V., Ginzburg N., Petelin M., ZhETF, 1979, **76**, 830.
4. *Sprangle P., Tang A., Manheimer W.*, Phys. Rev. A, 1980, **21**, 302.

MODE SELECTION IN FEL-OSCILLATORS BASED ON COUPLING OF PROPAGATING AND TRAPPED WAVES

N. S. Ginzburg, A. M. Malkin, N. Yu. Peskov, R. M. Rozental, A. S. Sergeev, V. Yu. Zaslavsky

Institute of Applied Physics RAS, Nizhny Novgorod, Russia

A novel Bragg FEL scheme, in which an electron beam synchronously interacts with a propagating wave and the latter is coupled on periodical corrugation with a trapped quasi cut-off mode, is discussed. The trapped feedback mode provides the self-excitation of the whole system while the efficiency in steady-state generation regime is determined by beam interaction with the propagating mode.

1. Introduction

A number of oscillator schemes based on the interaction between propagating and quasi cut-off trapped waves are known in microwave electronics. One of them is a scheme of a gyrotron [1] where an electron beam excites a quasi cut-off mode while the output of radiation is provided by the propagating wave, which is coupled with the trapped wave via corrugation of the waveguide side walls. One more example is a scheme of CRM [2] and FEL [3] in which the electron beam interacts both with a propagating wave (at the first harmonic) and a cut-off wave (at the second or third harmonic). The waves interact via electron beam modulation in the absence of direct coupling at microwave system. The trapped cut-off mode provides the oscillator self-excitation while the propagating wave is responsible for energy extraction in a steady-state regime.

In this paper we discuss a new variant of FEL based on the interaction between a propagating wave and a quasi cut-off wave [4]. In proposed scheme a beam of wiggling electrons interacts only with a propagating wave, but the latter is coupled with a quasi cut-off mode trapped inside the cavity. This coupling could be realised by either helical or azimuthally symmetric periodical waveguide corrugation. The trapped mode provides the feedback mechanism leading to the self-excitation of the whole system while the efficiency in steady-state regime of generation is almost completely determined by the interaction with the propagating wave, synchronous to the beam.

The main advantage of the proposed scheme is provision of higher selectivity over transverse mode index than traditional schemes of FEL with Bragg resonators where a feedback wave propagates in backward direction with rather high group velocity [5]. At the same time, this scheme is able to provide higher Doppler frequency up-shift in comparison with the scheme discussed in [2, 3], where the frequency is restricted by a number of the operating harmonic. The

novel feedback scheme will be tested at the JINR-IAP FEM [6] as a method of increasing oscillation frequency for fixed transverse size of interaction space.

Both helical and axial-symmetric corrugations can be used to realize coupling of propagating and cut-off modes. Nevertheless in the case of a helical corrugation the trapped mode scatters only in forward propagating wave and self-excitation should occur directly inside corrugated section. Possibility of single frequency generation in FEL with new modification of Bragg resonator is demonstrated both in model based on time domain averaged approach (Sect. 2) as well in direct PIC simulations (Sect. 3). In the case of axial-symmetric corrugation the trapped mode scatters both in forward and backward propagating waves. As a result such corrugation can be used to realize narrow band reflector in a more traditional two-mirror FEL scheme. In Sect. 4 a simple analytical model of Bragg reflector exploiting coupling of propagating and cut-off modes is developed and compared with results of "cold" tests.

2. FEL-oscillator based on coupling of propagating and trapped waves on helical corrugation

The fields of a propagating (index a) and a trapped quasi cut-off (index b) modes can be presented as

$$\mathbf{E} = \mathrm{Re}\left\{\left(a(t,z)\,\mathbf{E}_a(r_\perp)\mathrm{e}^{-ihz-im_a\varphi} + b(z,t)\,\mathbf{E}_b(r_\perp)\,\mathrm{e}^{-im_b\varphi}\right)\mathrm{e}^{i\omega_c t}\right\}, \qquad (1)$$

where ω_c is the carrier frequency, which is chosen to be equal to the cut-off frequency of the trapped mode and the functions $E_{a,b}(r_\perp)$ specify the transverse structure of the modes. Helical corrugation

$$r = r_0 + r_1\cos\left(\bar{h}z + \bar{m}\varphi\right) \qquad (2)$$

(r_0 is the mean radius of the waveguide, $\bar{h} = 2\pi/d$, d and $2r_1$ are the period and the depth of the corrugation correspondingly) under the Bragg resonance conditions

$$h \approx \bar{h}\,, \quad \bar{m} = m_a - m_b \qquad (3)$$

provides coupling of the waves (1) as shown on dispersion diagram Fig. 1.

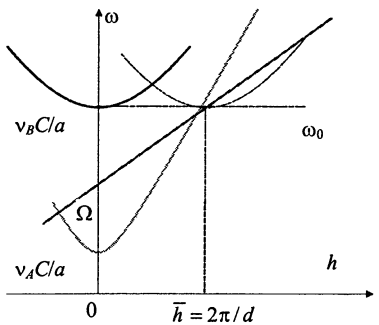

Fig. 1. Dispersion diagram corresponding to coupling of the propagating and quasi cut-off waves on the helical corrugation.

Forward propagating wave is synchronous to the electrons moving in the $+z$ direction under the resonance condition: $\omega - hv_{\|} \approx \Omega_b$, where Ω_b is the frequency of particle oscillations in a undulator field. Process of mutual scattering the waves (1) under the resonance (3) and amplification of the synchronous propagating wave can be described by the following system of equations:

$$\frac{\partial A}{\partial Z} + i\delta A = i\alpha B + \frac{C^3}{\pi}\int_0^{2\pi} e^{-i\theta} d\theta_0, \quad \frac{\partial B}{\partial \tau} + \frac{i}{2}\frac{\partial^2 B}{\partial Z^2} + \sigma B = -i\alpha A. \tag{4}$$

$$\frac{\partial^2 \theta}{\partial Z^2} = \mathrm{Re}\left(A(Z)e^{i\theta}\right), \quad \theta\big|_{Z=0} = \theta_0 \in [0, 2\pi), \quad \left.\frac{\partial \theta}{\partial Z}\right|_{Z=0} = \Delta. \tag{5}$$

In (4)–(5) $Z = z\bar{h}$, $\tau = \omega_c t$, $A = e\kappa\mu a / mc\omega_c\gamma_0$, $B = e\kappa\mu b\sqrt{N_b} / mc\gamma_0\sqrt{N_a}$, Δ is the initial mismatch of the electron-wave synchronism, θ is the electron phase in the field of the synchronous wave, C is the Pierce parameter, μ is the inertial bunching parameter, κ is the wave-electron coupling parameter proportional to the amplitude of the electron transverse oscillations [5], $N_{a,b}$ are the wave norms, σ is coefficient of the Ohmic losses for the quasi cut-off mode, $\delta = (\bar{\omega} - \omega_c)/\bar{\omega}$ is the normalized mismatch between the Bragg $\bar{\omega} = \bar{h}c$ and cut-off frequencies, and

$$\alpha_{\mathrm{TE}\to\mathrm{TE}} = \frac{r_1}{2hr_0^2}\frac{-\nu_b^2 + m_a m_b}{\sqrt{\left(\nu_a^2 - m_a^2\right)\left(\nu_b^2 - m_b^2\right)}}, \quad \alpha_{\mathrm{TE}\to\mathrm{TM}} = \frac{r_1}{2hr_0^2}\frac{m_a}{\sqrt{\nu_a^2 - m_a^2}} \tag{6}$$

is the wave coupling coefficient at the Bragg grating for the propagating wave "*a*" of a TE type and the quasi cut-off wave "*b*" of TE or TM type correspondingly, ν is roots of Bessel functions.

The amplitude of the propagating wave equals to zero at the beginning of the interaction space $A\ (Z = 0) = 0$. For the resonator with the cut-off narrowings boundary condition for the trapped mode can be presented in the form $B\ (Z = 0) = B\ (Z = L) = 0$. Initial condition can be defined as a small "seed" field of the trapped mode, i. e. $B\ (\tau = 0) = B_0\ (Z)$.

In nonlinear simulations of the FEL operation we assumed that the time of the changing the trapped mode amplitude B is substantially greater than the electrons transit time $l / v_{\|}$ and the forward wave propagation time l / v_{gr}. In this case it is possible to neglect time derivatives in the electron motion equations (5) as well as in the forward wave excitation equation. Process of establishment of a stationary regime of oscillation and spatial distribution of amplitudes of the partial waves in these regimes at different values of geometry mismatch δ is shown in Fig. 2. One can see excitation of modes with different longitudinal indices, dependent on δ. This conclusion corresponds to results of Ref. [4], where the approximation of the fixed structure of the trapped mode has been used. It is important to note that in optimal conditions the main part of electro-

magnetic energy, which is extracted from the electron beam, belongs to the propagating mode A but not dissipated with the trapped mode B.

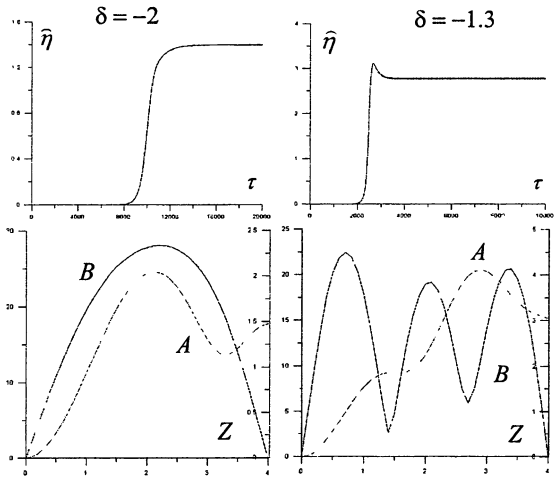

Fig. 2. Establishment of the steady state regime (up) and spatial distribution of the partial waves in this regime (down) at different values of the mismatch δ; $C = 10^{-2}$.

Using above analysis let us estimate possibility of creation of 4-mm FEL based on the accelerator LIU-3000 (JINR, Dubna) (1 MeV / 200 A / 200 ns). For the undulator of 3.9 cm period and the waveguide of 0.65 cm radius the two-fold helical corrugation ($\overline{m} = 2$) of 4.1 mm period provide the Bragg resonance conditions (4) for the pair of modes $TE_{1,1} \leftrightarrow TM_{1,3}$. For the conditions of the experiment the Pierce parameter $C \approx 10^{-2}$ and the length of interaction space would be $l \approx 20$ cm with the corrugation depth $r_1 \approx 0.1$ mm. The establishment of steady state regime for above parameters is shown in Fig. 2. Total electron efficiency amounts 15%.

3. KARAT PIC simulation of a planar FEL model

A FEL with coupling propagating and cut-off modes was simulated with the help of the KARAT PIC code (see. Fig. 3). We used a planar 2D model, in which the lowest TEM propagating mode was coupled to the H_2 mode of a planar waveguide via the corrugation of 8 mm period. Boundaries of the corrugated waveguide were matched with output regular waveguides (i. e. the cut-off narrowings were absent). Excitation of the second longitudinal mode was observed at the parameters $l = 40$ cm, $f = 37$ GHz, which are close to those of the planned experiment. The efficiency in the steady-state regime reached 20%.

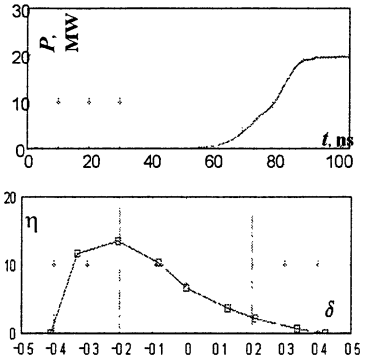

Fig. 3. Results of KARAT PIC code simulation: establishment of a steady-state regime (up) and the dependence of the stationary output efficiency on δ (down).

4. Narrow band reflector based on coupling of propagating and cutoff mode on symmetrical corrugation

In the case of symmetrical corrugation $\bar{m} = 0$ the coupling of propagating and cutoff modes can be used to realize a narrow band reflector. In this case the cut-off mode scatters both in forward and backward propagating waves: $\mathbf{E} = \mathrm{Re}\left(A_+\mathbf{E}_a(r_\perp)e^{i\omega t - ihz} + A_-\mathbf{E}_a(r_\perp)e^{i\omega t + ihz}\right)$. For monochromatic signal this process is described by the equations (compare with (4)):

$$\frac{dA_\pm}{dZ} \mp i\Omega A_\pm = \pm i\alpha B e^{\pm i\delta Z}, \quad \frac{1}{2}\frac{d^2B}{dZ^2} + \Omega A_\pm = \alpha(A_+ e^{-i\delta Z} + A_- e^{-i\delta Z}) \tag{7}$$

with boundary conditions:

$$A_+|_{Z=0} = A_0, \quad A_-|_{Z=L} = 0, \quad \left.\frac{dB}{dZ} \mp i\sqrt{2\Omega}B\right|_{Z=0,\,Z=L} = 0, \tag{8}$$

where $\Omega = (\omega - \omega_c)/\omega_c$ is the normalized frequency detuning. The boundary conditions for the quasi cut-off mode are written under assumption of the absence of the cut-off narrowings [8].

Based on Eqs. (7), (8) reflection coefficient from the Bragg structure with the length l = 20 см, radius $r_0 = 8.5$ mm, period of 10.7 mm and the corrugation depth of 0.3 mm was found in the case of coupling coefficient between the $TE_{1,1}$ and $TE_{1,2}$ modes (coupling coefficient $\alpha \approx 0.006$ cm^{-1}). Figure 4 demonstrates good agreement between results of the simulations under parameters closed to the parameters of "cold" tests and experimental data. Thus, the use of shallow symmetric corrugation for coupling of propagating and cut-off modes makes it possible realization of the reflector with a quite narrow reflection band. The 3D code simulation confirms this conclusion and indicates that the reradiaton to the

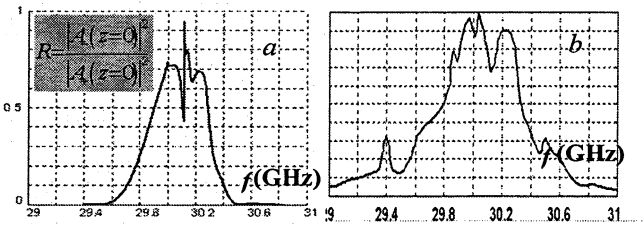

Fig. 4. Frequency dependence of the reflection coefficient: (*a*) simulations and (*b*) results of "cold" tests.

parasitic waveguide modes does not exceed 5% of total RF power. It should be noted that Bragg reflector based on coupling of propagating and trapped mode can be considered as one of variety of reflectors exploiting coupling with resonance mode [8].

Conclusion

As follows from the above consideration, a shallow corrugation ($r_1 / r_0 \approx$ ≈ 0.03) is sufficient for FEL self-excitation if the trapped cut-off mode is used to form a feedback loop. Thus, the use of a cut-off mode makes it possible to decrease effective coupling parameter required for the self-excitation of the oscillator in comparison with traditional Bragg FEL scheme, where the feedback wave possesses rather high group velocity [5]. Correspondingly in oversized microwave system, where Bragg conditions are satisfied for a large number of pairs of waves with different transverse indices, it is possible to provide selective excitation of a single pair consisting of the cut-off mode and operating propagating mode, which is amplified by the electron beam. Above method of mode control will be tested in JINR-IAP FEM [6] at Ka-band and then used as a method of increasing the operating frequency to W-band for fixed transverse size.

References

1. *Goldenberg A.L., Nusinovich G.N., Pavelyev A.B.*, Gyrotrons, IAP RAS, Gorky, Russia, 1980, p. 91 (in Russian).
2. *Savilov A.V., Bratman V.L., Phelps A.D.R., Samsonov S.V.*, Phys. Rev. E, 2000, **62**, 4207.
3. Savilov A.V., Peskov N.Yu., Samsonov S.V., Nucl. Instr. and Meth. Phys. Res. A, 2000, **A445**, 284.
4. *Ginzburg N.S., Malkin A.M., Peskov N.Yu. et al.*, Phys. Rev. ST AB, 2005, **8**, 040705.
5. *Ginzburg N.S., Bratman V.L., Denisov G.G., Petelin M.I.*, IEEE J. Quant. Electr., 1983, **QE-19**, 282.
6. *Ginzburg N.S., Kaminsky A.K., Peskov N.Yu. et al.*, Phys. Rev. Lett., 2000, **84**, 3574.
7. *Bratman V.L., Moiseev M.A., Petelin M.I., Erm R.E.*, Izv. VUZov, Radiophysica, 1973, **16**, 622 (in Russian).
8. *Denisov G.G., Lukovnikov D.A., Samsonov S.V.*, Int. J. Infrared and Millimeter Waves, 1995, **16**, 745.

ELECTRON BEAM CURRENT IN VACUUM DIODE WITH MAGNETICALLY ISOLATED EDGED CATHODE

A. V. Gromov, N. F. Kovalev, A. V. Palitsin, M. Fuks[1], *E. Schamiloglu*[1]

Institute of Applied Physics, RAS, Nizhny Novgorod, Russia
[1]University of New Mexico, Albuquerque, NM USA

The paper is devoted to the definition of an electron beam current forming in a magnetically insulated coaxial diode using a thin-walled tubular cathode with limited electron emission. Possible laws for electron emission and the development of a self-consistent problem are discussed. The structure of the electric field near the cathode edge and its dependence on the formed electron beam current are determined.

The analytical solution for the electron beam current from a coaxial diode (Fig. 1) with magnetic insulation comprising a thin-walled tubular cathode with unlimited electron emission of the cathode edge was found in [1]. This solution can be used as the reference for elaboration of numerical algorithms and theories for more complicated electron optics systems with thin-walled strongly magnetized electron beams.

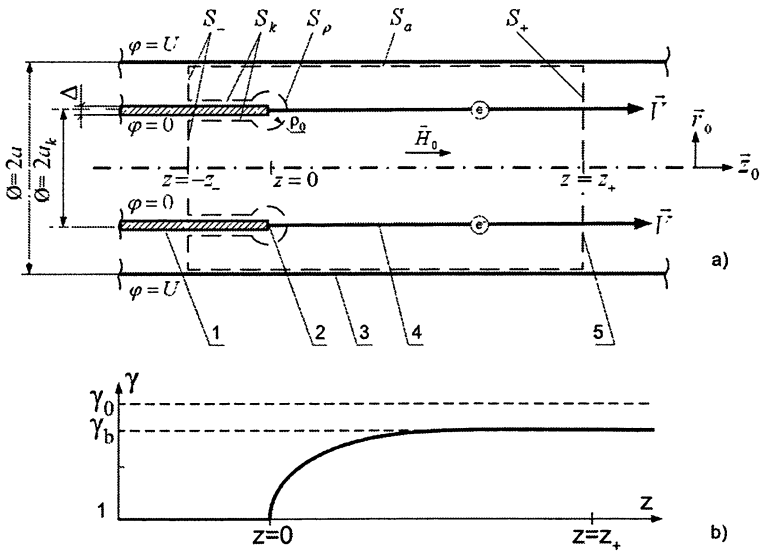

Fig. 1. Axisymmetric two-electrode electron gun with magnetized thin-walled cathode edge (*a*) and dependence $\gamma = \gamma(z)$ for studied electron beam state (*b*): *1* – thin-walled cathode; *2* – emitting cathode edge; *3* – anode; *4* – electron beam; *5* – closed contour for integrating (4).

In the present article we attempt to clarify the condition of unlimited emission from thin-walled cathode. Following [1], we consider the simplest model of an axisymmetric electron gun, which is comprised of a uniform anode with radius a and a thin-walled cathode (Fig. 1, *a*) in the approximation

$$(\Delta/a_c)^{1/4} << 1, \tag{1}$$

where Δ is the thickness of the cathode wall and a_c is the cathode radius. Transverse electron motion is neglected. We will study stationary processes in this system with perfectly conducting electrodes for electrons starting from the cathode edge with the zeroth velocity. Basic dimensions and directions of coordinate axes are shown in Fig. 1, *a*.

We consider the uniform system comprising the coaxial diode with a cathode potential $\varphi(r = a_c) = 0$ and an anode potential $\varphi(r = a) = U$. Following [1], we use the energy conservation law to calculate the electron beam current

$$(\gamma - 1)mc^2 = e\varphi, \tag{2}$$

and the z-th component of the total (fields and particles) momentum of the system yields

$$\oint_S \left\{ E_z\mathbf{E} + H_z\mathbf{H} - \frac{1}{2}(\mathbf{E}^2 + \mathbf{H}^2)\mathbf{z}_0 - 4\pi\frac{q}{e}\gamma m v_z \mathbf{v} \right\} d\mathbf{S} = 0. \tag{3}$$

Here $\mathbf{E} = -\nabla\varphi$ and $\mathbf{H}$ are the static electric and magnetic fields; φ is the electrostatic potential; $q > 0$ is the space-charge density of the beam; $e > 0$ and m are the charge and rest mass of an electron; $\mathbf{v} = v\mathbf{z}_0$ is the velocity of electrons, $\sigma > 0$ is the surface electron density.

We suppose that after acceleration the state of the electron beam becomes uniform when $z > z_+ >> a$ is achieved, for example, as way shown in Fig. 1, *b*. We apply the conservation laws (2) and (3) to the closed surface $S = S_+ + S_a + S_- + S_c + S_\rho$, which is shown in Fig. 1, *a* by the dotted lines. Surfaces S_+ and S_- are in regions $z_+ >> a$ and $z_- >> a$ where the field $\mathbf{E}$ and the electron beam state are uniform. As result, we receive the equations

$$I = \sqrt{\gamma_b^2 - 1}\,(\gamma_0 - \gamma_b)/\gamma_b, \tag{4a}$$

$$(\gamma_0 - 1)^2 - (\gamma_0 - \gamma_b)^2 - 2I\sqrt{\gamma_b^2 - 1} = D^2, \tag{4b}$$

where

$$D^2 = \frac{\ln(a/a_c)}{\pi}\left(\frac{e}{mc^2}\right)^2 \lim_{\rho_0 \to 0} \int_{S_\rho} \left\{ E_z\mathbf{E} - \frac{1}{2}\mathbf{E}^2 \right\} d\mathbf{S} \tag{5}$$

is the normalized limiting value of the field momentum flow through the emitting surface S_ρ with radius ρ_0; $\gamma_0 = 1 + eU/mc^2$; $\gamma_b = 1 + e\varphi_b/mc^2$; φ_b is the potential of the uniform electron beam in the region $z > z_+$; J is electron beam current, $I = 2\dfrac{eJ}{mc^3}\ln\dfrac{a}{a_c}$ is normalized value of it.

For

$$D^2 = 0 \tag{6}$$

(4) leads to the result

$$\gamma_b = \gamma_F \equiv \sqrt{2\gamma_0 + 0.25} - 0.5, \tag{7}$$

$$I = I_F \equiv (\gamma_0 - \gamma_F)\frac{\sqrt{\gamma_F^2 - 1}}{\gamma_F}, \tag{8}$$

which was first received in [1]. Accordingly [1], the equality (6) must be a consequence of the large emission of the cathode. In this case the current of the electron beam is limited by its own space charge. However, in contrast to the Child–Langmuir law for the planar diode with $\mathbf{E} = 0$ on the cathode, in the diode with a magnetized thin-walled cathode the self-consistent field E_z on the emitting cathode edge $(r = a_c, z = 0 + 0)$ has the singularity

$$E_z = -\frac{1}{\sqrt{3}} A_0 z^{-1/3}, \quad r = a_c, \quad 0 < z << a_c, \tag{9}$$

$$A_0 = \frac{\sqrt{3}}{(e/m)^{1/3}}\left(\frac{J_F}{a_c}\right)^{2/3}; \tag{10}$$

that is, near the cathode edge the field E_z is unlimited.

The derivation of (9) is based on the first term

$$\varphi_1 = A_0 \sigma^{2/3} \sin\left(\frac{2\theta}{3}\right), \quad 0 < \theta < \pi \tag{11}$$

in the expansion of the potential φ in terms of cylindrical harmonics with fractional indices in the local coordinate system (ρ, θ), which is shown in Fig. 2. On the cathode surface $(\theta = 0)$ the potential $\varphi = 0$, and on the beam surface $(\theta = \pi)$

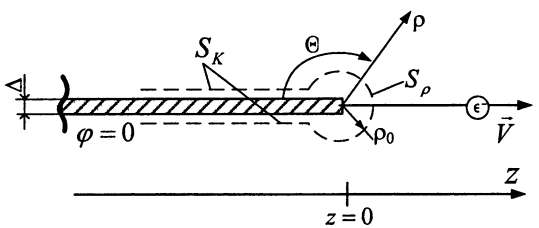

Fig. 2. Local two-dimensional coordinate system (ρ, θ). Fragment of the surface used for integrating (3) is shown by the dotted line.

$$E_\theta(\theta = \pi - 0) = -2\pi\sigma, \text{ or}$$

$$\frac{1}{\rho}\frac{\partial \varphi}{\partial \theta} = -\frac{J}{a_c}\sqrt{\frac{m}{2e\varphi}}. \tag{12}$$

In Eq. (12) symmetry of the potential φ is taken into account for $(\rho << a_c)$. For the diode under consideration, the current-voltage relationship $I = I(\gamma_0)$,

which is a solution of (7) and (8). For small voltages ($\gamma_0 - 1 << 1$) the current is determined by the equation

$$I_F = 2\left(\frac{\gamma_0 - 1}{3}\right)^{3/2}, \tag{13}$$

which is a direct consequence of the universal scaling relations (see, for example, [2]) and also scales as $J \sim A_0^{3/2}$ in (10). In the ultra-relativistic limit ($\gamma_0 >> 1$) the current is proportional to the voltage

$$I_F = \gamma_0 . \tag{14}$$

Note that electrons spend a very short time near the cathode ($0 < z << a_c$) because their motion begins with infinite acceleration that is associated with the singularity of the field E_z. Evidently this is also related to the short time that electrons dwell in the region of virtual cathodes $z = z_{vc}$ because the singularity of fields in the virtual cathodes has the same power dependence as in (9):

$$E_z \approx \left|z - z_{vc}\right|^{-1/3}.$$

When electron emission from a thin-walled cathode edge is limited, the limiting flow of the field momentum (5) does not reach zero, that is $D^2 \neq 0$, and a stronger singularity appears in the field E_z. In order to determine it, it is more convenient to represent the potential near the cathode edge as a series expansion in terms of cylindrical harmonics with other degrees:

$$\varphi \approx A\rho^{1/2}\sin\left(\frac{\theta}{2}\right) + \sum_{n=0}^{n_{max}} B_n \rho^{\frac{n+3}{4}} \sin\left(\frac{n+3}{4}\theta\right), \tag{15}$$

$0 < \theta < \pi,\ \rho << a_c$.

Amplitude B_n for each n-th harmonic is found from the differential boundary condition (12) with a strong singularity at $z = 0$ where $\varphi = 0$. Owing to this singularity, convergence of the series (15) is slow; nevertheless the series (15) can be used as an asymptotic one when only the first several terms are taken into account. We can calculate the asymptotic approximation of the integral in (5) and the limiting ($\rho_0 \to 0$) value for the normalized flow of the field momentum (5)

$$D^2 = \frac{\pi}{2} a_c \ln(a/a_c)\left(\frac{eA}{mc^2}\right)^2. \tag{16}$$

The relation (16) describes the dependence of the limiting momentum flow D^2 on amplitude A of the first term in the expansion (15) of the potential φ. This relationship explains all basic properties of, and peculiarities of the operation of thin-walled cathodes. For example, a value of the momentum flow cannot be negative because an imaginary amplitude of A has no physical sense. However, according to Eq. (4), the minimum allowable value of the flow $D^2 = 0$ corresponds to the maximum possible current ($I \geq 0$) of the electron beam from the cathode edge. Evidently, properties of the emitter do not determine this maxi-

mum current. This current is determined by the space-charge field of electrons, or by the attraction of electrons to their image charge that appears on the cathode.

According to (4) and (16) the amplitude A of the fundamental harmonic is determined by the electron beam current J. When the current increases, the amplitude A monotonically decreases.

The functional dependences

$$A = A(J),\ B_n = B_n(J, A) \tag{17}$$

describes the influence of the electron beam charge on the value and structure of the accelerating field near the cathode edge; that is, it characterizes the influence of reasons that prevent the increase of the current J. To find a self-consistent value of the current, we need one further characteristic, namely, the dependence of the current on the field near the cathode edge; that is, the law governing the emission of electrons for the particular cathode considered. When non-localness is accounted for only in the first approximation, then for thin-walled cathodes a convenient form of an emission law is

$$J = J(A). \tag{18}$$

For example, two possible versions of emission laws (18) are shown in Fig. 3. In the first case (*1*, Fig. 3) emission from a thin-walled cathode edge is high, and a self-consistent current is close to the maximum current J_F. In the second limiting case (*2*, Fig. 3) the electron beam current is determined by the emission capability of the cathode. When an emission law (18) is known, solution of the system of equations (17) and (18) for different voltages γ_0 yields a current-voltage characteristic of the electron gun that conditionally (as for planar guns) could be separated into an ascending branch that is determined by the space-charge field and a region of saturation. On the other hand, when a current-voltage characteristic is known (for example, from experiments) for some electron gun, then using dependences (17) it is possible to obtain curves (18) characterizing the individual properties of the cathodes, which would remain the same when these cathodes are used in other guns.

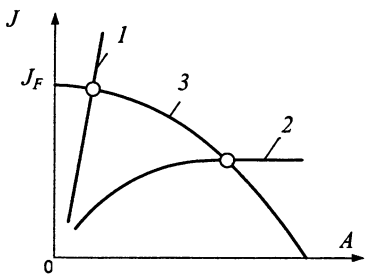

Fig. 3. Graphical solution of the system of equations (17) and (18) on the plane $A - J$ (*3*) for cathodes with high (*1*) and low (*2*) electron emission.

Conclusion

For low voltages ($\gamma_0 - 1 << 1$) the current-voltage characteristic of an electron gun with strongly magnetized thin-walled cathode edge with large emission

is described by the common Child–Langmuir law of "$J(V^{3/2})$". However, the accelerating electric field on the emitting cathode edge is infinite, contrary to planar diodes with the field equal to zero on the cathode. Because of this, a reason that prevents the electron current increase can only be an integral characteristic of the diode. As such, a characteristic chosen here is the amplitude of the first harmonic A in the expansion of the potential (15) because it is directly coupled with the momentum flow (16) and, accordingly, with a force acting on the emitted cathode edge. This quantity sufficiently changes the properties of electron guns with such cathodes, as well as interrelations of their basic parameters and characteristics of processes. A necessity arises for a more correct description of the properties of emitting edges. It is possible that the version of an emission law reported in this work is not alone its form. However, to determine the most convenient form of an emission law, additional investigations, including non-stationary regimes, are required.

References

1. *Fedosov A.I., Litvinov E.A., Belomytsev S.Ya., Bugaev S.P.*, On account of characteristics of an electron beam forming in diodes with magnetic insulation, Izv. VUZov, Fizika (Russian), 1977, no. 10, 134-135.
2. *Gaponov V.I.*, Electronics (in Russian), Moscow, Fizmatgiz, 1960.

PROJECT OF SUB-MILLIMETER BRAGG FEM BASED ON TWO-WAVE INTERACTION

N. Yu. Peskov, A. V. Savilov, Yu. K. Kalynov,
S. V. Kuzikov, D. Yu. Shchegol'kov, A. K. Kaminsky[1],
E. A. Perelshtein[1], *S. N. Sedykh*[1], *A. P. Sergeev*[1]

Institute of Applied Physics RAS, Nizhny Novgorod, Russia
[1]Joint Institute for Nuclear Research, Dubna, Russia

A project to generate powerful sub-mm pulses in JINR-IAP FEM-oscillator driven by 08 MeV / 200 A linac is in progress. Present paper describes recent design and key elements of the oscillator.

Introduction

Possibility to advance powerful microwave generators into sub-mm range is widely investigated currently. An attractive solution to achieve sub-mm wavelengths is an FEL-scattron, in which an external e.m. wave is used as a wiggler. In comparison with traditional FEMs having static magnetic wigglers an RF-wiggler makes it possible to get shorter period of electrons oscillations. Moreover, this scheme possesses twice higher factor of Doppler frequency up-conversion. As a result, FEL-scattron driven by mildly relativistic electron beam is able to operate at THz frequencies if mm pumping wave is applied.

To simplify device of such kind (when no additional powerful microwave sources is needed) an inter-cavity scattering can be used. Similar regime was realized experimentally in relativistic BWOs where cm backward waves scatter into powerful mm wavelength forward waves [1, 2]. We propose to realize this regime in Bragg FEM operating in two-wave (ubitron and scattron) resonance conditions. In the "ubitron" regime the beam electrons interact with the forward mm wave, the backward mm wave (forming in the Bragg resonator) is used a secondary wiggler to provide stimulated scattering into a sub-mm forward wave. To increase efficiency of the sub-mm generation we propose operation at a multiple frequency. In this case mm and sub-mm waves are coupled on the same electron beam and no feedback (resonator) is required for sub-mm wave.

FEM-oscillator with Bragg resonator is investigated during the last decade in collaboration between IAP RAS (N. Novgorod) and JINR (Dubna) based on linac LIU-3000 (08 MeV / 200 A) [3, 4]. At the present stage 30 GHz / 20 MW / 200 ns pulses with a spectrum width of ~ 10 MHz have been achieved. Possibility to advance of JINR-IAP FEM into sub-mm wavelength band is studied currently.

Operation principles

The FEM operates with a thin axial electron beam oscillating in a helical wiggler of periodicity d, a transverse field B_w, and a uniform guide field B_0, inside a circular waveguide. Dispersion diagram illustrating wave-beam interaction in a two-wave FEM is shown in Fig. 1. The traveling circularly polarized mm *wave "1"* is excited by the beam in the regime of the "ubitron" interaction at frequency

$$\omega_1 \approx (h_1 + h_w)v_{\|}, \tag{1}$$

$h_w = 2\pi/d$. The Bragg reflectors provide selective feedback for mm waves, the feedback loop is completed by the forward *wave "1"* and the backward *wave "2"*. To produce sub-mm radiation, the feedback *wave "2"* is used as a "secondary wiggler". This results in the wave scattering into the forward *wave "3"* (*"4"*) under the "scattron" resonance constraint

$$\omega_{3,4} \approx \omega_{1,2} + (h_{3,4} - h_2)v_{\|}. \tag{2}$$

It should be noted that the FEM possesses the "electron selectivity": i. e. a helical beam in a circular waveguide interacts only with the circularly polarized modes with an azimuthal index equal to 1.

As shown in [5], to increase the efficiency of sub-mm scattering the FEM should operate close to the cyclotron resonance. This can be achieved when (a) the *wave "2"* is close to cutoff and (b) a sufficiently strong guide field is used, i. e. $\omega_B \sim \omega_{1,2}$ ($\omega_B = eB_0/\gamma mc$ is the gyro-frequency). Moreover, the correct rotation of *wave "2"* should be provided. In the case of a reverse guide field orientation, which is used in the JINR-IAP FEM, the *waves "1"* and *"2"* should be counter-rotating. This can be achieved using Bragg mirrors, which couple forward and backward mm waves of opposite polarization (rotation).

To increase the efficiency of the sub-mm wave excitation we propose the use of the harmonic condition

$$\omega_{3,4} = s\omega_{1,2} \tag{3}$$

with s an integer, such that both the mm *wave "1"* and sub-mm *waves "3"* (*"4"*) couple to the same electron beam. In this case the (s-1)-th harmonic of the electron beam modulation due to the mm wave represents a modulation at the frequency of the combined "scattron" wave, $\omega_{3,4} - \omega_{1,2}$, which can be considered as an initial sub-mm seed. Thus feedback (resonator) for the sub-mm wave is unnecessary.

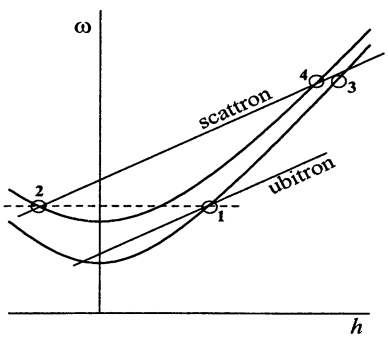

Fig. 1. Schematic dispersion diagram of the two-wave FEM.

Recent design

A schematic diagram of the JINR-IAP FEM experiments is shown in Fig. 2. The induction linac LIU-3000 (JINR) generates a 0.8 MeV / 200 A / 250 ns electron beam with a repetition rate of 1 Hz, which is injected into the FEM-oscillator immersed in a solenoid. A helical wiggler of 6 cm period pumps transverse velocity into the beam. This electron-optical system was tested in the FEM experiments at 30 GHz [3, 4]. A reversed guide field regime [6, 7] was chosen for the FEM operation. This regime provides high-quality beam formation in the tapered wiggler section with a low sensitivity to the initial beam spread and leads to high efficiency energy extraction from the beam [8] that was corroborated in performed experiments [3, 4].

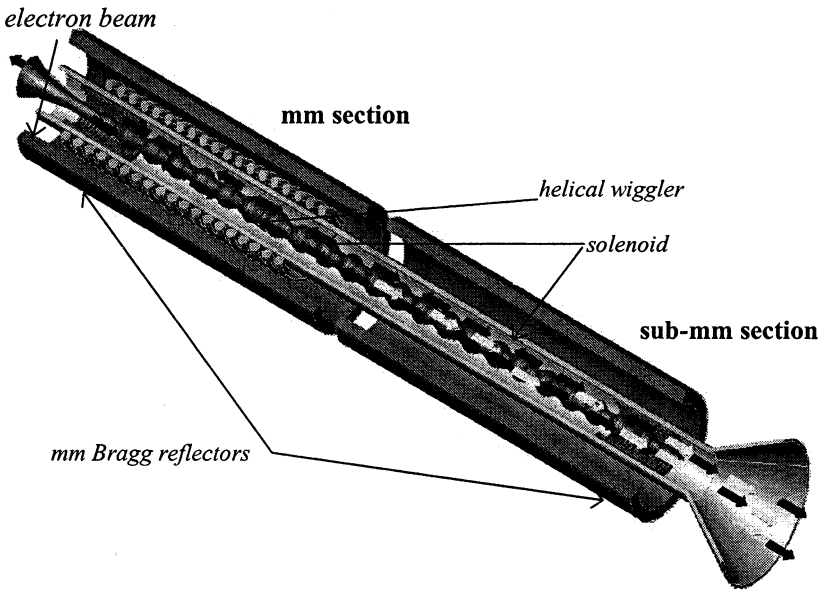

Fig. 2. Schematic diagram of a two-wave sub-mm FEM driven by linac LIU-3000

For sub-mm operation the FEM was designed with electron oscillating velocity of $\beta_\perp \sim 0.2$. The "ubitron" interaction with a 30 GHz circularly polarized $TE_{1,1}$ *wave "1"* in a circular waveguide is considered. The two-fold helically-corrugated Bragg mirrors, with 85% reflection, provide feedback of the counter-rotating $TE_{1,2}$ *wave "2"*. In order to increase wave-beam coupling in the scattering process the waveguide radius was chosen to be 0.87 cm, in this case the feedback wave $TE_{1,2}$ is close enough to the cut-off ($\beta_{gr} \sim 0.2$). Scattering of the

backward *wave "2"* into the $TE_{1,1}$ *wave "3"* and a $TE_{1,2}$ *wave "4"*, is calculated to be at 360 GHz for the $s = 12$ harmonic.

Simulations of the two-wave FEM based on LIU-3000 was done for both single-section and double-section variants (depicted in Fig. 2). In the last case the resonance conditions (1) and (2) are fulfilled in different sections. Evidently, separation of the "ubitron" and "scattron" interaction regions allows more freedom to optimize the radiation parameters. Results of simulations of the double-section variant are shown in Fig. 3, *a*. The simulations predict an output power of 300–400 kW at a frequency of 360 GHz. Under the optimal parameters of the wave-beam interaction the nonlinear competition between different waveguide modes results in establishment of a single-mode sub-mm oscillation. In particular, in Fig. 3, *a* the mode pattern in the output radiation contain practically only the $TE_{1,1}$ wave with a negligible (~20 kW) admixture of other modes with azimuthal index 1 ($TM_{1,1}$, $TE_{1,2}$, etc.).

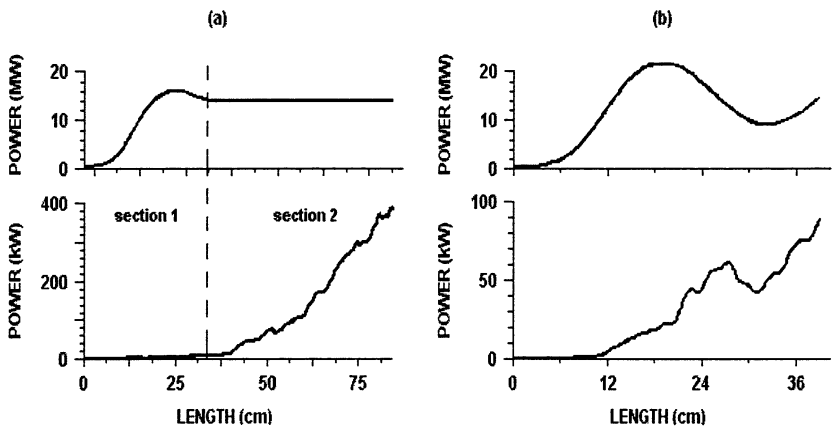

Fig. 3. Power of the "ubitron" mm wave (upper curves) and the "scattron" sub-mm wave (lover curves) versus the axial coordinate for guide field of 12 kG in the case of double-section (*a*) and configuration (*b*) of the two-wave FEM.

In a single-section variant of the two-wave FEL both interactions (1) and (2) occur simultaneously. In this case efficiency of sub-mm generation is 3–4 times lower (see Fig. 3, *b*) because optimal length for the "ubitron" and "scattron" interactions is different. Nevertheless, even in a single-section variant the output sub-mm power is calculated to be at 100-kW level. From the other hand, a single-section configuration of a two-wave FEM seems to be easy in the first experimental realization.

Sub-mm diagnostics

The main problem of a sub-mm diagnostics is the separation of radiation from a two-wave FEM, taking into account that the power of output mm wave is practically in order higher than the sub-mm power. One of the natural solutions with a good RF-breakdown strength is concerned with the use of a diffraction grating for the wave separation. The grating was designed with a mm wave mirror reflection and sub-mm wave reflection in the direction to the (–1)-st diffraction maximum so that different frequencies were spatially separated in directions shown in Fig. 4, *a*. This particular configuration of wave fluxes seems convenient for the experimental realization of the FEM. "Cold" test of the grating was carried out using mW-level BWO and demonstrated good agreement with the calculated parameters (Fig. 4, *b*).

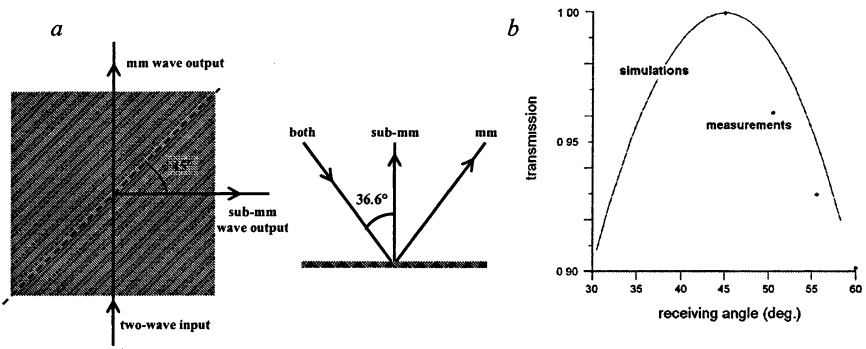

Fig. 4. Schematic of spatial separation of mm and sub-mm waves at the diffraction grating (*a*) and results of calculations and measurements of the separated sub-mm wave (*b*).

Conclusions

Bragg FEM based on simultaneous excitation of two types of the waves at different resonances (ubitron and scattron) is considered to generate sub-mm radiation using mildly relativistic electron beam. Simulations demonstrate possibility to achieve 100kW-power level at sub-mm wavelengths when optimizing the interaction. Project of 0.8 mm FEM based on LINAC LIU-3000 (0.8 MeV / 200 A / 200 ns) was designed. Key elements of the generator were manufactured and studied in "cold" tests. "Hot" experiments at 30 GHz demonstrated acceptable quality of the pumping wave. Diagnostics for sub-mm radiation were developed. Experimental study of the sub-mm generation in the FEM is in progress currently.

Acknowledgements. This work is supported partially by the Russian Foundation for Basic Research (grants №03-02-16530, №04-02-17118 and №05-02-16852) and the Russian Science Support Foundation.

References

1. *Zhukov P.G., Ivanov V.S., Rabinovich M.S., et al.*, JETP, 1979, **76**, 2065.
2. *Bratman V.L., Denisov G.G., Ginzburg N.S., et al.*, Int. J. of Electr., 1985, **59** (3), 247.
3. *Ginzburg N.S., Kaminsky A.K., Peskov N.Yu., et al.*, Phys. Rev. Lett., 2000, **84**, 3574.
4. *Kaminsky A.K., Elzhov A.V., Ginzburg N.S., et al.*, Proc. 5th Int. Workshop Strong Microwaves in Plasmas, N. Novgorod, Russia, 2002, **1**, 184.
5. *Savilov A.V., Peskov N.Yu., Kaminsky A.K.*, Phys. Res. A, Nucl. Instr. and Meth., 2003, **A507**, 162.
6. *Kaminsky A.A., Kaminsky A.K., Rubin S.B.*, Particle Accelerators, 1990, **33**, 189.
7. *Conde M.E., Bekefi G.*, Phys. Rev. Lett., 1991, **67**, 3082.
8. *Peskov N.Yu., Samsonov S.V., Ginzburg N.S., Bratman V.L.*, Phys. Res. A, Nucl. Instr. and Meth., 1998, **A407**, 107.

CONTROL OF QUASI-OPTICAL BEAMS BY GRATING BASED DEVICES

V. Erckmann[1], *V. N. Gorbatuschkov*[2], *J. L. Hirshfield*[3], *W. Kasparek*[4], *Yu. I. Koshurinov*[5], *V. G. Pavelyev*[5, 2], *M. I. Petelin*[2], *D. Yu. Shchegol'kov*[2], *I. V. Turchin*[2]

[1]MPI für Plasmaphysik (IPP), EURATOM Ass., Greifswald, Germany
[2]Institute of Applied Physics RAS, Nizhny Novgorod, Russia
[3]Omega-P, Inc., Yale University, New Haven, USA
[4]Institut für Plasmaforschung, Universität Stuttgart, Stuttgart, Germany
[5]Nizhny Novgorod State University, Nizhny Novgorod, Russia

The paper describes two quasi-optical devices capable to combine and redirect microwave flows in a discrete way. The first device – phase-controlled combiner-commutator – represents a 3 dB directional coupler based on a diffraction grating. Two beams of equal powers incident to the grating are combined into one reflected beam of double power so that by a phase shift between initial beams the combined beam is switched from one output to another. The second device – diplexer representing a quasi-optical cavity with two corrugated mirrors – separates (/combines) signals of different frequencies to two outputs (/from two inputs). A frequency shift switches the wave from one direction to another. The both devices were demonstrated at 34 GHz.

At millimeter wavelengths all components to control high power electromagnetic flows must be, obviously, quasi-optical [1]. This paper presents two relevant examples.

1. In future millimeter-wave-driven linear electron accelerators, it seems expedient to use a delay line distribution system (DLDS) [2] composed of binary phase-controlled combiner-commutators in the form of metal diffraction gratings [3]. Such a grating functions as a 3 dB hybrid in the following way [3] (Fig. 1). Let an incident plane wave (*I*) be divided by the grating into mirror (*M*) and (–1)st diffraction waves of equal power densities, so, that the (–1)st diffraction wave is anti-mirror (*AM*), i. e. its propagation vector belongs to the same plane as the groove direction and the propagation vector of the incident wave. All the waves are assumed of a common – either *E*, or *H* – polarization relative to the groove direction. The inverse wave propagation gives combining of two incident waves into one so, that changing the mutual phase between incident waves completely switches the combined plane wave from one direction to another.

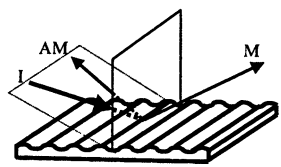

Fig. 1. Diffraction grating as a 3 dB hybrid (magic-Y).

For wave beams of a finite cross-section, even with properly matched density and phase distributions, some losses are inevitable because of dispersion properties of the grating. In the magic-Y, there are three kinds of diffractional power losses, namely filtration loss, polarization loss, and commutation loss. If

the input beams of the combiner-commutator are of Gaussian type, the combined beams are not pure Gaussian and have a small non-Gaussian content. So there will be filtration loss in case the output system is optimized only for transporting Gaussian beams. Polarization loss arises since linearly polarized Gaussian beams differ from *E*-polarized Gaussian beams by containing an *H*-component whose relative magnitude depends on the geometry and is inversely proportional by power to the second degree of beam width (a) normalized to the wavelength (λ). So the use of such beams will result in an additional loss. Commutation loss arises in switching. For example, let us suppose that as a result of two beams of equal powers combining there is only one reflected Gaussian beam. If the phase of one of the incident beams is shifted by π then the basic part of power will go in the direction alternative to the previous one, but there will still be a relatively weak wave going in the former direction. All three kinds of power loss are of the same order, namely $(\lambda/a)^2$, diminishing as the beam cross section increases.

Obviously, the frequency deviation from the design value will result in an extra loss which is mostly concerned with the deflection of the (–1)st beam. The corresponding frequency bandwidth is proportional to (λ/a).

The magic-Y was studied experimentally at 34.27 GHz. It was designed for a symmetric configuration: all the incident and reflected beams composed equal angles with all basic directions imposed by the grating; every beam had an 35.3° angle relative to the grating plane. The illuminated area at the grating plane was circular with a diameter by the intensity level e^{-1} equal to 70 mm. Accordingly, all wave beams were of elliptic Gaussian cross-section and had flat phase fronts at the grating. The chosen beam width was large enough to limit diffractional losses on the grating within ~1 %, but small enough to mitigate tolerances on mirror angular positioning. All the waves were *E*-polarized relative to the grove direction, that is favorable for withstanding high powers.

To provide the mutual coherence of quasi-optical beams incident to and scattered by the grating, a microwave source common for all the beams was used. The beam splitting and combining was performed by the same grating. The experimental set-up (Fig. 2), included: a transmit-receive transducer that matches the TE_{10} mode of a standard WR-28 rectangular waveguide to a Gaussian beam at the aperture of a 60 mm diameter horn; two matching mirrors *1*, *2*; flat grating *3* of 180×180 mm size, with a sinusoidal corrugation having a 7.58 mm period and a 3.05 mm amplitude and two identical focusing mirrors *4a*, *4b*.

The axisymmetric beam from the horn transformed by matching mirrors into the elliptical one is divided by the grating into two identical beams which, after having been reflected from the returning mirrors *4a* and *4b* come back to the grating and are combined by it. By moving one of the returning mirrors counter the incident beam, it is possible to change the phase shift between the beams being combined and so to redistribute the rf power between the direction to the horn (mirror *2* direction) and the alternative radiation direction (Fig. 2).

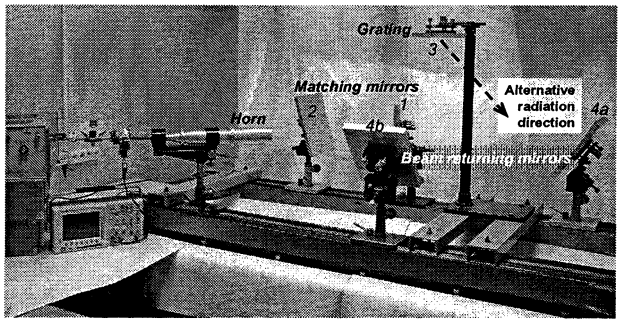

Fig. 2. A 34 GHz set-up for testing the magic-Y. Figures specify the numbers of mirrors in the sequence of their first beam path-tracing.

Figure 3 shows data for the power returned back into the horn as a function of the normal displacement of the mirror *4a* (Fig. 2). The maximum returned power was 92% of the initial power. The minimum returned power (when most of the power was radiated in the alternative direction) did not exceed 0.3%. When between the grating and one of the mirrors *4a* or *4b* a plate was inserted that reflected the beam aside, the relative power returned to the horn was about 23%. After replacement of the grating by a flat mirror about 94.5% of the power returned back, that means that the total two-pass loss due to the grating was about 2.5%.

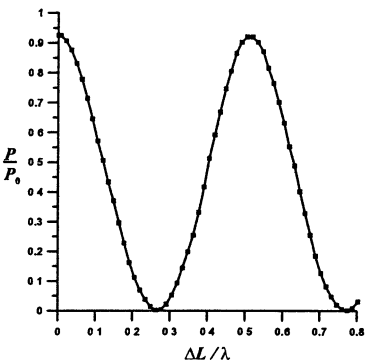

Fig. 3. Relative power in one of two magic-Y outputs vs mirror *4a* normal displacement determining the phase shift between the combined beams.

The results of the experiment indicate a high efficiency of the combiner-commutator magic-Y (96% taking into account the single-pass loss in transmitting matching system) and make it attractive for use in DLDS. Another important application of the magic-Y may be isolation of microwave source from the power reflected from the load.

2. Multiplexers [3–5] are devices used for combining and dividing signals of different frequencies. High frequency selectivities are provided with multiplexers of resonant types. In the millimeter wavelength range, resonant multiplexers should be quasi-optical [3, 5], exemplified with a symmetric four-mirror ring resonator schematically depicted in Fig. 4, *a*. The resonator is coupled to the input and the output by means of two identical corrugated mirrors *1* and *3*, the corrugation period and orientation being selected so that, upon the scattering of a wave incident onto the corrugated mirror *1*, only the (–1)-order diffraction beam would exist in addition to the mirror-reflected beam (non-resonant output

wave). For the sake of symmetry, it is appropriate to choose all angles of incidence to and reflection from the gratings equal to 45°, the grooves are oriented at 45° relative to the main planes of the resonator symmetry, the input and output beams are situated in the plane transverse to that of the beam circulation within the cavity.

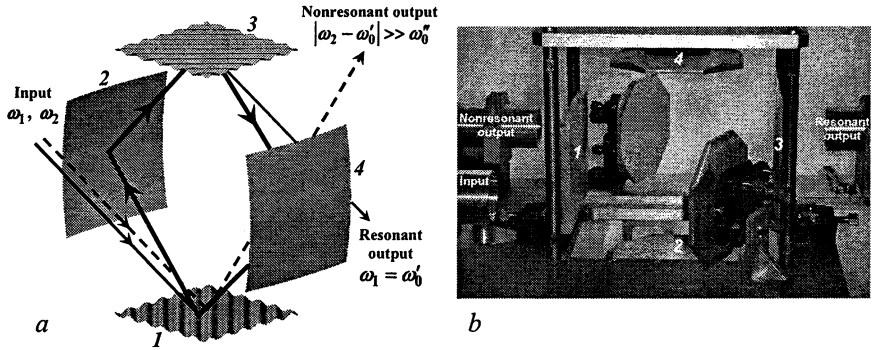

Fig. 4. Scheme of frequency separation by a four-mirror resonator with two corrugated mirrors (at the left) and an experimental 34 GHz diplexer (at the right).

The corrugation should be shallow enough to ensure that resonant bands of high-Q modes will not overlap, however deep enough to make the resonator overloaded. These conditions take the form $\omega L/c << Q_{rad} << Q_{ohm,\ diff}$, where L is the beam circulation length, Q_{rad} is the Q-factor determined by the wave scattering at the grating, Q_{ohm} and Q_{diff} are determined by the ohmic and diffusion loss. Under these conditions, all the power at the cavity eigen-frequency is extracted in the resonant output direction (Fig. 4, *a*). If the incident wave frequency is outside the resonance band, the field in the resonator is not excited and the incident wave is mirror reflected in the nonresonant output direction. Within the resonance band, the frequency dependence of the power transmission coefficients is described by Lorenz curve [5, 6] of $\omega/2Q_{rad}$ half-width.

The experimental diplexer (Fig. 4, *b*) had a beam circulation length of $L = 810$ mm. The wave field was E-polarized relative to the direction of corrugation grooves. The gratings were sine-corrugated and provided the (–1)st maximum diffraction coefficient of 13%. The focusing mirrors *2* and *4* represented segments of elliptic paraboloids shaping the circulating Gaussian beam so that its size in the circulation plane was half of that in the perpendicular direction (42 and 84 mm by intensity level e^{-1}) and, accordingly, the input and output Gaussian beams were axisymmetric. The radiation loaded quality factor of the resonator Q_{rad} was 2000, the unloaded quality factor $(1/Q_{ohm} + 1/Q_{diff})^{-1}$ was 50000.

The diplexer input and output systems (Fig. 4, *b*) were composed of horns and paraboloid mirrors. The microwave source represented a Gunn diode with a voltage-controlled capacity, and the signal frequency was modulated at a rate of 29 MHz/μs. Powers measured in the both output channels depended on the fre-

quency (Fig. 5) in a good accordance to the theory, the half-power line width being 18 MHz.

A high power experiment with a quasi-optical diplexer matched to a 140 GHz gyrotron is planned to be performed in Greifswald in 2006: the natural thermal frequency chirp of the pulsed gyrotron during the first ~100 ms should switch the wave beam from one output channel to another. The frequency scanning of high-power wave beams might be used for adaptive ECR suppression of hydrodynamic plasma instabilities in magnetic traps [7, 8].

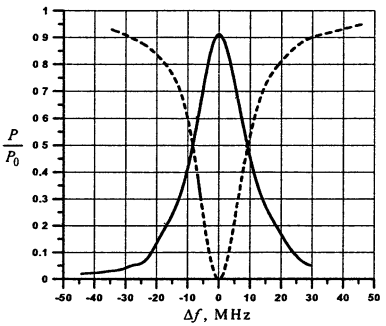

Fig. 5. Measured transmission coefficients of the diplexer into resonant (solid line) and nonresonant (dashed line) channels vs. frequency.

Such diplexers can also be combined into multiplexers [5] that might be used in long-range multi-channel communication and radar systems with synthesized frequency bands [3, 5, 9].

Acknowledgement

The work was supported by US DoE (project №DE-FG02-04ER-8403) and Russian Foundation for Basic Research (project №03-02-17107). Authors are grateful to M. Thumm and A. Litvak for valuable discussions.

References

1. *Petelin M.I.* in Quasi-Optics in High-Power Millimeter-Wave systems, RF-2003 Proc., Coolfont Resort.
2. *Mizuno H., Otake Y.* in A New RF Power Distribution System for X-band Linac Equivalent to an RF Pulse Compression Scheme of Factor 2**n, Proc. LINAC94, 1994.
3. *Petelin M.I., Caryotakis G. et al.*, AIP Conf. Proc. **474**, 304 (1998).
4. *Matthaei G., Young L., Jones E.M.T.*, Microwave Filters, Impedance-Matching Networks, and Coupling Structures, McGraw-Hill, NY, 1964.
5. *Turchin I.V.*, Radiotekh. Élektron. (Moscow) **48**, 684 (2003).
6. *Petelin M.I., Turchin I.V.*, Radiotekh. Élektron. (Moscow) **46**, 1445 (2001).
7. *Petelin M., Kasparek W.*, 6th IVEC Proc., 131 (2005).
8. *Gantenbein G., Zohm H. et al.*, Phys. Rev. Lett. **85**, 1242 (2000).
9. *Caryotakis G., Scheitrum G. et al.*, NATO Advance Research Workshop on Quasi-Optical Control of Intense Microwave Transmission Proc., Nizhny Novgorod, 2005 (Kluwer Academic, NY, in press).

ELECTRICALY CONTROLED DIFFRACTION GRATING FOR ACTIVE MICROWAVE PULSE COMPRESSORS

A. M. Gorbachev, S. V. Kuzikov, A. A. Vikharev

IAP RAS, Nizhny Novgorod, Russia

In the microwave pulse compressors proposed for high-gradient particle accelerators fed by millimeter waves it is natural to use quasi-optical resonators with the distributed power switches. A three-mirror pulse compressor with active diffraction grating is suggested. Switching the compressor from the regime of storage to the regime of extraction of microwave energy is provided by plasma discharge in the channels of grating.

Introduction

Currently future electron-positron linear colliders fed by Ka-band radiation are actively discussed [1–5]. Necessary accelerating gradient for such colliders is usually associated with high-power microwaves produced by means of pulse compressors.

To avoid breakdown and thermal heating fatigue it is natural to use pulse compressors based on multi-mirror resonators. Such compressors are able to provide a good selectivity [4–5].

Active pulse compressors allow achieving higher power gain and efficiency in comparison with the so-called passive compressors. In three-mirror active pulse compressor a diffraction grating as electrically controlled switch is preferable.

Numerical simulation of active diffraction grating

The quasi-optical traveling-wave resonators with a diffraction grating as a coupling device can be used as an active microwave pulse compressors, Fig. 1. To achieve this, the grating in the regime of energy storage provides reflection of a small portion of the incident power into the diffraction (–1st) beam to couple the resonator with the feeding line, Fig. 1, *a*. Then, to extract the energy the grating switches fast into the state in which a significant portion of the power is branched into the diffraction beam. As a result, the coupling of the resonator with the feeding line becomes stronger, and the energy stored in the resonator leaves in a short time, Fig. 1, *b*. This was done by changing properties of the diffraction grating using the gas-discharge plasma in grating channels which changes the distribution of RF field.

The reflecting diffraction grating was formed by a metal mirror and a periodical structure over it, Fig. 2, *a*. To avoid breakdown we chose the TE polarization of the electromagnetic waves at which the vector of the electric field is parallel to the grating grooves. In this case there is no noticeable increase of intensity of the electric field on the periodic structure. Operation of active dif-

fraction gratings was simulated by the means of the FDTD method [6]. The calculation scheme is shown in Fig. 2, *b*.

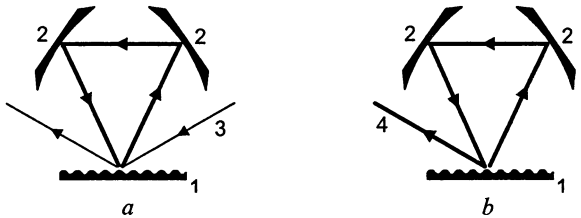

Fig. 1. Scheme of compression basing on the quasi-optical resonator: *1* – diffraction grating/switch; *2* – focusing mirrors; *3* – input pulse; *4* – output pulse; *a* – resonator in the regime of energy storage; *b* – resonator in the regime of extraction of the compressed pulse.

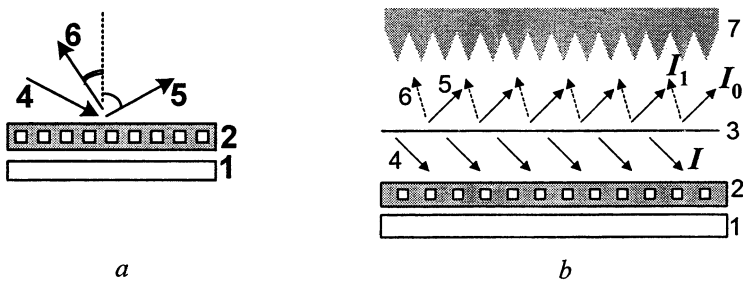

Fig. 2. Cut and calculation scheme of a controlled diffraction grating: *1* – metal mirror plate; *2* – diffraction grating; *3* – plane with set currents radiating a wave towards the grating; *4* – on the grating wave; *5* – reflected wave; *6* – diffraction wave (–1st maximum); *7* – absorber.

On the basis of calculations it was found that the gratings that consist of a relatively thick dielectric plate with channels in it (which serve as gas-discharge tubes) seem to be electrically reliable. Chosen type of the grating provides almost 98.5% mirror reflection in the absence of plasma in the channels, Fig. 3, *a*, and the lowest possible intensity of the electric field at these channels. To provide 1.5% branching into the diffraction wave the grooves parallel to the channel were made on both surfaces of the dielectric plate. When plasma is produced in each channel, a strong periodic inhomogeneity appears and 30% of the energy is branched into the diffraction wave, Fig. 3, *b*.

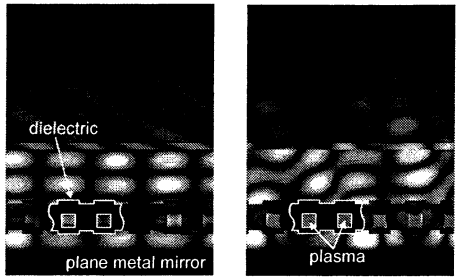

Fig. 3. Distributions of the instantaneous electric field during reflection of the plane wave from the diffraction grating made of polystyrene: *a* – in the regime of energy storage in the resonator; *b* – in the regime of energy extraction.

Study of quasi-optical three-mirror active compressor

The scheme of the experimental setup for studying the operation of the quasi-optical three-mirror active compressor is shown in Fig. 4. Compressor *1* is fed by a low-power continuous-wave generator *2* at the frequency of 34.27 GHz. The voltage produced by the high-voltage pulse generator *3* was fed to the elements of the controlled grating via a set of ballast resistors *4*. The radiation from the compressor output is received by detector *6* via attenuator *5* and then registered with a digital oscilloscope *7*. In order to measure the frequency characteristics of the compressor, generator *2* was switched into the regime of frequency sweeping. The spectrum of the transmitted pulse was analyzed with a network analyzer *8* to which the radiation was delivered via a directional coupler *9*.

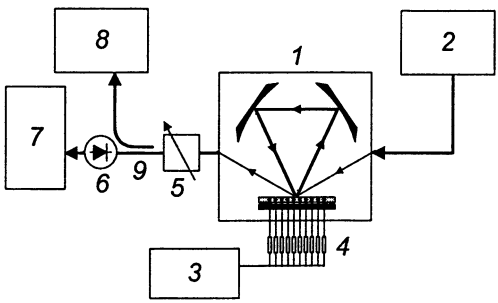

Fig. 4. The scheme of the experimental setup: *1* – quasi-optical three-mirror active compressor, *2* – microwave generator, *3* – high-voltage pulse generator, *4* – ballast resistors, *5* – attenuator, *6* – detector, *7* – oscilloscope, *8* – network analyzer, *9* – directional coupler.

In the series of experiments performed operation of the active compressor in SW-regime was studied when the resonator was tuned in such a way as to make the stored energy maximal. This was achieved by making the distance h between the polystyrene and metal plates of the grating such as to match the unloaded Q-factor of the resonator and the coupling Q-factor approximately equal. In this case the loaded Q-factor of the storing resonator was $QL \approx 14000$, and the signal in the mirror beam (having passed through the resonator) at the resonance frequency was weak.

To study the time of grating switching the focusing mirrors of the resonator were covered with an absorber. In the absence of plasma in the channels the intensity of the diffracted beam is low, and the incident power is reflected into the mirror beam. The signal registered by the detector was maximal. When the plasma appears in the grating channels in a high-voltage breakdown, the intensity of the mirror beam decreases, Fig. 5, curve 1. As seen from the Figure, the characteristic time of grating switching is of the order of 5 ns.

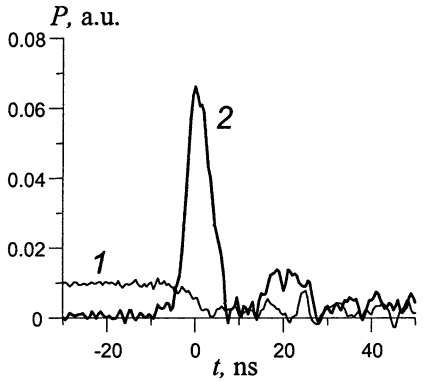

Fig. 5. Oscillograms of the output signals of the active compressor when plasma is produced in the channels of the diffraction grating: *1* – signal in the mirror beam in the presence of an absorber in the resonator; *2* – compressed pulse during energy output from the resonator.

In order to test whole compressor, the absorber was removed from the resonator. When the resonator was tuned to the resonance frequency, the signal having passed through the compressor (in the mirror beam) is close to zero. When plasma develops in the grating channels, the stored energy leaves the resonator in a diffracted beam, and, as a result, a compressed pulse is formed, Fig. 5, curve 2. In this case the half-height duration of the compressed pulse was 6–10 ns, and the power gain reached $G \approx 7$. The value of G depended on plasma homogeneity in different channels of the diffraction grating. In its turn homogeneity of the plasma depended on the gas pressure and simultaneity of breakdowns in the channels of the diffraction grating.

Efficiency of energy output from the resonator defined as the ratio of the energy in the compressed pulse and the energy stored in the resonator equaled approximately 40–50%. Evidently, a sufficiently low value of energy output efficiency (instead of 80–90%) is a result of the fact that the time of grating switching is comparable with and even longer than the time of the pass of the

electromagnetic wave through the ring resonator. During this time the gas discharge is propagated in the grating channels, there is no output of the energy from the resonator in the necessary direction, and a part of the energy stored is scattered on the grating and lost. This effect can be mitigated noticeably by making the length of the storing resonator longer.

Phase-shifter on the basis of active diffraction grating

In a case when the grating is placed inside the resonator it happens to be in a high power field and directly commutates stored power. There is a possibility of placing the grating outside the resonator, Fig. 6, then the grating stands in a less power field and switches the coupling between resonator and output.

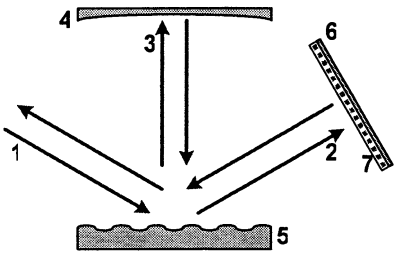

Fig. 6. The concept of future active compressor when diffraction grating is out of resonator and serves as a phase-shifter: *1* – incident beam, 2 – mirror beam, 3 – diffraction beam, 4 – metallic mirror, 5 – metallic grating, 6 – plane mirror, 7 – electrically controlled diffraction grating.

Conclusion

The experiments carried out with the use of the non-vacuum prototype of the three-mirror active compressor show the possibility to obtain efficient compression. At a low power level the power gain equal to 7 was obtained. On the gained experience the future experiments with vacuum set-up at high-power level are planned to be done to achieve higher compression rate.

References

1. *Wilson P.B.*, SLAC-PUB-7449, April, 1997.
2. *Tecker F.*, Highlights from CERN: http://clic-study.web.cern.ch/CLIC-Study/Presentations/20050904.pdf
3. *Denisov G.G., Kuzikov S.V., Bogdashev A.A., Chirkov A.V., Hirshfield J.L., Litvak A.G., Malygin V.I., Shmelyov M.Yu.*, Advanced Accelerator Concepts, 10th Workshop, C.E. Clayton and P. Muggli, eds, AIP Conf. Proc., 2002, **647**, 476.
4. *Petelin M.I.*, Advanced Accelerator Concepts, 10th Workshop, C.E. Clayton and P. Muggli, eds, AIP Conf. Proc., 2002, **647**, 459.
5. *Vikharev A.L., Danilov Yu.Yu., Gorbachev A.M., Kuzikov S.V., Koshurinov Yu.I., Pavelive V.G., Petelin M.I., Hirshfield J.L.*, Advanced Accelerator Concepts, 10th Workshop, C.E. Clayton and P. Muggli, eds, AIP Conf. Proc., 2002, **647**, 448.
6. *Yee K.S.*, IEEE Trans. Antennas and Propagation, 1966, **AP-14**, 302.

LOW-LOSS WAVEGUIDE COMPONENTS FOR TRANSMISSION AND CONTROL OF HIGH POWER MICROWAVE RADIATION IN ECW SYSTEMS

A. V. Chirkov, G. G. Denisov, D. A. Lukovnikov, V. I. Malygin, D. I. Sobolev

Institute of Applied Physics RAS, Nizhny Novgorod, Russia

Transmission lines for megawatt power level continuous wave gyrotrons should have small losses. Ohmic losses causes heating elements of a transmission line that demands their intensive cooling, and diffraction losses often result in arcing in a transmission line and worsening of wave beam structure at the output of the line. Straight corrugated waveguides, miter bends, polarizes, bellows, high-voltage DC breaks, monitors of transmitted and reflected power, mode filters, pumping ports are used in waveguide transmission lines. Each component should have small losses (less than 1%) in order to provide waveguide transmission of megawatt power level microwaves. This paper presents design features and high-power test results of new low-loss components for corrugated waveguide 31.75 mm diameter and 84 GHz frequency.

High power and high frequency of microwaves assume that waveguides for their transmission are oversized in order to provide low ohmic attenuation and low enough electric fields. Such lines are widely used in ECW systems of fusion installations [1, 2, 3]. For such transmission lines various components as miter bends, polarizes, bellows, high-voltage DC breaks, monitors of transmitted and reflected power, mode filters, pumping ports and straight corrugated waveguides are needed. For reduction diffraction losses in miter bends shaped mirrors are used, that essentially reduces diffraction losses [2, 3].

Minimization of diffraction losses in big (comparable with the waveguide diameter) waveguide gaps is a very important task because the gaps are basic elements for key waveguide components as waveguide bends, filters, pumping ports, DC breaks and others [1, 2, 3]. Numerous attempts were performed to make the losses smaller. It is also important to note that the achieved results are still rather far from the losses minimum. We found a systematic approach to the solution of this problem [4]. Using the approach it is possible to find the solution with minimum diffraction losses. It is very important to note, that such a solution complicates a waveguide, adding to it ends converters, but thus essentially improves the component parameters.

New low-loss waveguide components

Detailed calculations were performed for corrugated waveguide 31.75 mm diameter and 84 GHz frequency to design new low-loss components: HE_{11} waveguide mode filter and a miter bend. The calculations aimed to perform a design of a mode filter and a miter bend, which transmits HE_{11} mode with minimal losses and attenuates other modes (especially high-order modes). The mode filter consists of two mode converters (190 mm length) and a big gap

(70 mm) between them [4]. In this case the diffraction losses of HE_{11} mode are 0.3% and the field at the output of the waveguide converter can be approximated as a mixture of three waveguide modes: 81.8% HE_{11} (with zero phase), 17.5% HE_{12} (phase 1.01 radians) and 0.7% HE_{13} (phase 2.83 radians). A synthesized by a new method mode converter [5] has nearly 100% efficiency assuming six lowest forward-propagating waves with the same azimuth index. More precise calculations using a matrix code give the scattering loss of the converter of as 0.2%.

Low power measurements

At first the waveguide mode converter was tested with low power microwave oscillator. The HE_{11} mode exciter with high mode purity ($\eta_{HE11} \geq$ $\geq$ 99.0%) was used. The field structures were measured at the distances 5 mm, 35 mm and 70 mm at the converter output. After reconstruction of wave beam phase front, the mode content at the output of the waveguide mode converter was calculated. The mode content is the following 75.8% HE_{11} (with zero phase), 22.9% HE_{12} (phase 1.01 radians) and 0.5% HE_{13} (phase 2.58 radians). The experimental result agrees well with the theoretical calculation. After this the HE_{11} mode filter was tested with the same low power microwave oscillator (Fig. 1).

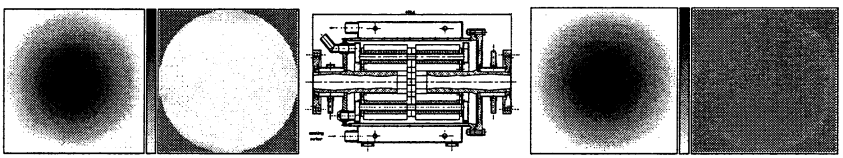

a *b* *c*

Fig. 1. HE_{11} waveguide mode filter: *a* – amplitude and phase distribution at the input (99.0% HE_{11}), *b* – drawing of HE_{11} waveguide mode filter, *c* – amplitude and phase distribution at the output (99.3% HE_{11}).

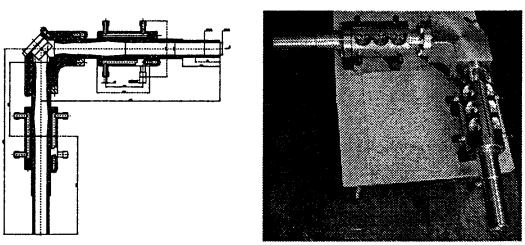

Fig. 2. The drawing and the picture of the miter bend

HE_{11} mode content 99.3% at the mode filter output was measured. So HE_{11} mode filter absorbed some spurious modes. The same results were achieved during the low power measurements of the miter bend (Fig. 2). This miter bend has the

similar construction, as a HE_{11} mode filter, excluding a flat mirror in the middle of the gap. This construction allows turning waveguide transmission line practically at any angle.

High power test results

The HE_{11} mode filter was designed for its use in the evacuated corrugated waveguide line of 31.75 mm diameter transmitting the microwave radiation of Gycom gyrotron (84 GHz / 200 kW / CW) at LHD installation (NIFS, Toki, Japan) (Fig. 3).

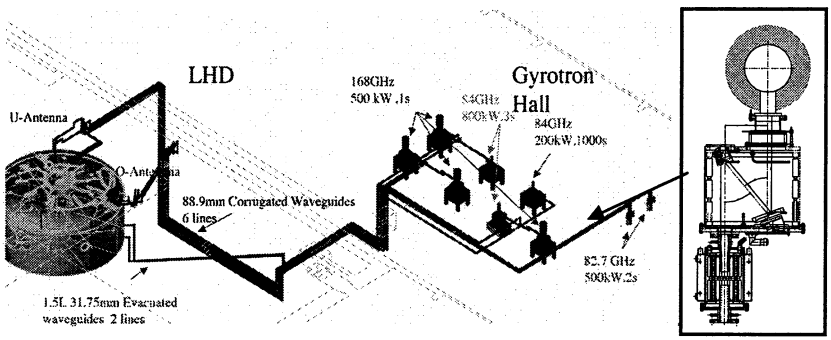

a *b*

Fig. 3. High power test of the HE_{11} waveguide mode filter at LHD: *a* – gyrotrons and transmission lines at LHD, *b* – Gycom gyrotron, MOU and HE_{11} mode filter in an assembly.

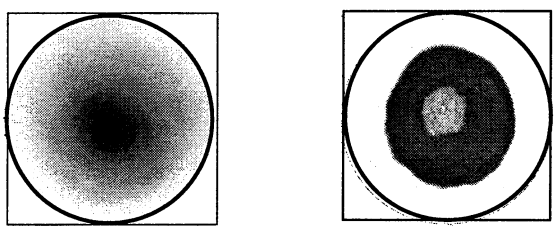

a *b*

Fig. 4. Power distribution at the input (*a*) and at the output (*b*) of the HE_{11} waveguide mode filter.

During a high-power experiment the HE_{11} mode filter was installed between matching optics unit (MOU) and a long (more 70 m) evacuated corrugated waveguide transmission line. The filter was designed to withstand 40% of the total power of a gyrotron. The calculated and measured HE_{11} mode

purity at the filter input was in the range of 96–97% (Fig. 4). In accordance with these figures the loss amount in the filter terminated with a well-matched load was 3– 4% of total power.

It was interesting to monitor the losses in the waveguide mode filter and in MOU for a long-pulse operation (up to 3900 s). First experiment was done with an empty chamber (without plasma) of the LHD and with a microwave power at the output of MOU 200 kW and pulse length t = 1000 seconds. At the beginning of the pulse the losses in the filter were the same as for a matched load. However after some time the losses increased about 3 times (Fig. 5).

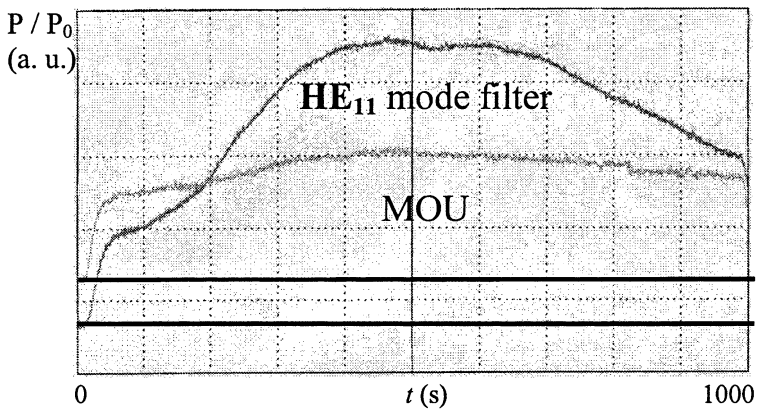

Fig. 5. Measured diffraction losses in MOU and in the HE_{11} waveguide mode filter (P = 200 kW, t = 1000 s).

This increase was caused probably by reflections from the line due to a misalignment caused by thermal expansions of the line sections or by arcing in remote waveguide sections. The power absorbed in MOU increased, however, by only 50%. Second experiment was done with a resonance plasma into the chamber of the LHD and with a microwave power at the output of MOU 170 kW and pulse length t = 3900 seconds. At the beginning of the pulse the losses in the filter were the same as for a matched load. However after some time the losses increased about 50–70%. The power absorbed in MOU increased, however, by only 10–15 % (Fig. 6).

So the HE_{11} waveguide mode filter protected the gyrotron against the reflected power. This allowed very long-pulse operation (200 kW/1000 s and 170 kW/3900 s) of the gyrotron-line system.

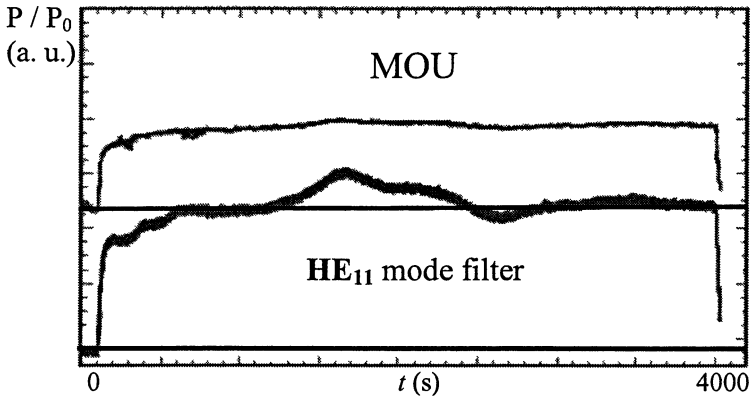

Fig. 6. Measured diffraction losses in MOU and in the HE_{11} waveguide mode filter (P = 170 kW, t = 3900 s).

Conclusion

New systematic approach to the task of diffraction losses minimization in quasi-optical gaps in oversized corrugated waveguides is used. The approach allows designing and optimizing important waveguide components as a miter bend and HE_{11} mode filter. The approach was proved in low and high power tests.

Acknowledgments

Authors are pleased to thank S. Kubo and E.M. Tai for the help and for the participation in the high-power test at LHD.

References

1. *Aleksandrov N.L., Belousov V.I., Bogdashov A.A., Chirkov A.V., Denisov G.G., Malygin V.I., Kuzikov S.V., Kapustin P.A., Lukovnikov D.A., Rodin Yu.V., Shmelyov M.Yu., Vinogradov D.V.*, Development of transmission lines for microwave radiation of powerful gyrotrons, Strong Microwaves in Plasmas, Proc. Int. Workshop, 2000. V. 2, p. 954-960.
2. *Belousov V.I., Chirkov A.V., Denisov G.G., Malygin V.I.*, Improved multi-function miter bends for corrugated waveguides of high-power millimeter transmission lines, Strong Microwaves in Plasmas, Proc. Int. Workshop, 2003. V. 1, p. 264-269.
3. *Belousov V.I., Chirkov A.V., Denisov G.G., Malygin V.I., Shmelyov M.Yu., Kurbatov V.I., Kazanskiy I.V., Solujanova E.A., Tai E.M.*, Transmission lines for microwave radiation of powerful continuous wave gyrotrons, Proc. Joint 29th Int. Conf. Infrared and Millimeter Waves and 12th Int. Conf. Terahertz Electronic, Ed. M. Thumm, W. Wiesbeck, Karlsruhe, 2004, p. 221-222.
4. *Chirkov A.V., Denisov G.G., Lukovnikov D.A., Malygin V.I., Sobolev D.I.*, Minimization of diffraction losses in big gaps of multi-mode waveguides, Int. J. Infrared and Millimeter Waves, 2005. V. 26, № 7, p. 1241-1254.
5. *Denisov G.G., Kalynova G.I., Sobolev D.I.*, Method for synthesis of waveguide mode converters, J. Radiophys. and Quantum Electron., 2004. V. 47, issue 8, p. 615-620.

PARTICLE ACCELERATOR AND MICROWAVE DEVICE APPLICATIONS USING AN ACTIVE MEDIUM

A. Kanareykin, P. Schoessow[1]

Euclid TechLabs, Solon OH, USA
[1]Tech-X Corporation, Boulder CO, USA

There has been considerable theoretical work on the so-called PASER concept [1], in which a particle beam is accelerated directly by absorbing energy from an active medium, analogous to the amplification of an optical signal in a laser. Use of an active microwave (maser) medium would have the advantage of requiring relaxed beam quality (mm vs. nm characteristic beam dimensions) compared to techniques based in optical frequencies. Recent work using electron paramagnetic resonance (EPR) techniques has demonstrated activity in the microwave regime (i. e. negative imaginary part of the magnetic susceptibility) for a class of organic compounds. A solution of fullerene (C_{60}) in a liquid crystal solvent has been reported in the literature to possess a maser transition in the X-band region. An external DC magnetic field is required to obtain the effect; the frequency of the maser transition is adjustable by varying the magnetic field strength. We report on the status of numerical and laboratory tools to evaluate the use of this material for accelerator applications, and eventually the feasibility of an accelerating structure based on an active microwave medium.

A charged particle (or particle bunch) traversing an active medium (i. e. one in which a population inversion has been generated) can absorb energy from the medium and be accelerated [1]. This technique has the potential to be the basis of a new method of acceleration providing high gradients. The effect is similar to the action of a maser or laser with the stimulated emission of radiation being produced by the virtual photons in the electromagnetic field of the beam. While this effect has been explored theoretically there has of yet been no experimental work in this area and little in the way of numerical simulations. We have initiated a research program that would lead to both an improved conceptual understanding of this technique through the development of sophisticated and physically realistic numerical models of the effect, tools for production and bench measurements of the material and eventually to a demonstration of particle acceleration by an active medium.

Until recently, existing solid state maser materials were usable only at cryogenic temperatures, limiting them to a few specialized applications like ultralow noise amplifiers for radio astronomy. Recently published work [2] reports the observation of maser amplification at near room temperature in an optically pumped Fullerene-based material at 9.4 GHz, an ideal frequency match to the beam parameters currently available at accelerator test facilities such as the Argonne Wakefield Accelerator.

While the physics of the masing transition in fullerene compounds is outside the scope of the paper, the basic effect is that an intense optical pulse creates a population inversion in the magnetic Zeeman levels of the molecules.

The material we plan to use must be cooled to –20 C, which is easily achieved with a Peltier device or with dry ice as a coolant. The material is a liquid but can be isolated from the beam channel by a thin walled quartz capillary.

There are a number of possible implementations of active media devices for particle acceleration. The first involves acceleration of a single bunch by the active medium (the basic PASER concept) without the use of a resonant structure. A second related technique would load the active medium in a resonant structure, similar to the dielectric wakefield accelerator, with the fundamental resonant frequency of the structure adjusted to correspond to the frequency of the masing transition. The device could then be used to amplify the wakefield of a drive beam for acceleration of a trailing witness beam. Yet another approach is to use the active medium, loaded into a resonant cavity of the appropriate frequency and with appropriate optical pumping as an rf power source to drive a conventional iris-loaded or dielectric structure directly.

We also plan to investigate applications of active media to compact microwave devices like low-noise amplifiers and adjustable frequency filters. Permanent magnets can be obtained with maximum remanent fields of 1.4 T, while the medium needs only ~0.3 T. Frequency adjustments could be made by mechanically deforming an external magnetic circuit containing a permanent magnet. A spatially varying magnetic field could be used to produce a bandpass filter with adjustable properties. The principal difficulty is injecting the pump radiation into the device, which may be overcome by using optical fibers.

Numerical simulations

We are developing a computer code to be able to reliably model an accelerating structure loaded with the active medium. The starting point of the computational effort will be the Arrakis code [6]. Arrakis was developed for the AWA/AATF program and has been used for many years to simulate wakefield and rf driven dielectric devices. Arrakis has proved to be an accurate and versatile tool for electromagnetic modeling of dielectric structures, especially in situations where material properties more complicated than constant permittivity/permeability are important. The code has been verified against AATF and AWA measurements and has been used to study nonlinear, anisotropic and lossy media effects.

An active gain medium can be treated as one in which the imaginary parts of the permittivity or permeability are negative rather than positive, so that an electromagnetic wave propagating in the medium gains energy rather than attenuates. From a numerical standpoint the situation is complicated by the frequency dependence of ε and μ, whereas we want to solve the problem of an accelerated beam in the time domain.

Consider a wakefield structure consisting of a dielectric tube, outer radius 1.5 cm, inner radius 0.75 cm. We assume that the medium has a permittivity

$\varepsilon = 2$ and an imaginary part of the permeability $\mu_i = -0.01$ [2]. This structure then has its fundamental TM_{01} mode at 9.4 GHz. We model the gain with a magnetic current term in Faraday's law:

$$\text{curl } \mathbf{E} = -\mu_r/c\ \partial\mathbf{H}/\partial t + 4\pi\ \sigma_M/c\ \mathbf{H}. \quad (1)$$

Here σ_M is the magnetic conductivity, and $\mu_i = 4\pi\ \sigma_M/\omega$. We compute the wakefield in this structure taking a rms bunch length $\sigma_Z = 0.5$ cm, sufficiently long that the TM_{01} mode predominates, so we can ignore any frequency dependence of σ_M. We also neglect saturation effects and dielectric losses. The longitudinal electric field in the vacuum gap is shown in Fig. 1.

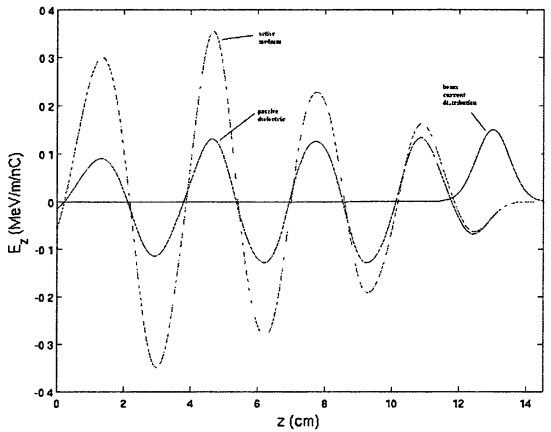

Fig. 1. Arrakis simulation of the longitudinal wakefields in 9.4 GHz structures loaded with an active medium and a conventional dielectric of the same permittivity.

We note in this case that the wakefield of the bunch is indeed amplified due to the activity of the medium. The accelerating gradient is enhanced by an easily detectable factor ~3 over the structure with no media activity.

A more realistic algorithm has recently been developed by Taflove and Hagness [4] to incorporate the effect of an active medium into a time-domain finite-difference code and also to include dispersive effects. This approach is based on the observation that a constitutive relation like $B(\omega) = \mu(\omega)\, H(\omega)$ where $\mu(\omega)$ is a quotient of polynomials in ω can be converted to an ordinary differential equation in the time domain using the inverse Fourier transform. The order of the auxiliary differential equation is the same as the highest power of ω present in either the numerator of denominator. At each time step, the constitutive relation is applied using the auxiliary differential equation to derive the magnetic field H from the induction B obtained from Faraday's law. H in turn is used to advance the electric field using Ampere's law.

If the permeability of the active medium is of the form

$$\mu(\omega)=1 + 4\pi\kappa/(\omega_0^2 - \omega^2 + i\omega/T) \quad (2)$$

the auxiliary differential equation is

$$d^2B/dt^2 + (1/T)dB/dt + \omega_0^2\, B(t) = d^2H/dt^2 + (1/T)dH/dt + (\omega_0^2 + 4\pi\kappa)\, H(t). \quad (3)$$

The algorithm for deriving H from B is

$$H(t) = \Sigma_{k=1}^{3}\, a_k\, H(t - k\Delta t) + \Sigma_{k=0}^{1}\, b_k\, B(t - k\Delta t), \quad (4)$$

where the a_k and b_k are chosen to make the expression correct to second order. (Mesh cell indices have been omitted for simplicity.) The algorithm requires additional memory backstorage but is otherwise straightforward to implement.

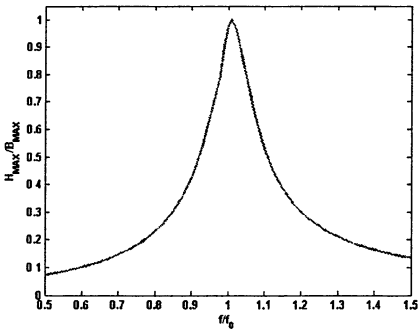

Fig. 2. Test of auxiliary differential equation algorithm (4) for the permittivity given by eq. (2). The material is driven by a spatially uniform sinusoidal magnetic field. The expected Lorentz behavior as a function of frequency is obtained. (The vertical axis scale is arbitrary).

Figure 2 shows the result of numerically solving the auxiliary differential equation (3). A sinusoidal magnetic field was applied to the active medium and the corresponding intensity calculated. The frequency was swept through the resonant frequency. The ratio of the field amplitudes shows the expected Lorentzian shape.

Another possibility is to use a running FFT of the fields and to invert the constitutive relation directly at the cost of additional memory since some portion of the time history for each finite difference mesh cell must be retained throughout the calculation. A similar technique [5] has been used to model dispersion in ferrites but to our knowledge has not been applied to active media.

EPR measurements

This work will rely heavily on development and EPR measurements of fullerene materials. We will develop a design for a prototype accelerating structure using this material with attention to details of pumping and maximizing energy gain. Preparation of the active material described in [2] a solution of C_{60} in a nematic liquid crystal, is not problematic. We have obtained initial samples of the active material and a number of related materials and are expecting the first results of the EPR testing very soon.

The basic EPR resonance condition in a paramagnetic spin system is $\omega = g\beta H$, where ω is the Larmor frequency, β is the Bohr magneton. The g-factor can vary between 1 and 2 depending on spin-orbit interactions in the material. A free electron has $g = 2$. Thus EPR frequencies are in the microwave regime ($\lambda \sim 3$ cm for $H \sim 3000$ Oe). The conventional way to detect EPR is to measure the change in the quality factor of a microwave cavity under the resonance condition. The sensitivity of EPR spectrometers is about 10^{10} spin/Oe. The ratio to magnetic units means that the sensitivity depends on line width and

the narrower the line, the easier it is to detect it. The conventional continuous wave EPR spectrometer uses a modulation of the magnetic field (usually 100 kHz) to observe the spectrum.

Transient signals excited for example by laser pump pulses can be time resolved by applying a pulse sequence and sampling at an increasing time offset with respect to the start of each pulse to obtain a time-resolved spectrum. In the case of exciting transient EPR spectra of C_{60} it is necessary to apply a laser pulse sequence directly into the microwave cavity. This technique is especially relevant to the diagnosis of activity in our samples since the generation of a population inversion in the fullerene-liquid crystal solution requires an optical pulse excitation.

Experiments carried out earlier showed that the EPR spectra and activity of C_{60} are strongly dependent on the solvent used. It is important for our purposes that C_{60} in different organic solvents or liquid crystals is light sensitive and undergoes reversible changes in the optical or EPR absorption spectra. Such light sensitive media demonstrate transient magnetization for about 1 s in duration after laser or xenon lamp pulse excitation. Thus the experiments can be carried out by either steady-state or time-resolved EPR in the presence of repetitive light pulses.

An absolute quantity of C_{60} in the $5\times10^{-4} - 2.5\times10^{-3}$ M range supplies no less than 3×10^{14} spins per probe; thus one can easily establish the requirements for EPR instrumentation sensitivity. These spins contribute to the C_{60} EPR signal that can be excited by 20–25 mJ/pulse irradiation with wavelengths of 200–350 nm. The EPR signal of the triplet state of C_{60} can be generated by pulses either from an excimer laser with a wavelength of 308 nm or from Nd:YAG laser at a second harmonic of 532 nm [2,7]. The pulse length of 10–12 ns with a repetition rate of 10–80 Hz is easily synchronizable with the EPR magnetic field sweep.

Summary

We are investigating a new microwave active material for accelerator applications. Initial work in this area will emphasize numerical modeling and sample preparation and characterization. If successful this effort will lead to beam tests of an active media based accelerator.

This work is supported by the US Department of Energy.

References

1. *Schachter L.*, Phys. Lett., 1995, **A205**, 355-358; *Schachter L.*, in Advanced Accelerator Concepts, APS Conf. Proc. **335**; *Schachter L.* Phys. Rev. Lett., 1999, **83,** 92-95.
2. *Blank A. et al.*, IEEE Trans. Microwave Theory and Techniques, 1998, **46,** 2137.
3. *Blank A., Levanon H.*, Appl. Phys. Lett., 2001, **79**, 1694.
4. *Taflove A.*, Computational Electrodynamics Artech, 1995.
5. *De Ford J. et al.*, Particle Accelerators, 1994, **45** (135).
6. *Schoessow P., Gai W.*, in Quantum Aspects of Beam Physics P. Chen ed., World Scientific, 1999.
7. *Closs G., et al.* J. Phys. Chem., 1992, **96**, 5228-5231; *Regev A., et al.* J. Phys. Chem. 1993, **97**, 3671-3679.

RADIATION SPECTRUM OF PLANAR FEM AT DIFFERENT CONDITIONS OF 2D DISTRIBUTED FEEDBACK REALIZATION

A. V. Arzhannikov, N. S. Ginzburg[1], *V. G. Ivanenko, P. V. Kalinin, A. S. Kuznetsov, S. A. Kuznetsov, N. Yu. Peskov*[1], *A. S. Sergeev*[1], *S. L. Sinitsky, V. D. Stepanov, V. Yu. Zaslavsky*[1]

Budker Institute of Nuclear Physics, SB RAS, Novosibirsk, Russia
[1]Institute of Applied Physics, RAS, Nizhny Novgorod, Russia

Results of investigations of radiation spectrum in planar FEM with a hybrid Bragg resonator at the ELMI-device are presented. Radiation spectrum measured in "hot" experiments is compared with results of computer simulations and "cold" tests of the resonator.

Introduction

Experiments with planar 4 mm Free Electron Maser (FEM) carried out in collaboration between BINP RAS and IAP RAS are directed on development of powerful source of spatially coherent radiation when the transverse size of the electron beam substantially exceeds the wavelength. To solve problem of transverse mode selection and spatial synchronization of radiation the use of 2D distributed feedback, which can be realized in 2D Bragg resonators, has been proposed [1, 2]. The operability and high selective properties of such resonators have been demonstrated experimentally [3]. Nevertheless implementation of 2D Bragg structures in "hot" experiments associates with some complications, which are mainly related to the compatibility with the beam transportation system. Special feature of the above structures is the transverse energy fluxes, which just serve for synchronization of emission from different parts of a large-size sheet electron beam. In ideal situation these fluxes should freely escape from the resonator [2, 3]. However in the real experimental conditions strong reflections of such fluxes from the side walls of the vacuum chamber should take place. These spurious reflections result in appearance of additional modes.

In recent experiments at the ELMI-accelerator (BINP RAS) a hybrid resonator consisting of up-stream 2D Bragg reflector and down-stream 1D Bragg reflector [4] was used (Fig. 1). In the ideal case of 2D Bragg structure, which is opened in the transverse directions, the hybrid resonator should posses only several high-Q modes in the vicinity of the precise Bragg frequency (75 GHz) with different longitudinal indexes. For experimental geometry shown in Fig. 1 frequency interval between these modes (which can be called "grating" modes) is ~250 MHz. Above modes were chosen for the FEM operation. However in the experiments alongside with excitation of the operating modes some parasitic generation at frequency bands of 73 and 78 GHz were observed.

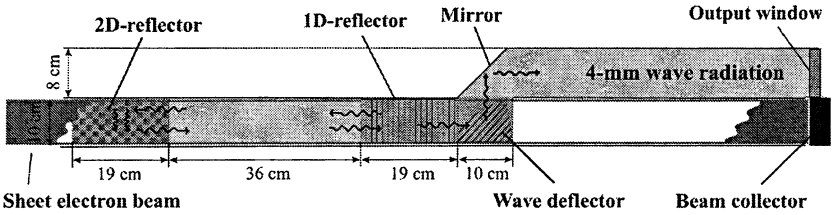

Fig. 1. Scheme of the planar FEM experiment at the ELMI-accelerator

Based on theoretical consideration this spurious generation is caused by appearance of additional modes due to the strong side-wall reflection inside the up-stream 2D Bragg structure. Obviously in the case of closed cavity the transverse propagating nearly cut-off energy fluxes form spectrum of the high-Q modes in the absence of grating. For such modes (which can be called "transverse" modes) the grating provides coupling of the transverse fluxes with longitudinally propagating fluxes and acts to decrease their Q-factors. Nevertheless under the certain conditions, because the forward propagating partial wave is synchronous to the electron beam, the self-excitation of such modes can be realized. (It should be noted that above mechanism of coupling the cut-off trapped mode with the propagating mode can be used for mode selection in the case of moderately oversized systems [5]). To suppress "transverse" parasitic modes in recent experiments the side walls of the 2D reflector were coated by a microwave absorber.

The present paper is devoted to the results of simulations, as well as "cold" and "hot" experiments, in which influence of side-wall reflections in the 2D Bragg structure on the mode spectrum and corresponding radiation spectrum of the FEM, was studied.

Results of simulations and "cold" tests

A scheme of planar FEM is shown in Fig. 1. A 3 kA / 1MeV sheet electron beam with a cross section of 0.4×7 cm propagates in a guide magnetic field of 1.2 T and the undulator field of about 0.2 T and 4 cm period. The hybrid resonator has a gap of 1 cm and consists of two Bragg reflectors and a regular waveguide section of 36 cm length between them. The up-stream 2D Bragg reflector has "chessboard" corrugation with 4 mm period in both directions and depth of 0.2 mm. The down-stream 1D reflector has corrugation in the form of parallel grooves with a period of 2 mm and depth of 0.07 mm.

Results of simulations for the frequency response of the hybrid resonator excited by a wide-band RF-pulse are shown in Fig. 2, *a*. Different lines correspond to different values of the side-wall reflection coefficient R for the 2D

Bragg structure. In the case of small side reflections ($R \sim 0.1$, thin line) three high-Q "grating" modes at the frequencies of 74.9, 75.1 and 75.3 GHz are presented in the resonator spectrum. In contrast, in the case of "closed" 2D reflector ($R \sim 0.99$, dashed line) the spectrum contains mainly "transverse" modes at the frequencies of 73.3 and 76.6 GHz. As mentioned above, these modes are originated from transverse energy fluxes trapped between closed ends of the reflector. For moderate reflections (thick line) both types modes are presented in the resonator spectrum.

In "cold" microwave tests of the resonator the modes of both types are registered as well. As seen from Fig. 2, *b* and 2, *c*, without the side-wall absorber the Q-factors of the "grating" and the "transverse" modes are close to 500 and 2000 respectively. Installation of "thin" absorber (side reflection coefficient was measured in "cold" tests as

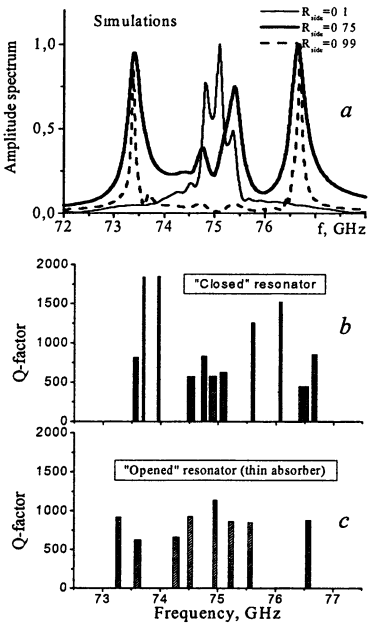

Fig. 2. Results of simulations (*a*) and "cold" measurements of the resonator mode spectrum in the case of different side-wall reflections (*b*, *c*).

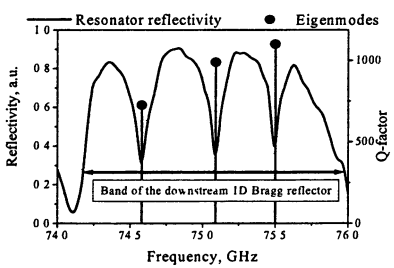

Fig. 3. Results of "cold" measurements of "grating" modes in hybrid resonator with "thick" absorber.

$R \sim 0.5$) results in decrease in the Q-factors of the "transverse" modes. Figure 3 demonstrates the position of operating "grating" modes observed in "cold" tests with "thick" side-wall absorber (side reflections were measured as $R \sim 0.15$). The Q-factor of the "grating" modes remains on the same level, i. e. ~1000, while the Q-factors of the "transverse" modes were ~500–800.

Spectral diagnostics

Two types of diagnostics of frequency spectrum of the FEM radiation have been developed. The first one is wide-band 4-channels quasi-optical diagnostics realized on the basis of a quasi-optical transmission line (Fig. 4, *a*) containing four

pass-band Fabry–Perot filters as spectrally selective elements. Each filter is represented by a pair of 2D "inductive" copper meshes deposited on a textolite substrate and has the following geometrical parameters (Fig. 4, *b*): $g = 1$ mm, $a = 0.32$ mm, $t = 0.018$ mm, $d = 0.9$ mm, $L \cong 8$ mm, a clear aperture size 100×100 mm. Typical values of transmission band and contrast of such filters are $\Delta\nu_{FWHM} \approx 0.68$ GHz and 25 dB respectively for the range of 73–77 GHz. The average frequency difference between the transmission maximums of neighboring filters is ~0.95 GHz (Fig. 4, *c*) that is provided by 100 μm variation of the intermesh gap L. The microwave signal after each Fabry–Perot filter is registered by a low-power detector and further digitized by an ADC with 5 ns time resolution.

The second diagnostics is a single-channel measuring system based on heterodyne technique with a frequency resolution of ±10 MHz. Such resolution is

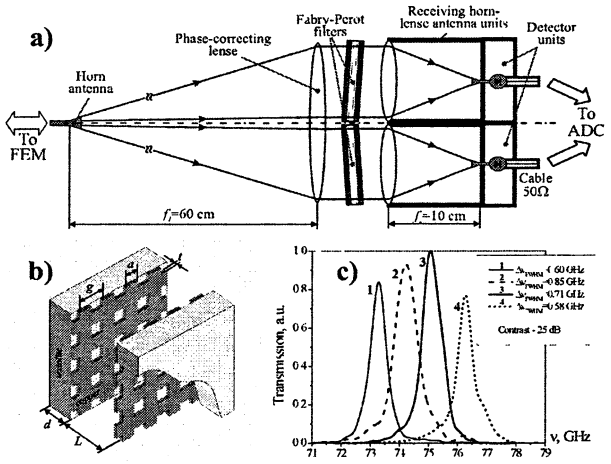

Fig. 4. Scheme of quasi-optical diagnostics (*a*) based on pass-band Fabry–Perot mesh filters (*b*); amplitude-frequency response of the four spectral channels (*c*).

determined by frequency instability of an industrial driving BWO-oscillator. The intercarrier frequency signal is registered by the digital oscilloscope with declared bandwidth 500 MHz. The measuring system includes a tunable pass-band filter with a bandwidth of ~1 GHz.

Results of "hot" experiments

Results of spectral measurements of the radiation obtained in a typical shot in the FEM with hybrid resonator having "thin" absorber at side walls are shown in Fig. 5, *a–e*. The analysis of time behavior of "Fabry–Perot" signals reveals the tendency that while the lower frequencies (bands 1, 2) are presented

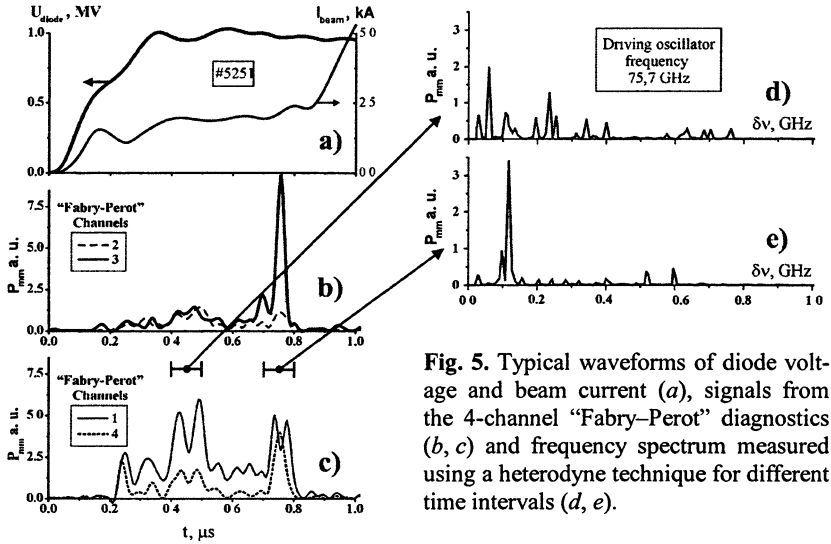

Fig. 5. Typical waveforms of diode voltage and beam current (*a*), signals from the 4-channel "Fabry–Perot" diagnostics (*b*, *c*) and frequency spectrum measured using a heterodyne technique for different time intervals (*d*, *e*).

both in the beginning and in the end of the radiation pulse at approximately the same level, excitation efficiency for higher frequencies (bands 3, 4) rises to the end of the pulse (see Fig. 5, *b*, *c*). Such retuning of the radiation spectrum might be explained both by changing the energy of the beam electrons and the mode competition effect. The analysis of Fourier decomposition of the heterodyne intercarier frequency signal for different time intervals of this radiation pulse (see Fig. 5, *d*, *e*) allows us to reveal the regime of single mode generation, which exists during ~100 ns interval. This behavior is in good correlation with the sharp growth of the signal in the channel 3 of the "Fabry–Perot" diagnostics. This effect is seen from the Fig. 5, *b*, *e* by the example of excitation of one of the "grating" modes.

Application of "thick" absorber in "hot" experiments permits us to observe the single- or quasi-single mode generation during 200 ns. As an example, we present in the Fig. 6 three shots demonstrating FEM operation at the modes with frequencies 75.1 GHz and 75.5 GHz. These heterodyne frequency measurements coincide with the results of "cold"

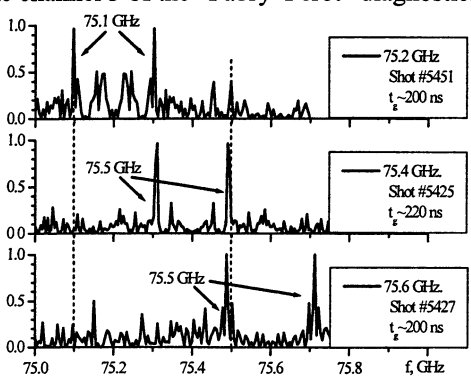

Fig. 6. Radiation spectrum demonstrating excitation of grating modes in three different shots (lines denoted by the arrows refer to the same frequency).

tests given in Fig. 3. At the bottom trace small shift of the mode near 75.1 GHz can be explained by the instability of the driving oscillator. Nevertheless spectrums measured by "Fabry–Perot" diagnostics showed a significant number of shots with generation at frequencies within the bands corresponding to the parasitic "transverse" modes of the resonator.

Conclusion

Both simulations and "cold" tests demonstrate the existence of the high-Q "grating" and "transverse" modes in the hybrid Bragg resonator with significant side-wall reflections. In the FEM experiments high level of the radiation spectral density near the frequencies corresponding to modes of both types has been observed. With installation absorber at side walls of 2D Bragg structure the regimes of narrow band generation with duration ~200 ns at the frequencies of the operating modes, i. e. "grating" modes of the 2D Bragg structure in the vicinity of 75 GHz, has been obtained.

It should be noted in conclusion that there are several ways to diminish influence of side wall reflections. One of them it is to install side reflector at some angle to the system axis so that the reflected wave-beams not fully returned back into the interaction space. Another way is circular connection of the transverse energy fluxes in up-stream 2D Bragg reflector by an additional loop that according to the simulation strongly increase Q-factor for the operating modes.

Acknowledgements. The work was partially supported by CRDF Grant NO-008-X1 and RFBR Grant 05-02-17036. The authors are grateful to Prof. M. Thumm for support in provision of the experiments and useful discussions.

References

1. *Arzhannikov A.V., Ginzburg N.S., Peskov N.Yu. et al.*, The 14th Int. FEL Conf., Kobe, Japan, 1992, p. 214.
2. *Ginzburg N.S., Peskov N.Yu., Sergeev A.S., Arzhannikov A.V., Sinitsky S.L.*, Nucl. Instr. Meth. in Phys. Res. A, 1995, **A358**, 189.
3. *Peskov N.Yu., Ginzburg N.S., Denisov G.G. et al.*, these proceedings, vol. 1, p. 321-329.
4. *Ginzburg N.S., Peskov N.Yu., Sergeev A.S., Arzhannikov A.V., Sinitsky S.L.*, Tech. Phys. Lett., 2000, **26**, 8.
5. *Ginzburg N.S., Malkin A.M., Peskov N.Yu. et al.*, these proceedings, vol. 1, p. 233-238.

MODE-LOCKING IN A DIELECTRIC WAKEFIELD RESONATOR ACCELERATOR

T. C. Marshall, I. N. Onishchenko[1], *N. I. Onishchenko*[1], *G. V. Sotnikov*[1]

Columbia University, New York City, U.S.A.
[1]NSC "Kharkov Institute of Physics and Technology", Kharkov, Ukraine

The multi-mode regime of wakefield excitation in a planar dielectric resonator by a regular sequence of electron bunches is studied. It is shown that the amplitude of the wakefield increases in comparison with a section of the waveguide of the same length. Moreover, the train of bunches provides mode-locking of the dielectric resonator.

Acceleration of charge bunches using wakefield in dielectric structures (DWFA) is a "two-beam" method of acceleration in which short relativistic driver bunches of large charge build up a high accelerating field for following "test" bunches. At BNL [1] it is proposed to use for excitation of the accelerating field the a sequence of supershort (duration of 3.5 fs) electron bunches with energy 500 MeV, and in experiments at ANL [2] the sequence of short (duration of 6.7 ps) electron bunches with energy 15 MeV is used.

The DWFA can operate in single-mode [2] or multimode [3] regimes. Wakefield amplitude in the multimode regime of DWFA is much higher than in the single-mode regime.

Below, we study the multimode excitation of wakefields by a sequence of electron bunches in the a planar dielectric resonator. The need for a resonator concept of DWFA arises in connection with the necessity of eliminating the undesirable effect of wakefield, which occurs with the group velocity with the waveguide dielectric structure [4]. The first results of theoretical examination [5] and numerical calculations with the PIC code KARAT [6], carried out for a cylindrical dielectric resonator geometry, showed that the strong restriction on the maximum number of bunches which may contribute to the growth of amplitude of the field, can be removed using the resonator concept of DWFA. Under optimum conditions, excitation of dielectric resonator by a sequence of bunches is similar to the excitation of an optical resonator by a mode-locked laser equipped with an "optical switch". At the moment when the short pulse of radiation reflected from the output of the resonator appears at the input, the optical switch injects the next impulse into the resonator. In cylindrical geometry it is difficult to realize a multimode condition of DWFA operation. Below, in planar geometry, we will consider the combination of the resonator together with the already described advantages of the dielectric waveguide, and the multimode and multibunch regimes.

Wakefield in the planar dielectric resonator

Let the rectangular metal resonator have a transverse size $a\,(-a/2 \le x \le a/2)$ and $b\,(-b/2 \le y \le b/2)$, its length equal to L. The resonator is filled by the a homogeneous dielectric with permittivity ε. Along the axis of the resonator there is a drift channel, the transverse dimensions which are small in compared with those of the resonator. We will suppose that monoenergetic, thin electron bunches are injected into the input of the resonator $z = 0$ and then move with a constant velocity v_0 along the axis. The distribution of current density of a single bunch has the form of:

$$j_z = Q_b \delta(x - x_0)\delta(y - y_0)\delta(t - t_{0i} - z/v_0) \times$$
$$\times [\theta(t - t_{0i}) - \theta(t - t_{0i} - L/v_0)]/v_0, \qquad (1)$$

where Q_b is the charge of a bunch, t_{0i} is the time of the i-th bunch injection into the resonator, x_0, y_0 are transverse coordinates of a bunch, $\theta(t)$ is the Heaviside function, $\delta(t)$ is the Dirac function.

Having solved the wave equation and taking into account the vanishing of the tangential components of electric field on the metal walls of the resonator, we obtaine the expression for the longitudinal electric field:

$$E_z = E_0 \sum_{i=1}^{N_b} \sum_{\substack{m,n=1 \\ l=0}}^{\infty} \cos(k_l z) \frac{\delta_l \omega_{100}}{\omega_{mnl}^2 - \omega_l^2} \left\{ \left[\frac{\omega_{mn0}^2}{\omega_{mnl}} \sin\omega_{mnl}(t - t_{0i}) - \omega_l \left(1 - \frac{c^2}{v_0^2 \varepsilon}\right) \times \right.\right.$$
$$\times \sin\omega_l (t - t_{0i}) \Big] \theta(t - t_{0i}) - (-1)^l \left[\frac{\omega_{mn0}^2}{\omega_{mnl}} \sin\omega_{mnl}(t - t_{0i} - L/v_0) - \right.$$
$$\left.\left. - \omega_l \left(1 - \frac{c^2}{v_0^2 \varepsilon}\right) \sin\omega_l (t - t_{0i} - L/v_0) \right] \theta(t - t_{0i} - L/v_0) \right\} G_{mn}(x, y, x_0, y_0), \qquad (2)$$

where: $E_0 = -16\pi Q_b v_0 / abL\varepsilon\omega_{100}$; $\omega_{mnl}^2 = c^2(\kappa_{xm}^2 + \kappa_{yn}^2 + k_l^2)/\varepsilon$; $\omega_l = k_l v_0$; $\kappa_{xm} = \pi m / a$; $\kappa_{yn} = \pi n / b$; $k_l = \pi l / L$; the function δ_l is equal 1 if $l = 0$ and is equal 2 if $l \ne 0$; N_b is the number of bunches in a sequence; $G_m(x, x_0) =$ $= \sin[\kappa_{xm}(x + a/2)]\sin[\kappa_{xm}(x_0 + a/2)]\sin[\kappa_{yn}(y + a/2)] \times \sin[\kappa_{yn}(y_0 + a/2)]$.

When all particles have left the resonator ($t > t_{0Nb} + L/v_0$) the field of the space charge (second expression in square brackets) disappears, and the expression for the longitudinal electric field is the sum of traveling forward and backward eigen-waves of the dielectric resonator:

$$E_z = E_0 \sum_{i=1}^{N_b} \sum_{\substack{m,n=1 \\ l=0}}^{\infty} \cos(k_l z) \frac{\delta_l \omega_{100}}{\omega_{mnl}^2 - \omega_l^2} \frac{\omega_{mn0}^2}{\omega_{mnl}} \left[\sin\omega_{mnl}(t - t_{0i}) - \right.$$

$$- (-1)^l \sin \omega_{mnl}(t - t_{0i} - L/v_0)\Big] G_{mn}(x, y, x_0, y_0). \quad (3)$$

We note, that for the condition

$$\omega_{mnl} = \omega_l \quad (4)$$

the relevant items in the sum (2), (3) become dominant. This condition is nothing but the condition of Cherenkov radiation in a slowing medium. This is why these resonant items can be treated as a Cherenkov field accumulated in the dielectric resonator. The rest of the field is the field of the transition radiation from both boundaries.

Because of the discreteness of the longitudinal wave numbers of the oscillation spectrum, the resonant condition for the optiomum sizes of the resonator, permittivity, and energy of the bunch can be fulfilled only approximately and only for a finite number of harmonics. Taking into account that we want to implement a multimode condition of DWFA, it makes sense to find the relation between the above quantities from the resonant requirement.

We now find the relation for a 2-d dielectric resonator (size in the y-direction is greater than the size in x-direction). Let the resonant condition be fulfilled for harmonic $m = 1$, $l = N$. Then from (3) we obtain

$$L = Na\sqrt{\beta_0^2 \varepsilon - 1}, \quad \beta_0 = v_0 / c, \quad (5)$$

i. e. the length of the resonator should be a multiple half-integer of wave lengths of the fundamental resonant harmonic. The condition of equal spacing is fulfilled automatically for harmonics $l = Nm$ ($m = 1, 2, \ldots$). Thus, the multimode operating regime of the DWFA is provided.

To obtain the coherent summation of fields in the resonator it is necessary, that the resonant frequency ω_{1N} be a multiple of the frequency of the following bunches. In the case when the bunches are injected at every period of the fundamental harmonic with frequency $f = \omega_{1N}$ of the wave, this condition sets the transverse size of the dielectric resonator as

$$a = v_0 / 2f\sqrt{\beta_0^2 \varepsilon - 1}. \quad (6)$$

Conditions (5) and (6) are the basis of the resonator concept of the dielectric wakefield accelerator. In such a resonator there will occur a multimode regime of field excitation and a coherent summation of fields from the injected bunches.

The wakefield from a sequence of bunches of finite size is obtained by integration of expression (2) over the time of injection t_{0i} and the locations x_0 of the point bunches.

We choose the following parameters for numerical calculations: dielectric permittivity $\varepsilon = 2.1$; frequency of bunch repetition $f = 2.85$ GHz; energy of the bunches is 4 MeV; transverse size chosen according to condition (6) $a = 5{,}045$ cm and the length of the resonator, chosen according to requirement (5), $L = 15.677$ cm (tenth longitudinal harmonic is chosen as resonant, $N = 10$);

the length of bunch $L_b = 1.7$ cm; the height of bunch $a_b = 0.1a$; $2Q_b / b = 0.32$ nC/cm.

In Figure 1 the time dynamics of the wakefield ($x = 0$) at the input of the dielectric resonator after injection of a single bunch is presented, the bunch having left the resonator at time $t \approx 1.75$ ns. The wakefield at the input of the resonator (as well as at any spatial point inside the resonator) has a nonregular behavior in time (see the left graph), even though the peaks of the wakefield follow with a period approximately equal to the period of the basic resonant mode.

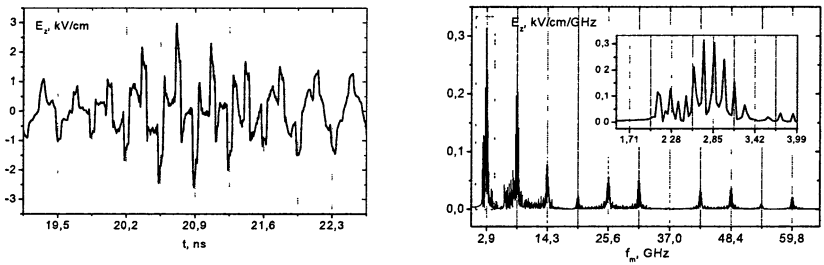

Fig. 1. Time dependence of longitudinal electric field at the input of the dielectric resonator (left) and its spectral density after injection of a single bunch (right).

The longitudinal distribution of the wakefield also has a nonregular character. The envelope of the field is nonuniform along the length of the resonator. Its structure varies with time; the maximum is periodically displaced from one wall of the resonator to another. The irregularity of the wakefield is related to the excitation by a single bunch of set of nonresonant longitudinal harmonics. These nonresonant harmonics can be attributed to the transition radiation [4], which has a wide spectrum. This is verified by the spectral density of the longitudinal electric field given in right part of Fig. 1. In this graph the peaks of spectral density corresponding to the excited longitudinal harmonics of the field are clearly visible.

In Figure 2 the axial distributions of wakefield build up by injecting a sequence of 101 bunches into resonator is presented: the left figure corresponds to the time $t = 1.738$ ns (the first 5 bunches are injected into the resonator) and the right figure corresponds to the time $t = 35.639$ ns (when the last bunch of the sequence is injected into the resonator).

At the initial stage, the amplitude of the field grows from the head of a sequence of the bunches to the location of the group wave front, excited by the first bunch, and then decreases backwards to the input of the resonator. The wakefield in the resonator before the first bunch leaves is qualitatively and quantitatively the same as the field in a semi-infinite waveguide. The shape of the wakefield impulses and their duration approximately repeats the shape and

duration of the bunches. At later times, after all the bunches have been injected into the resonator, a nearly homogeneous distribution of field amplitude is formed.

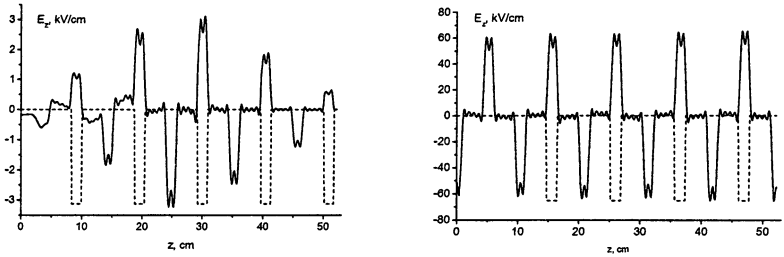

Fig. 2. Axial distributions of wakefield in the centre of resonator ($x = 0$) when injecting a train of bunches. Dashed lines show the shape and location of bunches.

The case in the semi-infinite waveguide in contrast to the resonator with regard to the increasing input to output distribution of field amplitude [4] is formed. The number of bunches participating in the build up to maximum amplitude is much lower, compared with the resonator. For a dielectric waveguide having the same length, transverse size and permittivity as the resonator, this number of bunches is equal 6. By comparison of the left and right graphs of Fig. 2 we conclude that all bunches of the sequence equally contribute to the formation of the longitudinal electric field amplitude in resonator: i. e., it is possible to excite a wakefield in the resonator with the amplitude considerably exceeding the amplitude of the field in the semi-infinite waveguide. The regularity of the oscillations is maintained.

We now show the mode-locking from the excitation of the dielectric resonator by a sequence of electron bunches. For this purpose we shall compare the temporal dynamics of the longitudinal electric field at a fixed point of the resonator when it is excited by a single bunch and by a train of 101 bunches. In Figure 3 (left part), the time dependence of the longitudinal electric field at the input end of the resonator is presented. The last bunch has left the resonator at time $t \approx 38$ ns. The wakefield at the input of the resonator has a pattern of a sequence of rectangular pulses with period equal to the period of the bunch repetition rate. The amplitude of the pulses varies weakly with time. At the right side of Fig. 3 the spectrum of the longitudinal electric field is presented. It is seen that wakefield contains only odd resonant frequencies. Non-resonant harmonics contribute very little to the amplitude of the wakefield.

We now compare this spectral density with the spectral density of the field, excited by a single bunch (see Fig. 1). It is seen that a train of bunches regularizes the wakefield, suppresses non-resonant longitudinal harmonics and strengthens the resonant harmonics of a field. In other words, the regular sequence of bunches realizes mode-locking of the dielectric resonator.

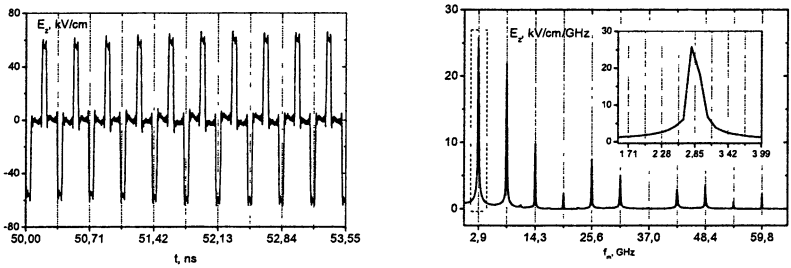

Fig. 3. Time dependence (left) of the longitudinal electric field and its spectral density (right) in the dielectric resonator after injection of 101 bunches.

Acknowledgments

This study was supported by CRDF Grant # UP2-2569-KH-04 and Ukr. DFFD 02.07/325.

References

1. *Marshall T.C., Wang C., Hirshfield J.L.*, Phys. Rev. STAB, 2001, **4**, 121301.
2. *Power J.G., Conde M.E., Gai W., Konecny R., Schoessow P., Kanareykin A.D.*, Phys. Rev. STAB, 2000, **3**, 101302.
3. *Zhang T.B., Hirshfield J.L., Marshal T.C., Hafizi B.*, Phys. Rev. E, 1997, **56**, 4647.
4. *Onishchenko I.N., Sidorenko D.Yu., Sotnikov G.V.*, Phys. Rev. E, 2002, **65**, 066501.
5. *Balakirev V.A., Onishchenko I.N., Sidorenko D.Yu., Sotnikov G.V.*, Tech. Phys. Lett., 2003, **29**, 589.
6. *Marshall T.C., Fang J-.M., Hirshfield J.L., Park S.J.*, In AAC Ninth Workshop, AIP Conf. Proc., № 569 (AIP, New York, 2001), p. 316.

PSEUDOSPARK-SOURCED ELECTRON BEAM GENERATION

A. W. Cross, H. Yin, W. He, K. Ronald, A. D. R. Phelps

Department of Physics, University of Strathclyde, Glasgow, G4 0NG, UK

A pseudospark discharge has been shown to be a promising source of high brightness, high intensity electron beam pulses. A pseudospark-sourced electron beam has two phases, an initial hollow cathode phase beam followed by a conductive phase beam. In our experiments, a 22 kV, 50 A hollow cathode phase beam of brightness 10^9–10^{10} A·m^{-2}·rad^{-2} followed by a 200 V, 200 A conductive phase beam of brightness 10^{11}–10^{12} A·m^{-2}·rad^{-2} were measured. Experiments have been conducted with the application of a hollow cathode phase beam in a Cherenkov interaction with no input seed wave and with post-acceleration of the conductive phase beam. The transportation of the pseudospark beams was investigated. An experiment has been designed using the hollow cathode phase beam from a pseudospark discharge in a Cherenkov maser amplifier driven by a 20 kW, 35 GHz pulsed magnetron. In this paper, some simulation results of electron beam formation from a pseudospark discharge will be presented.

1. Introduction

The pseudospark discharge was first discovered in 1977 and first developed as an electron beam source in 1978 by Christiansen and Schultheiβ at the University of Erlangen, Erlangen, Germany [1]. It is an axially symmetric, self-sustained, transient, low pressure (typically 50–500 mTorr) gas discharge and takes place in a special hollow-electrode geometry of a hollow cathode / planar anode configuration in various gases such as nitrogen, argon, hydrogen and xenon, etc. It operates on the left-hand side (with respect to the minimum) of the hollow-cathode analogy to the Paschen curve (Fig. 1). The breakdown voltage behaviour of a pseudospark discharge is characterized by being located on the left branch of a function similar to Paschens law. A fast voltage breakdown together with a fast current rise is typical for this discharge resulting in a class of high-power gas-phase switches used in pulsed power applications [2, 3]. Another remarkable feature of the pseudospark is the complex discharge development with different discharge phases, during which bright electron beams, ion beams and extreme ultraviolet (EUV) radiation can be generated. Therefore the breadth of unusual and interesting properties of pseudospark discharge has led to di-

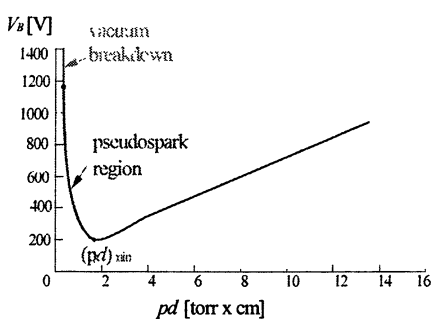

Fig. 1. Breakdown voltage as a function of pressure times anode-cathode distance showing pseudospark region of operation.

verse applications such as pulsed-power switching, electron beam generation and free electron masers, EUV generation and pseudospark microthrusters etc [4–7].

2. Pseudospark electron beam investigation

During a pseudospark discharge, a low temperature plasma is formed as a copious source of electrons and can be regarded as a low work function surface that facilitates electron extraction. Initial study of electron beam production was carried out on a single-gap pseudospark system for a wide range of parameters, including cathode cavity length, cathode hole size, applied voltage, external capacitance and the inductance in the discharge circuit [8]. Higher-energy electron beam production, more suitable for high power microwave generation, was studied using multi-gap pseudospark systems. Electron beam pulses of duration of tens of ns, current density (>10^8 A·m^{-2}), brightness of up to 10^{12} A·m^{-2}·rad^{-2} and emittance of tens of mm mrad were measured from a pseudospark discharge [9]. A typical pseudospark electron beam trace is shown in Fig. 2.

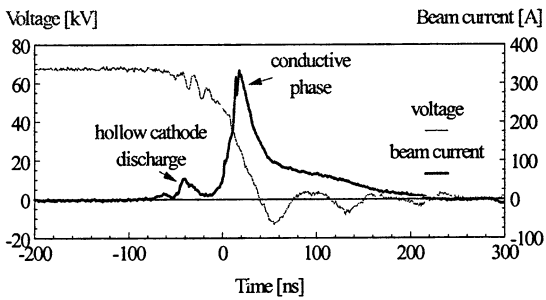

Fig. 2. Typical beam current and voltage traces from the 8-gap pseudospark discharge used for the Cherenkov maser experiments.

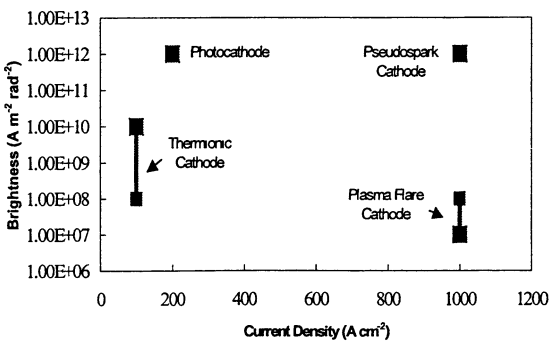

Fig. 3. Brightness as a function of current density for various electron beam sources.

This beam has a higher combined current density and brightness compared to electron beams formed from any other known type of electron source (Fig. 3).

The CP beam had been transported in a plasma induced ion background and simultaneously accelerated by an accelerating potential [10].

3. Cherenkov maser – simulation and experiments

The HCP beam was initially applied in a Cherenkov maser interaction with the background seed signal which was generated from the pseudospark discharge itself [11, 12]. The schematic setup of the initial pseudospark-based Cherenkov maser experiment is shown in Fig. 4. The main components of the experiment are the pseudospark-based electron beam source, the magnetic field for beam transport, the Cherenkov interaction region, electrical/beam diagnostics and the microwave launching/diagnostic system. The Cherenkov interaction cavity was made of a section of cylindrical waveguide, 9.5 mm in diameter, lined with a 1.75 mm thick layer of dielectric (alumina, $\varepsilon_r = 9.5$). The dielectric liner was used to slow down the normal electromagnetic modes in the cylindrical waveguide, allowing a resonant interaction to occur between a TM or HE waveguide mode and the rectilinear electron beam. Coherence of the generated radiation arises due to bunching of electrons in phase with respect to the electromagnetic wave. The calculated dispersion diagram in Fig. 5 shows the waveguide modes and the slow space charge mode of a 75 kV, 10 A electron beam [13]. It was found experimentally that significant microwave radiation was generated only when the dielectric was present in the interaction space, although if there was no dielectric in the cylindrical waveguide, then a very small background microwave output was detected.

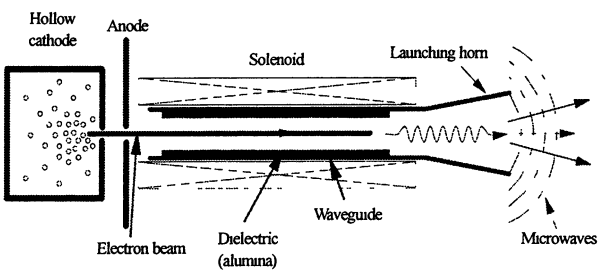

Fig. 4. Initial Cherenkov maser experiment outline

This demonstrated in conjunction with the observation that the microwave output signal was independent of the guide magnetic field over the range 0.13 to 0.26 T that the radiation from the experiment was due to the Cherenkov interaction mechanism. In addition, two components of the microwave pulse were observed corresponding to the two energy components of the electron beam during the pseudospark discharge breakdown. Another interesting result was the discovery that the small background signal was always present even without the guide B-field or dielectric lining in the waveguide. These results demonstrated that the

microwave radiation grew from a background seed signal, which was produced by the pseudospark discharge itself. The frequency range of the microwave radiation from the Cherenkov maser amplifier was measured to be between 25.5 and 28.6 GHz by applying different cylindrical cut-off filters in the waveguide.

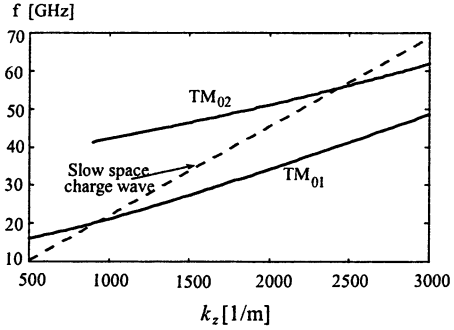

Fig. 5. Dispersion diagram showing the waveguide modes and slow space charge mode of the electron beam (75 kV, 10 A).

The output antenna pattern associated with the azimuthal E-field component was measured to be independent of the presence of the dielectric and close to zero, confirming the operation of a TM mode. The measured pattern was in good agreement with the results from bench experiments in which a 27 GHz TM_{01} microwave signal was launched using the same horn. This confirms the operation mode to be the TM_{01} mode. The peak power was measured to be around 2 ± 0.2 kW and the gain to be 29 ± 3 dB. A relative spectral energy distribution was obtained and approximately 65% of the radiation was found to lie in the 25–28.6 GHz frequency band.

4. Discussion, conclusion and future work

In future experiments we will investigate the Cherenkov interaction between a pseudospark electron beam and a seed signal produced by a 20 kW, 35 GHz pulsed magnetron. The experimental setup is similar to the one shown in Fig. 4 apart from the addition of an input coupler which is needed to introduce the seed signal from the magnetron. The interaction cavity has a similar structure as shown in Fig. 4, except that the dielectric liner is to be tapered at both ends to reduce reflections. The dispersion diagram is shown in Fig. 6, where the dispersion of a TM_{01} mode has been calculated analytically and simulated by a particle-in-cell (PIC) code MAGIC. It can be seen that the interaction between the TM_{01} wave mode and a 75 kV, 10 A electron beam occurs around 21 GHz, and for a 4 kV, 20 A beam the interaction takes place at around 34 GHz. The previous Cherenkov experiment demonstrated that microwave radiation was produced between 25.5 and 28.6 GHz, which is higher than 21 GHz as predicted from the calculation and simulation shown in Fig. 6.

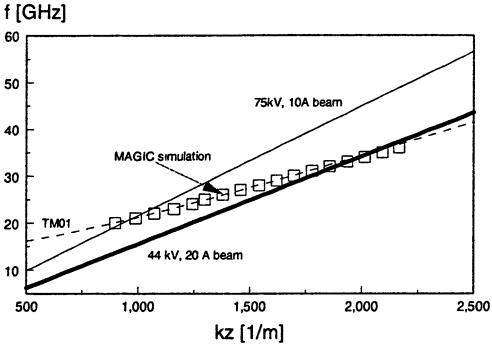

Fig. 6. Dispersion diagram of TM_{01} mode calculated and simulated by MAGIC code (squares) and slow space charge mode of the electron beams.

This discrepancy can be explained when dielectric charging [14] of the alumina by the electron beam is taken into account. Using MAGIC, the interaction frequency between TM_{01} mode and the electron beam was calculated against the beam voltage. It was found that the lower the voltage, the higher the interaction frequency.

A pseudospark-sourced electron beam was applied in a Cherenkov maser with no input seed signal. The microwave radiation was generated by Cherenkov amplification of the broadband emission from the pseudospark discharge itself. The frequency of the microwave output after the Cherenkov maser interaction was measured to be mainly around 25.5 GHz and the dominant mode was identified as being the TM_{01} mode. A peak power of 2 ± 0.2 kW and gain of 29 ± 3 dB was measured.

References

1. *Christiansen J., Schultheiss C.*, Z. Phys., 1979, vol. A290, p. 35.
2. *Bischoff R., Frank K., Iberler M., Petzenhauser I., Rainer A., Urban J.*, IEEE Trans. Plasma Sci., 2004, vol. 32, no. 1, Special Issue on Pseudospark Physics and Applications, p. 191-195.
3. *Heo H., Park S.S., Nam S.H.*, IEEE Trans. Plasma Sci., 2004, vol. 32, no. 1, Special Issue on Pseudospark Physics and Applications, p. 195-202.
4. *Gunderson M.A., Schaefer G.*, NATO ASI Ser. B, New York, Plenum, 1990.
5. *Frank K., Christiansen J.*, IEEE Trans. Plasma Sci., 1989, vol. 17, p. 748–753.
6. *Rosier O., Apetz R., Bergmann K., Jonkers J., Wester R., Neff W., Pankert J.*, IEEE Trans. Plasma Sci., 2004, vol. 32, no. 1, Special Issue on Pseudospark Physics and Applications, p. 240-245.
7. *Verboncoeur J.P., Chen H.P., Minnich A.*, Modelling of a MEMS Pseudospark Microthruster, Bull. Am. Phys. Society (APS), 2004, vol. 49, no. 8.
8. *Yin H., He W., Cross A.W., Phelps A.D.R., Ronald K.*, J. Appl. Phys., 2001, vol. 90, p. 3212–3218.
9. *Yin H., Phelps A.D.R., He W., Robb G.R.M., Ronald K., Aitken P., McNeil B.W.J., Cross A.W., Whyte C.G.*, Nucl. Instr. and Meth. Phys. Res. A, 1998, vol. 407, p. 175–180.
10. *Yin H., Cross A.W., He W., Phelps A.D.R., Ronald K.*, IEEE Trans. Plasma Sci., 2004, vol. 32, no. 1, Special Issue on Pseudospark Physics and Applications, p. 233-239.
11. *Liou R., Figueroa H., McCurdy A.H., Kirkman-Amemiya G., Temkin R.J., Fetterman H., Gundersen M.A.*, Appl. Phys. Lett. 1992, vol. 61, p. 2779.
12. *Ramaswamy K., Destler W.W., Rodgers J.*, J. Appl. Phys., 1998, vol. 83, p. 3514.
13. *Yin H., Robb G.R.M., He W., Phelps A.D.R., Cross A.W., Ronald K.*, Phys. Plasmas, 2000, vol. 7, p. 5195–5204.
14. *Garate E., Cook R., Heim P., Layman R., Walsh J.E.*, J. Appl. Phys., 1985, vol. 58, p. 627.

MICROWAVE INJECTOR FOR "ARCHIMEDES" NUCLEAR WASTE SEPARATOR

Yu. Ya. Brodsky, Yu. V. Bykov, A. V. Chirkov, G. G. Denisov, A. G. Eremeev, A. S. Fix, S. V. Golubev, A. A. Litvak, A. G. Litvak, L. V. Lubyako, N. V. Lunin, V. I. Malygin, V. V. Parshin, A. O. Perminov, S. Putvinski*, A. G. Shalashov, E. V. Suvorov*

Institute of Applied Physics, RAS, Nizhny Novgorod, Russia
*Archimedes Technology Group, San Diego, USA

Theoretical and experimental investigations have been carried out at Institute of Applied Physics supporting an alternative concept of neutral gas feed system for the "Archimedes" nuclear waste separator based on microwave heating and evaporation of the working matter injected into the vacuum chamber as a dispersed liquid aerosol.

Introduction

"Archimedes" facility has been designed for atom separation according to their masses basing on the idea of magnetron effect, and is proposed for extraction of radioactive fraction in the Hanford nuclear waste for improved utilizing [1]. In the original design it has been supposed that waste composed mainly of NaOH will be injected into the vacuum chamber in the form of vaporized gaseous flow, and then ionized by the plasma. An alternative concept of neutral gas feed system based on microwave heating and further evaporation of the working matter injected into the vacuum chamber as a dispersed liquid aerosol is discussed in the present communication. Theoretical and experimental investigations carried out at IAP to support the concept include the following main aspects:

- Theoretical modeling attesting that efficient evaporation can be realized with microwave sources of moderate power (up to 100 kW) provided that high-frequency conductivity of the working matter lies in a fairly broad range from 50 to 10^4 S/m.
- Measurements of high-frequency conductivity of molten NaON alkali resulting in the optimization of droplet size (diameters 0.5–1 mm).
- Design and assembling of the test facility for experimental demonstration of injector operation, including vacuum chamber with pump-out system, aerosol drop forming device, 20 kW / 83 GHz gyrotron microwave source, in-vessel electrodynamics system, and diagnostics.
- Demonstration of the injector operation with the productivity 1–5 g/s of evaporated mass both for pure molten NaOH with optimal droplet diameters and for $NaOH/Al_2O_3$ mixture (roughly modelling the nuclear waste composition).

Vaporizer concept based on microwave heating of aerosol

"Archimedes" facility has been designed to provide separation productivity of 1–5 g/s. Corresponding evaporation system based on microwave heating of the liquid droplets may be realized with microwave sources of moderate power. For example, taking specific evaporation heat $q_{ev} = 3.6$ kJ/g, productivity $G = 1$ g/s and neglecting all losses besides the aerosol heating, one can obtain the minimum power level $q_{ev} G = 3.6$ kW. It may be shown that accounting for all essential power losses under "Archimedes" conditions would result in the increase of required microwave power from few 10 up to 100 kW (the level which is accessible with industrial gyrotrons) provided that aerosol particle size and flow velocity are optimized in order to increase rf power deposition and to avoid parasitic effects, such as radiation scattering and vapor break-down.

Schematic view of the proposed evaporation system is shown in Fig. 1. This is a longitudinal cross-section of a cylindrical vacuum chamber. At "Archimedes" conditions the aerosol volume is optically thin for singe pass absorption of microwave radiation. In order to reach the estimated minimum power level the quasi-optical system is proposed which allows a finite number of microwave beam passes through the evaporation region. The number of beam passes (nine) is chosen in such a way that it is of the same order as number of passes limited due to absorption of rf radiation by the background plasma. Aerosol is heated mainly inside the working volume, where effective amplification of rf field intensity is provided. This volume coincides with the central (focused) part of rf beams. Important constrain on evaporation system design is implied by condition, that plasma rotation does not disturb the trajectory of aerosol particle inside the beam. To satisfy this condition the aerosol flow velocity must be high enough, what limits the maximum residence time of a droplet in the rf interaction volume.

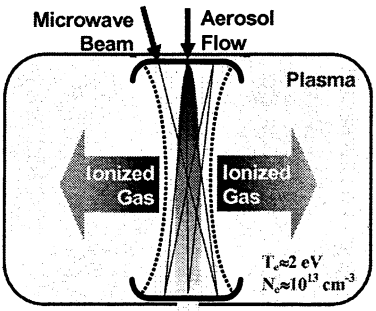

Fig. 1. Schematic view of the rf evaporation system.

Summarizing the results of feasibility study of the microwave evaporating system for the "Archimedes" facility, a basic scenario has been proposed in which the main part of mass is evaporated due to a single pass of aerosol particle through the system. Important parameters of this scenario are as follows: aerosol injection rate 1 g/s; reference microwave frequency 110 GHz; microwave power 100 kW for evaporation efficiency 85%; effective rf power density flux 70 kW/cm^2; aerosol flow velocity 30 m/s; optimal radius of aerosol particles 300 μm; evaporation time 10 ms; working volume about 10 cm^2×30 cm.

Further investigations supporting this concept were mainly aimed to demonstration of principal realization of microwave evaporating for molten nuclear

waste. Having available a limited power gyrotron (20 kW cw), the demonstrating experiments were performed with low aerosol flow velocity about 3 m/s. This essentially simplified construction of the droplet injector and up to one order of magnitude reduced the required rf power level. However electrodynamics components for quasi-optical cavity were designed having in mind application in the "Archimedes" facility with higher power loads up to 100 kW cw.

Mie modeling of rf power absorption by a spherical droplet under conditions of the performed experiments demonstrated that droplets with "optimal" diameters in a fairly broad range 0.5–1 mm may be effectively evaporated, i. e. loose significant part of their mass for residence time 100 ms, with input rf power 5 kW and more. With larger droplets (1–2 mm) it is also possible to reach the required evaporation rate about 1 g/s with reasonable level of rf power taking into account that at least about 2/3 of power is not absorbed but scattered; however one should keep in mind that in this case only a relatively small fraction of each particle is evaporated. With particle size decrease absorption efficiency drops tremendously, thus small particles (< 0.2 mm) would hardly been evaporated under any reasonable conditions of the experiment.

Measurements of high-frequency conductivity of molten alkali

To apply theoretical calculations to real experimental conditions it is rather important to specify the value of high-frequency conductivity of the evaporated matter. That was the motivation to perform measurements of high-frequency specific conductivity of molten NaOH alkali in mm wavelength range. Three independent techniques were used based on measurements of Q-factor of quasi-optical Fabry–Perot cavity, reflection coefficient from the plane surface of molten alkali, and thermal radiation from the same surface. The most reliable data related to frequency range 90–140 GHz were obtained by a rather sophisticated technique based on the measurements of Q-factor of quasi-optical Fabry–Perot cavity. Techniques based on the direct measurements of reflection coefficient and thermal radiation at 90 GHz from the sample surface of molten alkali are in agreement with the results following from Q-factor measurements.

The measured value of high-frequency conductivity of NaOH is more or less linearly increasing with temperature from about 150 S/m at 320 °C (melting) up to 400 S/m at 600 °C. These values of high-frequency conductivity satisfy the requirements for the evaporating system based on direct microwave heating of NaOH aerosol.

Test facility designed at IAP for evaporation of molten alkali

Scheme of the experimental facility is shown in Fig. 2. Radiation from the gyrotron (*1*) is transmitted by the quasi-optical matching optics unit (*2*) and injected into the vacuum chamber (*3*). The gyrotron (GCGT 83 GHz/20 kW) is

capable of operating in both cw and pulsed regimes with the output power in the range 2–20 kW. Microwave field intensity inside the working volume is increased by the quasi-optical system of 18 mirrors (*4*) placed inside the vacuum chamber and forming the "quasi-cavity". Wave beam trajectories inside this system are sketched in Fig. 3. Vertical aerosol flow is produced by a droplet injector (*5*) situated at the top of the chamber. The droplet forming is based on the development of Raleigh–Taylor instability in a free liquid jet formed by the pressure controlled syringe injector. The system provides molten NaOH droplet jet with initial velocity up to 2 m/s, droplet diameters within the range 0.6–3 mm, and temperatures up to 600 °C. The evaporated alkali is partially deposited on the walls of the vacuum chamber and partially pumped out by the vacuum system (*6*) consisting of a nitrogen trap, turbomolecular and fore-vacuum pumps (providing pump-out rate 500 l/s and initial pressure at the level 10^{-4} Torr).

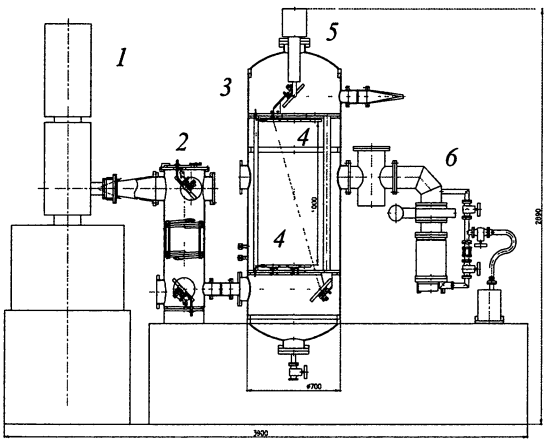

Fig. 2. The test stand: *1* – gyrotron microwave source; *2* – quasi-optical transmission line, MOU; *3* – vacuum chamber with diagnostics; *4* – in-vessel "quasi-cavity" mirrors; *5* – droplet injector; *6* – vacuum pump-out system.

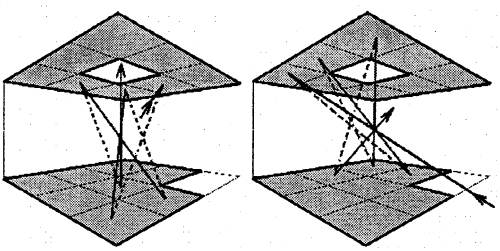

Fig. 3. Scematic view of Gaussian wave beam trajectories inside the "quasi-cavity": 9 rays from bottom mirrors to top mirrors are crossing the center axis.

In the course of experiments there was a possibility to measure droplet distributions over diameters and horizontal positions via three diagnostics ports:

the top one situated above the "quasi-cavity", the middle one looking into the waist of rf field distribution and the bottom one for droplet diagnostics after their interaction with rf field. Optical diagnostics of the droplet parameters is based on recording using a CCD camera of droplet shadows at the screen, when droplets are illuminated with laser radiation. Besides, the total evaporation efficiency has been more reliably determined by weighting of the non-evaporated fraction gathered into a special quartz cup placed in the bottom of vacuum chamber.

Throughout test of the facility with water droplets have been performed using low temperature injector before operation with alkali.

Experimental results on evaporation of molten NaOH alkali droplets

Experiments were performed with two injector nozzle diameters provided different droplet distributions over sizes. Droplet injector with nozzle diameter 0.3 mm provided productivity up to 1 g/s; in the droplet distribution pronounced peak was observed around diameter 0.6 mm. Reservoir volume of injector allowed investigating continuous droplet chain up to 40 s duration which was enough for statistical processing of droplet size distribution using the shadow photo diagnostics. Typical example of droplet distributions over diameters as seen in the top and the bottom diagnostics ports is shown in Fig. 4. It is clearly seen that after interaction with rf field narrow peak in the distribution is shifted to the diameter region around 0.2 mm, which corresponds to far above 90% mass evaporation efficiency. Unfortunately, the main part of mass (up to 70%) was concentrated in a large-scale fraction in the diameter region 0.7–1.5 mm that resulted in the essential decrease of the total evaporation efficiency as compared to 0.6 mm droplets (down to approximately 30% as measured by weighting of non-evaporated fraction).

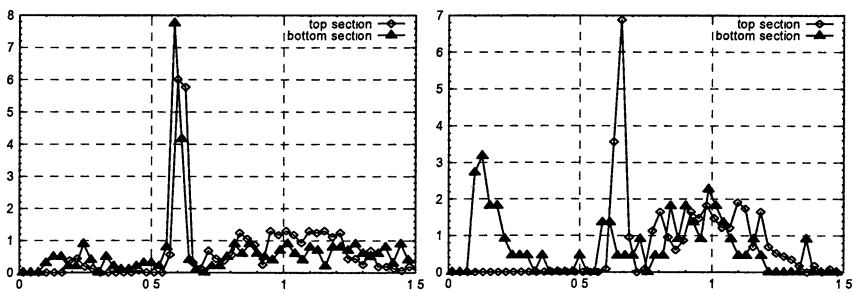

Fig. 4. Distribution of droplets over diameters in the top (◈) and bottom (▲) cross-sections for 0 kW (left) and 83 GHz/8 kW (right) rf power launched. Horizontal axis shows diameter in [mm], vertical axis shows distribution function in [mm^{-1}].

Thus the droplet injector with 0.3 mm nozzle failed in production of mono-size droplets which are evaporated with high efficiency. Moreover, injector with small nozzle from time to time had breaks in operation even with pure NaOH alkali as working substance due to jam formation inside the nozzle channel. The situation was even more drastic with small admixture of Al_2O_3 powder composed of rigid particles with a 10 μm characteristic size (first approach to the modeling of real nuclear waste composition). To overcome this problem the injector nozzle diameter was changed to 0.8 mm what resulted in formation of droplets with a rather broad diameter distribution within the range 1–2 mm. Under these conditions admixture of Al_2O_3 powder up to 10% never prevented the normal operation of the injector; injector productivity was a few g/s. The rate of evaporation obtained by the weighting procedure reached 2 g/s with evaporation efficiency 30–40% (corresponds to about 10–15% decrease in droplet size), which is close to the total evaporating efficiency obtained with the small nozzle. Chemical analysis of non-evaporated working matter showed that both fractions (NaOH and Al_2O_3) are in proportion corresponding to the initial composition of working matter.

After performed investigations it seems that the microwave injector concept will work in the real facility provided that a special system for utilization of non-evaporated substance is supplied. In particular, a multi-nozzle syringe injector producing 1–2 mm droplets with evaporation efficiency about 30% may be considered as alternative providing high productivity of evaporated working substance for the "Archimedes" facility.

References

1. http://www.archimedestechnology.com

WAKEFIELDS SET UP BY RELATIVISTIC ELECTRON BUNCHES AS A SOURCE OF HIGH INTENSITY PULSED MICROWAVES

T. C. Marshall[1], *S. V. Shchelkunov*[1], *Changbiao Wang*[2], *J. L. Hirshfield*[2,3]

[1]Applied Physics Department, Columbia University, New York City 10027, USA
[2]Omega-P, Inc., New Haven CT 06511, USA
[3]Physics Department, Yale University, CT 06520, USA

Energy radiated by a relativistic electron bunch passing through a dielectric liner can be a source of high intensity, broadband, microwave Cherenkov radiation. This radiation, confined within an enclosed structure, sets up wakefields which trail the bunch. We begin by showing how the wakefields may be enhanced by constructive superposition of the fields radiated by a bunch train, resulting in localized on-axis electric fields ~100 MeV/m. The spectrum of coherent bunch radiation extends to a wavelength somewhat shorter than the bunch length, and consists of a set of TM modes equally spaced in frequency; thus a bunch having RMS length of 0.3 ps will have a spectrum extending to THz frequency. Wakefield radiation can be extracted from the structure and brought to a remote focal spot, using a quasi-optical mirror. At this spot, a pulse intensity ~100 GW/cm^2 will result from a single, 1 nC, 0.3 ps, 100 MeV bunch.

Introduction

Wakefield accelerators are generally attractive because injection from an external source of rf energy is not required, and accelerating fields are generated from only bunches themselves. In the conventional dielectric wakefield accelerator (DWA), a dielectric-lined waveguide supports a longitudinal electric wakefield induced by the passage of an electron bunch. Phase velocities for the modes of dielectric-lined waveguide can be less than the speed of light, so that Cherenkov radiation occurs, manifesting itself as a wakefield that reflects periodically from the conducting wall and fills the waveguide behind the drive bunch. The source of power required for acceleration of the drive bunches can be provided by an efficient conventional rf linac. High acceleration fields are believed to be possible in the dielectric because it is exposed to intense fields for only a very short time. The breakdown limit of the wakefield structure is not determined by the slow filling time of the structure by electromagnetic energy, but rather by the much shorter time of the passing field pulses set up by the short bunches which build up the wakefields.

In 1999, some new refinements were proposed to boost the acceleration gradient in dielectric-lined waveguides [1]. Comparatively short drive bunches were suggested, so that excitation of a large number of high-amplitude TM_{0m} eigenmodes would form a high-amplitude wakefield. The waveguide design [2] would be chosen so that the wakefield is nearly periodic, with the same period

as that of the train of drive bunches. The interaction between the wakefield and electron bunches in cylindrical dielectric-lined waveguides has been theoretically analyzed in recent years [1, 3–6]. However, it has been pointed out that a rectangular structure made from slabs of dielectric is superior to the cylinder in that the mode dispersion is smaller and that the stability of the bunches is better; thus a longer train of bunches may be used to construct a larger wakefield than in the example of the cylinder. Rectangular structures for wakefield acceleration have been recently analyzed [7, 8, 9]. In this paper, we shall consider what is interesting in this topic from the point of view of the wakefield radiation [10], rather than accelerating particles. By proper choice of waveguide dimensions and dielectric, a distinctive sharply pulsed wakefield is found which trails the particles as they move along the axis of the channel in the dielectric. This wakefield can have a time signature in the ns-ps range with multi-megawatt power level [11], and the efficiency of bunch energy conversion into radiation is high (~30%). We begin with a schematic of the theory, present some examples, and show how the radiation might be extracted and directed onto a sample.

Theory

In cylindrical geometry, orthonormal wave functions can be found for the fields which separate into TE and TM classes for axisymmetric excitations, and into hybrid modes with mixed polarization otherwise. With axisymmetric bunch distributions, only TM modes have an electric field (E_z) that is finite at the bunch location, and that consequently contributes to the radiation generated. Axisymmetric TE modes have vanishing electric fields on axis. Non-axisymmetric modes that contribute to (unstable) transverse motions are excited by a bunch moving off-axis [3]. Conditions can be found where all TM modes have phase velocities equal to the speed of the electrons ($v \cong c$), and so wake fields move in synchronism with the bunches. We neglect contributions from transition radiation localized near axial boundaries of the dielectric insert [5].

To find wake fields induced by an electron bunch, one expands in orthonormal modes the solution of the inhomogeneous wave equation and constructs a Green's function. For instance, for a bunch containing N_b electrons distributed along a finite RMS length

$$\Delta z = 2\sqrt{\langle z^2 \rangle - \langle z \rangle^2} \tag{1}$$

in a Gaussian function (symmetrical distribution), one finds

$$E_z(r, z, t) = -E_0 \sum_m \left[f_m(r)/\alpha_m \right] \cos(\omega_m z_o / v) \exp\left(-\omega_m^2 \Delta z^2 / 8v^2\right). \tag{2}$$

Here, $E_0 = -eN_b / 2\pi\varepsilon_0 A^2$, and the results are valid only behind the bunch ($Z_0 < 0$), following the dictates of causality; in front of the bunch $E_z = 0$. Note

that only the radius of the hole A, and the bunch charge $-eN_b$ determine the total magnitude of the wake field, while the RMS bunch length Δz determines the distribution of amplitudes amongst the spectrum of normal modes. The energy loss dW/dz and total radiated power scale as N_b^2. Everywhere behind the Gaussian bunch

$$dW/dz = \frac{N_b^2 e^2}{4\pi\varepsilon_0 A^2} \sum_m \left(\exp(-\omega_m^2 \Delta z^2 / 8\nu^2)\right)^2 / \alpha_m \,. \tag{3}$$

An example of the power spectrum which we predict to be emitted from a typical well-focused bunch obtained at ATF, Brookhaven, is shown in Fig. 1, *a*. Radiation spectra from a Gaussian charge distribution having different RMS-lengths are shown. Most of the power is contained in the mm-wave portion of the spectrum. We have found that the choice of axial charge distribution is not important, providing each distribution is characterized by the same bunch RMS-length. In Figure 1, *b*, we show a spectrum generated by three different bunch shapes: a Gaussian, an asymmetrical triangular, and a rectangular charge distribution along the bunch length axis. For each example, the same RMS-length is chosen for the bunch. The result is quite interesting, as it shows that as long as the bunch RMS-length is used for comparison, the spectrum generated is almost the same. The physical reason for this result is that coherent bunch radiation requires generation of wavelengths which are longer than the bunch. These wavelengths cannot yield information about the fine-scale charge or current variation within the bunch. Accordingly, one finds, examining Fig. 1, *b*, that whatever sensitivity to the bunch charge profile is revealed only at the shortest wavelengths.

We can make a few general observations. First, the dielectric must be low loss, vacuum compatible, have a high breakdown strength, and be free of dispersion if the wakefield is to excite a large range of modes.

Secondly, theory largely treats a system that extends infinitely far in each direction; this however does not allow for end effects (e. g. transition radiation) which have been studied by others [5]. Third, dispersion arising from the geometry is more serious in the cylindrical configuration than in the rectangular configuration: this will limit the number of bunches in a train whose wakefields may be successfully superimposed. Fourth, stability considerations will set limits on the distance a bunch can propagate and the number of bunches which can be used to build up wake fields; it is found that stability for bunch motion in tall rectangular structures is superior to cylindrical structures. Finally, structures characterized by a large aperture and thin dielectric liner (or slab) support few modes, and can be designed to favor just one; whereas structures characterized by a small aperture and thick liner will set up a wide spectrum of TM modes if excited by a short bunch. Thus the radiation can be nearly monochromatic and appear as pulses lasting several nsec, or it may be broad-band and result in a single psec pulse or a pulse train.

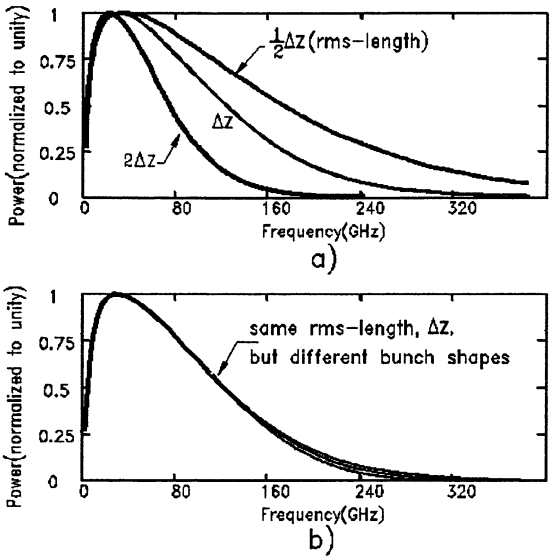

Fig. 1. Power spectrum that we predict from a typical well-focused bunch obtained at ATF-BNL. Radiation from a Gaussian charge distribution having different RMS-length[1]; Δz = 1.8 ps (*a*). Spectrum generated by three different bunch shapes: a Gaussian, an asymmetrical triangular (tail/head = 4/1), and a rectangular charge distribution along the bunch length axis (*b*). The normalized power emitted by each TM mode (shown as an unbroken line) is plotted, even though the mode spacing is ~2.8 GHz.

Examples

The first example we describe is that of the nearly single-mode wakefield, which can be developed at wavelengths ranging from mm's (ps bunches) [12] to μm's [11] (fs bunches) using narrow slabs of dielectric lining a rectangular structure. For injection into a rectangular-slab dielectric structure, a bunch with a slab shape can be made by distorting a circular cross section bunch using a quadrupole. When driven by a train of drive bunches spaced at the period of the most intense mode, a nearly sinusoidal wakefield results which will become progressively more monochromatic as the number of drive bunches is increased. In the case of a mm-dimensioned rectangular structure, there is the possibility of an application as a harmonic multiplier [13]. A rectangular dielectric slab structure lined with diamond as a dielectric has been designed to support a wakefield LSM mode at 102.8 GHz; this can be driven by bunches obtained from a source producing a bunch train at 34.2 GHz (0.877 cm bunch

[1] For the sake of convenience, we measure the RMS length in units of time, i. e. Δz = 1.8 ps corresponds to $c \times 1.8$ ps $\approx$ 540 μm.

spacing). (A powerful K-Band source is needed to generate a train of 1 MeV bunches that can be injected into this structure.) It has been shown [12, 13] that very large wake fields and high radiation power will be set up in the 103 GHz device by constructive superposition of wakefields arising from five 1 nC, 1 MeV bunches. The bunches radiate 11.6 MW from a beam having kinetic power of 34.3 MW (Table), and would have a duration equal to the transit time of the bunches in the dielectric structure (generally, ~1/2 ns).

The last bunches in the train set up very large retarding longitudinal wakefields, and therefore lose energy rapidly. To enhance efficiency, it would be necessary to recycle the energy of the "spent" bunches.

Parameters for a Five-zone DLA rf generator

frequency at design LSM_{21} mode	102.816 GHz
bunch spacing	0.82320 cm
bunch energy	1 MeV
bunch charge	1 nC
bunch number	5
bunch size	1 × 1 × 0.5 mm
waveguide height	8 mm
waveguide width	10.8 mm
beam aperture width	2.0 mm
width of dielectric slabs	0.4 mm
relative dielectric constant	5.7
group velocity	0.6630 *c*
radiation power	11.6 MW
average beam power	34.3 MW

Figure 2 shows a spectrum of LSM modes radiated by the bunches; LSE radiation is negligible. After 5 bunches, the waveform of the radiation is nearly sinusoidal.

There is interest in developing broadband (as well as narrow-band) sources in the THz range of frequencies at frequencies above 500 GHz. In some applications, radiation sources with psec pulse width or less are desirable, and have been demonstrated in the past by directing short-pulse lasers onto certain materials such as GaAs [14]. Radiation in the THz range can be provided by a suitable FEL or molecular laser as well. We point out that the multimode wakefield device also is useful for this purpose. We illustrate the potential of this method by using a 1 nC, 0.3 ps, 100 MeV bunch input into the alumina dielectric cylinder device which we have used at the Accelerator Test Facility, Brookhaven National Laboratory [15, 16]. In Figure 3 is shown the on-axis, axial electric

field which follows the moving charge. The sharp peak in the field behind the bunch is caused by reflection of the narrow Cherenkov cone of radiation emitted by the moving charge from the cylindrical walls of the structure. However, the sharpness of the peak (~3 ps) is determined more by the geometrical dispersion of the cylindrical structure rather than the wide spectrum of nearly-equally spaced TM modes which characterize the radiation in this model. One finds peak field ~11 MeV/m from just this single bunch. The axial electric field is nearly constant in amplitude across the vacuum aperture of the dielectric, and decreases rapidly at the dielectric-vacuum interface.

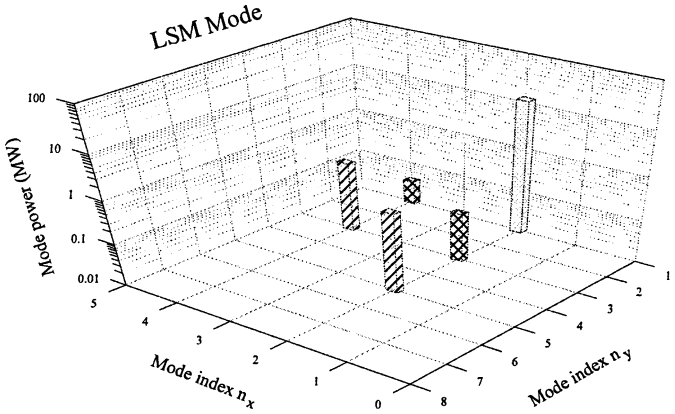

Fig. 2. Radiation power spectrum generated by a train of five 1-nC, 1-MeV bunches in a rectangular dielectric-lined structure with parameters: a_1 = 1.0 mm, and a_2 = 1.4 mm, b = 5.4 mm, and d = 4 mm, and ε_r = 5.7, and μ_r = 1. The bunch size is taken as 1×1×0.5 mm. LSM modes, above; LSE modes have much smaller amplitude. Note log scale.

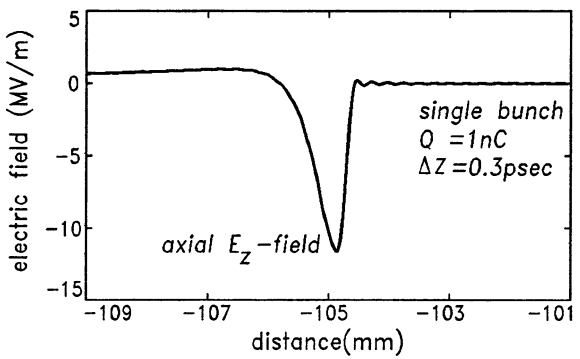

Fig. 3. On-axis pulse of electric field following a moving relativistic bunch of charge. The charge is to the right of the drawing (z = 0), moving toward the right.

Figure 4 shows the spectrum of TM modes emitted by this bunch, which extends up to 1 THz. It is assumed that the dielectric is not dispersive; this applies to alumina for frequencies as high as 500 GHz, but measurements beyond that have not been undertaken. The spectrum shows the power of the discrete TM modes that are excited by a bunch passing along a very long structure; however, if the length of the structure is very short (e. g. ~10 cm), the spectrum will become more nearly a continuum as the modes would be broadened by transit-time effects.

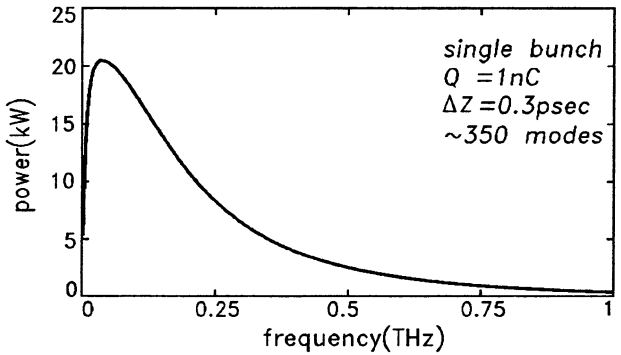

Fig. 4. Spectrum of the TM modes set up by the passage of a single bunch. The solid line connects the power radiated by each mode, shown as a continuum.

We now turn to the matter of a suitable antenna for the wakefield radiation, a matter that was left unfinished in our original publication [9]. The wakefield radiation is trapped inside the cylindrical structure, and for external use it is necessary to deflect away the bunches (readily done with a magnetic dipole), and reconstruct the tight "focus" of the bunch radiation. A possible scheme is shown in the sketch of Fig. 5, wherein the dielectric is extended as a conical surface beyond the metallic wall of the waveguide. This radiating surface (which resembles the sharpened end of a pencil, where by analogy the wood is the dielectric and the graphite is the vacuum hole through which the bunch moves) is machined to the complement of the Cherenkov angle (approximately 72 degrees in the case of alumina). When the bunch is at the tip of this structure, the Cherenkov radiation cone crosses the entire conical surface and the "rays" are directed normally outward from it as shown. A parabolic mirror surface machined into the cylindrical shell of the surrounding reflector will bring the parallel rays emerging from the Cherenkov front to a focal point beyond the hardware. This focal region should be comparable in size with the axial foci within the dielectric structure. A better representation of the reflector surface is shown in Fig. 6.

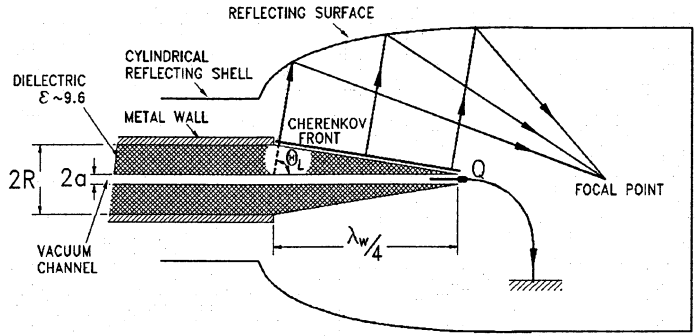

Fig. 5. Schematic of a possible antenna for focusing the wakefield radiation emitted by Q (a dipole deflects the charge away from the focal point). Mirror surface is only drawn schematically.

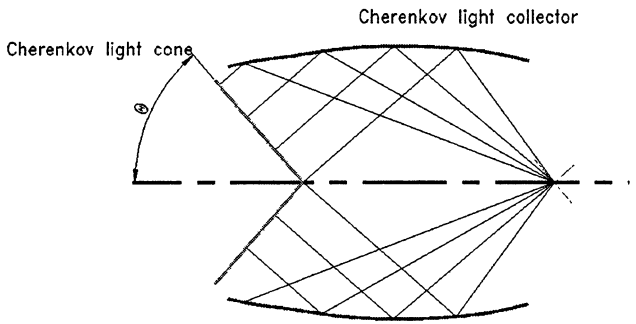

Fig. 6. Parabolic mirror surface of revolution will focus the rays directed from the Cherenkov front.

As an example, we take a single 3 nC, 1 ps, 100 MeV bunch which excites a 21 cm period wakefield in an alumina cylindrical dielectric structure (radius 1.93 cm, vacuum channel diameter 3 mm, dielectric coefficient 9.65). This charge emits a power of 1.1×10^7 W, and creates axial foci which trail the bunch where the axial field intensity is a maximum of 29 MV/m in a focal spot having a footprint of approximately 0.7 mm.

The Cherenkov front of radiation is normally incident upon the tapered dielectric-air interface, and most of the radiation propagates outward from there at the Cherenkov angle. A pulse of radiation, approximately 1psec in length (the width of the Cherenkov front), is emitted from the structure, carrying energy equal to that radiated by the charge in a quarter-wakefield-period of travel

(175 ps), namely $2 \cdot 10^{-3}$ J. The external mirror directs this energy onto a focal region beyond the structure resulting in a local intensity ~100 GW/cm^2. Such a large intensity would be useful to test the breakdown limits of dielectric materials.

Acknowledgment

Research supported by the US Department of Energy, High Energy Physics Division.

References

1. *Marshall T C., Zang T.-B., Hirshfield J.L.*, AIP Conf. Proc., ed. by W. Lawson, C. Bellamy, D. Brosius, 1999, **472**, 27.
2. *Fang J.-M., Marshall T.C., Hirshfield J.L., LaPointe M.A., Zhang T.-B., Wang X.J.*, Proc. Particle Accelerator Conf., 1999, p. 3627.
3. *Park S.Y., Hirshfield J.L.*, Phys. Rev. E, 2000, **62**, 1266.
4. *Power J.G., Gai W., Kanareykin A.*, Advanced Accelerator Concepts: Ninth Workshop, AIP Conf. Proc. ed. by P.L. Colestock, S. Kelley, 2001, **569**, p. 605.
5. *Onishchenko I.N., Sidorenko D.Yu, Sotnikov G.V.*, Phys. Rev. E, 2002, **65**, 066501.
6. *Schächter L., Byer R.L., Siemann R.H.*, Phys. Rev. E, 2003, **68**, 036502.
7. *Park S.Y., Wang C., Hirshfield J.L.*, Advanced Accelerator Concepts: Tenth Workshop, AIP Conf. Proc., ed. by Christopher E. Clayton, Patrick Muggli, 2002, **647**, 527.
8. *Wang C., Hirshfield J.L., Marshall T.C.*, Proc. Particle Accel. Conf., 2003, **3**, 1930, and references therein.
9. *Jing C., Lui W., Gai W., Schoessow P., Wong T.*, Phys. Rev. E, 2003, **68**, 01652.
10. *Zhang T.-B., Marshall T.C., Hirshfield J.L.*, IEEE Trans. Plasma Sci. 1998, **26**, 787.
11. *Wang C., Hirshfield J.L., Fang J.-M., Marshall T.C.*, Phys. Rev. ST Accel. Beams, 2004, **7**, 051301.
12. *Wang Changbiao, Yakovlev V.P., Marshall T.C., Hirshfield J.L.*, Rectangular Dielectric-Lined Two-Beam Accelerator Structure, Particle Accelerator Conf., 2005, paper TPAE013.
13. *Hirshfield J.L., Wang C., Marshall T.C.*, High Power Millimeter-Wave Harmonic Converter, Joint 30th Int. Conf. Infrared and Millimeter Waves, 13th Int. Conf. Terahertz Electronics, Williamsburg VA USA, 2005.
14. *Hu B.B., Zhang X.C., Auston D.H.*, Phys. Rev. Lett., 1991, **67**, 2709.
15. *Shchelkunov S.V., Marshall T.C., Hirshfield J.L., LaPointe M.A.*, Phys. Rev. Sci. & Technology, Accelerators and Beams, 2005, **8**, 062801.
16. *Shchelkunov S.V., Marshall T.C., Babzien M.A., Hirshfield M.A., LaPointe M.A.*, Observation of Superposition of Wakefields Generated by Electron Bunches in a Dielectric-Lined Waveguide, Particle Accelerator Conf., 2005, paper TPAE063.

RESEARCH ON WAKEFIELD EXCITATION IN A CYLINDRICAL DIELECTRIC WAVEGUIDE AND RESONATOR BY A SEQUENCE OF RELATIVISTIC ELECTRON BUNCHES

V. A. Kiselev, A. F. Linnik, T. C. Marshall[1], *I. N. Onishchenko, N. I. Onishchenko, G. V. Sotnikov, V. V. Uskov*

NSC Kharkov Institute of Physics and Technology, Kharkov, Ukraine
[1]Columbia University, New York City, USA

The excitation of wakefields in a cylindrical dielectric waveguide or resonator by a regular sequence of electron bunches for application to high-gradient particle acceleration has been investigated theoretically and experimentally using an electron linac «Almaz-2» (4.5 MeV, $6 \cdot 10^3$ bunches of duration 60 ps and charge 0.32 nC each). Measurements of the energy spectrum of electrons, radial topography and longitudinal distribution of wakefield, and excited wakefield energy were carried out by means of a magnetic analyzer, high frequency probe, and a sensitive calorimeter. The results establish the validity of the main theoretical assertions including the increase in the number of bunches coherently contributing to wakefield buildup.

1. Introduction

Dielectric wakefield acceleration (DFWA) is one of the novel methods of high gradient acceleration of charged particles, along with laser acceleration in plasma and vacuum. Three issues arise in connection with intense wakefield excitation in a dielectric. The wakefield in a dielectric (Cherenkov radiation) excited by charged particles can be enhanced by using a regular sequence of relativistic electron bunches (multi-bunch operation) [1], interference of many transverse modes to enlarge peak amplitude (multi-mode operation) [2], and resonant accumulation of wakefield in a cavity resulting from many bunches (resonator concept) [3]. We wish to exploit the third approach while retaining the other two. In the present work we attempt to clarify by theory and experiments the process of wakefield excitation in a cylindrical dielectric waveguide and resonator using a long sequence of relativistic electron bunches. The temporal evolution and spatial distribution of the excited wakefield are investigated by high frequency (HF) probes for both waveguide and resonator cases and comparison was made. Electron energy loss measured by a magnetic analyzer and the total energy of the excited HF wakefield measured by a calorimeter were compared to determine the energy balance. Conclusions concerning the increase in the number of coherently contributing bunches and the efficiency enhancement in the resonator approach are made.

2. Theory

For a semi-infinite dielectric waveguide without a channel for the bunches the problem of wakefield excitation was solved analytically [4]. There are two new peculiarities compared to the case of the infinite waveguide: appearance of transition radiation and wakefield removal with group velocity from the waveguide entrance. As a result, the net field amplitude grows from the entrance to the trailing edge of the first bunch field and then decreases to the position of the first bunch. The field amplitude at a given cross-section grows and after the passage of several bunches it saturates; however, the saturation level does not depend on the total number of bunches but is determined by the distance to the entrance.

The more complicated problem of including a hole for the bunches was solved in cylindrical geometry for a waveguide of finite length [5] and for a resonator [6]. Due to wakefields moving along the system with group velocity, the number of bunches whose wakefields can be coherently added giving maximum amplitude at the waveguide exit, is restricted in the first case by

$$N_{\max} \approx 1 + L/\Delta z\left(v_0/v_g - 1\right), \tag{1}$$

where L is waveguide length, Δz is distance between bunches, v_0 and v_g are the bunch velocity and group velocity, respectively. The presence of the hole results in the appearance of oscillations with the group velocity of light in vacuum. These oscillations move ahead of bunch and form a weak field precursor. For the resonator, a single bunch excites a multibunch wakefield which is the same as the field in a semi-infinite waveguide [4] until it is reflected from the resonator exit. Excitation by a sequence of bunches results, first in the excitation of only the resonant fundamental mode, the frequency of which coincides with the bunch repetition frequency (mode-locking) and, secondly, in the linear growth of the field amplitude with time in proportion to the number of injected bunches. The saturation level is determined by a nonlinear electron-wave interaction for the KIPT experiment with 4 MeV bunches [6]. It might be supposed that for higher energy (e. g. an experiment with 0.5 GeV bunches) the saturation could be caused the Q-factor of the resonator.

To demonstrate both multimode and multibunch regimes in a resonator case, the rectangular dielectric resonator (still without a vacuum channel) which provides equidistant resonant modes, was theoretically investigated [7]. It was shown that multimode operation is realized under the condition:

$$L = Na\sqrt{\beta_0^2\varepsilon - 1}, \quad \beta_0 = v_0/c, \tag{2}$$

i. e. the length of the resonator L should be a multiple N of half-integer wave lengths of the resonant fundamental mode; a is transverse size; the other transverse size b is supposed much larger, ε is permittivity. For coherent summing of wakefields from injected bunches the coincidence of the fundamental mode

frequency and the frequency f of bunch repetition should be fulfilled. This condition sets the transverse size of the resonator

$$a = v_0 / 2f\sqrt{\beta_0^2 \varepsilon - 1}\,. \qquad (3)$$

Conditions (5) and (6) are the basis of the resonator concept of the rectangular DWFA.

3. Experiment

Experiments to study the excitation of wakefields in a cylindrical dielectric structure (waveguide or resonator) were performed using the linear resonant electron accelerator "Almaz-2" at NSC KIPT.

3.1. Experimental setup. The scheme of the installation is shown in Fig 1. The electron beam had the following parameters: energy 4.5 MeV, current 0.5 A, impulse duration 2 μs, modulation frequency 2820 MHz. Therefore we had a regular sequence of $6 \cdot 10^3$ bunches, 60 ps duration each spaced by 300 ps. The diameter and length of each bunch were 1.0 cm and 1.7 cm, respectively.

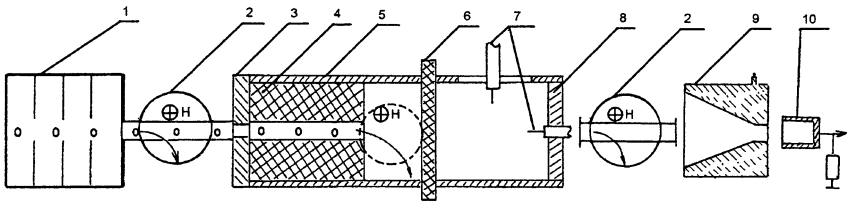

Fig. 1. Schematic of experimental installation: *1* – linac; *2* – magnetic analyzer; *3* – aperture; *4* – dielectric; *5* – copper tube; *6* – teflon plate; *7* – HF probes; *8* – movable metal screen; *9* – calorimeter; *10* – Faraday cup.

This sequence of electron bunches was injected into a dielectric structure made from Teflon (permittivity $\varepsilon = 2.1$, $\mathrm{tg}\delta = 1.5 \cdot 10^{-4}$ at frequency $f = 3 \cdot 10^9$ Hz). The length of the dielectric structure was varied up to 65 cm, the outer diameter was 8.6 cm and the diameter of the hole was 2.2 cm. The dielectric structure was placed into a copper tube of length 100 cm.

Behind the dielectric structure movable HF probes were installed to measure the wakefield amplitude. At the exit a movable metal screen or a matched load was positioned to provide either a resonator of variable length or an open waveguide. At the front of and at the end of the dielectric structure, magnetic analyzers were used for energy spectrum measurements. Also, a transverse magnetic field can be applied to obtain the entire electron energy spectrum on a glass plate of 3 cm thickness. In all cases the current of the bunch electrons was measured with a Faraday cup. The total power of excited wakefields was measured by a specially constructed sensitive calorimeter [8].

3.2. Wakefield spatial distribution. The *transverse* topography of the excited field is found to be almost azimuthally symmetric. The radial dependence of the E_r-component of the field shows a small value on the axis and a maximum near the tube wall. In the absence of the dielectric it is much smaller, which proves the Cherenkov nature of the excited field. The radial dependence of the longitudinal E_z-component shows a maximum on the axis and a small value near the wall. This topography of the excited field demonstrates that in the present experiment E_{0n}-waves are excited. Beyond-cutoff waveguides were used to estimate the contribution of higher radial modes. It was found that their total contribution is less than half of the fundamental mode. This result confirms theoretical conclusion [5] that coincidence of the bunch repetition frequency with the fundamental frequency but not with the difference frequency between the non-equidistant frequencies of the higher modes results in the survival of the resonant fundamental mode and the suppression of the other modes.

The *longitudinal* distribution of excited fields in the waveguide of finite length was measured the following way. The dielectric structure was cut into several pieces of various length (1, 2, 5, and 10 cm) and the electric field was measured at the exit of the structure, which is composed of a number of dielectric pieces to assemble the required length. The results of measurements of E_z after passing of $6 \cdot 10^3$ bunches are depicted in Fig. 2 (curve *1*). The linear growth of amplitude of the longitudinal component of the field along the dielectric waveguide was observed. This proves the theoretical result [5] according to which at the time when N_{max} bunches have passed through the structure a linear stationary longitudinal distribution of E_z has been established. The slope of this linear distribution is determined by the group velocity and bunch charge.

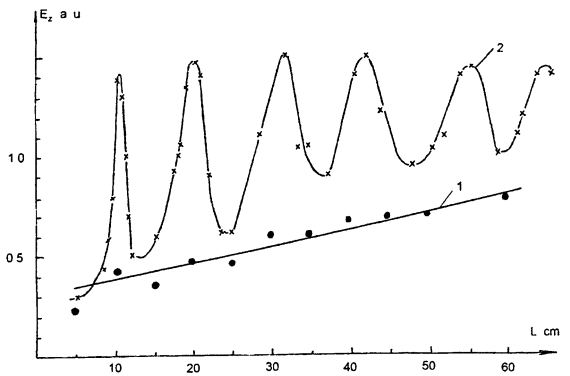

Fig. 2. E_z of wakefield in dependence on dielectric length: *1* – waveguide; *2* – resonator.

In the case of the resonator, the longitudinal distribution of E_z obtained by measuring E_z at the exit end of each dielectric insert consisting of a certain number of pieces is shown in Fig. 2 (curve *2*). The dielectric inserts were placed into the same copper tube with reflecting ends. By this way a dielectric resonator of variable length was realized.

As seen from Fig. 2, the resonator electric field amplitude is larger than the waveguide field. Also, the longitudinal dependence has a resonant character. Accumulation of wakefield in a dielectric resonator of appropriate length was proposed in [3] with the aim of enlarging the number of coherently contributing bunches. If the amplitude is proportional to the number of contributing bunches, we conclude that the resonator allows one to increase the number of contributing bunches approximately 4 times for length 10 cm and 2 times for length 65 cm. Resonant behavior is explained by the effective excitation at a coincidence (multiplicity) of resonator and bunch repetition frequencies.

3.3. Temporal evolution of wakefield excitation. To determine the increase in the number of coherently contributing bunches for the resonator case, we changed the duration of the beam current macro-pulse. This was achieved by using a time delay of the HF pulse of the master oscillator of the klystron feeding the linac, with respect to the high voltage pulse applied to the klystron. This results in the change of duration of the HF power pulse applied to the accelerating section and causes a beam duration in the range $\tau = 0.1$–2.0 μs without changing other beam parameters. In this way we could compose trains of bunches beginning with a minimum number of bunches 300 up to $6 \cdot 10^3$.

The results of measuring the dependence of the excited field amplitude upon beam pulse duration, i.e. upon the number of bunches, are shown in Fig. 3

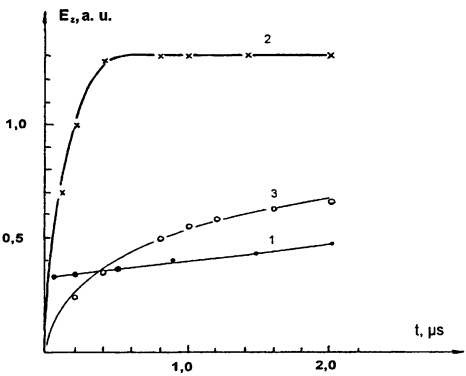

Fig. 3. Dependence of amplitude of the wakefield on pulse duration (number of bunches) for dielectric length 30 cm: *1* – waveguide; *2* – resonator, current 0.5 A; *3* – resonator, current 0.25 A.

at a dielectric length 30 cm. It is seen that for the waveguide case (curve *1*) the amplitude achieves saturation caused by the group velocity effect [4, 5] at a time < 0.1 μs (i. e. $N_{max} < 300$). According to theory (1) for experimental conditions $v_0/v_g = 2$, $N_{max}^{theory} = 3$. For the resonator case (curve *2*) the saturation time is much longer and occurs at 0.3 μs (i. e. $N = 900$ bunches). The number of contributing bunches in the waveguide case can be estimated from Fig. 2 from the amplitudes ratio 4 for $L = 30$ cm, and it should be $N_{max} = 225$. This greatly exceeds the theoretical value and such a discrepancy must be explained in further research. Also, the physical mechanism of amplitude saturation is not revealed

yet. Provisionally, we suppose that for low electron energy the reason for saturation is a nonlinear particle-wave interaction, but for super-relativistic bunches it might be the Q-factor. For smaller beam current (curve *3*) the amplitude grows slower and does not achieve saturation.

3.4. Energy loss of electron bunches. To estimate the dependence of bunch energy loss on wakefields excitation, the electron energy spectrum was measured by magnetic analyzers at the accelerator exit (initial spectrum) and after passing the dielectric structure at distance 100 cm from the linac exit (spectrum after excitation). In Figure 4 initial spectrum (*1*) and spectrum after excitation (*2*) for a dielectric length of 65 cm are presented for waveguide (Fig. 4, *a*) and resonator (Fig. 4, *b*). We find that the electron energy loss is 3% and 12%, respectively. A small number of accelerated electrons is observed for the resonator case.

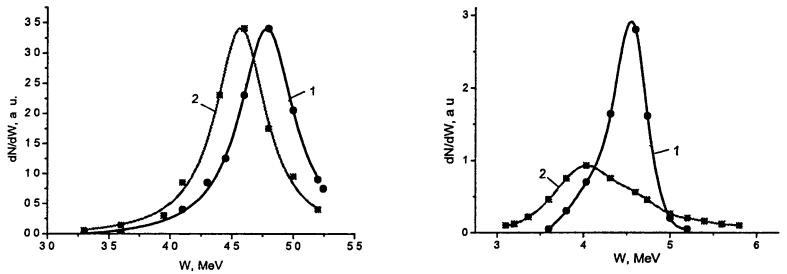

Fig. 4. Electron energy spectra for dielectric length 65 cm: *1* – initial spectrum; *2* – spectrum after passing resonator; *a* – waveguide; *b* – resonator.

The resonator results are in accordance with electron bunch imprints on a glass plate after electrons are deflected by a magnetic field and pass out of the copper tube wall (Fig. 5).

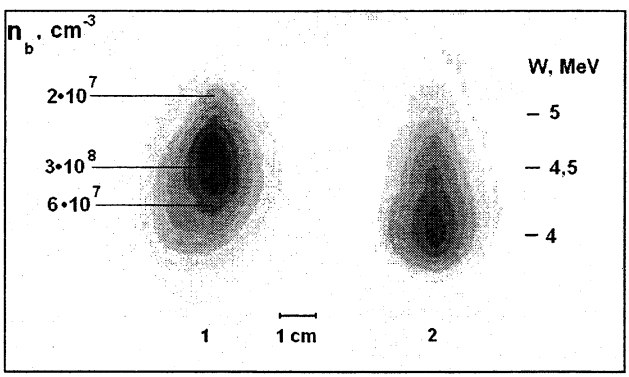

Fig. 5. Imprints of electrons deflected and passed through tube wall: *1* – without dielectric; *2* – dielectric resonator of length 65 cm.

From Figure 5 one sees the displacement of the spectrum as a whole by about 0.5 MeV at the low energy side (loss for wakefield excitation) and a spectrum transformation at the high energy side (evidence of electron acceleration by the wakefield).

3.5. Calorimeter measurements. The total energy of excited wakefields was measured by a specially constructed sensitive calorimeter [8]. Electron bunches were deflected by a magnetic field or passed through a hole in the calorimeter. It was found that the total excited energy in the waveguide case is 1.4% of the initial beam energy. The dependence upon the number of bunches in the macro-pulse is similar to the one observed in the amplitude measurements (Fig. 3, curve *1*). To explain this discrepancy of the calorimeter data with respect to the energy spectrum loss, we measured the damping of an excited field in the metal tube. It occurred that this damping is 3 dB, i. e. 2 times. Thus we conclude that the entire beam energy loss of about 3% is expended on wakefield excitation, within reasonable balance.

Conclusions

The process of wakefield excitation has been investigated theoretically and experimentally, resulting in the following conclusions:

1. The radial topography of excited wakefields was studied and it was established that the excited modes are of E_{0n}-type.

2. By changing the number of bunches in the train from $3 \cdot 10^2$ up to $6 \cdot 10^3$ it was shown that in the waveguide case the wakefield amplitude is built up by a small number of bunches (less than 300), caused by the excited field leaving the interaction region of waveguide with the wave group velocity.

3. The resonator concept was verified, so that for the right choice of resonator parameters and bunch repetition frequency, making the resonator length and the distance between bunches a multiple of the wavelength of the fundamental mode, all bunches may contribute coherently and the amplitude of the wakefield grows appreciably. In the resonator experiment the number of coherently contributing bunches and the field amplitude were increased 4 times for a dielectric length of 10 cm and 2 times for a dielectric length of 65 cm.

4. The electron energy spectra for waveguide and resonator cases were measured, from which it was concluded that for an electron energy of 4.5 MeV and current 0.5 A, and dielectric length of 65 cm, the energy loss during the interaction was 12% (resonator) and 3% (waveguide).

5. Calorimeter measurements were found to be in agreement with results from the HF-probes and allow one to determine the overall excited wakefield energy. This is 2.8% of the initial electron energy and is in satisfactory agreement with results from the energy spectra measurements. Hence it is demonstrated that almost all the electron energy loss is given to wakefield excitation.

Research supported by CRDF UP2-2569-KH-04 and Ukr DFFD 02.07/325.

References

1. *Onishchenko I.N., Kiseljov V.A., Berezin A.K., et al.*, Proc. of the PAC, New York, 1995 (IEEE, New York, 1995), p. 782.
2. *Zhang T.B., Hirshfield J.L., Marshall T.C., Hafizi B.*, Phys. Rev. E, 1997, **56**, 4647.
3. *Marshall T.C., Fang J.-M., Hirshfield J.L., Park S.J.*, AIP Conf. Proc., 2001, No. 569, p. 316.
4. *Onishchenko I.N., Sidorenko D.Yu., Sotnikov G.V.*, Phys. Rev. E, 2002, **65**, 066501-1-11.
5. *Onishchenko N.I., Sidorenko D.Yu., Sotnikov G.V.*, Ukr. Fiz. J., 2003, **48**, 16.
6. *Balakirev V.A., Onishchenko I.N., Sidorenko D.Yu., Sotnikov G.V.*, Technical Phys. Lett., 2003, **29**(7), 589.
7. *Marshall T.C., Onishchenko I.N., Onishchenko N.I., Sotnikov G.V.*, Mode-locking in a dielectric wakefield resonator accelerator, these proceedings, vol. 1, p. 277-282.
8. *Kiselev V.A., Linnik A.F., Onishchenko I.N., Uskov V.V.*, Pribory i technika experimenta, 2005, **2**, 103.

STATUS OF 30 GHz EXPERIMENT ON COPPER CAVITY HEATING

A. K. Kaminsky, A. V. Elzhov, N. S. Ginzburg[1], *A. P. Kozlov, S. V. Kuzikov*[1], *E. A. Perelstein, N. Yu. Peskov*[1], *M. I. Petelin*[1], *S. N. Sedykh, A. P. Sergeev, A. I. Sidorov*

Joint Institute for Nuclear Research, Dubna, Russia
[1]Institute of Applied Physics RAS, Nizhny Novgorod, Russia

The paper is devoted to progress in development and application of the JINR-IAP FEM. This Bragg FEM generates 30 GHz / 20 MW / 200 ns pulses. A test facility to study surface heating effects in a special copper cavity, which is modeled on a high-Q accelerating structure, has been constructed based on the FEM source. Results of the simulation of the FEM operation at a high-Q resonant load are presented. Experimental investigation of the cavity heating stress caused by 10^6 RF-pulses at a repetition rate of 1 Hz is in progress currently.

Introduction

Future electron-positron linear collider CLIC [1], which is under construction at CERN, will operate at the frequency of 30 GHz and average accelerating field of 150 MV/m. Repetitive pulse heating of the accelerating structure can be one of the reasons of copper surface damage. Collaboration of CLIC group (CERN) with JINR (Dubna) and IAP RAS (Nizhny Novgorod) is now realizing an experiment oriented on estimation of the lifetime of CLIC accelerating structure [2]. In the experiment specially designed copper cavity should undergo repetitive pulse heating by the radiation of 30 GHz JINR-IAP FEM-oscillator with Bragg resonator [3].

The test facility based on this FEM has been constructed and described in the paper. Results of the theoretical analysis of the possibility to use Bragg FEM-oscillator to drive a high-Q resonant load are discussed. Recent results of the experiment are presented.

Experimental set-up

A schematic diagram of the JINR-IAP FEM experiments is shown in Fig. 1. The induction linac LIU-3000 (JINR), which generates a 0.8 MeV / 200 A / 250 ns electron beam with a repetition rate of 1 Hz, drives the FEM-oscillator. Transverse velocity in the magnetically guided beam is pumped in a helical wiggler of 6 cm period. The main advantages of developed FEM is the use of a reversed guide field [4, 5], which provides high-quality beam formation in the tapered wiggler section with a low sensitivity to the initial beam spread, alongside with Bragg resonator having a step of phase of cor-

rugation [6, 7], which possesses high electrodynamical mode selection. As a result, stabile single-mode operation with high electron efficiency was achieved in the FEM [3]. At the present stage the FEM generates 20 MW / 200 ns pulses at 30 GHz with the spectrum width of about 10 MHz (Fig. 2). Stability of the radiation frequency, power and pulse shape was demonstrated over a sequence of 10^4 pulses.

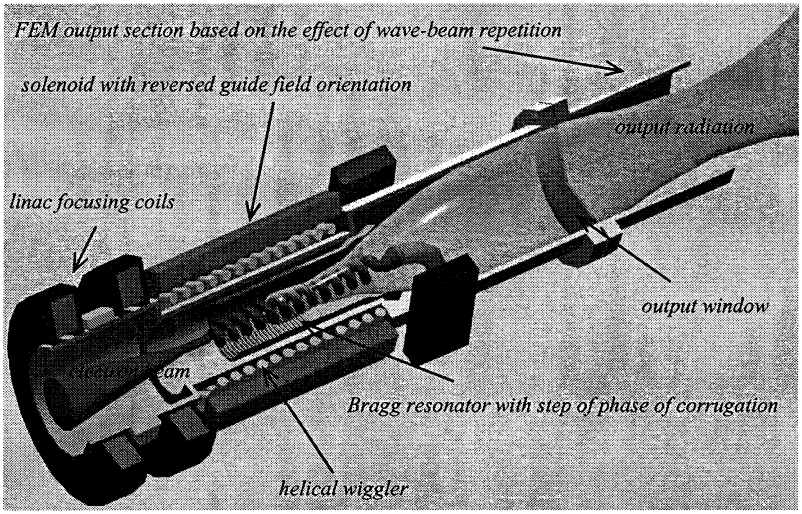

Fig. 1. Schematic diagram of the JINR-IAP FEM

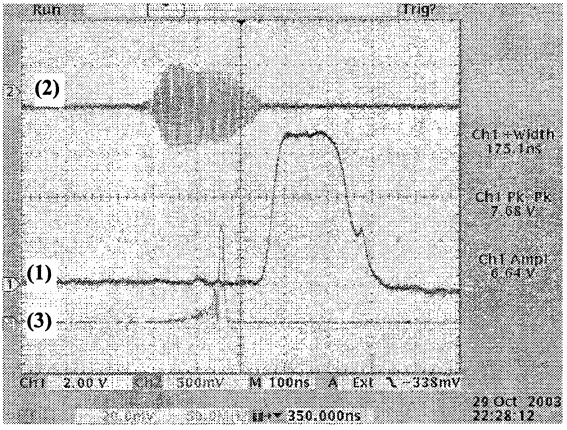

Fig. 2. Typical oscilloscope traces of RF-pulse (100 ns/div.) (*1*), heterodyne beating signal (*2*) and frequency spectrum (50 MHz/div.) (*3*).

The test facility to study surface heating effects at 30 GHz, which was constructed based on the FEM source [2], is shown in Fig. 3. The experimental set-up includes a two-mirror confocal transmission line and mode converters to transport the RF-power from the FEM to the test cavity. A special copper cavity operating with $TE_{0,1,1}$ mode and having Q-factor ~1000 was designed to model temperature regime in a high-Q accelerating structure of the CLIC project. The profile of the cavity surface was optimized to enhance the RF magnetic field in a certain zone and provide a temperature rise of up to 200 °C during each RF-pulse. The resonant frequency of the cavities is also mechanically tuned to coincide with the frequency of the FEM source. A directional coupler is included to control both the incident and reflected powers. After a certain number of pulses the Q-factor of the cavity would be monitored using a network analyzer to detect early signs of surface damage. "Cold" tests of all components of the experimental set up were carried out and demonstrated good agreement with designed parameters.

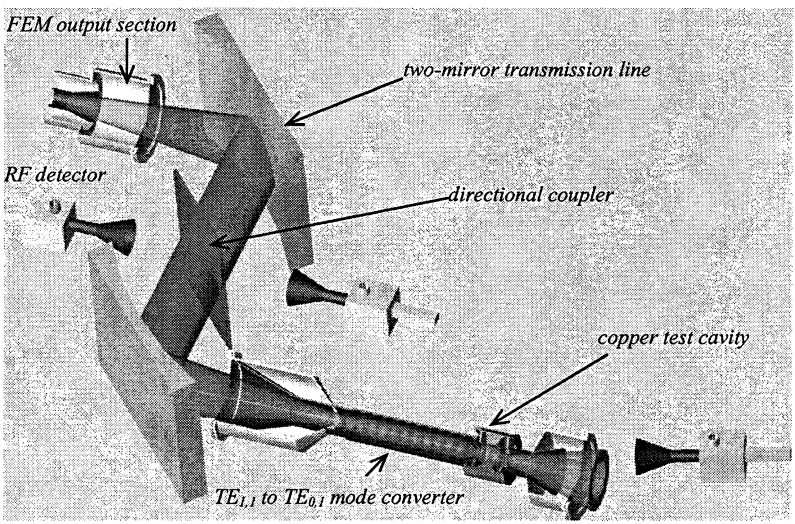

Fig. 3. Schematic diagram of the test facility for studying surface heating effects at 30 GHz based on JINR-IAP FEM.

Simulations of Bragg FEM operating at a high-Q resonant load

The key question for conducted experiments is ability of an FEM to operate with a high-Q load when taking into account parasitic reflections. Obviously, even in the case of ideal matching the load frequency to the FEM generation

frequency, strong reflections arise at the transient process when the RF-pulse just comes into the load. These reflections could affect on the process of generation.

Results of the modeling done in the frame of 1D time-domain approach are presented in Fig. 4. It was found that if the eigenfrequency of the load resonator coincides with the FEM operating frequency the load resonator becomes transparent and accumulation of the e. m. energy inside the resonator occurs. Detuning of the load-resonator frequency leads to strong reflections from this resonator what results in suppression of the FEM oscillations. At the same time, stability of the FEM operation can be improved when increasing (*a*) the time delay of the reflected from the load RF-pulse and (*b*) the RF-pulse losses in the transmission system.

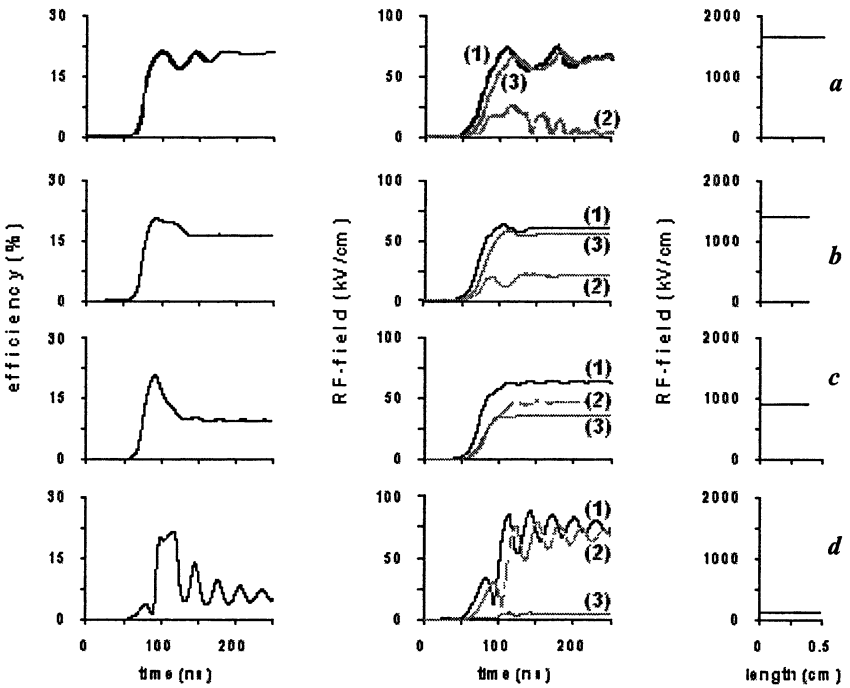

Fig. 4. Simulation of the FEM operation at the resonant load for parameters close to conditions of the CLIC-JINR-IAP experiment and different detuning between the load's and the radiation frequencies $\Delta\omega/\omega$: ideal matching (*a*), 0.01% (*b*), 0.05% (*c*), 0.5% (*d*); left column – time dependence of the FEM efficiency, middle column – time dependence of the signals: *1* – incident the load, *2* – reflected from the load, *3* – passed through the load, right column – the RF-field accumulated in the load at the steady-state stage.

Simulations carried out demonstrates principal ability of the FEM to be used for the aforementioned application. Results of the first experiments, which are shown in Fig. 5, also proved possibility of the FEM to operate at the high-Q load. When frequency of the test-cavity was tuned to the FEM generation frequency it was observed that during the RF-pulse the reflected signal decreased and the test-cavity became transparent. As a result, accumulation of the RF-power in the load was achieved.

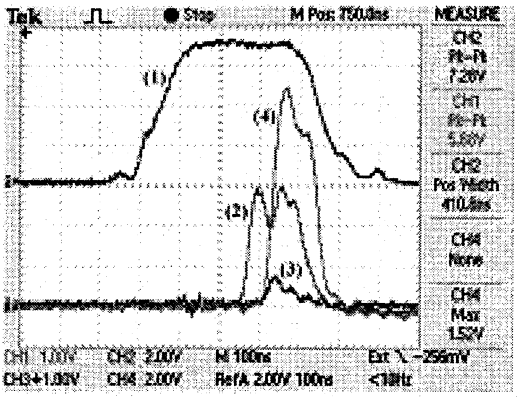

Fig. 5. Results of the first experimental studies of the FEM operating at the test resonator: oscilloscope traces of beam current at the FEM entrance (60 A / div.) (*1*), RF-pulse radiated from the FEM (5 MW / div.) (*2*), RF-pulse reflected from the test resonator (15 MW / div.) (*3*) and RF-pulse passed through the test resonator (0.5 MW / div.) (*4*); time scale is 100 ns / div.

The cavity heating stress is planned be studied during 10^6 RF-pulses, these experiments are currently in progress.

Acknowledgements. This work is supported partially by the Russian Foundation for Basic Research (grants №03-02-16530, №04-02-17118 and №05-02-16833) and INTAS.

References

1. *Wilson I.*, CLIC Note 52, Oct. 1987.
2. *Ginzburg N.S., Elzhov A.V., Ivanov I.N., et al.*, Proc. 22nd Int. FEL Conf., Durham, USA, 2000, p. II-41.
3. *Ginzburg N.S., Kaminsky A.A., Kaminsky A.K., Peskov N.Yu., et al.*, Phys. Rev. Lett., 2000, **84**, 3574.
4. *Kaminsky A.A., Kaminsky A.K., Rubin S.B.*, Particle Accelerators, 1990, **33**, 189.
5. Conde *M.E., Bekefi G.*, Phys. Rev. Lett., 1991, **67**, 3082.
6. *Kovalev N.F., Petelin M.I., Reznikov M.G.*, Resonator, USSR Athors Sert. no. 720592; Bull. no. 9, 1980.
7. *Bratman V.L., Denisov G.G., Ginzburg N.S., Petelin M.I.*, IEEE J. Quant. Electr., 1983, **QE-19**, 282.

COLLECTIVE ION WAKES IN COMPLEX PLASMAS

S. V. Vladimirov

University of Sydney, Sydney, Australia

The characteristics of plasma kinetics in the presence of flowing ions around stationary dust grain(s) are considered. Results of analytical considerations as well as numerical molecular dynamics simulation method are presented. The dynamics of plasma electrons and ions forming the wake structures as well as distributions of the electron and ion number densities, and the electrostatic plasma potential are obtained for various distances from the stationary test dust particle(s).

Complex "dusty" plasma is a multi-component plasma with solid particles, typically of a micron size [1]. In a series of experiments [2], formation of microscopic Coulomb crystals of solid particles in a plasma has been demonstrated. Associated with the Coulomb crystallization in strongly coupled complex plasmas, there have been indications of formation of pairs of particulates with relatively small separations. In a typical experiment, the dust is embedded in the sheath region [1, 2] where the balance between the gravitational and electrostatic forces is established, with often observed aligning of dust particle in the direction of the flow.

The fundamental question of importance for understanding the processes involving formation and evolution of various self-organized structures such as mentioned above colloidal crystals and other formations like dust clouds, dust voids, etc. [1] in a complex dusty plasma, is the interaction of dust grains with themselves and the surrounding plasma. Since in a typical laboratory discharge dust particles are negatively charged and usually levitate in the sheath or presheath region under the balance of gravitational, electrostatic (due to the sheath electric field) and plasma (such as the ion drag) forces, these interactions involve collective processes associated with specifics of the sheath plasma.

In the sheath region, the ion flow to the electrode is established thus naturally providing a distinctive direction, with plasma properties different in the direction parallel or perpendicular to the flow. The ion flow, providing a direct dragging influence, is also responsible for the generation of associated collective plasma processes. The latter strongly influence formation of the plasma-dust structures. A theory taking into account these features and suggesting that in the case of supersonic velocities of the ion flow the plasma wake is formed behind the levitating dust grain was proposed in Refs. [3, 4] and later developed in a number of studies [5–8]. It was demonstrated that the plasma wake can strongly modify interactions of dust grains between themselves and with the plasma; in particular, supporting a Cooper-pairing-like attraction of grains of the same sign of the charge [3]. The theory proved to be very successful in explaining the observed experimental phenomena (e. g., dust particle vertical alignments), and was confirmed in experiments [9].

Consider a possibility of formation of linear plasma wake behind a charged point-like particle. The mechanism is similar to the wake formation for moving charged particulate which involves excitation of the collective low-frequency electrostatic plasma excitations. We consider the situation close to laboratory experiments, namely, static dust particulates which can interact through the low-frequency oscillations in the ion flow which velocity exceeds the ion-acoustic velocity. Physically, the generation of the wake acoustic fields in this case is the same as the generation of the electromagnetic fields for the charge at rest placed in a medium moving faster than light. The stationary wake potential that is forming behind the charge in this case is shown in Fig. 1.

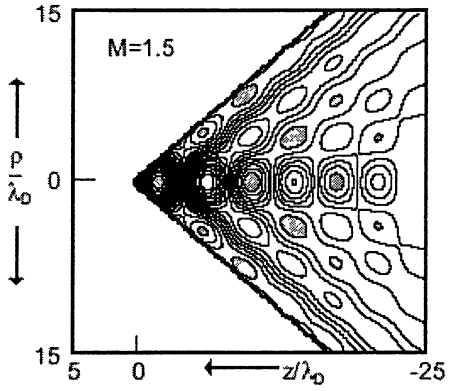

Fig. 1. The wake potential (the potential minima are shaded).

We see that the collective interaction of the static test dust particulate with the low-frequency perturbations in the ion flow can provide the attractive wake potential. The mechanism is similar to that which responsible for the Cooper pairing. We note that the physical idea of the Cooper pairing effect is that the test electron polarizes the medium by attracting positive ions. The excess positive ions, in turn, attract the second electron. If this attractive interaction is strong enough to overcome the repulsive screened Coulomb interaction, the effective attraction between two electrons can be realized, and the superconductivity results. For example, the jelium model leads to similar expression where one term is due to the screened Coulomb repulsion, whereas the other term corresponds to the attraction forces. In our situation, with static charged dust particulates, the moving ions of the flow create the polarization necessary for the resulting attraction. Thus, in order for the latter to be operative it is required that one has continuous ion flow which speed exceeds the ion-acoustic velocity. This condition is usually observed in the sheath region of low-temperature laboratory plasmas. The test particulates can attract to each other forming the quasi-lattice structures with the characteristic period which is close to experimental data [1, 2]. For the effective attraction, the speed of moving charged particles (in the frame where the background medium is at rest) should exceed the sound velocity. The larger are the ion velocities, the stronger are ballistic effects in the ion focusing; this is because fewer ions participate in the wave-particle resonance, and the Mach cone is narrower. The wake mechanism is the most effective when the particles' speed is quite close to the ion acoustic velocity (in this case the resonant interaction with phonons is maximum). We present in Fig. 2 the numerical result for $M = 1.1$ and two directions of the ion flow [10]. From these plots, we clearly see the wave character of the wake potential.

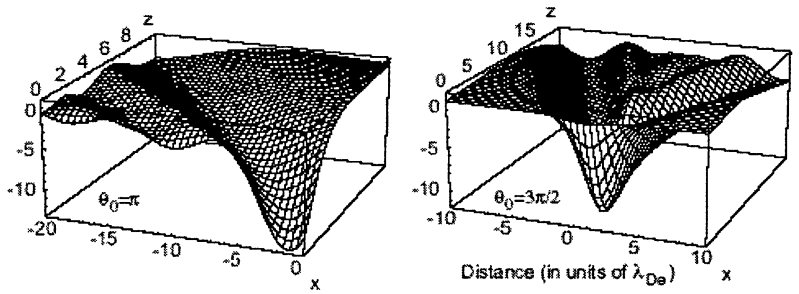

Fig. 2. The surface plot of the wake potentials for different directions of the ion flow [10].

Thus the ion flow provides not only a direct kinetic (dragging) influence but is also responsible for the generation of associated collective plasma processes which can strongly affect the vertical arrangement of dust grains [1, 2]. The problem of plasma kinetics in the presence of a macroscopic body is also connected to the charging of the body. For a typical situation of a low-temperature laboratory dusty plasma, the macro-particle charge appears as a result of charging plasma currents onto the particle surface. A number of experiments (see in Ref. [1]) have been performed to elucidate the character of the charge of an isolated particle; most of experimental techniques are complicated, requiring special measurement procedures, and, on the other hand, do not always give the precise results. Moreover, it is especially difficult to determine the particle charges for two particles, especially in the sheath region in the presence of the ion flow. In this case, the *ab initio* numerical simulation, being one of the most complete model description, can provide very important information on the character of the plasma kinetics and particles' charging. The complete problem of plasma dynamics around a macroscopic body in the presence of plasma flows is highly nonlinear and therefore its numerical analysis is of major importance. Among various numerical methods, direct integration of the equations of motions of plasma particles represents a numerical experiment whose significance approaches experiments in the laboratory.

The kinetics of plasma particles around one stationary dust grain in the presence of an ion flow studied using a three-dimensional molecular dynamics simulation method was studied in Ref. [11]. The model is self-consistent, involving the dynamics of plasma electrons and ions as well as charging of the dust grain. The effect of ion focusing is investigated as a function of the ion flow velocity, and distributions of electron and ion number densities, and electrostatic plasma potential, were obtained. The core of the numerical method includes consideration of the time evolution of the system consisting of N_i positively ("ions") and N_e negatively ("electrons") charged particles together with a macroscopic absorbing grain ("dust particle") of radius R with infinite mass and an initial (negative) charge Q. The walls bounding the simulation region are elastic; the ions are introduced in

the system as a uniform flow with the Mach number M and the temperature T_i. The paths of the ions and electrons are determined through numerical integration of the equations of motion. Simulating the charging process, the real electron/ion mass ratio was effectively taken into account by renormalizing the absorbed charge in the process of the electron-dust charging collision, so that the charge appearing on the grain corresponds to its value for the real electron/ion mass ratio. The charge of the dust particle was found to fluctuate around its average value weakly depending on the ion flow velocity.

Figure 3 presents contour plots of the (normalized) ion density for three values of the speed of the ion flow (subsonic with $M^2 = 0.6$, and two supersonic, $M^2 = 1.2$ and $M^2 = 2.4$). The strong ion focus is formed at the distance of a fraction of the electron Debye length behind the dust grain. The maximum value of the density at the ion focus is almost independent of the flow velocity, whereas the characteristic distance of the ion focus from the dust grain increases with increasing flow velocity.

Furthermore, the characteristics of plasma particle kinetics in the presence of ions flowing around two stationary dust grains aligned in the direction of the flow were numerically obtained [12]. Figure 4 gives the contour plot of the normalized ion density for five different distances between the grains corresponding to the range from a short distances much less than the Debye length up to distances relatively large with respect to the electron Debye length. For short distances, the wake is practically corresponding to that of one combined particle; on the other hand, for distances of the order of (or more than) the electron Debye length, the formation of quasi-wake features can be seen after the first grain, i.e. before the second one. The ion wake strongly influences the charge of the second grain located downstream with respect to the first particle. This influence is especially strong for intergrain distances small compared to the Debye length. It is interesting that there is also an influence of the downstream particle on the charge of the

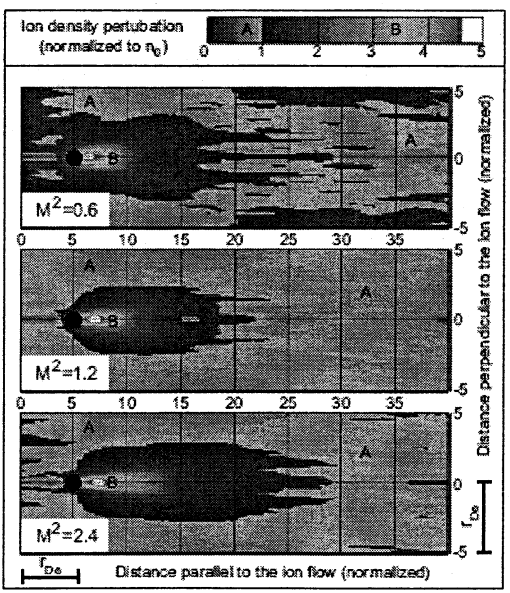

Fig. 3. Contour plot of the ion density, showing ion focusing, for three different velocities of ion flow. The ions are focusing behind the grain thus forming the region with highly enhanced ion density.

particle located upstream; this influence, however, is limited to distances of the order of the Debye length. The charge of the second particle, for the distances considered (up to four Debye lengths), is always less than the charge of the first particle, and this is attributed to the longrange influence of the plasma wake.

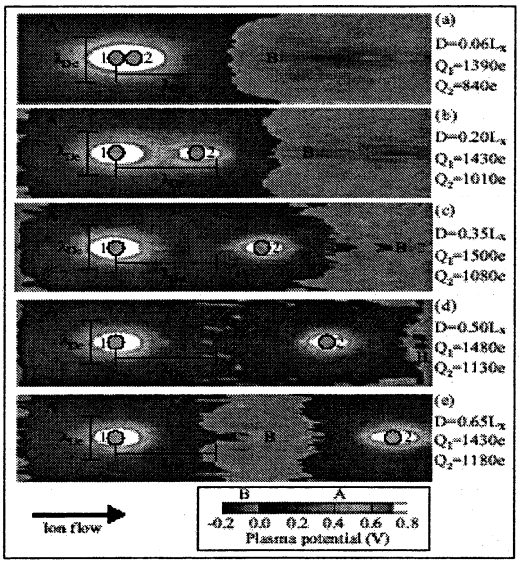

Fig. 4. Contour plot of the ion density for different distances between two dust grains. The potential well is formed behind the dust grains, and between the grains when the separation exceeds the Debye length.

Acknowldgement. This work was partially supported by the Australian Research Council and the Max Planck Society (Germany).

References

1. *Vladimirov S.V., Ostrikov K.*, Phys. Rep., 2004, **77**, 5551.
2. *Thomas H.M., Morfill G.E.*, Nature, 1996, **379**, 806.
3. *Vladimirov S.V., Nambu M.*, Phys. Rev. E, 1995, **52**, R2172.
4. *Vladimirov S.V., Ishihara O.*, Phys. Plasmas, 1996, **3**, 444.
5. *Schweigert V.A., et al.*, Phys. Rev. E, 1996, **54**, 4155.
6. *Ishihara O., Vladimirov S.V.*, Phys. Plasmas, 1997, **4**, 69.
7. *Benkadda S., et al.*, Phys. Rev. E, 1999, **60**, 4708.
8. *Lampe M., et al.*, Phys. Plasmas, 2000, **7**, 3851.
9. *Takahashi K., et al.*, Phys. Rev. E, 1998, **58**, 7805.
10. *Vladimirov S.V., Nambu M.*, Phys. Rev. E, 2001, **64**, 026403.
11. *Maiorov S.A., et al.*, Phys. Rev. E, 2001, **63**, 017401.
12. *Vladimirov S.V., et al.*, Phys. Rev. E, 2003, **67**, 016407.

PECULIARITIES OF MODE SPECTRUM OF PLANAR 2D BRAGG RESONATOR (THEORY AND EXPERIMENT)

N. Yu. Peskov, N. S. Ginzburg, G. G. Denisov, S. V. Kuzikov, A. S. Sergeev, A. V. Arzhannikov[1], P. V. Kalinin[1], R. M. Rozental, S. L. Sinitsky[1], M. Thumm[2], V. Yu. Zaslavsky

Institute of Applied Physics RAS, Nizhny Novgorod, Russia
[1]Budker Institute of Nuclear Physics RAS, Novosibirsk, Russia
[2]Forschungszentrum Karlsruhe, IHM, Germany

Electrodynamic properties of two-dimensional (2D) Bragg resonators of planar geometry realising two-dimensional distributed feedback are studied in the frame of the geometrical-optical approach and in 3D simulations. It was shown that the resonators possess high selectivity over both longitudinal and transverse mode indices and can be used in powerful microwave generators for provision of spatial coherence of radiation under large transverse oversize. Results of the theoretical analysis agrees with the data obtained in "cold" microwave measurements in the frequency band of 60 GHz. Transparency of the 2D Bragg structure in the vicinity of the Bragg frequency in the case of inclined wave-beam incidence has been observed. This effect corresponds to excitation of the fundamental eigenmode with the highest Q-factor.

Introduction

Two-dimensional (2D) Bragg structures of planar and coaxial geometries realizing 2D distributed feedback allow to develop powerful sources of coherent mm radiation based on high-current relativistic electron beams of either sheet [1] and tubular [2] geometry. The first successful operation of the novel feedback mechanism in both FEM geometries was demonstrated recently [3, 4].

The 2D Bragg resonators are modification of the traditional 1D Bragg structures, which were proposed for quantum lasers [5, 6] and relativistic masers [7, 8] to realize 1D distributed feedback. The use of these structures, which in the microwave frequency range can be realized by waveguide sections with shallow single-periodical corrugation providing coupling and mutual scattering of forward and backward (in the respect to the electron beam propagation) e. m. fluxes, allowed many successful experimental realization of high-power FEM-oscillators [8–11]. However such structures are able to provide mode selection only for system transverse sizes of a few wavelengths. As a result, the output power produced in FEMs exploiting 1D Bragg resonators did not exceed a few tens of MW [8–11]. The novel 2D Bragg structures possess double-periodical corrugation in two-directions with an angle to each other. The feedback loop arising on such a type of corrugation alongside with forward and backward e. m. fluxes includes as well the fluxes propagating in the transverse directions. These e. m. fluxes synchronise radiation from different parts of a large-size electron beam. Computer simulations in the frame of the geometrical-optical approach demonstrates the possibility of generation of coherent mm radiation of

a gigawatt power level in an FEM when driven by an electron beam of the transverse size up to 10^2–10^3 wavelengths and operating with 2D distributed feedback [1].

The present paper is devoted to detailed theoretical and experimental studies of the electrodynamical properties of 2D Bragg structures of planar geometry. In difference with previous papers, where the analysis of planar 2D structures was performed exceptionally in the frame of the geometrical-optical approach, in this paper we present 3D computer simulations which confirm results of analytical considerations. These results are proven also by the data obtained in "cold" tests of a 2D Bragg structure having double periodical sinusoidal corrugation. In accordance with theoretical analysis, in these experiments the high-Q modes inside the Bragg scattering zone were observed. The existence of such modes in the middle of the Bragg scattering zone without any defects of periodicity is the specific feature of 2D Bragg structures in difference with traditional 1D structures [5–8], as well as photonic band gap structures [12, 13].

Basic model (geometrical-optical approach)

A planar 2D Bragg resonator consists of two metal plates (Fig. 1, *a*) with the length l_z and width l_x, which are doubly corrugated as

$$a(x,z) = a_1 \cos(\bar{h}x)\cos(\bar{h}z), \tag{1}$$

where $2a_1$ is the corrugation depth, $\bar{h} = 2\pi/d$, d is the period over x- and z-coordinates. This structure provides coupling and mutual scattering of the four perpendicular-propagating partial waves

$$\mathbf{E} = \mathrm{Re}\left[\mathbf{E}_0\left(A_+ e^{-ihz} + A_- e^{ihz} + B_+ e^{-ihx} + B_- e^{ihx}\right)e^{i\omega t}\right] \tag{2}$$

of the same transverse structure $E_0(y)$ if the wavenumbers h of the partial waves satisfy to the Bragg resonance condition (Fig. 1, *b*):

$$h \approx \bar{h}\,. \tag{3}$$

One of the partial waves (let assume A_+ as this wave) propagates along the electron beam and provides an interaction with the electrons. Two other partial waves $B_\pm$ propagate in transverse directions and should provide synchronisation of radiation from different parts of a wide sheet electron beam. The backward (with the respect to the electron beam) wave A_- completes the feedback cycle.

In the frame of the geometrical-optics mutual scattering of the four partial waves (2) may be described by the set of coupled-wave equations for the slow functions $A_\pm(x,z)$, $B_\pm(x,z)$ [1]:

$$\frac{\partial A_\pm}{\partial z} \mp i\delta A_\pm \pm i\alpha\left(B_+ + B_-\right) = 0\,,\quad \frac{\partial B_\pm}{\partial x} \mp i\delta B_\pm \pm i\alpha\left(A_+ + A_-\right) = 0\,, \tag{4}$$

where $\delta = h - \bar{h}$ is the mismatch from the Bragg resonance (3) and α is the wave coupling coefficient, which for the case of scattering of the lowest propagating TEM-type partial waves has the form [1] $\alpha = a_1 h/4a_0$.

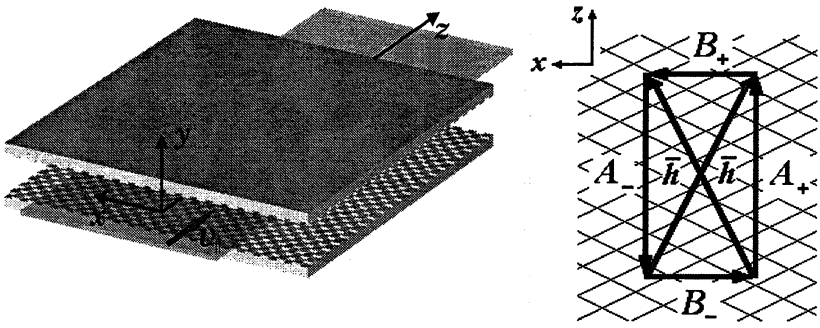

a *b*

Fig. 1. Scheme of a planar 2D Bragg resonator (*a*); Diagram illustrating 2D scattering of the four partial waves on the Bragg grating (*b*).

Eigenmodes of a planar 2D Bragg structure

The spectrum of the resonator eigenmodes may be found from the solution of the Eqs. (4) under the assumption that the e.m. energy fluxes from outside the resonator are absent and the partial waves are not reflected from the edges of the resonator, which corresponds to the boundary conditions for the partial waves in the form:

$$A_+(x,0) = 0 \ , \ A_-(x,l_z) = 0 \ , \ B_+(0,z) = 0 \ , \ B_-(l_x,z) = 0 \ . \qquad (5)$$

An analysis of Eqs. (4) with the boundary conditions (5) shows that the 2D Bragg resonator possesses a spectrum of high-Q modes, which may be divided into two families, whose eigenfrequencies are located (a) near the Bragg resonance $\delta \approx 0$ and (b) near $\delta \approx \pm 2\alpha$. Under the conditions of strong wave coupling $\alpha l_{x,z} >> 1$ the geometrical-optical solutions for the eigenmode frequencies $\omega_{n,m} \approx c\bar{h} + c\mathrm{Re}\delta_{n,m}$ and their Q-factors $Q_{n,m} \approx h/2\mathrm{Im}\delta_{n,m}$ are given as [1]

$$\delta_{n,m} = \pm\frac{\pi^2 mn}{2\alpha l_z l_x} + i\frac{\pi^2}{2\alpha^2 l_z l_x}\left(\frac{n^2}{l_z} + \frac{m^2}{l_x}\right) \qquad (6a)$$

near $\delta \approx 0$ and

$$\delta_{n,m} = \pm\left[2\alpha + \frac{\pi^2}{4\alpha}\left(\frac{n^2}{l_z^2} + \frac{m^2}{l_x^2}\right)\right] + i\frac{\pi^2}{2\alpha^2}\left(\frac{n^2}{l_z^3} + \frac{m^2}{l_x^3}\right) \qquad (6b)$$

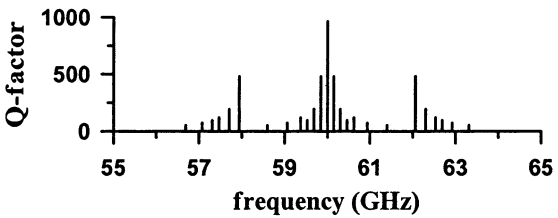

Fig. 2. Eigenmodes spectrum of 2D Bragg resonator

near $\delta \approx \pm 2\alpha$. According to (6) the 2D Bragg resonator possesses high selectivity over both the longitudinal (n) and the transverse (m) indices. This high selectivity is originated from output of the radiation not only in the longitudinal $\pm z$ directions (similar to 1D Bragg resonators), but additionally in the transverse $\pm x$ directions. Solutions (6) are shown in Fig. 2 for parameters used in "cold" tests (see below). The spectrum of eigenmodes is symmetrical over the Bragg resonance frequency $\bar{\omega} = \bar{hc}$ (i. e. $\delta = 0$) and the highest Q-factor is achieved at the precise Bragg frequency at the eigenmodes with indices $\{n = 0, m = 1\}$ or $\{n = 1, m = 0\}$ (these modes for the case of $l_x = l_z$ are degenerated on the Q-factor). Spatial profiles of the partial waves forming the fundamental mode are shown in Fig. 3.

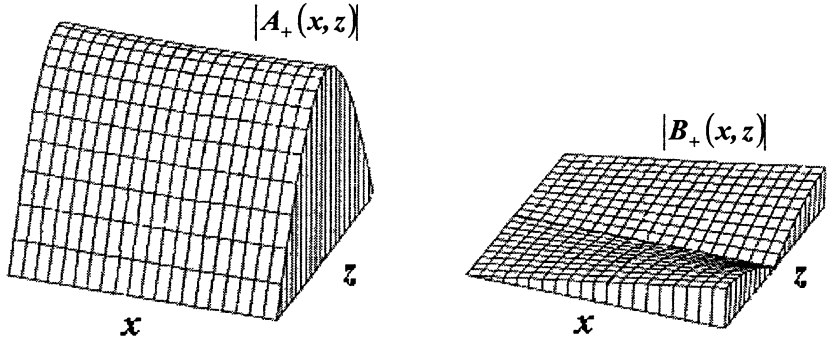

Fig. 3. Spatial profiles of the partial waves forming the fundamental mode

Simulations of excitation of 2D Bragg structures by an external wave

The frequencies and Q-factors of the resonator eigenmodes may be found also when modelling its excitation by a microwave beam coming in through one of the resonator edges. This modelling is necessary for interpretation of data obtained in "cold" resonator testing. In the frame of the geometrical-optical

approach, assuming an incident wave-beam (let us define A_+ as this wave), which enters at the resonator edge at $z = 0$, we get the boundary condition for the Eqs. (4) as

$$A_+(x,0) = A_0(x)e^{i\varphi(x)}. \quad (7)$$

The rest of the partial waves have zero amplitude on the corresponding edges of the resonator and satisfy the boundary conditions (5).

Figure 4 gives the frequency dependencies of the integral coefficients of reflection, transmission and scattering in transverse direction. The parameters in the simulations corresponded to the parameters used in the "cold" microwave experiments (see below). Obviously, excitation of different eigenmodes of the resonator depends on their spatial structure. Thus, in the case of the wave-beam with plane phase entering the resonator edge, i. e.

$$A_+(x,0) = 1, \quad (8)$$

the excitation of the eigenmodes having symmetrical structure (in respect with the middle of the resonator in the plane of incidence) of the partial waves takes place, i. e. the eigenmodes positioned in the vicinity of $\delta \approx \pm 2\alpha$. One can see from comparison of Fig. 2 and Fig. 4, *a* that the minima in the reflection coefficient as well as the maxima in the transmission and transverse-scattering coefficients correspond to the frequencies of these eigenmodes. In contrast, the eigenmodes with anti-symmetrical structure of the partial waves, which are situated near $\delta \approx 0$, are not excited by the plane wave-beam. This leads to the appearance of a non-transparent (forbidden) zone around the Bragg frequency for such wave incidence (similar to traditional 1D Bragg structures [5–8]).

It should be noted that in the case of the incident plane wave the fundamental highest-Q modes at the precise Bragg frequency are also not excited. This fact can be explained by peculiarities of these modes structure. For the eigenmode $\{n = 0, m = 1\}$ the amplitude of the partial waves $A_\pm$ is close to zero at the resonator edges in the directions of their propagation (similar to the standing wave), while the $B_\pm$ waves are anti-symmetrical (see Fig. 3). For the mode $\{n = 1, m = 0\}$ the structure of the partial waves corresponds to mutual exchange of the coordinates $x \leftrightarrow z$. As a result, the excitation of the mode $\{n = 0, m = 1\}$ from the resonator edge is not effective and the mode $\{n = 1, m = 0\}$ can be excited only by an anti-symmetrical wave-beam.

A simple way to form an anti-symmetrical wave-beam in the experiments is an inclined incidence of the incoming plane wave. Simulations show that optimal conditions for excitation of the fundamental mode correspond to a difference in phases of the incident wave over the resonator width of 2π, i. e.

$$A_+(x,0) = e^{2i\pi x/l_x}. \quad (9)$$

Results of simulations of Eqs. (4) with boundary conditions (9) are given in Fig. 4, *b*. One can see that for an anti-symmetrical (or inclined) incoming wave-beam, transparency of the structure in the vicinity of the Bragg frequency occurs. This effect corresponds to excitation of the fundamental eigenmode with

the highest Q-factor and other anti-symmetrical eigenmodes. Maxima in the transmission coefficient correspond to the frequencies of these eigenmodes (see Fig. 4, *b*). Symmetrical modes are not excited in the case of such wave incidence.

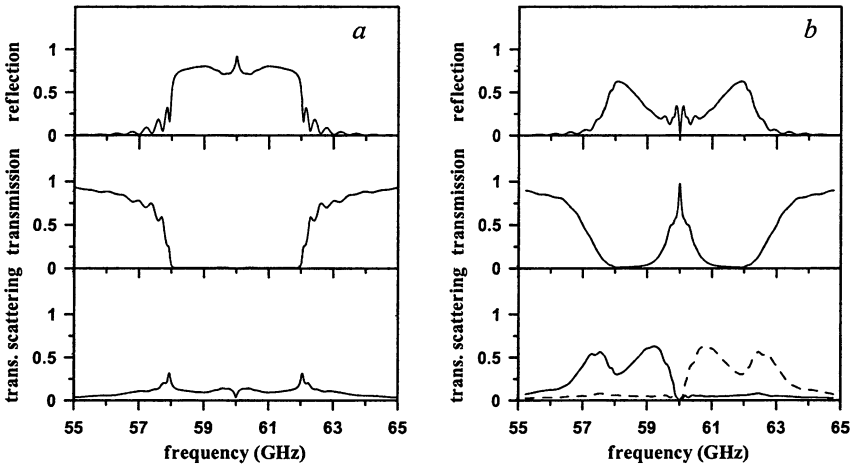

Fig. 4. Computer simulations of the integral coefficients of reflection, transmission and scattering in transverse direction in the frame of the geometrical-optical approach for the case of normal (*a*) and inclined (*b*) incidence of the plane wave-beam.

The simulation of excitation of a planar 2D Bragg resonator has been carried out also using the 3D code CST MicroWave Studio. To reduce simulation time the resonator was taken with $l_x = l_z = 15$ cm, i. e. a little smaller than used in the "cold" tests, but with deeper corrugation keeping the parameter $\alpha l_{x,z}$ constant. Results of simulations for different cases of the wave-beam incidence are shown in Fig. 5 and coincide well with the results obtained in the frame of the geometrical-optical approach.

To demonstrate selective properties of 2D Bragg resonators and the existence of a high-Q mode at the center of the Bragg reflection zone we exited the structure by a short (100 ps) incident e. m. pulse. In Figure 6, *a* one can see the evolution of field amplitude at some point inside the structure. In Figure 6, *b* the frequency spectrum is shown for different time intervals. The position of the central line in the spectrum at the final stage of the decay process corresponds to the fundamental mode having the Bragg frequency and the spectrum width defines the Q-factor of this mode as $Q \sim 1000$, which coincides well with the value found in the theoretical analysis given above. Thus direct simulations also confirm high selective properties of 2D Bragg resonators under large Fresnel parameter.

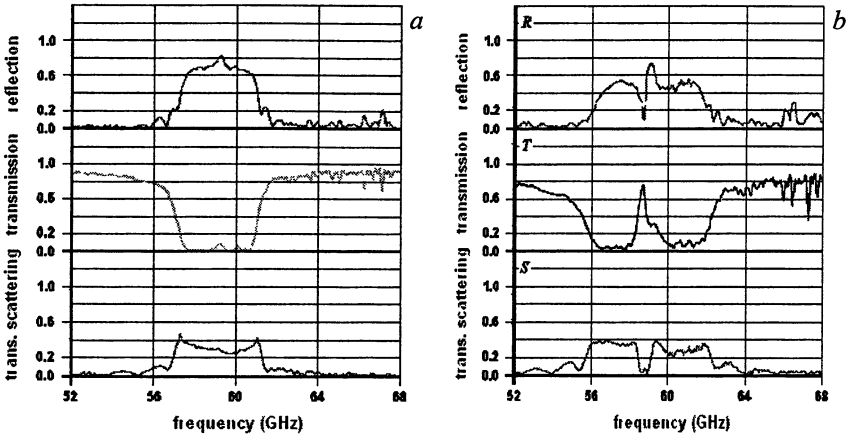

Fig. 5. The 3D computer simulations of the reflection, transmission and scattering in transverse direction for the case of symmetrical (*a*) and anti-symmetrical (*b*) incident wave-beam.

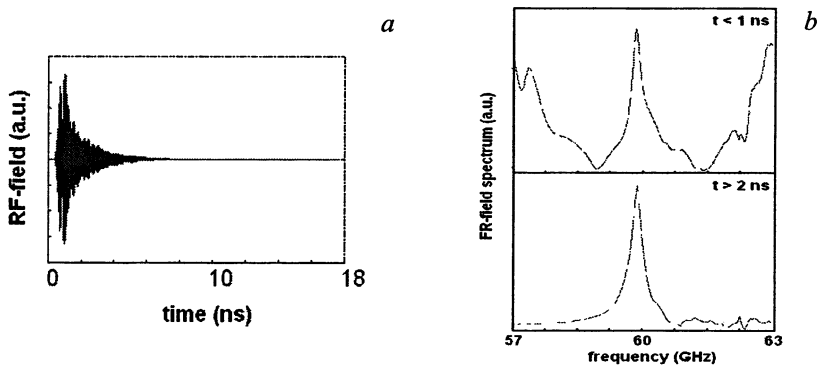

Fig. 6. Results of the 3D simulation of excitation of 2D Bragg resonator: time evolution of the RF-field (*a*) and frequency spectrum for different time intervals of the decay process (*b*).

Results of "cold" tests

For experimental study a resonator was constructed in the form of two parallel metal plates of the size 25×25 cm having a gap of 0.5 cm between them. On the inner surface these plates had a doubly-periodical sinusoidal corrugation of the depth 0.06 cm and the periods over both coordinates $d_x = d_z = 0.5$ cm, which in accordance with the Bragg resonance condition (3) provide a zone of effective Bragg scattering for TEM-modes near the central Bragg frequency of 60 GHz.

The resonators were tested using a scalar network analyser. For excitation of the resonator a wave-beam with TEM-mode structure and plane phase profile was formed at the resonator input using an additional quasi-optical transmission line of planar geometry [14]. In accordance with the calculations the zone of effective Bragg scattering was observed near 60 GHz. This zone corresponds to the mutual scattering of four partial TEM-type waves. The results of measuring of the coefficients T and S are presented in Fig. 7 and demonstrate good agreement with the simulations (compare Fig. 7 and Fig. 4). In particular, the coefficients are practically symmetrical with respect to the Bragg frequency. In the case of normal incidence of the wave-beam a non-transparent zone at the level of –25 dB was observed (Fig. 7, *a*). The width of this zone is determined by the wave coupling coefficient α. For scattering of TEM-waves it was calculated as $\alpha \approx 0.2$ cm^{-1} and corresponds well to the measured value. Two resonator modes were distinguished at the frequencies 57.3 GHz and 61.2 GHz. These modes were interpreted as the eigenmodes with one field variation over both coordinates, i. e. indices (1; 1), located at the border of the effective Bragg scattering zone $\delta \approx \pm 2\alpha$ (they are easy to be seen at the transverse scattering coefficient, see Fig. 7, *b*). The Q-factors of these modes were measured to be about 600 and 500 respectively.

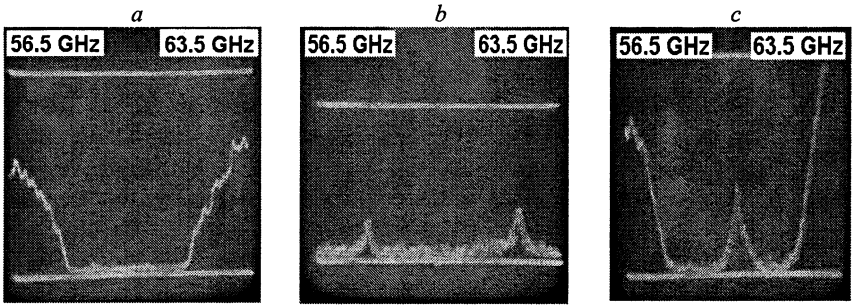

Fig. 7. Results of "cold" measurements of transmission (*a*) and transverse-scattering (*b*) coefficients for normal incidence of plane wave-beam and transmission coefficient (*c*) for inclined incidence of plane wave beam.

Inclined incidence of the wave-beam was realized in the experiment by turning the transmission line so that the difference in the rays path at the different resonator edges was equal to 5 cm (i. e. one wavelength) and this corresponds to difference in phase of the wave-beam over the resonator width of 2π. For such wave incidence transparency of the structure in the middle of the Bragg zone was observed (see Fig. 7, *c*). In accordance with the simulations the fundamental mode was measured at the frequency of 59.75 GHz with a Q-factor of about 900.

Conclusions

For a Bragg structure of planar geometry analysis of the eigenmodes spectrum has been carried out in the frame of the geometrical-optical approach and direct 3D simulations based on the CST MicroWave Studio code. Both approaches demonstrate high selective properties of above structures for large Fresnel parameters. Scattering coefficients were found for the cases of normal and inclined incidence of the wave-beam. Frequency dependences of the scattering coefficients at the Bragg structure with 2D sinusoidal corrugation were measured in "cold" tests and coincide well with theoretical predictions. Principal difference of the transmission coefficient in the vicinity of the Bragg frequency for different cases of wave-beam incidence was observed experimentally. Transparency of the structure in the vicinity of the Bragg frequency in the case of inclined wave-beam incidence was obtained that corresponds to excitation of the fundamental eigenmode of the 2D Bragg structure. Frequencies for the few first eigenmodes and their Q-factors were measured in good agreement with simulations. Thus, theoretical and experimental investigations carried out demonstrated the performance of 2D Bragg structures and their high potential to be used as selective resonators for relativistic free electron masers.

Acknowledgements. This work is supported partially by the Russian Foundation for Basic Research (grants №04-02-17118 and №05-02-17036).

References

1. *Ginzburg N.S., Peskov N.Yu., Sergeev A.S., et al* , Phys. Rev. E, 1999, **60**, 935.
2. *Cross A.W., Konoplev I.V., Ronald K., et al.*, Appl. Phys. Lett., 2002, **80**, 1517.
3. *Arzhannikov A.V., Ginzburg N.S., et al.*, these proceedings, vol. 1, p. 271-276.
4. *Konoplev I.V., Cross A.W., Ginzburg N.S., et al.*, ibid p. S34.
5. *Kogelnik H., Shank C.V.*, J. Appl. Phys., 1972, **43**, 2327.
6. *Yariv A.* Quantum Electronics. John Wiley and Sons Inc., N.Y., 1975.
7. *Kovalev N.F., Petelin M.I., Reznikov M.G.,* Resonator, USSR Athors Sert. no. 720592; Bull. no. 9, 1980.
8. *Bratman V.L., Denisov G.G., Ginzburg N.S., Petelin M.I.*, IEEE J. Quant. Electr., 1983, **QE-19**, 282.
9. *Chu T.S., Hartemann F.V., Danly B.G., Temkin R.J.*, Phys. Rev. Lett., 1994, **72**, 2391.
10. *Zambon P., Witteman W.J., Van der Slot P.J.M.*, Nucl. Instr. Meth. Phys. Res. A, 1994, **A341**, 88.
11. *Ginzburg N.S., Kaminsky A.K., Peskov N.Yu., et al.*, Phys. Rev. Lett., 2000, **84**, 3574.
12. *Yablonovitch E.*, Phys. Rev. Lett., 1987, **58**, 2059.
13. Photonic Bandgaps and Localization, Ed. by C.M. Soukoulis. Plenum, N.Y., 1993.
14. *Peskov N.Yu., Ginzburg N.S., Denisov G.G., et al.*, Opt. Comm., 2001, **187**, p. 311.

NOVEL QUASI-OPTICAL PASSIVE PULSE COMPRESSORS

S. V. Kuzikov, Yu. Yu. Danilov, G. G. Denisov, J. L. Hirshfield[1], *Yu. I. Koshurinov*[2], *V. G. Paveliev*[2], *M. I. Petelin, M. E. Plotkin*[2], *D. Yu. Shegol'kov, I. Syratchev*[3], *A. A. Vikharev, S. A. Yashunin*[2]

Institute of Applied Physics RAS, Nizhny Novgorod, Russia
[1]Omega-P, Inc., New Haven, USA
[2]Nizhny Novgorod State University, Nizhny Novgorod, Russia
[3]CERN, Geneva, Switzerland

Pulse compressors, based on a propagation of phase-modulated pulse in a dispersive media, are optimized in viewpoint of compression efficiency and compactness. The propagation of a phase-modulated pulse in a dispersive media is considered by means of spectral formalism. This allows formulating a synthesis procedure for input phase modulation and frequency dispersion which provide desirable shape of the output pulse. An idea to use a set of the cylindrical multi-mode cavities as a compact delaying line is investigated. Results of low-power tests are discussed. A new idea to avoid two-channel scheme with 3 dB coupler used for SLED-II pulse compressors is analyzed.

Introduction

Amplitude and phase distributions of a RF pulse are very important for many applications of high-power microwaves. This means the problem how to synthesize a pulse compressor with desirable pulse shape.

High-energy particle accelerators usually require flat-top pulse shape for feeding. That is why, SLED-II pulse compressors, based on long delay lines, are attractive. Unfortunately, smooth waveguides have too small delaying time (~3 ns/m). This leads to extremely long (tens meters) SLED-II compressors. New compact quasi-optical compressors are necessary.

Synthesis of pulse compressors

Let us consider theoretical problem of a propagation of the phase-modulated RF pulse in a media with frequency dispersion. The spectrum of the output pulse $s_{out}(\omega)\cdot\exp(j\varphi_{out}(\omega))$ is given by Fourier transformation of the input pulse $a_{in}(t)\cdot\exp(j\psi_{in}(t))$ increased on the dispersion $\exp(j\chi(\omega))$ of a reflectionless media:

$$F[a_{in}(t)\cdot\exp(j\psi_{in}(t))]\cdot\exp(j\chi(\omega)) = s_{out}(\omega)\cdot\exp(j\varphi_{out}(\omega)), \qquad (1)$$

where ω is a frequency, and t is a time. The formula (1) might be considered as an equation for the unknown phase modulation $\psi_{in}(t)$ and dispersion $\chi(\omega)$, if one substitutes in the left side of the equality (1) parameters of the given input pulse and parameters of the desired output pulse in the right side correspondingly. This equation is suggested to solve using two-step iteration procedure [1]:

$$\chi^i(\omega) = \varphi_{out}(\omega) - \arg\left\{F[a_{in}(t)\cdot\exp(j\psi_{in}(t)]\right\}, \quad (2)$$

$$\psi_{in}^{i+1}(t) = \arg\left\{F^{-1}[s_{out}(\omega)\cdot\exp(j\varphi_{out}(\omega) - \chi^i(\omega))]\right\}. \quad (3)$$

This procedure is similar to that has been published in [2] and allows finding the next (j+1)th approach using the previous jth approach for the mentioned unknown functions.

Let us analyze the proposed method for a synthesis of pulse compressors. The first example is actually conversion of the experimentally measured (30 GHz, 200 ns) pulse (Fig. 1) into a desired pulse to be 4 times higher on power. The iteration procedure (2)–(3) results the input phase modulation and dispersion of media shown in Figs. 2, 3 correspondingly. The output phase, which was desired to be flat, is shown in Fig. 4. Iterations were stopped when efficiency (similarity of the desired and resulted output pulses) reached 99%.

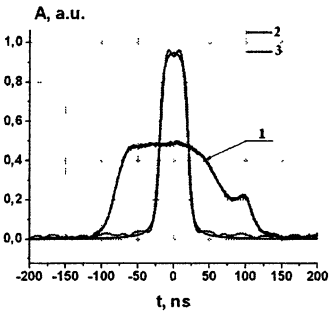

Fig. 1. Envelopes of incident (*1*), desired (*2*) and resulted (*3*) RF pulses.

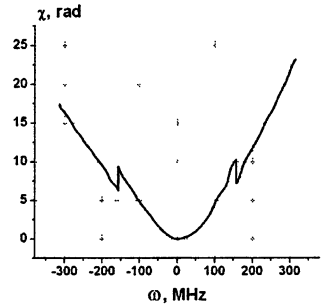

Fig. 2. The synthesized dispersion

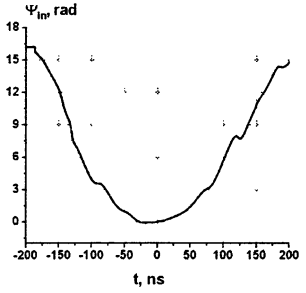

Fig. 3. The synthesized phase modulation

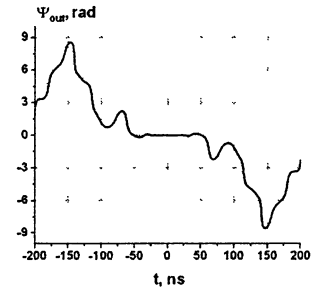

Fig. 4. The resulted phase in output RF pulse.

In order to provide found synthesized dispersion $\chi(\omega)$ by means of a real physical device, it is proposed to use a helically corrugated waveguide that dispersion is formed by coupling of one traveling mode and another standing azimuthally counter rotating mode [6]. In particular, a waveguide of the elliptical

cross-section with TE_{11} transmitting mode coupled with the rotating TM_{11} mode seems attractive. The period P, the amplitude l_0 and the length of corrugation l should be optimized in order to obtain the best approach of the waveguide dispersion $h(\omega)\times l$ to the synthesized dispersion $\chi(\omega)$. This condition means a search of minimum of the function:

$$f(P,l_0,l)=\int_{\omega_2}^{\omega_2}(\chi(\omega)-h(\omega,P,l_0)\cdot l)^2\,d\omega, \tag{4}$$

where $\Delta\omega = \omega_2 - \omega_1$ – is a bandwidth of the RF pulse.

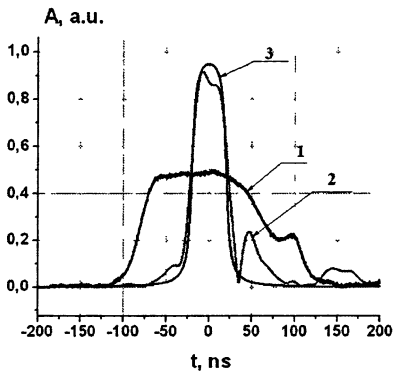

Fig. 5. Envelopes of incident (*1*), desired (*2*) and resulted (*3*) RF pulses

The optimal parameters (P = 1.08 cm, l_0 = 0.01 cm, l = 31.4 cm) of the helical waveguide with average radius 0.6 cm provide the final efficiency 94%. Here the output phase distribution was taken into account. The resulted pulse shape is plotted in Fig. 5.

Compressors based on a set of cylindrical multi-mode cavities

A SLED-II pulse compressor consists of two delay lines, operated with TE_{01} modes, which are coupled by means of 3 dB coupler [3]. In order to reduce a length of delay waveguides, an idea to use a set of cavities, which are to be an equivalent of delay line, was suggested [4]. The example of such 11.424 GHz cavity is shown in Figs. 6, 7. The incident power in a form of TE_{01} mode passes many times inside the cavity. This provides very large delay time in comparison with a smooth waveguide of the same length. Several cavities, connected in a chain, can provide delay time up to hundreds of nanoseconds.

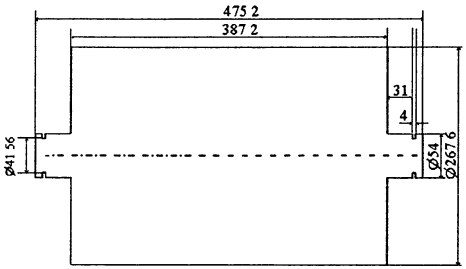

Fig. 6. The 11.4 GHz elementary delay cavity

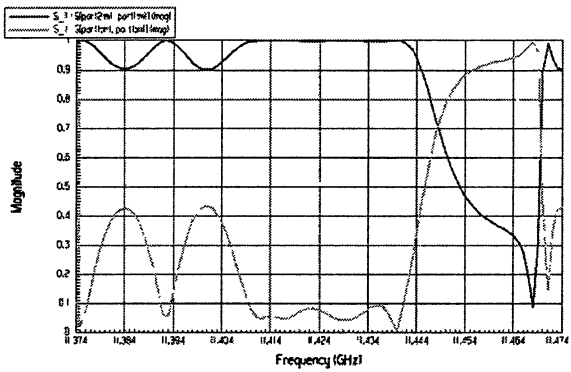

Fig. 7. Reflection and transmission for the 4-cavity chain

The necessary condition for the mentioned solution is that spurious high-Q resonances are to be avoided in frequency band which should be wider than spectrum width of the output compressor's pulse: this condition is satisfied, in particular, if a cavity has spectrum of eigen modes consisted of the quasi-degenerated modes. This situation takes place in a solution presented in [4]. This is confirmed by calculations of eigen mode spectrum of this cavity (Fig. 8).

In order to test at 34 GHz such compact pulse compressor, the cavities with the shape, shown in Fig. 6, were chosen with scaling of their parameters for the mentioned frequency. The used cavities provide at 34 GHz delay time 23 ns/m.

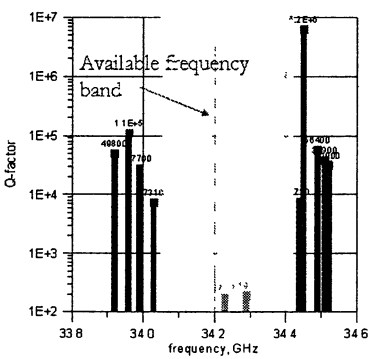

Fig. 8. Eigen modes of delay cavity

The low power tests were carried out with the 4-cavity prototype shown schematically in Fig. 9. The last cavity was closed by means of movable cut off reflector for frequency tuning. The coupling diaphragm before the first cavity was calculated to provide maximal efficiency in accordance with the chosen compression ratio 5.

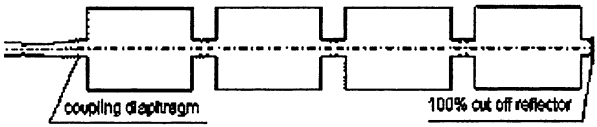

Fig. 9. Scheme of the tested 4-cavity pulse compressor

The observed experimentally compression with the π-phase flip (Fig. 10) is well agreed with a theory. The power gain was about 4.5, the output pulse duration was 40 ns.

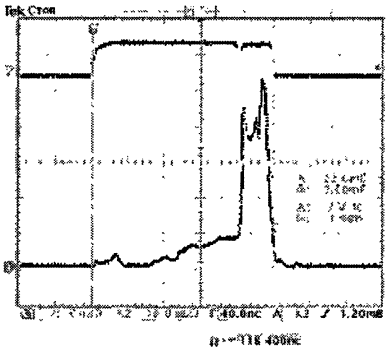

Fig. 10. Measured envelopes of the input and output RF pulses

Calculations show that at 30 GHz the 150 ns/m delay time is easily achievable. Such dramatic reduction of a length allows using of multi-stage pulse compressors which combine high power gain as well as high efficiency.

One-channel SLED-II pulse compressor

In SLED-II pulse compressor two delay lines are coupled by means of a 3 dB coupler. This allows an isolation of RF source from the compressor's reflection. Unfortunately, 3 dB coupler is a weak part of any SLED-II pulse compressor, because this coupler includes a lot of brazed junctions of single mode waveguides. The higher frequency, the more complicated problem is. A necessity to tune two delay lines, which ideally should be identical ones, is also disadvantage of the conventional compression scheme.

Fortunately, any ring-like cavity, operated with a traveling eigen mode, does not reflect a power. Let us consider version of such cavity consisted of axis-symmetrical waveguides and operated with axis-symmetrical TE modes (Fig. 11) [5]. An eigen mode of the cavity consists of TE_{02} and TE_{03} modes which propagate toward each other. These modes are completely converted each to other in the both ends of the cavity by means of selective reflecting converters.

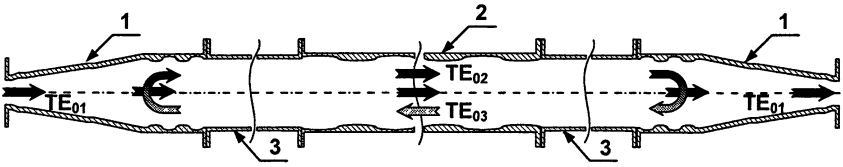

Fig. 11. One channel SLED-II pulse compressor: *1* – TE_{02}–TE_{03} reflective mode converter, *2* – TE_{01}–TE_{02} mode converter (coupler), *3* – delay waveguides.

The TE_{01} mode is assumed to be a feeding wave. This transmitting mode is coupled with the forward TE_{02} mode only by means of selective mode converter placed in the middle of the cavity. This converter plays a role of the coupler and provides an optimal level of mutual conversion TE_{01}–TE_{02} in order to provide high compression efficiency.

Let us consider an operation of the suggested compressor. The phase-modulated RF pulse feeds the compressor. The feeding TE_{01} wave propagates to TE_{01}–TE_{02} mode converter where a part of the incident power is converted into the forward TE_{02} wave. The arisen TE_{02} wave propagates to the right reflective TE_{02}–TE_{03} converter and completely transformed into the backward TE_{03} wave, which propagates to the left end reflector without losses. At the left end the TE_{03} mode has full conversion into the forward TE_{02} mode. At the TE_{01}–TE_{02} mode converter this wave is added to a new portion of power produced by the feeding TE_{01} mode. Like in any SLED-II pulse compressor RF power is stored inside the compressor. At first time the transmitting signal at the output decreases then it grows again, nevertheless, being less than the input signal. When π-phase step comes in the compressor the stored power begins to leak outside being in the same phase as a phase of the incoming TE_{01} power. This means an emissive splash of RF power at the output.

Note that amongst eigen modes of the considered cavity there is an absolutely degenerated eigen mode. This mode consists of the same mixture of the TE_{02} and TE_{03} modes, but directions of propagation are quite opposite in comparison with the described operating eigen mode. This parasitic mode leads to reflection of some RF power and splitting of eigen frequencies of the cavity. In order to avoid these undesirable phenomena, spurious coupling between the operating eigen mode and the degenerated spurious mode should be as small as possible.

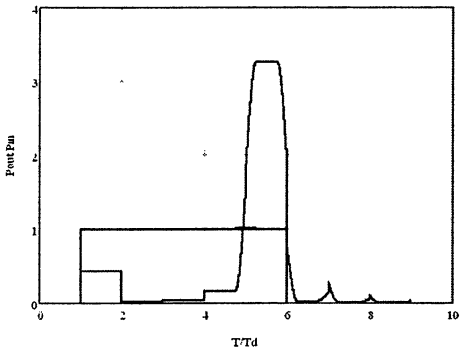

Fig. 12. Simulation of compression by the one-channel SLED-II

Calculations aimed to simulate 34 GHz pulse compressor show that high efficiency is achievable. In particular, at 34 GHz we anticipate the power gain 3.3, efficiency 66% for 100 ns output pulse duration taking into account losses and realistic 50 ns phase flip (Fig. 12).

Conclusion

Synthesis procedure, which provides a desired output pulse, helps to find the best approach for the phase modulation and frequency dispersion. The synthesized dispersion might be embodied by means of waveguides with helical corrugation.

SLED-II pulse compressors due to TE_{0n} mode cavity chains allow a reduction of the length by 10–50 times. Designs of such cavities should provide an existence of a lot of the degenerated eigen modes. The proposed compact single-channel SLED-II pulse compressor does not require a 3 dB coupler.

References

1. *Kuzikov S.V.* Optimization and Synthesis of Passive Pulse Compressors Based on Reflectionless Cavities, Int. J. IRMMW, Vol. 19, No. 5, 1998, p. 771-784.
2. *Katsenelenbaum B.Z. et al.*, Radiotekhnika i Electronika, No. 12, 1967, p. 244-251 (in Russian).
3. *Wilson P.B. et al.*, SLED-II: A new method of RF pulse compression, presented at the Linear Accelerator Conference, Albuquerque, NM, September 10-14, 1990.
4. *Kazakov S.*, Multi-mode delay lines, ISG-XI, KEK, December 2003.
5. *Kuzikov S.V. et al.*, Multi-Mode SLED-II Pulse Compressors, Proc. LINAC 2004 Conf., Lubeck, Germany, 2004, p. 660-662. http://bel.gsi.de/linac2004/PAPERS/THP28.PDF
6. *Burt G. et al.*, Dispersion of helically corrugated waveguides: Analytical, numerical, and experimental study, Phys. Rev. E, Vol. 70, No. 4, 2004, p. 046402.

A DESIGN SCHEME FOR QUASI-OPTICAL MODE CONVERTERS OF COAXIAL CAVITY GYROTRONS

G. Michel[1], *O. Prinz*[2], *T. Rzesnicki*[2]

[1]Max-Planck-Institut für Plasmaphysik, Teilinstitut
Greifswald, EURATOM Ass., Wendelsteinstraße 1,
17491 Greifswald, Germany
[2]Forschungszentrum Karlsruhe EURATOM Ass., IHM,
Postfach 3640, 76021 Karlsruhe, Germany

This paper describes the peculiarities of mode converters of coaxial cavity gyrotrons. The high order and the characteristic field pattern of these volume modes makes it difficult to design a quasi-optical mode converter with a dimpled wall launcher and (possibly) Yeti-footprint-mirrors. A method to obtain the vector potential out of the elcetric field is presented which allows the use of MoM codes to produce the input field for the mirror design codes. In the second section a method which tries to synthesize smooth mirrors in the presence of helical wave fronts ("vortices") is presented.

Introduction

The limiting factor for the mode order in hight power gyrotrons (i. e. the size of the resonator for a given wavelength) is the mode selectivity, as the mode spectrum becomes denser with growing resonator size. A well known method for the reduction of the density of the mode spectrum is the introduction of a coaxial insert in the cylindrical gyrotron cavity. Therefore, coaxial gyrotrons can operate at higher order modes (i. e. larger Bessel roots) than conventional gyrotrons. This allows bigger resonators and hence, higher power levels.

Launcher modeling

The European ITER gyrotron [2] operates at the $TE_{34,19}$ mode with a Brillouin angle of about 60° at the launcher output. According to the asymptotic theory [1], the minimal launcher length for the longitudinal bunching of the field is more than 500 mm for the given overmoding factor, which is unfeasible in a real gyrotron. Therefore – at least for the longitudinal bunching – one has to live with an imperfect output pattern which produces edge diffraction at the launcher cut or decrease the overmoding significantly, which complicates the cooling and increases the risc of post-cavity interaction. As this gyrotron aims at 2 MW, CW operation, stray radiation in the tube is very critical. The correct modeling of the launcher output is the basis for the assessment of the beam quality and, more important, it is the basis for the design of the internal mirrors [3].

Numerically optimized launchers allow to shorten the mode converter. They have low edge diffraction but also low gaussian content.

The most accurate way of calculating the launcher output is the direct solution of Maxwell's equations. With the method of moments (MoM) this becomes feasible in spite of the large size compared to the wavelength. At FZK the MoM code from CCR [4] is used. It solves the electric field integral equation (EFIE) for the unknown surface currents on the launcher wall. Then the electric field on the top of the launcher is calculated from the known surface currents. However, the mirror design codes are based on the z-component (along the gyrotron axis) of the electric vector potential $\mathbf{F}$:

$$\mathbf{E} = -\frac{1}{\varepsilon_0}\nabla \times \mathbf{F}. \tag{1}$$

If there is only a z-component of $\mathbf{F}$ (in the longitudinal direction), we speak of TE-waves. Practical calculations show, that the E-field in a x-y-plane a few millimeters over the top of the launcher is still an almost pure TE-wave (the z-component of $\mathbf{E}$ is less than –30 dB). With this knowledge we can neglect E_z and calculate an F_z which produces the known $\{E_x, E_y\}$. This is done with a variational approach by minimizing the least squares difference between the known $\{E_x, E_y\}$ and the unknown $\{\partial F_z/\partial y, \partial F_z/\partial x\}$. In other words, we look for a "best solution" of (1) by minimizing the functional

$$I = \iint \left[\left(-E_x - \frac{\partial F_z}{\partial y} \right)^2 + \left(E_y - \frac{\partial F_z}{\partial x} \right)^2 \right] dxdy. \tag{2}$$

The ε0 is omitted here as we are only interested in the distribution and not in the total power. Now $-E_x$ is expanded into a 2D Fourier series:

$$-E_x(x, y) = \sum_i \sum_k a_{ik} e^{j(ix+ky)}. \tag{3}$$

Similarly E_y is expanded into b_{ik} and F_z into c_{ik}. Then the derivatives of F_z become

$$\frac{\partial F}{\partial x} = \sum_i \sum_k jic_{ik} e^{j(ix+ky)}, \tag{4}$$

$$\frac{\partial F}{\partial y} = \sum_i \sum_k jkc_{ik} e^{j(ix+ky)}. \tag{5}$$

Now the known a_{ik} and b_{ik} as well as the unknown c_{ik} are substituted into (2) and the functional is made stationary by setting $\partial I/\partial c_{ik} = 0$. Due to the orthogonality of the basis functions this gives a simple equation for the unknown c_{ik}:

$$c_{ik} = \left(ka_{ik} + ib_{ik}\right) / \left(j(i^2 + k^2)\right). \tag{6}$$

Note that c_{00}, the constant part, is still undefined (because $\mathbf{F}$ is defined via its derivatives). As the field is a quickly oscillating wave, this constant part can be set to zero. Now F_z can be obtained with a Fourier backtransform of the c_{ik}.

As the field was calculated shortly over the top of the launcher, it must now be backprojected to the beginning of the cut via plane wave decomposition. This is now the initial or source distribution for the mirror design. The Figure below shows $|E_\perp|$ and the resulting $|F_z|$ in comparison.

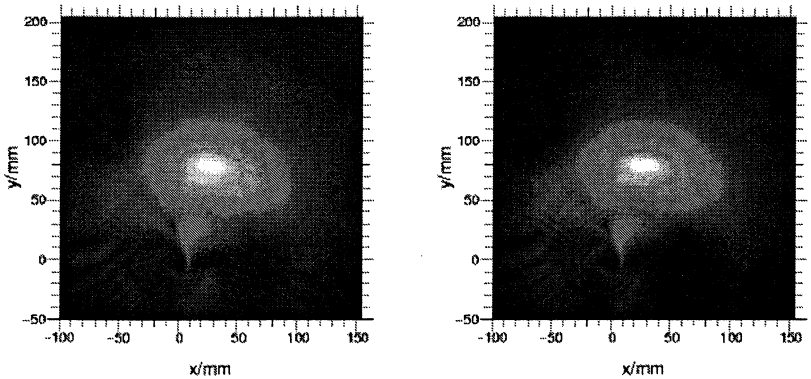

$|E_\perp|$ (left) and $|F_z|$ (right) for a $TE_{22,6}$ launcher

The field patterns look pretty identical which confirms that we are in the radiating near field region of the launcher and the distribution of F_z is very close to H_z.

Currently there is not yet a calculation for a radiation pattern of the $TE_{34,19}$ launcher as the dimensions are quite large compared to the wavelength and the Microsoft®Windows™ version of the MoM-code is only capable of allocating 2 GB of RAM which is too little for this problem. A Linux version of the code is now avaliable at FZK and work is in progress for the modeling of this launcher.

Mirror design

As we have an imperfect launcher radiation, there will be most likely the need for Yeti-footprint mirrors in order to fit a maximum fraction of the power trough the gyrotron window and to achieve a high Gaussian content. These mirrors are synthesized with the Katzenelenbaum – Semenov algorithm. A common problem with these mirrors are helical phasefronts or "vortices" in some places. It is impossible to transform such a helical phasefront into a smooth one with a smooth mirror. There must be phase jumps somewhere on the mirror to fulfill this goal.

In order to minimize the negative effect of these phase jumps (stray radiation), they should be placed in locations where the field amplitude is low which will reduce stray radiation and cross polarization. A smooth mirror surface $f(x, y)$ can be transformed into an exact phase corrector $u(f)$ by

$$u(f) = \varphi + 2\pi \mathrm{nint}\left(\frac{f-\varphi}{2\pi}\right). \tag{7}$$

Here, φ is the exact phase corrector and nint is the nearest integer; f is exact when $|f - u(f)| = 0$. This condition will be hard to fulfill when f is smooth and there are helical phasefronts. A minimization of the cost function $|f - u(f)| \cdot A^2$, with A being the field amplitude, allows errors in regions with little or no field ampli-

tude. In these regions a higher error is possible which allows the surface to remain smooth in the vicinity of vortices.

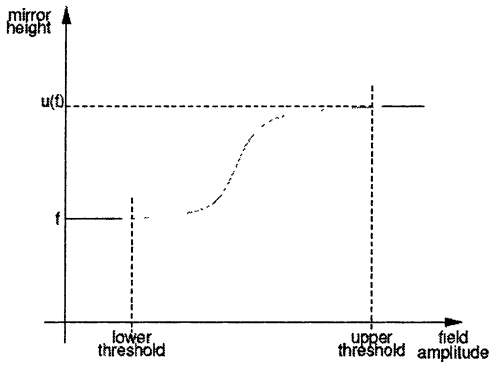

This is achievend by means of a sigmoid function S (see Figure above). First, a smooth curl-free phase corrector is calculated with [5]. This is $f(x, y)$. Then $u(f)$ is calculated by means of (7). The final surface (mirror height) $z(x, y)$ is now calculated by

$$z = S(f, u, A^2). \tag{8}$$

The Figure below shows the mixture of an $TEM_{0,0}$ and a $TEM_{1,1}$ Gauß – Hermite mode with four vortices. The contour lines represent the amplitude and the color represents the error of the unwrapped phase corrector. The hard adjustment contains no errors but jumps, the soft adjustmet contains no jumps but errors in high-amplitude regions. The medium adjustment has no jumps and errors in low-amplitude regions.

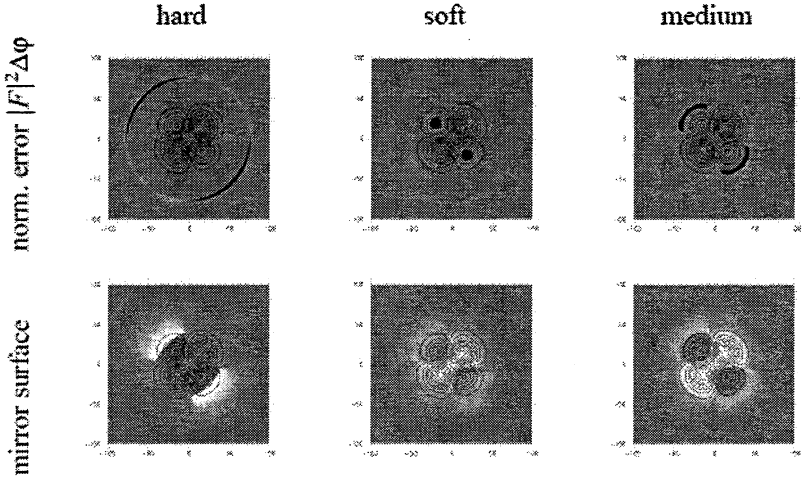

Academic example: phase error of a curly phase front for three different adjustments of the sigmoid function.

Conclusions

The use of a MoM code for the modeling of the initial field distribution gives the most accurate results in the final design. The problem of the interconnection between the vectorial MoM code and the scalar mirror code has been resolved.

Even with advanced synthesis algorithms for the launcher, the output beam is not perfect in the case of high order volume modes. These beams contain helical wave fronts which can be handled with some success by the proposed method of allowing a higher error in places where the amplitude is low. Both methods are used in the design of the mode converter for the European ITER gyrotron.

References

1. *Bogdashov A.A., Denisov G.G.,* Asymptotic Theory of High-Efficiency Converters of Higher-Order Waveguide Modes into Eigenwaves of Open Mirror Lines, Radiophys. Quantum Electron., 2004. Vol. 47, No. 4, p. 283 ff.
2. *Piosczyk B. et al.*, Progress in the Development of the 170 GHz Coaxial Cavity Gyrotron for ITER, these proceedings, vol. 1, p. 91-99.
3. *T. Rzesnicki et al.*, 170 GHz, 2 MW Coaxial Cavity Gyrotron – design verification of the new RF output system, 30th Int. Conf. IRMMW/THz, Williamsburg, USA, 2005, p. 519 ff.
4. *Neilson J., Bunger R.*, Surface Integral Equation Analysis of Quasi-Optical Launchers, IEEE Trans. Plasma Sci., 2002. Vol. 30, No. 3, p. 794 ff.
5. *Michel G., Thumm M.*, Spectral Domain Techniques for Field Pattern Analysis and Synthesis, Surveys on Mathematics for Industry, 1999, 8, 259-270.

A METHOD OF WAVEGUIDE MODE CONVERTER SYNTHESIS

G. G. Denisov, D. I. Sobolev

Institute of applied physics Russian academy of sciences, Nizhny Novgorod, Russia

An iterative method for synthesis of waveguide mode converters is described. The method is applicable to various types of irregular waveguides. Examples of new synthesized components are presented.

Introduction

Development of multi-mode waveguide transmission lines requires design of components ensuring that waveguide modes be preserved or converted from one into another when the transmission line is bent or its parameters (e. g., radius) are varied. The synthesis methods developed to date (see, e. g., [1]) were in some respects unsatisfactory, both in regard to converter parameters, such as the length and the conversion coefficient, and computer resources. The objective of this paper is to formulate and to illustrate a new efficient iterative algorithm for synthesis of waveguide mode converters.

1. Description of the method

Let us consider a system of linear differential equations of the form:

$$da_j/dz = ih_j(z)a_j + i\sum_{k\neq j}\kappa_{jk}(z)a_k \ . \qquad (1)$$

In particular such a system corresponds to the problem of one-dimensional propagation of waves in an inhomogeneous waveguide (with time dependence as $e^{-i\omega t}$). In this case, a_j and h_j are the amplitude and wave number of the j-th mode, respectively, and $\kappa_{jk}(z)$ are the coupling coefficients of the k-th and j-th modes. In the simplest case when all waves propagate without losses in the positive direction of the z axis, the wave numbers are positive. The eigenvalues and coupling coefficients for the modes of a metal waveguide are obtained in [2, 3]. In this case, wave numbers can be considered either constant (if a waveguide with small deformations is analyzed by the perturbation method) or dependent on the z coordinate (if inhomogeneous waveguides are considered by the cross-section method). By renormalization of the amplitudes, it can be ensured that the relationship $\kappa_{jk}(z) = \kappa^*_{kj}(z)$ is satisfied. Here, the asterisk indicates the complex conjugation. The energy conservation law takes the form $\sum_j |a_j|^2 = 1$.

We assume that the total length of the converter is constant and specify two possible boundary conditions on its ends, namely, the wave amplitude vector $a_j(0)$, corresponding to a given field, at the beginning of the waveguide and a desired amplitude vector $a_j(L)$ at the end of the waveguide. Denote the wave amplitude distribution obtained with the use of the first boundary condition as $a_j^{(1)}(z)$. After this, one can obtain the wave amplitude distribution with the use of the second boundary condition. Denote this distribution as $a_j^{(2)}(z)$. In the case where the waveguide profile ensures complete conversion of the initial amplitude vector to the desired one, the equality $a_j^{(1)}(z) = a_j^{(2)}(z)$ will be satisfied for all j and z. If the conversion is not complete, then, correspondingly, $a_j^{(1)}(z) \neq a_j^{(2)}(z)$.

To provide an iterative procedure for synthesis of coupling coefficients, we find the correction for coupling coefficients in each step as

$$\Delta\kappa = \pi \operatorname{Im}(a_1^{(1)*} a_2^{(2)} - a_1^{(2)*} a_2^{(1)} + a_2^{(1)*} a_1^{(2)} - a_2^{(2)*} a_1^{(1)})/2L, \qquad (2)$$

where L is length of the converter.

To determine the necessary deformation of the waveguide surface, we consider the simplest case where coupling coefficients are products of constants dependent on types and indices of the waves and the function describing the deformation (e. g., the curvature in the case of bending a regular waveguide or the tangent of the inclination angle of the waveguide generatrix in the case of axis-symmetric deformation), namely,

$$\kappa_{jk}(z) = \gamma_{jk} f(z). \qquad (3)$$

Corrections from each pair of interacting waves are added: $\Delta f(z) = \sum_{j \neq k} \Delta f_{jk}(z)$. At each iteration of the process the difference of the distributions $a_j^{(1)}(z)$ and $a_j^{(2)}(z)$ for the current value of $f(z)$ is found and the correction $\Delta f(z)$ and the corresponding change in the waveguide profile are calculated.

This method was applied to various types of waveguide geometry, for which the coupling coefficients can be represented in the form of (3). The first type is a bent circular waveguide with constant cross-section, where the coupling coefficients are proportional to the waveguide curvature, so that it is expedient to choose the latter as the function $f(z)$. The second one is a straight circular waveguide with variable radius, where the coupling coefficients are proportional to the waveguide radius derivative. The method is also applicable to the more general types of 2-D waveguide deformation (see the last example).

Converter of the TE_{01} mode to TE_{11} mode

The converter was designed for frequency 28 GHz, waveguide length 56 cm, and the waveguide diameter 32 mm. We took into account 21 modes, i. e. all propagating modes at the given frequency which are excited by the TE_{01} mode in a bent waveguide. The content of the desired wave amounted to 99%. Total time of calculation (several tens of iterations) using a 2 GHz processor is less than one minute. Figure 1 shows interior view of the disassembled converter fabricated in two parts. Converter test results agree well with the calculations.

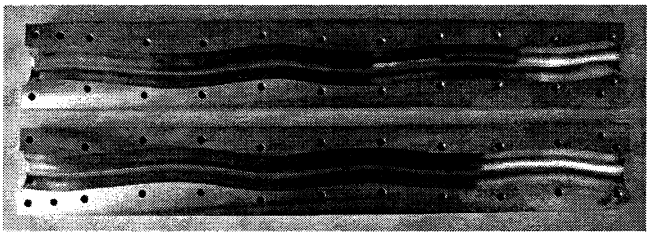

Fig. 1. View of the TE_{01}-to-TE_{11} efficient mode converter

90° TE_{01} waveguide bend

The design parameters are: frequency 10 GHz, waveguide length 50 cm, waveguide diameter 54 mm. For these parameters of the waveguide, the bent angle is close to Jouguet angle and, therefore, an almost complete undesirable conversion of the TE_{01} mode into the TM_{11} mode occurs if the waveguide curvature is constant. However, owing to coupling with the waves with are not degenerate with the TE_{01} wave (mainly, TE_{11} and TE_{12} in this case, see Fig. 2), we obtained up to 99.98% of the power in the TE_{01} mode at the bend end as a result of the iterative synthesis. In the calculations, we took into account all propagating modes at the given frequency (9 modes). The total time of calculation using a 2 GHz processor was about one minute.

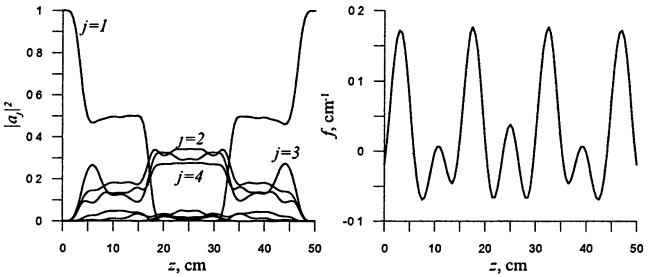

Fig. 2. TE_{01} waveguide bend. Powers of waves – $|a_j|^2$ (left) and waveguide curvature – f (right). The first wave is TE_{01}, the second – TE_{11}, the third – TM_{11}, and the fourth – TE_{12}.

Analyzing the synthesized waveguide profile, it can be noted that the waveguide curvature has oscillating components which provide coupling of TE_{01} wave with certain auxiliary waves. As a result of this coupling the wave degeneracy is removed and the necessary wave is realized at the output. This example illustrates that the proposed method permits to find solutions even if the initial and the desired waveguide profiles strongly differ.

Despite the strong dependence of the curvature on the longitudinal coordinate, the waveguide profile does not look complicated (see Fig. 3) since upon double integration, which is required for obtaining the waveguide trajectory.

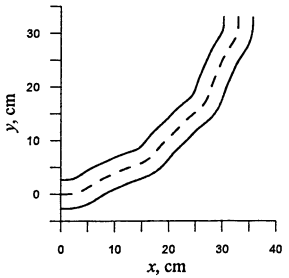

Fig. 3. Cross section of the waveguide bend with the TE_{01} mode preserved. The waveguide axis is shown by a dashed curve.

Filter of HE_{11} mode of the corrugated waveguide

The filter was designed for 84 GHz frequency and 31.75 mm waveguide diameter. The filter consists of two identical waveguide converters (190 mm length) separated with a big (70 mm) gap. The first converter transforms HE_{11} mode into converging Gaussian wave beam. The beam parameters are chosen so that after the gap the phase front curvature changes its sign but has the same value. Such a beam propagates through the gap with very small diffraction losses: 0.3%. The second converter is symmetrical and it converts the diverging wave beam back into HE_{11} mode. Any other waveguide mode is effectively attenuated due to diffraction losses in the gap.

The synthesized mode converter has nearly 100% efficiency assuming six lowest forward-propagating waves. More precise calculations using a matrix code give the scattering loss of the converter as 0.2%. Figure 4 shows the shape of the converter and the electric filed at its end.

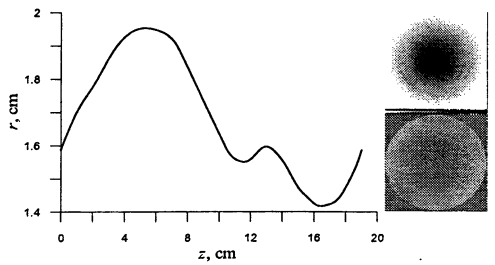

Fig. 4. Mode converter shape (left part) and electric field on its end (right part: amplitude – top, phase – bottom).

The filter was tested as a separately and as a part of a high-power transmission line (200 kW, CW). Both tests showed good agreement with the calculations (for details see [5]).

Short gyrotron converter

The converter operates at frequency 118 GHz, waveguide diameter is 40.16 mm. Input $TE_{22,6}$ mode is transformed into Gaussian wave beam. Existing high-efficiency converters [6] with such parameters are slightly less than 200 mm long. Using a 2-dimensional implementation of the method, we were able to decrease the converter's length to nearly 100 mm at the cost of deeper and more complicated waveguide deformation (Fig. 5).

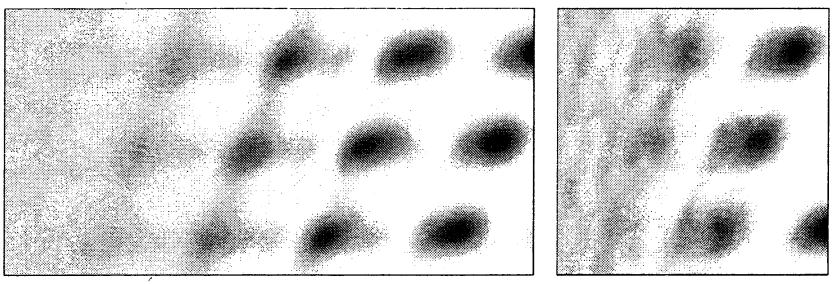

Fig. 5. Field intensity on the border of the gyrotron converter. Left part – previously existing variant (L = 195 mm), right part – the new one (L = 100 mm). Gaussian mode content in radiation patterns exceeds 99% for both cases.

Conclusion

A new iterative method for synthesis of waveguide mode converters is proposed, realized as a computer code and checked in experiments. The method offers fundamentally new solutions to the problem of mode converter design.

References

1. *Plaum B., Wagner D., Kasparek W., Thumm M.*, Proc. of 25th IRMMW Conf., 2000, Beijing, China. p. 219.
2. *Katsenelenbaum B.Z.*, Theory of Irregular Waveguides with Slowly Varying Parameters [in Russian], USSR Acad. Sci., Moscow, 1961.
3. *Kerzhentseva N.P.*, Radiotekh. & Elektron., 1958, 3, No. 5, 649.
4. *Denisov G.G., Kalynova G.I., Sobolev D.I.*, Method for synthesis of waveguide mode converters, J. Radiophys. Quantum Electron., 2004, 47, No. 8, 615.
5. *Sobolev D.I., Chirkov A.V., Denisov G.G., Lukovnikov D.A., Malygin V.I.*, Minimization of diffraction losses in big gaps of multi-mode waveguides, Int. J. Infrared and Millimeter Waves, 2005, 26, No. 7, 953.
6. *Bogdashov A.A., Denisov G.G.*, Asymptotic Theory of High-Efficiency Converters of Higher-Order Waveguide Modes into Eigenwaves of Open Mirror Lines, J. Radiophys. Quantum Electron., 2004, 47, No. 4, 283.

SURFACE TEXTURES AND REFLECTION LOSSES AT MILLIMETRE WAVELENGTHS

S. Cirant

Istituto di Fisica del Plasma, CNR, Milano, Italy

In most applications of microwaves the power reflected at the Snell's angle is lower than predicted, even for good quality mirrors, because of a non-smooth shape of the real surface. Scope of this work is twofold: first, to work out a model for loss enhancement based on the effective area increase in rough surfaces, applicable to the case in which the wavelength is much longer than roughness (both amplitude and scale length), and the skin depth is not necessarily much smaller than roughness. Second, to apply surface texturing for the evaluation of the likely effect of roughness on long-term mirror reflectivity.

Goal of this task is to build and validate a model for reflection loss enhancement with respect to theoretical estimates assuming perfectly smooth resistive mirror surface, which is due to surface roughness. The motivation is the development of a predictive tool for extra thermal loading of the plasma facing ECRH mirrors, possibly due to exposure to thermonuclear plasmas, once the shape of the damaged surface is given. The model must be validated by experiments.

Brief description of the model

The model holds in the approximation $(4\pi\sigma/\lambda)^2 << 1$, i. e. the wavelength λ is much longer than the roughness σ, which in turn is in the order of, or much less than, the skin depth δ.

Enhanced losses are assumed to be due to the effective area increase of the layers carrying the skin current, which is caused by roughness. Skin currents in the metallic body match standard reflection conditions, and are not affected by surface roughness. The local resistive power density dissipation is therefore given by:

$$\frac{dP}{dV} = \eta J^2, \tag{1}$$

where J is the local skin current density given by reflection from perfectly smooth surface. The total resistively dissipated power in the mirror body is given by:

$$P = \eta J_0^2 \int_{S} \int_{d>>\delta} \Gamma dS e^{-2z/\delta} dz, \tag{2}$$

where Γ is the surface enhancement factor due to roughness. The exponential decay of the skin currents in the mirror body is taken into account by the weighted average:

$$\frac{P_{rough}}{P_{smooth}} = \int_{d>>\delta} \frac{\Gamma(z)e^{-2z/\delta}}{\int_{d>>\delta} e^{-2z/\delta}dz} dz. \tag{3}$$

Surface textures

The Γ function for a "monocromatic" rough surface, i. e. the surface characterized by a purely periodic roughness, is given by:

$$\Gamma(z) = \begin{cases} \left(\frac{2}{\pi^2}\right)\int_0^{\pi} x\sqrt{1+\left[\pi\frac{\sigma-z}{\lambda}\right]^2}\sin(x)^2 dx, & 0 \le z \le \sigma; \\ 1, & z > \sigma, \end{cases} \tag{4}$$

which in practice is the surface of revolution of a sinusoid around the symmetry axis, $(\sigma - z)$ being the peak-to-peak amplitude and λ the transverse wavelength. See Fig. 1 for further details.

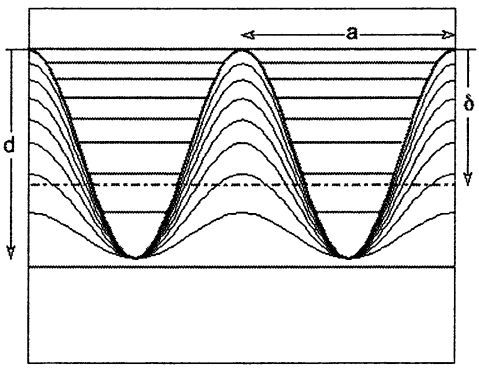

Fig. 1. A modeling of the periodic roughness, which takes into account the fact that for depths larger than the roughness amplitude, the current sheets are unperturbed flat planes.

The texture of a generic surface is described by its Power Spectral Density (PSD) $S(k)$, defined as the Fourier transform of the autocorrelation function of a set of vertical displacements $z(x)$ of the real surface with respect to the ideal mean plane (x is the transverse coordinate, z the displacement from the zero reference plane). It can be demonstrated that the integral of PSD over the wave number spectrum is equal to the average displacement squared:

$$\int_{k_0}^{\infty} S(k)dk = \int_0^L z^2(x)dx = \sigma^2. \tag{5}$$

We assume that the surface enhancement factor γ is therefore given by:

$$\gamma = \frac{\langle A \rangle}{A_0} = \frac{1}{A_0} \frac{\int_{k_{min}}^{\infty} S(k)\langle A_k \rangle dk}{\sigma^2}. \tag{6}$$

The assumption has to be verified by comparing the predictable loss enhancement given by (6) and actual reflectivity measurements.

Textures classification

If all processes concurring to the surface erosion do not have any particular preferred transverse scale length, or any preferred wavelength range, they are stochastic, and it is observed from micrometric to galactic scale that the scaling $\sigma^2 \propto D$ holds, D being the size of the sample [1]. Therefore, the PSD in this case is given by:

$$S_s(k) = \frac{2\pi\kappa_T}{k^2}, \tag{7}$$

κ_T being called "*topothesy*" of the surface.

In machined surfaces, longer wavelengths are suppressed by mechanical removal of mirror material, and the PSD can be given by [2]:

$$S_m(k) = \frac{\kappa_T}{1+(k/k_c)^2}, \tag{8}$$

$k_c = 2\pi/\lambda_c$ being the cut-off wave number above which the surface can be considered stochastic.

A periodic surface has a dominant wave length $\lambda_g = 2\pi/k_g$, with a Gaussian distribution of wave numbers having a width $w = \delta k/k_g$:

$$S_p(k) = \zeta \cdot K \cdot \exp\left[-\left(\frac{k/k_g - 1}{w}\right)^2\right] + (1-\zeta) S_m(k), \tag{9}$$

where ζ represents the weight of the periodic content of the roughness spectrum over a machined-stochastic one ($\zeta = 1$: purely periodic, $\zeta = 0$: purely machined-stochastic).

Figure 2 shows an example of three PSD with the same σ (100 μm). Because of the different shape, they have a different γ.

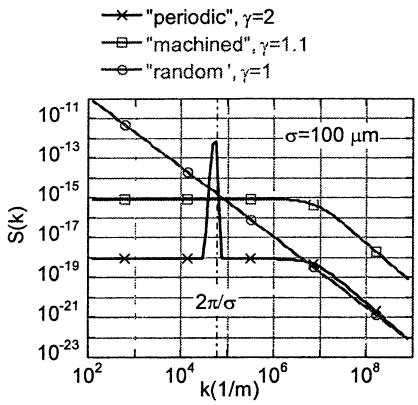

Fig. 2. PSD for three different surface textures. The average roughness σ is the same for all surfaces, but the average surface enhancement γ is much different.

Loss enhancement from textured surfaces

Assuming that the area increase is the dominant effect in reflection loss enhancement, Eq. (6) can be used to predict the effect of roughness on losses. We use as a reference case a circular surface with a diameter $D = 5$ cm which corresponds to the most energetic part of a mm-wave beam in an high power system for Electron Cyclotron Heating and Current Drive.

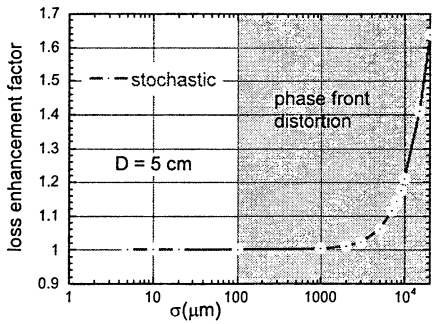

Fig. 3. γ factor dependence with σ, in case of a stochastic surface

Figure 3 shows the predicted loss enhancement dependence with the average rugosity σ over the sensitive area. Because of the dominance of long scale length perturbations, which produce a very low area increase, the loss increase is negligible unless surface perturbations are extremely large, in which case the phase front distortion would be a much worst effect.

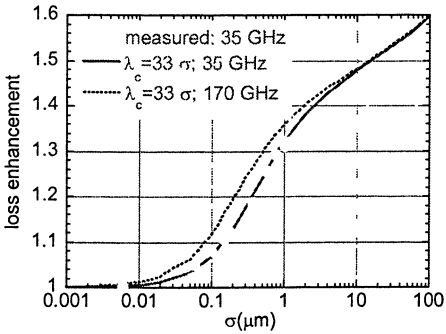

Fig. 4. γ factor dependence with σ, in case of a machined copper surface, which is stochastic on scale lengths shorter than 33σ. The calculation is made for two frequencies, and compared with experimental data (dots) at 35 GHz [3].

Figure 4 shows γ calculated for a machined surface, stochastic on scale lengths shorter than 33σ. For this specific PSD the γ factor agrees quite well with experimental values obtained at 35 GHz.

Fig. 5. γ factor dependence with σ, in case of a periodic surface having a wavelength peaked at 2.1σ. The calculation is made for two frequencies, and compared with experimental data (dots) at 35 GHz [3].

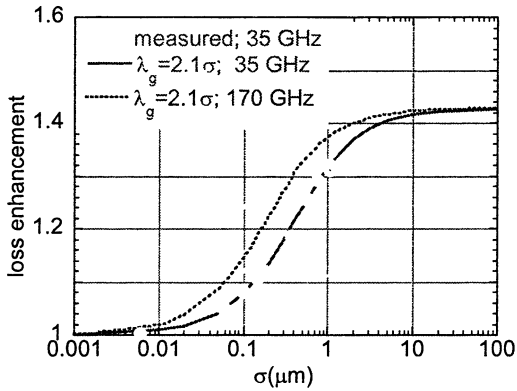

Figure 5 is similar to Fig. 4, but in this case the shape of the rugosity is periodic, with a wavelength peaked at the plausible value of 2.1σ. Also in this case the agreement with experimental data is good, which means that different PSD can give the same loss enhancement. This is not surprising since the area increase is an integral factor. It follows that for a validation of the model several loss measurements with different roughness and, possibly, the e.m. measurement on the sample should be accompanied by its accurate texture and dimensional characterization.

Model validation

In order to validate the model, it is necessary to proof that loss enhancement scales as $\langle A \rangle_d / A_0$, independently on the specific texture and PSD.

To this end, samples (60 mm diameter, 2 mm thick) made of copper, σ = 20, 2, 0.2, 0.03 μm, and of SS AISI 304L as a second material with higher resistivity, are being manufactured. Samples will be characterized both with respect to reflection loss enhancement (at 170 GHz), and to their surface texture, PSD and $\langle A \rangle_d / A_0$.

Conclusions

Measured extra-losses at reflection of millimeter wave beams from metallic surfaces are consistent with a the assumption that they are due to the effective surface increase created by roughness. The agreement between prediction and measurement is achieved with different surface textures and PSD function. In order to validate the model a direct comparison between γ and reflection losses is necessary.

Assuming that the area-model is correct, purely stochastic processes like erosion/redeposition should not cause a significant loss enhancement per se. Mirror surface can be machined to low losses ($\sigma \leq 0.2$ μm for copper), and ageing do not necessarily cause severe long-term reflectivity degradation. Therefore erosion should not be a major problem for plasma facing mirrors, while the main focus should be on surface contamination by resistive films thicker than the skin depth in the film material.

References

1. *Sayles R.S., Thomas T.R.*, Nature, **271** (1978) 431.
2. *Mulvanney J., Newland D.E., Gill K.F.*, Wear **132** (1989) 173.
3. Tischer, IEEE Transactions **MTT-24** (1976).
4. *Myasnikova S.E. et al.*, IRMMW (2004).
5. *Kasparek W. et al.*, IJIRMMW, **22** (2001) 1695.

SELECTIVE RE-RADIATION OF WAVES IN MULTIMODE WAVEGUIDES WITH SHALLOW SINGLE AND DOUBLE CORRUGATIONS

M. Goykhman, A. Gromov, N. Kovalev, M. Fuks[1], *E. Schamiloglu*[1]

Institute of Applied Physics, RAS, Nizhny Novgorod, Russia
[1]University of New Mexico, Albuquerque, USA

We present a method to improve the selective properties of a waveguide resonator with Bragg reflectors on both ends, a passive device that is widely used in microwave engineering and optoelectronics. It is shown that additional mode conversions lead to a significantly rarefied spectrum of eigenoscillations with different transverse field structures. In particular, this can be achieved by using doubly periodic Bragg reflectors with different azimuthal symmetries forming four wave resonant field structures.

1. Introduction: problem and solution

Bragg reflectors and resonators (Fig. 1) are used for precise selection of different transverse field structures in oversized high-power microwave (HPM) oscillators driven by high-current relativistic electron beams. The main advantage of Bragg reflectors is their ability to selectively convert waves with practically any transverse field structures in narrow frequency bands (stopbands). For simple waveguide reflectors with homogeneous periodic corrugations, as, for example, cylindrical reflectors with sinusoidal profile

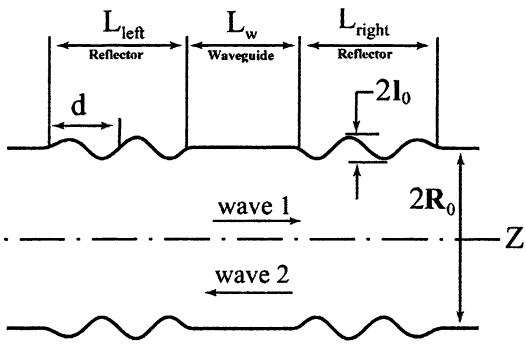

Fig. 1

$$R(\theta, z) = R_0 + l_0 \cos\left(\bar{m}\theta + \bar{h}z\right) \tag{1}$$

(where $\bar{h} = 2\pi / d$, $\bar{m}$ is number of folds of spiral corrugation), conditions for resonant reradiation of rotating waves $\mathbf{E}, \mathbf{H} \sim A(r)\exp\left[i\left(\omega t - m\varphi - hz\right)\right]$ are

$$h_1 - h_{-2} - \bar{h} = 2\delta, \quad \delta << k \tag{2}$$

$$m_1 - m_{-2} = \bar{m}. \tag{3}$$

Here, $h_1 = \sqrt{k^2 - g_1^2}$ and $h_{-2} = -\sqrt{k^2 - g_{-2}^2}$ are longitudinal wavenumbers of the incident and reflected waves, δ is the mismatch in the Bragg resonance

condition, $g_{1,-2}$ are transverse wavenumbers of each wave pair, and $m_{1,-2}$ are the azimuth indexes of the waves. In this case the number of stopbands and, accordingly, the number of combinations of reradiated waves are very large, and the density of their spectrum

$$4k^2 = \left(\bar{h} + 2\delta\right)^2 + 2\left(g_1^2 + g_{-2}^2\right) + 2\left(g_1^2 - g_{-2}^2\right)^2 \Big/ \left(\bar{h} + 2\delta\right)^2, \qquad (4)$$

rapidly condenses as the waveguide's cross section of electrodynamic systems increases for increasing radiated energy of high-power microwave sources.

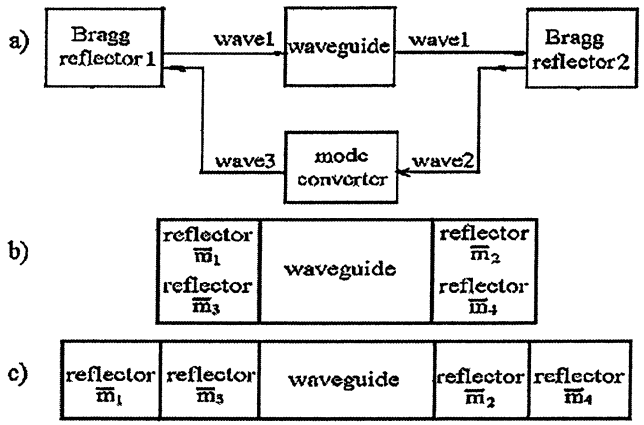

Fig. 2

The effective way to significantly rarify the spectral density is to enhance the number of waves forming eigenoscillations in the resonators [1, 2]. This can be attained, for example, as is shown at Fig. 2. Selectivity is provided when the bands of conversions of partial waves in the operating field structure overlap, whereas the bands of other mode combinations do not.

2. Initial idealizations and derivation of equations

We consider a hollow waveguide with smooth shallow periodicallycorrugated perfectly conducting walls of arbitrary profile. The electric fields on the waveguide surface satisfies

$$\left(\tau \mathbf{E}\right)_s = 0. \qquad (5)$$

We use one of the simplest perturbation method [3] by replacing (5) with approximate boundary conditions on a uncorrugated surface S_0 –

$$E_x(s) = \sum_{n=0}^{\infty} \frac{l^n}{n!} \frac{\partial^n E_x}{\partial x^n}\bigg|_{S_0}. \qquad (6)$$

Here, the fields are written in the local coordinate system (Fig. 3), where the coordinate x is orthogonal to the surface S_0 and directed into metal. Eq. (5) for circular waveguide with corrugation (1) can be written as:

$$\begin{cases} E_z \approx -\sum_{n=0}^{\bar{n}} \frac{l}{n!}\left\{ \frac{l}{n+1}\frac{\partial^{n+1}E_z}{\partial\rho^{n+1}} + \frac{\partial l}{\partial z}\frac{\partial^n E_\rho}{\partial\rho^n} \right\}_{\rho=R_0} \\ E_\varphi \approx -\sum_{n=0}^{\bar{n}} \frac{l}{n!}\left\{ \frac{l}{n+1}\frac{\partial^{n+1}E_\varphi}{\partial\rho^{n+1}} + \frac{1}{r}\frac{\partial l}{\partial\varphi}\frac{\partial^n E_\rho}{\partial\rho^n} \right\}_{\rho=R_0} \end{cases} \quad (7)$$

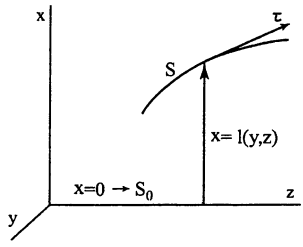

Fig. 3

The equations for desired fields $\mathbf{E},\mathbf{H}$ of considered waveguide with corrugation (1) can be found by integrating Lorentz's lemma, in which, as additional fields is used a complete system of rotating eigenmodes of regular waveguide with perfectly conducting wall S_0 $\left(\hat{\mathbf{E}}^j,\hat{\mathbf{H}}^j\right)=\left(\mathbf{E}^j(\rho),\mathbf{H}^j(\rho)\right)e^{-i\left(h_j z+m_j\varphi\right)}$, over a thin transverse slice of a regular circular waveguide:

$$\frac{dp_j}{dz}+ih_j p_j = -\frac{e^{-ih_j z}}{N_j}a_0\int_0^{2\pi}\rho_0\left[\hat{\mathbf{H}}^{-j}\times\mathbf{E}\right]_{\rho=a_0}d\varphi, \quad (8)$$

where we used $\mathbf{E}_\perp,\mathbf{H}_\perp$ as expansions in terms of the eigenmodes in the region $r<R_0$: $\mathbf{E}_\perp=\sum_\nu p_\nu\mathbf{E}_\perp^\nu e^{-im_\nu\varphi}$, $\mathbf{H}_\perp=\sum_\nu p_\nu\mathbf{H}_\perp^\nu e^{-im_\nu\varphi}$.

We derive a convenient system of approximate equations in coordinate form by replacing the field $\mathbf{E}$ in (8) with its approximate value given by (7). For example, for $\bar{n}=0$ [4]:

$$\frac{dp_j}{dz}+ih_j p_j \approx \frac{R_0}{N_j}\int_0^{2\pi}\left[ikl\left(H_\varphi^{-j}H_\varphi+H_z^{-j}H_z+E_\rho^{-j}E_\rho+\frac{H_z^{-j}E_\varphi}{ik\rho}\right)e^{im_j\varphi}+\right.$$

$$\left.+\,e^{-ih_j z}\frac{\partial}{\partial z}\left(l\hat{H}_\varphi^{-j}E_\rho\right)\right]_{\rho=R_0}. \quad (9)$$

Here the fields without indices are total fields, that is, fields that depend on both z and φ.

3. Bragg reflectors with helical sinusoidal corrugation

We assume that (2) and (3) for the resonant interaction between the forward wave with number $j=1$ and the backward wave with $j=-2$ are satisfied. If the amplitude of corrugation is sufficiently small (9) reduces to equations for complex amplitudes $A_1(z)=p_1\sqrt{N_1}e^{i(h_1-\delta)z}$, $A_{-2}(z)=p_{-2}\sqrt{N_2}e^{i(h_{-2}+\delta)z}$

$$\frac{dA_1}{dz}+i\delta A_1=-fA_{-2}e^{-i\beta},\quad \frac{dA_{-2}}{dz}-i\delta A_{-2}=-fA_1e^{i\beta}, \tag{10}$$

where $f=\left(\pi kR_0\, l_0/\sqrt{N_1N_2}\right)\left(H_{\varphi,1}H_{\varphi,2}+H_{z,1}H_{z,2}+E_{\rho,1}E_{\rho,2}\right)_{\rho=R_0}$ is the purely real coupling coefficient, and β is the initial corrugation phase. Solution of (10) give the boundaries for the stopbands $\delta=\pm f$. For the derivation of complex reflection coefficients R_{right}, R_{left} is used the continuity of amplitudes A_j at the interface of a regular waveguide with a corrugated one

$$A_j(z=0+0)=A_j(z=0-0);\quad A_j(z=\pm L+0)=A_j(z=\pm L-0).$$

As result,

$$R_{right}=\left(\frac{-ie^{i\beta}f\sinh(\kappa_0L)}{\delta\sinh(\kappa_0L)-i\kappa_0\cosh(\kappa_0L)}\right)_{right},\quad R_{left}=\left(\frac{ie^{-i\beta}f\sinh(\kappa_0L)}{\delta\sinh(\kappa_0L)-i\kappa_0\cosh(\kappa_0L)}\right)_{left}.$$

4. Resonator with simple helical Bragg reflectors

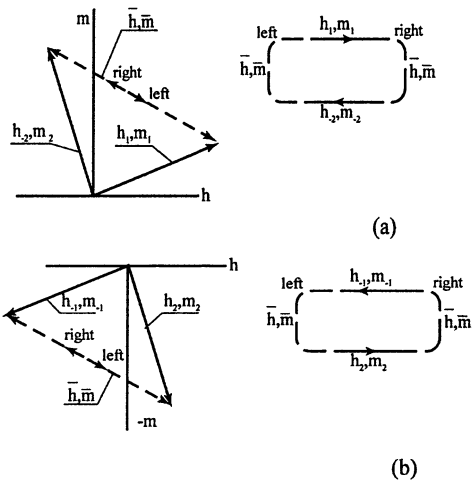

Fig. 4. Wave vectors of partial waves (solid lines) and vectors of corrugation (dashed lines) in the (*h, m*) plane; arrows on the dashed lines indicate the direction of re-radiation in the left and right reflectors; *a* – the diagram for waves with indices $j=1$ and $j=-2$, and *b* – the diagram for waves with indices $j=-1$ and $j=2$. The directions of propagation and the re-radiation of partial waves are indicated on the right.

It is convenient to explain the interaction of partial waves in Bragg resonators and reflectors using diagrams of wave vectors in the plane (*h, m*) as, for example, is shown in Fig. 4, where the solid lines are vectors of partial waves and the dashed lines are vectors of corrugations. The vectors of corrugation are always two mutual opposite vectors for resonators with identical helical reflectors. Evidently indices m_j and $\bar{m}$ can only be integer.

According to the conditions of Eqs. (2) and (3), resonant re-radiation is possible only in cases when vectors of two waves and the vector of the corrugation form a closed triangle (we call this property (a)). When the directions of propagation of partial waves (that is, the signs of h_j) are opposite, then the stop-band appears (property (b)).

It is possible to illustrate these properties and estimate the region of their applicability from simple geometrical considerations that take into account the width of the stopband. From Fig. 4, *a* it follows that there is another diagram (Fig. 4, *b*) that is symmetric with the initial one. The spectrum of the Bragg resonator with simple helical reflectors as a result of the symmetry is twice degenerate (for frequencies and also for Q factors). Also, from the diagrams it follows that the degeneracy is absent for axisymmetric waves where $h_{-2} = h_1$ in a resonator with axisymmetric reflectors.

The existence of high Q oscillations in resonator (Fig. 1) is possible because of the overlapping stopbands of partial waves of the left and right reflectors $\left|\overline{h}_{left} - h_1 - h_{-2}\right| < \left|f_{left}\right|$ and $\left|\overline{h}_{right} - h_1 - h_{-2}\right| < \left|f_{right}\right|$. The necessary condition for the existence of high oscillations is the identical symmetry of reflectors, that is, left and right reflectors have the same number and direction of spiral corrugations $\overline{m}_{left} = \overline{m}_{right}$. The spectrum of complex eigenfrequencies is found from the dispersion relation $R_{left} R_{right} e^{-i(h_1+h_2)L_w} = 1$.

5. Bragg resonators with combined reflectors

Accordingly to property (a) listed earlier, an infinite combination of partial waves with overlapping stop-bands occurs in resonators with simple helical Bragg reflectors, and inside these bands in each combination there are eigenmodes with slightly different Q factors because of small differences in the values of the coupling coefficient f.

Another situation appears when you replace of one of the simple helical reflectors (for example, the left reflector) with a combined reflector with corrugation described by the formula

$$R = R_0 + l_1 \sin\left(\overline{h}_1 z + \overline{m}_1 \varphi + \beta_1\right) + l_2 \sin\left(\overline{h}_2 z + \overline{m}_2 \varphi + \beta_2\right), \qquad (11)$$

choosing combinations of partial waves with identical central frequency $k = \overline{k}_{res}$, yielding resonance conditions

$$2m_1 = \overline{m}_1, \quad 2h_1 = \overline{h}_1 + 2\delta_1; \quad 2m_2 = \overline{m}_2, \quad 2h_2 = \overline{h}_2 + 2\delta_2. \qquad (12)$$

The conditions for the right simple helical reflector

$$m_1 + m_2 = \overline{m}_{right}, \qquad h_1 + h_2 = \overline{h}_{right} + 2\delta_{right} \qquad (13)$$

are satisfied.

For resonator with left combined reflector and right simple helical reflector the diagram of wave vectors with chosen combination of partial waves is shown in Fig. 5 for the case $\overline{m}_1 > 0, \overline{m}_2 < 0$. This diagram, with directions of propagation and re-radiation of four partial waves, allows us to form the general disper-

sion relation without any additional considerations, in which deviations of the central frequencies k_{res} of stopbands relative to one another are permissible.

$$\left[\left(i\delta+\kappa_0\coth(\kappa_0 L)f^{-1}e^{i\beta}\right)\right]_{left1,left2}\times$$
$$\times\left[\left(i\delta+\kappa_0\coth(\kappa_0 L)f^{-1}e^{i\beta}\right)\right]_{right}e^{2i(h_1+h_2)L_w}=1, \qquad (14)$$

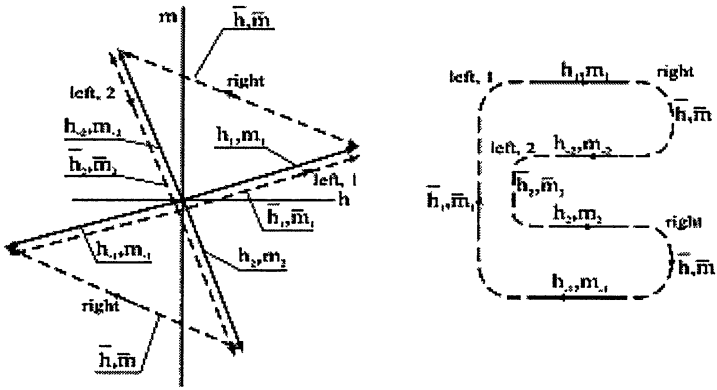

Fig. 5. Left: Vector diagram of a Bragg resonator with simple reflector (*right*) and combined (*left, 1* and *2*) reflectors; right: direction of propagation and re-radiation of partial waves.

For each reflector the mismatch δ is connected with frequency by different relations (Eqs. (12) and (13)); thus, the resonant frequencies and attenuation decrements are solutions of the complicated system of transcendental equations given by Eqs. (12) – (14). However, in order to receive visible qualitative relations we can use simplifying assumptions about the approximate equality of all stop-bands and attenuation decrements for operating wave combinations. In this case there is the same coupling coefficient f for all reflectors.

These simplifications lead to approximate relations for the resonance frequencies:

$$4\arcsin(\delta/f)+2(\bar{h}+2\delta)L_w+\beta=2\pi q\,, \qquad (15)$$

where $\beta=\beta_1+\beta_2-2\beta_{right}$. Equaton (15) shows that $\beta=\text{const}$ is invariant for the initial system of Eqs. (14); that is, variations of mutual phasings of corrugations do not lead to any variations in the spectrum of eigenmodes.

According to Eq. (14), in long resonators with $fL_w >> \pi$, the total number of oscillations in the operating stop-band with $k_{res}=\bar{k}_{res}$, taking into account the degeneracy, yields

$$M \approx 4\left(1+\frac{fL_w}{\pi}\right), \tag{16}$$

which coincides with the total number of oscillations for the initial Bragg resonator with simple helical reflectors, and with the maximum shift between oscillations

$$\Delta k_{\max} \approx \frac{\pi h_1 h_2}{k_{res}\bar{h}\left(L_w + 1/f\right)} \tag{17}$$

becoming half that compared with one in initial Bragg resonator. Therefore, using combined reflectors leads only to the removal of the degeneracy in the spectrum of eigenmodes from the operating stop-bands with $k_{res} = \bar{k}_{res}$.

Resonant frequencies of of Tamm's oscillations are determined by the relation

$$k \approx \bar{k}_{res} + 2\frac{h_1 h_2}{\bar{k}_{res}\bar{h}} f \sin\left(\frac{\pi}{2}q - \frac{\beta}{4}\right), q = 0,1; \quad \beta \in [0, 2\pi). \tag{18}$$

When $\beta \neq 0$, in the stop-band there are two non-degenerate Tamm's resonances. However, when $\beta = 0$ in the stop-band one non-denegerate and really solitary Tamm's oscillation with frequency $k = \bar{k}_{res}$ and with maximum quality (see Eq. (19)) can exist.

With the assumption of equality of average frequencies of operating stop-bands, we can obtain from Eq. (14) the general expression for the maximum value of the Q of the eigenmodes with $k = \bar{k}_{res}$:

$$Q \approx \frac{\bar{k}_{res}^2}{4} \frac{\left(2L_w + \frac{1}{|f|_{right}}\right)\frac{\bar{h}}{h_1 h_2} + \frac{1}{h_1 |f|_{left1}} + \frac{1}{h_2 |f|_{left2}}}{\left(e^{-2|f|L}\right)_{left1} + \left(e^{-2|f|L}\right)_{left2} + 2\left(e^{-2|f|L}\right)_{right}}, \tag{19}$$

which is applicable for longer lengths $|fL|_{left1} >> \pi$, $|fL|_{left2} >> \pi$, $|fL|_{right} >> \pi$.

Therefore, the replacement of a simple helical reflector with a combined one (described by Eq. (11)) leads only to small variations in the spectrum of the high Q oscillations with the chosen combination of partial waves because all stop-bands overlap in this case. For competing mode combinations the stop-bands diverge to one degree or another. The smaller the cross-section of the resonator, the greater is the divergence for permanent corrugation depth. When transverse dimensions are chosen so that the stop-bands do not overlap for competing wave combinations, the eigenmodes of this combination will be outside the stop-band; therefore, they will be low Q oscillations.

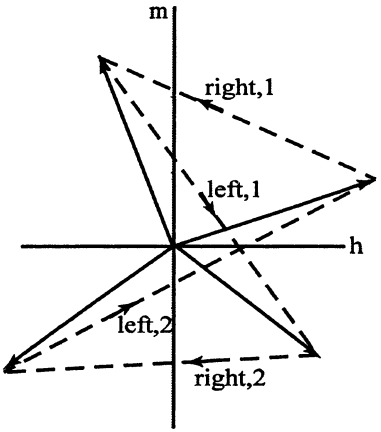

Fig. 6. Vector diagram for the combination of partial waves with opposite directions of rotation in a Bragg resonator with two combined reflectors.

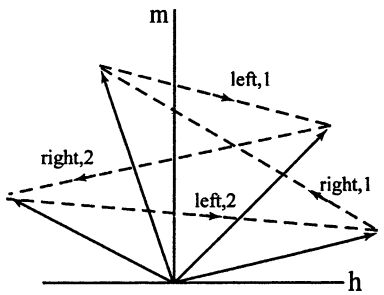

Fig. 7. Vector diagram for the combination of partial waves with identical directions of rotation in a Bragg resonator with two combined reflectors.

The Bragg resonator under consideration, namely, with one combined reflector and one simple helical reflector, is not unique. The more common case is a resonator comprised of two combined reflectors on the ends of a regular waveguide with partial waves having different transverse wave numbers g_j or different azimuthal values $|m_j|$. Examples of two types of vector diagrams with operating wave combinations for such resonators are shown in Figs. 6 and 7. From Eq. (4) it can be shown that selective properties of the resonator, which correspond to the second diagram (Fig. 7), are less than that of the resonator, whose schematic of wave interactions is shown in Fig. 6; that is, resonators with operating waves having different directions of rotation have greater selectivity than resonators in which the partial waves rotate in the same direction.

When all partial waves have frequencies far from cut-off, then the diagrams (Figs. 6 and 7) readily lead to the dispersion relation:

$$\left[\frac{\kappa_0 \coth \kappa_0 L + i\delta}{f} e^{i\beta}\right]_{right,1}\left[\frac{\kappa_0 \coth \kappa_0 L + i\delta}{f} e^{i\beta}\right]_{right,2} \times$$

$$\times\left[\frac{\kappa_0 \coth \kappa_0 L + i\delta}{f} e^{i\beta}\right]_{left,1}\left[\frac{\kappa_0 \coth \kappa_0 L + i\delta}{f} e^{i\beta}\right]_{left,2} e^{2iL_w \sum_{n=1}^{4} h_n} . \quad (20)$$

We will not analyze this equation here; we only note that the basic relations that were derived above are applicable here as well. Therefore, all conclusions about resonant frequencies, quality factors, and mode selectivity are correct for

such resonators. Equation (20) describes the basic properties of the bands of eigenmodes of resonators with combined reflectors.

Conclusion

We present one method to improve the selective properties of Bragg resonators by forming four-mode resonant transverse field structures that provide a way to substantially enlarge their cross sections without coincidence of stopbands of applied Bragg reflectors for competitive mode combinations.

On the base of the simplest model of a circular waveguide with shallow corrugated walls, the most common formulas for reflection coefficients, accounting for reradiation to other modes, were obtained that allow us to calculate dispersion relations for resonators with any number of mode conversions and any relations between phases of reflectors.

In spite of this approach of using schematic diagrams to obtain the dispersion relations, the conclusion about the universal and broad possibilities of applications of this method of selection of resonant transverse field structures are strongly justified.

To take into account additional factors limiting the applicability of the present work, we plan to consider more detailed situations with quasi-transverse waves, that is, waves near cutoff, for which, it is possible to obtain the maximum efficiency of this technique. Above all, we plan to consider the following in future:

1) irregular, in particular, conical resonators, in which divergence of the stopbands can be observed even for simple helical reflectors;

2) open and dielectric waveguide systems;

3) resonators with intermediate wave conversions;

4) the influence of losses because of finite conductivity of walls, in addition to other material properties.

References

1. *Fuks M.I., Kovalev N.F.,* Device for amplification of electromagnetic oscillations, Copyright 1828325 with priority from 20.11.90, Bulletin of inventions (in Russian), 1996, vol. 32.
2. *Fuks M.I., Kovalev N.F.,* Selective multichannel feedback, IEEE Trans. Plasma Sci., 2002, vol. 30, p. 1147-1150.
3. *Katsenelenbaum B.Z., Mercader del Rio L., Pereyaslavets M., Sorolla Ayza M., Thumm M.,* Theory of nonuniform waveguides, Institute of Electical Engineers, London, United Kingdom, 1998.
4. *Fuks M.I., Goikhman M.B., Kovalev N.F., Palitsin A.V., Schamiloglu E.,* Waveguide resonators with combined bragg reflectors, IEEE Trans. Plasma Sci., 2004, vol. 32, No. 3, p. 1323-1333.

HIGH POWER FERROELECTRIC SWITCHES AT CENTIMETER AND MILLIMETER WAVE LENGTHS

V. P. Yakovlev[1], *O. A. Nezhevenko*[1], *J. L. Hirshfield*[1,2]

[1]Omega-P, Inc., New Haven, CT 06511, USA
[2]Yale University, Physics Department, New Haven, CT 06520, USA

High-power ultra-fast, electrically-controlled switches for accelerator applications in the centimeter and millimeter wavelength ranges that employ ferroelectric elements are discussed. Examples of fast switches and phase shifters for pulse compression and power distribution systems at X- and Ka-band are presented.

Introduction

Future linear accelerators with high accelerating gradient [1] rely on pulse compression to achieve the high peak RF power levels required to drive the accelerator structures (500–600 MW in ~400 ns pulses at X-band, for example). A number of RF pulse compression systems have been under consideration recently including versions of the Delay Line Distribution System (DLDS) [2], and SLED-II [3]. The mechanisms upon which these compressors operate are *passive*, in that no element in the compressor structure has time-dependant properties. Common limitations of these systems are their relatively low compression ratio (~4:1), and/or their very long runs (100's of km) of low-loss vacuum waveguide [4]. In an attempt to circumvent these limitations, various concepts of *active* RF pulse compression have recently received attention [5, 6, 7]. To date, none of the tested versions of active pulse compressors have achieved power levels high enough for accelerator application.

Electrically-controlled ferroelectric elements represent an attractive option for either active pulse compression and/or power distribution systems [8, 9]. Ferroelectric elements have an **E**-field-dependent dielectric permittivity $\varepsilon(\mathbf{E})$ that can be very rapidly altered by application of a bias voltage pulse. The switching time in most instances would be limited by the response time of the external electronics that generates the high-voltage pulse, and can therefore be in the nsec range. Modern bulk ferroelectrics, such as barium strontium titanate (or BST), have high enough dielectric breakdown fields (100–200 kV/cm) and do not require too high a bias electric field (~20–50 kV/cm) to effect a significant change in ε [10]. Ferroelectrics are already successfully used in RF communication technology and radar applications. Euclid Concepts, LLC recently developed and tested for Omega-P a bulk ferroelectric [11] that has a permittivity $\varepsilon = 500$, and a 20% change in permittivity for a bias electric field of 50 kV/cm. The best loss tangent already achieved is 4×10^{-3} at 35 GHz that should correspond to 1.3×10^{-3} at 11 GHz [10]. Development of production techniques for this material continues, with the expectation of further lowering of the loss tangent to values of less than 1×10^{-3}.

Ferroelectric switches

1. In active pulsed compressors with resonance switches, the RF source supplies electromagnetic energy to fill a low-loss storage cavity coupled through an electrically-controlled resonance switch to a load (the accelerating structure). Compressor operation involves two steps: *first*, that of energy storage when the coupling to the storage cavity is small in order to provide good efficiency of filling; and *second*, that of energy extraction when the coupling is high to provide fast energy discharge into the accelerating structure. The coupling of the storage cavity with the RF source is controlled by changing the resonance frequency of the switch cavity. A schematic diagram of a proposed active pulse compressor is shown in Fig. 1. This example is based on the design of Omega-P's two-channel Active Bragg Compressor (ABC) [12] that employs resonance plasma switches. As shown in Fig. 1, two cylindrical TE_{01}-mode storage cavities (*8*) are each coupled through an electrically-controlled switch cavity (*7*).

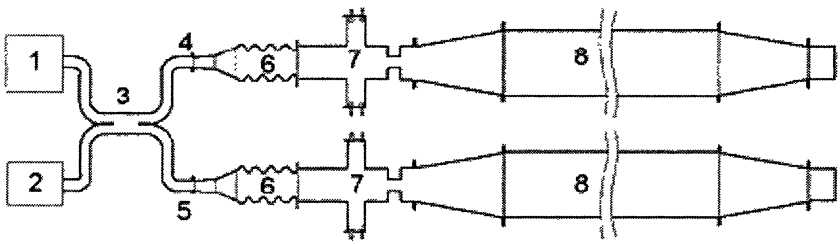

Fig. 1. Schematic diagram of the two-channel ABC

Waveguides (*4* and *5*) are fed from the RF source (*1*) after the source power is split using a 3-dB hybrid coupler (*3*). Mode converters (*6*) transform the mode from TE_{10}-rectangular to TE_{01}-circular. Compressed output pulses are combined and absorbed in the load, i. e. the accelerator structure (*2*). Main design parameters of the proposed ferroelectric active pulse compressor are given in Table 1. The entire proposed ferroelectric switch arrangement is shown in Fig. 2, including the matching diaphragm and two TE_{031} switch cavities containing ferroelectric rings. Two cavities are necessary in order to reduce both RF electric fields and losses in the ferroelectrics. The cavity resonance frequency is altered by application of a bias voltage pulse across the ferroelectric rings. The two cavities are located in an external evacuated chamber. In order to apply biasing voltages up to 100 kV, part of the end walls of each cavity are separated from the rest of the cavity by circular non-radiating slots. Parameters found for the X-band switch cavity are listed in Table 2.

Table 1. Parameters of the active pulse compressor

operating frequency f_0	11.424 GHz
input power P_o	50 MW
input pulse duration t_f	1 μs
power gain k	10
peak output power $P_{out} = kP_o$	500 MW
output half-height pulse duration $t_{0.5}$	~40 ns

Table 2. Parameters of TE_{031} switch cavity

operating mode	TE_{031}
cavity length, mm	20
ferroelectric ring width, mm	20
ferroelectric ring inner diameter, mm	106
ferroelectric ring radial thickness, mm	3
maximum electric field in ferroelectric, kV/cm	16

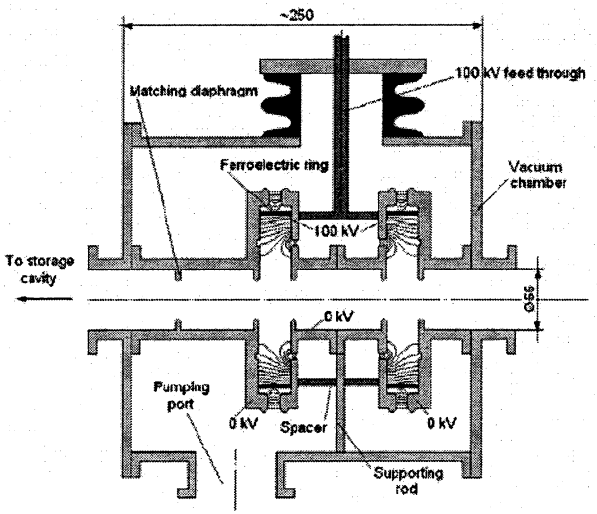

Fig. 2. A conceptual arrangement of the X-band ferroelectric switch, showing the bias electric field lines. Dimensions are in mm.

In the energy storage regime, when both switch cavities have resonance frequencies of about 11.350 GHz, transmission at the operating frequency is about –14 dB that provides optimal coupling of the storage cavities with the

line. In the energy extraction regime, the ferroelectric permittivity of the switch cavities is decreased from 500 to 400, and the resonance frequencies are close to the operating frequency. At resonance the transmission of both cavities is close to 100%.

2. In order to develop RF technology in the millimeter wavelength domain for a future CLIC-like multi-TeV electron-positron linear collider, it is necessary to test in realistic regimes accelerating structures and high power RF components, and to determine limits of breakdown and metal fatigue. The typical required power for such tests at Ka-band falls in the range of 200–300 MW with a pulse width of 70–150 ns [13]. This goal can be achieved by creation of a long pulse RF source and then employing an RF pulse compressor. For example, if one has an RF power source of 30–50 MW with a pulse width of 0.5–1 μs, and if one could develop an active pulse compressor with a compression ratio of 10:1, it would be possible to achieve the required power of 200–300 MW in ~100 ns pulses. Development of an active pulse compressor with a ferroelectric switch is partly motivated by the first successful test results of the 34.3 GHz third-harmonic magnicon amplifier [14, 15]. The main design parameters of the proposed Ka-band active pulse compressor with ferroelectric switches are given in Table 3. A design concept for the ferroelectric switch cavity is scaled from that shown in Fig. 2. Parameters found for the switch cavity are listed in Table 4.

Table 3. Parameters of the 34.272 GHz active pulse compressor

operating frequency, MHz	34.272
output power, MW	200
input power, MW	30
output pulse width, ns	70
input pulse width, ns	700
compression ratio	10
efficiency, %	67.5
bias voltage, kV	35

Table 4. Parameters of 34.272 GHz TE_{031} switch cavity

operating mode	TE_{031}
cavity length, mm	6.7
coupling iris diameter, mm	9.3
coupling diaphragm thickness, mm	3
ferroelectric ring width, mm	6.7
ferroelectric ring inner diameter, mm	35.7
ferroelectric ring radial thickness, mm	0.95

3. In principal, the most efficient power combining system should be DLDS. However, in its original incarnation, DLDS required ~300 km of waveguides and waveguide components [4]. It has been recognized that a substantial reduction in the length of waveguides could be achieved if an *active* DLDS system could be developed. Figure 3 illustrates the layout of an active DLDS for the case of one waveguide feed for four accelerator modules [4]. The key element is a high power microwave switch, which must quickly divert ~500 MW of power sequentially from a main feed line in and out of the accelerator modules.

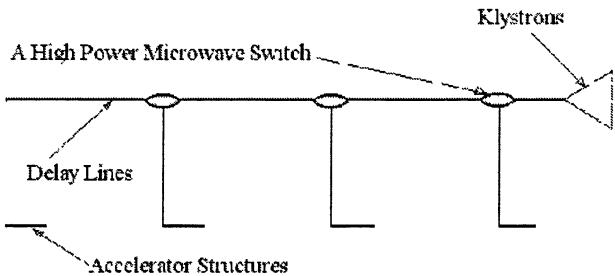

Fig. 3. Schematic for an active DLDS that feeds four accelerator modules [4]

High-power microwave switches must be able on command to redirect the full microwave power from a main feed line to one accelerator module after another within the RF pulse, with a switching time of tens of ns. One possible scheme for such a switch is shown in Fig. 4. The circuit consists of two 3-dB hybrid couplers and an electrically-controlled phase shifter. In this circuit, input power is supplied to one waveguide at the left. The hybrid splits the input power into two equal portions which, with the phase shifter unbiased, combine into one of the right-most output channels. In order to switch RF power from one output to the other, one has to change the phase difference between the two input signals by 180°. This phase shifter should thus be designed to operate with at least half of the full RF power (500/2 = 250 MW).

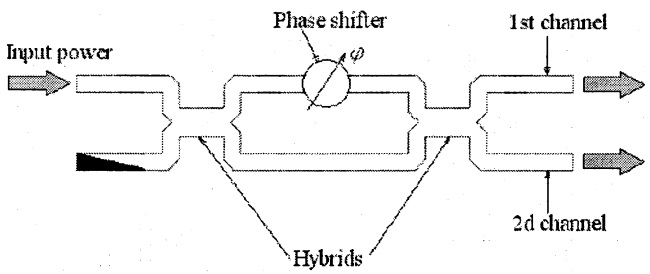

Fig. 4. A possible arrangement of a switch for an active DLDS

As with the switch considered above, a phase shifter can be constituted as a set of RF cavities partially-filled with ferroelectric whose dielectric constant is electrically-controlled. A change in resonance frequency of the cavities causes a phase change for the transmitted signal. The cavities should sustain the full power of 250 MW without breakdown, and should possess low dielectric losses. These requirements limit the maximum available phase shift that can be achieved in one cavity to about ~50°. Thus, in order to achieve the required phase shift of 180°, a sequence of four identical cavities should be used. In order to achieve maximum transmission over a wide frequency range, a quarter-wave filter-like arrangement may be used. The results for optimized parameters found for the phase shifter are listed in Table 5. A concept for the phase shifter that will be suitable for high-power use is shown in Fig. 5. The phase shifter design made for Omega-P by AES, Inc is shown in Fig. 6. The four cavi-ties are located in an external evacuated chamber. Evaluation of the phase shifter with RF power levels up to 50 MW using the Omega-P/NRL 11.4 GHz magnicon [16] is currently planned. The arrangement of the test bed for evaluation of the phase shifter is shown in Fig. 7. Because the magnicon has two outputs with equal power [16], the test bed for the phase shifter doesn't require a power splitter. The power from the two outputs is combined in a 3-dB hybrid [7]. Finally the power from the outputs of the two hybrids is absorbed in high-power SLAC-type vacuum loads. Varying the biasing pulse generator will allow redirection of the full magnicon power from one output arm of the 3-dB hybrid to the other.

Table 5. Parameters of an X-band phase shifter

operating frequency, GHz	11.424
bias voltage for ~200° phase shift, kV	100
number of cavities	4
cavity operating mode	TE_{031}
waveguide mode	TE_{01}
transmitted (switched) power, MW	250 (500)
peak power losses (tan δ = 0.0013), MW	18 (3.6%)
efficiency, %	> 96
RF electric field in ferroelectric, kV/cm	24

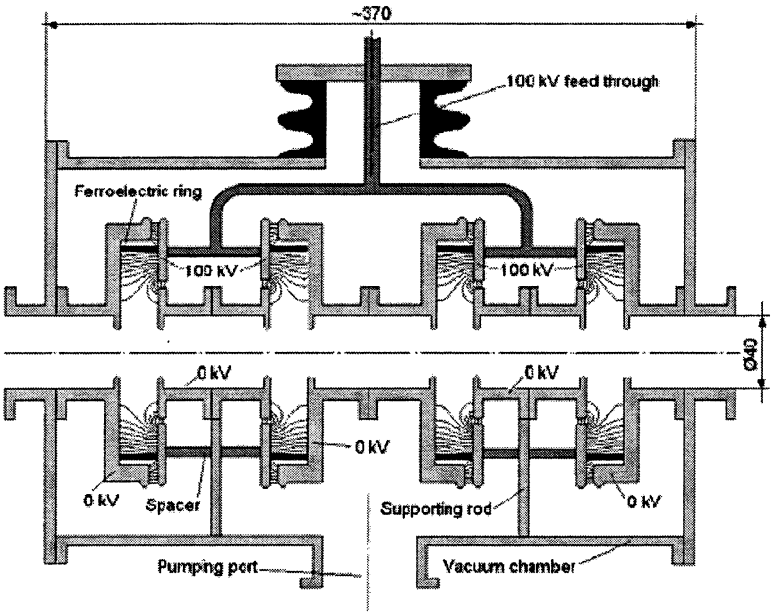

Fig. 5. A concept of an X-band phase shifter design, showing the bias electric field lines. Dimensions in mm.

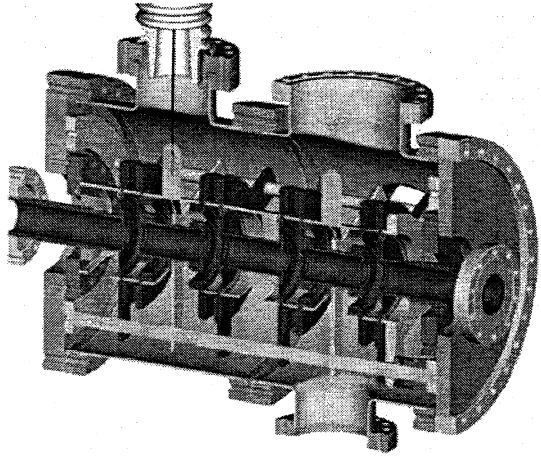

Fig. 6. A phase shifter design

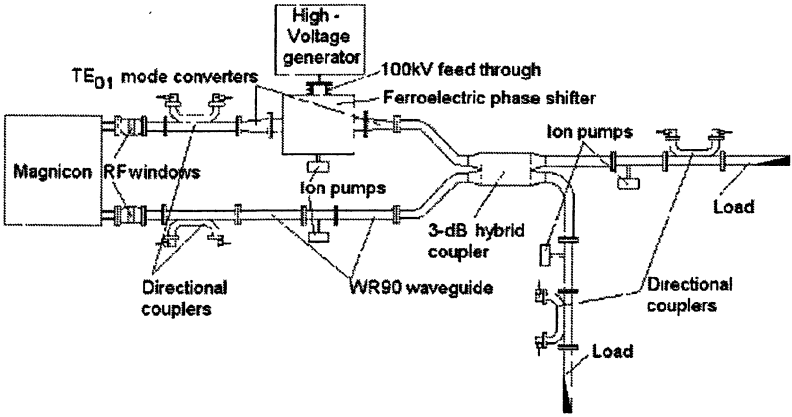

Fig. 7. Arrangement for testing the X-band phase shifter up to 50 MW

References

1. International Linear Collider Technical Review Committee, 2nd Report, SLAC-R-606, SLAC, 2003.
2. *Mizuno H., Otake Y.*, KEK 94-112, Oct. 1994.
3. *Wilson P.B. et al.*, SLAC-PUB-5330.
4. *Tantawi S.*, SLAC-PUB-8582.
5. *Tantawi S. et al.*, SLAC-PUB-7368.
6. *Tamura F., Tantawi S.*, LINAC 2000, p. 751-753.
7. *Vikharev A.L. et al.*, AIP **472**, p. 975.
8. *Yakovlev V.P., Nezhevenko O.A., Hirshfield J.L.*, PAC 2003, p. 1147.
9. *Yakovlev V.P., Nezhevenko O.A., Hirshfield J.L.*, AIP **737**, p. 643.
10. *Sengupta L.C. et al.*, IEEE Trans. Ultrasonics, Ferroelectrics and Freq. Control, 1997, vol. 44, p. 792.
11. *Kanareykin A. et al.*, AIP **737**, p. 1016.
12. *Vikharev A.L. et al.*, AIP **569**, p. 741.
13. *Braun H. et al.*, CLIC Note 596, August 2004.
14. *Nezhevenko O.A. et al.*, IEEE Trans. Plasma Sci., 2004, vol. 32, No. 3, p. 994-1001.
15. *Nezhevenko O.A. et al.*, **WPAT026**, PAC 2005, Knoxville, May 16-20, 2005 (to be published).
16. *Nezhevenko O.A. et al.*, **WPAT027**, PAC 2005, Knoxville, May 16-20, 2005 (to be published).

BULK BST FERROELECTRIC FOR ACCELERATOR APPLICATIONS

A. D. Kanareykin[1], *E. A. Nenasheva*[2], *V. P. Yakovlev*[3]

[1]Euclid Techlabs LLC, Solon, OH, USA
[2]Ceramics Ltd., St.Petersburg, Russia
[3]Omega-P, Inc., New Haven, CN, USA

We discuss a newly developed nonlinear ferroelectric material especially for accelerator applications. This is a BST (Barium-Strontium Titanium oxide) and MgO composite material, or BSM. The ferroelectric ceramic has an electric field-dependent dielectric permittivity that can be altered by applying a bias voltage. Bulk BSM ferroelectrics can be used as active elements of electrically controlled switches and phase shifters in pulse compressors or power distribution circuits of future linear colliders as well as tuning layers for dielectric based accelerating structures. The chemical composition, features of the manufacturing process, and mechanical and electrical properties of the material are discussed.

Introduction

A ferroelectric ceramic is a material with an electric-field-dependent dielectric permittivity that can be very rapidly altered by an applied bias voltage pulse. Typical representative ferroelectric materials are $(Ba,Sr)TiO_3$ or a $BaTiO_3$ - $SrTiO_3$ solid solution (BST). The BST material can be synthesized in polycrystalline, ceramic layer and bulk forms. Ferroelectrics have unique intrinsic properties that make them extremely attractive for high-energy accelerator applications. The response time is $\sim 10^{-11}$ s for the crystalline and $\sim 10^{-10}$ s for ceramic compounds. Unlike semiconductors and plasma devices, ferroelectrics allow control of their properties in two directions using a single external control pulse, offering unique capabilities for high-power switching device design. High dielectric breakdown strength, low gas permeability and simplicity of mechanical treatment make ferroelectric ceramics promising candidates for the loading material in accelerator tuning and switching devices.

Frequency control of any accelerating structure is a fundamental issue. Synchronization between the electron beam velocity and the phase velocity of the accelerating field must be maintained in order for the bunch to gain energy. Lack of frequency control causes problems for multistage accelerators where one has to match the accelerating field frequency and phase between adjoining sections. A method to vary the resonant frequency of a *dielectric loaded accelerating* **(DLA)** structure by an *electrically-controlled thin layer of ferroelectric* has been proposed and demonstrated [1].

In order to develop rf technology for a future CLIC-like multi-TeV electron-positron linear collider in the millimeter wave frequency band, it is necessary to test the proposed accelerating structures and high power rf components

in realistic regimes to be able to determine the rf breakdown and metal fatigue limits. The typical required power for such tests in the Ka-band falls in the range of 200–300 MW with a pulse of 70–150 ns [2]. This goal can be achieved by using of a long pulse rf source and by employing an rf pulse compressor. For example, if one has an rf power source of 30–50 MW with a pulse width of 0.5–1 μs along with an active pulse compressor with a compression ratio of 10:1, it would be possible to achieve the required power level of 200–300 MW for the ~100 ns pulses. The key element of the active pulse compressor is the fast, electrically-controlled high power ferroelectric microwave switch proposed in reference [2].

Note that ultra-fast, electrically controlled switches based on ferroelectric elements may also be used in the 1.3 GHz rf system of the superconducting linear collider. These elements may be incorporated into rf couplers. The coupler feeding the rf structure already has a built in DC bias in order to suppress multipacting. This bias may be used for tuning a ferroelectric element with the possibility of adjusting the coupling of the rf cavity to the feed line.

The new BSM ferroelectric typically shows a loss tangent of $4–6\times10^{-3}$ at X-band and Ka-band, and some samples have even showed better results. The BSM ceramic exhibits a high tunability factor: a bias voltage of 50 kV/cm reduces the permittivity from 500 to 400. The newly developed ferroelectric technology will be experimentally applied at Omega-P Inc./Yale University in cooperation with Euclid Techlabs LLC for the development and demonstration of a high power microwave switch and fast ferroelectric phase-shifter [2] in 2005–2006.

BSM ferroelectric development

We have fabricated and experimentally tested BST ferroelectric samples which, when a dc bias field is applied allow varying of the effective dielectric constant of the rf resonator/waveguide loading and, therefore, tuning and control of the operating frequency of the device [3, 4]. We have developed BST-MgO ferroelectric samples to be able to test the dielectric response in the 3–35 GHz frequency range as well as to define the tunability factor. We have studied the phase composition depending on the initial raw material and additives introduced. Microstructure of the samples and, in particularly, the shape and size of the crystals indicated a method of improving the dielectric parameters of the final BST-MgO composition. The effects of the sintering technology used in manufacturing the material on the loss factor was also studied. We have developed and sintered large (up to 11 cm in diameter) ferroelectric rings (Fig. 1) and long tubes with thin walls (Fig. 2) for the key ferroelectric switching and control elements. We have studied the dielectric response of our BST-MgO samples with short (tens of ns) leading and tailing edge pulses.

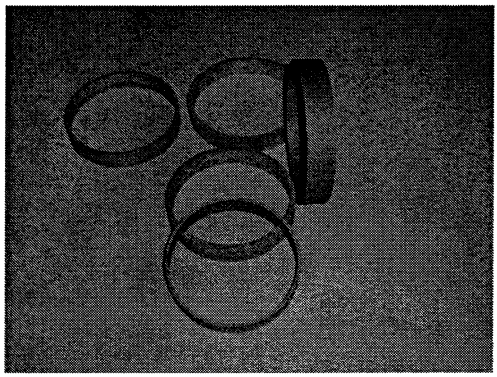

Fig. 1. Fabricated 110 cm diameter ferroelectric ring for the X-band phase-shifter. Ring thickness is 2.8 mm.

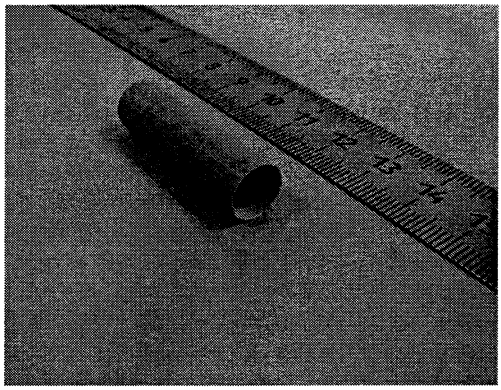

Fig. 2. Ceramic waveguide layer made of BST-MgO (BSM) ferroelectric with wall thickness 600 μm, diameter 10 mm and length of 4.5 cm. The sample was fabricated for the 11.424 GHz tunable DLA structure project [1].

The main requirement for the electrical properties of ceramic materials to be used in accelerator devices is a combination of a relatively low dielectric constant in the range from 300 to 600 at an electric field tunability not less than 10–20% (electric field magnitude ~20–50 kV/cm (or 2–5 V/μm) and low dielectric losses in the microwave range (tan $\delta \leq 0.005$ at 10 GHz) [3, 4].

The required range of dielectric constants in $(Ba,Sr)TiO_3$ solid solutions with perovskite structure can be achieved by increasing the content of strontium titanate which is accompanied by a shift of the Curie temperature. Barium strontium titanate solid solutions $(Ba_xSr_{1-x})TiO_3$ (x = 0.45–0.55) were synthesized by ceramic processing from titanium dioxide (TiO_2) and strontium and barium carbonates ($SrCO_3$, $BaCO_3$) or prefabricated barium and or strontium titanates ($BaTiO_3$, $SrTiO_3$). The initial materials were treated mechanically by mixing them in a vibration mill for three hours to achieve a particle size of 1 μm.

Bulk BST-MgO (BSM) ferroelectric samples have been fabricated. We used pre-synthesized barium and strontium titanates ($BaTiO_3$ and $SrTiO_3$) with grain sizes in the range of 1 μm and 0.3–0.7 μm. We manufactured disk ferroelectric samples for dielectric response measurements in the 1 MHz frequency range.

Regularities in the variation of dielectric properties (Curie temperature T_c, dielectric constant, tunability by dc bias voltage, and dielectric losses at rf and from 3.5 to 11.5 GHz) of the BSM samples have been studied as a function of the solid solution composition, Mg-containing additives, and the quality of raw materials. The proportions of the components were determined by the required range of ε = 400–600, electric field tunability 1.22–1.29 at $E \sim 4.5$ V/μm, and Q-factor 110–290 at $f \sim 11$ GHz. The compounding and processing technology we have developed provides stability and reproducibility of ferroelectric properties.

Active high power ferroelectric switches and phase-shifters require large diameter ferroelectric rings with electrical properties similar to those mentioned in the previous section. Recently we fabricated and tested a 110 mm BSM ferroelectric ring (Fig. 1), the ring thickness of 2.8 mm has been achieved. We have also developed an ultra-thin BST ferroelectric tube for a tunable DLA accelerating structure: the required thickness in the 600 micrometer range has been achieved, Fig. 2.

We have also performed loss factor measurements of an X-band reflective resonator partially filled with BST-MgO (BSM) ceramic substrate (Fig. 3). A 7.8 GHz bulk dielectric resonator has also been measured: both methods yielded loss factors of $(4–6)\times10^{-3}$ in the 8–12 GHz frequency range with some samples exhibiting smaller values in the $(3–4)\times10^{-3}$ range. An overall frequency shift of 100–160 MHz of the X-band prototype tunable accelerating structure has been demonstrated over a 1.7–2.5 V/μm range of bias field strengths using transparent electrode technology, Fig. 4.

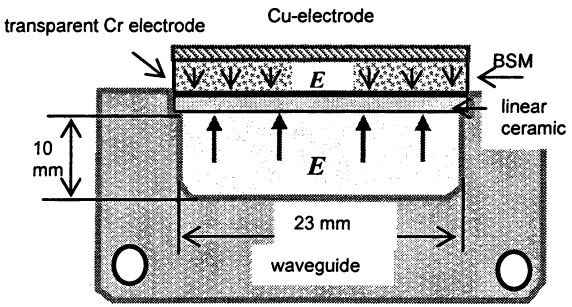

Fig. 3. Transparent electrode technology for the X-band cavity resonator. Parameters of the structure: 23×10 mm^2, thickness of ferroelectric layer 0.5 mm, ε = 500; thickness of linear dielectric layer 1 mm, ε = 100.

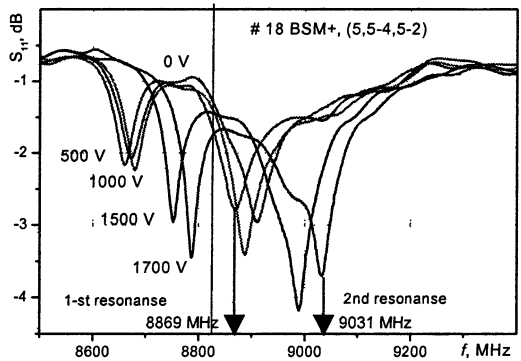

Fig. 4. Frequency shift of 100–160 MHz, transverse biasing field of 17–25 kV/cm applied using transparent electrode technology as shown in Fig. 3.

Summary

We have developed new ferroelectric materials with applications to tuning and switching accelerator components. The bulk BST-MgO composition has been identified as the best candidate for use in these devices. The dielectric constant of the material is in the range of 400–500, the loss tangent at 10 GHz does not exceed $(4–6)\times10^{-3}$ at X-band and Ka band and the tunability factor (dielectric constant relative variation) is in the range of 1.22–1.29 at a 4.5 V/μm (45 kV/cm) dc biasing field. The new BSM ferroelectrics have been studied for use in a fast ferroelectric switch and phase shifter for the LC active pulse compression scheme. 110 cm diameter, 2.8 mm thickness ferroelectric rings for the X-band phase-shifters were developed.

References

1. *Kanareykin A., Gai W., Power J., Altmark A., Sheinman I.,* AIP Conf. Proc., 2002, **647**, p. 565-575; 2002 N. J. Deophys. Res., 1992, **77**, 5551.
2. *Yakovlev V.P. et al.*, Proc. PAC 2005, Knoxville, May 16–20, 2005 (to be published).
3. *Nenasheva E., Kanareykin A., Kartenko N., Karmanenko S.,* J. Electroceramics, 2004, **13**, p. 235-238.
4. *Kanareykin A., Nenasheva E., Karmanenko S., Yakovlev V.,* AIP Conf. Proc. 2004, **737**, p. 1016-1024.

APPLICATION OF RECOMBINATION CONTINUUM EMITTED BY A SLAB OF THE Cs-Xe DC DISCHARGE FOR IMAGING OF FIELD PATTERN OF MODERATE-POWER MILLIMETER WAVES

M. S. Gitlin, M. Yu. Glyavin, V. V. Golovanov, A. G. Luchinin, V. V. Zelenogorsky

Institute of Applied Physics, Russian Academy of Sciences,
Nizhny Novgorod, Russia

Millimeter wave field patterns have been imaged using the recombination continuum emitted by a slab of the positive column of the Cs-Xe DC discharge. The spatial distributions of millimeter wave intensity at the output of waveguide transmission lines measured by this technique agreed well with the calculated field patterns. In K_a-band energy flux sensitivity of the imaging technique of about 10^{-5} J/cm^2 and dynamic range about 10 dB have been demonstrated. It has been measured that its temporal resolution is 1 μs. Imaging of the W-band gyrotron output field pattern made it possible to identify its operating mode and measure relative intensity of the counter-rotating mode.

Design of microwave transmission lines and microwave sources, i. e. magnetrons, gyrotrons, gyroklystrons, etc., often require determination of the spatial distribution of the millimeter wave (MMW) intensity [1, 2]. To our knowledge, there is no technique, which would make it possible to measure field patterns of moderate-power millimeter waves for submillisecond pulse duration. Thermal methods are unsuitable for measuring the spatial structure of relatively short-pulse millimeter waves due to their low energy sensitivity. Arrays of semiconductor microwave detectors have low spatial resolution, besides, possible irreversible microwave breakdowns also limit their application essentially.

For imaging moderate-power millimeter waves and measuring the spatial distribution of their intensity we propose to use the recombination continuum (RC) emitted by a plasma slab of the positive column (PC) of a Cs-Xe DC discharge [3].

To demonstrate the possibility of using this imaging technique for measuring the field patterns at the output of a waveguide line or a MMW source, we performed model experiments on imaging of the spatial structure of the TE_{01} mode of a circular waveguide. The scheme of the experimental setup (top view) is shown in Fig. 1. In our experiments on millimeter wave imaging a sealed discharge tube described in detail in [3] was used for generation of the slab of positive column of the Cs-Xe DC discharge. A hollow rectangle parallelepiped glued from plane-parallel fused quartz plates was located in the middle of the tube. Two square plane quartz windows (*1*) with their apertures 10×10 cm were set at the distance of 2 cm between their internal surfaces. These windows allowed injecting the microwave beam into the tube with small reflection and without distortions. Two plane anodes (*2*) and two heated cathodes (*3*) were

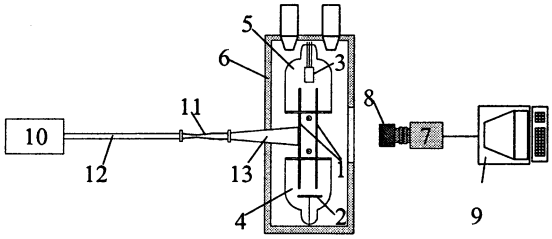

Fig. 1

placed in glass cylinders (*4*) and (*5*) 10 cm in diameter. The glass cylinders were glued to the quartz cell. Each pair of the electrodes was connected to a separate current source. The discharge tube was filled with xenon at the pressure of 45 Torr. This relatively high gas pressure is necessary to provide a locality of the additional electron heating under the action of microwaves. For xenon pressure of about 50 Torr the spatial resolution of this imaging technique is of the order of a millimeter. The discharge tube had sidearms, in which drops of cesium metal were placed. To obtain the required density of cesium vapor, the discharge tube was heated in an oven (*6*). The oven had a quartz window 20 cm in diameter. A monochrome CCD camera (*7*) was used to record the spatial distribution of RC intensity. A set of optical filters (*8*) transmitting only RC radiation in the visible region, was placed in front of the camera lens. The signal from the CCD camera was fed to a framegrabber installed in a computer (*9*). Millimeter waves with the frequency of 35.4 GHz were generated by a magnetron (*10*) with a maximum power of 20 W in the long-pulse operation (pulse duration is 0.1 s). The leading edge of the microwave pulse was less 100 ns. A Marier converter (*11*) was used to transform the TE_{01} mode of a rectangular waveguide (*12*) into the TE^{O}_{01} mode of a circular waveguide. To increase the transverse size of the microwave beam, we used a conical horn antenna (*13*) with flare angle 6°. Its output aperture diameter was 56 mm. The input window of the discharge tube was connected to the horn and we measured the spatial distribution of millimeter wave intensity in the near zone.

Millimeter wave imaging experiments were performed for the discharge current of 1.5 A and tube temperature 95–100 °C (the longitudinal electric field in PC was 1.0–1.2 V/cm). Under these conditions, the PC of the Cs-Xe discharge had the form of a uniform slab, which filled the entire tube aperture with its size about 10×8 cm. The electron number density in PC was 3×10^{12} cm^{-3} and the electron temperature was 0.4 eV [4]. In the continuum spectrum emitted by the uniform PC of the Cs-Xe discharge recombination continuum of xenon dominated in visible region. The RC intensity is very sensitive to electron temperature variations due to the action of millimeter waves. The measurements performed in [3] showed that variation of RC intensity ΔI is directly proportional to the intensity of millimeter waves incident on the plasma W, if W is less than half of the breakdown value. For K_a-band microwaves the threshold of microwave breakdown of the positive column of Cs-Xe discharge was equal $W_{br} = 5$ W/cm^2. The function $\Delta I(W)$ for $W_{br}/2 < W < W_{br}$ is weakly nonlinear.

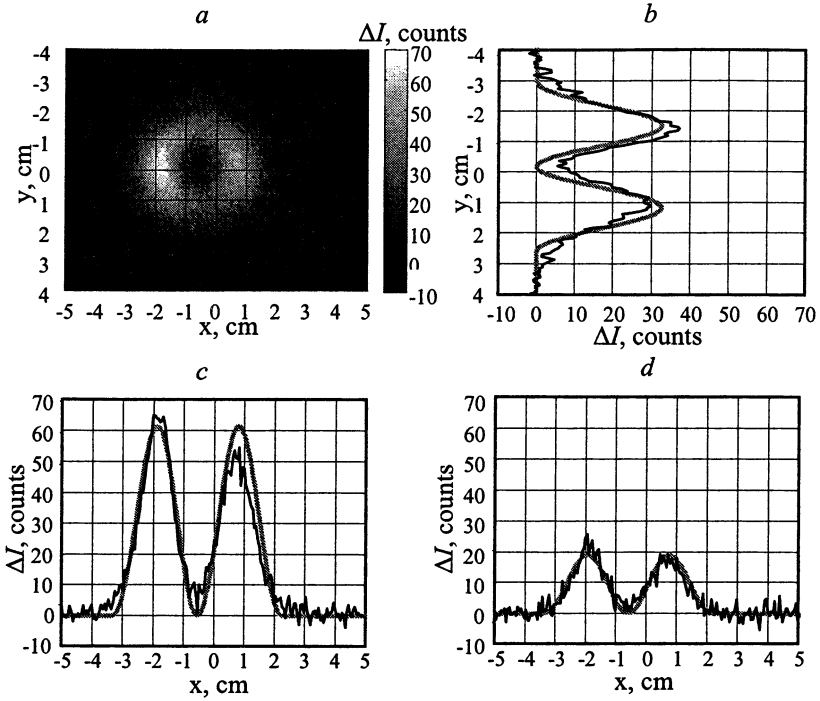

Fig. 2

Figure 2, *a* shows the two-dimensional distribution of the RC intensity variation $\Delta I(x, y)$ under the action of millimeter waves at the output of the conical horn. Here, x and y are the longitudinal and transverse coordinates with respect to the discharge current, respectively. Millimeter waves intensity was $W_m = 1$ W/cm^2 at the field maximum and its value was below microwave breakdown threshold. The CCD camera exposure time was 100 μs. It is seen in Fig. 2, *a* that the pattern of the recombination continuum glow corresponds to the TE^{O}_{01} mode with a small admixture of other modes. The pattern rotated by the angle $\pi/2$ if a rectangular waveguide twisted by the angle $\pi/2$ was set before the Marier converter. Figures 2, *b*, and 2, *c* show the dependence of the RC intensity variation under the action of millimeter waves on transverse coordinate y and the longitudinal coordinate x. For the TE^{O}_{01} mode, the dependence of the microwave electric field $|E_\varphi(r)|$ on the radius r is described by the first-order Bessel function [5]: $|E_\varphi(r)| \sim [J_1(3{,}832r/R)]$, where R is the waveguide radius. The power absorbed in the discharge is proportional to the square of the electric field. It follows from Figs. 2, *b*, and 2, *c* that the plots of the measured RC intensity variations $\Delta I(x, 0)$ and $\Delta I(0, y)$ (black lines) coincide fairly well with the plots of the squared first-order Bessel function (gray lines). This experiment demonstrates the feasibility to apply the proposed method for imaging the millimeter wave intensity spatial distribution at the output of

a waveguide transmission line or a MMW source. Dynamic range of this imaging technique is about 10 dB.

Energy flux sensitivity of the imaging technique in our experiments was limited by the noise of the CCD camera. Figure 2, *d* shows the dependence of the RC intensity variation $\Delta I(x, 0)$ under the action of millimeter waves at the output of the conical horn antenna vs the longitudinal coordinate x measured for the CCD camera exposure time 10 μs. Intensity of millimeter waves at the maximum was $W_m = 4$ W/cm^2. It is seen in Fig. 2, *d* that the signal-to-noise ratio (*S/N*) was about five for the millimeter wave energy flux at the field maximum about 40 μJ/cm^2. Thus, the one-pulse threshold energy flux sensitivity ($S/N = 1$) about 10^{-5} J/cm^2 was achieved in our experiments.

The characteristic response time of the RC intensity on the action of millimeter waves was measured by a photomultiplier. In the course of the experiments the photomultiplier was set into the place of CCD camera. The optical filter transmitting only the RC was mounted in front of the photomultiplier. Figure 3 shows time history of the RC intensity and intensity of millimeter waves incident on the plasma slab after switching the magnetron on. As follows from the oscillogram, the temporal resolution of this imaging technique is about 1 μs.

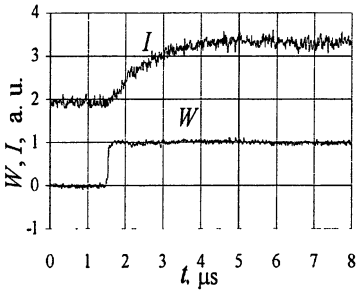

Fig. 3

In the second part of this paper, we describe the experiments on imaging the output field pattern of a 110 GHz moderate-power gyrotron with a pulsed magnetic field [6]. The maximum gyrotron pulse duration was 60 μs. The design operating mode of the gyrotron was the rotating mode of a circular waveguide TE^0_{32}. The millimeter waves were output from the gyrotron via a circular waveguide 16 mm in diameter without mode conversion. The MMWs were transmitted to the discharge tube with a circular waveguide 16 mm in diameter and 640 mm long, which was connected to the waveguide of the gyrotron. At the output of the circular waveguide a conical horn antenna with its flare angle 5°, 140 mm long, and aperture diameter 40 mm was set. The CCD camera exposure time was 64 μs.

In the first series of experiments on imaging of W-band millimeter waves, the length of the gyrotron cavity was by 1.5 times longer than optimal for its high efficiency operation. Because of this, the maximum output power of the gyrotron was about 3 kW. Figure 4, *a* shows the two-dimensional distribution of RC intensity variation under the action of millimeter waves. This distribution was measured at the output of the waveguide transmission line, when the power of the gyrotron was $P = 1$ kW. For this gyrotron power millimeter wave intensity did not exceed the threshold of microwave breakdown of the PC of the Cs-Xe discharge. As seen from Fig. 4, *a*, the recombination continuum image corresponds to the TE^O_{32} mode pattern. The standing-wave pattern in the azimuthal direction occurred due to the presence of an admixture of the TE^O_{32} counter-rotating mode

(about 0.5% in power) at the output of the gyrotron. Evidently, appearance of this counter-rotating mode was caused by insufficiently good matching of the uptaper at the output end of the gyrotron cavity with the waveguide. The microwave breakdown threshold of the PC of the Cs-Xe discharge for W-band millimeter waves should be of the order of 100 W/cm^2. Figure 4, *b* shows the image of the spatial distribution of RC recorded at the output of the transmission line for gyrotron power P = 3 kW. At such a power level the intensity of millimeter waves in their maxima exceeded the breakdown value. Due to the strong increase of RC intensity in the breakdown regions, the image (see Fig. 4, *b*) of the spatial distribution of millimeter wave intensity was distorted (much more contrasting than it was actually).

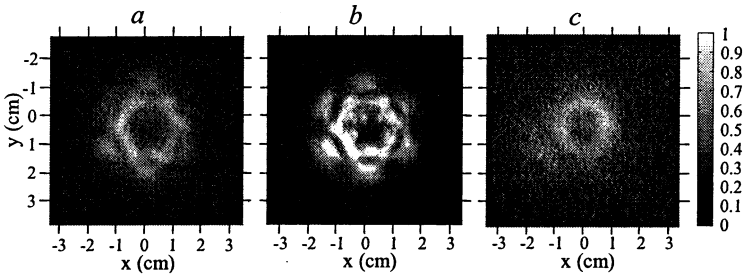

Fig. 4

In the second experimental series the cavity installed in the gyrotron had the optimal length for high efficiency operation (6 wavelengths). As the result, the maximum gyrotron power increased up to about 10 kW. The length of the uptaper at the cavity output was also made longer. Figure 4, *c* shows the two-dimensional distribution of RC intensity variation recorded at the output of the transmission line at gyrotron power 1 kW. For this gyrotron power millimeter wave intensity did not exceed the microwave breakdown threshold. The imaged pattern corresponded to the rotating mode TE^{O}_{32}. Admixture of the counter-rotating TE^{O}_{32} mode was less than 0.1% in power.

Acknowledgments. The authors gratefully acknowledge useful discussions with V. L. Bratman, S. V. Golubev, A. G. Litvak, V. I. Malygin, and V. E. Semenov. We would like to thank B. G. Bocharov, A. A. Mantsvetov, and D. P. Plokhikh for manufacturing the CCD camera. This work was supported in part by the Russian Foundation for Basic Research under Grant № 04-02-17132.

References

1. *Malygin V.I., Paveljev A.V.* Int. J. Infrared Millim. Waves, 1999, **20**, 33.
2. *Idehara T., Ogawa I., et al.,* Int. J. Infrared Millim. Waves, 2002, **23**, 973.
3. *Abubakirov I.E., Gitlin M.S., et al.,* Radiophys. Quantum Electron., 2003, **46**, 722.
4. *Bogatov N.A., Gitlin M.S., et al.,* Phys. Rev. Lett., 1997, **79**, 2819.
5. *Harvey A.F.* Microwave engineering, Academic Press, 1963.
6. *Gitlin M.S., Glyavin M.Yu., et al.,* IEEE Trans. Plasma Sci., 2005, **33**, 380.

CONTENTS OF VOLUME 1

STRONG MICROWAVES IN PLASMAS

PROCEEDINGS
OF THE INTERNATIONAL WORKSHOP

In two volumes

Volume 1

Institute of Applied Physics,
Russian Academy of Sciences

46 Ul'yanov Street, 603950 Nizhny Novgorod, Russia

Printed by Printing House №2, "Nauka" Publishers,
6 Shubinsky Pereulok, 121099 Moscow